Titre: Title:	Numerical Analyses of the Stability and Geomechanical Behavior of Side-exposed Backfill Associated with Closure of Rock Walls
Auteur: Author:	Ruofan Wang
Date:	2021
Type:	Mémoire ou thèse / Dissertation or Thesis
Référence: Citation:	Wang, R. (2021). Numerical Analyses of the Stability and Geomechanical Behavior of Side-exposed Backfill Associated with Closure of Rock Walls [Thèse de doctorat, Polytechnique Montréal]. PolyPublie. https://publications.polymtl.ca/9961/

URL de PolyPublie: PolyPublie URL:	https://publications.polymtl.ca/9961/
Directeurs de recherche: Advisors:	Li Li
Programme: Program:	Génie minéral

POLYTECHNIQUE MONTRÉAL

affiliée à l'Université de Montréal

Numerical analyses of the stability and geomechanical behavior of side-exposed backfill associated with closure of rock walls

RUOFAN WANG

Département des génies civil, géologique et des mines

Thèse présentée en vue de l'obtention du diplôme de *Philosophiæ Doctor*

Génie minéral

Décembre 2021

POLYTECHNIQUE MONTRÉAL

affiliée à l'Université de Montréal

Cette thèse intitulée:

Numerical analyses of the stability and geomechanical behavior of side-exposed backfill associated with closure of rock walls

présentée par **Ruofan WANG**

en vue de l'obtention du diplôme de *Philosophiæ Doctor*

a été dûment acceptée par le jury d'examen constitué de:

Benoît COURCELLES, président
Li LI, membre et directeur de recherche
Shaocheng JI, membre
Ali SAEIDI, membre externe

DEDICATION

To my family

To my homeland

ACKNOWLEDGEMENTS

RÉSUMÉ

La récupération des piliers en minerai requiert un remblai stable lors de son exposition latérale. Comprendre le comportement géomécanique et déterminer la cohésion minimale requise (c_{min}) d'un remblai exposé latéralement sont essentiels pour assurer une production minière sécuritaire et économique. La plupart des études antérieures consistent à évaluer la stabilité d'un remblai explosé latéralement en considérant trois ou deux murs encaissants immobilisés d'un chantier isolé. Les solutions ont été validées contre des résultats d'essais d'instabilité de remblai en boîte sur des remblais mous. Dans la pratique, les remblais sont souvent exposés après une longue période lorsqu'ils deviennent suffisamment résistants (et durs). Une convergence des épontes rocheuses peut avoir lieu lors de l'excavation d'un chantier secondaire adjacent et du fluage des épontes rocheuses. Une bonne compréhension de l'influence de la convergence des épontes rocheuses sur la stabilité et la c_{min} d'un remblai exposé latéralement est nécessaire.

Pour atteindre cet objectif, des simulations numériques tri- dimensionnelles ont été réalisées avec FLAC^{3D} afin d'évaluer la stabilité et de déterminer la c_{min} d'un remblai exposé latéralement en considérant la convergence instantanée des épontes rocheuses associée avec une extraction adjacente. L'instabilité d'un remblai exposé latéralement est déterminée en évaluant la fusion des zones en plasticité. Les résultats numériques montrent que lorsque la profondeur de la mine et la convergence des épontes rocheuses sont faibles, le mécanisme de rupture dominant est le glissement. Une faible convergence des épontes rocheuses améliore la stabilité du remblai exposé latéralement. La c_{min} diminue avec l'augmentation de la profondeur de mine, la rigidité du remblai, le coefficient de pression des terres, et la résistance (angle de frottement et l'adhérence) des interfaces entre le remblai et les épontes rocheuses. Augmenter la rigidité du massif rocheux, la hauteur et la largeur des chantiers augmente la c_{min}. Lorsque la profondeur de mine et la convergence sont très grandes, l'écrasement devient le mécanisme de rupture dominant du remblai expos latéralement. La c_{min} devient insensible à la variation de la résistance des interfaces entre le remblai et les épontes rocheuses. Elle augmente avec l'augmentation de la profondeur de mine, la hauteur et la longueur du chantier primaire, la rigidité du remblai et le coefficient de pression des terres de la roche. Elle diminue avec l'augmentation de la largeur des chantiers et la rigidité du massif rocheux. Dans tous les cas, la stabilité d'un remblai exposé latéralement peut être améliorée par l'utilisation d'un remblai ayant un angle de frottement interne élevé.

Une autre étude numérique a été réalisée avec FLAC^{3D} pour évaluer la stabilité d'un remblai explosé latéralement en fonction du temps, associée avec la déformation de fluage des épontes rocheuses. L'évolution des propriétés mécaniques du remblai cimenté avec le temps de cure a été considérée. Les résultats numériques montrent que la période ouverte du chantier primaire n'affecte pas significativement la stabilité et la c_{min} du remblai exposé latéralement. Lorsque la profondeur de mine est faible ou/et le massif rocheux montre peu de fluage, il est préférable d'attendre plus longtemps avant d'excaver le chantier secondaire adjacent pour permettre au remblai d'acquérir plus de résistance. Lorsque la profondeur de mine est grande ou/et le massif rocheux montre de grands fluages, l'instabilité du remblai exposé latéralement peut être dictée par une rupture en écrasement. Une simple augmentation de la teneur en liant du remblai n'est pas forcément le meilleur choix parce qu'un remblai plus résistant est aussi plus dur et susceptible à être écrasé. En revanche, un remblai plus mou avec une teneur en liant plus faible ou/et avec une période de cure plus courte pourrait être préférable. Une fois exploité, le chantier secondaire adjacent doit être remblayé aussi tôt que possible pour prévenir des ruptures du remblai exposé latéralement. Une optimisation des dimensions des chantiers primaire et secondaire est nécessaire pour minimiser le coût global du remblai.

La rigidité d'un remblai a été montré d'être un facteur d'influence important sur la stabilité et la c_{min} d'un remblai exposé latéralement. Cependant, elle a été considérée comme une constante dans le modèle d'élasto-plastique de Mohr-Coulomb. Une étude comparative est donc nécessaire pour identifier un modèle constitutif applicable à décrire la dépendance de contrainte de la compressibilité des remblais non-cimentés ou de faible teneur en liant. L'applicabilité du modèle élasto-plastique de Mohr-Coulomb, du modèle à double seuils d'écoulement (Double Yield), et du modèle de sol mou (Soft Soil) à décrire la compressibilité de remblai a été évaluée en reproduisant numériquement certains résultats de laboratoire existants, obtenus par des essais de consolidation unidimensionnelle et des essais de compression triaxiale en conditions consolidée et drainée réalisés sur un remblai de faible teneur en ciment. Les résultats montrent que le modèle du sol mou peut décrire correctement la compressibilité des remblais légèrement cimentés avec de faibles cohésions. L'application du modèle de Mohr-Coulomb et du modèle à double seuils d'écoulement montre une mauvaise description de la compressibilité du remblai soumis à des charges importantes et cycliques.

L'analyse de l'effet de fluage sur la stabilité d'un remblai exposé latéralement nécessite un modèle constitutif de fluage approprié pour les roches. On constate premièrement que la plupart des modèles de fluage existants ne peuvent pas représenter la rupture à la phase tertiaire des roches. On constate aussi que la régression a été couramment utilisée dans les études antérieures sur tous les résultats expérimentaux disponibles pour obtenir une ou plusieurs séries de paramètres de modèle. La capabilité de prédiction du modèle de fluage calibré aux conditions non testées est inconnue. Par conséquent, un nouveau modèle de fluage a été développé pour décrire et prédire la déformation de fluage et le temps à la rupture des roches. Le modèle de fluage proposé a été validé contre des résultats expérimentaux disponibles dans la littérature. Les paramètres de modèle ont été obtenus par une calibration sur une partie des résultats expérimentaux. La capacité de prédiction du model calibré est testé sur l'autre partie des résultats expérimentaux. Les bonnes corrélations entre les résultats expérimentaux et le model de fluage indiquent que le modèle de fluage proposé peut décrire et prédire les déformations de fluage et la rupture de la phase tertiaire des roches.

ABSTRACT

Ore pillar recovery requires backfill to be stable upon side exposure. Understanding the geomechanical behavior and determining the minimum required cohesion (c_{min}) of side-exposed backfill are important for ensuring safe and economic mining productions. Most previous studies evaluated the stability of side-exposed backfill by considering three or two immobile confining walls of one isolated stope. The solutions were validated against experimental results of box instability tests on very soft backfill. In practice, backfill is usually exposed after long enough curing time when it becomes strong (and hard) enough. Significant closure of rock walls occurs due to adjacent excavation and creep behavior of rock walls. A good understanding of the influence of rock wall closure on the stability and the c_{min} of side-exposed backfill is needed.

To this end, three-dimensional numerical simulations were conducted with FLAC^{3D} to evaluate the stability and determine the c_{min} of side-exposed backfill by considering the instantaneous closure of rock walls due to adjacent extraction. The instability of side-exposed backfill is determined by evaluating the yield zones coalescence. Numerical results show that when the mine depth and rock-wall closure are small, the governing failure mechanism is sliding. Small rock-wall closure improves the stability of side-exposed backfill. The c_{min} decreases with the increase of mine depth, fill stiffness, rock pressure coefficient, and fill-rock interface strength (friction angle and adhesion). Increasing rock mass stiffness, stope height and width leads to an increase in c_{min}. When the mine depth and rock-wall closure are large, crushing becomes the dominant failure mechanism of side-exposed backfill. The c_{min} becomes insensitive to the variation of fill-rock interface strength. It increases with the increase of mine depth, stope height and length, fill stiffness and rock pressure coefficient and decreases with the increase of stope width and rock mass stiffness. In all cases, the stability of side-exposed backfill can be improved by using backfill of larger internal frictional angle.

A further numerical study was conducted using FLAC^{3D} to evaluate the time-dependent stability of side-exposed backfill associated with creep deformation of rock walls. The evolution of mechanical properties of cemented backfill with curing time is considered. Numerical results show that the open period of primary stope does not significantly affect the stability and c_{min} of side-exposed backfill. When the mine depth is small or/and the rock mass exhibits little creep, it is better

to wait longer time before excavating the adjacent stope for backfill to gain more strength. When the mine depth is large or/and the rock mass exhibits heavy creep, the instability of side-exposed backfill can be dictated by crushing failure. Simply increasing binder content of backfill may not be the best choice because a stronger backfill is also harder, and more prone to be crushed. Rather, a softer backfill using lower binder content or/and with a shorter curing time can be better. Once mined out, the adjacent secondary stope should be filled as soon as possible to prevent failure of side-exposed backfill. An optimization of sizes of the primary and secondary stopes is needed to minimize the overall cost of backfill.

The stiffness of backfill has been shown to be an important influencing factor on the stability and c_{min} of side-exposed backfill. It was however considered as a constant in the commonly used Mohr-Coulomb elasto-plastic model. A comparative study is thus necessary to identify a constitutive model applicable to describing the stress-dependent compressibility of uncemented or low-cement content backfill. The applicability of the Mohr-Coulomb elasto-plastic, double-yield, and Soft Soil models is assessed by numerically reproducing some existing laboratory results, obtained by one-dimensional consolidation tests and consolidated drained triaxial compression tests on lowly cemented backfill. Results show that the Soft Soil model can properly describe the compressibility of lightly cemented backfill with small cohesions. The application of the Mohr-Coulomb model and double-yield model shows poor description on the compressibility of the backfill submitted to large and cycle loading.

Consideration of creep effect on the stability analysis of side-exposed backfill needs a proper constitutive creep model for rocks. One first noted that most creep models cannot represent the delayed failure of rocks. One also noted the common application of curve-fitting technique in previous studies on all available experimental results of creep strain to obtain one or several sets of model parameters. The predictive capability of creep model for untested conditions is unknown. Therefore, a new creep model is developed to describe and predict the creep strain and time to failure of rocks. The developed creep model is validated against some experimental results available in the literature. The model parameters are obtained by calibration on a part of experimental results. Validity of the calibrated model is tested by predicting the other part of test results. The quite good agreements between the experimental results and creep model indicate that the developed creep model can describe and predict the creep strain and delayed failure of rocks.

TABLE OF CONTENTS

LIST OF TABLES

LIST OF FIGURES

LIST OF SYMBOLS AND ABBREVIATIONS

Symbols

a	Hoek-Brown parameter
a_c	centrifugal acceleration (m/s^2)
A_{sc}	material parameter (s^{-1} or h^{-1})
A_{tc}	material parameter (s^{-1} or h^{-1})
B	width of backfill (m)
B_D	width of the numerical model (m)
c	cohesion (kPa or MPa)
c_b	bond strength along interface of backfill and back wall (kPa)
c_i	interface cohesion (kPa)
c_{min}	minimum required cohesion of side-exposed backfill (kPa or MPa)
c_R	cohesion of rock mass (MPa)
c_s	cohesion of sill mat (MPa)
C_u	coefficient of uniformity
C_v	volumetric solid concentration
D	mine depth (m)
D_{10}	effective grain size
D_R	disturbance factor
e_{ini}	initial void ratio
E	Young's modulus (MPa or GPa)
E_K	Young's modulus of Kelvin-Voigt element
E_M	Young's modulus of Maxwell element
E_R	Young's modulus of rock mass (GPa)
E_s	Young's modulus of sill mat (GPa)
f^*	normalized stress
$F_\sigma^{\beta c}$	normal force on a micro crack plane (N)
$F_\tau^{\beta c}$	shear force on a micro crack plane (N)
g	gravitational acceleration (m/s^2)
G	shear modulus (kPa or MPa)

G_e	shear modulus of spring element (MPa)
G_K	shear modulus of Kelvin-Voigt element (GPa)
G_M	shear modulus of Maxwell element (GPa)
G_{max}	upper limit of shear modulus (GPa)
G_R	shear modulus of rock mass (GPa)
h	height (m)
H	height of backfill (m)
H_D	height of the numerical model (m)
H_s	height of sill mat (m)
k_n	interface normal stiffness (Pa/m)
k_s	interface shear stiffness (Pa/m)
K	bulk modulus (kPa or MPa)
K_0	at-rest earth pressure coefficient
K_a	Rankine's active earth pressure coefficient
K_e	bulk modulus of spring element (MPa)
K_i	stress intensity factor (MPa·m$^{1/2}$)
K_t	threshold of stress intensity factor (MPa·m$^{1/2}$)
K_c	critical value of stress intensity factor (MPa·m$^{1/2}$)
K_{max}	upper limit of bulk modulus (GPa)
K_r	rock stress coefficient
K_R	bulk modulus of rock mass (GPa)
L	strike length of backfill (m)
L_b	strike length of primary stope (m)
L_s	strike length of secondary stope (m)
L_D	length of numerical model (m)
m	ratio of crack initiation threshold and short-term peak strength
m_b	Hoek-Brown parameter
m_i	Hoek-Brown parameter
m_b^r	residual value of Hoek-Brown parameter
M_s	slope of critical state line in Soft Soil model

n	material parameter
n_1	material parameter
p	mean stress (kPa or MPa)
p_0	surcharge (kPa)
p_c	cap pressure (MPa)
q	deviatoric stress (kPa or MPa)
R	material constant
r_a	interface friction angle ratio
r_s	interface adherence ratio
s	Hoek-Brown parameter
t	time (s or day)
t_0	initial time (s)
t_c	curing time (day)
t_{cr}	critical time when internal stress reach the Coulomb envelop (s)
t_d	delayed time before filling the primary stope (day)
t_e	exposure time before filling the secondary stope (day)
$t_f^{\beta_c}$	time to failure along a micro crack plane (s)
t_f	time to failure of rocks (s)
t_{fin}	time period of 28 days for backfill parameters evolution
t_i	initial timestep (s)
t_m	maximum timestep (s)
T	tensile strength
T_R	tensile strength of rock mass (kPa)
V_c	subcritical crack growth velocity (m/s)
$V_\tau^{\beta_c}$	increasing rate of shear stress along micro crack plane (MPa/s)
α	inclination angle of sliding plane (°)
α_c	angle between stress path and normal stress axis (°)
β	inclination angle of stope (°)
β_c	angle between micro crack plane and major principal stress (°)
β_{cr}	critical angle in rock sample (°)

β_s	parameter controlling transition between peak and residual strength
ε_t	total strain
ε_1^e	axial elastic strain
ε_e	instantaneous elastic strain
ε_{pc}	creep strain of primary creep stage
ε_{sc}	creep strain of secondary creep stage
ε_{tc}	creep strain of tertiary creep stage
ε_v	volumetric strain
ε_{sc}^c	creep strain due to micro crack propagation of the secondary creep stage
ε_{sc}^v	visco-elastic creep strain of the secondary creep stage
ε_v^p	plastic volumetric strain
e_3^p	plastic confining strain component
$\dot{\varepsilon}_{sc}$	rate of secondary creep strain
$\dot{\varepsilon}_{sc}^c$	non-linear creep strain rate attributed to micro crack propagations
$\dot{\varepsilon}_{sc}^v$	linear visco-elastic creep strain rate
θ_l	Lode angle (°)
θ_c	angle between micro crack plane and normal stress axis (°)
θ_{cr}	critical angle of stress state in Mohr plane (°)
σ_1	major principal stress (kPa or MPa)
σ_2	intermediate principal stress (kPa or MPa)
σ_3	minor principal stress (confining pressure) (kPa or MPa)
σ_a	applied deviatoric stress (MPa)
σ_c	short-term peak strength in terms of deviatoric stress (MPa)
σ_{ci}	uniaxial compressive strength of intact rock (MPa)
σ_{CI}	value of crack initiation threshold (MPa)
σ_h	horizontal stress (kPa)
σ_v	vertical stress (kPa)
σ_{STF}	short-term peak strength (MPa)
σ_Y	yield strength (kPa or MPa)

$\sigma_t^{\beta c}$	normal stress on a micro crack plane (MPa)
$\sigma_{t_0}^{\beta c}$	initial normal stress on a micro crack plane related to time t_0 (MPa)
$\sigma_{t_{cr}}^{\beta c}$	critical normal stress on a micro crack plane related to time t_{cr} (MPa)
σ_{ci}^r	residual value of uniaxial compressive strength (MPa)
$\tau_t^{\beta c}$	shear stress on a micro crack plane (MPa)
$\tau_{t_0}^{\beta c}$	initial shear stress on a micro crack plane related to time t_0 (MPa)
$\tau_{t_{cr}}^{\beta c}$	critical shear stress on a micro crack plane related to time t_{cr} (MPa)
ϕ	internal friction angle (°)
ϕ_s	friction angle of sill mat (°)
ϕ_R	internal friction angle of rock mass (°)
ρ	density (kg/m^3)
ψ	dilation angle (°)
ψ_R	dilation angle of rock mass (°)
ψ_s	dilation angle of sill mat (°)
δ	interface friction angle (°)
ν	Poisson's ratio
ν_R	Poisson's ratio of rock mass
ν_s	Poisson's ratio of sill mat
λ	scale factor (ratio) between centrifugal and gravitational accelerations
λ^*	slope of normal consolidation line
λ_f	critical value of scale factor when centrifugal model fails
λ_{tc}	material parameter
γ	unit weight (kN/m^3)
γ_R	unit weight of rock mass (kN/m^3)
γ_s	unit weight of sill mat (kN/m^3)
γ_{tc}	material parameter
κ^*	slope of swelling line
η	parameter controlling slope of stress-strain curve

η_K viscosity coefficient of Kelvin-Voigt element (Pa·s or GPa·h)

η_M viscosity coefficient of Maxwell element (Pa·s or GPa·h)

η_{SC} viscosity coefficient of Newton dashpot (Pa·s or GPa·h)

Abbreviations

AE	acoustic emissions
CIT	crack initiation threshold
CPB	cemented paste backfill
CVISC	Burgers-creep viscoplastic
FLAC^{3D}	Fast Lagrangian Analysis of Continua in 3 Dimensions
FS	factor of safety
GSI	geological strength index
HB	Hoek-Brown
lfob	lower limit of unbalanced force ratio
MC	Mohr-Coulomb
NCL	normal consolidation line
RMR	rock mass rating
SL	swelling line
UC	ubiquitous-corrosion
UCC	ubiquitous-corrosion-Coulomb
UCS	uniaxial compressive strength
ufob	upper limit of unbalanced force ratio
UFR	unbalanced force ratio
VCL	vertical central line

LIST OF APPENDICES

CHAPTER 1   INTRODUCTION

1.1 Definition of the problem

Mining plays an essential role in resources supply and economics in Canada. In mining activities, the creation of mine openings and processing of minerals can result in a substantial amount of mine wastes in terms of waste rock and tailings. Mine wastes are typically disposed on the surface in tailings ponds or as waste rock piles. The surface disposal of mine wastes will, however, leave long-term geotechnical and geochemical issues and has an important influence on the environment (Bussière 2007; Benzaazoua et al. 2008; Aubertin 2013). A more environmental-friendly management is applying mine wastes to backfill mined-out voids in underground mines. In addition to its environmental benefits, mining backfills can maintain regional ground stability, improve ore recovery rate, reduce dilution, and control subsidence (Hassani & Archibald 1998; Brady & Brown 2002; Potvin et al. 2005; Darling 2011). This explains why backfill has become an integral part of most underground mines in Canada.

Backfill can be cemented or uncemented. In open stoping mining method, cemented backfill is commonly used to allow the recovery of rib ore pillars (secondary stope) (Hamrin 2001; Bullock 2011). In underhand cut-and-fill mining, cemented backfill can also serve as an artificial roof under which mining operations are conducted (Darling 2011; Stephan 2011). In these cases, the stability of backfill upon exposure becomes a critical issue as an instable backfill significantly dilutes the blasted ore and threatens the safety of workers and equipment. The improvement of backfill strength typically relies on an increased consumption of binders that constitutes a considerable part of the mining cost. Therefore, determining the minimum required strength of backfill upon exposure is a critical issue for the mining industry to reach a safe and economic design of backfill.

Evaluating the stability and determining the minimum required strength of exposed backfill requires a good understanding of its mechanical performance and the interactions with surrounding rock walls. Most of previous studies on side-exposed backfill were performed by considering two or three immobile walls (Mitchell et al. 1982; Li & Aubertin 2012, 2014; Li 2014a, 2014b; Yang et al. 2017; Liu et al. 2018; Zhao et al. 2019). In practice, excavating adjacent stopes results in instantaneous closure of rock walls. Moreover, most rocks exhibit more or less degree of time-dependent creep deformation (Griggs 1939; Cristescu & Hunsche 1998; Malan 1999; Brantut et al.

2013). Both the instantaneous and creep deformation closures of rocks can become significant as the underground mining activities advancing to large depth with high in-situ stresses (Anderson 2014; Ranjith et al. 2017). These closures can compress the backfill in the stope and affect its stability of side-exposed backfill. However, there are few studies dedicated to this aspect in the past. The effects of instantaneous and time-dependent closures of rock walls on the stability of side-exposed backfill thus constitute the main scopes of this thesis.

1.2   Thesis objectives and methodology

The overall objective of this research is to obtain a better understanding of the effects of rock wall closures on the stability, minimum required strength, and mechanical behavior of backfill upon vertical exposure. It is achieved through the realization of the following sub-objectives:

1. Analyze the stability of backfill upon a vertical exposure considering an adjacent extraction

    - Develop 3D numerical model to evaluate the failure mechanisms and minimum required cohesion of side-exposed backfill under the influence of instantaneous rock-wall closure associated with adjacent extraction.

    - Conduct parametric analyses to investigate the effects of mine depth, stope geometry, shear strength of fill-rock interface, mechanical properties of backfill and rock mass on the minimum required cohesion of backfill.

2. Evaluate the time-dependent stability of side-exposed backfill considering creep of rocks

    - Develop 3D numerical model to estimate the minimum required cohesion of side-exposed backfill by considering the evolution of fill mechanical properties with curing time and creep of rocks.

    - Investigate the influence of time factors on the stability and minimum required cohesion of side-exposed backfill.

3. Identify a constitutive model applicable to describing the compressibility of mining backfill

4. Develop a creep model to describe and predict the creep strain and delayed failure of rocks.

1.3   Contributions

The main scientific contribution of this project is a thesis including one accepted and three published articles in peer-reviewed journals:

Article 1:

Wang R, Zeng F, Li L. (2021) Stability analyses of side-exposed backfill considering mine depth and extraction of adjacent stope. *International Journal of Rock Mechanics and Mining Sciences*. 142: 104735. https://doi.org/10.1016/j.ijrmms.2021.104735. This article is presented in Chapter 3.

Article 2:

Wang R, Li L. (2022) Time-dependent stability analyses of side-exposed backfill considering creep of surrounding rock mass. *Rock Mechanics and Rock Engineering*. Accepted. This article is presented in Chapter 4.

Article 3:

Wang R, Zeng F, Li L. (2021) Applicability of constitutive models to describing the compressibility of mining backfill: A comparative study. *Processes*. 9(12): 2139. https://doi.org/10.3390/pr9122139. This article is presented in Chapter 5.

Article 4:

Wang R, Li L, Simon R. (2019) A model for describing and predicting the creep strain of rocks from the primary to the tertiary stage. *International Journal of Rock Mechanics and Mining Sciences*. 123: 104087. https://doi.org/10.1016/j.ijrmms.2019.104087. This article is presented in Chapter 6.

The contributions of this project also include following four conference papers:

Wang R, Li L. (2018) Burgers creep model used for describing and predicting the creep behaviour of a rock under uniaxial and triaxial compression test conditions. In *Proceedings of the 71st Canadian Geotechnical Conference* (*GeoEdmonton 2018*), Edmonton, Alberta, Canada.

Wang R, Li L. (2019) A non-stationary power law model to predict the secondary creep rate of rocks. In *Proceedings of the 8th International Conference on Case Histories in Geotechnical*

Engineering: Geotechnical Materials, Modeling, and Testing (*Geo-Congress 2019*), Philadelphia, PA, United States. https://doi.org/10.1061/9780784482124.048.

Wang R, Zeng F, Li L. (2021) Stability evaluation of side-exposed backfill considering adjacent extraction at different mine depths. In *Proceedings of the 74th Canadian Geotechnical Conference* (*GeoNiagara 2021*), Niagara Falls, ON, Canada.

Wang R, Li L. (2021) Time-dependent stability of side-exposed backfill influenced by the creep of rock walls. *Presented at the 5th International Symposium on Mine Safety Science and Engineering*, Katowice, Poland.

The realization of this project leads to a better understanding of the mechanical behavior of side-exposed backfill interacting with the surrounding rock walls. The relationship between the minimum required strength of side-exposed backfill and mine depth, stope geometry, in-situ rock stresses as well as the mechanical properties of backfill and rock mass is better understood. It can be expected that the application of part of the results presented in this thesis may lead to several benefits for the mining industry, including for instance:

- A significant cost reduction due to the optimized strength estimation of side-exposed backfill;

- An improved risk control through a better understanding of the stability of side-exposed backfill and the stress state within backfill associated with the rock-wall closure;

- An increase in productivity and a decrease in stope turnaround time by optimizing time schedule of mining operations, backfill properties and stope dimensions.

1.4   Outline of the thesis

The thesis is presented in a paper-based format.

Chapter 1 provides a general introduction about the problem definition, objectives, contributions, and the content of the thesis.

Chapter 2 gives a comprehensive literature review on relevant themes, including underground mining methods with backfill, properties of mining backfill, stresses estimation in backfilled stopes, stability evaluation of side-exposed backfill, and creep behavior of rocks.

Chapter 3 contains the main numerical results for stability analyses of backfill upon a vertical exposure considering adjacent extraction. The different failure mechanisms and minimum required cohesion (c_{min}) of side-exposed backfill influenced by the walls instantaneous closure are investigated using FLAC^{3D}. The effects of mine depth, stope geometry, shear strength of fill-rock interfaces, mechanical properties of backfill and rock mass on the c_{min} of backfill are analyzed. The developed numerical model is verified against some centrifugal model test results published in the literature.

Chapter 4 investigates the time-dependent stability of side-exposed backfill associated with the creep of surrounding rock mass using FLAC^{3D}. Mechanical properties evolution of backfill with curing time is considered. The influences of delayed filling time of primary stope, curing time of backfill, exposure time of the backfill after the excavation of adjacent secondary stope, stope geometry, mechanical properties of backfill and rock mass on the time-dependent stability and c_{min} of backfill are analyzed. The ability of numerical model in describing time-dependent closure around underground openings is verified against in-situ measurements of creep deformation in a tunnel, reported in the literature.

Chapter 5 presents the main results of identifying a constitutive model applicable to describing the compressibility of mining backfill. Some constitutive models commonly used in geotechnical engineering are briefly recalled. They are used to reproduce some existing laboratory tests results obtained by one-dimensional consolidation tests and consolidated drained triaxial compression tests on slightly cemented backfill. The identified model is further used to analyze the stresses in backfill overlying a sill mat.

Chapter 6 presents a new creep model developed to describe and predict creep strain and delayed time to failure of rocks under different stress states. The developed model is tested against some triaxial compression creep tests results available in the literature. Part of the test results is used to calibrate the creep model. The calibrated creep model is then applied to predict the other part of the test results.

Chapter 7 gives a general discussion of the presented results in the thesis.

Chapter 8 presents the conclusions and recommendations for further studies.

More details and relevant information are given in several appendices, including the validations of FLAC^{3D} (Appendix A), the Burgers-creep viscoplastic model and its validation in FLAC^{3D} (Appendix B), a method to build numerical model by applying varied mesh sizes for different areas (Appendix C), sensitivity analyses and additional results related to Chapter 3 (Appendix D), comparisons between numerical and analytical solutions related to Chapter 3 (Appendix E), sensitivity analyses and additional results related to Chapter 4 (Appendix F), and a FISH program for backfill parameters evolution within curing time in FLAC^{3D} (Appendix G).

CHAPTER 2   LITERATURE REVIEW

This chapter starts by an introduction of underground mining methods with backfill to show the role and necessity of backfill. The commonly used backfills along with their typical properties are presented. Stresses estimation in backfilled stopes and stability analysis of backfill upon side exposure as well as creep behavior of rocks are reviewed.

2.1   Underground mining with backfill

Extraction of underground mineral resources requires using proper mining methods which depend on the characteristics of the deposit and the geomechanical conditions of rock masses. Underground mining methods can be typically divided into three categories: naturally supported, artificially supported and unsupported methods (Brady & Brown 2004). Figure 2.1 shows some commonly used mining methods applied in modern underground mines.
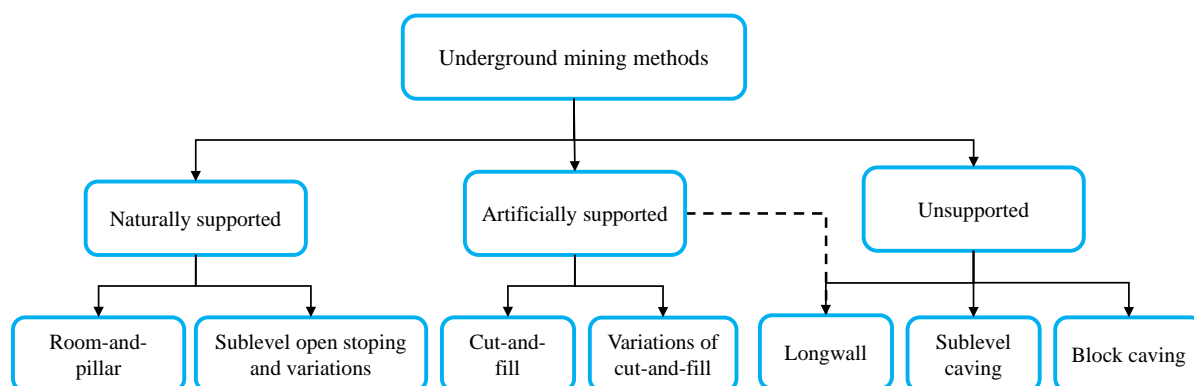
Figure 2.1: Illustration of different underground mining methods (modified based on Brady & Brown 2004 with permission)

2.1.1 Naturally supported mining method

2.1.1.1   Room-and-pillar mining method

Room-and-pillar mining method is applied in flat-laying deposits with relatively small and uniform thickness (Hamrin 2001). Ore pillars are left in place between rooms to provide support on the roof and restrict the convergence of surrounding rock mass (Roberts et al. 2007; Tesarik et al. 2009). In order to increase the recovery rate, the size of pillars should be as small as possible. The mine depth for this mining method should not be very large to avoid excessive stresses in pillars (Hamrin

2001). In some cases, the empty room may be backfilled with cemented backfill acting as artificial pillars which permit the extraction of adjacent ore pillar. The rooms are usually backfilled from around outer pillar towards the center of the section. In this case, the stability of exposed backfill during adjacent extraction and building stable barricades to retain fill are essential to the success of the mining operation (Hamrin 2001; Stebbins & Schumacher 2001).

2.1.1.2 Sublevel open stoping and its variants

Sublevel open stoping is a productive mining method typically applies for orebodies with steep dip (from 50° to 90°) and large thickness (Hamrin 2001). The stopes in sublevel open stoping are usually large which requires that the orebody and surrounding rock mass should be sufficiently stable (Hamrin 2001; Brady & Brown 2004). Figure 2.2a shows a layout of sublevel open stoping mining method. Classically, the mining area can be divided along strike direction as stopes and rib pillars. Several drifts are created at different heights (sublevels) from which blast holes with a length of 20–30 m are drilled into the blocks. Ore in the stope is blasted and withdrawn from the draw-points at the base level of the stope. The extracted stope is then left empty and the rib pillar supports the hanging wall. This means that the ore pillars are lost resulting in a reduction of ore recovery rate. Nowadays, more and more mines apply the mining backfill as an integral part of the sublevel open stoping mining method (Hamrin 2001). When the backfill is applied, the orebody can be divided as the primary and adjacent secondary stopes. After extracting the primary stope, it can be filled with uncemented fill or low cement content backfill to improve the local stability of host rock mass if the extraction of secondary stope is not required. When the secondary stope needs to be recovered, the primary stope must be filled with cemented backfill while the secondary stope can be filled with uncemented backfill. It is because that extracting the adjacent secondary stope will expose the backfill in primary stope on one side which makes its stability a critical issue. In this case, determining the minimum required cohesion of cemented backfill in the primary stope is a key task for the mining industry to ensure stability and minimize the cost.

(a)   (b)
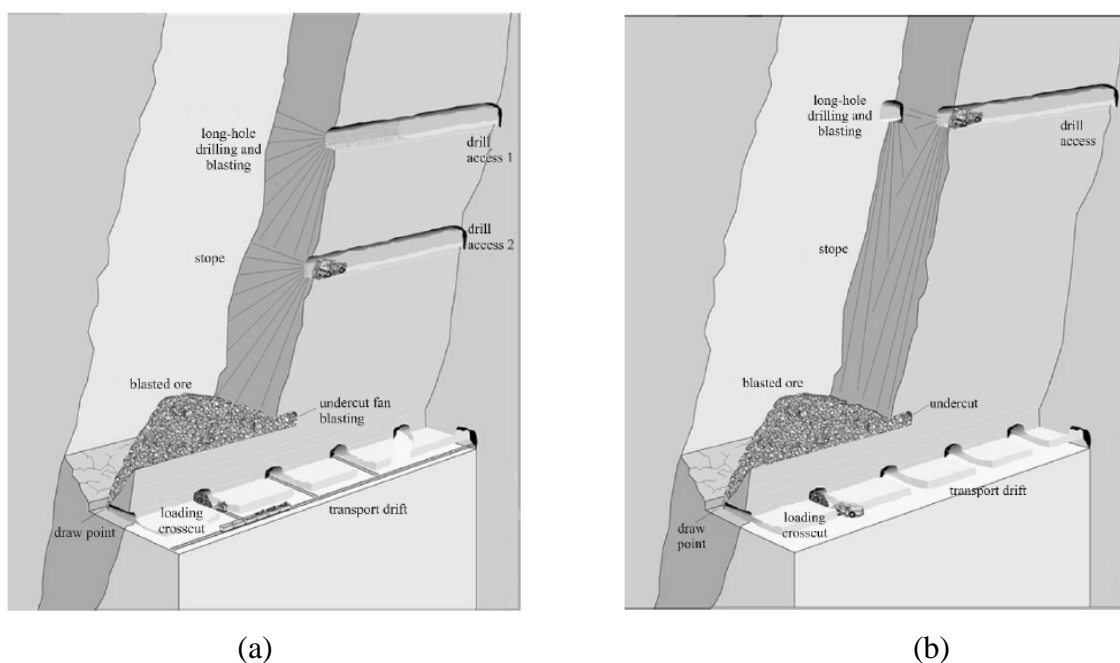
Figure 2.2: Schematic layout for (a) sublevel open stoping and (b) bighole open stoping mining methods (reproduced of Hamrin 2001 with the permission of Society for Mining, Metallurgy & Exploration (SME), smenet.org)

Bighole stoping is a scaled-up variant of sublevel stoping mining method. Its typical layout is shown in Figure 2.2b and is similar as sublevel stoping. In bighole stoping, blast hole with a longer length up to 100 m and a larger diameter of 140–165 mm are drilled using the in-the-hole (ITH) technique (Hamrin 2001). Compared to sublevel stoping, the space between sublevels in bighole stoping can also be larger which simplifies developments. Cemented backfill can be applied in bighole stoping to fill the extracted primary stopes and permit excavating the secondary stopes with less dilution.

Shrinkage stoping is a method parallel to sublevel open stoping. It is usually applied to very narrow orebody (Bullock 2011). In Shrinkage stoping, ore is extracted upward in horizontal slices from the bottom of stopes. During extraction, part of broken ore is left in the empty stope working as a platform and a temporary support for surrounding rocks. The miners stand on the broken ore and drill short vertical blast holes into the crown of previously excavated slice. After each blasting, part of ore (30 to 35%) is drawn to ensure enough work space in the stope (Brady & Brown 2004). The miners then reenter the created void and drill for the next slice. When reaching the upper end of the designed stope, the broken ore left in the stope can be recovered and the extracted stope can be

backfilled to enable excavating the adjacent stopes. The shrinkage stoping has low dilution due to short blast holes and support for rock walls form the broken ore. However, it is labour-intensive and dangerous because that the miners work under unsupported ore.

Vertical crater retreat (VCR) mining is a variant of sublevel stoping mining methods and shrinkage stoping. It is originally developed and patented by Canadian mining company INCO (Hamrin 2001). In this mining method, the stope is mined vertically upward. Larger diameter blast holes are drilled from drilling level (overcut) downward to the undercut level. Short charges are placed into the hole slightly above the crown of the undercut. As each layer is blasted, part of broken rock is extracted to maintain void for next blasting while the rest ores remain in the stope to support the walls. When the extracting level reaches the upper border of the stope, all broken ore in the stope can be recovered and the stope can be backfilled. Similar to the sublevel stoping mining method, when the adjacent secondary stope is extracted, the stability of side-exposed backfill in the primary stope is an important issue for the mining operation.

2.1.2 Artificially supported mining method

In artificially supported mining method, backfill is applied to assist the production and to provide support for rock walls. The artificially supported mining methods mainly involve cut-and-fill mining and some variants (Hamrin 2001; Brady & Brown 2004).

2.1.2.1 Cut-and-fill mining

In cut-and-fill mining, ore is extracted in horizontal or inclined slices. The slice is required to be backfilled immediately after each extraction to support exposed rock walls and facilitate the continuation of mining. This mining method is applicable for orebodies with irregular geometry because the blasting and extraction can be selective (Hamrin 2001). The most common form of cut-and-fill mining is overhand cut-and-fill mining as schematically shown in Figure 2.3a. The ore is removed in horizontal slice from the bottom of stope towards upward. The void is backfilled with hydraulic sand tailings or waste rock (Hamrin 2001). Cement is added in the last pour to form an artificial floor to access higher level for subsequent mining.

(a)   (b)
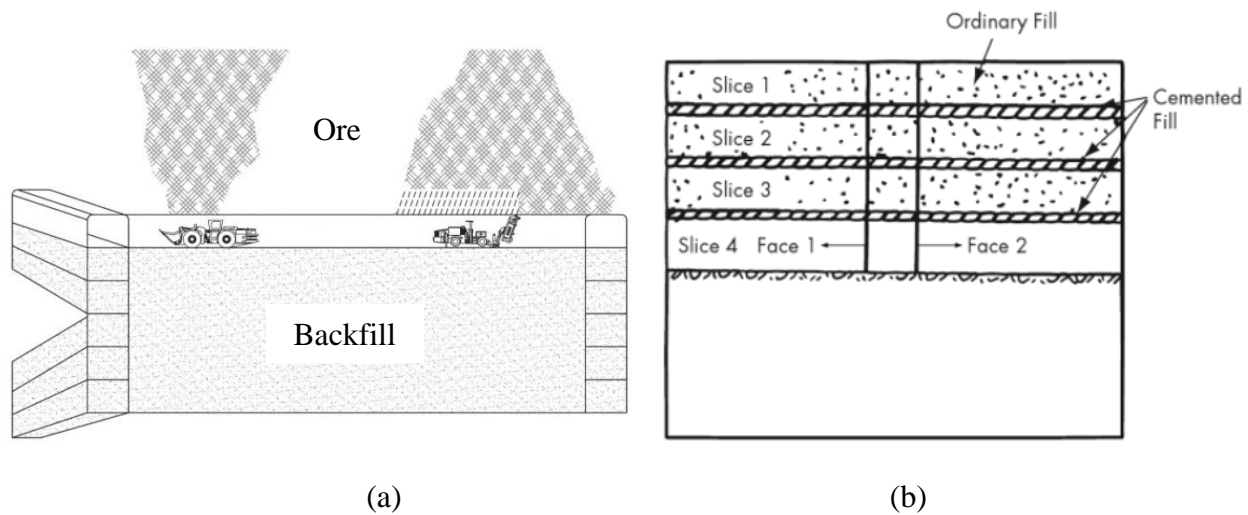
Figure 2.3: Schematic layout for (a) overhand (reproduced of Stephan 2011 with the permission of SME, smenet.org) and (b) underhand cut-and-fill mining methods (reproduced of Bullock 2011 with the permission of SME, smenet.org)

On the other hand, underhand cut-and-fill mining method can be used classically when the ore is narrow and inclined. When the surrounding rock mass is very weak such as having a rock mass rating (RMR) of 20–40, the underhand cut-and-fill can also be used (Darling 2011). The layout of an underhand cut-and-fill mining is shown in Figure 2.3b. The ore in this method is extracted in horizontal slices, but starting from top overcut and advancing downward. Once a slice is mined out, a layer of cemented backfill is poured with or without reinforcements to form a sill mat (Bullock 2011). The rest space can be left unfilled or can be backfilled with uncemented fill. In this case, the sill mat will serve as an artificial roof under which next production cycle occurs. In Lucky Friday mine, underhand cut-and-fill mining is used to control the risk of rockburst because that miners and equipment can work under the backfill instead of rock mass. The stability and minimum required cohesion of sill mat are thus important tasks in this mining method (Mitchell 1991; Sobhi & Li 2015; Pagé et al. 2019; Keita et al. 2021a, 2021b).

2.1.2.2   Variants of cut-and-fill mining

Figure 2.4 illustrates main variants of cut-and-fill mining including: Avoca mining (Figure 2.4a), drift-and-fill mining (Figure 2.4b) and post room-and-pillar mining (Figure 2.4c). When the rock mass has good strength, two slices at different heights can be created using the Avoca mining method as shown in Figure 2.4a. Then the vertical blast holes can be drilled from the floor of upper

slice to the top of lower slice. The blasted ore is removed from the lower slice and the stope is mined by retreat extraction. Along with the extraction, the void is backfilled using waste rocks from the opposite of the stope (Bullock 2011). After one level is finished, same operations are repeated on a higher level.
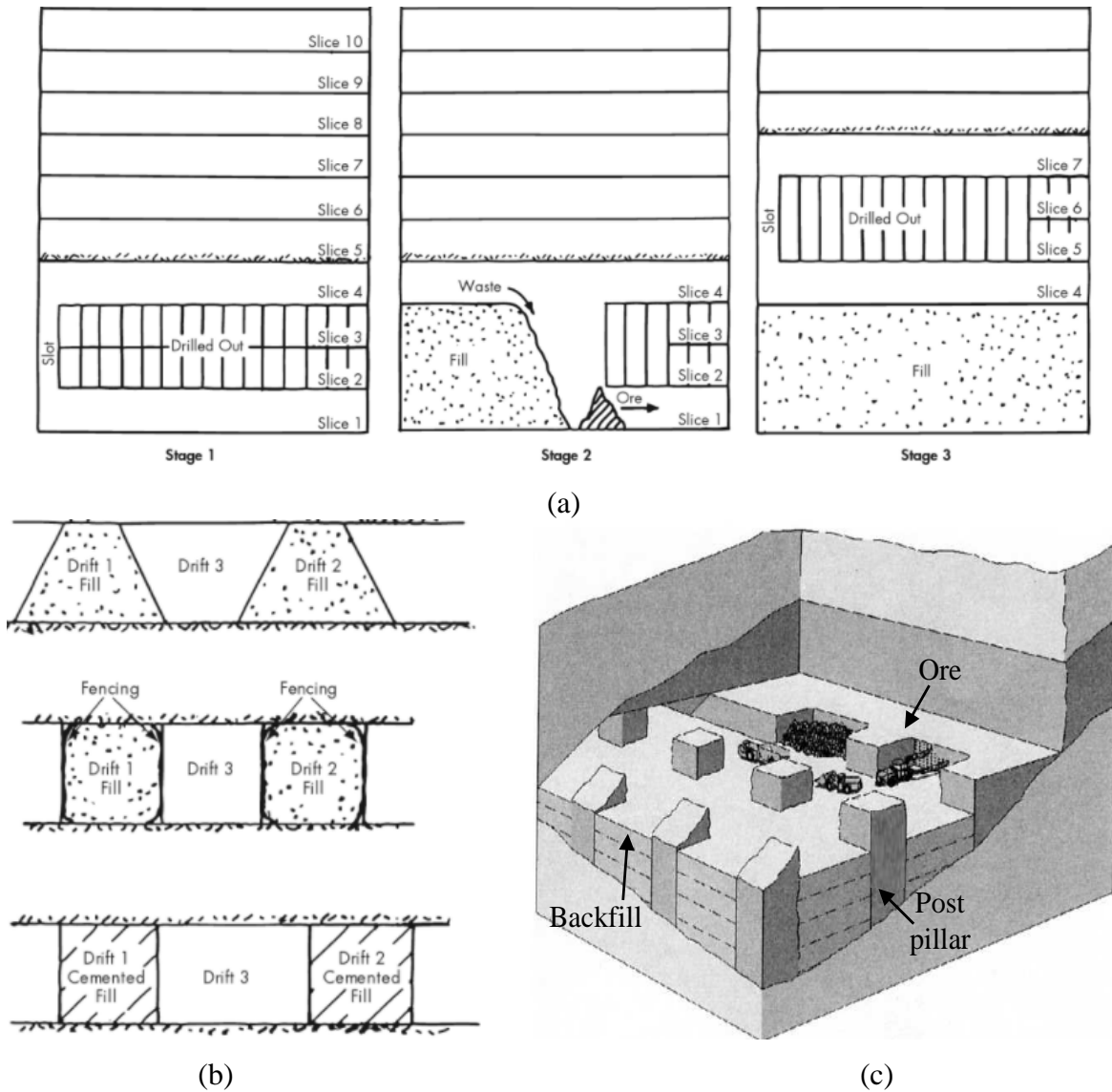
Figure 2.4: Schematic layout for (a) Avoca mining (reproduced of Bullock 2011 with the permission of SME, smenet.org), (b) drift-and-fill mining (reproduced of Bullock 2011 with the permission of SME, smenet.org) and (c) post room-and-pillar mining (reproduced of Hamrin 2001 with the permission of SME, smenet.org)

When the orebody has a large width, drift-and-fill method can be applied which is quite similar to room-and-pillar mining. In drift-and-fill mining, primary drifts are created side by side and are then backfilled with cemented backfill. After that, the remaining pillars (secondary drifts) between backfilled drifts can be recovered with less dilution. In this mining method, the drifts may have various shapes. The primary drifts are usually designed to be narrow to reduce the cost for cement (Bullock 2011).

Post room-and-pillar mining is applied for orebodies of large thickness and width (Hamrin 2001). With this method, a classic room-and-pillar mining is conducted in the lowest slice and rooms are then backfilled. The next upper slice is extracted from the surface of backfill along vertical extension of the pillars (Bullock 2011). The process repeats until that whole stope is mined out. In post room-and-pillar mining, pillars are left to provide additional support and can cross several layers of backfill. Meanwhile, with the confining effect from fill, the pillars can have a smaller size which increases the ore recovery rate.

2.1.3 Unsupported mining method

The unsupported mining method mainly includes block caving, sublevel caving and longwall mining. Figure 2.5a shows a schematic layout of block caving method. Block caving is an economical and mass mining method applicable to orebodies with large heights (Brady & Brown 2004). The production level is created beneath the divided block. Above the production level, a horizontal undercut level is developed which removes the support of the ore. The fracturing and breaking of the block are achieved under the effect of gravity. Small pieces of broken ore then fall and pass through drawpoints.

Figure 2.5b illustrates the conceptual layout of a sublevel caving. Sublevel caving is applicable for steeply inclined orebody (Hamrin 2001; Brady & Brown 2004). Drifts are developed at various sublevels from which blast holes are drilled into the orebody. The blasting is performed with a retreat pattern along the drifts. After blasting, parts of ore pieces fall into the drift and can be removed which results in gravitational flow of broken ore and caved waste (Brady & Brown 2004; Bullock 2011). When high degree of dilution occurs, the extraction of stopes and mining operations retreat.

Longwall mining is a method applicable to flat-lying ore with large and uniform horizontal extent. It is usually applied to mine coal and potash layers (Nieto 2011; Hamrin 2001). Figure 2.5c shows the schematic of the longwall mining. Parallel haulage drifts are created in which belt conveyor is installed. Ore is extracted along a straight front (longwall) between haulage drifts. The mining can be conducted by blasting or using the mechanized cutter. When one slice is cut, it is moved to haulage drifts with the chain conveyor. The mining area is under the protection of a system of hydraulic roof supports. Along the extraction, the chain conveyor, and hydraulic supports advances while roof behind the longwall face collapses. The caved rocks occupy the goaf restricting the deflection of the upper level. Therefore, longwall mining is a method between supported and caving mining (Brady & Brown 2004).

(a)

(b)

(c)
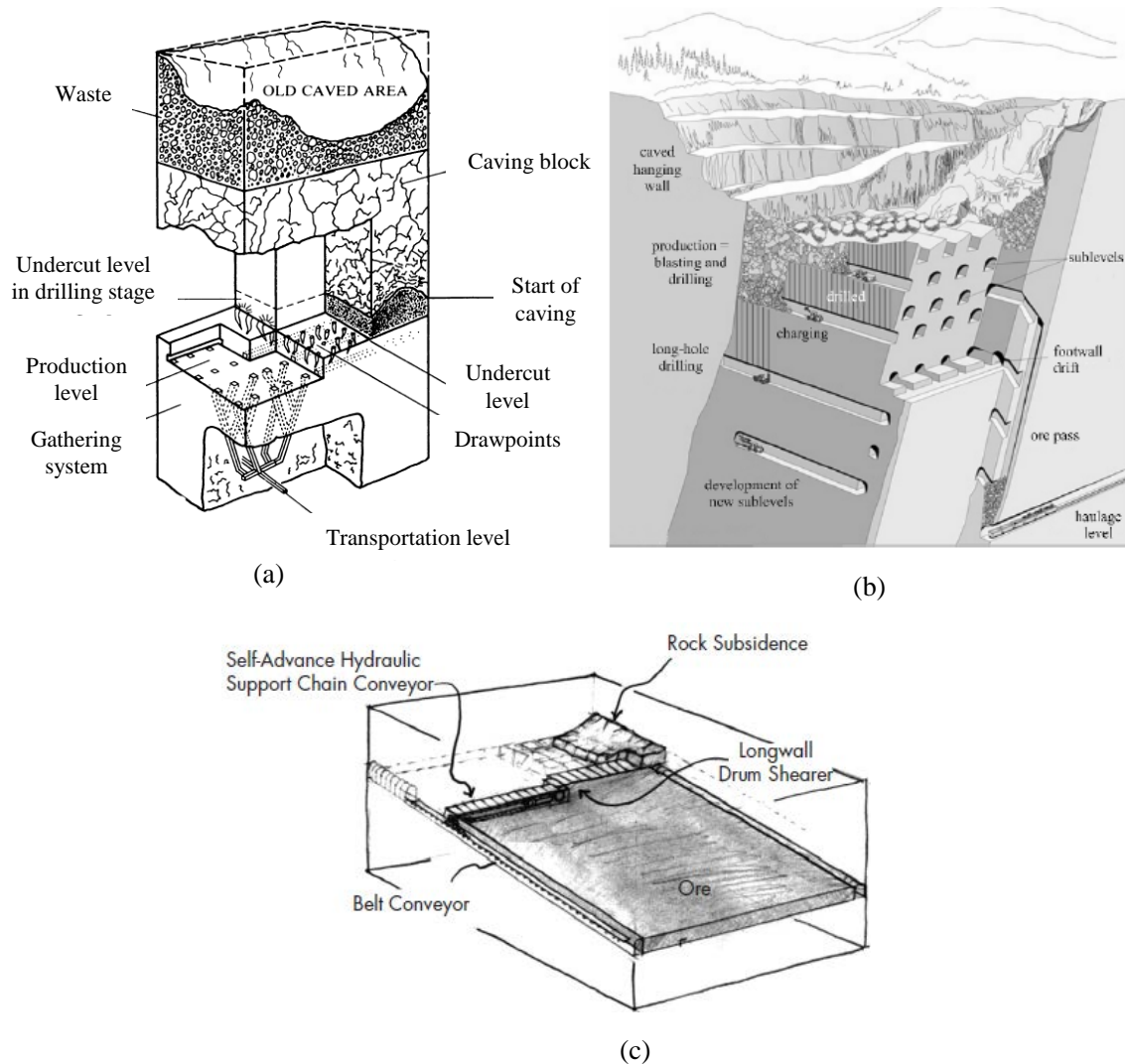
Figure 2.5: Schematic layout for (a) block caving (reproduced of Brady & Brown 2004 with permission), (b) sublevel caving (reproduced of Hamrin 2001 with the permission of SME, smenet.org) and (c) longwall mining method (reproduced of Nieto 2011 with the permission of SME, smenet.org)

Mining backfill can be used in longwall mining, but is hardly used in block caving and sublevel caving. In longwall mining, waste rocks can be used to backfill goaf behind the working face. Application of backfill can minimize the subsidence and reduce the forces applied on the hydraulic supports (Palarski 2014; Zhang et al. 2015).

2.2 Mining backfills

In underground mines, a backfill material can be made of any sources as long as it meets the physical, mechanical and chemical requirements. Several types of mining backfill can exist. Here, only the three commonly used mining backfills are presented, including rockfill, hydraulic fill and paste fill.

2.2.1 Rockfill

Rockfill is typically made of waste rock, quarried rocks or aggregate generated from mine development or natural sites (Hassani & Archibald 1998; Potvin et al. 2005). It can be placed by trucks and dumped into the stopes. Rockfill can be uncemented if adjacent extraction is not necessary. When the recovery of transverse pillar is required, a thin diaphragm wall (pillar) has to be left to retain the uncemented rockfill (Askew & McCarthy 1978; Kuganathan 2005). More commonly, source materials such as waste rocks or other aggregate can be modified by adding fines, crushing, and adding binders (Grice 2001; Salvoldi et al. 2019) to achieve a new rock fill. The binders used for mining backfill mainly involve Portland cement and pozzolans such as fly ash, slag and gypsum. Cemented rockfill usually has a binder content ranging from 1.5% to 6% (Emad et al. 2015).

Physical properties of rockfill

Rockfill has a wide range of grain sizes while minus 10 mm particles are usually considered fine (Kuganathan 2005; Saw et al. 2011). Optimal grading is important for rock fill design. Excessive

coarse particles result in loose fill with poor flowability during placement. Excessive fines will increase the surface area of particles causing an increase in binder consumption. The Talbot grading (Talbot & Richart 1923) is usually applied to make optimum particles distributions of waste rock for rockfill design. Quesnel et al. (1989) suggested that 25% of fine aggregates is an optimal content of waste rocks to maximize the strength. Waste rocks typically have a coefficient of uniformity C_u (=D_{60}/D_{10}) of 8 to 18 (Bussière 2007). Its dry unit weight and void ratio range from 1500 to 2300 kg/m^3 and 0.48 to 0.85 (Williams & Walker 1985; Williams & Kuganathan 1992; Kuganathan 2005).

Hydraulic properties of rockfill

Measurements on typical waste rocks showed that the hydraulic conductivity should be higher than 10^{-5} m/s (Aubertin 2013). Based on the column test, Peregoedova (2012) reported that waste rock at Lac Tio Mine has a hydraulic conductivity ranging from 5.4×10^{-2} to 2.2×10^{-1} cm/s. Williams & Kuganathan (1992) measured the hydraulic conductivity of coal mine waste rocks at New Hope Colliery. The coarse coal wastes have a hydraulic conductivity of 4×10^{-2} m/s while a mixture of coarse wastes and coal mine tailings has a value of around 5×10^{-5} m/s. Lessard (2011) conducted infiltration tests on a waste rock pile at Tio mine and reported that the hydraulic conductivity is between 4×10^{-5} and 3×10^{-3} m/s.

Mechanical properties of rockfill

Typically, uncemented rockfill only has frictional shear strength and its cohesion approaches zero. The value of internal friction angle of rockfill is usually between 35° to 55° that is similar to its repose angle (Farsangi 1996; Kuganathan 2005). The strength of cemented rockfill is commonly evaluated using uniaxial compressive test. Sainsbury & Sainsbury (2014) conducted uniaxial compression tests on cemented rockfill and reported that the UCS increases from 1500 to 3500 kPa at 28 curing days as the cement content increases from 3 to 5%. As the curing time increases, UCS also increases for different cement contents. Similar trend is also seen in the study of Lingga (2018) who proposed a linear relationship between the UCS and curing time. Shrestha et al. (2008) reported that UCS of cemented rockfill with 6% cement content can reach 11.5 MPa with 28 days of curing.

The Young's modulus of cemented rockfill is usually positively related to its UCS and increases with the increase of binder content. Sainsbury & Sainsbury (2014) shows that the Young's modulus of cemented rockfill with 5% cement content can increase from 111 to 148 MPa as the curing time increases from 7 to 28 days. Tesarik et al. (2003) reported a Young's modulus of 2900 MPa for a rockfill with 5.5% content of cement after curing time of 7 to 8 months based on their in-situ measurements at Cannon mine.

2.2.2 Hydraulic fill

Hydraulic fill is a high-density slurry delivered through boreholes and pipelines. Figure 2.6 shows an example of stope backfilling with a hydraulic fill through pipeline at Sondershausen mine. To enable the hydraulic transportation, hydraulic fill must have a large amount of water which needs drainage after the placement. When hydraulic fill is made using mill tailings, desliming is required (usually by hydrocyclone) to increase the permeability. Before placement, porous barricades or barricades with pipes needs to be built in the drift around the bottom of stope to retain hydraulic fill and to permit the drainage (Sivakugan et al. 2015; Yang & Li 2017). When the adjacent pillar recovery is not required, and the drainage condition is good, hydraulic fill can be placed without adding binders. However, binders are needed to generate cohesive strength if the backfill is expected to be exposed or there is a risk of liquefaction.

Figure 2.6: Backfilling a stope with hydraulic fill through pipeline at Sondershausen mine
(reproduced of Marx et al. 2005 with the permission of Dr. Heiner Marx)

Physical properties of hydraulic fill

Hydraulic fill usually has a particle size ranging from 1 to 1000 μm. In order to ensure a proper permeability, hydrocyclone technology needs to be used to make the effective grain size D_{10} larger than 10 μm (Brady & Brown 2002; Kuganathan 2002; Grice 2005). Herget & De Korompay (1978) suggested that the typical value for D_{10} of hydraulic fill is 35 μm.

Figure 2.7 shows the practical size distributions of different hydraulic fills used in Australian mine. The practical size distributions of hydraulic fills fall within a narrow band. Hydraulic fill can thus be classified as silty sand. Rankine et al. (2006) reported that C_u of hydraulic fill is around 6 while Gupta & Paul (2017) suggested that C_u can fall to a value between 6.14 to 7.0 for hydraulic fill made of coal mine overburden dumps material.

The specific gravity of hydraulic fill can change from 2.8 to 4.5, depending on the source materials (Rankine et al. 2006). Slurries of hydraulic backfill typically have a volumetric solids concentration of 40 to 50% or a solid content of 65 to 75% (Grice 1998; Rankine et al. 2006; Sivakugan et al. 2013).
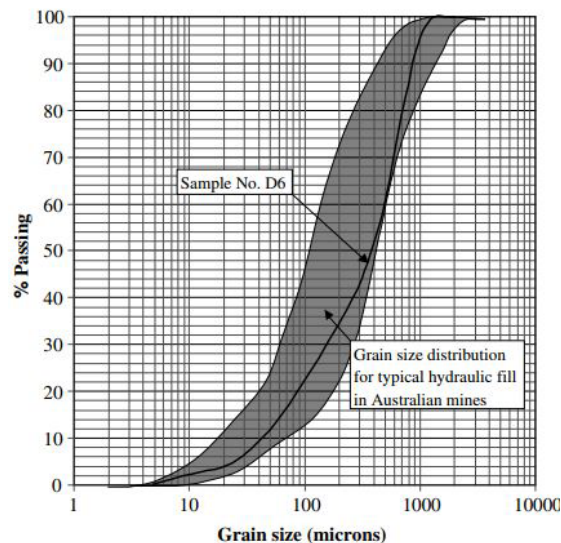
Figure 2.7: The band of particles size distributions of 24 different hydraulic fills used in Australian mine (reproduced of Rankine et al. 2006 with permission)

Hydraulic properties of hydraulic fill

Adequate drainage is essential for the application of hydraulic fill. Hydraulic conductivity (or coefficient of permeability) is thus one of the most important parameters for hydraulic fill. Its value

can be measured by using infiltration test or be estimated using Kozeny-Carman equation (Aubertin et al. 1996; Mbonimpa et al. 2002; Chapuis & Aubertin 2003; Rankine 2005). The mining industry often desires a hydraulic conductivity higher than 100 mm/h for hydraulic fill to ensure drainage (Herget & De Korompay 1978). However, this value is considered conservative according to Sivakugan (2008) who studied the hydraulic conductivity of 25 different hydraulic fill samples. Sivakugan (2008) reported that the hydraulic backfilling has been practiced well with typical values of hydraulic conductivity between 10 to 40 mm/h. Grice (1998) reported that hydraulic conductivity of large-scale uncemented hydraulic fill is 30 to 75 mm/h while for cemented hydraulic fill, the value reduces to 14 mm/h. Liston (2014) suggested a coefficient of permeability of 36 mm/h as the lower band for hydraulic fill. Mitchell et al. (1975) reported that hydraulic conductivity of cemented hydraulic fill reduces exponentially with curing time from 54 mm/h at 20 days to 25 mm/h at 150 days.

Mechanical properties of hydraulic fill

The friction angle of cemented hydraulic fill ranges from 30° to 48° (Askew et al. 1978). It is seen that the friction angle of hydraulic fill can be higher than common granular soil. This is considered due to the angular particles of crushing waste rock without experiencing geological weathering. Rankine et al. (2006) proposed that the friction angle of hydraulic fill is positively related to its specific gravity through a power law equation. The cohesion of cemented hydraulic fill can be affected by the binder content, curing time, segregation and stress conditions during curing. Grice (1998) reported that the UCS of a hydraulic fill with 6% cement content can be 750 kPa after 28 curing days. Askew et al. (1978) shows that for a hydraulic fill at 112 days of curing, its cohesion can increase from 0.1 to 1.5 MPa with the increase of cement content from 3% to 17%. The Young's modulus of hydraulic fill is positively related to binder content and curing time while in the field, it can increase with the depth (Börgesson 1981).

2.2.3 Paste fill

Paste fill is made by mixing full stream tailings with water and binders. It requires at least 15% by weight of fine particles smaller than 20 μm to retain water and make a non-segregating slurry with high density (Brummer 1991; Henderson et al. 2005). Figure 2.8 shows the paste backfill being

deposited into a stope through a pipeline. Due to its non-segregating behavior, paste fill does not require a critical delivery velocity and allows a slow pipeline rate to reduce wear effect (Henderson et al. 2005). Ideal paste fill demonstrates the non-Newtonian Bingham plastic flow characteristic. Before mobilizing the paste fill, a sufficient yield stress must be overcome which is largely dependent on the water content.
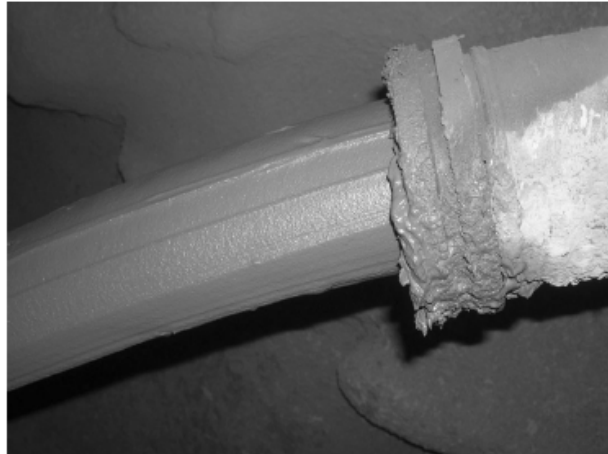
Figure 2.8: Paste fill being poured into a stope through pipeline (reproduced of Sivakugan et al. 2015 with permission)

Since part of water is retained in paste fill, it is prone to liquefaction caused by some disturbances such as the blasting from adjacent stope (Grabinsky 2010; Zheng & Li 2020). The liquefied paste fill will significantly increase the pressure in stope and on barricade. This may further cause the failure of barricade and threaten the safety of workers. Therefore, a small percentage of cement is always necessary for paste fill to generate bonds between particles and reduce some water by hydration, thus avoiding liquefaction. Been et al. (2002) reported that a cement content of at least 1% is needed for cemented paste backfill (CPB). Aref et al. (1989) stated that the liquefaction is prevented for CPB with a cement content of 3%.

Physical properties of paste fill

Paste fill can have a high solid content ranging from 75 to 85% and a binder content of 2 to 10% to generate cohesive strength (Potvin et al. 2005). Rankine & Sivakugan (2007) reported that typical CPB has a solid content of 79% and a cement content of 3.5%. Paste fill can be made using mixing full stream tailings. Figure 2.9 shows an example of particle size distributions of mill

tailings at Cayeli Mine. The tailings are very fine with over 40% by weight finer than 20 μm. The water content, void ratio and degree of saturation of CPB are affected by the tailing type, binder content, curing time and drainage. Belem et al. (2006) reported that a CPB sample cured 91 days in a drained column can have a void ratio ranging from 0.77 to 0.91 and a typical saturation degree from 75 to 93%.
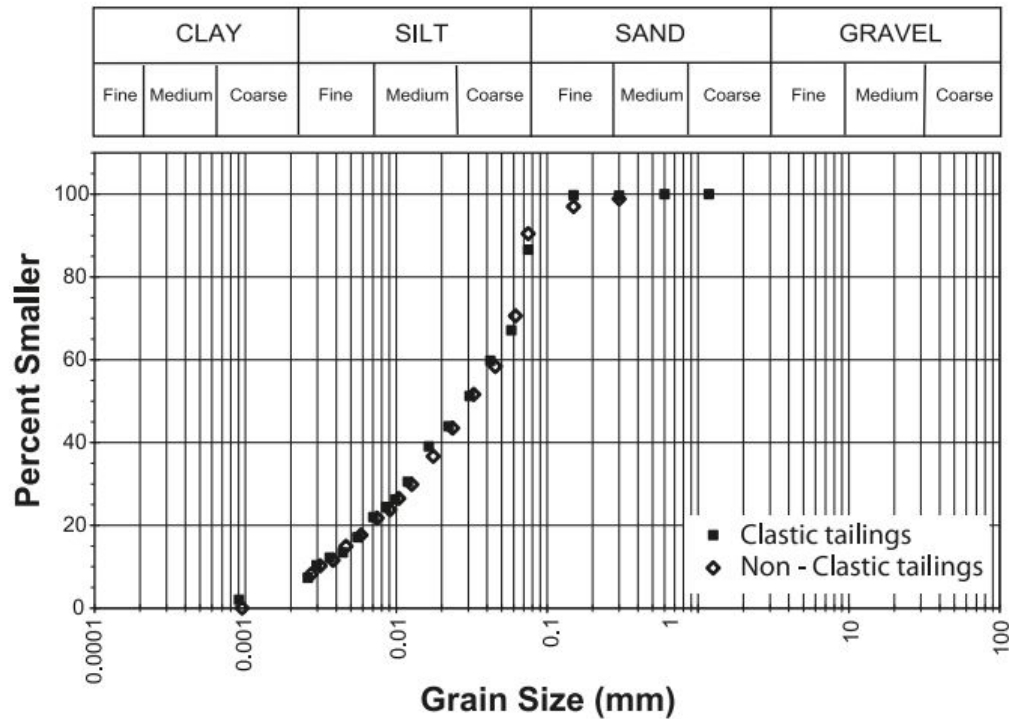
Figure 2.9: Particle size distributions of mill tailings at Cayeli Mine (reproduced of Thompson et al. 2012 with permission)

Hydraulic properties of CPB

The hydraulic conductivity of cemented paste backfill is affected by binder content and type, curing time, curing stress, content of fine particles and water/cement (*w/c*) ratio. Godbout et al. (2007) conducted falling head permeameter tests on CPB using different contents of binder made by Portland cement and slag. Their results shown in Figure 2.10 indicate that the hydraulic conductivity of CPB decreases with the increase of curing time and binder content. For a binder content of 4.5%, the hydraulic conductivity reduces from 4.5×10^{-7} to 2.5×10^{-8} m/s after 14 days of curing. As the binder content reduces to 1%, the initial value of hydraulic conductivity becomes

6×10^{-7} m/s and decreases to 1×10^{-7} m/s at 14 days. Belem et al. (2001) reported that the decrease of hydraulic conductivity of CPB is mainly within the first 7 curing days, after which the change in permeability is insignificant. Fall et al. (2009) reported that the permeability of CPB at 28 curing days decreases from 4×10^{-7} m/s to around 5×10^{-8} m/s as the content of fine particles (< 20 μm) increase from 20 to 45%.
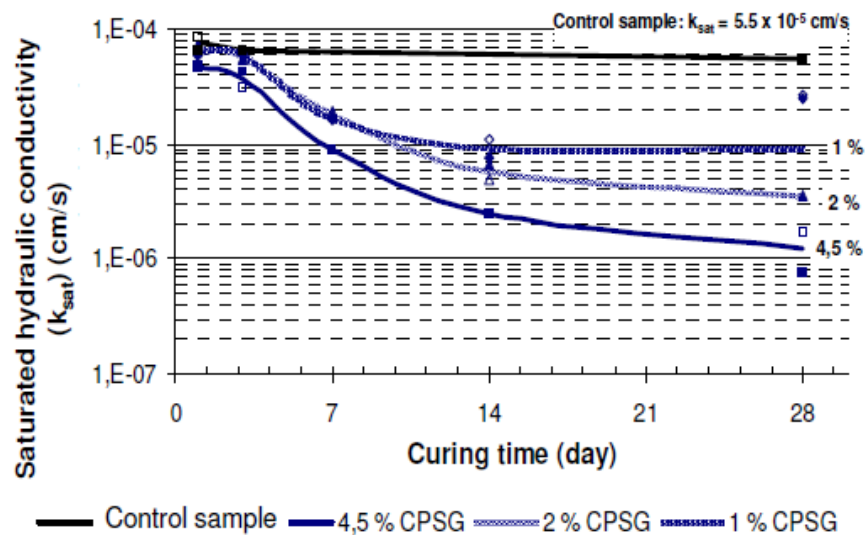
Figure 2.10: Saturated hydraulic conductivity of CPB as a function of curing time for different contents of binder (reproduced of Godbout et al. 2007 with the permission of Prof. Bruno Bussiere)

Rheological properties of CPB

A yield stress must be overcome to mobilize the CPB. If the applied shear stress is lower than the yield stress, the CPB behaves as an elastic material without any movement. The yield stress of CPB can be indirectly measured using shear vane test or slump test. In shear vane test, a vane is inserted into the CPB sample and then rotated. The maximum torque to maintain a constant rotation is recorded and is used to calculate the yield stress (Simon & Grabinsky 2013; Niroshan et al. 2018). Slump test is more commonly used in practice to measure the slump height of CPB slurry (Tan et al. 2017; Niroshan et al. 2018; Behera et al. 2019). In slump test, a cone is used to contain CPB. After removal of the cone, the reduced height is measured as the slump of the material. According to Ferraris & de Larrard (1998), yield stress of CPB can be estimated from slump height by using

an empirical equation. CPB used in underground mine typically has a yield stress ranging from 200 to 700 kPa (Amaratunga & Yaschyshyn 1997; Potvin et al. 2005; Sivakugan et al. 2015). In some cases, for increasing the flowability for transportation of CPB by pipelines, superplasticizer can be added into CPB mixture (Koohestani et al. 2018; Haruna & Fall 2020).

Mechanical properties of CPB

Pierce (1999) reported that the cohesion of CPB increases significantly with the increase of binder content and curing time, but the friction angle slightly decreases as curing time increases. Belem et al. (2000) reported that as the binder content of CPB increases from 3 to 6%, its cohesion at 112 curing days increases but the friction angle shows a decreasing trend. Veenstra (2013) indicated that the cohesion of CPB can increase from 40–130 kPa at 7 curing days to 240–680 kPa at 21 curing days based on direct shear tests. Fall et al. (2007) reported that both the peak stress and Young's modulus of CPB increase with increase of cement content. Johnson et al. (2015) indicated that the UCS is around 4.15 MPa and Young's modulus ranges from 1.1 to 3.59 GPa for CPB at Lucky Friday Mine.

2.3   Stress state in backfilled stopes

Estimation of stress state in a backfilled stope is important for its design. When a backfill is placed in a stope, it has a downward moving tendency driven by the weight. The surrounding rock walls are usually much stiffer than the backfill and tend to retain the backfill in the original place. The relative movement of backfill against the rock walls leads to the generation of shear stresses along the fill-rock interfaces, resulting in a reduction of the stresses in the backfilled stopes. This is known as arching effect. Arching effect can be significant in a narrow backfilled stope and is also seen in other geotechnical structures such as retaining walls and ditches. In this subsection, some analytical solutions for evaluating stress state in backfilled stopes are briefly reviewed. It should be noted that only the dry condition is considered in this subsection.

Marston (1930) solution

Marston (1930) applied the arching theory to estimate the vertical stress σ_v at a depth h (m) within the fill placed in a trench. The analytical solution is given as:

$$\sigma_v = \frac{\gamma \cdot B}{2K \cdot \tan \delta} \left[1 - exp\left(-2K \cdot \tan \delta \frac{h}{B}\right)\right] \tag{2.1}$$

where K is the earth pressure coefficient; γ (kN/m³) denotes the unit weight of fill material; δ (°) denotes the friction angle of fill-wall interface. B (m) is the width of trench.

Cohesion of fill is not considered in Marston (1930) solution. Rankine's active earth pressure coefficient K_a was recommended by Marston (1930) as the value of K in the equation. However, based on the analytical and numerical analyses, Yang et al. (2018) indicated that K along center of cohesionless backfill can either be active or at-rest (K_0) earth pressure depending on the values of Poisson's ratio v and internal friction angle ϕ of backfill.

Aubertin et al. (2003) solution

Aubertin et al. (2003) introduced the Marston (1930) solution to calculate the vertical stress σ_v and horizontal stress σ_h at a depth h (m) in a vertical backfilled stope. The formulations are given as:

$$\sigma_v = \frac{\gamma \cdot B}{2K \cdot \tan \phi} \left[1 - exp\left(-2K \cdot \tan \phi \frac{h}{B}\right)\right] \tag{2.2}$$

$$\sigma_h = \frac{\gamma \cdot B}{2 \tan \phi} \left[1 - exp\left(-2K \cdot \tan \phi \frac{h}{B}\right)\right] \tag{2.3}$$

where γ (kN/m³) is the unit weight of backfill; ϕ (°) is the effective friction angle of backfill; B (m) is the width of the stope; K is the earth pressure coefficient.

Aubertin et al. (2003) further conducted numerical simulations with PHASES2 to analyze the stress distribution in a narrow stope. The numerical results of vertical and horizontal stresses along stope height were compared with analytical solutions by considering different values of K. However, in all cases, the numerical results are significantly larger than the analytical results. This is because in the numerical simulations, the backfill was placed before applying in situ stresses. It is similar to a case where very small slice cut-and-fill mining method was applied. The rock-wall closure caused by the very small slice extraction applies fully on the backfill, resulting in high compression stresses in the backfilled stope.

Li et al. (2003) simulated the stress state in a two-dimensional backfilled stope using FLAC. The mining and filling sequence in Li et al. (2003) study is different form those in the study of Aubertin et al. (2003). The whole stope was extracted first after which the numerical model was solved to

equilibrium state. Then the displacement was reset to zero and backfill was placed in the stope. By using this simulation sequence, the closure of rock walls caused by stope extraction was not applied on the backfill. Li et al. (2003) compared the numerical results of vertical and horizontal stresses in backfill with Marston (1930) solution. It was found that Marston (1930) solution understates the vertical and horizontal stresses along the vertical central line of backfill. For the stresses along walls, the horizontal stress is still understated by Marston (1930) solution while the vertical stress is overestimated.

Ting et al. (2011) solution

Ting et al. (2011) developed a two-dimensional arching solution with a new equation of modified earth pressure coefficient K_β for estimating stress distribution within an inclined backfilled stope by considering parallel inclined walls. The solution contains some assumptions including: the vertical stress distributes uniformly along stope width; fill-rock interfaces have the same cohesion with backfill; shear and normal stresses acting on inclined side walls are considered identical. The proposed solutions for the vertical stress and K_β are given as:

$$\sigma_v = \frac{\gamma B - 2c(1+\sin 2\beta \tan \delta)}{2K_\beta \tan \phi}\left[1 - exp\left(-2K_\beta \tan \delta \frac{z}{B}\right)\right] + q exp\left(-2K_\beta \tan \delta \frac{z}{B}\right) \tag{2.4}$$

$$K_\beta = \left(\frac{1+K_0}{2} + \frac{1-K_0}{2}\cos 2\beta + K_0 \tan \delta \sin 2\beta\right) \tag{2.5}$$

where γ (kN/m^3) is the unit weight of backfill; B (m) is the width of the stope; β (°) is the stope dip angle; c (kPa) denotes the backfill cohesion; δ (°) is the friction angle of fill-rock interface and its value is taken as $2/3\phi$; ϕ (°) is the effective frictional angle of backfill; z (m) is the depth in the stope; q (kPa) is the surcharge; K_0 is the at-rest earth pressure coefficient.

Ting et al. (2011) reported that on account of arching effect and stope inclination, the vertical stress acting on the bottom of stope is reduced by 65 to 70% compared to the overburden. It was suggested that the influence of friction angle of backfill on the stress distribution within backfilled stope becomes negligible as its value exceeds 30°.

Jahanbakhshzadeh et al. (2017) solution

Jahanbakhshzadeh et al. (2017) suggested that the earth pressure coefficient K in the backfilled stope is not a constant and is dependent on the stope geometry, the specific position in the stope and the internal frictional angle of backfill. A reference model as shown in Figure 2.11 was used by Jahanbakhshzadeh et al. (2017) to calculate the modified earth pressure coefficient K_β and drive the arching solution based on the equilibrium state of a horizontal thin layer.
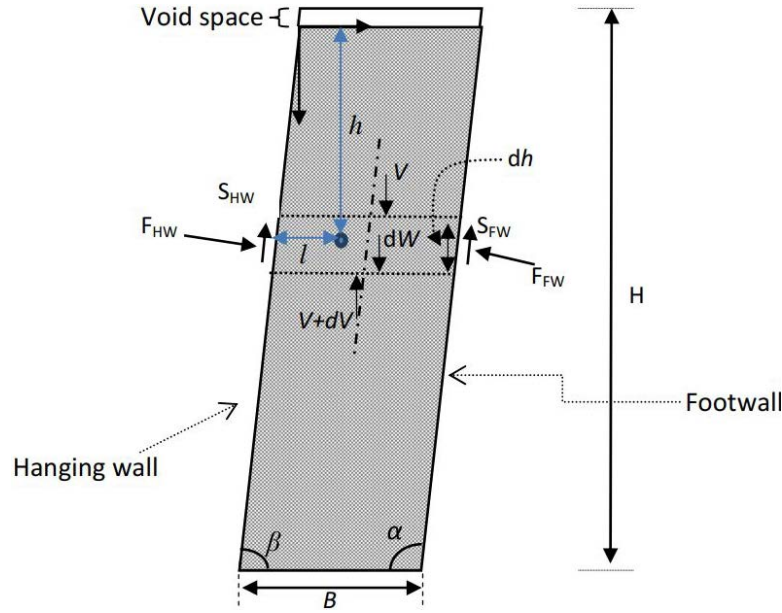
Figure 2.11: A reference model for inclined backfilled stope (reproduced of Jahanbakhshzadeh et al. 2017 with permission)

Jahanbakhshzadeh et al. (2017) proposed the following equation for K_β in the backfilled stope:

$$K_\beta = K_a \cdot f_h \cdot f_w \tag{2.6}$$

where K_a is Rakhine' active earth pressure coefficient; f_h and f_w are two parameters expressed as:

$$f_h = 1 + \cos\beta - \left(\frac{h}{H}\tan\phi\cos^2\beta\right) \tag{2.7}$$

$$f_w = \left[1 + 3\tan\phi\cos(\beta - 10°)\left(1 - \frac{l}{B}\right)^4\right] \tag{2.8}$$

where β (°) is walls inclination angle; H (m) and B (m) are the height and width of stope respectively; l (m) is the distance from a point in the stope to the hanging wall; h (m) is the distance from a point in the stope to the top of the backfill; ϕ (°) is the internal frictional angle of backfill.

It can be seen that K_β in the Jahanbakhshzadeh et al. (2017) solution is a function of stope geometry, the specific position in the stope and the backfill friction angle. The arching solution proposed by Jahanbakhshzadeh et al. (2017) for the vertical stress σ_v at a depth h (m) in backfilled stope is then expressed as:

$$\sigma_v = \frac{\gamma B \sin \beta}{2 K_\beta \tan \phi}\left[1 - exp\left(-2 K_\beta \tan \phi \frac{h}{B \sin \beta}\right)\right] \tag{2.9}$$

where γ (kN/m^3) denotes the unit weight; B (m) is the stope width; β (°) is the inclination angle.

Jahanbakhshzadeh et al. (2017) compared the analytical solution with numerical results of stresses along profiles of hanging wall, footwall and central line of the backfill. The comparisons show good agreements. However, Jahanbakhshzadeh et al. (2017) solution has some limitations one of which is the assumption that backfill is always attached to the hanging wall. When the dip angle is small, the backfill can be detached from the hanging wall which was not considered by Jahanbakhshzadeh et al. (2017). Moreover, Jahanbakhshzadeh et al. (2017) solution is only applicable for two-dimensional plane strain condition that implies the length of the stope is much larger than its width.

Li & Aubertin (2008) solution

Li & Aubertin (2008) modified the two-dimensional Marston (1930) solution by considering nonuniform vertical stress along the width of the stope while the horizontal stress was still considered uniform. The proposed equations for the vertical stress σ_{vx} at a point in the stope and horizontal stress σ_h are given as:

$$\sigma_{vx} = \frac{\gamma B}{2K \tan \delta}\left[1 - exp\left(-2K \tan \delta \frac{h}{B\left(1-\frac{a}{2^b(b+1)}\right)}\right)\right] \times \left[1 - a\left(\frac{|x|}{B}\right)^b\right] \tag{2.10}$$

$$\sigma_h = \frac{\gamma B}{2 \tan \delta}\left[1 - exp\left(-2K \tan \delta \frac{h}{B\left(1-2^b(b+1)\right)}\right)\right] \tag{2.11}$$

where γ (kN/m^3) denotes the unit weight; B (m) is the width of the stope; h (m) is the distance from the top of backfill to the calculation point; x (m) represents a distance from the centreline to the calculation point with a range of $-B/2$ to $B/2$; δ (°) is the friction angle of fill-rock interface and its value can be considered equal to the internal frictional angle of backfill when rock walls are

sufficiently rough; K is the earth pressure coefficient; a and b are two parameters controlling the vertical stress distribution curvature along the width of the stope.

In Li & Aubertin (2008) solution, the vertical stress in the stope is not only affected by stope geometry and backfill properties, but also a function of the relative position in the stope. The parameters a and b in the equation can be determined by calibrating the analytical solution with numerical or laboratory results.

Jaouhar et al. (2018) solution

Most analytical solutions are based on the analysis of the equilibrium state of a thin horizontal layer element. The vertical and horizontal stresses acting on this layer element are considered as principal stresses which facilitate the use of the earth pressure coefficient. However, this is only valid near the center of the stope while rotation of principal stresses occurs near the walls of the stope. Jaouhar et al (2018) developed a modified solution to analyze the circular arc distribution of stresses at a point (x, y) in a vertical backfilled stope by considering the arc layer elements. The proposed equations of vertical stress $\sigma_{v(x, y)}$ and horizontal stress $\sigma_{h(x, y)}$ are expressed as:

$$\sigma_{v(x,y)} = \sigma_{1(x,y)} \left[1 - \left(1 - K_{ps}\right) \left(\frac{x}{Bk}\right)^2 \right] \tag{2.12}$$

$$\sigma_{h(x,y)} = \sigma_{1(x,y)} \left[K_{ps} + \left(1 - K_{ps}\right) \left(\frac{x}{Bk}\right)^2 \right] \tag{2.13}$$

where B (m) represents the half width of the stope; x (m) is a distance from the centreline to the calculation point. $\sigma_{1(x, y)}$ is the major principal stress at the calculation point and its equation is given as:

$$\sigma_{1(x,y)} = \frac{Q}{S} \left\{ 1 - exp \left[-\frac{S}{P} \left(y - \left(Bk - \sqrt{Bk^2 - x^2}\right) \right) \right] \right\} \tag{2.14}$$

Other parameters in Jaouhar et al (2018) solution are given as:

$$K_{ps} = \tan^2(45^\circ - \phi/2) \tag{2.15}$$

$$k = \frac{1}{\sin(45^\circ - \phi/2)} \tag{2.16}$$

$$Q = \gamma Bk \sin \omega_w \tag{2.17}$$

$$S = \frac{\tan \delta}{\cos \omega_w} \left(\sin^2 \omega_w + K_{ps} \cos^2 \omega_w \right) \tag{2.18}$$

$$P = Bk \sin \omega_w \tag{2.19}$$

$$\omega_w = \sin^{-1} \frac{1}{k} \tag{2.20}$$

Li et al. (2005) solution for 3D stope

Li et al. (2005) considered a three-dimensional backfilled stope as shown in Figure 2.12. Based on the derivation of the equilibrium state of a thin layer element, Li et al. (2005) developed a 3D analytical arching solution for estimating stress distribution in cohesive backfill contained in a vertical narrow stope. The formulations for vertical stress σ_v and horizontal stress σ_{hi} along the ith ($i = 1$–4) rock wall are given as:
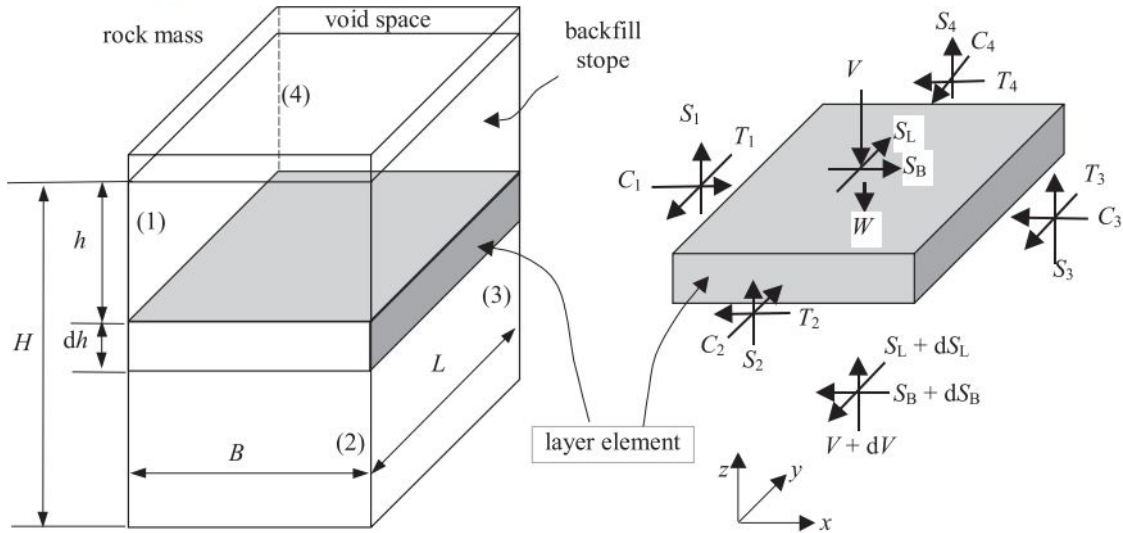
Figure 2.12: A three-dimensional model of a backfilled stope with a thin horizontal layer element (reproduced of Li et al. 2005 with permission).

$$\sigma_v = \frac{\gamma - (\kappa_{13} 2B^{-1} + \kappa_{24} L^{-1})}{(\lambda_{13} B^{-1} + \lambda_{24} L^{-1})} \left[1 - exp\left(-h(\lambda_{13} B^{-1} + \lambda_{24} L^{-1}) \right) \right] \tag{2.21}$$

$$\sigma_{hi} = K_i \sigma_v + 2c \tan \alpha_i \tag{2.22}$$

where γ (kN/m³) denotes the unit weight; B (m) and L (m) are the width and length of the stope respectively; c (kPa) is the cohesion of backfill; K_i and α_i are the earth pressure coefficient and backfill state angle on the ith wall; λ_{13}, λ_{24}, κ_{13} and κ_{24} are parameters which are expressed as:

$$\lambda_{13} = K_1 \tan \delta_1 + K_3 \tan \delta_3 \tag{2.23}$$

$$\lambda_{24} = K_2 \tan \delta_2 + K_4 \tan \delta_4 \tag{2.24}$$

$$\kappa_{13} = c_1 + c_3 + 2c(\tan \alpha_1 \tan \delta_1 + \tan \alpha_3 \tan \delta_3) \tag{2.25}$$

$$\kappa_{24} = c_2 + c_4 + 2c(\tan \alpha_2 \tan \delta_2 + \tan \alpha_4 \tan \delta_4) \tag{2.26}$$

where δ_i (°) and c_i (kPa) are the friction angle and adhesion of the ith fill-wall interface.

Li et al. (2005) solution is general because the fill-rock interfaces can have different properties and the earth pressure coefficient can also differ along different directions. The limitations of this solution include that it is not applicable for backfill (or interface) with very large cohesion. Its application also largely depends on the estimation of earth pressure coefficient in the backfilled stope.

Pirapakaran & Sivakugan (2007) solution for 3D stope

Pirapakaran & Sivakugan (2007) modified Marston (1930) solution to estimate the stress state in backfill contained by a three-dimensional rectangular stope. The four vertical rock walls are assumed having same geomechanical properties. The equation of vertical stress in Pirapakaran & Sivakugan (2007) solution is expressed as:

$$\sigma_v = \frac{\gamma B}{2K \tan \delta} \left(\frac{L}{L+B}\right) \left[1 - exp\left(-2\left(\frac{L+B}{LB}\right)Kh \tan \delta\right)\right] \tag{2.27}$$

where γ (kN/m³) denotes the unit weight of backfill; B (m) and L (m) are the width and length of the stope respectively; h (m) is a depth in the stope; δ (°) is the friction angle of fill-rock interface; K is the earth pressure coefficient.

Since the surrounding rock mass is much stiffer than fill material, Pirapakaran & Sivakugan (2007) suggested that the displacement of rock walls due to the placement of backfill can be neglected while K in the solution can thus be considered as at-rest pressure coefficient K_0. The value of δ was recommended as 2/3 of the internal frictional angle of backfill.

2.4 Stability of side-exposed backfill

2.4.1 Conventional overburden solutions

Before the 1980s, the required strength of side-exposed backfill was mainly estimated using two traditional solutions by considering the overburden stress (Li et al. 2014a, 2014b). One considers the side-exposed backfill as a free-standing vertical face and requires the uniaxial compressive strength (UCS) of backfill larger than overburden stress at any depth z (m). The formulation of this solution is given as:

$$\text{UCS} \geq \gamma z \tag{2.28}$$

where γ (kN/m^3) is the unit weight of backfill.

According to this method, the side-exposed backfill can have a zero UCS at the top which increases linearly with the increase of the depth reaching the maximum value at the bottom of stope (Mitchell et al. 1982; Li et al. 2014a, 2014b).

The other approach considers the UCS of backfill as a constant for different depths and its value is required larger than the overburden stress at the half height of the stope (Mitchell et al. 1982). The equation of this solution for UCS of side-exposed backfill is given as:

$$\text{UCS} \geq \frac{1}{2}\gamma H \tag{2.29}$$

where H (m) is the height of side-exposed backfill.

The second solution is simpler for the application in practice. Nevertheless, traditional overburden solutions are conservative because the arching effect generated within backfilled stopes and confining effects of side walls are not considered (Mitchell et al. 1982; Li et al. 2014a, 2014b). Applying these conservative solutions can result in an overestimation of backfill strength and mining cost. More representative solutions for evaluating the stability and estimating the minimum required strength of side-exposed backfill are needed.

2.4.2 Wedge sliding model and Mitchell et al. (1982) solution

Mitchell et al. (1982) proposed a three-dimensional wedge sliding model with a vertical open face to evaluate the stability of the side-exposed backfill. The model is schematically shown on Figure

2.13. The side and back walls of the model are confined by the remaining rock walls. Mitchell et al. (1982) assumed that the side-exposed backfill fails by sliding along an inclined plane making an angle of $\alpha = 45° + \phi/2$ to the bottom of the stope (ϕ (°) is the friction angle of the backfill) as shown in the figure.
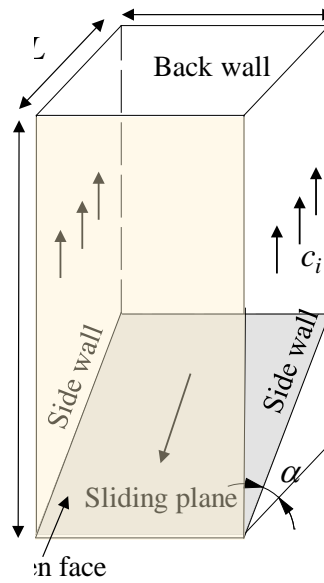
Figure 2.13: Schematic of wedge sliding model for vertical cemented backfill upon a side exposure (adapted from Mitchell et al. 1982 with permission)

The weight of the sliding block in the Mitchell model is partially resisted by the side walls. Mitchell et al. (1982) simplified the shear resistance along the fill and side wall interfaces as a constant cement bond shear strength c_i (kPa). The factor of safety (FS) of side-exposed backfill in this model is considered as a ratio of resisting forces to the driving forces on the failure plane. The equation of FS is given as:

$$FS = \frac{\tan \phi}{\tan \alpha} + \frac{2cB}{(H - \frac{L \cdot \tan \alpha}{2})(\gamma B - 2c_i) \sin 2\alpha} \tag{2.30}$$

where γ (kN/m³) is the unit weight of the backfill; c (kPa) is the cohesion of the backfill; H (m), B (m), and L (m) are the height, width, and length of the side-exposed backfill.

In the case that $c_i = c$ and $H \gg L$, the required cohesion for side-exposed backfill can be calculated as follows by considering FS = 1:

$$c = \frac{\gamma H}{2\left(\frac{H}{B}+\tan\alpha\right)} \qquad (2.31)$$

Based on the assumption that considering the friction angle ϕ of backfill as 0 (Mitchell et al. 1982), the UCS of backfill relates to its cohesion as UCS $= 2c$. The above solution for c of side-exposed backfill can then be simplified to calculate the UCS of fill as (Mitchell et al. 1982):

$$\text{UCS} = \frac{\gamma H}{\frac{H}{B}+1} \qquad (2.32)$$

In order to verify the proposed analytical solution, Mitchell et al. (1982) conducted the physical box stability tests of cemented tailings and cemented sand. The physical model had a steel frame and a fixed back and bottom formed by laminated plywood as shown in Figure 2.14. The front of the box was formed using various horizontal timbers with a height of 100 mm. Waterproof calking, rubber straps, and plastic sheeting were applied to seal the box while drainage facilities were built under the box with pea gravel. The adjustment bolts were installed on sides of the box to allow closure applied to fill material. The box was in a relatively small scale with a height of around 2 m which requires the reduction of strength of fill material to achieve the failure. Therefore, cemented fills with a low cement content of 2.2% and a short curing time of 2.5–5 h were used in Mitchell et al. (1982) tests. After mixing within 20–40 min, the fill material was poured into the box. When the desired strength of fill was reached by conducting confined compression and direct shear tests on control samples, the drainage valve at the bottom was opened to reduce the pore water pressure in fill. Then the timbers on the front wall were removed from top to bottom to determine the stable height of the vertical exposure. 30 tests with various box geometries, unit weights and strengths of fill, walls roughness and closures were conducted by Mitchell et al. (1982). The comparison between the experimental results and the analytical solution for UCS proposed by Mitchell et al. (1982) show good agreement.
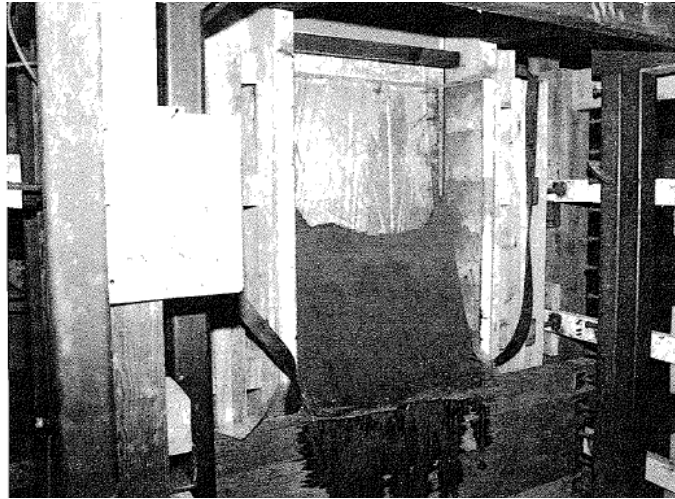
Figure 2.14: A photo of one box instability test (reproduced of Mitchell et al. 1982 with permission).

The Mitchell et al. (1982) solution for estimating the required UCS of side-exposed backfill has been commonly used in backfill design. However, Mitchell et al. (1982) considered that the adhesion of fill-side wall interfaces equals to the cohesion of backfill which is only valid when the rock walls are sufficiently rough. The nil friction angle of backfill also implies that this solution is only applicable for backfill under undrained or partially drained condition. The box instability tests used to verify the analytical solution were also conducted with very soft backfill under undrained or partially drained conditions. This was confirmed by Liu et al. (2016a) who reproduced the box instability tests of Mitchell et al. (1982) with FLAC^{3D} using undrained shear strength parameters. These limitations of box instability tests can explain that Mitchell et al. (1982) suggested that rock wall closure has little effect on the stability of side-exposed backfill.

In practice, cemented backfill will cure a long time (typically 28 days) before side exposure which becomes hard under drained condition. Excavating a stope removes the support for rock mass and causes the stress redistribution. This results in the instantaneous rock-wall closure. When the induced stress in rock walls is large or the rock mass is weak, long-term creep deformation of rock walls can occur. The compression caused by rock walls closure will thus increase the stress state in the backfilled stope and may crush the side-exposed backfill which causes a different failure mechanism from the sliding failure considered by Mitchell et al. (1982). A more representative

solution is needed to evaluate the stability and determine the minimum required cohesion of side-exposed backfill by considering the closure of rock walls

2.4.3 Other analytical solutions based on the wedge sliding model

Mitchell (1989) solution

Mitchell (1989) compared the by Mitchell et al. (1982) solution with some centrifugal model tests made on side-exposed fill with 28 curing days. It was found that Mitchell et al. (1982) solution largely overestimates the required strength of side-exposed backfill under the drained condition. Mitchell (1989) further proposed the following empirical solution to estimate the required UCS of a side-exposed backfill:

$$\text{UCS} = \frac{0.4 \gamma H \sin \beta}{1 + \frac{H}{L}} \tag{2.33}$$

where γ (kN/m^3) is the unit weight of the backfill; H (m), and L (m) are the height, and length of the side-exposed backfill; β (°) is the inclination angle of the backfill.

The Mitchell (1989) solution is empirical based on curve fitting with some centrifugal model test results. The equation is lack of clear physical meaning and its predictive capability needs to be verified with more tests or simulation results.

Li & Aubertin (2012) solution

Li & Aubertin (2012) proposed a modified version of Mitchell et al. (1982) solution (MM solution) by considering a surcharge P_0 (kPa) applied on the top of backfill, and a smaller cohesion for fill-rock interface c_i (kPa). Under a high aspect ratio condition (HAR, $H > L \cdot \tan\alpha$, α (°) is the inclination angle of failure plane to the bottom and $\alpha = 45° + \phi/2$; H (m) and L (m) are backfill height and length), the sliding plane was considered within backfill while the formulations of MM solution for FS and required cohesion are given as:

$$\text{FS} = \frac{\tan \phi}{\tan \alpha} + \frac{2c}{\left[p_0 + (H - \frac{L \cdot \tan \alpha}{2})(\gamma - 2\frac{c_i}{B}) \right] \sin 2\alpha} \tag{2.34}$$

$$c = \frac{(p_0 + \gamma(H - \frac{L \cdot \tan \alpha}{2}))/2}{\left[\left(\text{FS} - \frac{\tan \phi}{\tan \alpha} \right) \sin 2\alpha \right]^{-1} + \frac{r_s(H - \frac{L \cdot \tan \alpha}{2})}{B}} \tag{2.35}$$

where ϕ (°) is the friction angle of backfill; c (kPa) is the cohesion of side-exposed backfill; r_s is the adhesion ratio of fill-rock interface ($r_s = c_i/c$) with a range of 0 to 1; γ (kN/m³) is the unit weight of backfill; B (m) is the width of backfill.

For the side-exposed backfill with a low aspect ratio (LAR, $H < L \cdot \tan\alpha$), Li and Aubertin (2012) assumed that the sliding plane in the backfill will reach the top surface rather than the back wall. In this condition, the MM solutions are given as:

$$\text{FS} = \frac{\tan\phi}{\tan\alpha} + \frac{2c}{\left[p_0 + H\left(\frac{\gamma}{2} - \frac{c_i}{L}\right)\right]\sin 2\alpha} \tag{2.36}$$

$$c = \frac{p_0 + (\gamma H)/2}{2\left[\left(\text{FS} - \frac{\tan\phi}{\tan\alpha}\right)\sin 2\alpha\right]^{-1} + \frac{r_s H}{B}} \tag{2.37}$$

The MM solution does not consider the frictional stresses along the remaining side walls.

Li (2014a) solution

Li (2014a) developed a generalized solution for determining FS and required cohesion of side-exposed backfill based on the solution proposed by Mitchell et al. (1982). The frictional stresses along the side walls and the bond strength on the back wall c_b ($= r_b \cdot c$, $0 \le r_b \le 1$) were considered. Arching solutions (Aubertin et al. 2003) were employed to calculate the horizontal stress within side-exposed backfill which thus allow a calculation of shear stresses along side walls. For stopes with a HAR, FS and the required cohesion c are calculated as:

$$\text{FS} = \frac{\tan\phi}{\tan\alpha} + \frac{2}{\sin 2\alpha}\left(\frac{p'}{c} - r_b \frac{H - L\tan\alpha}{L} - 2r_s \frac{\left(H - \frac{L \cdot \tan\alpha}{2}\right)}{B}\right)^{-1} \tag{2.38}$$

$$c = p'\left[\frac{2}{(\text{FS} - \tan\phi/\tan\alpha)\sin 2\alpha} + r_b \frac{H - L\tan\alpha}{L} + 2r_s \frac{\left(H - \frac{L \cdot \tan\alpha}{2}\right)}{B}\right]^{-1} \tag{2.39}$$

where parameter p' (kPa) is given as:

$$p' = \frac{B}{2K\tan\delta}\left\{\gamma - \frac{1}{L\tan\alpha}\left(\frac{\gamma B}{2K\tan\delta} - p_0\right) \times \left[exp\left(-\frac{2K\tan\delta}{B}(H - L\tan\alpha)\right) - exp\left(-\frac{2K\tan\delta}{B}H\right)\right]\right\} \tag{2.40}$$

where δ (°) ($= r_a \cdot \phi$, $0 \le r_a \le 1$) is the frictional angle of fill-rock interface; K is the earth pressure coefficient.

For stopes with a LAR, the FS and the required cohesion of a side-exposed backfill are given as:

$$FS = \frac{\tan \phi}{\tan \alpha} + \frac{2}{\sin 2\alpha} \left(\frac{p''}{c} - r_s \frac{H}{B} \right)^{-1} \tag{2.41}$$

$$c = p'' \left[\frac{2}{(FS - \tan \phi / \tan \alpha) \sin 2\alpha} + r_s \frac{H}{B} \right]^{-1} \tag{2.42}$$

where parameter p'' (kPa) is given as:

$$p'' = \frac{B}{2K\tan\delta} \left\{ \gamma - \frac{1}{H} \left(\frac{\gamma B}{2K\tan\delta} - p_0 \right) \times \left[1 - exp \left(-\frac{2K\tan\delta}{B} H \right) \right] \right\} \tag{2.43}$$

The above solutions for LAR stopes do not consider the tension cracks. In some cases, tension cracks can occur near the top of side-exposed backfill. Its depth H_t (m) can be calculated as:

$$H_t = \frac{2c}{\gamma \tan \left(45° - \frac{\phi}{2} \right)} \tag{2.44}$$

By considering this tension crack within side-exposed backfill under a LAR condition, the equations for FS and c are given as:

$$FS = \frac{\tan \phi}{\tan \alpha} + \frac{2}{\sin 2\alpha} \left(\frac{p'''}{c} - r_s \frac{H + H_t}{B} \right)^{-1} \tag{2.45}$$

$$c = p''' \left[\frac{2}{(FS - \tan \phi / \tan \alpha) \sin 2\alpha} + r_s \frac{H + H_t}{B} \right]^{-1} \tag{2.46}$$

where parameter p''' (kPa) is given as:

$$p''' = \frac{B}{2K\tan\delta} \left\{ \gamma - \frac{1}{H - H_t} \left(\frac{\gamma B}{2K\tan\delta} - p_0 \right) \times \left[exp \left(-\frac{2K\tan\delta}{B} H_t \right) - exp \left(-\frac{2K\tan\delta}{B} H \right) \right] \right\} \tag{2.47}$$

Li (2014a) recommended that the value of K in the solutions can be taken as the Rankine active earth pressure coefficient. It should be noted that using the arching solution can overestimate the horizontal stress in side-exposed backfill because the effect of removing a lateral wall on the stress redistribution is neglected. Meanwhile, in the arching solution, shear stresses along side walls are considered fully mobilized which is not valid when the cohesion of fill-rock interface is large.

Li (2014b) solution for side-exposed backfill containing a plug

Li (2014b) developed a new analytical solution to evaluate the stability of side-exposed backfill containing a plug pour. The plug pour has a thickness of H_p (m), a unit weight of γ_p (kN/m³), a cohesion of c_p (kPa), a friction angle of ϕ_p (°), The final pour has a height of H_f (m), a unit weight of γ (kN/m³), a cohesion of c (kPa), and a friction angle of ϕ (°). The friction angle of plug pour is

considered equal to that of the final pour while the cohesion of the plug pour was considered as a proportion of the final pour cohesion (i.e., $c_p = r_p c$, $r_p \geq 1$). The sliding plane was assumed having an inclination angle of $\alpha = 45° + \phi/2$. The elevation of the intersection between the sliding plane and back wall is H_s (m). The total height H (m) of side-exposed backfill can be calculated as $H = H_f + H_p$. The adhesions of interfaces of the side walls with the final pour and the plug pour are c_{if} ($c_{if} = r_{sf} c$, $0 \leq r_{sf} \leq 1$) and c_{ip} ($c_{ip} = r_{sp} c$, $0 \leq r_{sp} \leq 1$).

When the sliding plane extends within the plug pour, the net weight W_n (kN) of wedge block above the failure plane is expressed as:

$$W_n = p_0 BL + \left(\gamma B - 2c_{if}\right)H_f L + \left(\gamma_p B - 2c_{ip}\right)H'L \tag{2.48}$$

where p_0 (kPa) is a surcharge on the top surface of side-exposed backfill. H' (m) is given as:

$$H' = H_p - H_s - \frac{B \tan \alpha}{2} \tag{2.49}$$

The solutions for FS and the required cohesion c of final pour are given as:

$$\text{FS} = \frac{\tan \phi}{\tan \alpha} + \frac{2r_p c}{\left[p_0 + \left(\gamma - \frac{2r_{if}}{B}c\right)H_f + \left(\gamma_p - \frac{2r_{ip}r_p}{B}c\right)H'\right]\sin 2\alpha} \tag{2.50}$$

$$c = \frac{p_0 + \gamma H_f + \gamma_p H'}{\frac{2r_p}{(\text{FS} - \tan \phi/\tan \alpha)\sin 2\alpha} + 2r_{if}\frac{H_f}{B} + 2r_{ip}r_p\frac{H'}{B}} \tag{2.51}$$

In the case that the sliding plane interacts with the top of the plug pour, the net weight of the wedge block is expressed as:

$$W_n = p_0 BL + \left(\gamma B - 2c_{if}\right)H^*L + \left(\gamma_p B - 2c_{ip}\right)\frac{\left(H_p - H_s\right)^2}{2 \tan \alpha} \tag{2.52}$$

where H^* (m) is a parameter given as:

$$H^* = H_f - \frac{\left(L \tan \alpha - H_p + H_s\right)^2}{2L \tan \alpha} \tag{2.53}$$

The formulations for FS and c in this condition are:

$$\text{FS} = \frac{\tan \phi}{\tan \alpha} + \frac{c}{\sin^2 \alpha}\frac{\tan \alpha + (r_p - 1)\frac{H_p - H_s}{L}}{p_0 + \left(\gamma - \frac{2r_{if}}{B}c\right)H^* + \left(\gamma_p - \frac{2r_{ip}r_p}{B}c\right)\frac{\left(H_p - H_s\right)^2}{2L \tan \alpha}} \tag{2.54}$$

$$c = \frac{p_0 + \gamma H^* + \gamma_p \frac{(H_p - H_S)^2}{2L \tan \alpha}}{\frac{\tan \alpha + (r_p - 1)\frac{H_p - H_S}{L}}{(FS - \tan \phi / \tan \alpha) \sin^2 \alpha} + \frac{2}{B}\left[r_{if}H^* + r_{ip}r_p\frac{(H_p - H_S)^2}{2L \tan \alpha}\right]}$$ (2.55)

The required cohesion is affected by the ratio of plug pour cohesion to the final pour cohesion r_p. For the backfill design with a given backfill geometry, the required cohesion for the final pour and plug pour can be determined be following 3 steps as recommended by Li (2014b): 1. calculating the minimum required cohesion of final pour with Eq. (2.55) by considering $H_p = H_s$; 2. determining the optimal value of r_p by using Eq. (2.50) with $H_s = 0$ and Eq. (2.54) with $H_s = H_p$; 3. calculating the minimum required cohesion of plug pour by using the optimal r_p. Li (2014b) solution is an improved version of MM solution. However, this solution is not applicable for stops with a LAR. The frictional stresses along fill-walls interface are not considered which makes it conservative.

Li & Aubertin (2014) solution

Li & Aubertin (2014) investigated the stability of side-exposed backfill with FLAC^{3D}. Numerical results of displacement and corresponding vectors of a side-exposed backfill are shown in Figure 2.15. The triangular block at the lower part of sliding wedge tends to move along the sliding plane while the upper block of backfill tends to move vertically downwards. Based on the equilibrium state of lower and upper part of wedge block, Li & Aubertin (2014) proposed a new analytical solution for FS and required cohesion c of side-exposed backfill as:
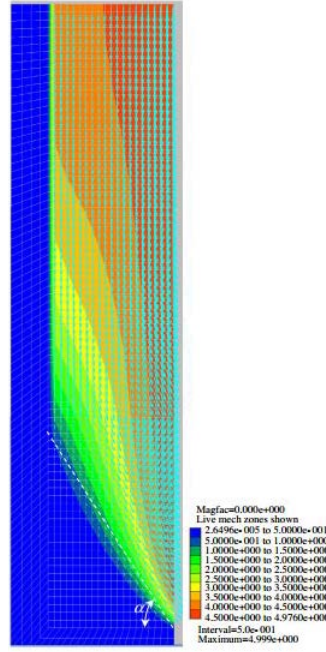
Figure 2.15: Numerical results of displacement and corresponding vectors of a backfilled stope upon side exposure obtained with FLAC^{3D} (reproduced of Li & Aubertin 2014 with permission)

$$\text{FS} = \frac{\tan\phi}{\tan\alpha} + \frac{c\left(\frac{1}{\cos\alpha}+r_s\frac{H'}{B}\right)+\frac{(\gamma/M-p_1)\left[\frac{(1-exp(-MH'))}{MH'}-1\right]+\gamma H'/2}{1+B/L}}{(p_1+\gamma H'/2)\sin\alpha} \tag{2.56}$$

$$c = \frac{D'(p_0+\gamma(H-H')-G')+\frac{\gamma A'H'}{2}\left(1+\frac{B}{L}\right)\sin\alpha-\gamma\left(\frac{C'}{M}+\frac{H'}{2}\right)}{B'\left(1+\frac{B}{L}\right)+D'(H-H')\left(\frac{2r_s}{B}+\frac{r_b}{L}\right)} \tag{2.57}$$

where γ (kN/m^3) is the unit weight of backfill; H (m), L (m), and B (m) are the height, strike length and width of backfill respectively; r_s is the adhesion ratio of interface along the side walls; r_b is the adhesion ratio of interface along the back wall. p_0 is a surcharge on the top surface of backfill. Other parameters of p_1 (kPa), G' (kPa/m), A', B', C', D', H' (m), M (m^{-1}) in the equations are given as:

$$p_1 = p_0 + (H - H')\left[\gamma - c\left(\frac{2r_s}{L} + \frac{r_b}{B}\right)\right] \tag{2.58}$$

$$G' = \frac{1}{1+L/B}\left[\gamma(H-H') + \left(p_0 - \frac{\gamma}{M}\right)\left(1 - exp(-(H-H')M)\right)\right] \tag{2.59}$$

$$A' = \text{FS} - \frac{\tan\phi}{\tan\alpha} \tag{2.60}$$

$$B' = \frac{1}{\cos \alpha} + r_s \frac{H'}{L} \tag{2.61}$$

$$C' = \frac{1 - exp(-MH')}{MH'} - 1 \tag{2.62}$$

$$D' = A' \left(1 + \frac{B}{L}\right) \sin \alpha + C' \tag{2.63}$$

$$H' = L \tan \alpha \tag{2.64}$$

$$M = 2K(L^{-1} + B^{-1}) \tan \delta \tag{2.65}$$

where K is the earth pressure coefficient and its value was recommended as Rankine's active earth pressure coefficient; δ (°) is the friction angle of fill-rock interface ($\delta = r_a \cdot \phi$, $0 \leq r_a \leq 1$).

Li & Aubertin (2014) conducted numerical modeling of a side-exposed backfill with cohesions of 0, 10, 20, 30 kPa. By evaluating the iso-counter of total displacement in side-exposed backfill, Li & Aubertin (2014) determined that the minimum required cohesion of backfill is between 20 to 30 kPa. This verified their proposed solution which predicts a value of 22.04 kPa.

Yang et al. (2017) solution considering the tension crack

By considering the tensile crack around the top surface in wedge model. Yang et al. (2017) developed an analytical solution to estimate the FS and required cohesion c of side-exposed backfill as:

$$FS = \frac{\tan \phi}{\tan \alpha} + \frac{2}{\sin 2\alpha} \left(\frac{p}{c} - \frac{H_t}{L_t} - r_s \frac{2H - L_t \tan \alpha}{B}\right)^{-1} \tag{2.66}$$

$$c = p \left[\frac{2}{(FS - \tan \phi / \tan \alpha) \sin 2\alpha} + \frac{H_t}{L_t} + r_s \frac{2H - L_t \tan \alpha}{B}\right]^{-1} \tag{2.67}$$

where H_t (m) is the depth of tension crack and L_t (m) is the distance from front face to the tension crack. The formulations for H_t, L_t and the parameter p (kPa) are given as:

$$H_t = \frac{2c}{\gamma \tan\left(45° - \frac{\phi}{2}\right)} \tag{2.68}$$

$$L_t = \frac{H - H_t}{\tan \alpha} \tag{2.69}$$

$$p = \frac{B}{2K tan\delta} \left\{\gamma - \frac{1}{L_t \tan \alpha} \left(\frac{\gamma B}{2K tan\delta} - p_0\right) \times \left[exp\left(-\frac{2K tan\delta}{B} H_t\right) - exp\left(-\frac{2K_a tan\delta}{B} H\right)\right]\right\} \tag{2.70}$$

Yang et al. (2017) solution has the similar form as the Li (2014a) solution when the tension crack is considered. Yang et al. (2017) verified their analytical solutions by comparing with some numerical results of the minimum required cohesion using FLAC^{3D}.

Liu et al. (2018) solution considering pressures on the back wall of backfill

In open stoping mining, uncemented backfill can be used to fill the extracted secondary stope. Due to the mining sequence, some primary stopes filled with cemented backfill can connect with an uncemented backfill and expose on the opposite side. In this condition, the stability of side-exposed backfill can be affected by the pressure on its back wall caused by the uncemented backfill. Liu et al. (2018) proposed an analytical solution to calculate the FS and required cohesion c of side-exposed backfill in this condition:

$$\text{FS} = \frac{cLB/\cos\alpha + [Y + 2S_s \sin\phi]\tan\phi}{Z - 2S_s \cos\phi} \tag{2.71}$$

$$c = \frac{Z\cos\phi - Y\sin\phi - 2X}{LB\frac{\cos\phi}{\cos\alpha} + 2LH^* r_s} \tag{2.72}$$

where H^* (m) is the equivalent height of the wedge block; L (m) and B (m) are strike length and width of the cemented backfill respectively; ϕ (°) is the friction angle of backfill; α (°) is the inclination angle of failure plane to the bottom and is calculated as $\alpha = 45° + \phi/2$; r_s is the adhesion ratio of interface along the side walls with a range of 0 to 1; S_s (kPa) is the shear strength along the side walls; Equations for H^*, S_s, and parameters of X, Y, and Z are given as:

$$H^* = H - \frac{L\tan\alpha}{2} \tag{2.73}$$

$$S_s = LH^* r_s c + X \tag{2.74}$$

$$X = \frac{LB}{2}\left[\gamma H^* - \left(\frac{\gamma L}{2K\tan\delta} - p_0\right)\right] + \frac{B^2}{4K\tan\alpha\tan\delta}\left(\frac{\gamma B}{2K\tan\delta} - p_0\right)\left(exp\left(\frac{-2K\tan\delta}{B}H'\right) - exp\left(\frac{-2K\tan\delta}{B}H\right)\right) \tag{2.75}$$

$$Y = W'\cos\alpha - P_b\sin\alpha \tag{2.76}$$

$$Z = W'\sin\alpha + P_b\cos\alpha \tag{2.77}$$

where H (m) is the full height of the cemented backfill; γ (kN/m^3) is the unit weight of the cemented backfill; p_0 (kPa) is a surcharge on the top surface of backfill; K is the earth pressure coefficient; δ (°) is the friction angle of fill-rock interface along the side walls; H' (m) is the height of wedge

block on the back wall; W' (kN) is the effective weight of the wedge block; P_b (kN) is the force acting on the back of backfill due to uncemented backfill. The formulations for H', W', and P_b are given as:

$$H' = H - L \tan \alpha \tag{2.78}$$

$$W' = (\gamma H^* + p_0)BL \tag{2.79}$$

$$P_b = \frac{1}{2}\gamma_u B(H - L \tan \alpha)^2 \tag{2.80}$$

where γ_u (kN/m^3) is the unit weight of the uncemented backfill.

The comparison between the Liu et al. (2018) solution and numerical results of minimum required cohesion obtained using FLAC^{3D} generally shows good agreement. The analytical solution tends to overestimate the required cohesion for side-exposed backfill when its height exceeds 40 m or the width is smaller than 8 m. The calculation of horizontal stresses on side walls in the Liu et al. (2018) solution is based on the arching solution (Aubertin et al. 2003; Li et al. 2014a) which may be inaccurate because the stress redistribution due to removal of the front wall is not considered. The assumption that the shear resistances along side walls are fully mobilized is not applicable when the backfill has large cohesion.

Dirige et al. (2009) solution for inclined side-exposed backfill

Dirige et al. (2009) modified the Mitchell et al. (1982) solution to calculate the FS of inclined side-exposed backfill. The wedge sliding model used by Dirige et al. (1982) is schematically shown in Figure 2.16. In the figure, H (m), L (m), and W (m) are the height, strike length and width of backfill respectively; β (°, $\beta \leq 90°$) is the stope inclination angle; ϕ (°) is the friction angle of backfill; c (kPa) is the cohesion of side-exposed backfill; the intersection lines of footwall and sliding plane and the bottom make an angle of α (°, $\alpha = 45° + \phi/2$); H^* (m) is the equivalent height of the sliding wedge ($H^* = H - L\tan\alpha/2$). The resistance along hanging wall was not considered when β is less than 90°.
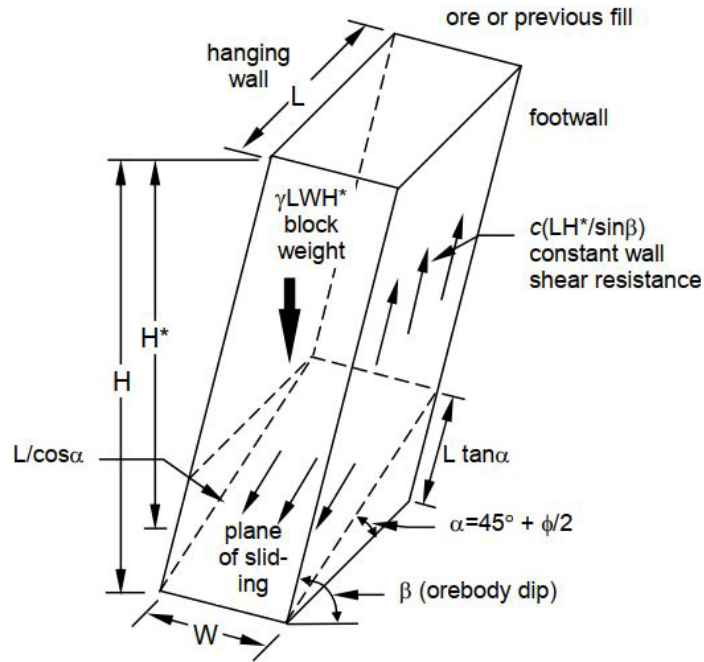
Figure 2.16: Wedge sliding model for inclined side-exposed backfill (reproduced of Dirige et al. 2009 with the permission of Dr. Philip Dirige)

When the rock wall is smooth, the bond strength along footwall is neglected, and the equation of FS is:

$$FS = \frac{\tan\phi}{\tan\alpha} + \frac{c\frac{L}{\cos\alpha}W}{F_V\sin\alpha} + \frac{\cos\beta\tan\phi}{\sin\alpha} \tag{2.81}$$

where F_V (kN) is the net weight of the sliding wedge and its equation is:

$$F_V = (\gamma WLH^*) - (\gamma WLH^* \cos\beta \tan\phi) \tag{2.82}$$

When the rock walls are rough, both friction stress and bond strength along footwall are considered, and the equation of FS is expressed:

$$FS = \frac{\tan\phi}{\tan\alpha} + \frac{c\frac{L}{\cos\alpha}W}{F_V\sin\alpha} + \frac{\cos\beta\tan\phi}{\sin\alpha} + \frac{cL\frac{H^*}{\sin\beta}}{F_V\sin\alpha} \tag{2.83}$$

where F_V in this condition is given as:

$$F_V = (\gamma WLH^*) - \left(\gamma WLH^* \cos\beta \tan\phi + cL\frac{H^*}{\sin\beta}\right) \tag{2.84}$$

The above equations only apply for $\beta < 90°$. For vertical backfill, the resistances along both hanging wall and footwall are considered and the equations for FS and F_V become:

$$\text{FS} = \frac{\tan\phi}{\tan\alpha} + \frac{c\frac{L}{\cos\alpha}W}{F_V\sin\alpha} + \frac{2\cos\beta\tan\phi}{\sin\alpha} + \frac{2cL\frac{H^*}{\sin\beta}}{F_V\sin\alpha} \tag{2.85}$$

$$F_V = (\gamma WLH^*) - \left(2\gamma WLH^*\cos\beta\tan\phi + 2cL\frac{H^*}{\sin\beta}\right) \tag{2.86}$$

Dirige et al. (2009) solution is an improved form of the solution proposed by Mitchell et al. (1982) which can be applied on inclined condition. However, the equations for F_V developed by Dirige et al. (2009) are not accurate without considering the equilibrium state of sliding wedge along different directions. The normal forces acting on the backfill from the footwall is not accounted. Neglecting the resistance along hanging wall can also be inaccurate when the inclination angle is large (close to the subvertical condition). The has been shown by Chai (2020) though numerical modeling with FLAC*3D*. Moreover, Dirige et al. (2009) solution inherits some limitations of the Mitchell et al. (1982) model including that it only applies to stopes with a HAR while the surcharge on the top of backfill is not considered.

2.4.4 Numerical simulations of side-exposed backfill

Analytical solutions for evaluating the stability of side-exposed backfill are useful in practice due to its simplicity and ability to investigate different influential factors. However, analytical solutions suffer from significant limitations resulted from simplifying assumptions. Compared to analytical solutions, numerical modeling is a powerful and efficient method. Some previous studies on the stability of side-exposed backfill using numerical simulations are reviewed in this subsection.

Cundall et al. (1978) used a three-dimensional finite difference program to study the stability of vertical side-exposed backfills. The in-situ stress condition equivalent to a depth of 1200 m in the Canadian Shield was considered. Both the rock and backfill obey the Mohr-Coulomb criterion with a tension cut-off. It was reported that when the mechanical properties of hydraulic fill with a cement to tailings ratio of 1:30 was applied, the stability is governed by gravity. However, for the cemented rock fill, the instability upon side exposure is controlled by walls deformation associated with the pillar extraction. This can be explained as that the cemented rock fill used in numerical simulation

with a Young's modulus of 2.1 GPa is much stiffer than the cemented hydraulic fill with a Young's modulus of 0.25 GPa. Therefore, the cemented rockfill is more prone to be crushed.

Coulthard & Dight (1980) reported a case study about numerical simulations of a failed side-exposed backfill at ZC/NBHC mine. The backfill has a height of 49 m, a length of 13 m and was cured for more than one year before exposure. The 2D finite program TNJTEP was used for simulation. The rock mass was omitted and side exposure was modelled by freeing boundary restriction along one side of fill. Shear strengths of backfill with different curing days including 50, 224, and 700 days were applied to reproduce the failure of side-exposed backfill. It was found that the simulation with 50-day fill strength was most consistent with the field observation, and a factor of safety of 1.5 on fill cohesion was thus suggested. The differences between the numerical results and field observations may partially be explained by the neglection of rock-wall closure associated with the adjacent extraction.

Coulthard (1980) analyzed the stability of side-exposed backfill with a height of 60 m using a three-dimensional finite element program NONSAP. The surrounding rock mass was not constructed while the cemented backfill was modeled with the linear elastic model. The convergence of rock walls due to adjacent extraction was modeled by applying inward horizontal movement with different values of 20 and 100 mm on backfill. The applied rock-wall convergence has a maximum value at the mid-height of the backfill and linearly decreases along the height reaching a nil value at the top and bottom. The convergence also linearly increases along the length of backfill from zero at the back wall to the maximum value at the front wall. Coulthard (1980) reported that numerical results by considering 20 mm closure are similar to those in which side walls are fixed. A closure of 20 mm was found slightly reducing the tensile stresses in backfill around side and back walls. When a closure of 100 mm was applied, the volume of overstress in backfill significantly increases which indicates a deep-seated failure. Coulthard (1980) used the linear elastic model to analyze the stresses distribution within backfill which can be inaccurate because the yield under large shear stress condition was not considered. The minimum required cohesion of backfill was not analyzed. Using the volume of overstress area as an instability criterion can be subjective since there is not a limiting value. Moreover, the linearly distributed convergence along walls can be different from reality in which rock-wall closure due to stope extraction is nonlinear and affected by other factors such as mine depth, in-situ stress, and rock mass properties.

Pierce (1999) investigated the stability of side-exposed backfill using FLAC^{3D} by considering the rock-wall closure due to excavating a new stope. The surrounding rock mass was built as thin elements around backfill. The rock-wall closure was achieved by setting small inward velocity for side walls. Pierce (1999) used the yield state and convergence of the numerical model to determine the instability of backfill. It was reported that a rock-wall closure of 0.33% strain increases the stability of side-exposed backfill by increasing the normal and shear stresses along side walls. However, applying a rock-wall closure of 2% strain causes the shear failure of open face backfill. This study has similar limitations as the numerical model of Coulthard (1980). The uniformly distributed rock-wall closure along side walls is not in accordance with the reality. The minimum required cohesion of side-exposed backfill was not investigated while the influence of other factors such as mine depth and rock mass properties on the results were not studied.

Sainsbury & Urie (2007) performed numerical simulations with FLAC^{3D} to analyze the stability of narrow backfill upon side and base exposures at Raleigh mine. The stope has a height of 16.5 m, a width of 2.5 to 3.5 m and a strike length of 15 m. Linear elastic model was applied for the rock mass while the Mohr-Coulomb model with strain softening was used for the cemented backfill. Sainsbury & Urie (2007) used the extent of yielding area as the instability criterion. The conditions of exposed backfill were divided to be no yielding, minor yielding, significant yielding, crushing failure, and caving failure. It was reported that the stability of exposed backfill with a width of 3.5 m is governed by tensile failure when its UCS is smaller than 70 kPa. As the rock walls convergence increases, the required UCS for exposed backfill increases to prevent the crushing failure. However, Sainsbury & Urie (2007) reported that a fill UCS larger than 275 kPa will not further increase the stability against the crushing failure because of the increase in elastic modulus. It should be noted that modeling the rock mass as linear elastic material is inaccurate because the rock mass around stopes can yield due to large induced stresses. The effects of different mine depths, stope geometries, mechanical properties of backfill and rock mass on the stability of exposed backfill were not studied by Sainsbury & Urie (2007).

Emad et al. (2012, 2014) investigated the influence of blasting vibration due to adjacent mining on the stability of backfill by conducting three-dimensional dynamic numerical modeling with FLAC^{3D}. It was found that blasting in an adjacent stope can result in the wedge failure initiating from the top of side-exposed backfill shown by the tensile stress development. The maximum total

velocity was detected in these tensile stress areas. This is different from the commonly applied wedge sliding model which predicts a sliding block around the bottom of the backfill. By further comparing with static analysis results, Emad et al. (2012, 2014) reported that using the static limit equilibrium method can underestimate the required strength of side-exposed backfill. It was also reported that the yielding of side-exposed backfill can be reduced by decreasing the peak blasting load.

Karim et al. (2013) evaluated the stability of side-exposed backfill at Kencana underground gold mine using a distinct element method (DEM) 3DEC. Figure 2.17 shows the numerical model. The extracted stope has a width of 16 m, a strike length of 35 m, and a height of 20 m while it is surround by cemented backfill on west, north, and south sides. Mechanical properties of cemented backfill with cement contents of 6%, 12%, and 14% under a curing time of 7 days were used in numerical simulations. The instability of backfill was evaluated by analyzing the maximum horizontal and vertical displacements on the open face. However, this instability criterion is unclear because Karim et al. (2013) did not provide the limiting value of displacement. For instance, the west open face was concluded stable with a cement content of 14% for a horizontal displacement of 2.5 cm. As the cement content reduces to 6%, the horizontal displacement increases to 7.01 cm and the open face was considered instable without much explanations.
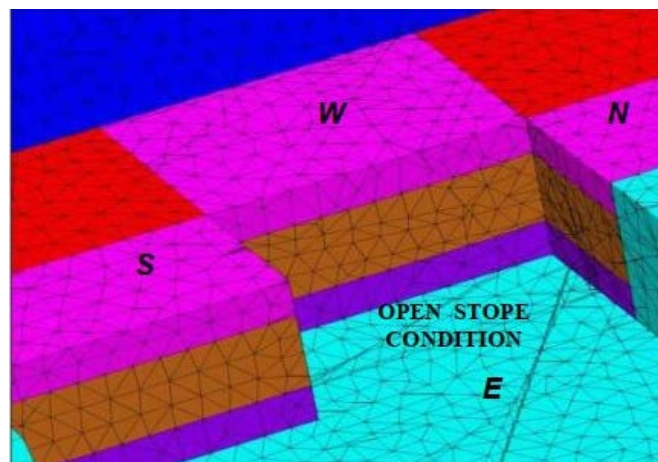
Figure 2.17: DEM model of cemented backfill exposed on west, north and south faces
(reproduced of Karim et al. 2013 with permission)

Falaknaz (2014) analyzed the stability of backfill with a vertical open face using FALC^{3D}. The primary and secondary stopes locate at a mine depth of 300 m. The surrounding rock mass was

modeled as the linear elastic material while the cemented backfill obeys the Mohr-Coulomb model. The effect of different stope geometries and mining sequences on the stability of side-exposed fill was investigated. By evaluating the stress distribution within backfill before and after removing the secondary stope, Falaknaz (2014) reported that the horizontal stresses in backfill increase due to adjacent extraction. This can be understood as that excavating a pillar leads to the rock-wall closure which compresses the backfill. Falaknaz (2014) further determined the minimum required cohesion of side-exposed backfill by evaluating the displacement and strength-stress ratio. Numerical results of displacement contours of stable and unstable backfills are illustrated in Figure 2.18. However, one should note that displacement is not an objective instability criterion because it does not have a limiting value. The linear elastic model can not capture the yielding of rock mass under large induced stress condition. This aspect accompanying with a small mine depth of 300 m caused that the rock-wall closure is small and only the sliding failure of backfill occurred. As the mine depth becomes large and the rock-wall closure increases due to yielding of rock mass, the backfill can be crushed upon side exposure due to significant compression which was not addressed by Falaknaz (2014). Moreover, the effects of in-situ stress, properties of backfill and rock mass on the minimum required cohesion were not studied.
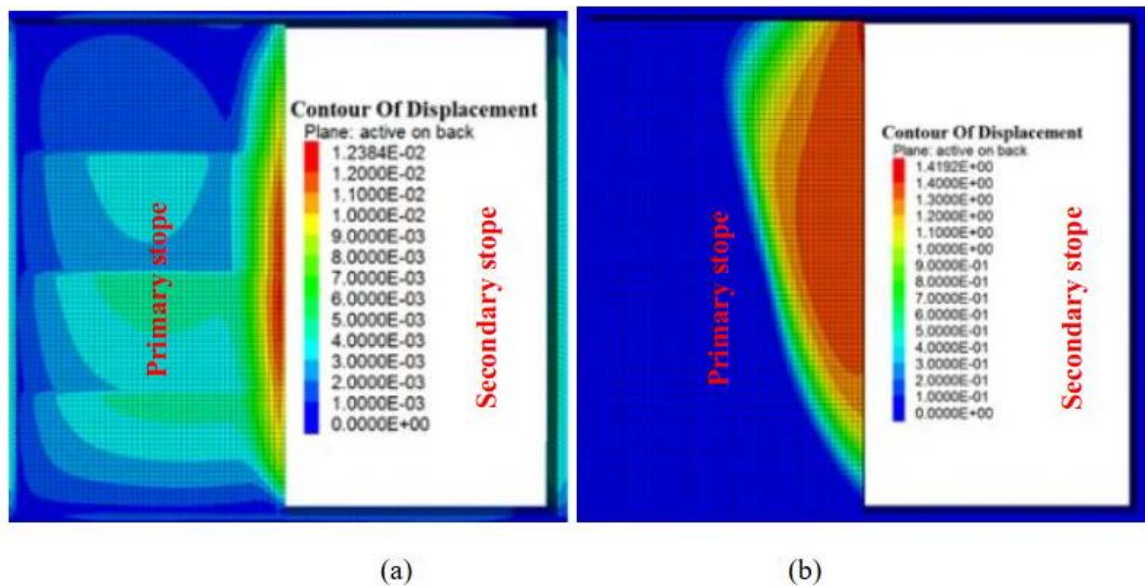
Figure 2.18: Displacement contours of side-exposed backfill under (a) stable and (b) unstable conditions (reproduced of Falaknaz 2014 with the permission of Dr. Nooshin Falaknaz)

2.5   Challenges for deep underground mines

Underground mining is advancing towards large depth since shallow mineral resources are becoming exhausted (Brown 2012; Counter 2014; Ranjith et al. 2017; Wagner 2019; Xie et al. 2019). For example, Kidd Creek mine in Canada, as one of the deepest metal mines in the world, has reached an underground level of 3000 m (Counter 2014). Nickel Rim South Mine in Sudbury has extended to a depth of 1710 m below ground surface (Jalbout & Simser 2014). The mine depth of Tau Tona gold mine in South Africa is reported to be over 4000 m (Fairhurst 2017). In United States, Lucky Friday mine reaches a depth of over 2000 m (Seymour et al. 2017). Moreover, there have been around 47 coal mines in China having a mine depth of over 1000 m (Xie et al. 2019).

Compared to shallow mining, deep mining is conducted in rock mass characterized by high in-situ stresses. The high in-situ stresses are dominant factor related to severe rock mechanics challenges including rock burst (seismic events), large creep deformation and squeezing conditions (Malan & Basson 1998; Nordlund 2013; Anderson 2014; Ranjith et al. 2017). Rockburst is a form of rock rupture usually accompanied with projection of broken rock. On account of its violence and suddenness, rockburst in deep mines is dangerous and threatens the safety of miners and equipment (Ortlepp 2005; Durrheim & Riemer 2012).

Rock mass in deep mines can demonstrate significant time-dependent creep deformation (Malan et al. 1997; Malan 1999). Creep deformation can also occur at a shallow depth for weak rock (Bonini et al. 2009; Barla et al. 2010). Guler (1998) reported a stope closure rate of 10 mm/day at East Driefontein Mine and a creep rate of 5 mm/day at Deelkraal Mine in South Africa. Raffaldi et al. (2019) monitored time-dependent closure of stope which resulted in an increase of stresses in the backfilled stope after a blasting at Luck Friday Mine. Excessive creep deformation of rock mass can thus affect the interactions between backfill and rock walls (Malan 2002; Paraskevopoulou & Diederichs 2018; Qi & Fourie 2019).

In addition to above challenges of rockburst and creep of rocks, deep mining also has risks due to high temperature, long distance of transportation and ventilation, and management. Theses risks tend to increase the overall mining cost. Therefore, when estimating the required strength of side-exposed backfill, mine depth and complex geomechanical performance of rock mass such as its long-term creep deformation should be considered.

2.6 Creep behavior of rocks

Creep is a time-dependent behavior of rock, by which the rock submitted to a constant load (but below its peak strength) exhibits a continuous deformation. It can take place accompanied with micro seismic activities (Griggs 1939; Hardy et al. 1969).

The creep of rocks can be attributed to pressure solution, dislocations in crystalline structures, diffusion mechanism, and propagation of micro cracks. Pressure solution is a transfer process of material governed by chemical erosion. It reflects dissolution of minerals at the grain boundary under relatively high stress and deposition in areas of low stress (McClay 1977; Green 1984). The dislocation creep is due to the movement of weak bond within crystal lattice of crystalline rocks. Diffusion creep is initially investigated for metals which is then adapted to the field of rock creep behavior. All rocks contain vacancies on the atomic scale such as pores and impurities. With an applied stress or/and a relatively high temperature, the diffusion of vacancies through crystal lattice and the closure of pores can occur resulting in creep strain. The magnitude of diffusion creep strain rate is usually minor (lower than 10^{-9}/s) (Ohring 1995; Weijermars et al. 1997). The evidence of diffusion creep on rocks has been provided by many researchers who conducted long-term creep tests under small stress level (0.1 to 2.5 MPa) lasting months to decades (Ito 1991; Bérest et al. 2015; Nopola and Roberts 2016). The long-term creep tests under small stress level also indicate that diffusion creep of rocks almost has no stress threshold and will not lead to the failure. On the other hand, when the applied stress state exceeds a threshold value, micro cracks propagate. This propagation of micro cracks is the origin of the acoustic emission (AE) activities. This is thus a mechanism responsible for the creep behavior of rocks under a stress lower than its peak strength but higher than a threshold (Freiman, 1984; Damjanac & Fairhurst 2010). The rate of creep is governed by the rate of crack propagation. The threshold value of stress is known as the crack initiation threshold (CIT). Its value can be determined from the start of deviation of the axial stress-radial strain curve from the linearity, start of acoustic emission, or start of dilation (Aubertin et al. 2000; Diederichs et al. 2004; Li et al. 2017). When the applied stress is sufficiently large, the micro cracks within rocks can develop, coalesce, and lead the rock to rupture.

Most rocks have a more or less degree of creep. It has been observed in many experimental tests (Obert et al. 1946). Soft rocks usually demonstrate more obvious creep phenomenon (more creep

strain) than hard rocks (Cristescu & Hunsche 1998). However, creep of hard rocks can also be significant under high stress conditions. The long-term creep deformation has been observed in many rock structures such as tunnels, dams and slopes (Ladanyi and Gill 1988; Chang et al. 2015; Paraskevopoulou & Diederichs, 2018). In underground mines, the redistributed stresses around excavations can result in the creep of surrounding rock walls after the instantaneous deformation (Malan et al. 1997; Malan 1999). Figure 2.19 illustrates the significant rock-wall creep deformation in a drift at a Quebec mine. In the figure, one can see that excessive deformation due to creep reduces the cross section of drift.

Figure 2.19: Time-dependent creep deformation of rock mass around a drift at a Quebec mine (photo from personal collection of Li Li)

For a backfilled stope, the long-term creep deformation of rockwalls can compact and generate stresses within the fill that influences its stability upon exposure (Guler1998; Raffaldi et al., 2019). Therefore, it is necessary to understand creep behavior of rocks and incorporate it in the stability analyses of side-exposed backfill.

2.6.1 Characteristics of rock creep behavior

The main influential factors for rock creep behavior (creep strain rate) are the magnitude of stress and temperature while it can also be affected by the humanity and chemical active substance in initial cracks of rocks. When a rock specimen is subjected to a maintained stress condition, Farmer (2012) proposed three types of creep strain-time curve as:

(a) If the maintained stress is above the critical crack density level, unstable cracks will rapidly develop leading to the failure of the specimen;

(b) If the stress is well below the critical crack density level, creep strain is slow with a decaying rate. Micro cracks are stable and the specimen will not fail;

(c) If the maintained stress is in the intermediate zone, just below the critical crack density level, micro cracks will continually grow leading to the failure of rock specimen.

Figure 2.20 shows typical creep strain and creep strain rate curve of rocks. From the figure, one can see that a rock subjected to a constant load exhibits an instantaneous deformation, followed by creep deformation. A typical creep strain-time curve of rock is composed of three stages, including:

(1) Primary (transit) creep stage: the creep strain increases with a continuously declined rate;

(2) Secondary (steady) creep stage: the creep strain almost linearly increases with a constant strain rate;

(3) Tertiary (accelerating) creep stage: the creep strain increases with an accelerating rate leading to the failure of rock.

The secondary creep stage is usually associated with long-term deformation of rocks. The duration of each creep stage is affected by the applied stress and the properties of rocks. The tertiary creep stage is sometimes absent for ductile rock such as rock salt even after a very long creep period. For hard rocks, the creep strain rate can be small that the secondary creep stage seems to be absent (Lockner, 1993).
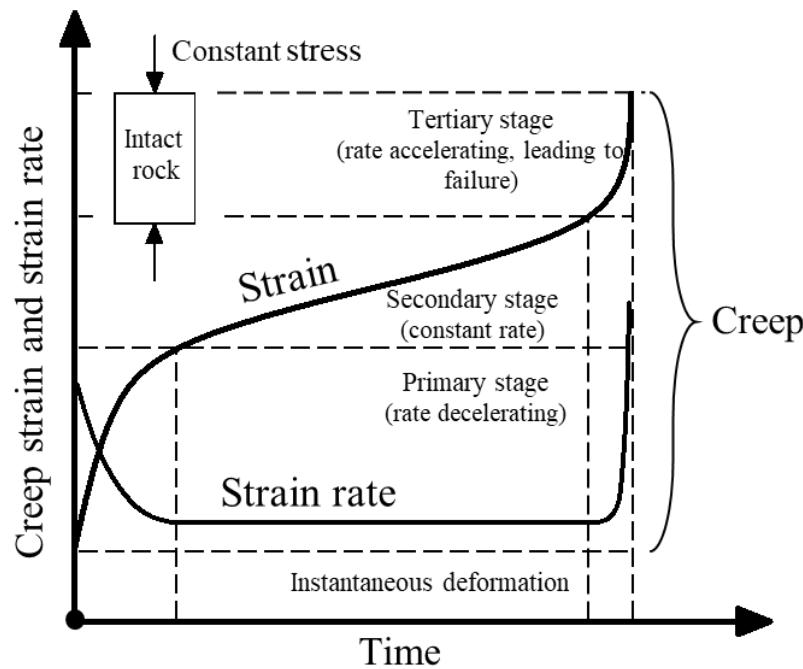
Figure 2.20: A schematic presentation of typical creep strain-time and creep strain rate-time curves of rock (reproduced of Wang et al. 2019 with permission)

The CIT is an important stress value below which no cracks are considered extending. The time-dependent deformation of rocks under a stress lower than CIT is associated with diffusion creep which can be described by the visco-elasticity (Ito 1991; Aydan et al. 2014). The creep behavior of rocks under a stress larger than CIT is due to the propagation of micro cracks (Maranini & Yamaguchi 2001; Damjanac & Fairhurst 2010; Wang et al. 2019; Yang et al. 2021). In order to identify the mechanism of rock creep behavior, the CIT must be determined by analyzing the deviation of axial stress-radial strain curve from linearity, start of acoustic emission or dilation. The CIT can also be roughly estimated by using a ratio to the short-term strength of rocks. The ratio typically ranges from 30–70 % for low porosity rock which is sometimes simplified as 50% (Lajtai & Schmidtke 1986; Aubertin et al. 2000).

Ngwenya et al. (2001) conducted triaxial creep tests on sandstones under different confining stresses with room temperature. Figure 2.21 shows an example of variations of the steady creep strain rate as a function of differential stress under confining pressures of 20.7, 27.6, and 34.6 MPa, respectively. From the figure, one can see that the creep strain rate increases as the differential stress increases. Conversely, the secondary creep strain rate decreases with the increase of

confining pressure. Similar phenomenon was reported by Heap et al. (2009, 2011) and Brantut et al. (2012) on westerly granite and Etan basalt. Ngwenya et al. (2001) further showed that the positive relationship between the creep strain rate and differential stress can be represented by a power law formulation. However, they did not mention how confining pressure be considered in creep model.
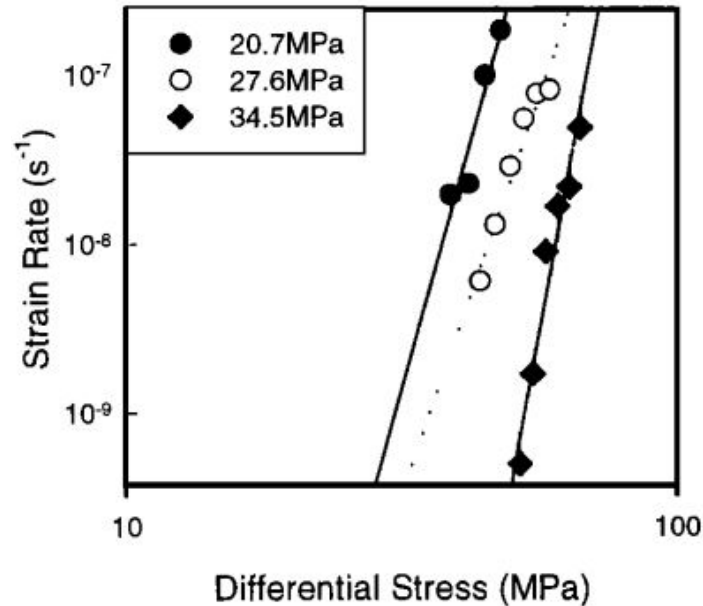
Figure 2.21: Variation of steady creep strain rate of sandstone as a function of differential stress under different confining pressures (reproduced of Ngwenya et al. 2001 with permission)

Hao et al. (2017) conducted creep tests on granite and marble at room temperature and room humidity. During the experiments, the delayed failure time and steady (secondary) creep rate were recorded. The results show that the average creep deformation rate (equals to the ratio of total creep deformation and total measured time) demonstrates a common power-law relationship with the creep strain rate in the steady creep stage. It tends to suggest that with the increase of creep strain rate, rocks will have shorter time to reach the final failure. It should be noted that, however, Hao et al. (2017) did not consider the effect of confining pressure on the results.

Lajtai & Schmidtke (1986) conducted uniaxial creep tests on granite and anorthosite. Their results showed that the tertiary creep stage of rocks does not happen unless the applied stress exceeding the long-term strength of rocks. It was found that the long-term strength can be less than 60% of the instantaneous strengths of rocks. Similarly, Paraskevopoulou et al. (2018) performed a series

of creep tests on Jurassic and Cobourg limestones under the unconfined condition. A total of 17 rock samples were tested under different stress levels above CIT until the failure. Figure 2.22 shows the variation of time to failure for different driving stress ratios which are the ratio between applied stress to UCS. The time to failure of rocks decreases with the increase of applied stress. These results are in accordance with the conclusions of Hao et al. (2017) because that a larger stress level also results in a larger creep strain rate. Paraskevopoulou et al. (2018) recommended a logarithmic function to describe the time to failure based on curve fitting as shown in Figure 2.22. The tests of Lajtai & Schmidtke (1986) and Paraskevopoulou et al. (2018) are all under unconfined condition while the effect of confining pressure and friction angle on the time to failure of rocks was not investigated.
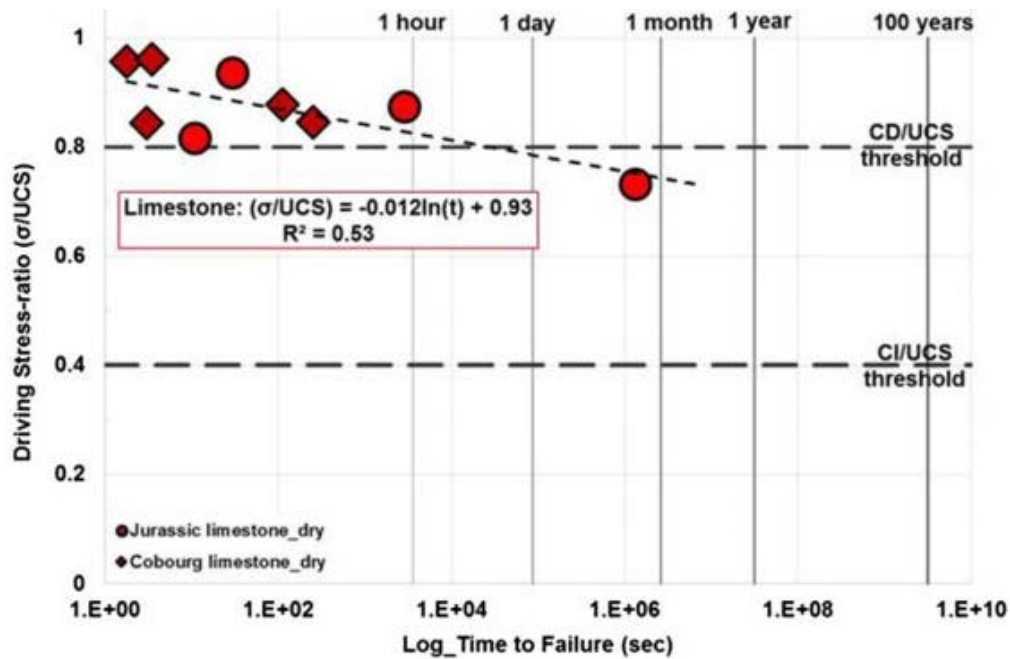
Figure 2.22: Variation of time to failure a function of driving stress ratio (reproduced of Paraskevopoulou et al. 2018 with permission)

Kranz (1980) investigated the effects of confining pressure and deviatoric stress on the time to failure of Barre granite. Confining pressures including 0.1, 55, 101, and 198 MPa were applied. The maintained load for the creep tests were set as 75 to 90% of the short-term strength at the corresponding confining pressures. The results show that the time to failure of rocks decreases with the increase of applied deviatoric stress which agree with most uniaxial creep tests. Meanwhile,

the time to failure significantly increases with the increase of confining pressure. For instance, a deviatoric stress of around 200 MPa leads to a time to failure of 12 s under a confining pressure of 0.1 MPa. However, as the confining pressure increases to 101 MPa, a larger deviatoric stress of 550 MPa results in the delayed failure after 33 h. Kranz (1980) suggested that the effect of confining pressure is due to an increase in the activation enthalpy for the stress corrosion cracking which results in a decrease in dilatancy growth and crack interaction. Therefore, the confining pressure has a significant effect on the creep behavior of rock.

The creep strain rate and delayed time to failure of rocks are all related to the stress state. A larger applied stress results in higher creep strain rate with shorter duration before failure (Bieniawski 1970; Ngwenya et al. 2001; Brantut et al. 2013). So, it implies that the delayed failure time of rocks may be predicted by using the stress state or creep strain rate. On the other hand, shear failure is a common failure form in creep tests of rocks (Brantut et al. 2013; Liu et al. 2016). Figure 2.23 shows a comparison between the fractured rock samples in a creep test and in a conventional constant strain rate test. The two samples demonstrate highly similar shear band which makes an angle to the plane of axial stress. This suggests that the failure of rock in creep and conventional compression tests is controlled by shear and may be described by the Coulomb criterion.

Creep tests   Conventional constant
strain rate tests
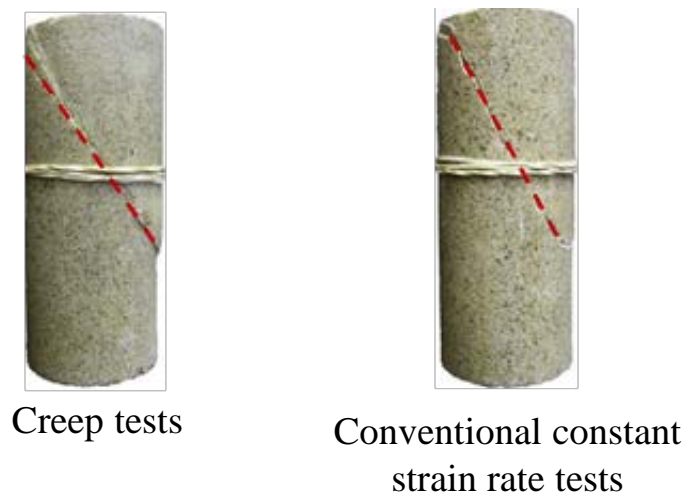
Figure 2.23: Comparison between the fractured rock samples in a creep test and in a conventional constant strain rate test (reproduced of Brantut et al. 2013 with permission)

Evidences of micro crack propagation within rocks during creep were reported in many studies. Figure 2.24 shows micrographs of Darley Dale sandstone samples under an intact condition and a

fractured condition after a creep test. During the creep, micro cracks initiate and develop through the whole sample which explain the creep strain under a stress level higher than CIT. The coalescence of micro cracks around the shear band leads to the delayed failure of rocks.
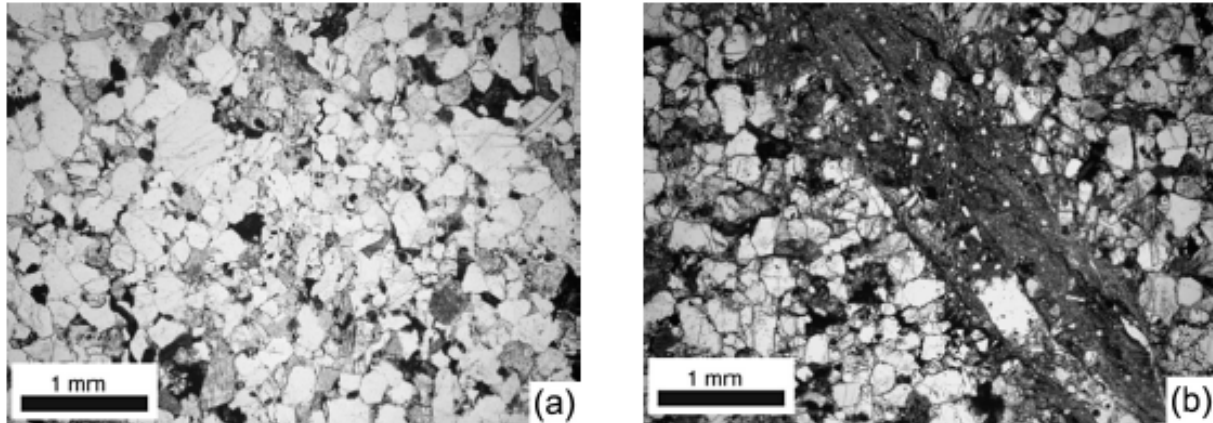
Figure 2.24: Micrographs of Darley Dale sandstone samples under (a) an intact condition and (b) a fractured condition after creep test (reproduced of Brantut et al. 2013 with permission)

Heap et al. (2009) performed creep tests on Darley Dale sandstone. The constant stresses were applied as 80% to 90% of the short-term strength of the rock to obtain all three stages of creep. During the creep tests, the AE activities were recorded continuously using transducers. Figure 2.25 plots AE hypocenters in the rock sample for primary, secondary, and tertiary creep stages. During the primary and secondary creep stages, AE activities indicate that there are micro crack propagations distributed throughout the full sample. During the tertiary creep, the micro crack development as shown by the AE hypocenters localizes around the shear plane. The monitored AE activities indicate that micro crack propagations govern the creep strain and delayed failure of rocks once the applied stress exceeds CIT.
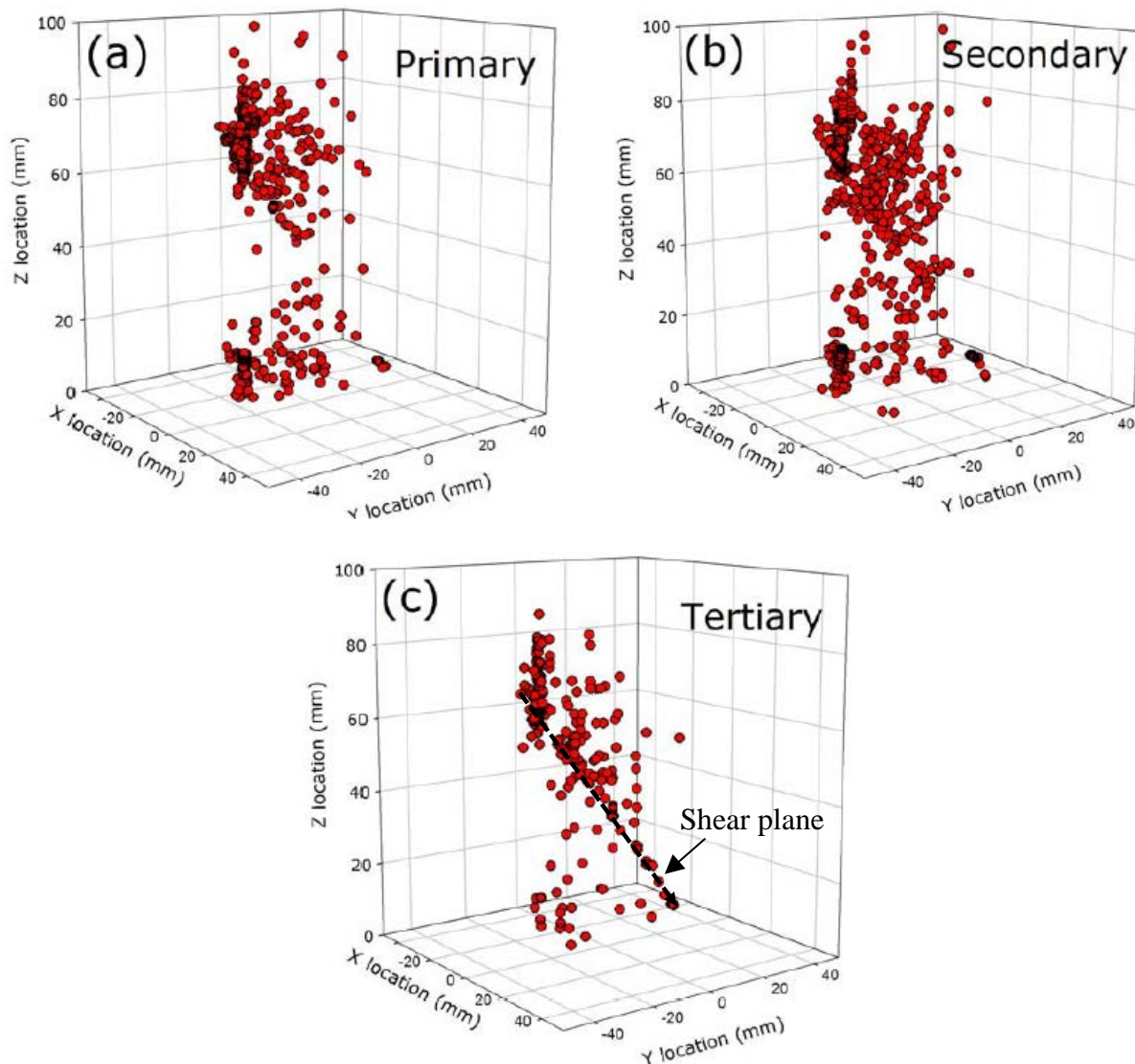
Figure 2.25: AE hypocenters at the (a) primary creep, (b) secondary creep, and (c) tertiary creep stages of a Darley Dale sandstone (reproduced of Heap et al. 2009 with permission)

The creep deformation can reduce the strength of rocks (Adachi and Takase 1981; Sulistianto et al. 2010; Brantut et al. 2013). For example, Sulistianto et al. (2010) performed the shear creep tests on sandstone rock samples with two different sizes. The small drill core sample has a diameter of 45 mm while the large square sample was sheared along a shear plane of 250 mm × 250 mm. In the creep tests, the drill core sample demonstrated a creep strain of 0.35% while the square sample exhibited a creep strain of 0.28% after the secondary creep stage. Table 2.1 shows the comparisons between short-term strength parameters (i.e., cohesion c and friction angle ϕ) and those obtained

after creep tests (long-term parameters) for two rock samples. It can be seen that the strength of rock reduces during the creep.

Table 2.1: Comparisons between short-term and long-term shear strength parameters of sandstone rock samples (based on Sulistianto et al. 2010)

Sample	Shear strength parameters	Short-term	Long-term
Drill core sample	c (MPa)	0.106	0.07
	ϕ (°)	57.25	45.76
Square sample	c (MPa)	0.552	0.197
	ϕ (°)	45.29	32.37

Based on the uniaxial compression creep tests made on Oya tuff and Cappadocia tuff, Aydan and Nawrocki (1998) proposed a relation to calculate the time-dependent uniaxial compressive strength $\sigma_c(t)$ of rock as:

$$\frac{\sigma_c(t)}{\sigma_c} = 1 - b \cdot \ln\left(\frac{t}{t_s}\right) \tag{2.87}$$

where σ_c is the short-term strength; t is time; t_s is the short-term test duration; b is a material parameter. In this equation, the value of b ranges from 0.0186 to 0.0583 for most rocks (Aydan and Nawrocki 1998). According to this equation, the strength of rock decreases with the increase of creep time or creep strain.

2.6.2 Creep models

The existing fundamental creep models for rocks can be divided as: empirical solutions (Mirza 1978; Jeffieys 1958; Aydan et al. 2003) and rheological model-based formulations (Boukharov et al. 1995;). Based on empirical and rheological solutions and some creep theories, more powerful and advanced creep models were developed (Yahya et al. 2000; Fahimifar et al. 2015; Wang et al. 2019). Some fundamental empirical creep models and rheological creep models are reviewed in this section. Some advanced creep models developed by researches will also be reviewed.

Empirical creep models

Under a maintained stress state, the total strain ε_t (a sum of instantaneous strain ε_e and creep strain ε_c) demonstrated by rocks shown in Figure 2.20 can be calculated as

$$\varepsilon_t = \varepsilon_e + \varepsilon_{pc} + \varepsilon_{sc} + \varepsilon_{tc} \tag{2.88}$$

where ε_{pc}, ε_{sc}, and ε_{tc} are the creep strains of the primary, secondary, and tertiary creep stages, respectively. Some empirical models are mostly developed to describe the creep strain in one stage. For example, the primary (transient creep) stage of rocks and metals is commonly described by a power law function:

$$\varepsilon_{pc} = C_1 \cdot t^{1/C_2} \tag{2.89}$$

where t is time; C_1 and C_2 are constants varying with temperature and can be calibrated based on experimental results. According to the previous studies on the creep behavior of metals (Andrade 1910, 1914), C_2 usually has a value of 3. This model is independent on the stress state which implies that it cannot be applied for different stress conditions.

Another commonly used empirical model to describe the primary creep stage is a logarithmic law proposed by Lomnitz (1957) as follows:

$$\varepsilon_{pc} = C_1 \cdot \ln(1 + C_2 \cdot t) \tag{2.90}$$

where C_1 and C_2 are constants. This model also has a limitation of stress independency.

For the description of the secondary creep stage, Norton's law (Penny and Marriott 1995; Farmer 2012) is usually used which is given as:

$$\varepsilon_{sc} = C_1 \cdot \sigma^{C_2} t \tag{2.91}$$

where C_1 and C_2 are material constants; σ is applied deviatoric stress.

For a creep model involving the tertiary creep stage, one can mention the form of Garofalo's expression (Garofalo 1965; Maruyama et al. 1990) which is usually applied on metals:

$$\varepsilon_t = C_1 \cdot (1 - e^{-C_2 \cdot t}) + C_3 \cdot (e^{C_4 \cdot t} - 1) \tag{2.92}$$

where C_1, C_2, C_3, C_4 are material constants.

The model of Garofalo (1965) is theoretically applicable to all the three creep stages. Table 2.2 shows some more empirical formulations to describe the creep behavior of rocks.

Table 2.2: Empirical creep models to describe the creep behavior of rocks (based on Mirza 1978)

Empirical creep models
$\varepsilon_c = C_1 \cdot t^{C_2}$
$\varepsilon_c = C_1 + C_2 \cdot t^{C_3}$
$\varepsilon_c = C_1 + C_2 \cdot t + C_3 \cdot t^{C_4}$
$\varepsilon_c = C_1 \cdot t^{C_2} + C_3 \cdot t^{C_4} + C_5 \cdot t^{C_6} + C_7 \cdot t^{C_8}$
$\varepsilon_c = C_1 \cdot t^{C_2} + C_3 \cdot t^{C_4} + C_5 \cdot t^{C_6} + C_7 \cdot t^{C_8} + \cdots$
$\varepsilon_c = C_1 \cdot \log t$
$\varepsilon_c = C_1 + C_2 \cdot \log t$
$\varepsilon_c = C_1 \cdot \log(C_2 + t)$
$\varepsilon_c = C_1 \cdot \log(C_2 + C_3 \cdot t)$
$\varepsilon_c = C_1 + C_2 \cdot \log(C_3 + t)$
$\varepsilon_c = C_1 + C_2 \cdot \log(t + C_3 \cdot t)$
$\varepsilon_c = C_1 \cdot t / (1 + C_2 \cdot t)$
$\varepsilon_c = C_1 + C_2 \cdot \sinh C_3 \cdot t^{C_4}$
$\varepsilon_c = C_1 + C_2 \cdot t - C_3 \cdot exp(-C_4 \cdot t)$
$\varepsilon_c = C_1 + C_2 \cdot [1 - exp(-C_3 \cdot t)]$
$\varepsilon_c = C_1 \cdot [1 - exp(-C_2 \cdot t)] + C_3 \cdot [1 - exp(-C_4 \cdot t)]$
$\varepsilon_c = C_1 + C_2 \cdot \log t + C_3 \cdot t^{C_4}$
$\varepsilon_c = C_1 + C_2 \cdot t^{C_3} + C_4 \cdot t$
$\varepsilon_c = C_1 + C_2 \cdot \log t + C_3 \cdot t$
$\varepsilon_c = \log t + C_1 \cdot t^{C_2} + C_3 \cdot t$
$\varepsilon_c = C_1 \cdot \log[1 + (t/C_2)]$
$\varepsilon_c = C_1 \cdot [1 - exp(C_2 - C_3 \cdot t^{C_4})]$
$\varepsilon_c = C_1 \cdot [1 - exp(-C_2 \cdot t)]$
$\varepsilon_c = C_1 \cdot \exp(C_2 \cdot t)$
$\dot{\varepsilon}_{sc} = C_1 \dfrac{\sigma_d^{C_2}}{d^{C_3}} \cdot f_w^{C_4} \exp\left(-\dfrac{E_a + P_c \cdot \Delta V}{R_g T_a}\right)$

C_i ($i = 1, 2, 3, \ldots, 8$) in the table is material constant.

It should be noted that the last equation in Table 2.2 is commonly used by geologists and geophysicists to describe the steady-state creep strain rate $\dot{\varepsilon}_{sc}$ of mineral polycrystalline aggregates and rocks. In this equation, C_1 is the pre-exponential factor; σ_d represents the differential stress; C_2 is the stress exponent; d is the grain size; C_3 is the grain size exponent; f_w is the water fugacity; C_4
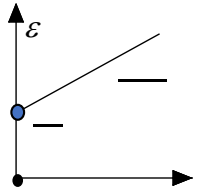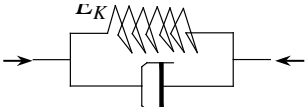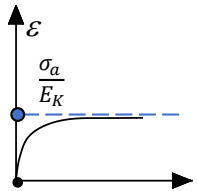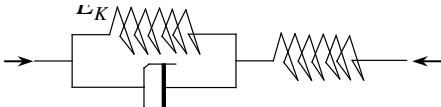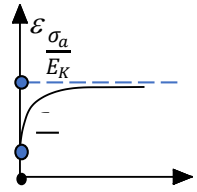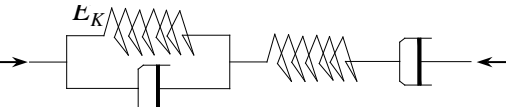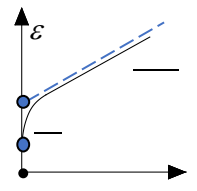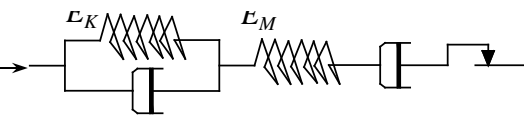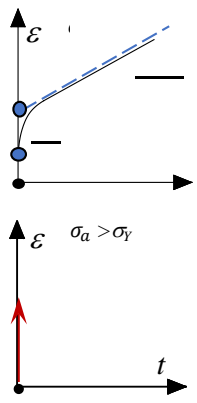
is the water fugacity exponent; E_a is the activation energy; P_c represents the confining pressure; Δ V denotes the volume of activation; R_g is the gas constant; T_a is the absolute temperature. When this equation is applied to describe the Nabarro-Herring diffusion creep, $C_2 = 1$ and $C_3 = 2$. For the Coble creep, $C_2 = 1$ and $C_3 = 3$. $C_2 = 3$–5 and $C_3 = 0$ for dislocation creep.
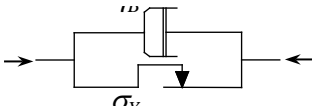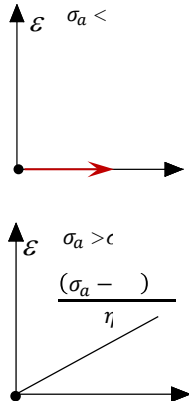
Most empirical creep models are phenomenal, based on creep strain-time curve observations. The empirical formulations are usually simple and easy to be used by applying calibration technique. However, the parameters in most empirical model are often lack of clear physical meaning. Some empirical creep models do not involve stresses which makes it inapplicable for different stress conditions. The confining stress is omitted in some empirical models. For these formulations, the effect of confining stress on the creep behavior of rocks can not be captured. Furthermore, the time to delayed failure of rocks cannot be predicted by most empirical models. Therefore, the empirical models are usually applied to phenomenally reflect the creep behavior of rocks while their capability in predicting creep deformations is limited.

Rheological models

Table 2.3 shows some basic one-dimensional rheological models. The rheological models typically consist of different mechanical elements coupled in parallel or series including the elastic spring and dashpot (Goodman 1989; Jaeger et al. 2009). For the Maxwell, Kelvin-Voigt, generalized Kelvin-Voigt and Burgers creep models, these models can describe the creep strain in the primary or/and secondary creep stages, but they cannot reflect the tertiary creep strains. When a plastic slider element is involved such as in the CVISC and Bingham creep models (Farmer 2012), the models are able to reflect the plasticity and yielding, but the time to delayed failure cannot be represented. One should note that the Bingham creep model postulates that the creep strain of rocks is possible only when the applied load exceeds the shear strength of the plastic slider element (a threshold). This is not in accordance with the reality because that many long-term creep tests revealed that creep of rocks occurs under very low stress conditions (Ito 1991; Bérest et al. 2015; Nopola and Roberts 2016).

Table 2.3: A summary of some fundamental rheological models (based on Goodman 1989; Jaeger et al. 2009) (E = elastic modulus, η = viscosity coefficient, σ_Y = yield strength, σ_a = applied stress)

Creep model	Schematic and formulation	Strain-time curve	Description
Maxwell	E_M $$\varepsilon_t = \frac{\sigma_a}{E_M} + \frac{\sigma_a \cdot t}{\eta_M}$$		Visco-elastic model for instantaneous and secondary creep strains
Kelvin-Voigt	E_K $$\varepsilon_t = \frac{\sigma_a}{E_K} \cdot \left[1 - exp\left(-\frac{E_K \cdot t}{\eta_K}\right) \right]$$		Visco-elastic model for primary creep strain
Generalized Kelvin-Voigt	E_K $$\varepsilon_t = \frac{\sigma_a}{E_e} + \frac{\sigma_a}{E_K} \cdot \left[1 - exp\left(-\frac{E_K \cdot t}{\eta_K}\right) \right]$$		Visco-elastic model for instantaneous and primary creep strains
Burgers	E_K $$\varepsilon_t = \frac{\sigma_a}{E_M} + \frac{\sigma_a \cdot t}{\eta_M} + \frac{\sigma_a}{E_K} \cdot \left[1 - exp\left(-\frac{E_K \cdot t}{\eta_K}\right) \right]$$		Visco-elastic model for instantaneous, primary and secondary creep strains
CVISC	E_K E_M $\sigma_a < \sigma_Y$: $$\varepsilon_t = \frac{\sigma_a}{E_M} + \frac{\sigma_a \cdot t}{\eta_M} + \frac{\sigma_a}{E_K} \cdot \left[1 - exp\left(-\frac{E_K \cdot t}{\eta_K}\right) \right]$$ $\sigma_a > \sigma_Y$: Plastic yield		Elasto-visco-plastic model for instantaneous, primary and secondary creep strains. Phenomenal description of the tertiary creep stage

| Bingham | $\sigma < \sigma_Y$: $\varepsilon_t = 0$ $\sigma > \sigma_Y$: $\varepsilon_c = \dfrac{(\sigma_a - \sigma_Y) \cdot t}{\eta_B}$ | | Visco-plastic model for secondary creep strain |

Among fundamental rheological models shown in Table 2.3, one can mention that the Burgers model (or CVISC model as its variation) is widely used one to represent the creep behavior of rocks. Wang & Li (2018) applied the Burgers model to describe and predict the creep strain of green sandstone and lherzolite under uniaxial and triaxial compression test conditions. The Burgers model shows good agreement with the experimental results. The applications of the Burgers model on more kinds of rocks were summarized by Paraskevopoulou et al. (2018). In order to describe the tertiary creep stage, some more advanced rheological models were developed with damage variables by relating mechanical parameters such as elastic modulus and viscosity coefficient with creep strain (Liu et al. 2016; Zhao et al. 2017).

In contrast to the empirical models, the rheological model-based formulations have more sophisticated forms. The number of model parameters increases considerably with the complexity of the rheological behavior and the desired ability or applicability of the model (Liu et al. 2016). On the other hand, the model parameters of rheological model-based formulations are usually of obvious physical meaning (e.g., viscosity coefficient, elastic modulus, and yielding strength). The curve-fitting technique is commonly used to identify these parameters to obtain good agreements between analytical and experimental results for describing the creep behavior of rocks (Liu et al. 2016; Zhao et al. 2017). This results in a problem that the predictive capability of the models remains unknown in different stress conditions. Most rheological models neglect the confining pressure and friction angle. This is a typical feature of frictionless materials such as metals, but it is not the typical feature of geomaterials like rocks (Brantut et al. 2013; Ngwenya et al. 2001). Meanwhile, traditional rheological models cannot reflect the relationship between microscopic

crack extension and macroscopic failure of rocks in creep process.

Advanced creep models

Many advanced creep models were developed based on the fundamental empirical and rheological models and creep theories (Ashby & Sammis 1990; Perzyna 1966). Some of these advanced creep models are presented as follows.

Maranini & Yamaguchi (2001) proposed a non-associated constitutive model to describe the elastic and viscoplastic properties of Inada granite. The formulas of model were in the form of polynomial expression and composed of an elastic component and a viscoplastic component. The model considers dependency of the shear and bulk modulus on the mean stress. The comparisons between the proposed model and the creep test results show good agreements on low deviatoric level while on high deviatoric level, some differences can be observed. The polynomial expressions proposed by Maranini & Yamaguchi (2001) have a large number of coefficients which need to be determined based on the experimental results. This increases the difficulties for its application.

Yahya et al. (2000) developed an internal state variable (ISV) model to describe the ductile behavior of rock salt based on a viscoplastic model proposed by Aubertin et al. (1991a, 1991b, 1998). The elastic strain of the model is described by the generalized Hooke's law. The inelastic strain is given by a kinetic law depending on the deviatoric stress, yield strength, drag stress and the tensorial back stress. Yahya et al. (2000) indicated when the inelastic deformation occurs during loading process for a specimen and only a part of deviatoric stress is active. The active stress equals to the applied stress minus the internal stress which is constituted by the yield strength and tensorial back stress. The proposed model was compared with some experimental results of stress-strain and strain-time curves of rock salt under different stress states available in literatures. However, the parameters in the model were adjusted using a computer code SIDOLO to minimize the discrepancies which is a calibration technique. This makes the predictive capability of the proposed model remaining unknown.

Shao et al. (2006) developed a constitutive model to describe the anisotropic damage and creep deformation of cohesive frictional geomaterials such as rocks and concrete. In this model, the creep deformation is considered attributed to the sub-critical propagation of micro cracks associated with stress corrosion. This is in accordance with experimental observations as presented in previous

sections. By considering this important feature of rocks, a second order damage tensor was defined in the model to estimate the crack density. The proposed model of Shao et al. (2006) shows good agreements with the experimental results of Lac de Bonnet granite. However, this model cannot explain the localization of micro cracks around the shear band in the tertiary creep. Meanwhile, it cannot be applied to predict the time to delayed failure of rocks.

Zhao et al. (2017) proposed a nonlinear constitutive model to describe creep strains and strain rate in three creep stages of lherzolite. In the model, a Hooke spring element was adopted to represent instantaneous elastic behavior while a parallel combination of a spring element and a plastic slider was used to describe instantaneous plastic behavior. A Kelvin element was used to describe visco-elastic behavior in the primary creep stage. A generalized Bingham element was employed to describe the visco-plastic strain. In the Bingham element, the viscosity coefficient is related to the creep time through a damage variable which enables to capture the time to failure in a creep process. Zhao et al. (2017) further compared the proposed model with the creep strains of rock samples under a confining pressure of 6 MPa and different deviatoric stress states. The comparisons are shown in Figure 2.26 which demonstrate good agreement. One should note that this correlation was obtained by calibrating (or curve fitting) the model with test results under each different stress states. The model thus has different sets of parameters for each stress state which makes it application difficult in practice.
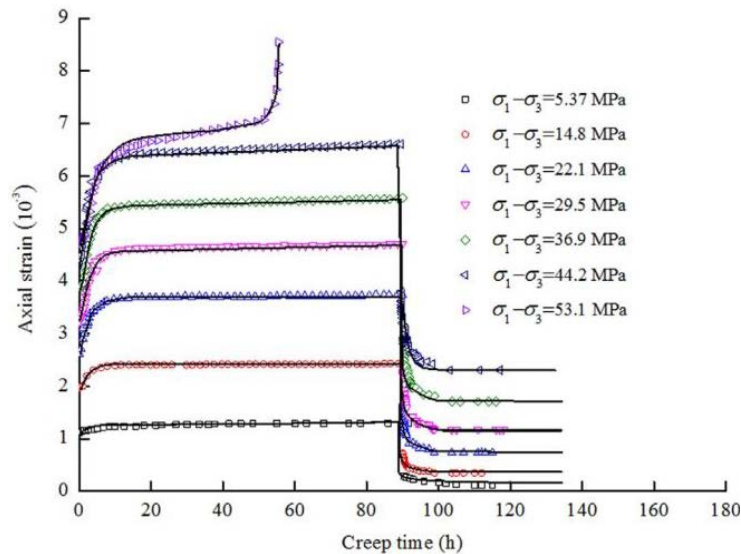
Figure 2.26: Comparisons between the creep model (solid lines) and experimental results (points)

of creep strain under different stress states based on calibration technique (reproduced of Zhao et al. 2017 with permission)

Ashby & Sammis (1990) proposed a model to describe the creep behavior of rocks by taking the crack interactions into consideration in a global way. It is assumed that the extension of crack wings leads to a reduction of contact area in rocks which further results in an increase in the internal stresses. When the increased internal stresses are sufficiently large, the delayed failure of rock occurs. However, the model of Ashby & Sammis (1990) cannot explain the formation of shear plane of rocks by micro cracks in the macroscopic scale.

Recently, Innocente et al. (2021) suggested that the empirical logarithmic form function fits well with the time to failure of rocks. The experimental results of delayed time to failure were plotted against driving stress ratio which is a ratio between the applied stress and UCS. The good correlations between the analytical solution and test results were obtained based on curve-fitting. However, when the ratio between the applied stress and UCS was taken as the stress variable in the model, the effect of confining pressure on the time to failure was neglected. Kranz (1980) showed that the increase of confining pressure results in an increase in the time to failure of rocks. Therefore, the logarithmic solution suggested by Innocente et al. (2021) cannot be applied to estimate the time to failure of rocks under different confining pressures. It implies that this solution is inapplicable for underground rock structures which are usually submitted to complicated stress conditions. For frictional materials like rocks, the effects of both deviatoric stress and confining stress on the creep behavior should be considered.

2.6.3 Numerical simulations of backfilled stope considering creep of rocks

Despite that the creep behavior of rocks can lead to the long-term closure of underground excavations, there are relatively few numerical models developed to study its influence on the performance and stability of backfilled stopes. Qi & Fourie (2019) investigated the stress distribution in a backfilled stope using a two-dimensional plane strain model built with FLAC. The CVISC creep model was applied for the rock mass while the backfill was modeled with the Mohr-Coulomb elasto plastic model. The increases of the cohesion and Young's modulus of backfill with time was considered. It was concluded the rock mass displacement increases with the increase of time which results in an increase in both horizontal and vertical stresses within backfill. However,

in this study, the viscosity coefficient of rock mass was taken as 10^{20} Pa·s that is much larger than typical value of rocks. The earth pressure coefficient in this study was taken as 2 to obtain the initial elastic equilibrium state followed by the excavation and the application of the CVISC parameters. This procedure needs discussion because that an earth pressure of 2 results in deviatoric stresses in the model, which can further cause the time-dependent creep (or stress relaxation) of rocks even without any excavations. Meanwhile, the stope was filled in a single step which affects the results because the placed backfill in a numerical model should be in a quasi-static state (Li & Aubertin 2009). Qi & Fourie (2019) suggested that the delayed placement of fill significantly influence the rock displacement and stresses in the stope. However, the sum of delayed filling time and curing time in this study is a constant (21 days). The varied results may thus be attributed to different cuing time instead of different delayed filling time.

Yan et al. (2021) developed an analytical solution to estimate the stress distribution around a circular backfilled excavation. The creep of surrounding rocks was considered by using a power law function proposed by Xu et al. (2018). Without much explanations, the solutions for the circular excavation were extended to the rectangular backfilled stope. Yan et al. (2021) further conducted the numerical modeling with a two-dimensional plane strain model to verify the proposed solution. In the numerical simulations, the Yong's modulus of backfill was 300 MPa and different delayed filling time of backfill was applied. It was reported that the stresses in a backfilled is affected by the arching effect and squeezing from creep deformation of rock walls. The creep of rock mass causes an increase in stresses withing the backfilled stope. It was also reported that the increase of delayed filling time leads to a decrease in stresses in fill. The vertical stress in the proposed solutions was calculated based on the Rankine's passive earth pressure coefficient which was not justified due to the significant shear stress along fill-rock interface caused by creep of walls. The effect of delayed filling time on the generated stresses may be caused by the large initial elastic modulus of 300 MPa of backfill. In practice, the cemented backfill is very soft during the early period of curing and becomes stiff as time increases.

2.7   Summary

The reviews have shown that most previous analytical solutions for evaluating the stability of side-exposed backfill were developed based on limit equilibrium analysis by considering a wedge

sliding model proposed by Mitchell et al. (1982) with two or three immobile walls. The effect of rock-wall convergence on the stability was neglected. The justification was based on some box instability tests conducted by Mitchell et al. (1982) using very soft backfill with a cement content of 2.2% and a curing time of 2.5–5 hours. The tests are thus deemed only valid for undrained or partially drained conditions, not for side-exposed backfill in practice which undergoes a quite long curing time (typically 28 days) and are under drained condition.

In underground mines, excavating a stope will result in stress redistribution around the stopes and instantaneous rock-wall closure applied on the side-exposed backfill. The induced stress around the extracted stopes can also cause the creep deformation of rock mass, which affects the stress state and stability of side-exposed backfill. As the cemented backfill in underground mines can be hard due to the high cement content and long curing time, it will interact with the rock-wall closure.

Numerical modeling is an ideal method to analyze the effect of deformation of rock walls caused by stope extraction and creep on the stability of side-exposed backfill. However, there are relatively few numerical models of side-exposed backfill considering rock walls instantaneous closure. Furthermore, the influence of creep deformation of rocks on the stability of side-exposed backfill has never been analyzed by previous studies. The effects of different mine depths, stope geometries, properties of backfill and rock mass on the failure mechanism and the minimum required cohesion of side-exposed backfill were not properly investigated. Therefore, it is necessary to develop new numerical models to analyze the stability and determine the minimum required cohesion of side-exposed backfill by considering rock-wall closure associated with adjacent extraction and creep deformation of rocks.

CHAPTER 3   ARTICLE 1: STABILITY ANALYSES OF SIDE-EXPOSED BACKFILL CONSIDERING MINE DEPTH AND EXTRACTION OF ADJACENT STOPE

Ruofan Wang, Feitao Zeng, and Li Li

Abstract: Pillar recovery requires stable backfill upon side exposure in open stoping mining methods. Until now, the solutions used to estimate the required strength of side-exposed backfill are mainly based on a wedge model where the effect of rock-wall closure was neglected. In this paper, the influence of mine depth and adjacent extraction on the stability of side-exposed backfill is analyzed through numerical modeling with FLAC^{3D}. The failure mechanism and minimum required cohesion (c_{min}) of backfill are investigated. Results show that the governing failure mechanism can be sliding or crushing, depending on the magnitude of rock-wall closure. When the mine depth and rock-wall closure are small, sliding failure is dominant and rock-wall closure has effect to improve the stability of exposed backfill. The values of c_{min} can become even smaller than those obtained with immobile rock walls solutions. When the sliding failure is dominant, the c_{min} decreases with the increase of mine depth, fill stiffness, rock pressure coefficient, and fill-rock interface strength (friction angle and adhesion). Increasing rock mass stiffness, stope height and width leads to an increase in c_{min}. When mine depth and rock-wall closure are large, the crushing failure is dominant. The c_{min} increases with the increase of mine depth, stope height and length, fill stiffness and rock pressure coefficient. It decreases with the increase of stope width and rock mass stiffness, and is insensitive to the variation of fill-rock interface strength. In all cases, the stability of side-exposed backfill is improved by increasing its internal frictional angle.

3.1 Introduction

Mining backfill is used in underground mines for safety, economic, and environmental benefits. For example, it improves ground stability, reduces dilution, increases ore recovery, and minimizes surface deposal (Hassani and Archibald 1998; Li et al. 2003; Potvin et al. 2005; Benzaazoua et al. 2008). In metal mines with open stoping mining method, cemented backfill is used to fill mined-out primary stopes and acts as an artificial pillar to allow extraction of the secondary stope (Barrett and Cowling 1980; Tesarik et al. 2009). The extraction of a secondary stope results in side exposure of the backfill in the primary stope, as schematically shown in Figure 3.1. The cemented backfill is usually exposed under fully drained condition without any more free water. However, if the backfill does not have enough strength to remain stable, it may fail upon the wall exposure and threat the safety of workers and equipment and dilute the blasted ore (Askew et al. 1978; Coulthard and Dight 1980; Mitchell 1986), which requires to determine the minimum required cohesion (c_{min}) with optimized cement content to ensure the stability with a reasonable cost (Mitchell et al. 1982; Grice 1998; Belem and Benzaazoua 2008).
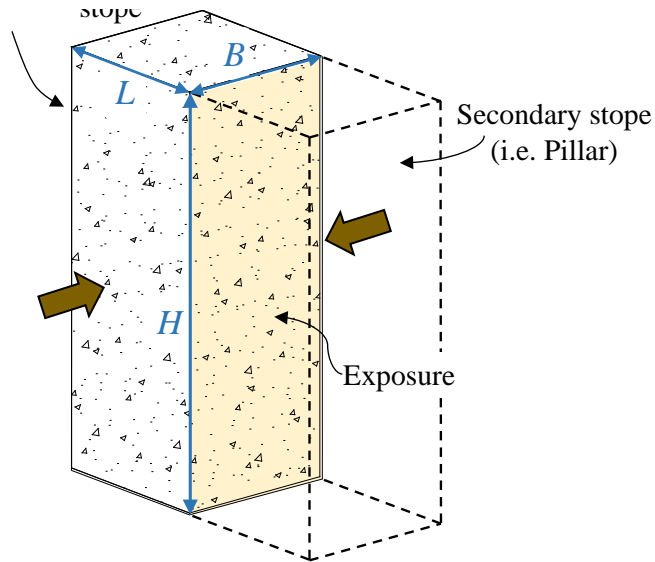
Figure 3.1: Backfill in a primary stope upon side exposure associated with extraction of the secondary stope (L (m), B (m) and H (m) are the strike length, width, and height of the backfill in the primary stope, respectively)

Several analytical solutions (Mitchell et al. 1982; Li and Aubertin 2012; Li 2014a, 2014b; Li and Aubertin 2014; Yang et al. 2017; Liu et al. 2018) that estimate the c_{min} of side-exposed backfill were mainly developed by using a wedge model proposed by Mitchell et al. (1982). The influence of rock-wall closure during the extraction of adjacent pillar was neglected based on the box instability tests (Mitchell et al. 1982) using a backfill with 2.2% cement by mass and cured only 2.5 to 5 hours when the backfill remains very soft. The conclusion based on these experimental results can only be valid when the backfill is very soft under undrained or partial drained conditions. In underground mines, however, the backfill in primary stopes is usually exposed after a quite long period of curing time (typically 28 days). This had been further confirmed by Mitchell (1989), who showed that wall closure affects the stability of side-exposed backfill under fully drained condition with a curing time of 28 days. Thus, the effect of walls closure should be considered when estimating the c_{min} of backfill.

Rock-wall closure due to the excavation of the secondary stope depends on several influencing factors, such as the mechanical properties of rock wall and backfill, stope geometries, excavation rate, mining sequence, local support and mine depth. When a stope is located at shallow depth with low in-situ stresses and surrounded by hard rocks, the wall closure could be very small when an adjacent secondary stope is excavated. When a stope is located at a large depth with high in-situ stresses and surrounded by soft rocks, the excavation of an adjacent secondary stope or the removal of an adjacent pillar can result in remarkable rock-wall closure (Malan and Basson 1998; Malan et al. 2007; Brown 2012; Anderson 2014; Fairhurst 2017; Ranjith et al. 2017; Seymour et al. 2017; Wagner 2019). The side-exposed backfill can fail by crushing due to the excessive compression associated with the rock-wall closure. When the backfill is very soft due to very low cement content or very short curing time, the side-exposed backfill can also fail by sliding. The dynamic loading is another influencing factor on the stability of side-exposed (Emad et al. 2018). It is however beyond the scope of the paper and not further discussed in this study.

Numerical model is a useful way to analyze the stability of backfill (Barrett et al. 1978; Coulthard 1999; Falaknaz 2014). Coulthard (1980) analyzed the stability of a side-exposed backfill pillar with a linearly elastic finite element program. The backfill was modeled as a linearly elastic material and its stability was determined by estimating the range of overstressed area. The convergence was assumed linearly distributed along the rock walls. It was reported that wall displacement of

approximately 20 mm could slightly promote the stability of side-exposed backfill by reducing the tensile stresses near the side and back walls, while wall displacement of 100 mm would cause a large-scale failure of the exposed face. Similarly, Pierce (1999) simulated the surrounding rock mass of a side-exposed backfilled stope with the thin rigid elements in FLAC^{3D}. The wall closure was simulated by applying specific displacements to the side walls. It was claimed that a horizontal closure microstrain of 3.3×10^3 could increase the stability of backfill while a horizontal closure microstrain of 2×10^4 could induce a shear failure of exposure. Sainsbury and Urie (2007) investigated the stability of the side and base exposed backfill with FLAC^{3D} by considering the effect of adjacent extraction and showed that the required uniaxial compressive strength (UCS) of fill increases as the rock-wall convergence increases. Falaknaz (2014) investigated the response of side-exposed backfill during sequential excavation and claimed that the increase of stope height and width leads to an increase in required fill strength. However, in previous studies the different failure mechanisms and the c_{min} of side-exposed backfill were not evaluated while effects of some factors including mine depth, mechanical properties of backfill and rock mass, were not analyzed.

In this study, three-dimensional numerical models are developed with FLAC^{3D} to assess the stability of side-exposed backfill in metal mines by considering extraction of the secondary stope. The failure mechanism and c_{min} of backfill are investigated. Parametric studies are performed to evaluate the effects of mine depth, stope geometry, mechanical properties of backfill and rock mass, and fill-rock interfaces on the results. Additional simulations considering immobile rock walls are also conducted for comparison. Further, in order to verify the applicability of the numerical models, comparisons between the numerical models and Mitchell's centrifuge model tests are made in Appendix I. This study aims at revealing the failure mechanisms of side-exposed backfill and providing the variation of c_{min} with different factors. It is expected to help mining engineers evaluating the required strength of backfill and optimizing the operating cost.

3.2 Numerical model

The stability and c_{min} of side-exposed backfill associated with the excavation of the secondary stope are analyzed through numerical modeling with FLAC^{3D} code (Itasca 2013). The physical model is shown in Figure 3.1. H, L and B are the height, length and width of the backfill, respectively.

The cemented backfill obeys the Mohr-Coulomb (MC) elasto-plastic model with tension cut-off. The MC failure criterion has been commonly used for mining backfill (Sainsbury and Urie 2007; Li and Aubertin 2014; Yang et al. 2017; Liu et al. 2018) and shows good agreement with experimental data (Pierce 1999; Belem et al. 2000; Rankine 2004). The MC model in FLAC^{3D} has been validated by comparing with analytical solutions for the problem of a cylinder hole developed by Salencon (1969). The cemented backfill is characterized by dry unit weight γ, Young's modulus E, Poisson's ratio ν, cohesion c, internal friction angle ϕ and dilation angle ψ. It should be noted that the Poisson's ratio ν and internal friction angle ϕ are interrelated through $\nu = (1 - \sin\phi)/(2 - \sin\phi)$ to ensure a consistent at-rest earth pressure coefficient K_0 (Falaknaz 2014; Yang 2016; Jahanbakhshzadeh et al. 2017, 2018a, 2018b). Moreover, the tensile strength T of cemented backfill is taken as 1/10 of the UCS (Mitchell and Wong 1982). Mechanical parameters of backfill for a reference case are shown in Table 3.1.

Table 3.1: Backfill parameters for a reference case

γ (kN/m³)	E (MPa)	ν	ϕ (°)	c (MPa)	ψ (°)	T (kPa)
18	300	0.33	30	1	0	346

The rock mass is simulated by the Hoek-Brown (HB) elasto-plastic model with strain softening. The nonlinear HB criterion has largely been shown to be capable of describing the shear strengths of a wide range of rock types, especially at high confining pressures (Pariseau 2007; Benz and Schwab 2008). The strain softening can describe the post failure behavior of rock mass (Cundall et al. 2003; Alejano et al. 2010). The validity of HB model with strain softening in FLAC^{3D} has been checked against analytical solutions for the problem of a cylinder hole developed by Carranza-Torres (2004). The rock mass is characterized by unit weight γ_R, Young's modulus E_R, Poisson's ratio ν_R, dilation angle ψ_R, geological strength index GSI, disturbance factor D_R and Hoek-Brown parameters of σ_{ci} (UCS), m_i, m_b, s and a (Hoek and Brown 1997; Hoek et al. 2000; Hoek and Brown 2019). Strain softening behavior of rock mass is featured by specifying the changing of σ_{ci} and m_b according to the plastic confining strain component e_3^p. Residual values of σ_{ci} and m_b are calculated by (Cundall et al. 2003):

$$\sigma_{ci}^r = (1 - \beta)\sigma_{ci} \tag{3.1}$$

$$m_b^r = (1 - \beta)m_b \tag{3.2}$$

where β_s $(0 \leq \beta_s \leq 1)$ controls the transition between the peak and the residual strength. e_3^p is given by[47]:

$$e_3^p = -\frac{\beta\sigma_{ci}}{2G_R}\left(\frac{\eta+1}{\eta}\right)\left(m_b\frac{\sigma_3}{\sigma_{ci}} + s\right)^a \frac{K_{\psi R}}{K_{\psi R}+2} \tag{3.3}$$

where G_R is the shear modulus of rock mass; $K_{\psi R} = (1 + \sin\psi_R)/(1 - \sin\psi_R)$; η $(\eta > 0)$ controls the slope of stress-strain curve in the softening stage. The rock mass is perfectly-ductile when $\eta \to 0$ and perfectly-brittle when $\eta \to \infty$. Table 3.2 summarizes the parameters of hard rock mass for a reference case, as suggested by Hoek and Brown (1997).

Table 3.2: Rock mass parameters for a reference case (based on the values suggested by Hoek and Brown 1997)

γ_R (kN/m³)	E_R (GPa)	v_R	ψ_R (°)	GSI	D_R	σ_{ci} (UCS) (MPa)	m_i	m_b	s	a	β_s	η
27	42	0.22	0	75	0	150	25	10.24	0.06	0.5	0.85	∞

Figure 3.2 shows the corresponding numerical model built with FLAC^{3D}. Half of the model is simulated due the symmetry plane $(y = 0)$. A void space of 1 m high is left on the top of the backfill to represent the poor contact between the fill and stope roof. The adjacent secondary stope has the same dimensions as those of the primary stope.

The interface model is utilized for the interface between the backfill and the rock walls. The interface model parameters are normal stiffness k_n, shear stiffness k_s, adherence cohesion $c_i = r_s \cdot c$, $(0 \leq r_s \leq 1)$, interface friction angle $\delta = r_a \cdot \phi$ $(0 \leq r_a \leq 1)$. According to the recommendation of the manual of FLAC^{3D} (Itasca 2013), k_n and k_s are determined by:

$$k_n = k_s = 10\frac{\left(K + \frac{4}{3}G\right)}{\Delta z_{min}} \tag{3.4}$$

where K and G are the bulk and shear modulus of backfill respectively, Δz_{min} is the smallest backfill element size for the fill-rock interface. Since the rock mass is much stiffer than the backfill, the interface model and Eq. (3.4) are applied to the backfill to minimize the influence of interface on the numerical model (Itasca 2013).

The depth D (m) of stopes is measured from the ground surface to the origin of the model, which locates at the central point of the excavation. Gravity is set along the negative direction of the z-axis in Figure 3.2. The lateral earth pressure coefficient $K_r = 2$ is employed due to the typical stress regime of the Canadian Shield (Herget 1988). The average interpolation method in FLAC^{3D} is used for contours which means the value of zone-based data is averaged to grid points and linearly interpolated to zone interior (Itasca 2013). In terms of the boundary conditions, the top boundary is set free where a surcharge is applied to simulate the overburden in case the model height is limited; normal displacements are restricted for the four lateral boundaries while the displacements in all three directions are prohibited for the bottom boundary. Sensitivity analyses considering different domain sizes, ranges with fine grids, mesh sizes, and filling layers were conducted to determine optimal values of these parameters that ensure stable results and a reasonable runtime. Based on the sensitivity analyses, the sizes of the numerical model are determined as $L_D = B_D = H_D = 900$ m to minimize the boundary effect. Stopes and backfill are meshed with uniform brick-shaped elements of 0.5 m while the rock mass is meshed with radially graded grids. The number of zones ranges from 1.4×10^5 to 5.1×10^5 depending on the size of stope. Detailed mesh generation method is addressed in Appendix II. All elements in the model are hexahedrons while aspect ratio, orthogonality, and face planarity are used to describe the zone quality in FLAC^{3D} (Itasca 2013). For the numerical model in this study, the aspect ratio and orthogonality range from 0.25 to 1 and 0.53 to 1 respectively, while face planarity is always 0. The runtime for one case is roughly 4 hours on a 3.4 GHz Intel i7-6700 CPU computer.
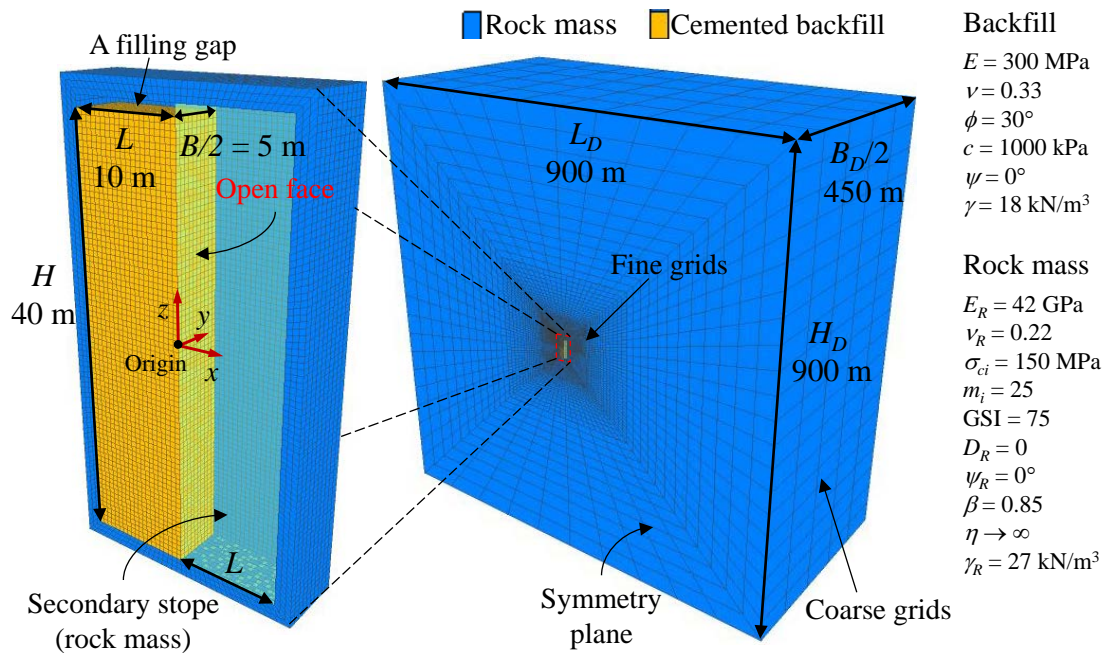
Figure 3.2: A numerical model built with FLAC^{3D} of side-exposed backfill in a primary stope and an adjacent excavated secondary stope surrounded by the rock mass

The numerical simulations are conducted by the following four steps, as illustrated in Figure 3.3:

1) Obtaining the initial stress state before any excavation;

2) Excavating the primary stope in one step and solving to the equilibrium state;

3) Resetting the displacement of rock mass induced by excavation to zero, followed by placing backfill using a multilayer method. The numerical model is solved to achieve the equilibrium state as each layer of backfill is placed;

4) Excavating the whole adjacent secondary stope in one step and solving to achieve the equilibrium state.
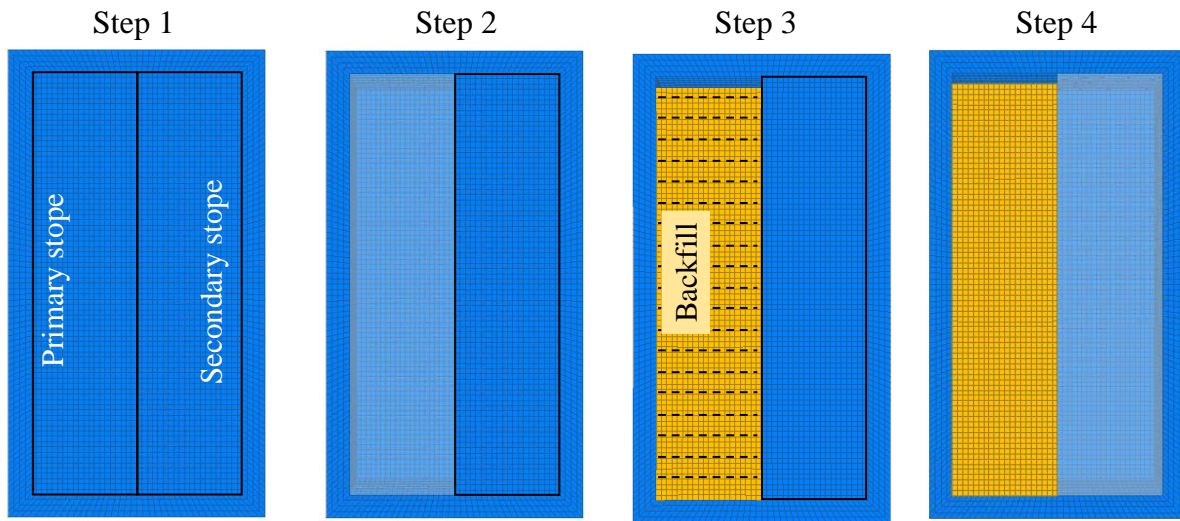
Figure 3.3: Steps for the numerical simulations

The thickness of filling layer in step 3 of simulation is determined as 2 m based on the sensitivity analyses. Figure 3.4 shows the variation of the vertical and horizontal (σ_{yy}) stresses along vertical central line of a backfilled stope with $H = 60$ m, $L = 25$ m, $B = 25$ m before excavating the adjacent secondary stope by considering different layer thicknesses. It is found that when the layer thickness reduces to 2 m, the numerical results tend to be stable. Further increasing of filling layer would not greatly affect the results.
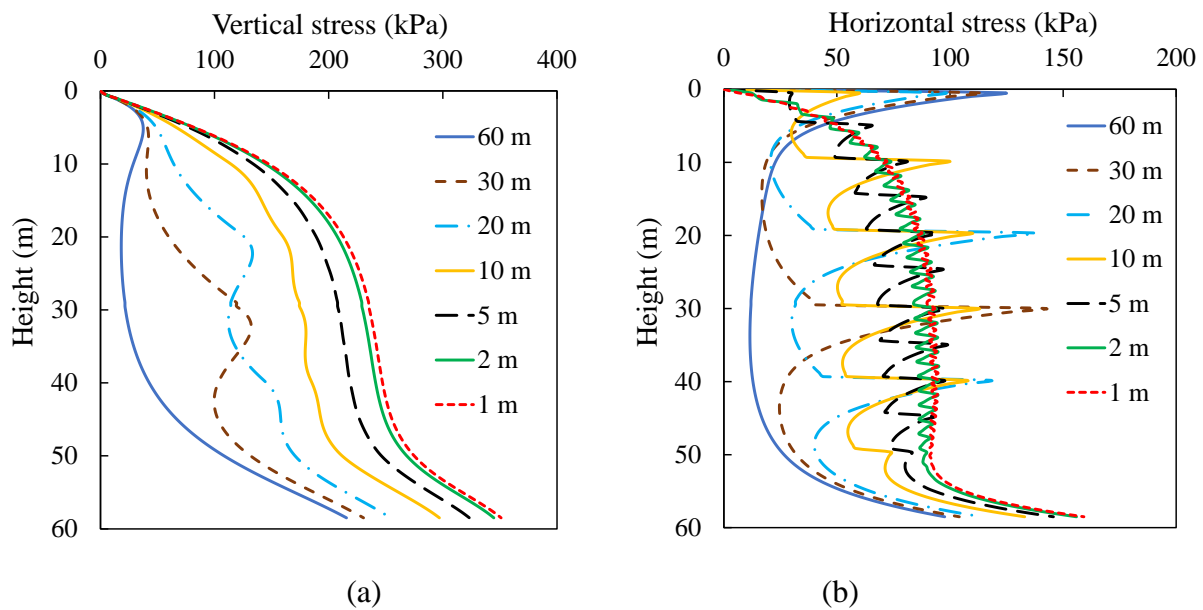
Figure 3.4: Variation of the (a) vertical stress and (b) horizontal stress (σ_{yy}) along vertical central line of a backfilled stope ($H = 60$ m, $L = 25$ m, $B = 25$ m) before excavating the adjacent secondary stope by applying fill parameters in Table 3.1 and different thicknesses of filling layer

The equilibrium state of simulation is obtained by using the "STEP" command and monitoring the stress and displacement in backfill and rock mass until observing the convergence. For example, Figure 3.5 shows the variation of the horizontal stress (σ_{yy}) and x-displacement at the central point of open face after adjacent extraction for a reference case. It can be seen that numerical results converge as the iteration steps increase to 5.2×10^4, indicating the equilibrium state and that simulation can be stopped. The unbalanced force ratio is not used as an indicator for equilibrium state because it limiting value varies as the variation of grid number and stress magnitude. However, it should be noted that for rare cases in which results are not able to converge due to the very small cohesion, simulation stops at a nonconvergent state.
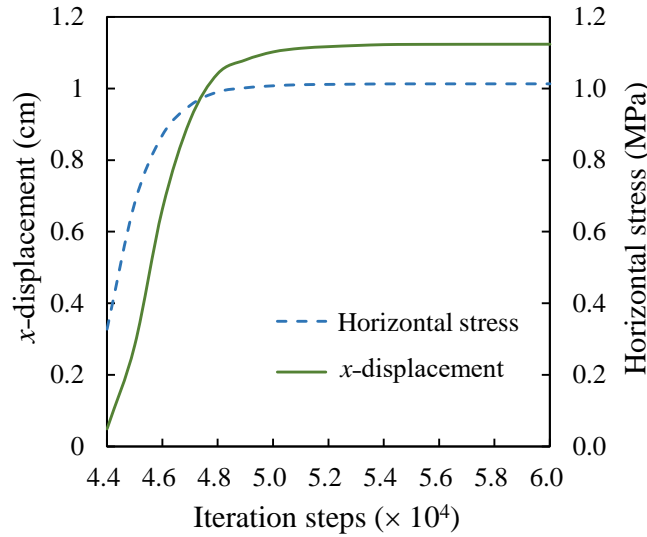
Figure 3.5: Variation of the horizontal stress (σ_{yy}) and x-displacement at the central point of open face as the iteration step increases after adjacent extraction for a reference case

Since the rock-wall deformation at the large depth can be significant, the large strain option of FLAC^{3D} is used to account for the geometrical nonlinearity (Itasca 2013). All FISH functions of FLAC^{3D} used in this study are identical for both small and large strain modes.

Numerical cases with immobile rock walls are also conducted which are less practical, but are used for comparison to show the influence of rock-wall closure. In these cases, small domain sizes L_D,

B_D, and H_D are used and the displacement of rock mass is constrained in all directions. Mine depth D is not considered while other material and modeling parameters remain the same. A series of orthogonal numerical simulations are conducted to investigate the effect of different factors.

All conducted cases are summarized in Table 3.3. Constant parameters are presented in the caption while the variables, including stope geometry, mechanical properties of backfill and rock mass, and fill-rock interfaces, are listed in the table. Each case in Table 3.3 is simulated by changing one parameter in the conditions with and without rock-wall closure. When considering the rock-wall closure, cases are conducted with D ranging from 100 m to 2000 m to investigate the effect of mine depth. Case 1 with $H = 40$ m is taken as the reference case.

Table 3.3: Characteristics of the numerical simulation cases (with $\gamma = 18$ kN/m^3, $\nu = 0.33$, $\psi = 0°$ for cemented backfill, $\gamma_R = 27$ kN/m^3, $\nu_R = 0.22$, GSI = 75, $D_R = 0$, $\sigma_{ci} = 150$ MPa, $m_i = 25$, $\psi_R = 0°$, $m_b = 10.24$, s = 0.06, $a = 0.50$, $\beta_s = 0.85$, $\eta \rightarrow \infty$ for rock mass)

Case	Stope geometry			Backfill		Fill-rock interface		Rock mass		Mine depth (m)
	H (m)	L (m)	B (m)	E (MPa)	ϕ (°)	r_s	r_a	E_R (GPa)	K_r	
1	20–60	10	10	300	30	1	1	42	2	
2	40	5–25	10	300	30	1	1	42	2	
3	40	10	5–25	300	30	1	1	42	2	
4	40	10	10	10–500	30	1	1	42	2	
5	40	10	10	300	20–40	1	1	42	2	100–2000
6	40	10	10	300	30	0–1	1	42	2	
7	40	10	10	300	30	1	1/3–1	42	2	
8	40	10	10	300	30	1	1	12–72	2	
9	40	10	10	300	30	1	1	42	0.5–2	

It should be noted that in the specific cases with a relatively small depth, the geometry of H_D shown in Figure 3.2 needs to be modified accordingly. For example, there is no element above $z = 100$ m in the cases of $D = 100$ m.

3.3 Instability determination of side-exposed backfill

3.3.1 Failure mechanism

Failure mechanisms of side-exposed backfill are influenced by the rock-wall closure, and needs to be determined before evaluating the c_{min}. The backfill upon side exposure can either fail with a sliding plane (Mitchell et al. 1982; Mitchell 1989; Dirige and De Souza 2013) or be crushed (Pierce 1999; Sainsbury and Urie 2007), depending on the rock-wall closure magnitude. The displacement trends of side-exposed backfill are different with different failure mechanisms. For example, Figure 3.6a illustrates the displacement distribution and corresponding vectors for Case 1 upon failure with $H = 40$ m, $D = 100$ m, and $c = 27$ kPa. It is found that the movement of backfill during the extraction of adjacent secondary stope is mainly downward along a sliding plane, indicating the sliding failure mechanism. Figure 3.6b shows the displacement distribution and corresponding vectors for the same case upon failure with $D = 1000$ m and $c = 295$ kPa. As the mine depth increases from 100 m to 1000 m, the side-exposed backfill mainly demonstrates a horizontal movement from sidewalls toward the symmetry plane ($y = 0$) while the backfill around the central line moves to the open face. The upward bulging at the bottom of the backfill is resulted from the heave of rock mass caused by the adjacent excavation which removes some compressions on the floor. The displacement vectors in Figure 3.6b indicate the crushing failure mechanism. The cases in Figures 3.6a and 3.6b fail with different values of cohesion because of the different failure mechanisms and mine depths. The failure mechanism of side-exposed backfill can thus be identified by the evaluation of its displacement vectors.
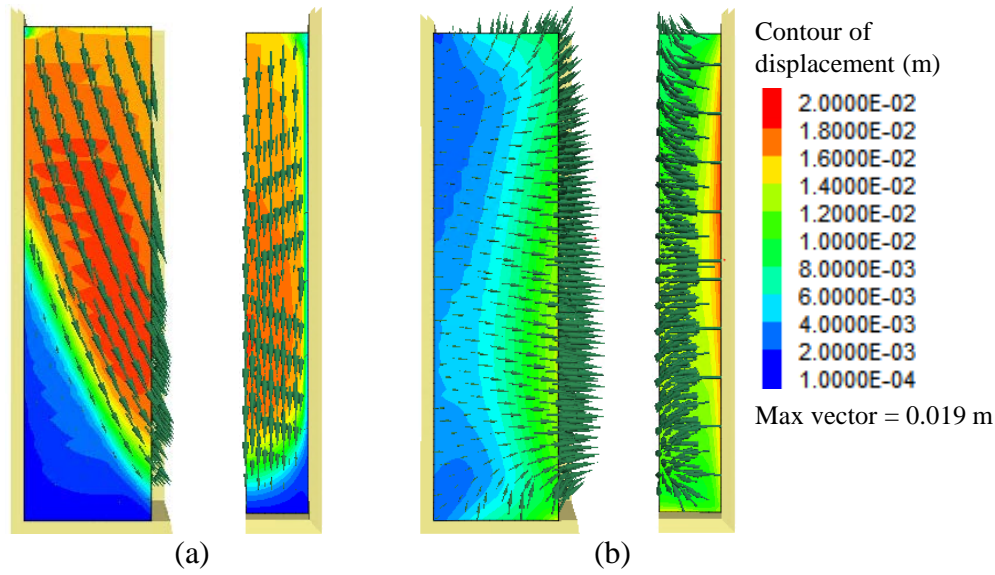
Figure 3.6: Displacement distribution and corresponding vectors of side-exposed backfill for Case 1 in Table 3.3 with (a) $H = 40$ m, $D = 100$ m, $c = 27$ kPa, and (b) $H = 40$ m, $D = 1000$ m, $c = 295$ kPa

3.3.2 Instability criterion of side-exposed backfill

The c_{min} of side-exposed backfill is a critical value to ensure stability and is determined by repeating the steps 3 and 4 of simulation with gradually reduced c. In order to evaluate whether the backfill is stable or unstable at a given state, several indicators have been used, including yield state, convergence of numerical calculation, displacements and strength-stress ratio (Barrett et al. 1978; Cundall et al. 1978; Pierce 1999; Coulthard and Dight 1980; Dirige and De Souza 2013; Falaknaz 2014; Liu et al. 2016a; Caceres et al. 2017; Yang et al. 2017; Pagé et al. 2019). When the yield state or strength-stress ratio is analyzed to evaluate the stability, the evaluation can become subjective when the yield areas are sparse. Therefore, a more objective instability criterion is needed. The divergence of numerical simulation can take place when the model is not able to converge. Nevertheless, applying this criterion usually leads to nonconservative design because of the underestimation of required strength. Several researchers suggested that the rapid increases of displacement can indicate the instability of side-exposed backfill (Karim et al. 2013; Li and Aubertin 2014; Yang et al. 2017; Liu et al. 2018). Figure 3.7 shows the variation of the total displacement value at the central point of open face after adjacent extraction as a function of the

cohesion c (Case 1 with $H = 40$ m, $D = 1000$ m in Table 3.3). Based on the entire curve in Figure 3.7, the displacement starts to significantly increase as c reduces to 50 kPa while the value of c_{min} should be between 50 kPa (unstable) and 100 kPa (stable). However, if one evaluates the subset of the displacement curve as c ranges from 250 kPa to 500 kPa, c_{min} can also be determined as between 300 kPa (unstable) and 350 kPa (stable). Therefore, the displacement is helpful to define the range of required cohesion, but it can be subjective as a criterion to determine the c_{min} because the result depends on the selected axis scales.
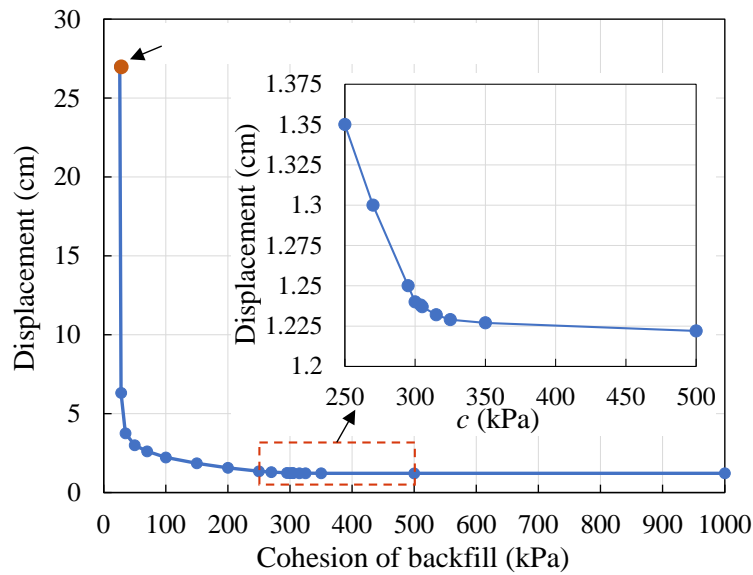
Figure 3.7: Variation of the total displacement value at the central point of the open face with different cohesions of backfill (Case 1 in Table 3.3 with $H = 40$ m, $D = 1000$ m)

Figure 3.8 shows the yield state of the side-exposed backfill of Case 1 with $H = 40$ m, $D = 1000$ m when the backfill cohesion $c = 1000$, 305, 295, 200 and 26 kPa, respectively. When $c = 305$ kPa, the yield area appears in the backfill close to the sidewalls, due to the rock wall compression associated with the extraction of the secondary stope. The yield area propagates horizontally through the symmetry plane ($y = 0$) when c reduces to 295 kPa, indicating a contiguous yielding line joining two sidewalls. It suggests that the stress states around the open face exceed the yield surface of backfill. Therefore, the surficial crushing failure on the open face may occur, which can cause a sloughing of backfill when c reduces to 295 kPa. This crushing failure is caused by the horizontal convergence of rock walls. The yield area increases to 4 m deep from the open face indicating a more pronounced crushing failure when the cohesion further reduces to 200 kPa and a

nonconvergent case occurs when c decreases to 26 kPa, as shown in Figure 3.8. The yield area shown in Figure 3.8 corresponds well with the trend of displacement curve shown in the subset of Figure 3.7. The value of c_{min} is thus 305 kPa. It should be noted that minor yield area around the base of backfill caused by bottom heave (as shown in Figure 3.8b) is considered not affecting the stability because it is at local area without joining to other surfaces.

Failed: ■ (shear) ■ (tensile)

(a) (b) (c) (d) (e)
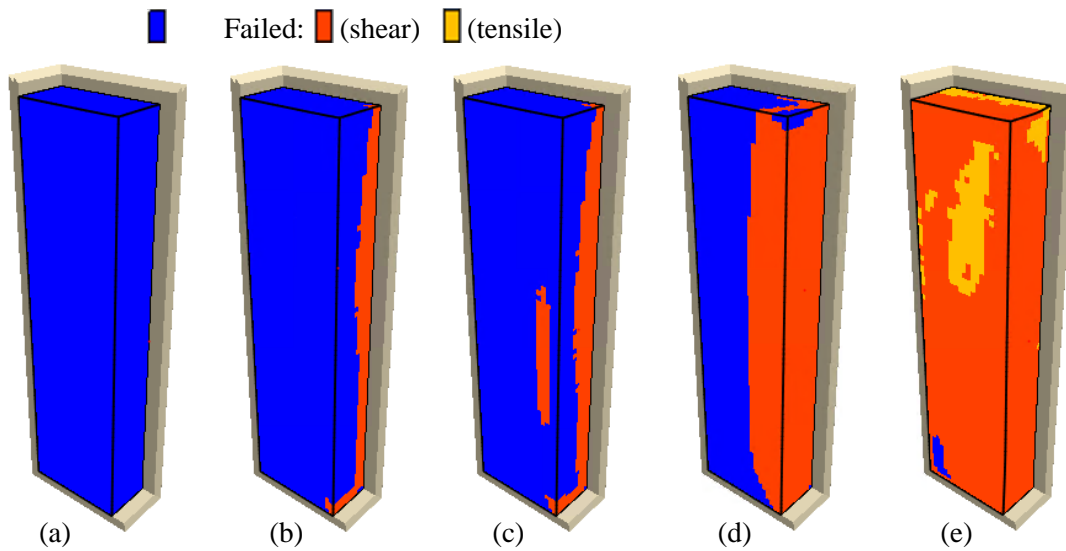
Figure 3.8: Development of the yield area in the side-exposed backfill with the cohesion c equaling: (a) 1000 kPa; (b) 305 kPa; (c) 295 kPa; (d) 200 kPa; (e) 26 kPa for Case 1 in Table 3.3 with $H = 40$ m and $D = 1000$ m

However, if the governing failure mechanism is sliding, the propagation of the yield area can be different from that in the crushing failure case. For example, the sliding failure is identified for Case 1 with $H = 40$ m, $D = 100$ m. Figure 3.9 shows the development of the yield area in this case with $c = 100$, 34, 29, 28, and 27 kPa, respectively. As the cohesion reduces from 34 to 27 kPa, the yield area extends from the toe of exposure toward the back wall. This trend of yielding propagation corresponds well with the displacement vector shown in Figure 3.6a, but is different from the lateral propagation of the yield area in the crushing failure mechanism. When c decreases from 28 kPa to 27 kPa, the yield area on Figure 3.9 joins the front and back wall which forms a sliding plane. This sliding failure is caused by the self-weight of backfill. The value of c_{min} is 28 kPa for this case. Thus, joining of the yield area is used to determine the occurrence of failure and the c_{min} of side-exposed backfill hereafter. The variation of displacement of side-exposed backfill can be used in

some cases to be combined with the yield area development, but the displacement cannot be considered as a main independent instability criterion. The instability criterion can be further verified by the comparisons between the numerical modes and Mitchell's centrifugal model tests (Mitchell 1986) presented in Appendix Ⅰ.
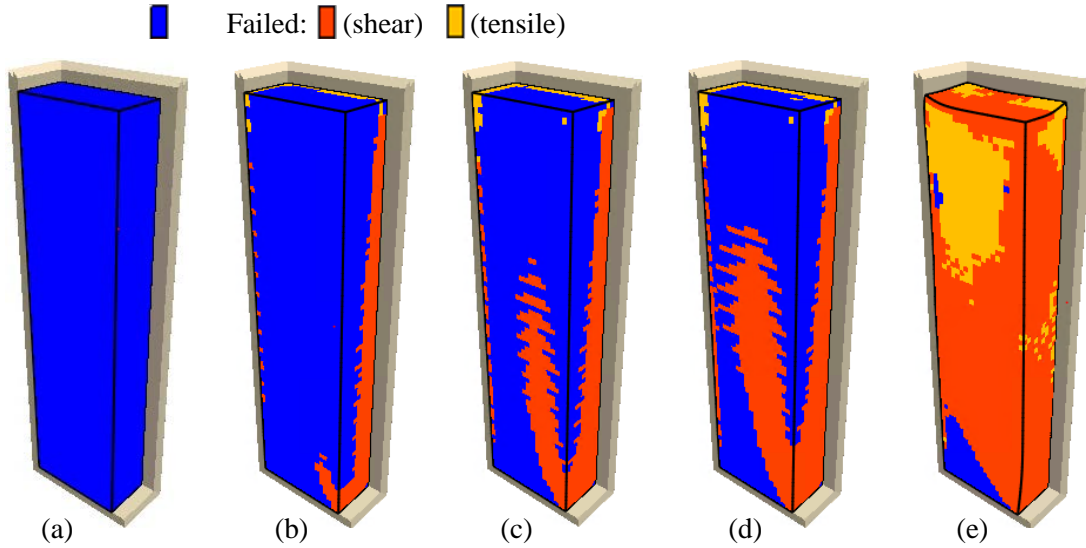
Figure 3.9: Development of the yield area in the side-exposed backfill with the cohesion c equaling: (a) 100 kPa; (b) 34 kPa; (c) 29 kPa; (d) 28 kPa; (e) 27 kPa for Case 1 in Table 3.3 with $H = 40$ m and $D = 100$ m

3.4   Numerical results

Sliding failure mechanism is identified for all cases considering immobile rock walls in Table 3.3. However, the governing failure mechanism differs for cases considering rock-wall closure. The c_{min} for each case and the effect of different factors on the results are discussed in this section.

3.4.1 Effect of stope geometry

Figure 3.10 shows the variation of the c_{min} of the side-exposed backfill as a function of the mine depth ranging from 100 m to 2000 m with different stope heights. It is found that for a given depth, the value of c_{min} increases as the H increases from 20 m to 60 m. As the mine depth increases, a constant trend of c_{min} is shown in Figure 3.10 with immobile rock mass. When rock-wall closure is considered, the sliding failure of side-exposed backfill is identified for cases of $D = 100$ m while

the crushing failure is discovered for other cases. The values of c_{min} for cases of $D = 100$ m are smaller than those without considering wall closure for a given stope height. This is because the rock-wall closure caused by adjacent extraction is not able to crush the backfill when the in-situ stress is small at a shallow depth. Conversely, rock wall confines the fill and improves the shear resistance along the fill-rock interfaces. As the mine depth becomes larger, the crushing failure mechanism becomes dominant while it is straightforward to see the increase of cohesion with mine depth. Moreover, the c_{min} increases with the stope height because that the extraction of a higher adjacent pillar results in a larger rock-wall closure. The region with c_{min} large than that with immobile rock mass is marked as the crushing region with transparency as shown in Figure 3.10, and the stability in the rest unmarked region is dominated by the sliding failure mechanism.
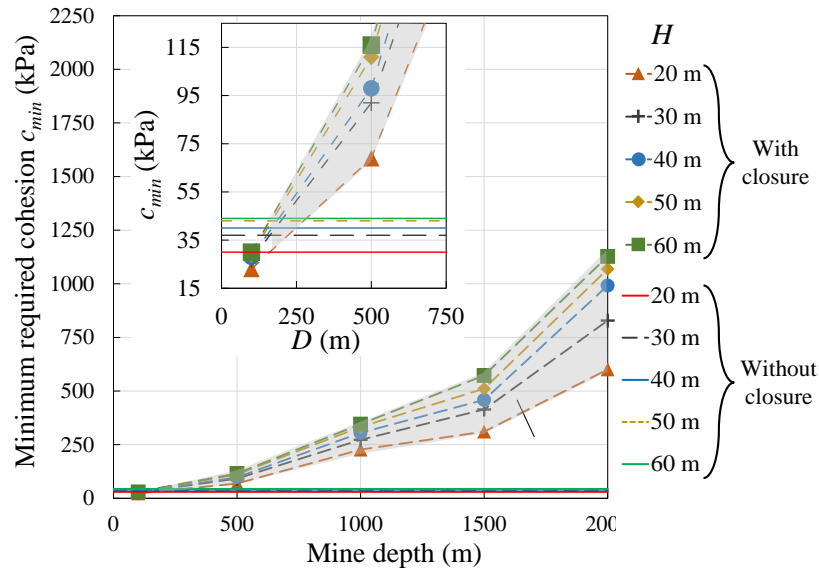
Figure 3.10: Variation of the minimum required cohesion c_{min} of the side-exposed backfill as a function of the mine depth D for different stope heights H (Case 1 in Table 3.3)

Figure 3.11 shows the changing of the c_{min} at different depths for various stope lengths. The tendency of the c_{min} is quite similar to that in Figure 3.10. When the crushing is dominant failure mechanism, the value of c_{min} increases as the increase of mine depth and L ranging from 5 m to 25 m. This is because extracting a longer pillar leads to larger closure at the pillar center and a higher strength is required for backfill to prevent crushing. Meanwhile, sliding failure is identified for cases of $D = 100$ m where the c_{min} is averagely 8 kPa smaller than the result without rock-wall

closure. The reason is minor rock mass deformation of 4 mm confines the backfill and increases the shear resistance along the fill-rock interfaces.
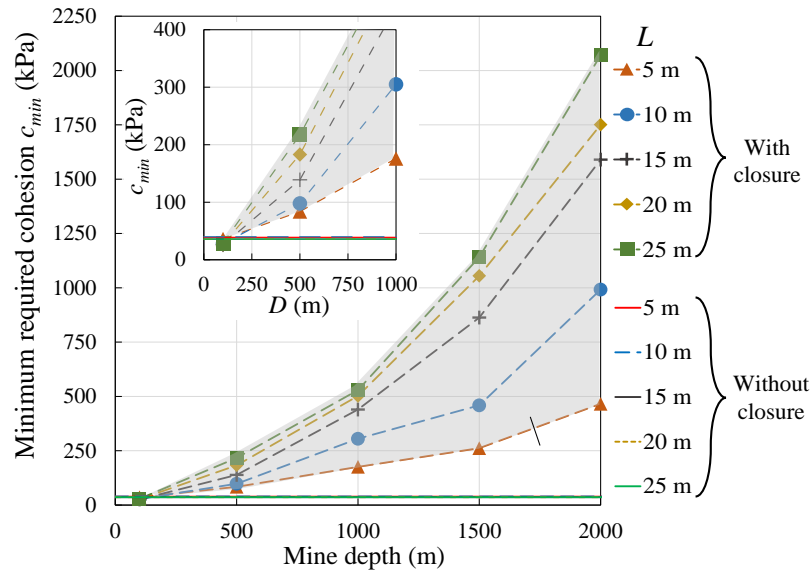
Figure 3.11: Variation of the minimum required cohesion c_{min} of the side-exposed backfill as a function of the mine depth D for different stope lengths L (Case 2 in Table 3.3)

Figure 3.12 illustrates the variation of the c_{min} as a function of the mine depth for different stope widths. The sliding failure is identified for cases with c_{min} smaller than those with immobile rock walls while the crushing failure is the governing failure mechanism for the other cases, as marked with transparency. When the sliding failure is dominant, the c_{min} decreases as the increase of mine depth, but increases as B increases due to the reduction of the arching effect (Aubertin et al. 2003; Li et al. 2003). When the crushing failure is governing, the c_{min} increases as the mine depth increases and decreases with the increase of B as shown in Figure 3.12. These results tend to suggest that a wider side-exposed backfill could be more stable when the dominant failure mechanism is crushing, which is somewhat counterintuitive. It is because a wider backfill has smaller horizontal strains and lower compressive stresses generated by rock-wall closure. The backfill thus becomes less prone to be crushed. Therefore, a larger width can help to prevent the horizontal crushing but it rises the risk of sliding failure for side-exposed backfill.
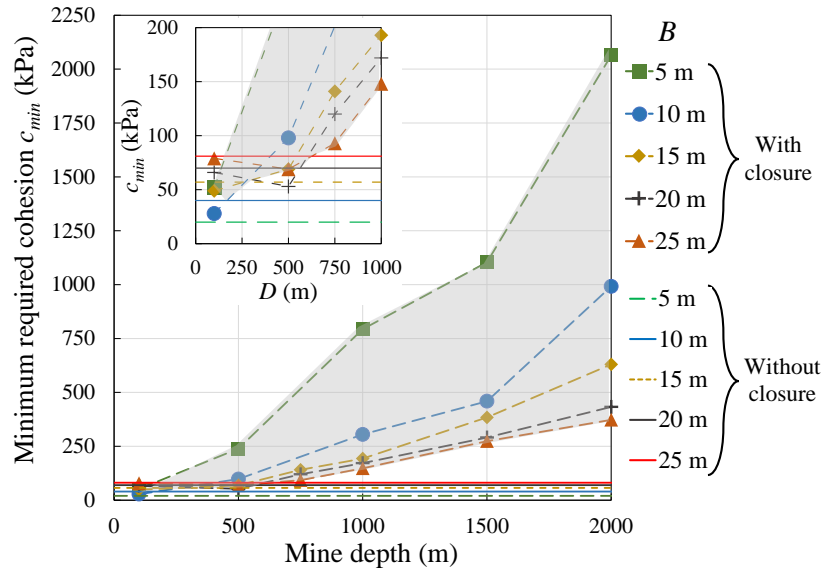
Figure 3.12: Variation of the minimum required cohesion c_{min} of the side-exposed backfill as a function of the mine depth D for different stope widths B (Case 3 in Table 3.3)

3.4.2 Effect of backfill modulus and friction angle

Young's modulus and internal friction angle of cemented backfill could affect the minimum required cohesion. Young's modulus increases with the increase of curing time, binder content, and particle size (Pierce 1999; Fall et al. 2007). Figure 3.13 illustrates the variation of the c_{min} of the side-exposed backfill at different depths considering various E. In the figure, the c_{min} without considering rock-wall closure is around 40 kPa and is independent on backfill Young's Modulus. With the effect of rock-wall closure, the value of c_{min} increases as the increase of E and mine depth when crushing failure is dominant. The sliding failure is also identified for some cases as shown by the unmarked region in the subset of Figure 3.13, where c_{min} is smaller than those with immobile rock walls. For cases with sliding failure, increase of E and mine depth reduces the value of c_{min}. It is because the increase of E leads to higher compressive stresses in fill under a certain rock-wall convergence. Therefore, a higher E can improve the fill stability at shallow depth but it leads to a higher required cohesion when the stability is governed by crushing at the large depth.
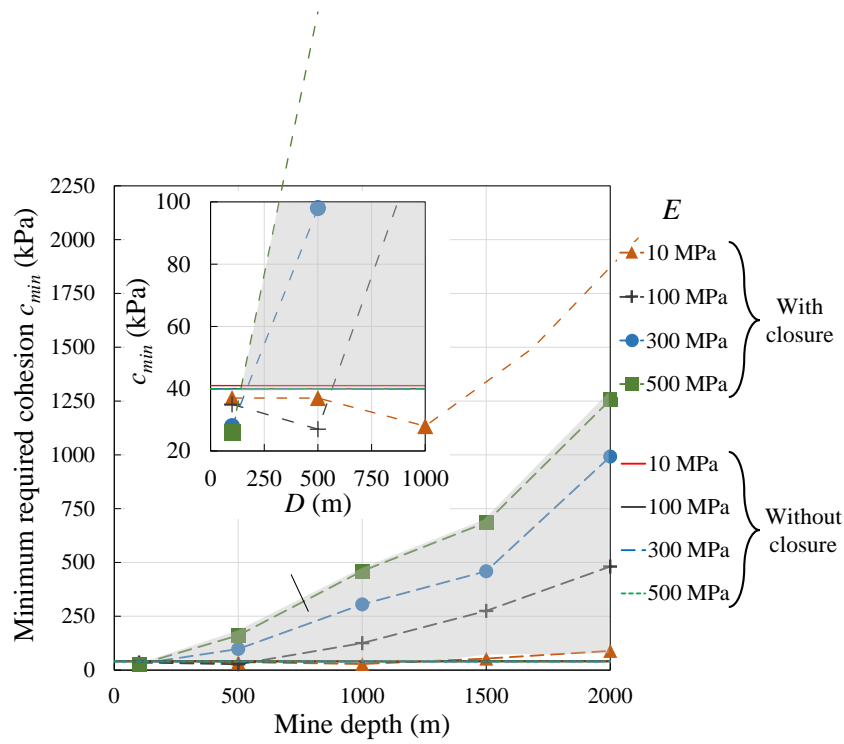
Figure 3.13: Variation of the minimum required cohesion c_{min} of the side-exposed backfill as a function of the mine depth D considering different backfill Young's modulus E (Case 4 in Table 3.3)

Internal friction angle of backfill can be affected by curing time, particle size, binder type and content (Belem et al. 2000; Rankine 2004; Wang et al. 2013). The variation of the c_{min} as a function of mine depth for different friction angles of backfill is shown in Figure 3.14. Sliding failure is identified for the cases with $D = 100$ m in which the c_{min} are smaller compared with those considering immobile rock walls due to the improvement of stability by rock-wall closure. For the cases with crushing failure, an increasing tendency of c_{min} is found as mine depth increases. In all cases, the c_{min} decreases as ϕ increases from 20° to 40°, because the increase of friction angle expands the failure surface of backfill, which makes the side-exposed backfill more stable regardless of the failure mechanism.
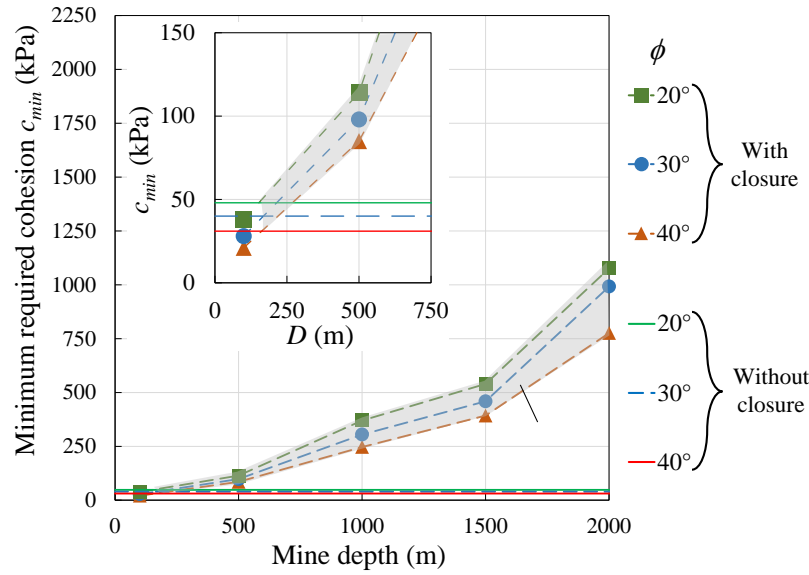
Figure 3.14: Variation of the minimum required cohesion c_{min} of the side-exposed backfill as a function of the mine depth D for different backfill friction angles ϕ (Case 5 in Table 3.3)

3.4.3 Effect of interface properties

The resistance along fill-rock interfaces affects the stability of cemented backfill, but the measurements of the parameters for interface are quite limited. The interface bond can be broken by the blast vibration from the adjacent pillar, and the interface friction angle increases as the asperities become rougher. In practice the interface friction angle (δ) ranges from 1/2 to 2/3 of ϕ while adhesion ratio (r_s) ranges from 0.5 to 1 (Canadian Geotechnical Society 1978; Bowles 1996). Figure 3.15a shows the variation of the c_{min} of side-exposed backfill as a function of mine depth considering different r_s. The c_{min} increases as the interface adhesion decreases for the cases with immobile rock walls. Similar tendency is observed for the cases of $D = 100$ m where the sliding failure is governing and the c_{min} are smaller than those without rock-wall closure. On the other hand, crushing failure is identified for the other cases in which the c_{min} increases with the mine depth, but is almost independent on the interface adhesion.
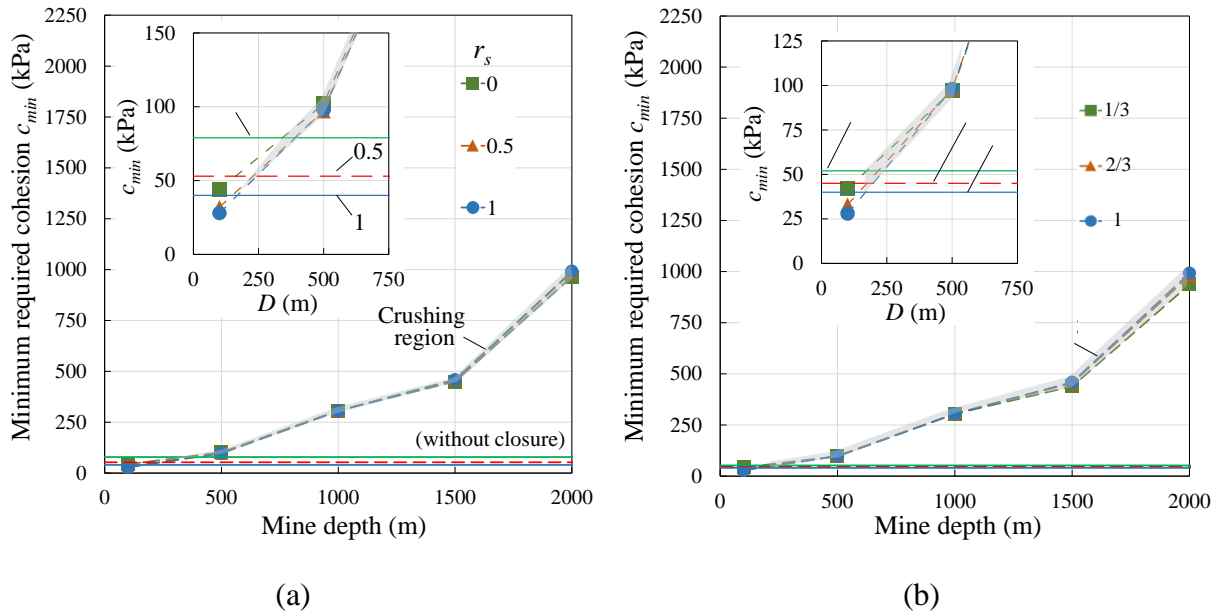
Figure 3.15: Variation of the minimum required cohesion c_{min} of the side-exposed backfill as a function of the mine depth D considering different (a) adhesion ratios r_s and (b) friction angle ratios r_a (Case 6 and Case 7 in Table 3.3)

Figure 3.15b illustrates the variation of the c_{min} at different mine depths D for various r_a. The trend of c_{min} in Figure 3.15b is quite similar to that in Figure 3.15a. One sees that the c_{min} increases as the interface friction angle decreases for the cases of $D = 100$ m and those without wall closure in which sliding is the governing failure mechanism. The c_{min} increases as the mine depth further increases because the failure mechanism becomes crushing, while its value is almost identical for different interface friction angles. Therefore, Figure 3.15 suggests that friction angle and adhesion of fill-rock interface affect the stability of side-exposed backfill at shallow mine depth. However, their influence on the stability is minor when the failure mechanism of crushing is dominant at the large mine depth.

3.4.4 Effect of rock mass properties and rock stresses

Figure 3.16 shows the variation of the c_{min} as a function of mine depth considering different rock mass Young's modulus and rock pressure coefficients. Figure 3.16 illustrates that the c_{min} of the cases considering immobile rock walls are independent on E_R and K_r. In Figure 3.16a, sliding failure is the governing failure mechanism for the cases of $D = 100$ m with $E_R = 42$ and 72 GPa, while the c_{min} slightly reduces from 32 kPa with $E_R = 72$ GPa to 28 kPa with $E_R = 42$ GPa. The

values of c_{min} for these cases are smaller than those with immobile rock walls, that has been explained as minor rock-wall closure improves the backfill stability. When the crushing failure is dominant, the c_{min} grows with the mine depth for a given E_R while it increases as E_R reduces from 72 to 12 GPa at a given depth. It is explained that increasing mine depth or decreasing E_R results in larger wall closure, thus leading to a higher required cohesion when the stability of side-exposed backfill is governed by crushing failure at the large depth.
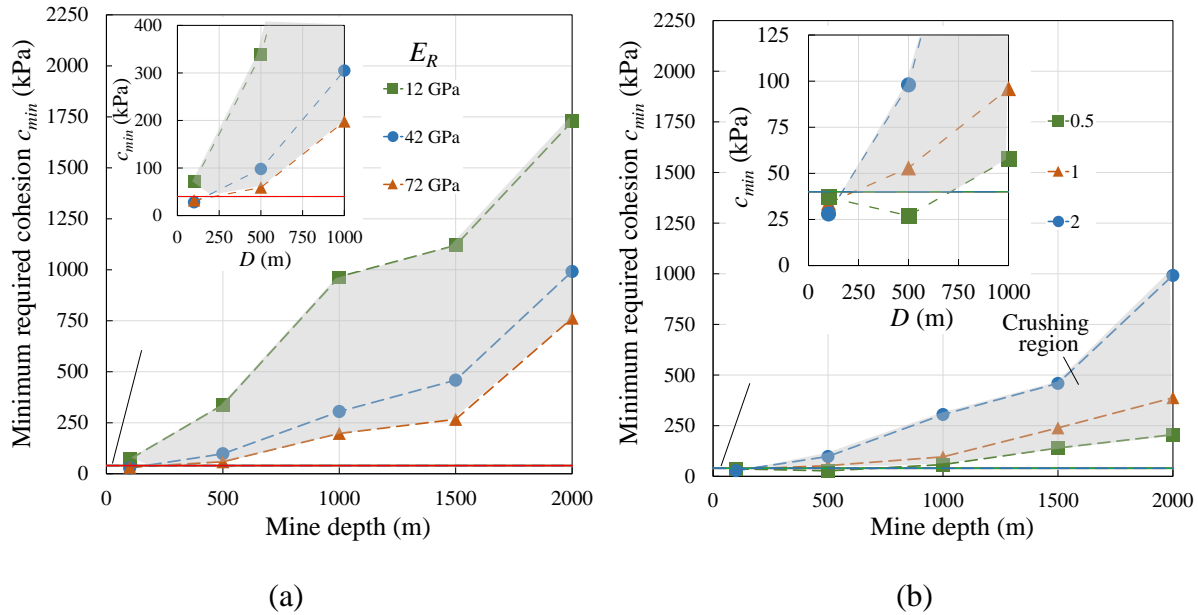
Figure 3.16: Variation of the minimum required cohesion c_{min} of the side-exposed backfill as a function of the mine depth D considering different (a) rock mass Young's modulus E_R and (b) rock pressure coefficients K_r (Case 8 and Case 9 in Table 3.3)

Figure 3.16b illustrates when the crushing failure is dominant, c_{min} increases with the increase of K_r and mine depth. However, the c_{min} slightly decreases as the increase of K_r and mine depth when the sliding failure is dominant as shown by the unmarked region in the subset of Figure 3.16b. It is because the increasing of rock pressure coefficient rises the initial lateral stresses in the rock mass which corresponds to more pronounced wall deformation. Therefore, as K_r increases, side-exposed backfill becomes more stable when the governing failure mechanism is sliding at shallow depth, but tends to be crushed at the large depth.

Numerical results show that the c_{min} of side-exposed backfill are affected by a wide range of factors. Nonetheless, the general trend of c_{min} for each specific factor in Figures 3.10–3.16 can be quantified

by considering the average value. Within the range of this study, when the sliding failure is dominant, the c_{min} averagely decreases by 8% with the increase of 200 m in mine depth, 77% in fill stiffness, 0.5 in rock pressure coefficient, 32% and 48% in fill-rock interface friction angle and adhesion respectively. Increasing rock mass stiffness by 40%, stope height by 49% and width by 7% leads to an average increase of 8% in c_{min}. When the stability is governed by the crushing failure, the c_{min} averagely increases by 8% with the increase of 50 m in mine depth, 22% in stope height, 16% in stope length, 15% in fill stiffness and 0.06 in rock pressure coefficient. Increasing stope width by 16% and rock mass stiffness by 26% results in an average decrease of 8% in c_{min}. In all cases, the c_{min} averagely decreases by 8% as the internal frictional angle of backfill increases by 5°.

3.5 Discussion

Three-dimensional numerical models are developed with FLAC^{3D} to evaluate the stability of side-exposed backfill considering the extraction of adjacent stope at different mine depths. The dominant failure mechanism of side-exposed backfill is found changing from sliding to an unusual crushing failure with the increase of mine depth. The effects of stope geometry, mechanical properties of backfill, rock mass and fill-rock interface have been investigated. This study improves the confidence in predicting the required strength of backfill and the mining cost. It is also helpful to improve the safety and efficiency during pillar recovery with less dilution.

It should be noted that some studies (Barrett et al. 1978; Barrett and Cowling 1980; Coulthard and Dight 1980) employed two-dimensional (2D) numerical models to analyze the stability of side-exposed backfill. The 2D model is efficient, but it implies that the width of stope is large while it is not allowed to consider the rock-wall closure and the arching effect along side walls.

3.5.1 Cost analysis

Previous studies (Belem et al. 2000; Fall et al. 2007) show the nearly linear relationship between the UCS of cemented paste backfill and the cement content within the range of 1.5% to 6%. Combining it with the numerical results in this study, the cost analysis of cemented backfill considering the adjacent extraction can be conducted. For instance, the cement content for Case 4 with a Young's modulus of 10 MPa can be slightly reduced by around 0.04% as the mine depth

increases from 100 m to 1000 m. The effect of this small reduction of cement content on the cost can be minor. However, most cases with a depth larger than 500 m demonstrate the crushing failure and the cement content considerably increases with depth. For Case 1 with a height of 40 m, the cement content needs to be increased by 1.5% approximately as the mine depth increases from 500 to 1500 m. Assuming a pouring rate of 1000 t per day for cemented backfill, the annual cement consumption will increase by over 5400 t. With an assumed price of $120 per ton, an increasing of $0.65 million for annual mining cost should be considered. Nevertheless, the overall economics can benefit from the optimized cemented backfill by increasing the pillar recovery efficiency and reducing the surface disposal of mine waste. The cost analysis above is for the total extraction of secondary stope. Advantages may be obtained by using low cement content with partial extraction or leaving thin pillar for containing backfill (Askew et al. 1978; Mitchell et al. 1982). Moreover, furnace slag, fly ash, and pozzolan can be partially used in place of cement and reduces the cost (Barrett and Cowling 1980; Belem et al. 2000).

3.5.2 Limitations

Even if the numerical modeling is able to assess the stability and required strength of side-exposed backfill in depth, the numerical models involve several hypotheses and limitations discussed as follows.

1) The geometry of stopes is simplified as a vertical rectangular prism while the secondary stope is assumed with the same size as the primary stope. In practice, the shape of underground stope is usually irregular and inclined. More works are needed to investigate the effect of irregular geometry and inclination on the stability of side-exposed backfill.

2) Open stoping mining method with whole adjacent pillar extracted in one step is applied in the numerical model. However, the secondary stope can be extracted in layers which causes the sequential exposure of backfill. Moreover, rock mass conditions do not always permit an open stoping while cut and fill mining method applies when the surrounding rock is weak (Grice 1998). The effect of different mining methods and mine sequencing needs to be studied.

3) This study focuses on the long-term mechanical behavior of side-exposed backfill which is assumed under fully drained condition. Moreover, blast vibrations in open stoping may

influence the stability of adjacent backfilled stope (Emad et al. 2018). This aspect is not considered in this study.

4) In this study, the improvement effect of rock-wall closure on backfill stability is determined when the value of c_{min} is smaller than that considering immobile rock mass. This has been explained as that minor wall closure confines the backfill and increases the shear resistance along interface. However, in reality there may be some void spaces between backfill and rock walls due to shrinkage of fill or blast vibration, which can affect the resistance along fill-rock interface. More efforts are needed to investigate this aspect.

5) Mechanical parameters of backfill, i.e., cohesion, friction angle, and Young's modulus, are all considered as independent parameters. However, few experimental results suggest they can be coupling. For example, Belem et al. (2000) found the friction angle of backfill decreases as the cohesion and cement content increase. And a stiffer fill usually has a higher cohesion (Gonano and Kirkby 1977; Blight and Clarke 1983; Fall et al. 2007). The coupling of parameters can affect the c_{min} of side-exposed backfill. More works are required to assess the stability of side-exposed backfill considering the relationship between these parameters.

6) Backfill is assumed homogeneous and isotropic, and characterized by the elasto-perfectly plastic Mohr-Coulomb model. However, the stress-strain behavior of backfill can be more complicated in plasticity (Pierce 1999; Belem et al. 2000; Rankine 2004). The backfill can also be non-homogeneous and anisotropic due to segregation and different pouring stages (Grabinsky and Bawden 2007; Yumlu and Guresci 2007).

3.6　Conclusions

Numerical modeling is performed with FLAC^{3D} to investigate the stability of side-exposed backfill considering mine depth and adjacent extraction. The failure mechanism and the minimum required cohesion (c_{min}) are determined by considering the joining of yield area, and displacement vectors. Numerical results show that with the influence of rock-wall closure, the dominant failure mechanism of side-exposed backfill can be sliding or horizontal crushing, depending on the magnitude of rock-wall closure. When the mine depth and rock-wall closure are small, sliding failure is dominant and rock-wall closure has effect to improve the stability of exposed backfill.

The values of c_{min} can become even smaller than those obtained with immobile rock walls solutions. Within the range of this study, the c_{min} decreases (8% on average) with the increase of mine depth (per 200 m), fill stiffness (77%), rock pressure coefficient (per 0.5), and fill-rock interface strength (friction angle 32% and adhesion 48%). Increasing rock mass stiffness (40%), stope height (49%) and width (7%) leads to an increase in c_{min} (8% on average). When mine depth and rock-wall closure are large, the crushing failure is dominant. The c_{min} of side-exposed backfill becomes insensitive to the variation of fill-rock interface strength, and increases (8% on average) with the increase of mine depth (per 50 m), stope height (22%) and length (16%), fill stiffness (15%) and rock pressure coefficient (per 0.06). The increase of stope width (16%) and rock mass stiffness (26%) results in the decrease in c_{min} (8% on average). In all cases, the stability of side-exposed backfill is improved by increasing its internal frictional angle.

3.7   Appendix I: Comparisons between numerical models and laboratory tests

The applicability of numerical models and instability criterion of side-exposed backfill can be verified by comparing with the laboratory tests. The stability of side-exposed backfill has been investigated using FLAC^{3D} by simulating the backfill with the Mohr-Coulomb elasto-plastic model as shown by Liu et al. (2016a) through the reproduction of the box instability tests of Mitchell et al. (1982). In this section, three centrifuge model tests of Mitchell (1986) performed to investigate the stability of side-exposed backfill will be reproduced by numerical simulations with FLAC^{3D}. The three tests denoted as 1, 1a, and 4a by Mitchell (1986) were selected because of the same testing conditions (i.e., all cured in a strong box and exposed in the same direction). The first one will be used as calibration to obtain the missing parameters for the numerical model of FLAC^{3D} while the last two will be used to test the predictability of the calibrated numerical model of FLAC^{3D}.

The cemented fill is 33 cm in height and 20 cm in length. The exposure is facing laterally in a 15 cm wide strongbox. Figure 3.17a shows a cemented fill sample for one of the physical model tests. After curing for 28 days, the fill was exposed while the strongbox was laid down and mounted in the centrifuge. The centrifuge test was then conducted by increasing centrifuge speed which produces an increased acceleration a_c (m/s^2) along the fill height until the failure of the side-exposed fill. A scale factor λ was adopted to define the ratio of a_c over the gravitational acceleration

g (m/s^2), and λ_f denotes the λ when the centrifuge model fails. Figure 3.17b shows a numerical model built in FLAC^{3D} by using the same dimensions of the physical test. For boundary conditions, the displacement of strongbox is constrained in all directions as shown in Figure 3.17b. The fill is sequentially placed in the strongbox with 1 cm per layer. The equilibrium state is first simulated with the gravitational acceleration vector $(0, 0, -g)$. Then the vector changes to be $(0, g, 0)$ to represent the change of natural gravity direction relative to the fill sample when mounting the strongbox. Centrifugal acceleration $\lambda \cdot g$ is simulated by modifying the z-component of gravitational acceleration vector which becomes $(0, g, -\lambda \cdot g)$.

(a)   (b)
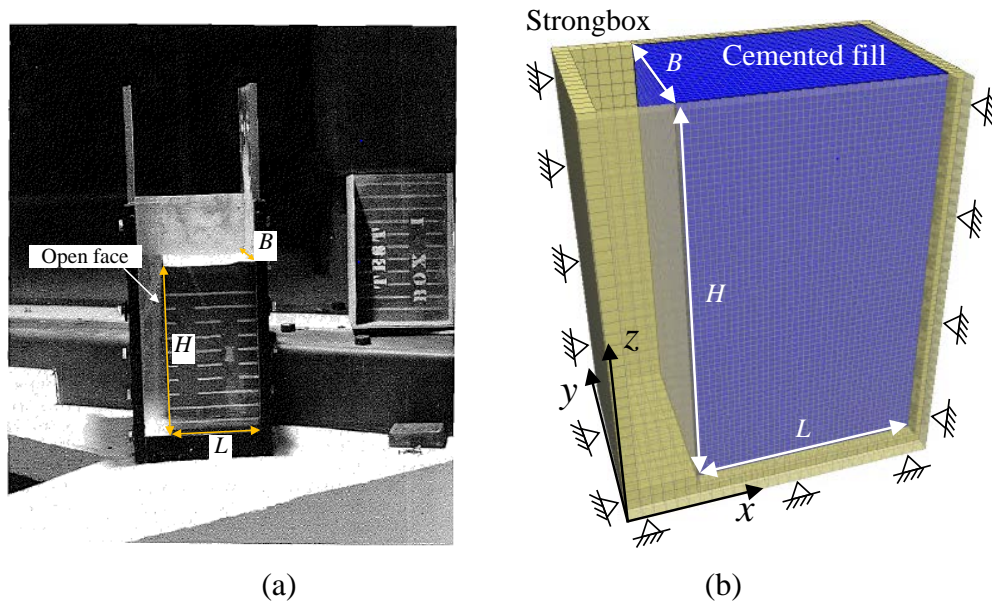
Figure 3.17: A photographic view of (a) a strongbox containing cemented fill to be exposed laterally (modified based on Mitchell 1986) and (b) a numerical model of centrifuge model tests

The density ρ (kg/m^3) and UCS for each model were provided by Mitchell (1986). The tensile strength T is taken as 1/10 of UCS while the interface friction angle δ is taken as 2/3 of ϕ according to previous studies (Canadian Geotechnical Society 1978; Mitchell and Wong 1982; Bowles 1996). Several trial-and-error numerical simulations have been conducted to calibrate the model according to the experimental result of model test 1. Based on calibration, the Young's modulus E for the cemented fill is 150 MPa, the Poisson's ratio v is 0.3, the friction angle ϕ is set as 36° and the interface adhesion ratio r_s is estimated as 0.54. Centrifuge model 1 of Mitchell (1986) failed with $\lambda_f = 62$, as shown in Figure 3.18a. The yield states of model test 1 are shown in Figure 3.18b. The

yield area propagates along a sliding plane as the centrifugal acceleration increases, and it joins the front wall and top with $\lambda_f = 64$ which indicates the failure of the side-exposed fill. This calibrated final scale factor is 2 larger than the experimental result and is considered remarkably close. Moreover, the tensile yielding area around the top of numerical model reasonably agrees with the tensile cracks in the physical tests.
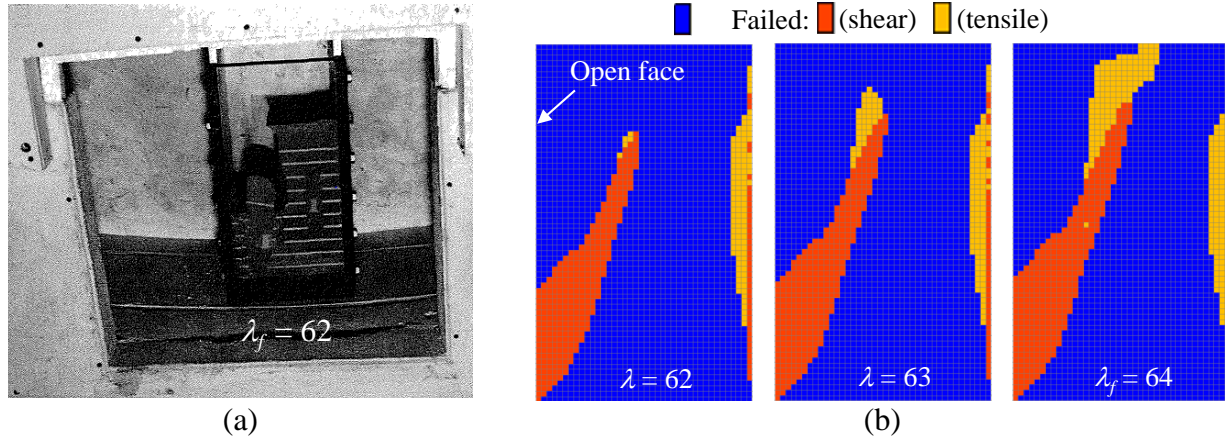
Figure 3.18: (a) Failure in the centrifuge model test 1 (taken from Mitchell 1986); (b) Yield states of the side-exposed fill obtained from numerical simulations for model test 1

The calibrated parameters are then applied to predict the model tests 1a and 4a of Mitchell (1986). It is noted that Young's modulus and Poisson's ratio of cemented fill can vary for different sand to cement ratios. However, the influences of Young's modulus and Poisson's ratio on the fill stability are minor in numerical simulations of these centrifuge model tests. The comparisons of predicted and experimental results are summarized in Table 3.4. For model test 1a, $\lambda_f = 149$ is predicted from the numerical result while $\lambda_f = 159$ was for the experimental result. For model test 4a, $\lambda_f = 237$ is predicted from the numerical result while $\lambda_f = 215$ was for the experimental result. The predicted results show good agreements with the experimental results. Therefore, the numerical models of FLAC^{3D} are partly validated by the experimental results of Mitchell (1986) and can be used to investigate the stability of side-exposed backfill. Meanwhile, the instability criterion for side-exposed backfill in this study is verified.

Table 3.4: Characteristics of the centrifuge model tests conducted by Mitchell (1986), and numerical simulations with $E = 150$ MPa, $\nu = 0.3$, $\phi = 36°$, $r_s = 0.54$, $\delta = 2\phi/3$, $T = $ UCS/10.

	Test	Ratio of sand to cement	H (cm)	ρ (kg/m³)	UCS (kPa)	Scale factor at failure λ_f	
						Test	FLAC^{3D}
Calibration	1	40:1	33	1800	96.4	62	64
Prediction	1a	27:1	34.3	1830	233	159	149
	4a	20:1	33.4	1870	380	215	237

3.8 Appendix II: Mesh generation method

The mesh of the numerical model shown in Figure 3.2 is generated by applying the primitive shape of radial brick in FLAC^{3D} to construct one-quarter of the model. The whole model is then generated through the reflection of this part along the vertical and horizontal symmetry planes, as shown in Figure 3.19a. The radial brick mesh consists of brick-shaped mesh and surrounding radially graded mesh (Itasca 2013). In the numerical model, stopes and backfill are meshed with uniform brick-shaped elements of 0.5 m while the rock mass is meshed with radially graded grid. For meshing the surrounding rock mass, fine grids (radial ratio 1.05) of 0.5 m are applied in a region of 45 m around excavations. The area out of this range is meshed with coarse grids (radial ratio 1.1) to save runtime for a large model. The numerical model needs to be attached before calculation. In order to reduce discontinuity at the attached area, the size of coarse grids follows a multiple integer ratio (e.g., 2 to 1, 3 to 1) to that of fine grids (Itasca 2013), as shown in Figure 3.19b.

(a)

(b)
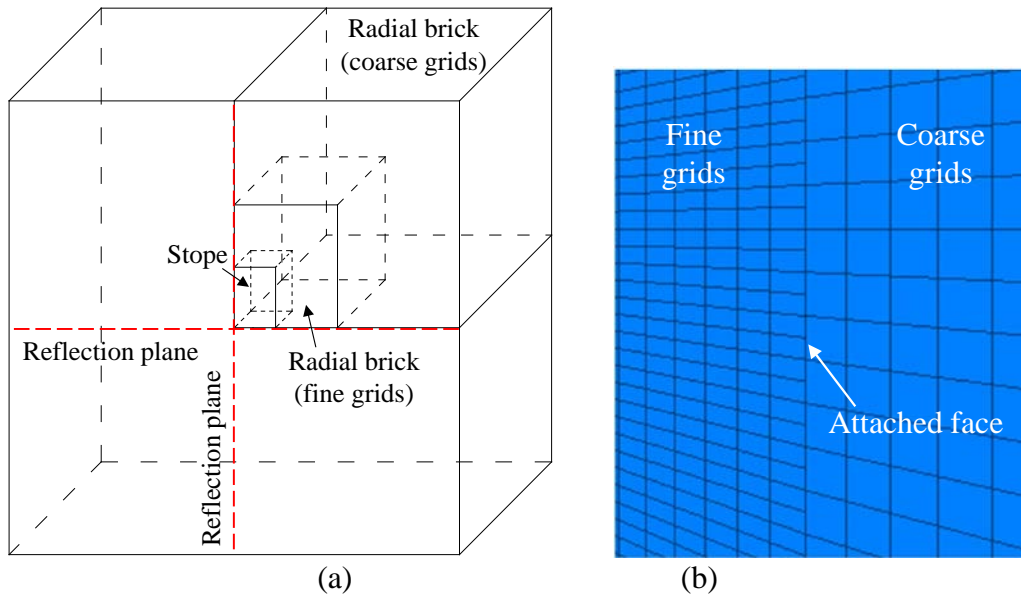
Figure 3.19: Illustrations of (a) the model development of side-exposed backfill utilizing the primitive shape of radial brick and reflection in FLAC^{3D} and (b) the attached area with different zone sizes that follow an integer ratio of 2 to 1

Acknowledgements

3.9   References

Alejano, L.R., Alonso, E., Rodriguez-Dono, A., & Fernandez-Manin, G. (2010). Application of the convergence-confinement method to tunnels in rock masses exhibiting Hoek-Brown strain-softening behaviour. *International Journal of Rock Mechanics and Mining Sciences*, 47(1), 150–160.

Anderson, T. (2014). A comparison of shallow and deep mining. *Proceedings of the 7th International Conference on Deep and High Stress Mining*. Sudbury, Canada, Australian Centre for Geomechanics, 181–187.

Askew, J., McCarthy, P.L., & Fitzgerald, D.J. (1978). Backfill research for pillar extraction at ZC/NBHC. *Proceedings of 12th Canadian Rock Mechanics Symp*. Sudbury, Canada, Canadian Institute of Mining and Metallurgy, 100–110.

Aubertin, M., Li, L., Arnoldi, S., Belem, T., Bussière, B., Benzaazoua, M., & Simon, R. (2003). Interaction between backfill and rock mass in narrow stopes. *Proceedings of 12th Panamerican Conference on Soil Mechanics and Geotechnical Engineering and 39th U.S. Rock Mechanics Symp*.Cambridge, Massachusetts, United States of America, 1157–1164.

Barrett, J.R., Coulthard, M.A., & Dight, P.M. (1978). Determination of fill stability. *Proceedings*

of 12th Canadian Rock Mechanics Symp. Sudbury, Canada, Canadian Institute of Mining and Metallurgy, 85–91.

Barrett, J.R., & Cowling, R. (1980). Investigations of cemented fill stability in 1100 orebody, Mount Isa Mines, Ltd., Queensland, Australia. *Institution of Mining and Metallurgy Transactions, Section* A, 89, A118–A128.

Belem, T., Benzaazoua, M., & Bussière, B. (2000). Mechanical behaviour of cemented paste backfill. *Proceedings of 53rd Canadian Geotechnical Conference*. Montreal, Canada, Canadian Geotechnical Society, 373–380.

Belem, T., & Benzaazoua, M. (2008). Design and application of underground mine paste backfill technology. *Geotechnical and Geological Engineering*, 26(2), 147–174.

Benz, T., & Schwab, R. (2008). A quantitative comparison of six rock failure criteria. *International Journal of Rock Mechanics and Mining Sciences*, 45(7), 1176–1186.

Benzaazoua, M., Bussière, B., Demers, I., Aubertin, M., Fried, É., & Blier, A. (2008). Integrated mine tailings management by combining environmental desulphurization and cemented paste backfill: Application to mine Doyon, Quebec, Canada. *Minerals Engineering*, 21(4), 330–340.

Blight, G.E., & Clarke, I.E. (1983). Design and properties of stiff fill for lateral support of pillars. *Proceedings of International Symp on Mining with Backfill*. Lulea, Sweden, 303–307.

Bowles, L. (1996). *Foundation analysis and design*. New York: McGraw-hill.

Brown, E.T. (2012). Progress and challenges in some areas of deep mining. *Mining Technology*, 121(4), 177–191.

Caceres, C., Moffat, R., & Pakalnis, R. (2017). Evaluation of flexural failure of sill mats using classical beam theory and numerical models. *International Journal of Rock Mechanics and Mining Sciences*, 99, 21–27.

Canadian Geotechnical Society. (1978). *Canadian foundation engineering manual*. Canada: BiTech Publishers Ltd.

Carranza-Torres, C. (2004). Elasto-plastic solution of tunnel problems using the generalized form of the Hoek-Brown failure criterion. *International Journal of Rock Mechanics and Mining*

Sciences, 41(3), 480–481.

Coulthard, M.A., & Dight, P.M. (1980). Numerical analysis of failed cemented fill at ZC/NBHC Mine, Broken Hill. *Proceedings of 3rd Australia-New Zealand Conference on Geomechanics*. Wellington, New Zealand, Institution of Professional Engineers New Zealand, 145–151.

Coulthard, M.A. (1999). Applications of numerical modelling in underground mining and construction. *Geotechnical and Geological Engineering*, 17(3-4), 373–385.

Coulthard, M.A. (1980). Numerical analysis of fill pillar stability: Three dimensional linearly elastic finite element calculations. *Technical Report*. Australia: Division of Applied Geomechanics, Commonwealth Scientific and Industrial Research Organization;.

Cundall, P., Carranza-Torres, C., & Hart, R. (2003). A new constitutive model based on Hoek-Brown criterion. *Proceedings of 3rd International Symp on FLAC and FLAC3D Numerical Modelling in Geomechanics*. Sudbury, Canada, 17–25.

Cundall, P., Shillabeer, J.H., & Herget, G. (1978). Modelling to predict rock fill stability in transverse pillar extraction. *Proceedings of 12th Canadian Rock Mechanics Symp*. Sudbury, Canada, Canadian Institute of Mining and Metallurgy, 92–99.

Dirige, A.P.E., & De Souza, E. (2013). Mechanics of failure of paste backfill face exposure during adjacent mining. *Proceedings of 23rd World Mining Congress*. Montreal, Canada.

Emad, M.Z., Mitri, H., & Kelly, C. (2018). Dynamic model validation using blast vibration monitoring in mine backfill. *International Journal of Rock Mechanics and Mining Sciences*, 107, 48–54.

Fairhurst, C. (2017). Some challenges of deep mining. *Engineering*, 3(4), 527–537.

Falaknaz, N. (2014). *Analysis of the geomechanical behavior of two adjacent backfilled stopes based on two and three dimensional numerical simulations* (Ph.D. thesis, École Polytechnique de Montréal).

Fall, M., Belem, T., Samb, S., & Benzaazoua, M. (2007). Experimental characterization of the stress-strain behaviour of cemented paste backfill in compression. *Journal of Materials Science*, 42(11), 3914–3922.

Gonano, L.P., & Kirkby, R.W. (1977). In situ investigation of cemented rockfill in the 1100 orebody, Mount Isa Mine, Queensland. *Technical Report*. Australia: Division of Applied Geomechanics, Commonwealth Scientific and Industrial Research Organization.

Grabinsky, M.W., & Bawden, W.F. (2007). In situ measurements for geomechanical design of cemented paste backfill systems. *Proceedings of 9th International Symp on Mining with Backfill*. Montreal, Canada, Canadian Institute of Mining, Metallurgy and Petroleum, 1–8.

Grice, T. (1998). Underground mining with backfill. *Proceedings of 2nd Annual Summit-Mine Tailings Disposal Systems*. Brisbane, Australia, 24–25.

Hassani, F., & Archibald, J. (1998). *Mine backfill*. Canadian Institute of Mine, Metallurgy and Petroleum.

Herget, G. (1988). *Stresses in rock*. Rotterdam: AA Balkema.

Hoek, E., & Brown, E.T. (1997). Practical estimates of rock mass strength. *International Journal of Rock Mechanics and Mining Sciences*, 34(8), 1165–1186.

Hoek, E., & Brown, E.T. (2019). The Hoek–Brown failure criterion and GSI–2018 edition. *Journal of Rock Mechanics and Geotechnical Engineering*, 11(3), 445–463.

Hoek, E., Kaiser, P.K., & Bawden, W.F. (2000.). *Support of underground excavations in hard rock*. Rotterdam: AA Balkema.

Itasca. (2013). *FLAC3D—Fast Lagrangian analysis of continua in 3 dimensions; user's guide*. version 5.01. Minneapolis, MN: Itasca Consulting Group.

Jahanbakhshzadeh, A., Aubertin, M., & Li, L. (2017). A new analytical solution for the stress state in inclined backfilled mine stopes. *Geotechnical and Geological Engineering*, 35(3), 1151–1167.

Jahanbakhshzadeh, A., Aubertin, M., & Li, L. (2018a). Analysis of the stress distribution in inclined backfilled stopes using closed-form solutions and numerical simulations. *Geotechnical and Geological Engineering*, 36(2),1011–1036.

Jahanbakhshzadeh, A., Aubertin, M., & Li, L. (2018b). Three-dimensional stress state in inclined backfilled stopes obtained from numerical simulations and new closed-form solution. *Canadian Geotechnical Journal*, 55(6), 810–828.

Karim, R., Simangunsong, G.M., Sulistianto, B., & Lopulalan, A. (2013). Stability analysis of paste fill as stope wall using analytical method and numerical modeling in the Kencana underground gold mining with long hole stope method. *Procedia Earth and Planetary Science*, 6, 474–484.

Li, L., Aubertin, M., Simon, R., Bussière, B., & Belem, T. (2003). Modeling arching effects in narrow backfilled stopes with FLAC. *Proceedings of 3rd International Symposium on FLAC and FLAC3D Numerical Modelling in Geomechanics*. Sudbury, Canada, 211–219.

Li, L., & Aubertin, M. (2012). A modified solution to assess the required strength of exposed backfill in mine stopes. *Canadian Geotechnical Journal*, 49(8), 994–1002.

Li, L., & Aubertin, M. (2014). An improved method to assess the required strength of cemented backfill in underground stopes with an open face. *International Journal of Mining Science and Technology*, 24(4), 549–558.

Li, L. (2014a). Generalized solution for mining backfill design. *International Journal of Geomechanics*, 14(3), 04014006.

Li, L. (2014b). Analytical solution for determining the required strength of a side-exposed mine backfill containing a plug. *Canadian Geotechnical Journal*, 51(5), 508–519.

Liu, G., Li, L., Yang, X., & Guo, L. (2018). Required strength estimation of a cemented backfill with the front wall exposed and back wall pressured. *International Journal of Mining and Mineral Engineering*, 9(1), 1–20.

Liu, G., Li, L., Yang, X., & Guo, L. (2016a). Stability analyses of vertically exposed cemented backfill: A revisit to Mitchell's physical model tests. *International Journal of Mining Science and Technology*, 26(6), 1135–1144.

Malan, D.F., & Basson, F.R.P. (1998). Ultra-deep mining: the increased potential for squeezing conditions. *Journal of the Southern African Institute of Mining and Metallurgy*, 98(7), 353–363.

Malan, D.F., Napier, J.A.L., & Janse V.R. (2007). Stope deformation measurements as a diagnostic measure of rock behaviour: a decade of research. *Journal of the Southern African Institute of Mining and Metallurgy*, 107(11), 743–765.

Mitchell, R.J., Olsen, R.S., & Smith, J.D. (1982). Model studies on cemented tailings used in mine backfill. *Canadian Geotechnical Journal*, 19(1), 14–28.

Mitchell, R.J., & Wong, B.C. (1982). Behaviour of cemented tailings sands. *Canadian Geotechnical Journal*, 19(3), 289–295.

Mitchell, R.J. (1986). Centrifuge model tests on backfill stability. *Canadian Geotechnical Journal*, 23(3), 341–345.

Mitchell, R.J. (1989). Model studies on the stability of confined fills. *Canadian Geotechnical Journal*, 26(2), 210–216.

Pagé, P., Li, L., Yang, P., & Simon, R. (2019). Numerical investigation of the stability of a base-exposed sill mat made of cemented backfill. *International Journal of Rock Mechanics and Mining Sciences*, 114, 195–207.

Pariseau, W.G. (2007). Fitting failure criteria to laboratory strength tests. *International Journal of Rock Mechanics and Mining Sciences*, 44(4), 637–646.

Pierce, M.E. (1999). *Laboratory and numerical analysis of the strength and deformation behaviour of paste backfill*. (Master thesis, Queen's University).

Potvin, Y., Thomas, E., & Fourie, A. (2005). *Handbook on mine fill*. Perth, Australia: Australian Centre for Geomechanics publication.

Ranjith, P.G., Zhao, J., Ju, M., De Silva, R.V.S., Rathnaweera ,T.D., & Bandara, A.K. (2017). Opportunities and challenges in deep mining: a brief review. *Engineering*, 3(4), 546–551.

Rankine, R.M.A. (2004). *The geotechnical characterisation and stability analysis of BHP Billiton's Cannington Mine paste fill*. (Ph.D. thesis, James Cook University).

Sainsbury, D.P., & Urie, R. (2007). Stability analysis of horizontal and vertical paste fill exposures at the Raleigh Mine. *Proceedings of 9th International Symp on Mining with Backfill*. Montreal, Canada, Canadian Institute of Mining, Metallurgy and Petroleum.

Salencon, J. (1969). Contraction quasi-statique d'une cavité a symétrie sphérique ou cylindrique dans un milieu elastoplastique. *Ann Ponts Chaussées*, 4, 231–236.

Seymour, J.B., Raffaldi, M.J., Abraham, H., Johnson, J.C., & Zahl, E.G. (2017). Monitoring the in situ performance of cemented paste backfill at the Lucky Friday Mine. *Proceedings of 12th International Symp on Mining with Backfill*. Denver, United States of America, 19–22.

Tesarik, D.R., Seymour, J.B., & Yanske, T.R. (2009). Long-term stability of a backfilled room-and-pillar test section at the Buick Mine, Missouri, USA. *International Journal of Rock Mechanics and Mining Sciences*, 46(7), 1182–1196.

Wagner, H. (2019). Deep mining: a rock engineering challenge. *Rock Mechanics and Rock Engineering*, 52(5), 1417–1446.

Wang, J.J., Zhang, H.P., Tang, S.C., & Liang, Y. (2013). Effects of particle size distribution on shear strength of accumulation soil. *Journal of Geotechnical and Geoenvironmental Engineering*, 139(11), 1994–1997.

Yang, P., Li, L., & Aubertin, M. (2017). A new solution to assess the required strength of mine backfill with a vertical exposure. *International Journal of Geomechanics*, 17(10), 04017084.

Yang, P. (2016). *Investigation of the geomechanical behavior of mine backfill and its interaction with rock walls and barricades*. (Ph.D. thesis, École Polytechnique de Montréal).

Yumlu, M., & Guresci, M. (2007). Paste backfill bulkhead monitoring: A case study from Inmet's Cayeli Mine, Turkey. *Proceedings of 9th International Symp on Mining with Backfill*. Montreal, Canada, Canadian Institute of Mining, Metallurgy and Petroleum, 146–155.

CHAPTER 4   ARTICLE 2: TIME-DEPENDENT STABILITY ANALYSES OF SIDE-EXPOSED BACKFILL CONSIDERING CREEP OF SURROUNDING ROCK MASS

Ruofan Wang and Li Li

Abstract: The stability of side-exposed backfill is essential to ensure a successful mining operation. Until now, it has been analyzed without considering the creep of rock mass. In practice, stope excavation and backfilling are always scheduled with different time during which fill mechanical properties can evolve and rocks exhibit more or less creep deformation. In this study, time-dependent stability and minimum required cohesion (c_{min}) of side-exposed backfill associated with the creep of surrounding rock mass are, for the first time, analyzed through numerical modeling with FLAC^{3D}. A distinction is made between the cohesion at failure and c_{min}. Results show that the empty time of primary stope does not significantly affect the stability and c_{min}. When mine depth is small and the rock exhibits little creep, it deserves to wait longer time before adjacent extraction for the backfill to gain more strength. When the mine depth is large or/and the rock exhibits heavy creep, the instability of side-exposed backfill can be dictated by crushing failure. A stronger backfill means also a harder backfill, which absorbs larger compressive stress and is more prone to be crushed. In this condition, a softer backfill can be better through the use of lower binder content or/and with a shorter curing time. The adjacent secondary stope should be filled as soon as possible to avoid failure of side-exposed backfill. More simulations were done on the effects of stope geometry and mechanical properties of backfill and rock mass on the stability and c_{min} of side-exposed backfill.

4.1 Introduction

Cemented backfill is commonly used in underground metal mines to decrease ore dilution, increase ore recovery and improve the stability condition of underground openings (Askew et al. 1978; Barrett and Cowling 1980; Hassani and Archibald 1998; Potvin et al. 2005; Belem and Benzaazoua 2008). In open stoping mining method or in drift-and-fill mining method, the stopes are commonly divided into primary and secondary stopes (Hartman 1992; Darling 2011). The backfill in the primary stopes must gain enough strength before side exposure associated with the excavation of adjacent secondary stopes. The minimum required cohesion (c_{min}) of side-exposed backfill is therefore of particular interest to ensure its stability and minimize binder consumption and associate cost.

The first analytical solution by considering the confining effect of rock walls was proposed by Mitchell et al. (1982). The friction angle of backfill was taken as nil and the interface cohesion between rock walls and backfill was assumed to be equal to the backfill cohesion. The analytical solution was validated by laboratory box instability test results. Through numerical modeling, Liu et al. (2016a) have shown that the analytical solution and laboratory tests of Mitchell et al. (1982) are all for backfill under undrained condition for short-term stability analysis, not for backfill under fully drained condition for long-term stability analysis.

In practice, the backfill in primary stopes is commonly exposed after a long enough, typically for a curing period of 28 days in order for the backfill to gain enough strength. At that time, the backfill typically becomes stiff and unsaturated due to drainage and hydration of binder. Analytical solutions by considering drained backfill for long-term stability analysis is thus necessary. In addition, several studies have shown that the fill-rock interface cohesion is usually smaller than the backfill cohesion (Nasir and Fall 2008; Fall and Nasir 2010; Fang and Fall 2018, 2019, 2020, 2021). The consideration of these limitations led to several improved analytical solutions developed to estimate the c_{min} of side-exposed backfill (Li and Aubertin 2012, 2014; Li 2014a, 2014b; Yang et al. 2017; Liu et al. 2018; Zhao et al. 2019). All these improvements were based on the confined wedge model of Mitchell et al. (1982). Rock walls were thus considered as stiff and immobile, independently on the filling and side-stope excavation. In reality, the rock walls can deform and exercise compression on the backfill upon side-stope excavation, affecting significantly the

stability and c_{min} of side-exposed backfill. This has been shown by several researchers (e.g., Coulthard 1980; Pierce 1999; Sainsbury and Urie 2007; Wang et al. 2021) through numerical modeling by considering the rock mass to have an elastic or elasto-plastic behavior. The closure due to side-stope excavation and rock-wall deformation considered in previous studies are thus instantaneous while the factor of time is not accounted.

In many cases, rock can exhibit significantly creep behavior. When a rock is submitted to a sufficiently high (but lower than its peak strength) and constant mechanical load, it can react and deform instantaneously, followed by continuous deformation with time. This phenomenon of time-dependent mechanical behavior is well-known as creep of rocks (Griggs 1939; Dusseault and Fordham 1993). Creep deformation can generally exhibit three stages: primary, secondary and tertiary (Hardy et al. 1969; Farmer 2012; Wang et al. 2019). Figure 4.1 shows the typical variation of strain and strain rate of rocks with time upon a constant load. In the primary stage, rocks deform with progressively decreased strain rate as time increases. The secondary stage is featured with an almost constant creep strain rate and mainly relates to the long-term deformation of rocks. If the load exceeds the long-term strength of rocks, the tertiary stage occurs in which the creep strain rate accelerates leading to failure of the material (Lajtai and Schmidtke 1986; Cristescu and Hunsche 1998). These stages depend on the deviatoric and confining stresses (Kranz 1980; Ngwenya et al. 2001; Amitrano and Helmstetter 2006; Brantut et al. 2013; Hao et al. 2017) as long as the thermal conditions (Heap et al. 2009).
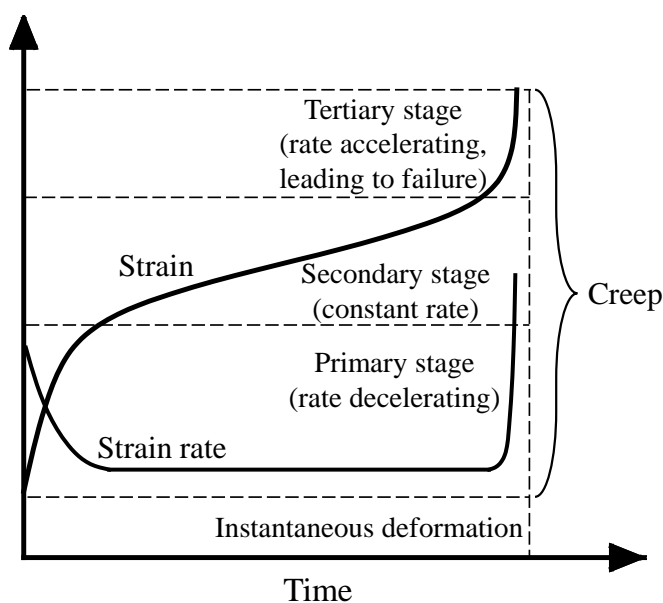
Figure 4.1: Schematic illustration of creep strain and strain rate of rocks (modified based on Wang et al. 2019)

The creep deformation of surrounding rocks can be significant for a soft rock mine (e.g., rock salt, shale, limestone) or with a deep hard rock mine where the stresses and temperature can become very high (Malan 1999; Paraskevopoulou et al. 2018; Wang and Li 2019; Bérest et al. 2019). For example, King et al. (1989) reported a stope closure rate of 6 mm/day for 37 days after the blasting at Hartebeestfontein Mine. Guler (1998) monitored a closure rate of 10 mm/day for a stope with soft lava hanging wall at East Driefontein Mine and a stope closure rate of 5 mm/day at Deelkraal Mine. At Lucky Friday Mine, an increase of stope closure and an increase of horizontal stress in the backfill at a rate of 0.15 MPa/month after an undercut were observed for a period of 60 days (Raffaldi et al. 2019). At Kidd Mine, stress increase with time in a backfilled stope after adjacent extraction was also reported (Thompson et al. 2009). Recently, Qi and Fourie (2019) have shown that stress states in a backfilled stope increase with time when rock walls demonstrate creep deformation based on numerical simulations with FLAC.

Despite the above mentioned evidences of creep behavior of rocks and its significant impact on the stresses in backfilled stopes, the effect of time on the stability and c_{min} of side-exposed backfill has never been studied. In practice, instantaneous excavation and backfilling of a stope are impossible. Time is always necessary not only for these operations, but also before or after each of these operations. During these times, the mechanical properties of cemented backfill can change due to cement hydration and rock-wall closure can evolve with the creep deformation of rock masses. It still remains unknown on how the stability and required strength of side-exposed backfill be influenced by time-dependent behaviors of cemented backfill and rock mass.

To fill this gap, a series of numerical simulations were performed with FLAC^{3D}. The time-dependent stability and minimum required cohesion c_{min} of side-exposed backfill associated with the creep of surrounding rock mass are for the first time investigated. A distinction is made between the cohesion at failure and the c_{min}. Mechanical parameters evolution of backfill with curing time is considered. The effect of waiting time between the excavation and filling of a primary stope, the effect of curing time between the filling of the primary stope and excavation of a secondary stope and the effect of waiting time between the excavation and filling of the secondary stope on the

stability and c_{min} of side-exposed backfill are for this first time analyzed. The effects of mine depth, stope geometry, mechanical properties of backfill and rock mass are also investigated.

4.2 Numerical model

Figure 4.2 shows a schematic presentation with primary stope backfilled with cemented backfill, aside a secondary stope already excavated, all at a mine depth D measured from the ground surface to the stope roof. The stopes are surrounded by the rock mass which can cover a wide range of rocks (e.g., rock salt, sandstone, schist, lherzolite, and granite) since most rocks have more or less degree of creep. In the figure, H and B are the height and width of the stopes, respectively; L_b and L_s denote the strike lengths of the primary and secondary stopes, respectively. This problem will be treated by numerical modeling with FLAC^{3D} (Itasca 2013).
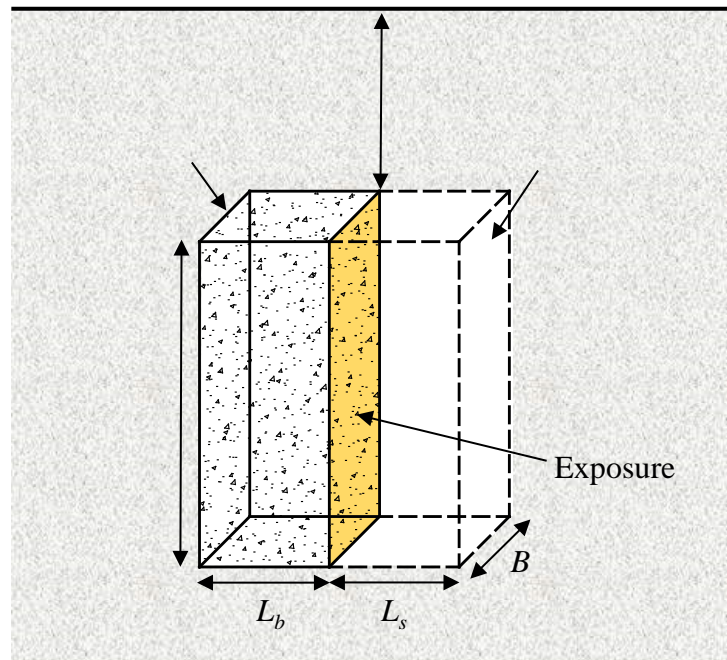
Figure 4.2: Schematic presentation of a backfilled primary stope aside an excavated secondary stope

The rock mass is described by Burgers-creep viscoplastic (CVISC) model (Jaeger 1969; Itasca 2013). The CVISC model is composed by the Burgers viscoelastic model and the Mohr-Coulomb (MC) elasto-plastic model in series. The Burgers model composed of a Kelvin-Voigt element and a Maxwell element is used to capture the creep behavior while the MC model is used to describe

the failure of rocks when the stress state exceeds the yield criterion envelope of MC. A detailed presentation of the CVISC model is provided in Appendix B. The CVISC model is applicable for different kinds of rocks which may act as the host rock mass in Figure 4.2 (Barla et al. 2010; Pałac-Walko and Pytel 2014; Hasanpour et al. 2015; Paraskevopoulou and Diederichs 2018; Qi and Fourie 2019). The applicability of the Burgers model (the part of CVISC model for creep behavior) on green sandstone and lherzolite has been shown by Wang and Li (2018) against measured creep strains under uniaxial and triaxial compression test conditions. The applications of the Burgers model on more kinds of rocks including but not limited to shale, limestone, schist, potash, and granite are summarized by Paraskevopoulou et al. (2018). In Appendix B, the applicability and capability of the CVISC model built in FLAC^{3D} are further verified by comparing with experimental creep strains of rock salt.

The rock mass is characterized by bulk modulus K_R (Pa), shear modulus G_M (Pa) and viscosity coefficient η_M (Pa·s) of the Maxwell element, shear modulus G_K (Pa) and viscosity coefficient η_K (Pa) of the Kelvin-Voigt element, unit weight γ_R (kN/m^3), cohesion c_R (MPa), internal friction angle ϕ_R (°), dilation angle ψ_R (°), tensile strength T_R (Pa). Note that G_M and K_R are related to the instantaneous elastic strain. They can be obtained by calculation from Young's modulus E_R (Pa) and Poisson's ratio v_R. Table 4.1 shows the mechanical property parameters of fair rock mass for the reference case by considering some values reported in the literature (see Appendix B) and those recommended by Hoek and Brown (1997).

Table 4.1: Mechanical parameters of fair rock mass for the reference case

γ_R (kN/m^3)	E_R (GPa)	v_R	c_R (MPa)	ϕ_R (°)	ψ_R (°)
27	10	0.25	3.5	35	0
T_R (kPa)	K_R (GPa)	G_K (GPa)	η_K (Pa·s)	G_M (GPa)	η_M (Pa·s)
150	6.67	3	3×10^{14}	4	5×10^{15}

The dry cemented backfill is considered as elasto-plastic obeying the MC criterion with tension cut-off. The validity of the MC model in FLAC^{3D} has been verified against the analytical solutions of Salencon (1969) developed for the problem of a cylinder hole. The cemented backfill is characterized by dry unit weight γ, Young's modulus E, Poisson's ratio v, cohesion c, internal friction angle ϕ and dilation angle ψ. The tensile strength T of the cemented backfill is taken as

1/10 of its uniaxial compressive strength (UCS) (Mitchell and Wong 1982). The stiffness and strength of the cemented backfill are considered to linearly increase with curing time and reach the maximum values at a curing time of 28 days, after which the mechanical properties become constant (Belem et al. 2000; Cao et al. 2018). The increase of the cemented backfill strength is mainly attributed to the increase of cohesion while the fill friction angle is considered as constant with curing time (Rankine 2004; Ghirian and Fall 2015). In addition, the values of γ, ν, and ψ of the cemented backfill are also considered as constant with curing time.

Figure 4.3 shows the evolution of E, c, and T. They linearly increase with time within a period of $V = 28$ days, after which they become constant. The values V of E, c, and T of cemented backfill in the numerical model at a time t can be expressed as:

$$V = \begin{cases} \dfrac{V_f}{t_f}t, & t < t_{fin} \\ V_f, & t \geq t_{fin} \end{cases} \tag{4.1}$$

where t (s) is time; V_f denotes the final values of E, c, and T after a curing time of $t_{fin} = 28$ days.
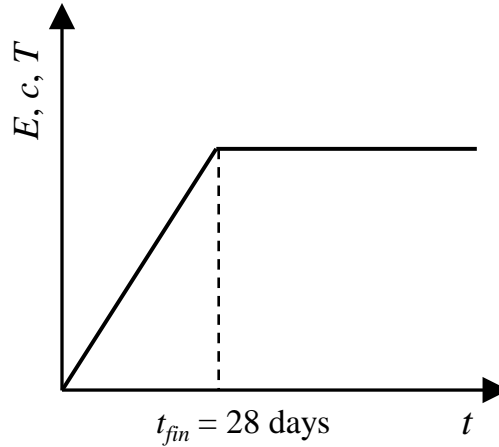
Figure 4.3: Evolution of E, c, and T of cemented backfill with time

In the numerical simulations with FLAC^{3D}, the initial E, c, T of backfill are applied with values at $t = 1$ day. The evolution and update of E, c, and T of the cemented backfill based on Eq. (4.1) after every 24 hours are achieved through a program made of FISH language of FLAC^{3D} which is provided in Appendix G.

Table 4.2 shows the mechanical parameters of the cemented backfill used as reference case. The values of E, c and T are those corresponding to the final values at a curing time of 28 days.

Table 4.2: Mechanical parameters of the cemented backfill for the reference case

γ (kN/m³)	E (MPa)	v	ϕ (°)	c (kPa)	Ψ (°)	T (kPa)
18	300	0.3	30	500	0	173

Figure 4.4 shows the numerical model built with FLAC^{3D} for the reference case with a side-exposed backfill confined by rock walls. The numerical model must involve the surrounding rock mass because that the creep deformation of rocks caused by the induced stresses can influence the fill stability. This is the main objective of this study. The stopes in the reference case locate at a mine depth D of 350 m and are 40 m in height, 10 m in width and 8 m in length as shown in Figure 4.4. The vertical plane of symmetry at $y = 0$ is taken into account. The numerical model is developed by using the primitive shape of radial brick in FLAC^{3D} which consists of brick-shaped mesh and radially graded mesh. There is a void space of 1 m between the top of backfill and the stope roof to represent a poor contact. The top face of the numerical model is set to be free to represent the ground surface. The bottom is fixed along all directions. Along the four lateral boundaries of the numerical model, displacements perpendicular to the surfaces are prohibited while displacements in other directions are allowed. Gravity is set along the negative direction of the z-axis. The lateral earth pressure coefficient K_r is applied as 1 to obtain the initial equilibrium state of a creep model (Boulianne et al. 2004; Aubertin et al. 2018; Paraskevopoulou and Diederichs 2018). Interface elements are introduced between the backfill and rock walls. The shear strength parameters (i.e., friction angle and cohesion) of interface are assumed equal to those of backfill by considering rough rock walls (Li et al. 2003; Liu et al. 2016b). The interface normal stiffness k_n (Pa/m) and shear stiffness k_s (Pa/m) are determined based on an equation suggested in the manual of FLAC^{3D} (Itasca 2013) as:

$$k_n = k_s = 10 \frac{K + 4G/3}{\Delta z_{min}} \tag{4.2}$$

where K (Pa) and G (Pa) are bulk modulus and shear modulus of backfill; Δz_{min} (m) is the smallest backfill element size. The input value of interface stiffness should ensure that the numerical results are not affected. It is justified by comparing the stresses in a backfilled stope with and without interface.

In order to ensure stable numerical results, sensitivity analyses were conducted to determine optimal values of domain size, ranges with fine grids, mesh size and filling layers. This results in an optimal value of 1000 m for both length L_D and width B_D of the numerical model and an optimal value of 890 m for height H_D of the numerical model with $D = 350$ m. The stopes and the rock mass in a range of 10 m around the excavations are simulated with brick-shaped meshes of a 0.5 m size. The rock mass out of this range is meshed with coarse radially graded grids which have a size following an integer multiple ratio (e.g., 2 to 1) to that of fine grids. For the numerical model in this study, the number of zones ranges from 1.4×10^5 to 2.5×10^5 depending on the size of stope. The aspect ratio and orthogonality range from 0.33 to 1 and 0.58 to 1 respectively while face planarity is 0.
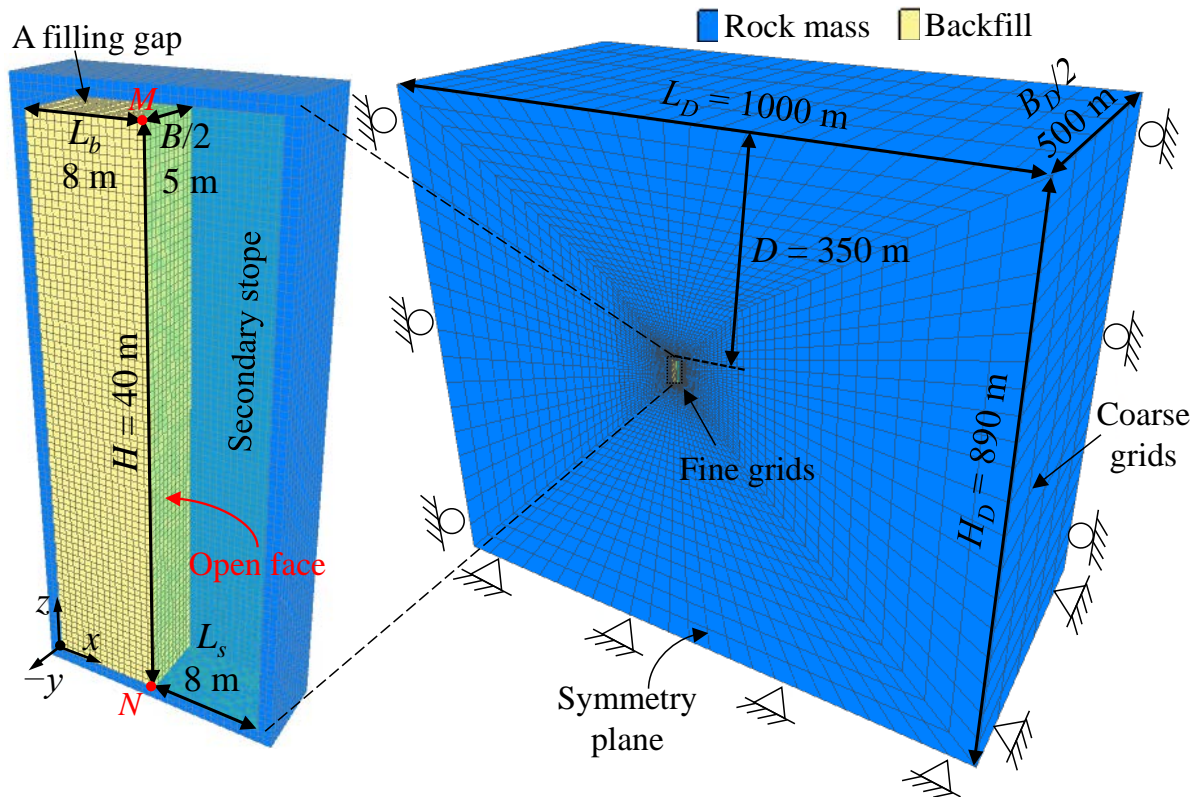
Figure 4.4: A reference numerical model of a backfilled primary stope with surrounding rock mass aside an excavated secondary stope, built with FLAC^{3D}

Static analysis is the default calculation in FLAC^{3D} which reaches a static or steady-state solution when the changing of kinetic energy approaches a negligible value. In static calculation, timestep is an artificial quantity of iteration used for stepping to steady-state solution. However, in the

numerical simulations of creep, timestep represents the real time and its duration can change during the calculation. The unbalanced force ratio (UFR) which represents the ratio of the maximum unbalanced force to the average gridpoint force is used for the adjustment of timestep. The timestep will be increased by multiplying 1.05 if UFR falls below a lower limit *lfob*, and decreased by multiplying 0.95 if UFR exceeds an upper limit *ufob*. A latency can be set which defines the minimum number of steps that must run before adjustment of the timestep to ensure a stable simulation. There is a limit for the maximum duration t_m of timestep to make the model in quasi-static equilibrium during the creep calculation. For the CVISC model, the limit of t_m can be calculated as (Itasca 2013):

$$t_m = \min\left(\frac{\eta_K}{G_K}, \frac{\eta_M}{G_M}\right) \tag{4.3}$$

In this study, the t_m is set as 1000 s. The initial timestep t_i is 30 s, latency is 50 steps, *lfob* is 1×10^{-6}, and *ufob* is 3×10^{-6} based on sensitivity analyses.

To mimic the primary stope excavation and backfilling and secondary stope excavation as well the creep behavior of rock walls, a numerical model needs at least seven steps of numerical simulation as follows:

1) Initial state before any excavation;

2) Primary stope excavation;

3) Creep calculation for delayed filling time t_d;

4) Primary stope backfilling;

5) Creep calculation for curing time t_c;

6) Secondary stope excavation;

7) Creep calculation for exposure time t_e;
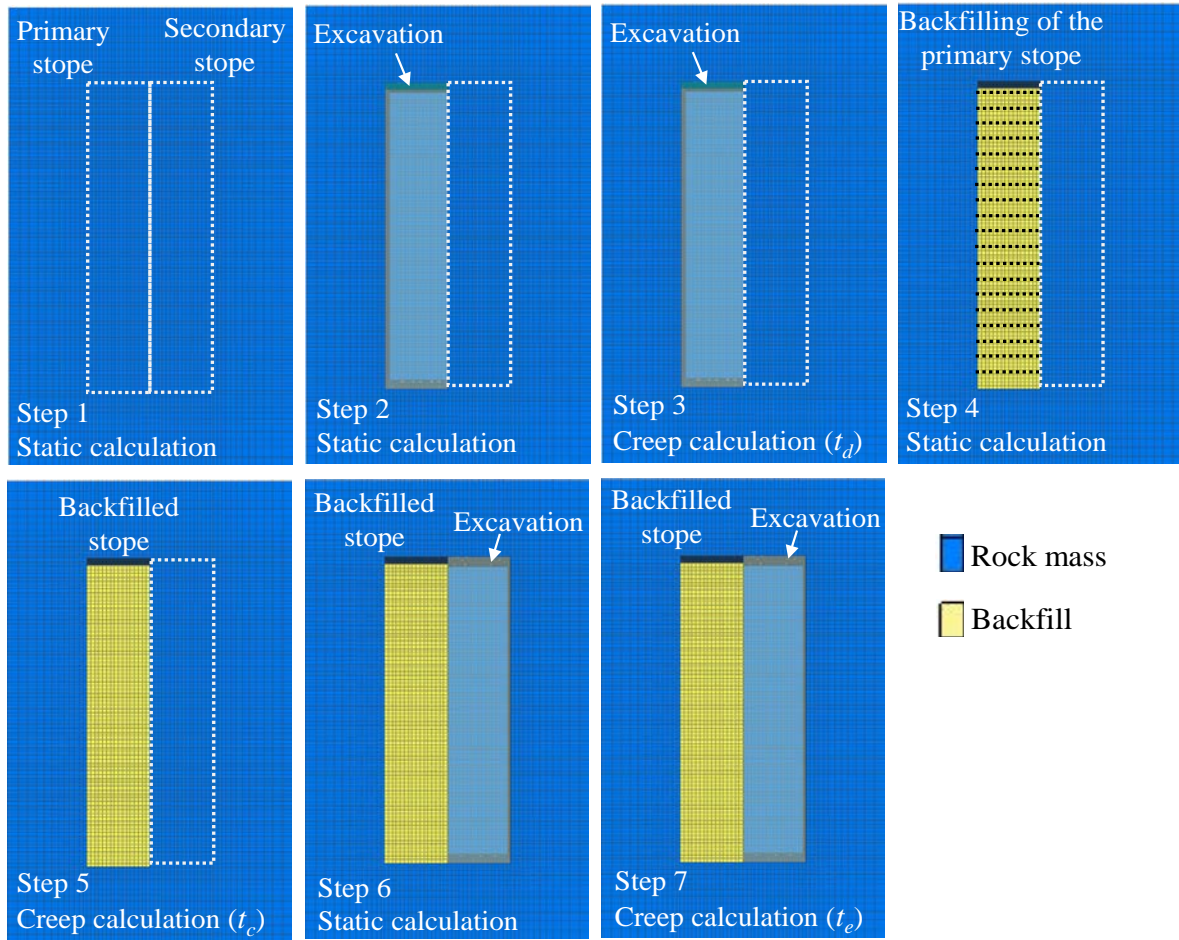
Figure 4.5: Illustration of different simulation steps

The steps of numerical simulation are further shown in Figure 4.5. In Step 1, static calculation is conducted to obtain the initial state of the numerical model before any excavation. In Step 2, the whole primary stope is extracted in one step and the numerical model is solved to the equilibrium state with static analysis. In Step 3, The numerical simulation of creep is conducted for delayed filling time t_d to calculate the creep deformation of rock walls before backfilling the primary stope. In Step 4, displacements are reset to zero after which the primary stope is backfilled using a multilayer method with 2 m per layer. This step is performed with static calculation while numerical model is solved to the equilibrium state as each layer of backfill is placed. In Step 5, displacements are reset to zero, and creep calculation is conducted for curing time t_c during which mechanical parameters of the cemented backfill evolve with time as shown in Figure 4.3. In Step 6, displacements are reset to zero, after which the whole secondary stope is excavated in one step

and static calculation is performed to solve to the equilibrium state. In Step 7, creep calculation is conducted for exposure time t_e to represent a period before backfilling the extracted secondary stope. t_d, t_c, and t_e are counted from the beginning of corresponding steps 3, 5, 7, respectively.

Numerical simulations are conducted using the large strain option to account for the geometrical nonlinearity. The equilibrium state of static calculation is determined by using the "STEP" command and monitoring the stress and displacement in the backfill and rock mass until observing the convergence. The default value of UFR given in FLAC^{3D} is not used as an indicator for the equilibrium state because its limiting value varies significantly with grid number or stress magnitude. In some cases, the numerical simulation with a side-exposed backfill may not be able to converge when the value of c is too small. This is because the side-exposed backfill is physically instable and the numerical calculation thus stops at a non-convergent state.

Figure 4.6 shows an example of horizontal closure on the side wall center of a reference case presented in Figure 4.4 during 28 days after extracting the primary stope (Step 3). Material parameters for rock mass are shown in Table 4.1. The rock wall demonstrates an instantaneous displacement of 8 mm after excavation. The displacement then increases to 20 mm with a reducing rate as time increases to 5 days which is related to the primary creep stage. This is followed by an increase of displacement to 30 mm at 28 days with a constant rate that corresponds to the secondary creep stage. However, the tertiary creep stage is not represented which is one of the limitations of the CVISC model. The results shown in Figure 4.6 are typical closure profile of underground excavations. In Appendix, the applicability of numerical model to describing the time-dependent closure of underground openings are further verified against in-situ measurements of creep deformation in a tunnel.
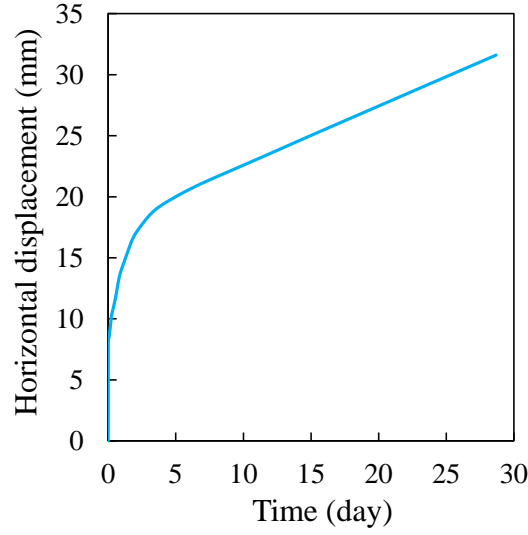
Figure 4.6: Horizontal closure at the side wall center of the reference case during 28 days after extracting the primary stope by considering parameters shown in Table 4.1

Table 4.3 presents the program of numerical simulations by considering mine depth D ranging from 0 to 500 m. The effects of delayed time before filling the primary stope, curing time, exposure time, stope geometry, properties of backfill and rock mass on the value of c_{min} are studied by changing one parameter for each case.

Table 4.3: Characteristics of numerical simulation cases (with $\gamma = 18$ kN/m³, $\nu = 0.3$, $\psi = 0°$, $T =$ UCS/10 for cemented backfill, $\gamma_R = 27$ kN/m³, $\nu_R = 0.25$, $c_R = 3.5$ MPa, $\phi_R = 35°$, $\psi_R = 0°$, $T_R =$ 150 kPa, $G_K = 3$ GPa, $\eta_K = 3 \times 10^{14}$ Pa·s, $G_M = 4$ GPa for rock mass, and mine depth D ranging from 0 to 500 m)

Case	Time (day)			Stope geometry (m)				Backfill		Rock mass	
	t_d	t_c	t_e	H	L_b	B	L_s	E (MPa)	ϕ (°)	E_R (GPa)	η_M (Pa·s)
1	VAR	28	0	40	8	10	8	300	30	10	5×10^{15}
2	3	VAR	0	40	8	10	8	300	30	10	5×10^{15}
3	3	28	VAR	40	8	10	8	300	30	10	5×10^{15}
4	3	28	0	VAR	8	10	8	300	30	10	5×10^{15}
5	3	28	0	40	VAR	10	8	300	30	10	5×10^{15}
6	3	28	0	40	8	VAR	8	300	30	10	5×10^{15}
7	3	28	0	40	8	10	VAR	300	30	10	5×10^{15}
8	3	28	0	40	8	10	8	VAR	30	10	5×10^{15}

9	3	28	0	40	8	10	8	300	VAR	10	5×10^{15}
10	3	28	0	40	8	10	8	300	30	VAR	5×10^{15}
11	3	28	0	40	8	10	8	300	30	10	VAR

4.3 Determination of c_{min} for side-exposed backfill

The minimum required cohesion c_{min} of side-exposed backfill should be considered different from the cohesion at failure. The cohesion at failure is a value of the backfill cohesion at which the side-exposed backfill starts to become instable. The c_{min} is the minimum required value of the backfill cohesion at which the side-exposed backfill remains stable. The two critical values are very close to each other when the factor of safety (FS) equals to 1. They can be determined by conducting numerical simulations with different c ranging from a high value to a low value until an instability occurs.

4.3.1 Failure mechanism

The failure mechanism of side-exposed backfill associated with stiff and immobile rock walls has been investigated by Mitchell and coworkers (Mitchell et al. 1982; Mitchell 1986, 1989) through laboratory tests, which show that wedge sliding is the main control failure mechanism. This has been further confirmed by Li and coworkers (Li and Aubertin 2014; Liu et al. 2016a, 2018; Yang et al. 2017) through numerical modeling when the backfill cohesion is low. When the backfill cohesion is high, tension cracks can occur on top part of the side-exposed backfill and the instability is mostly exhibited by the fall of a spoon-like block (Yang et al. 2017). When rock-wall closure associated with the excavation of an adjacent secondary stope occurs, Wang et al. (2021) have shown that the side-exposed backfill can fail by sliding along a plane for small rock-wall closure at a shallow depth. When the rock-wall closure is significant at a large depth, the horizontal compressive stress associated with walls closure can exceed the yield surface of backfill which leads to a crushing failure (Wang et al. 2021).

The failure mechanism of side-exposed backfill associated with the creep of rock walls has never been investigated. But a similar phenomenon as that with the consideration of rock-wall closure can be expected.

Figure 4.7 shows the displacement distribution and vectors of the side-exposed backfill upon failure for Case 1 (Table 4.3) with $t_d = 3$ days when the mine depth is 0 and 350 m, respectively. When $D = 0$ m, the side-exposed backfill exhibits a downward movement along an inclined plane, indicating a failure mechanism by sliding (Figure 4.7a). As D increases to 350 m, the side-exposed backfill shows a horizontal outside movement toward the excavated secondary stope, indicating a failure mechanism by horizontal crushing (Figure 4.7b).
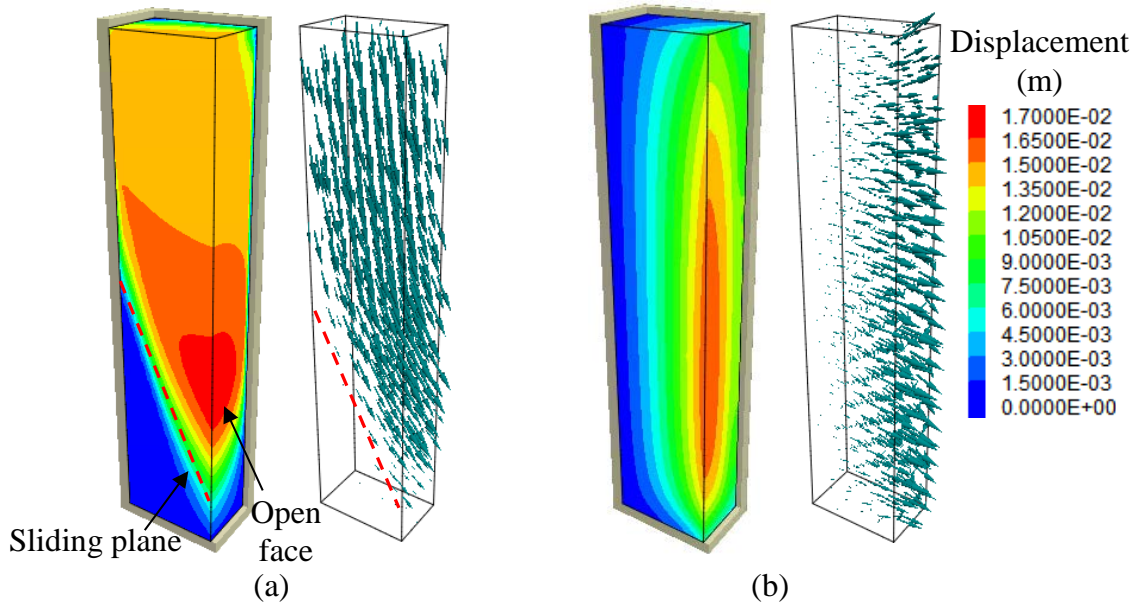
Figure 4.7: Displacement distribution and vectors of side-exposed backfill upon failure for Case 1 in Table 4.3 with $t_d = 3$ days when the mine depth D increases from (a) 0 to (b) 350 m

4.3.2 Instability indicator

To reduce the subjectivity in evaluating the instability and c_{min} of side-exposed backfill, the coalescence of yield zones when the backfill cohesion gradually decreases from a large value to a small enough value is used. The variations of backfill displacement for different cohesion can be combined with yield zones in some cases. However, the displacement is not a main independent instability indicator because there is not a limiting value and its variation trend depends on the selected axis scales.

Figure 4.8 shows the yield state and total displacement at the center on the open face of side-exposed backfill for Case 1 with $t_d = 3$ days and $D = 350$ m when the backfill cohesion c decreases

from 500 to 120 kPa. One sees that the displacement of side-exposed backfill rapidly increases when c reduces from 200 to 170 kPa. However, it is difficult to evaluate the transition point between stability and instability because the displacement curve shows a gradual increase without a clear jump. From the figure, one sees also that yield zones appear in the backfill around sidewalls as c reduces to 300 or 181 kPa. The yield zones propagate horizontally from the two sidewalls and coalesce at the center on the symmetry plane when c further reduces to 175 kPa, indicating an instability of the side-exposed backfill by horizontal crushing. The value of cohesion at failure for this case is determined as 175 kPa while the minimum required cohesion c_{min} is 181 kPa.
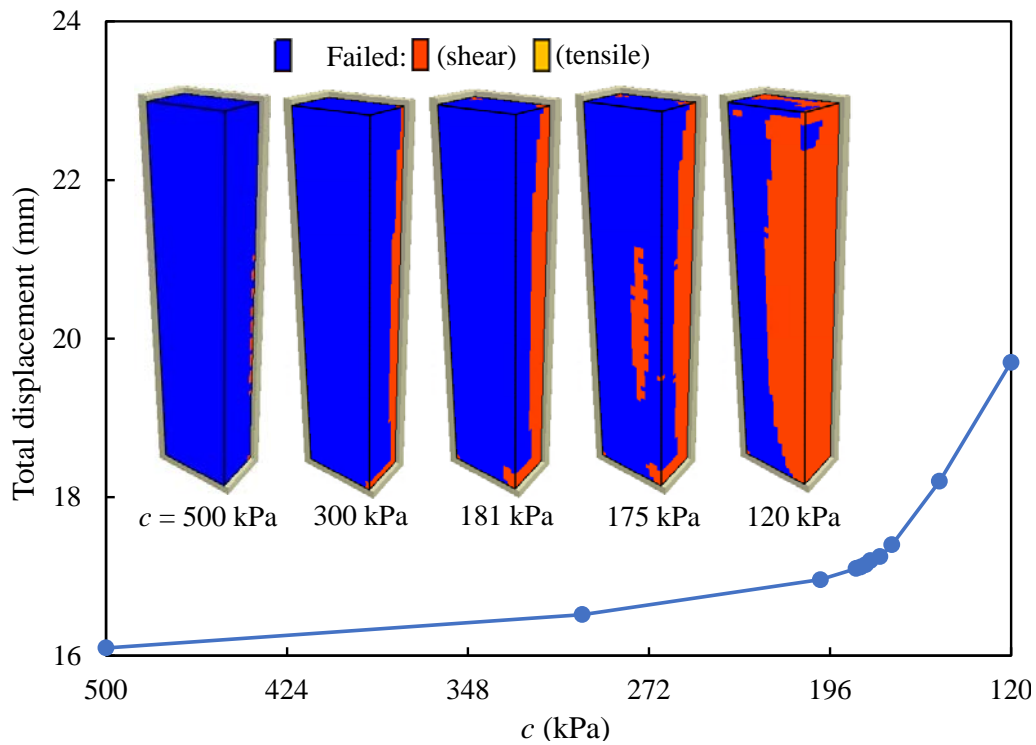
Figure 4.8: Yield zone development and variation of total displacement at the center on the side-exposed face of backfill as a function of the backfill cohesion c for Case 1 in Table 4.3 with $t_d = 3$ days and $D = 350$ m

Figure 4.9 illustrates the development of yield zones and total displacement at the center on the open face of side-exposed backfill for Case 1 with $t_d = 3$ days and $D = 0$ m when the backfill cohesion c varies from 100 to 28 kPa. Compared to the case with crushing failure, the yield zones shown in Figure 4.9 propagate from the toe of open face toward the back wall as c decreases, and forms a sliding plane with a clear sliding wedge as c reduces to 28 kPa. The numerical model

becomes non-convergent with $c = 28$ kPa. The instability of the side-exposed backfill for this case is clearly attributed to a failure mechanism by sliding. Meanwhile, one sees a significant increase of backfill displacement as c decreases from 32 to 28 kPa which also indicates the instability. The cohesion at failure for this case is determined as 28 kPa while the minimum required backfill cohesion c_{min} is 32 kPa. The instability and c_{min} of side-exposed backfill in this study are thus determined by mainly evaluating the coalescence of yield zones. The jump of displacement can be combined with the yield zones development in some cases, but the displacement is not a main instability criterion. The yield zone development within side-exposed backfill was validated by Wang et al. (2021) through the comparisons with some centrifugal model tests conducted by Mitchell (1986).
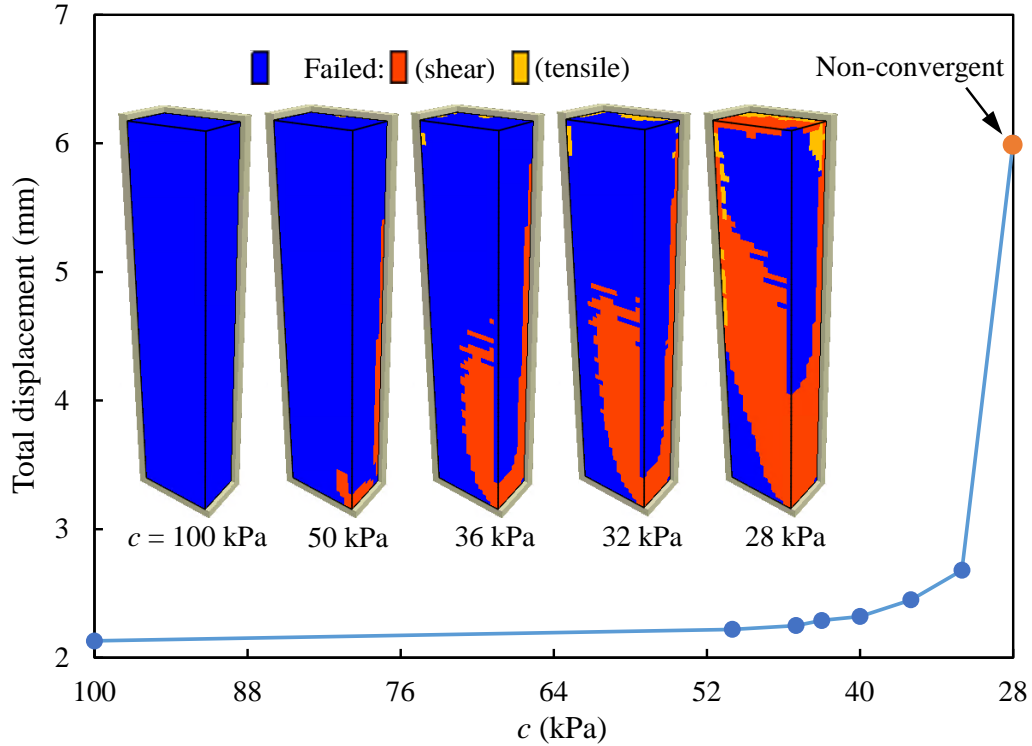
Figure 4.9: Yield zone development and variation of total displacement at the center on the side-exposed face of backfill as a function of the backfill cohesion c for Case 1 in Table 4.3 with $t_d = 3$ days and $D = 0$ m

4.4 Numerical results

Figure 4.10 shows the distributions of horizontal stress σ_{yy} (Figure 4.10a) and vertical stress σ_{zz} (Figure 4.10b) along a vertical line *MN* in the backfilled primary stope before side exposure (Step 5) for Case 1 with $t_d = 3$ days, $D = 350$ m, and $c = 300$ kPa as curing time t_c increases from 1 to 28 days. The horizontal stress is along the normal direction of side walls. From the figure, one sees that when t_c is shorter than 3 days, both horizontal and vertical stresses are smaller than overburden horizontal ($K_0 \cdot \gamma \cdot h$, K_0 is at-rest earth pressure coefficient, h is height) and vertical ($\gamma \cdot h$) pressures due to the arching effect. As t_c further increases, the horizontal and vertical stresses increase and exceed the overburden pressures. This is because the creep deformation of surrounding rock mass increases with time which results in larger compressive strain in backfill. Meanwhile, the backfill becomes harder with larger elastic modulus as t_c increases which leads to larger compressive stress with the same closure. The increase of stress states in the backfilled primary stope with t_c is thus a combined effect of backfill hardening and increase of closure. Given this compression condition of backfill during t_c, its minimum required cohesion c_{min} upon side exposure can be quite different from that without considering creep.
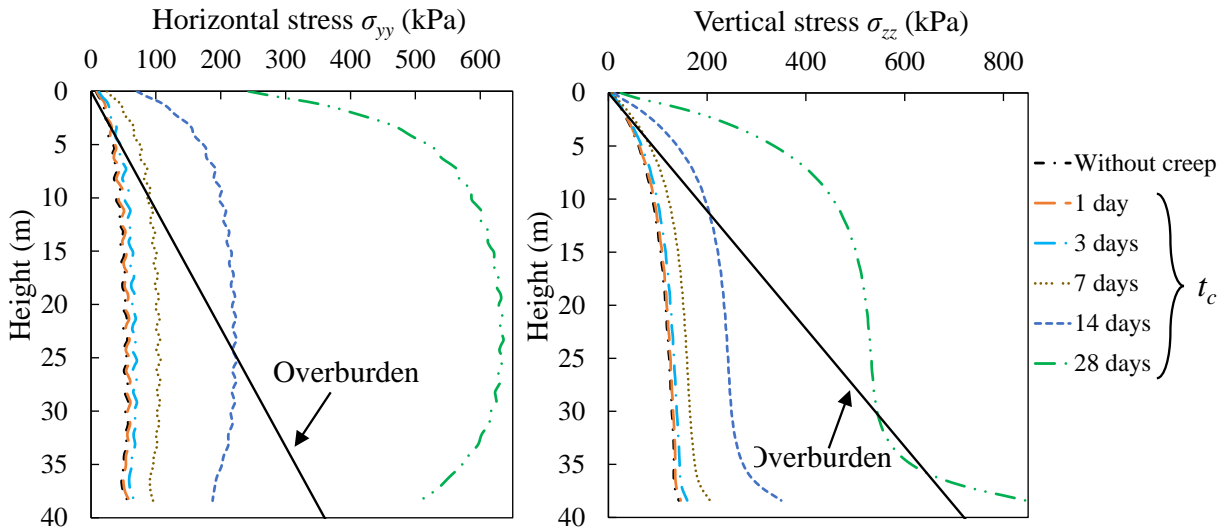
Figure 4.10: Distributions of (a) horizontal stress (σ_{yy}) and (b) vertical stress (σ_{zz}) along a vertical line *MN* in the backfilled primary stope before side exposure (Step 5) for Case 1 in Table 4.3 with $t_d = 3$ days, $D = 350$ m, $c = 300$ kPa as t_c increases from 1 to 28 days

Figure 4.11 shows the variation of the c_{min} of side-exposed backfill for Case 1 with $t_d = 3$ days as a function of the mine depth D. The results without any creep calculation and those considering immobile rock mass are also plotted in Figure 4.11. In the figure, the cases governed by crushing failure have been marked using the grey color. For the rest unmarked cases (white areas) in the figure, the dominant failure mechanism is sliding. When D is small and sliding failure is governing, the c_{min} of side-exposed backfill is smaller than those with immobile rock mass and decreases as D increases. It is because that the small compressive stresses in backfill caused by small walls closure at a shallow depth is not able to crush the backfill. Conversely, the small compressive stresses increase the lateral confining and improve the stability of side-exposed backfill to avoid sliding failure. As D further increases, the instability is dictated by crushing failure and the values of c_{min} thus increase with the mine depth. Compared to the cases without any creep, the c_{min} of side-exposed backfill by considering walls creep is slightly smaller at $D = 0$ m, but is significantly larger at a large mine depth. This is explained as that the creep deformation of surrounding rock mass generates compressive stresses in the backfilled primary stope during curing time t_c. Therefore, the backfill upon side exposure becomes more stable at a shallow mine depth, but requires a higher strength when the mine depth is large and stability becomes governed by crushing failure.

Figure 4.11: Variation of the minimum required cohesion c_{min} of side-exposed backfill as a function of the mine depth D for Case 1 in Table 4.3 with $t_d = 3$ days in conditions of considering creep of rock mass, without creep, and with immobile rock mass respectively

4.4.1 Effect of delayed time before filling the primary stope

Figure 4.12 shows the variation of the c_{min} of side-exposed backfill as a function of the mine depth by considering various delayed time t_d before filling the primary stope. In the figure, one sees that the c_{min} increases with D, but is almost identical for different delayed filling time t_d at a given depth. After excavating the primary stope, the surrounding rock mass enters the primary creep stage in which its creep strain rate reduces as t_d increases as shown in Figure 4.6. When t_d is long enough, the rock mass will exhibit the secondary creep stage with a constant creep strain rate. Since the primary stope is backfilled after t_d, the variation of delayed filling time can cause different rate of walls creep deformation that applies on backfill at the early period of curing. Nevertheless, backfill is very soft at the beginning of curing with an increased stiffness as time increases. Therefore, though the walls creep deformation during the early curing stage can vary with t_d, it will not result in significantly different compressive stresses in backfill in the primary stope due to its small stiffness. This explains that delayed filling time t_d does not greatly influence the stability and c_{min} of side-exposed backfill.
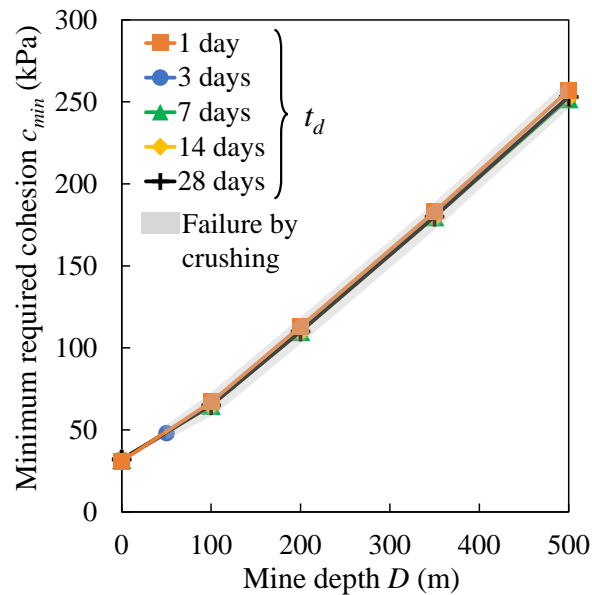
Figure 4.12: Variation of the minimum required cohesion c_{min} of side-exposed backfill as a function of the mine depth D for different delayed time t_d before filling the primary stope (Case 1 in Table 4.3)

4.4.2 Effect of curing time

Figure 4.13 shows the variation of the c_{min} as a function of D for different curing time t_c. The c_{min} slightly reduces from 36 to 30 kPa as curing time t_c increases from 7 to 42 days at $D = 0$ m, and also decreases as D increases from 0 to 200 m for $t_c = 7$ days. Sliding failure is dominant for these cases. As the mine depth increase, the governing failure mechanism for side-exposed backfill becomes crushing as marked with the grey color in Figure 4.13. The c_{min} then increases with the increase of D and t_c. The variation of the c_{min} with t_c is the combined effects of hardening of the backfill and walls creep deformation. The backfill hardens and rock walls creep deformation increases as t_c increases which result in larger compressive stresses in fill. Increasing t_c thus improves the stability of side-exposed backfill at a shallow mine depth, but requires a larger shear strength for side-exposed backfill to prevent crushing when the mine depth is large or the walls creep displacement is significant. It should be noted that in Figure 4.13, the mechanical properties of E, c, T of backfill for cases with t_c of 7 and 14 days are not in final values. The determined c_{min} for these cases is related to relatively short curing time. Results in Figure 4.13 suggest that it deserves to wait a longer time before excavating adjacent stope in order for the backfill to gain more strength with curing time as long as the mine depth is small and the rock walls demonstrate little creep deformation. When the mine depth is large or/and rock walls exhibit pronounced creep deformation, simply increasing the binder content may not be the best choice. It is because a stronger backfill means also a harder backfill, which absorbs larger compressive stress with a given rock-wall closure and is thus more prone to be crushed. In this condition, a softer backfill can be better through the use of lower binder content or/and with a shorter curing time.
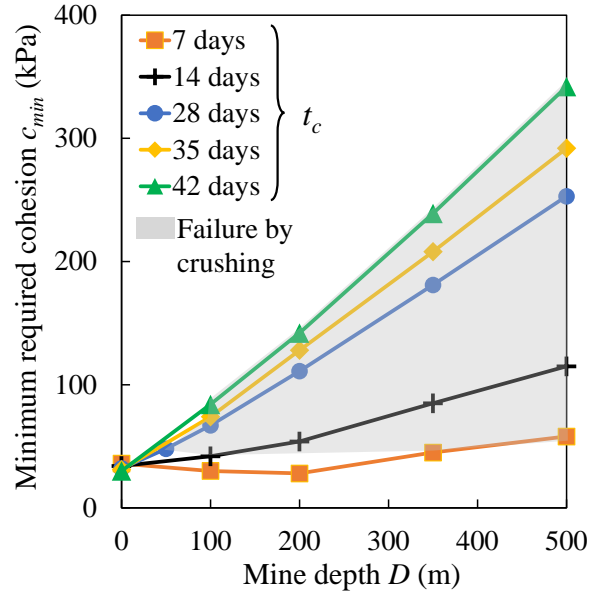
Figure 4.13: Variation of the minimum required cohesion c_{min} of side-exposed backfill as a function of the mine depth D for different curing time t_c (Case 2 in Table 4.3)

4.4.3 Effect of exposure time before filling the secondary stope

Figure 4.14 shows the variation of the c_{min} as a function of D for various exposure time t_e before filling the secondary stope. In the figure, one sees that exposure time t_e of side-exposed backfill does not influence the value of c_{min} at $D = 0$ m where sliding failure is dominant. It is because that small walls creep deformation during t_e at a shallow depth slightly improves the stability of side-exposed backfill after adjacent extraction. However, this improvement of stability with exposure time will not change the c_{min} because the backfill must remain stable once the adjacent secondary stope is excavated. As the mine depth and the walls creep deformation become large, stability of side-exposed backfill is governed by crushing failure. The c_{min} then increases with the increase of D and t_e due to the increased compressive stresses in side-exposed backfill. Results in Figure 4.14 indicate that the excavated secondary stope should be filled as soon as possible to maintain the stability of backfill in the primary stope when the mine depth is large or/and the creep of surrounding rock mass is significant.
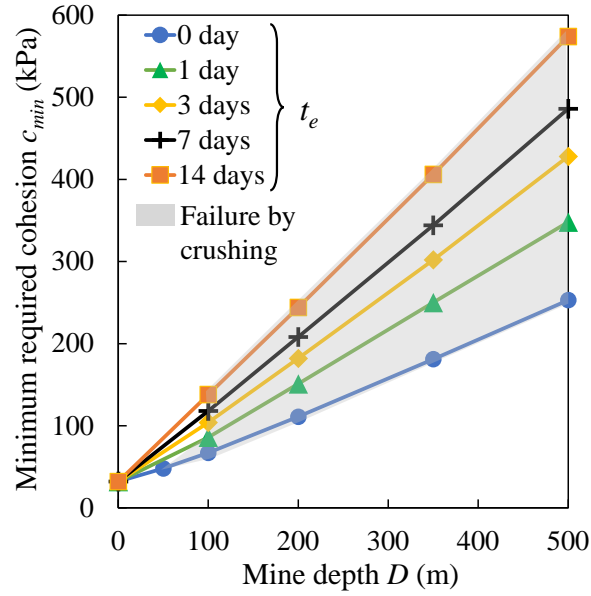
Figure 4.14: Variation of the minimum required cohesion c_{min} of side-exposed backfill as a function of the mine depth D for different exposure time t_e before filling the secondary stope (Case 3 in Table 4.3)

4.4.4 Effect of stope geometry

Figure 4.15 shows the variation of the c_{min} of side-exposed backfill as a function of the mine depth D for different heights H, lengths L_b, and widths B of the backfilled primary stope. For $D = 0$ m, the c_{min} shows a minor increase from 30 to 32 kPa as H increases from 30 to 50 m, and slightly decreases from 34 to 30 kPa as L_b increases from 4 to 14 m. The c_{min} also increases with the increase of B at $D = 0$ m due to the reduction of arching effects (Aubertin et al. 2003; Li et al. 2003), and decreases as D increases from 0 to 50 m for $B = 15$ m. Sliding failure is dominant for these cases. As D further increases, crushing failure becomes governing and it is straightforward to see the c_{min} increasing with the increase of D. The increase of H and L_b leads to the increase of c_{min} because that both walls creep and instantaneous deformation increase as the stope becomes higher and longer. Figure 4.15c shows that when the mine depth is large, increasing B causes a reduction in c_{min} which can be counterintuitive. It is explained as that when the backfill becomes wider, the horizontal compressive strain due to walls convergence becomes smaller which results in lower compressive stress in backfill. The side-exposed backfill with a larger width thus becomes less prone to be crushed, but tends to fail by sliding at a shallow mine depth.

(a)

(b)

(c)
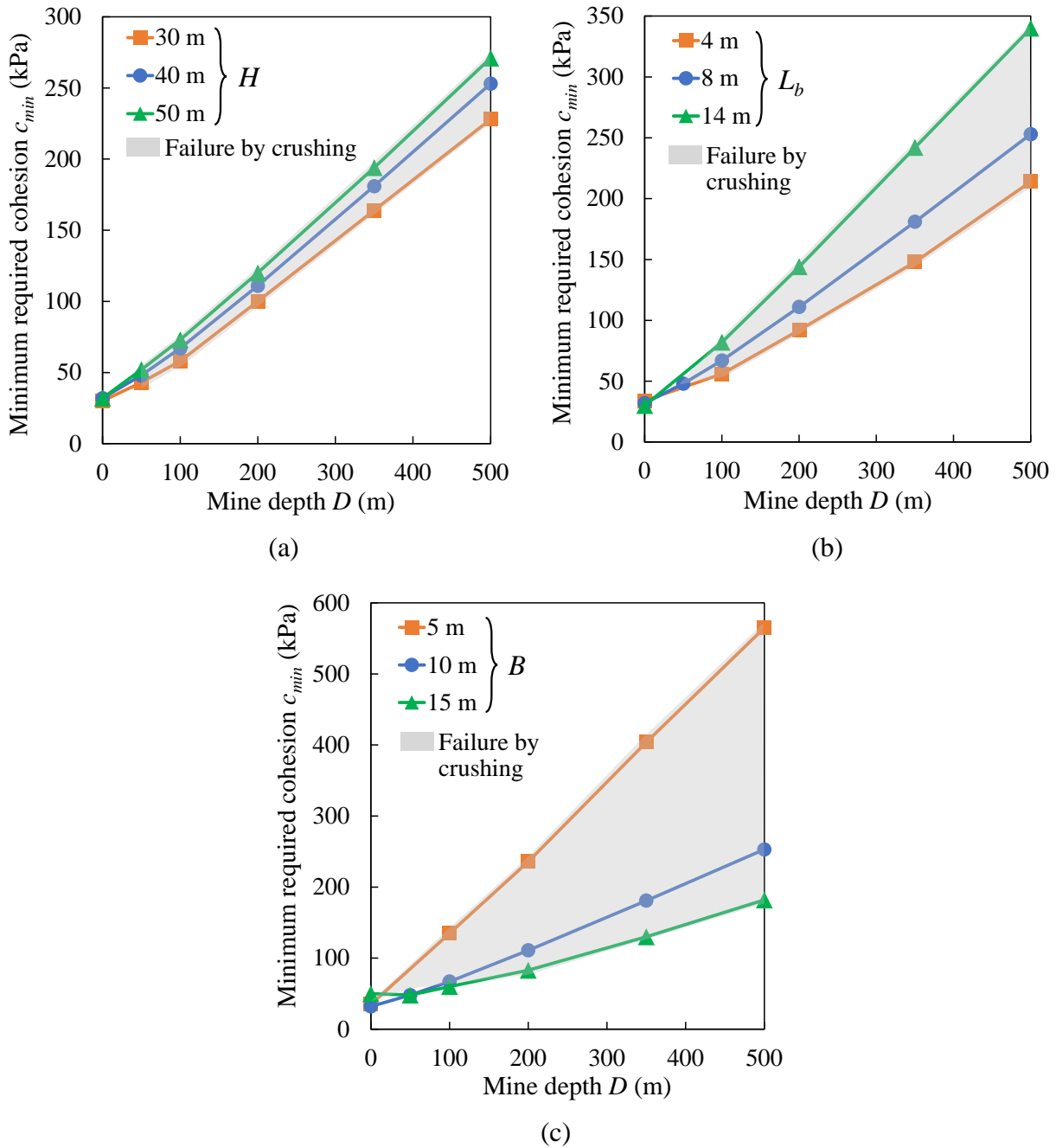
Figure 4.15: Variation of the minimum required cohesion c_{min} of side-exposed backfill as a function of the mine depth D for different (a) heights H (Case 4 in Table 4.3), (b) lengths L_b (Case 5 in Table 4.3), and (c) widths B (Case 6 in Table 4.3) of the backfilled primary stope

Figure 4.16 illustrates the variation of the c_{min} as a function of D for various lengths L_s of the adjacent secondary stope. The c_{min} slightly decreases from 33 to 31 kPa as L_s increases from 4 to 14 m at $D = 0$ m. When the mine depth is large, the stability of side-exposed backfill becomes

governed by crushing and the c_{min} increases with the increase of D and L_s. It is because that excavating a longer adjacent pillar results in larger walls closure and higher compressive stress in the side-exposed backfill. This result tends to indicate that it would be better to use small secondary stope. On the other hand, large secondary stopes are preferred because non-cemented or low binder content backfill can be used to fill the secondary stopes. An optimization is thus needed to minimize the overall cost of backfill for the primary and secondary stopes.
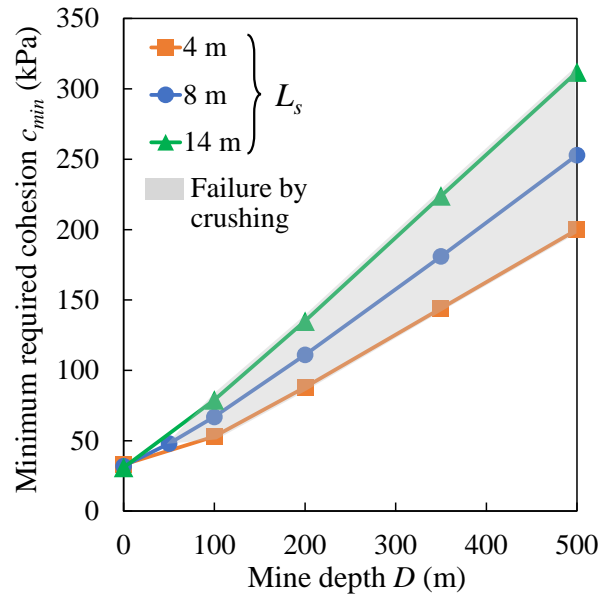
Figure 4.16: Variation of the minimum required cohesion c_{min} of side-exposed backfill as a function of the mine depth D for different lengths L_s of the adjacent secondary stope (Case 7 in Table 4.3)

4.4.5 Effect of backfill properties

Figure 4.17a shows the variation of the c_{min} as a function of mine depth for different Young's modulus E of backfill. When the rock mass exhibits little creep deformation at the shallow depth, the c_{min} decreases with the increase of D and E. This is because that the increase of Young's modulus and mine depth results in larger compressive stresses in backfill generated by walls closure. The side-exposed backfill thus becomes more stable when D is small and stability is governed by sliding failure. However, when the rock walls creep deformation is significant at a large depth, increasing D and E leads to the increase of c_{min} for side-exposed backfill to prevent crushing.
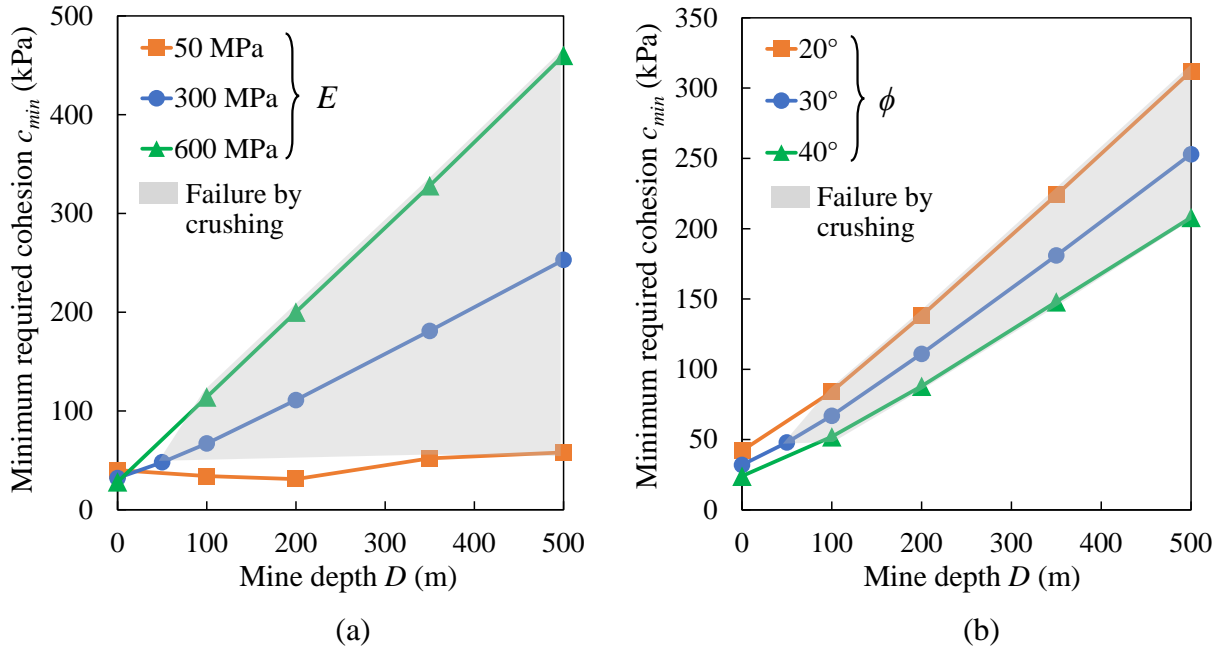
Figure 4.17: Variation of the minimum required cohesion c_{min} of side-exposed backfill as a function of the mine depth D for different (a) Young's modulus E (Case 8 in Table 4.3), and (b) internal frictional angles ϕ (Case 9 in Table 4.3) of backfill

Figure 4.17b illustrates the variation of the c_{min} as a function of D for different internal frictional angles ϕ of backfill. One sees that in all cases, increasing ϕ from 20° to 40° leads to the decrease of the c_{min} of side-exposed backfill. This is because that the failure surface of backfill expands as ϕ becomes larger, which improves its stability upon side exposure despite different failure mechanisms caused by rock walls convergence.

4.4.6 Effect of rock mass properties

Figure 4.18a shows the variation of the c_{min} as a function of D for different Young's modulus E_R of rock mass. The changing of E_R affects the instantaneous rock-wall closure associated with extraction. When the mine depth is 0 m with small in-situ stress, sliding failure is dominant while the values of c_{min} increase from 32 to 34 kPa as E_R increases from 10 to 50 GPa. When the mine depth is large, the governing failure mechanism becomes crushing. The values of c_{min} then increase with the increase of D, but decrease as E_R increases from 10 to 30 GPa. This is because that increasing E_R results in smaller rock-wall closure associated with adjacent extraction which makes the side-exposed backfill less prone to be crushed. However, as E_R further increases from 30 to 50

GPa, one sees that the c_{min} becomes almost identical at a given D. It is because that the backfill in the primary stope before side exposure is under a compression condition with excessive compressive stresses generated by walls long-term creep deformation. Excavating the adjacent secondary stope removes the confining for backfill from one side which makes the stress state around the open face exceeding its yield surface if the cohesion is not adequate. Therefore, when the rock walls instantaneous closure is small, the c_{min} of backfill can be dominated by walls long-term creep deformation before side exposure.
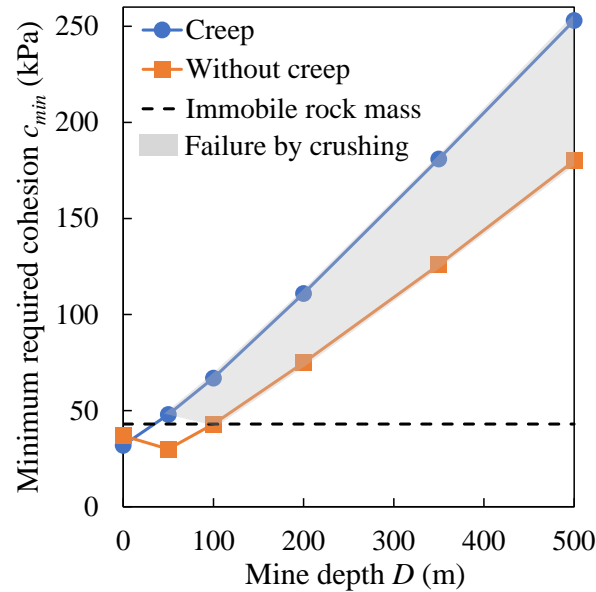

(a) (b)
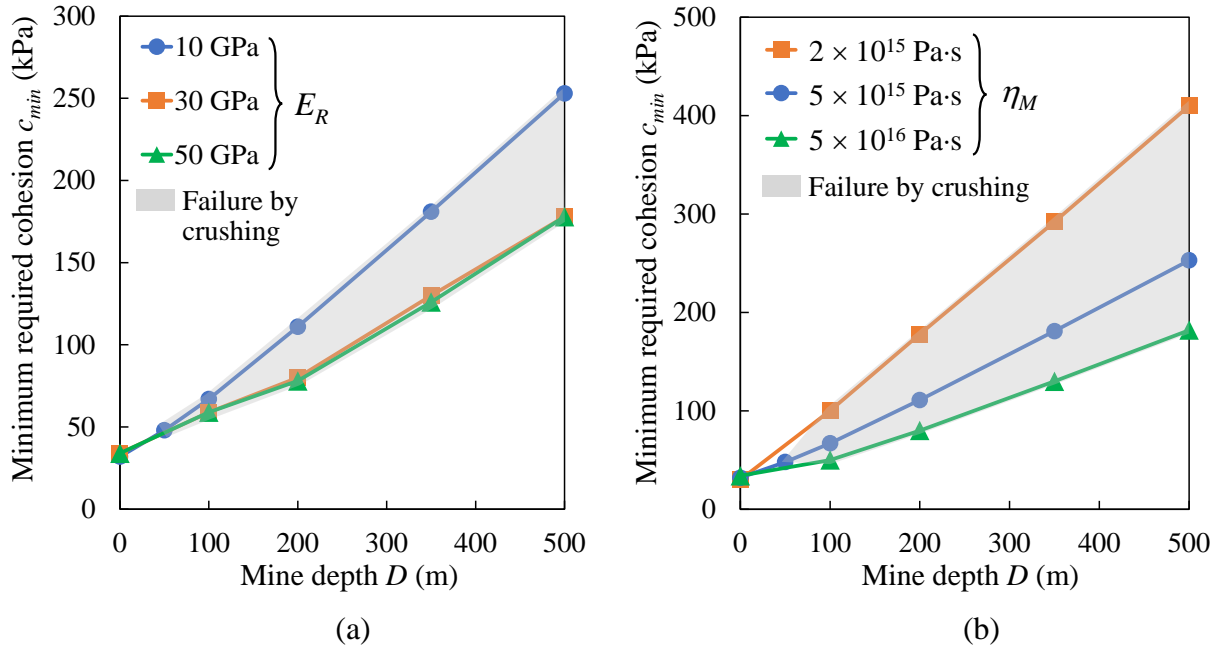
Figure 4.18: Variation of the minimum required cohesion c_{min} of side-exposed backfill as a function of the mine depth D for different (a) Young's modulus E_R (Case 10 in Table 4.3), and (b) Maxwell viscosity coefficient η_M (Case 11 in Table 4.3) of rock mass

Figure 4.18b illustrates the variation of the c_{min} as a function of D for various Maxwell viscosity coefficient η_M of rock mass. η_M is the factor affecting the rate of long-term creep deformation of rock mass (see Appendix B). When the in-situ stress is small at $D = 0$ m, increasing η_M from 2×10^{15} to 5×10^{16} Pa·s leads to the slight increase of c_{min} from 30 to 34 kPa. As the mine depth becomes large, the stability is governed by crushing and the c_{min} shows an increasing trend with the decrease of η_M, and increases as D increases. It is because that reducing η_M causes the increase of walls creep deformation and thus generating larger compressive stresses in backfill. Therefore,

the side-exposed backfill needs a larger strength to avoid crushing as η_M reduces at a large mine depth.

4.5 Discussion

The time-dependent stability of side-exposed backfill associated with the creep of surrounding rock mass is, for the first time, evaluated through three-dimensional numerical modeling with FLAC^{3D}. This numerical model is considered more representative of underground mining conditions. A distinction is made between the cohesion at failure and the minimum required cohesion c_{min}. Effects of delayed time before filling the primary stope, curing time, exposure time and parameters evolution of backfill on the c_{min} are analyzed. With the influence of rock walls creep behavior, other factors including mine depth, stope geometry, mechanical properties of backfill and rock mass are also investigated.

4.5.1 Comparison between the current cohesion and c_{min} of side-exposed backfill

In this study, the current cohesion of backfill linearly increases with curing time t_c for 28 days after which the cohesion remains constant. Therefore, the results for Case 2 can also be interpreted by comparing the varied current cohesion and c_{min} of side-exposed backfill within $t_c = 28$ days. The comparisons at mine depths D of 100 and 500 m are shown in Figure 4.19 as examples. In Figure 4.19a, one can see that for the side-exposed backfill at $D = 100$ m with c_{min}, its current cohesion falls below the minimum requirement as t_c becomes shorter. In this case, a stable side-exposed backfill with short curing time can also remain self-standing as t_c increases. However, a backfill exposed with a long curing time may not be strong enough to be exposed at a shorter t_c. As D increases to 500 m, Figure 4.19b shows that the current cohesion of side-exposed backfill with $t_c = 28$ days exceeds the c_{min} at shorter t_c of 7 and 14 days. It is because a shorter curing time results in softer fill and smaller walls creep deformation both of which reduce the compressive stresses within backfill and improve the stability. The comparisons between the current cohesion and c_{min} for Case 2 further clarify the analyses in the previous section. The time-dependent stability thus should be considered in backfill design for better economics and risk control.
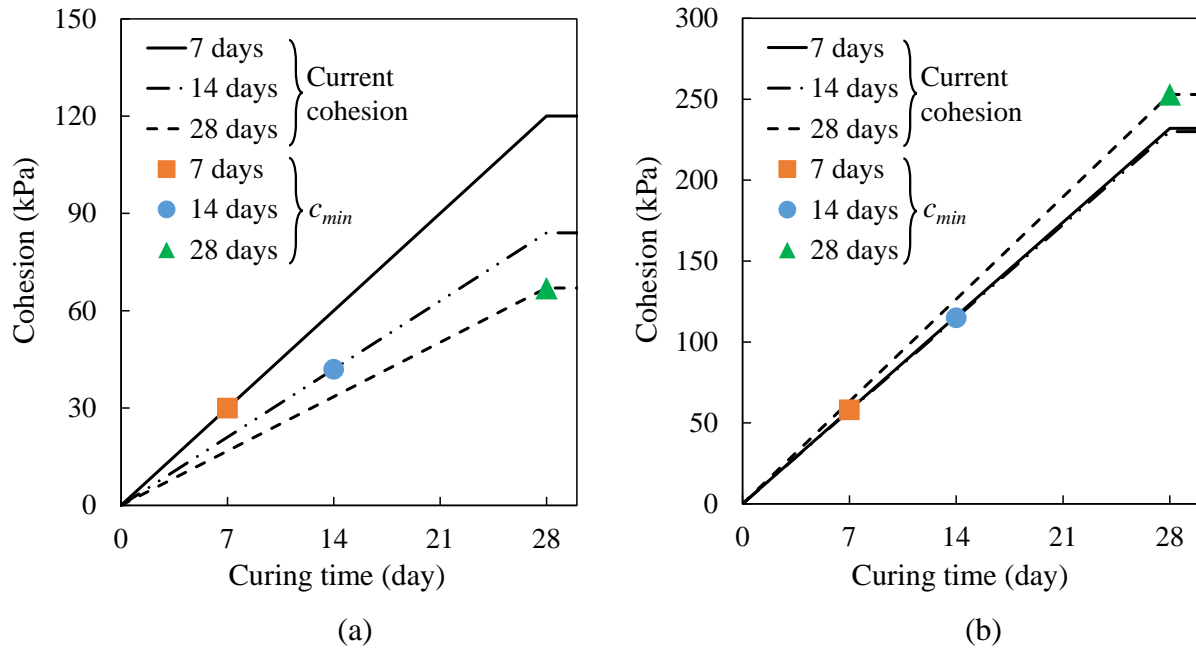
Figure 4.19: Comparisons between the c_{min} and current cohesion of side-exposed backfill for Case 2 with different curing time at mine depth of (a) 100 m and (b) 500 m

4.5.2 Limitations

The numerical model in this study is simplified from the engineering practice of backfilled stopes in underground mines. In the model, both the primary and secondary stopes are assumed to have a vertical rectangle shape while an underground stope usually has irregular geometry with inclinations. The secondary stope in this study is extracted in one step which is close to a sublevel stoping or long-hole stoping mining. In practice, the secondary stope could also be mined in layers such as the vertical retreat mining that can result in a sequential exposure of backfill. The vicinity of a backfilled stope can have various excavations such as drifts, declines, and previous stopes which are not considered here. The effect of blasting vibration generated by neighboring workings on the fill stability is not accounted. Moreover, both rock mass and cemented backfill in practice can be non-homogeneous and anisotropic due to discontinuities for the former and segregation and different pouring stages for the latter (Grabinsky and Bawden 2007; Wittke 2014). More works are needed to analyze the time-dependent stability of side-exposed backfill by overcoming the above limitations.

When the influence of geological conditions on rocks needs to be considered, the Rock Mass Rating (RMR) system can be used (Bieniawski 1989). RMR includes ratings on six parameters: uniaxial compressive strength (UCS); rock quality designation (RQD); groundwater conditions; spacing, condition, and orientation of discontinuities. The shear strength parameters (c_R and ϕ_R) and deformation modulus of in-situ rock mass can then be estimated based on the RMR (Aydan and Kawamoto 2000; Nejati et al. 2014). The in-situ viscosity coefficient can be determined by calibrating based on the measured closure profiles of underground excavations (Malan et al. 1997; Qi and Fourie 2019). The measured different earth stresses along varied orientations can also be applied in the numerical model. In this case, the creep of rock mass occurs at the initial state (without any excavation) due to the deviatoric stresses. After calculating the initial equilibrium state of a creep model, the earth pressure coefficient will change and be close to a nil deviatoric stress condition.

The CVISC model is applicable to describing the creep behavior of wide kinds of rocks (Wang and Li 2018; Paraskevopoulou et al. 2018), but it still has several limitations. The CVISC model exhibits the linear relationship between the stress and long-term creep strain rate which captures the creep behavior of rocks when the applied stress is low. However, as the applied stress increases and exceeds the crack initiation threshold, the creep strain rate of rocks shows nonlinear relationship with the applied stress (Brantut et al. 2013; Aydan et al. 2014; Wang et al. 2019) which is not represented by the CVISC model. The omission of the mean stress term in the constitutive equation (see Appendix B) indicates that the CVISC model cannot account the effect of friction angle on the creep strain rate for frictional material (Ngwenya et al. 2001; Wang et al. 2019). The CVISC model is also not able to predict the time to delayed failure and creep strains of rocks in the tertiary creep stage. This can cause an underestimation of walls creep deformation applied on backfill when the time to exposure is very long. A more representative model is thus needed to better simulate the time-dependent behavior of rocks in future works. More works are also required to account the effect of temperature on the results.

Numerical results show that stress states in a backfilled stope can significantly increase due to the walls creep deformation. However, the volumetric yield under high isotropic loading and pressure dependent behavior of backfill (Pierce 1999; Rankine 2004) are not considered in this study. The cemented backfill is simulated in dry condition that means the dissipation of pore water pressure

during curing time is not considered (Godbout et al. 2007; El Mkadmi et al 2014). The evolution of the backfill properties during curing time can be more complex than a linear function as shown in Figure 4.3 (Belem et al. 2000). More effort is needed to better represent above aspects.

Mechanical parameters of cemented backfill can be coupled and affected by the stress condition during curing time. For example, some experimental results showed that E of cemented backfill increases with the increase of c (Gonano and Kirkby 1977; Fall et al. 2007). More effort is needed to consider the coupled effect on the backfill mechanical parameters. Yilmaz (2018) reported that UCS and E of cemented backfill increase as the applied compressive stress increases during curing time. However, one should note that in the tests of Yilmaz (2018), the compaction effect was achieved by applying stress which is independent on the backfill parameters evolution. In this study, the compaction on backfill is governed by the walls creep deformation which interacts with backfill properties. As the backfill becomes harder under walls compaction, it further reduces the deformation of rocks. Therefore, the interaction between backfill parameters evolution and compaction governed by rock walls creep deformation (strain) is expected to be analyzed in future, but it is beyond the scope of this study.

In this study, the cohesion at failure and the minimum required cohesion of side-exposed backfill are considered very close to each other in a condition that FS equals to 1. In practice, a larger FS is recommended which can lead to a larger required cohesion for side-exposed backfill.

The applicability of FLAC^{3D} in studying the stability of side-exposed backfill has been verified by Liu et al. (2016a) and Wang et al. (2021) through the reproductions of box instability (Mitchell et al. 1982) and centrifugal model tests (Mitchell 1986). Nonetheless, more experimental works are still needed to verify the numerical model considering creep of rock mass. It is also worth mentioning that some studies used two-dimensional model to estimate the stress state in a backfilled stope with or without considering creep, and evaluate the stability of side-exposed backfill (Coulthard and Dight 1980; Li et al. 2003; Qi and Fourie 2019). The two-dimensional model is efficient and may be applied when the width of stope is large. However, the two-dimensional model is inapplicable when the arching stress and closure from side walls need to be considered.

4.6 Conclusions

The time-dependent stability and minimum required cohesion (c_{min}) of side-exposed backfill associated with the creep of surrounding rock mass are, for the first time, investigated through three-dimensional numerical modeling with FLAC^{3D}. A distinction is made between the cohesion at failure and the c_{min}. Mechanical parameters evolution of backfill with curing time is considered. Results show that the empty time of primary stope does not significantly affect the stability and c_{min}. When mine depth is small and the rock exhibits little creep, it deserves to wait longer time before excavating adjacent stope in order for the backfill to gain more strength with curing time. When the mine depth is large or/and the rock exhibits heavy creep, the instability of side-exposed backfill can be dictated by crushing failure. A stronger backfill means also a harder backfill, which absorbs larger compressive stress with a given rock-wall closure and is more prone to be crushed. In this condition, simply increasing the binder content may not be the best choice. Rather, a softer backfill can be better through the use of lower binder content or/and with a shorter curing time. Once the adjacent secondary stope is mined out, it should be filled as soon as possible to avoid failure of side-exposed backfill.

The c_{min} of side-exposed backfill can be significantly reduced with a thick ore vein or through the use of secondary stopes with small height and length when the mine depth is large or/and rock walls exhibit pronounced creep deformation. On the other hand, large secondary stopes are preferred because non-cemented or low binder content backfill can be used to fill the secondary stopes. An optimization is thus needed to minimize the overall cost of backfill for the primary and secondary stopes. The results also show that for the backfill with a large internal frictional angle, the c_{min} can be decreased. The soft rock mass with small stiffness and viscosity coefficient leads to the decrease of c_{min} at a shallow mine depth, but requires a larger c_{min} for side-exposed backfill to prevent crushing when the walls creep deformation is significant at a large mine depth. When the walls instantaneous closure is small, the c_{min} of side-exposed backfill can be dominated by the long-term creep deformation of rock mass during curing time.

4.7 Appendix: Verification of the applicability of numerical model to describing the time-dependent closure of underground openings

The simulated time-dependent closure of stope shown in Figure 4.6 is a typical closure profile of underground openings (Malan 1999; Barla et al. 2010; Qi and Fourie 2019). The numerical results and the ability of numerical model can be further verified by comparing with the in-situ measurement of creep deformation around a tunnel. The Frejus tunnel between France and Italy is 12.78 km long and has a typical cross-section as shown in Figure 4.20a (Sulem et al. 1987). It was excavated in schist under a depth of 600 to 1200 m. During the construction of Frejus tunnel, the face advance was stopped for 22 days during which the walls time-dependent convergence along line *M'N'* was monitored at a section that is 29 m behind the face. The measured results were reported by Sulem et al. (1987) and is shown here in Figure 4.20b. Since the face advance is interrupted, the closure shown in the Figure 4.20b is only attributed to the creep behavior of rocks. The measured results will be reproduced using FLAC^{3D} to verify the ability of the model. Due to that the the actual stress conditions and rock properties are not accurately known, some parameters will be assumed and the numerical reproduction is performed by calibrating the viscoelastic parameters.

(a) (b)
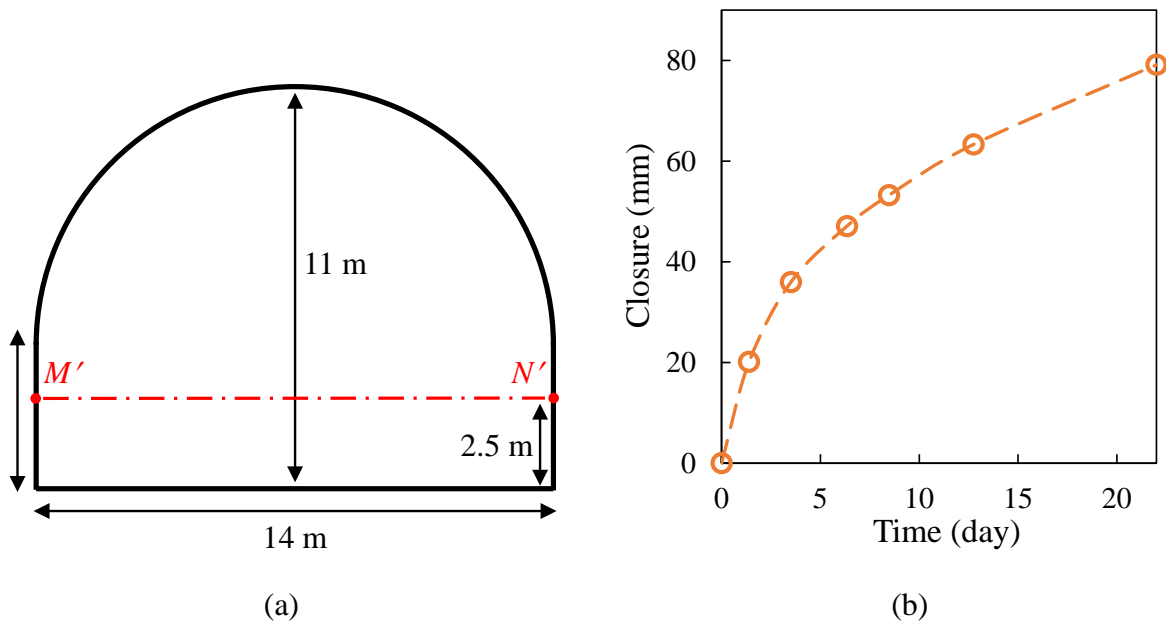
Figure 4.20: (a) Cross-section and (b) measured time-dependent closure along line *M'N'* in a section of the Frejus tunnel (adopted from Sulem et al. 1987)

Figure 4.21 shows the plane strain numerical model of Frejus tunnel built with FLAC^{3D}. The numerical model has a height of 411 m and a length of 414 m. Gravity is along the negative direction of the y-axis. The average depth of 900 m is considered and the lateral earth pressure coefficient K_r is applied as 1. The CVISC model is applied for the rock mass. The assumed parameters for rock mass include $\gamma_R = 27$ kN/m^3, $E_R = 10$ GPa, $v_R = 0.25$, $c_R = 2$ MPa, $\phi_R = 40$, $\psi_R = 0°$, $T_R = 150$ kPa. One should note that elastic modulus and strength parameters mainly affect the instantaneous deformation which is not the objective here. Creep modeling parameters involve $t_m = 1000$ s, $t_i = 30$ s, latency of 50 steps, $lfob = 1 \times 10^{-6}$, and $ufob = 3 \times 10^{-6}$. In the numerical model, displacement along the third direction (z-axis) is restricted. Lateral displacements are prohibited along the left and right boundaries while for the bottom, all displacements are restricted. After solving to the equilibrium state by excavating the tunnel, the instantaneous deformation is reset to 0. The time-dependent closure along line $M'N'$ is then calculated for 22 days. Based on calibration, the applied viscoelastic parameters are $G_K = 5.62$ GPa, $\eta_K = 1.07 \times 10^{15}$ Pa·s, $\eta_M = 9.75 \times 10^{15}$ Pa·s.
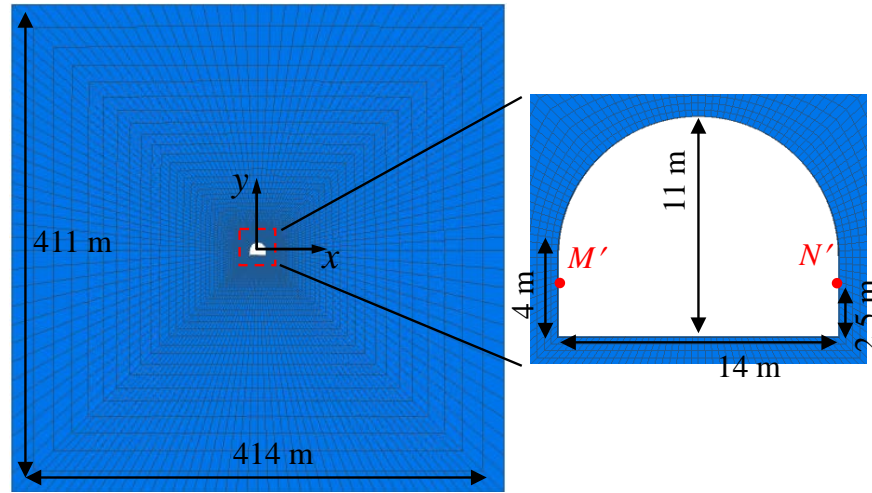
Figure 4.21: Plane strain numerical model of the Frejus tunnel built with FLAC^{3D}

Figure 4.22 shows the comparisons between the numerical results and in-situ measurements of walls time-dependent closure in the Frejus tunnel. The good agreement verifies that the numerical model is able to reflect the creep deformation around underground openings as illustrated in Figure 4.6.
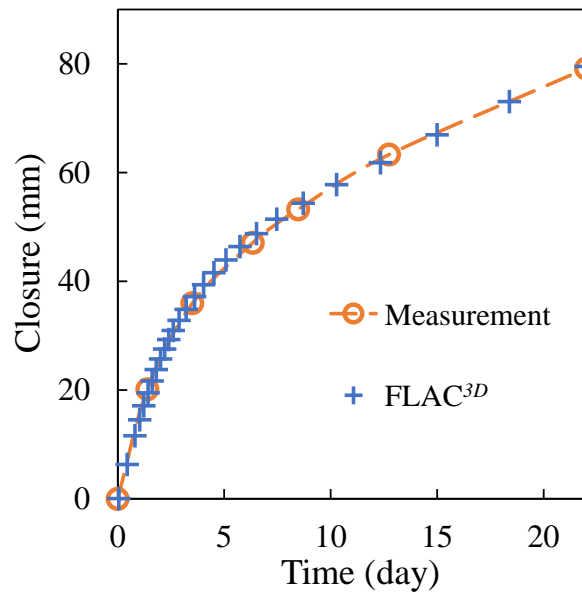
Figure 4.22: Comparisons between the numerical results of walls time-dependent closure and in-situ measurements reported by Sulem et al. (1987) in the Frejus tunnel

Acknowledgements

4.8 References

Amitrano, D., & Helmstetter, A. (2006). Brittle creep, damage, and time to failure in rocks. *Journal of Geophysical Research: Solid Earth*, 111, 1–17.

Askew, J., McCarthy, P.L., & Fitzgerald, D.J. (1978). Backfill research for pillar extraction at ZC/NBHC. *Proceedings of 12th Canadian rock mechanics symposium*. Institute of Mining and Metallurgy, Sudbury, 100–110.

Aubertin, M., Li, L., Arnoldi, S., Belem, T., Bussière, B., Benzaazoua, M., & Simon, R. (2003). Interaction between backfill and rock mass in narrow stopes. *Proceedings of 12th*

panamerican conference on soil mechanics and geotechnical engineering and 39th U.S. rock mechanics symposium. Cambridge, USA, 1157–1164.

Aubertin, J.D., Hoentzsch, S., Diederichs, M.S., & Milton, H. (2018). Influence of the creep law on pillar response based on numerical simulations of an underground salt mine. *Proceedings of 52nd U.S. rock mechanics/geomechanics symposium.*, American Rock Mechanics Association, Seattle, Washington.

Aydan, Ö., & Kawamoto, T. (2000). The assessment of mechanical properties of rock masses through RMR rock classification system. *Proceedings of the GeoEng 2000 symposium.* Sydney, Australia.

Aydan, Ö., Ito, T., Özbay, U., Kwasniewski, M., Shariar, K., Okuno, T., Özgenoğlu, A., Malan, D.F., & Okada, T. (2014). ISRM suggested methods for determining the creep characteristics of rock. *Rock Mechanics and Rock Engineering*, 47(1), 275–290.

Barla, G., Bonini, M., Debernardi, D. (2010). Time dependent deformations in squeezing tunnels. *Proceedings of the 12th ISSMGE international conference of international association for computer methods and advances in geomechanics*. Goa, India, 4265–4275.

Barrett, J.R., & Cowling, R. (1980). Investigations of cemented fill stability in 1100 orebody, Mount Isa Mines, Ltd., Queensland, Australia. *Mining Technology IMM Transactions section A*, 89, A118–A128.

Belem, T., Benzaazoua, M., & Bussière, B. (2000). Mechanical behaviour of cemented paste backfill. *Proceedings of 53rd Canadian geotechnical conference*. Canadian Geotechnical Society, Montreal, 373–380.

Belem, T., & Benzaazoua, M. (2008). Design and application of underground mine paste backfill technology. *Geotechnical and Geological Engineering*, 26(2), 147–174.

Bérest, P., Gharbi, H., Brouard, B., Brückner, D., DeVries, K., Hévin, G., Hofer, G., Spiers, C., & Urai, J. (2019). Very slow creep tests on salt samples. *Rock Mechanics and Rock Engineering*, 52(9), 2917–2934.

Bieniawski, Z.T. (1989). *Engineering rock mass classifications: a complete manual for engineers and geologists in mining, civil, and petroleum engineering*. New York: Wiley.

Boulianne, M., Simon, R., & Aubertin, M. (2004). A numerical investigation of the creep (viscoplastic) behaviour of circular opening and pillar in rock salt. *Proceedings of 57th Canadian geotechnical conference and the 5th joint CGS-IAH conference*. Quebec City, 25–32.

Brantut, N., Heap, M., Meredith, P., & Baud, P. (2013). Time-dependent cracking and brittle creep in crustal rocks: A review. *Journal of Structural Geology*, 52, 17–43.

Cao, S., Yilmaz, E., & Song, W. (2018). Evaluation of viscosity, strength and microstructural properties of cemented tailings backfill. *Minerals*, 8(8), 352.

Coulthard, M.A. (1980). Numerical analysis of fill pillar stability: Three dimensional linearly elastic finite element calculations. *Technical report*. Division of Applied Geomechanics, CSIRO, Australia.

Coulthard, M.A., & Dight, P.M. (1980). Numerical analysis of failed cemented fill at ZC/NBHC Mine, Broken Hill. *Proceedings of 3rd Australia-New Zealand conference on geomechanics*. Institution of Professional Engineers New Zealand, Wellington, 145–151.

Cristescu, N., & Hunsche, U. (1998). *Time effects in rock mechanics*. New York: Wiley.

Darling, P. (2011). *SME mining engineering handbook*. Denver: Society for Mining, Metallurgy and Exploration.

Dusseault, M.B., & Fordham, C.J. (1993). *Time-dependent behavior of rocks. In: Hudson JA (ed) Rock testing and site characterization*. Pergamon, 119–149.

El Mkadmi, N., Aubertin, M., & Li, L. (2014). Effect of drainage and sequential filling on the behavior of backfill in mine stopes. *Canadian Geotechnical Journal*, 51(1), 1–15.

Fall, M., Belem, T., Samb, S., & Benzaazoua, M. (2007). Experimental characterization of the stress-strain behaviour of cemented paste backfill in compression. *Journal of Materials Science*, 42(11), 3914–3922.

Fall, M., & Nasir, O. (2010). Mechanical behaviour of the interface between cemented tailings backfill and retaining structures under shear loads. *Geotechnical and Geological Engineering*, 28, 779–790.

Fang, K., & Fall, M. (2018). Effects of curing temperature on the shear behaviour of cemented paste backfill-rock interface. *International Journal of Rock Mechanics and Mining Sciences*, 112, 184–192.

Fang, K., & Fall, M. (2019). Chemically induced changes in the shear behaviour of the interface between rock and tailings backfill undergoing cementation. *Rock Mechanics and Rock Engineering*, 52, 3047–3062.

Fang, K., & Fall, M. (2020). Shear behavior of the interface between rock and cemented backfill: effect of curing stress, drainage condition and backfilling rate. *Rock Mechanics and Rock Engineering*, 53, 325–336.

Fang, K., & Fall, M. (2021). Shear behaviour of rock–tailings backfill interface: effect of cementation, rock type, and rock surface roughness. *Geotechnical and Geological Engineering*, 39, 1753–1770.

Farmer, I.W. (2012). *Engineering behaviour of rocks*. Springer Science & Business Media.

Ghirian, A., & Fall, M. (2015). Coupled behavior of cemented paste backfill at early ages. *Geotechnical and Geological Engineering*, 33(5), 1141–1166.

Godbout, J., Bussière, B., & Belem, T. (2007). Evolution of cemented paste backfill saturated hydraulic conductivity at early curing time**.** *Proceedings of 60th Canadian geotechnical conference and the 8th joint CGS/IAH-CNC groundwater conference*. Ottawa, 2230–2236.

Gonano, L.P., & Kirkby, R.W. (1977). In situ investigation of cemented rockfill in the 1100 orebody, Mount Isa Mine, Queensland. *Technical Report*. Australia: Division of Applied Geomechanics, Commonwealth Scientific and Industrial Research Organization.

Grabinsky, M.W., & Bawden, W.F. (2007). In situ measurements for geomechanical design of cemented paste backfill systems. *Proceedings of 9th international symposium on mining with backfill*. Canadian Institute of Mining, Metallurgy and Petroleum, Montreal, 1–8.

Griggs, D. (1939). Creep of rocks. *The Journal of Geology*, 47(3), 225–251.

Guler, G. (1998). *Analysis of the rock mass behaviour as associated with Ventersdorp Contact Reef stopes, South Africa*. (Master's thesis, University of the Witwatersrand, Johannesburg).

Hao, S., Liu, C., Wang, Y., & Chang, F. (2017). Scaling law of average failure rate and steady-state rate in rocks. *Pure and Applied Geophysics*, 174(6), 2199–2215.

Hardy, H.R., Kim, R. Y., Stefanko, R., & Wang, Y. J. (1969). Creep and microseismic activity in geologic materials. *Proceedings of the 11th US Symposium on Rock Mechanics (USRMS)*. American Rock Mechanics Association, 377-414.

Hartman, H.L. (1992). *SME mining engineering handbook, 2nd edn.* Society for Mining, Metallurgy, and Exploration, Littleton.

Hasanpour, R., Rostami, J., & Barla, G. (2015). Impact of advance rate on entrapment risk of a double-shielded TBM in squeezing ground. *Rock Mechanics and Rock Engineering*, 48(3), 1115–1130.

Hassani, F., & Archibald, J. (1998). *Mine backfill*. Canadian Institute of Mine, Metallurgy and Petroleum.

Heap, M.J., Baud, P., & Meredith, P.G. (2009). Influence of temperature on brittle creep in sandstones. *Geophysical Research Letters*, 36(19), L19305.

Hoek, E., & Brown, E.T. (1997). Practical estimates of rock mass strength. *International Journal of Rock Mechanics and Mining Sciences*, 34(8), 1165–1186.

Itasca. (2013). *FLAC3D—Fast lagrangian analysis of continua in 3 dimensions, user's guide, version 5.01*. Minneapolis: Itasca Consulting Group.

Jaeger, J.C. (1969). *Elasticity, fracture and flow: with engineering and geological applications*. London: Chapman and Hall.

King, R.G., Jager, A.J., Roberts, M.K.C., & Turner, P.A. (1989). Rock mechanics aspects of stoping without back-area support. *Research Report*. CSIR, Pretoria.

Kranz, R.L. (1980). The effects of confining pressure and stress difference on static fatigue of granite. *Journal of Geophysical Research: Solid Earth*, 85(B4), 1854–1866.

Lajtai, E.Z., & Schmidtke, R.H. (1986). Delayed failure in rock loaded in uniaxial compression. *Rock Mechanics and Rock Engineering*, 19(1), 11–25.

Li, L., Aubertin, M., Simon, R., Bussière, B., & Belem, T. (2003). Modeling arching effects in

narrow backfilled stopes with FLAC. *Proceedings of 3rd international symposium on FLAC and FLAC3D numerical modelling in geomechanics*. Sudbury, 211–219.

Li, L. (2014a). Generalized solution for mining backfill design. *International Journal of Geomechanics*, 14(3), 04014006.

Li, L. (2014b). Analytical solution for determining the required strength of a side-exposed mine backfill containing a plug. *Canadian Geotechnical Journal*, 51(5), 508–519.

Li, L., & Aubertin, M. (2012). A modified solution to assess the required strength of exposed backfill in mine stopes. *Canadian Geotechnical Journal*, 49(8), 994–1002.

Li, L., & Aubertin, M. (2014). An improved method to assess the required strength of cemented backfill in underground stopes with an open face. *International Journal of Mining Science and Technology*, 24(4), 549–558.

Liu, G., Li, L., Yang, X., & Guo, L. (2016a). Stability analyses of vertically exposed cemented backfill: A revisit to Mitchell's physical model tests. *International Journal of Mining Science and Technology*, 26(6), 1135–1144.

Liu, G., Li, L., Yang, X., & Guo, L. (2016b). A numerical analysis of the stress distribution in backfilled stopes considering nonplanar interfaces between the backfill and rock walls. *International Journal of Geotechnical Engineering*, 10(3), 271–282.

Liu, G., Li, L., Yang, X., & Guo, L. (2018). Required strength estimation of a cemented backfill with the front wall exposed and back wall pressured. *International Journal of Mining and Mineral Engineering*, 9(1), 1–20.

Malan, D.F., Vogler, U.W., & Drescher, K. (1997). Time-dependent behaviour of hard rock in deep level gold mines. *Journal of the Southern African Institute of Mining and Metallurgy*, 97(3), 135–147.

Malan, D.F. (1999). Time-dependent behaviour of deep level tabular excavations in hard rock. *Rock Mechanics and Rock Engineering*, 32(2), 123–155.

Mitchell, R.J., Olsen, R.S., & Smith, J.D. (1982). Model studies on cemented tailings used in mine backfill. *Canadian Geotechnical Journal*, 19(1), 14–28.

Mitchell, R.J., & Wong, B.C. (1982). Behaviour of cemented tailings sands. *Canadian Geotechnical Journal*, 19(3), 289–295.

Mitchell, R.J. (1986). Centrifuge model tests on backfill stability. *Canadian Geotechnical Journal*, 23(3), 341–345.

Mitchell, R.J. (1989). Model studies on the stability of confined fills. *Canadian Geotechnical Journal*, 26(2), 210–216.

Nasir, O., & Fall, M. (2008). Shear behaviour of cemented pastefill–rock interfaces. *Engineering Geology*, 101(3), 146–153.

Nejati, H.R., Ghazvinian, A., Moosavi, S.A., & Sarfarazi, V. (2014). On the use of the RMR system for estimation of rock mass deformation modulus. *Bulletin of Engineering Geology and the Environment*, 73(2), 531–540.

Ngwenya, B.T., Main, I.G., Elphick, S.C., Crawford, B.R., & Smart, B.G.D. (2001). A constitutive law for low-temperature creep of water-saturated sandstones. *Journal of Geophysical Research: Solid Earth*, 106(B10), 21811–21826.

Pałac-Walko, B., & Pytel, W. (2014). The effect of the presence of salt formations above extracted copper ore as determined by numerical modelling. *Proceedings of the seventh international conference on deep and high stress mining*. Australian Centre for Geomechanics, Perth, 409–420.

Paraskevopoulou, C., & Diederichs, M. (2018). Analysis of time-dependent deformation in tunnels using the Convergence-Confinement Method. *Tunnelling and Underground Space Technology*, 71, 62–80.

Paraskevopoulou, C., Perras, M., Diederichs, M., Loew, S., Lam, T., & Jensen, M. (2018). Time-dependent behaviour of brittle rocks based on static load laboratory tests. *Geotechnical and Geological Engineering*, 36(1), 337–376.

Pierce, M.E. (1999). *Laboratory and numerical analysis of the strength and deformation behaviour of paste backfill*. (Master's thesis, Queen's University).

Potvin, Y., Thomas, E., & Fourie, A. (2005). *Handbook on mine fill*. Perth: Australian Centre for

Geomechanics.

Qi, C., & Fourie, A. (2019). Numerical investigation of the stress distribution in backfilled stopes considering creep behaviour of rock mass. *Rock Mechanics and Rock Engineering*, 52(9), 3353–3371.

Raffaldi, M.J., Seymour, J.B., Richardson, J., Zahl, E., & Board, M. (2019). Cemented paste backfill geomechanics at a narrow-vein underhand cut-and-fill mine. *Rock Mechanics and Rock Engineering*, 52(12), 4925–4940.

Rankine, R.M.A. (2004). *The geotechnical characterisation and stability analysis of BHP Billiton's Cannington Mine paste fill*. (Ph.D. thesis, James Cook University).

Sainsbury, D.P., & Urie, R. (2007). Stability analysis of horizontal and vertical paste fill exposures at the Raleigh Mine. *Proceedings of 9th international symposium on mining with backfill*. Canadian Institute of Mining, Metallurgy and Petroleum, Montreal.

Salencon, J. (1969). Contraction quasi-statique d'une cavité a symétrie sphérique ou cylindrique dans un milieu elastoplastique. *Ann Ponts Chaussées*, 4, 231–236.

Sulem, J., Panet, M., & Guenot, A. (1987). Closure analysis in deep tunnels. *International Journal of Rock Mechanics and Mining Sciences & Geomechanics Abstracts*, 24(3), 145–154.

Thompson, B.D., Grabinsky, M.W., Bawden, W.F., & Counter, D.B. (2009). In-situ measurements of cemented paste backfill in long-hole stopes. *Proceedings of the 3rd CANUS rock mechanics symposium*. Toronto, 197–198.

Wang, R., & Li, L. (2018). Burgers creep model used for describing and predicting the creep behaviour of a rock under uniaxial and triaxial compression test conditions. *Proceedings of the 71st Canadian geotechnical conference*. Canadian Geotechnical Society, Edmonton.

Wang, R., & Li, L. (2019). A non-stationary power law model to predict the secondary creep rate of rocks. *Proceedings of 8th international conference on case histories in geotechnical engineering*. American Society of Civil Engineers, Philadelphia, 476–483.

Wang, R., Li, L., & Simon, R. (2019). A model for describing and predicting the creep strain of rocks from the primary to the tertiary stage. *International Journal of Rock Mechanics and Mining Sciences*, 123, 104087.

Wang, R., Zeng, F., & Li, L. (2021). Stability analyses of side-exposed backfill considering mine depth and extraction of adjacent stope. *International Journal of Rock Mechanics and Mining Sciences*, 142, 104735.

Wittke, W. (2014). *Rock mechanics based on an anisotropic jointed rock model (AJRM).* Berlin: Ernst & Sohn.

Yang, P., Li, L., & Aubertin, M. (2017). A new solution to assess the required strength of mine backfill with a vertical exposure. *International Journal of Geomechanics*, 17(10), 04017084.

Yilmaz, E. (2018). Stope depth effect on field behaviour and performance of cemented paste backfills. *International Journal of Mining, Reclamation and Environment*, 32(4), 273–296.

Zhao, X., Fourie, A., & Qi, C. (2019). An analytical solution for evaluating the safety of an exposed face in a paste backfill stope incorporating the arching phenomenon. *International Journal of Minerals, Metallurgy and Materials*, 26(10), 1206–1216.

CHAPTER 5   ARTICLE 3: APPLICABILITY OF CONSTITUTIVE MODELS TO DESCRIBING THE COMPRESSIBILITY OF MINING BACKFILL: A COMPARATIVE STUDY

Ruofan Wang, Feitao Zeng, and Li Li

Abstract: The compressibility of mining backfill governs its resistance to the closure of surrounding rock mass which should be well reflected in numerical modeling. In most numerical simulations of backfill, Mohr-Coulomb elasto-plastic model is used, but is constantly criticized for its poor representativeness to the mechanical response of geomaterials. Finding an appropriate constitutive model to better represent the compressibility of mining backfill is critical and necessary. In this paper, Mohr-Coulomb elasto-plastic model, double-yield model, and Soft Soil model are briefly recalled. Their applicability in describing the backfill compressibility is then assessed by comparing numerical results in FLAC^{3D} with some experimental results of one-dimensional consolidation and consolidated drained triaxial compression tests made on lowly cemented backfills available in the literature. The results show that the Soft Soil model can be used to properly describe the experimental results while the application of the Mohr-Coulomb model and double-yield model shows poor description on the compressibility of the backfill submitted to large and cycle loading. A further application of the Soft Soil model to the case of a backfilled stope overlying a sill mat shows stress distributions close to those obtained by applying the Mohr-Coulomb model when the rock-wall closure is not applied. However, after excavating the underlying stope, rock-wall closure is generated and exercises a compression on the overlying backfill. Compared to the results obtained by applying the Soft Soil model, an application of the Mohr-Coulomb model tends to overestimate the stresses in the backfill when the mine depth is small and underestimate the stresses when the mine depth is large due to the poor description of fill compressibility. The Soft Soil model is recommended to describe the compressibility of uncemented or lightly cemented backfill with small cohesions under external compressions associated with rock-wall closure.

Key-words: Mining backfill; Compressibility; Constitutive models; Numerical modeling.

5.1 Introduction

Backfill is being considered as an integral part of several underground mining methods. It is used as working platform in overhand cut-and-fill mining method or for creating safer working space in underhand cut-and-fill mining method. Using mine wastes as underground mining backfill helps minimize the surface disposal of mine wastes (Hassani and Archibald 1998; Benzaazoua et al. 2008; Stephan 2011; Kortnik 2021). However, the major objective of backfilling the mined-out space is to effectively control the rock-wall closure and maintain the regional ground stability (Potvin et al. 2005; Newman and Agioutantis 2018; Zhao et al. 2018; Vasichev 2019; Wang et al. 2021). The compressibility of backfill plays an important role in resisting the closure of surrounding rock walls associated with adjacent extraction or/and creep behavior. Previous studies showed that a backfill with a low compressibility can carry significant stresses generated by walls convergence and provide considerable support for surrounding rocks (Falaknaz et al. 2015; Sobhi and Li 2017; Newman and Agioutantis 2018; Raffaldi et al. 2019; Qi and Fourie 2019). Understanding and properly describing the compressibility of mining backfill is thus of specific interest for mining industry to evaluate fill performance and stability of underground structures.

Numerical modeling provides an efficient and cost-effective method to study the complex mechanical behavior of backfill. Nonetheless, the reliability and applicability of a numerical model largely depends on the capability of applied constitutive model. There are many constitutive models of geomaterial proposed in literatures with various levels of complexity (Brinkgreve 2005; Helinski et al 2007; Li et al. 2010; Cui and Fall 2015). Until now, the Mohr-Coulomb elasto-plastic model is the most used one to simulate the mining backfill due to the simplicity and clear physical meaning of model parameters (Aubertin et al. 2003; Li et al. 2003; Pirapakaran and Sivakugan 2007; Emad et al. 2012; Li and Aubertin 2014; Liu et al. 2017; Pagé et al. 2019; Keita et al. 2021a). The justification of the Mohr-Coulomb model is usually attributed to the good fit with the shear strength of backfill (Pierce 1999; Belem et al. 2000; Rankine 2004; Fall et al. 2007; Jafari et al. 2021). However, it is well-known that the Mohr-Coulomb elasto-plastic model suffers from its linearly elasticity and the neglection of volumetric yielding. In reality, geomaterial can have a nonlinear behavior before yielding while a mining backfill can become denser upon a large compression generated by wall closure. Given the restrictions of the Mohr-Coulomb elasto-plastic model, it

remains unknown which constitutive model should be applied to better represent the compressibility of mining backfill.

There are few researches devoted to identify a constitutive model applicable of describing the compressibility of mining backfill. Among these studies, Oliver and Landriault (1989) investigated the convergence resistance of backfill by simulating the oedometer test of dense sand with the Mohr-Coulomb and the Strain-Softening models. Different values of Young's modulus and Poisson's ratio were applied. Results show that numerical model remains elastic over the full strain range except when a very small Poisson's ratio is applied. The predicted compressive stresses of two constitutive models are almost identical and significantly smaller than the experimental results. Clark (1991) reproduced the non-linear stress-strain response of the dewatered tailings backfill in uniaxial compression tests with a cap model in FLAC. The input parameters for the cap model were obtained by curve fitting with all experimental results. The good agreements between the numerical model and experimental results do not mean that the calibrated numerical model can be used to correctly predict the mechanical behavior of the backfill under an untested stress condition. Fourie et al. (1993) performed a finite element analysis by making use of the linear elastic, Mohr-Coulomb, Drucker-Prager, and Modified Cam-Clay models to simulate a backfilled stope at a mine depth of 2000 m with a finite element program. The hanging wall convergence for the Modified Cam-Clay model was found 11% larger than the results of other three models due to the plastic volumetric strain of backfill. The numerical results were not further compared with physical test data. Lagger et al. (2016) used the double-yield model in FLAC^{3D} to simulate the oedometer test of pea gravel as a filling material. The cap pressure of the double-yield model was calibrated based on the experimental results in a stress range of 0 to 6 MPa. Within this range, numerical results reasonably correlate with the test data, but the comparisons for higher load stage was not shown. Therefore, more works are necessary to identify a suitable constitutive model to describe the compressibility of mining backfill, particularly by analyzing its predictive capability and comparing with physical results.

In this study, the Mohr-Coulomb, double-yield, and Soft Soil models are recalled. Their ability in describing the compressibility of backfill is identified by comparing the numerical results in FLAC^{3D} with the experimental results of one-dimensional consolidation and consolidated drained triaxial compression tests of backfill available in the literature. Some unknown model parameters

are calibrated based on part of the experimental results and the calibrated models are applied to predict the other part of the experimental results. The identified model is then benchmarked with the Mohr-Coulomb model in simulating a backfilled stope overlying a sill mat at different mine depths. The applicability of identified model and the significance of modeling fill compressibility will be shown and discussed.

5.2   Commonly used constitutive models in geotechnical engineering

For the sake of completeness, a few constitutive models commonly used in geotechnical engineering, including the Mohr-Coulomb, double-yield, and Soft Soil models, are briefly recalled. Compression stresses are positive and tension is negative. All the strength parameters are in terms of effective stresses.

5.2.1 Mohr-Coulomb elasto-plastic model

The Mohr-Coulomb elasto-plastic model considers a material as linearly elastic and perfectly plastic once the stress state reaches a state of yield (Labuz and Zang 2012). It is the most commonly used constitutive model in modeling the mechanical behavior of mining backfill.

Figure 5.1 plotted the envelope of the Mohr-Coulomb model in p-q space and the typical stress-strain relation. In the figure, ϕ and c are the friction angle and cohesion, respectively; ε_q is the deviatoric strain; p and q are the mean and deviatoric stresses, respectively expressed as:

$$p = \frac{(\sigma_1 + \sigma_2 + \sigma_3)}{3} \tag{5.1}$$

$$q = \sqrt{\frac{(\sigma_1 - \sigma_2)^2 + (\sigma_2 - \sigma_3)^2 + (\sigma_3 - \sigma_1)^2}{2}} \tag{5.2}$$

where σ_1, σ_2 and σ_3 are the major, intermediate and minor principal stresses, respectively.

The linear stress-strain relation in the elastic regime (below the envelope) is described using a constant Young's modulus E and Poisson's ratio v and assumed to follow the Hooke's law. Once the stress state reaches the yield envelop defined by the Mohr-Coulomb criterion, infinite plastic shear strain occurs under constant load.
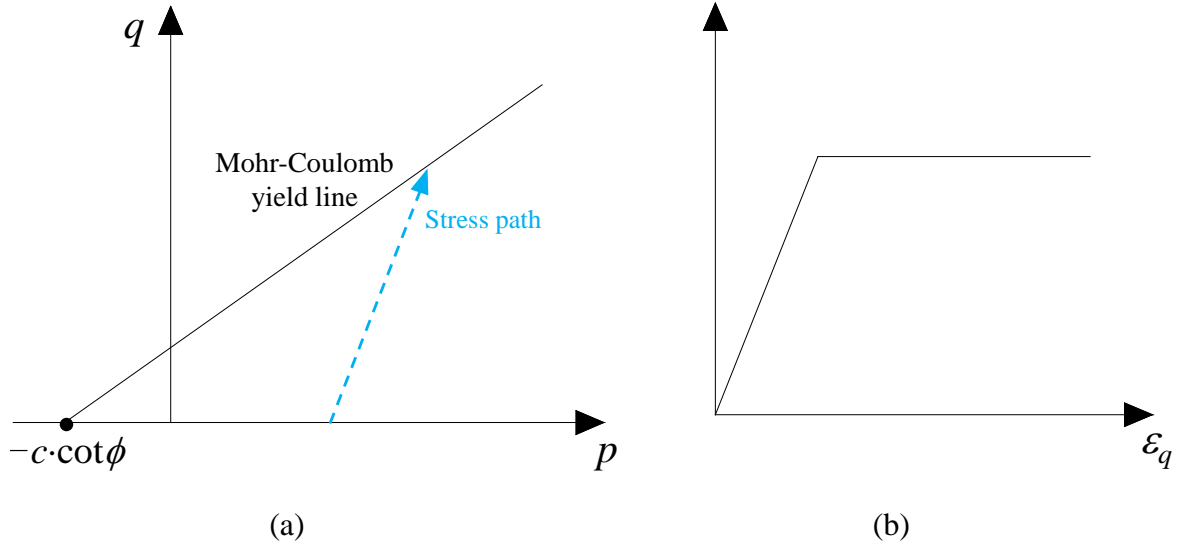
Figure 5.1: Schematic (a) yield surface and (b) stress-strain behavior of the Mohr-Coulomb model

The stress-strain relation in the elastic region is expressed as:

$$\varepsilon_x = \frac{1}{E}\left[\sigma_x - v(\sigma_y + \sigma_z)\right] \tag{5.3}$$

$$\varepsilon_y = \frac{1}{E}\left[\sigma_y - v(\sigma_x + \sigma_z)\right] \tag{5.4}$$

$$\varepsilon_z = \frac{1}{E}\left[\sigma_z - v(\sigma_x + \sigma_y)\right] \tag{5.5}$$

$$\gamma_{xy} = \frac{2(1+v)}{E}\tau_{xy}, \quad \gamma_{yz} = \frac{2(1+v)}{E}\tau_{yz}, \quad \gamma_{xz} = \frac{2(1+v)}{E}\tau_{xz} \tag{5.6}$$

where σ_x, σ_y, σ_z, τ_{xy}, τ_{yz}, τ_{xz} are the components of stress tensor; ε_x, ε_y, ε_z, γ_{xy}, γ_{yz}, γ_{xz} are the components of strain tensor.

The Mohr-Coulomb yield criterion can be considered as a combination of the Mohr circle of stress state (Mohr 1900) and Coulomb criterion (Coulomb 1773) which is defined with the friction angle ϕ and cohesion c. The Coulomb criterion describes a linear relation between shear strength τ and corresponding normal stress σ given by:

$$\tau = c + \sigma \cdot \tan \phi \tag{5.7}$$

The Mohr-Coulomb yield criterion in terms of principal stresses can be expressed as:

$$\frac{(\sigma_1 - \sigma_3)}{2} - \frac{(\sigma_1 + \sigma_3)}{2} \cdot \sin \phi - c \cdot \cos \phi = 0 \tag{5.8}$$

An 3D generalization of Eq. (5.8) in terms of stress invariants is given as (Pietruszczak 2010):

$$q + \left(\frac{3\sin\phi}{\sin\theta_l \cdot \sin\phi - \sqrt{3}\cos\theta_l}\right)p + \left(\frac{3\cos\phi}{\sin\theta_l \cdot \sin\phi - \sqrt{3}\cos\theta_l}\right)c = 0 \tag{5.9}$$

where θ_l is the Lode angle.

The Mohr-Coulomb criterion correlates well with the shear strength of backfill but tends to overestimate the tensile strength since it is a linear criterion (Mitchell and Wong 1982). A tensile strength T, called tension cut-off, thus usually applies for mining backfill. A dilation angle ψ is introduced in the Mohr-Coulomb model to describe the a nonassociated flow rule and model the plastic volume change due to shearing. The Mohr-Coulomb model does not capture the plastic volumetric strain under isotropic compression.

5.2.2 Double-yield model

The double-yield model is introduced in FLAC (Itasca 2019) which involves shear and tensile yield criteria of the Mohr-Coulomb model, and a volumetric yield surface. Its stress-strain relation in the elastic region is described by the Hooke's law. Figure 5.2 illustrates the schematic yield surface and stress-strain behavior of the double-yield model.
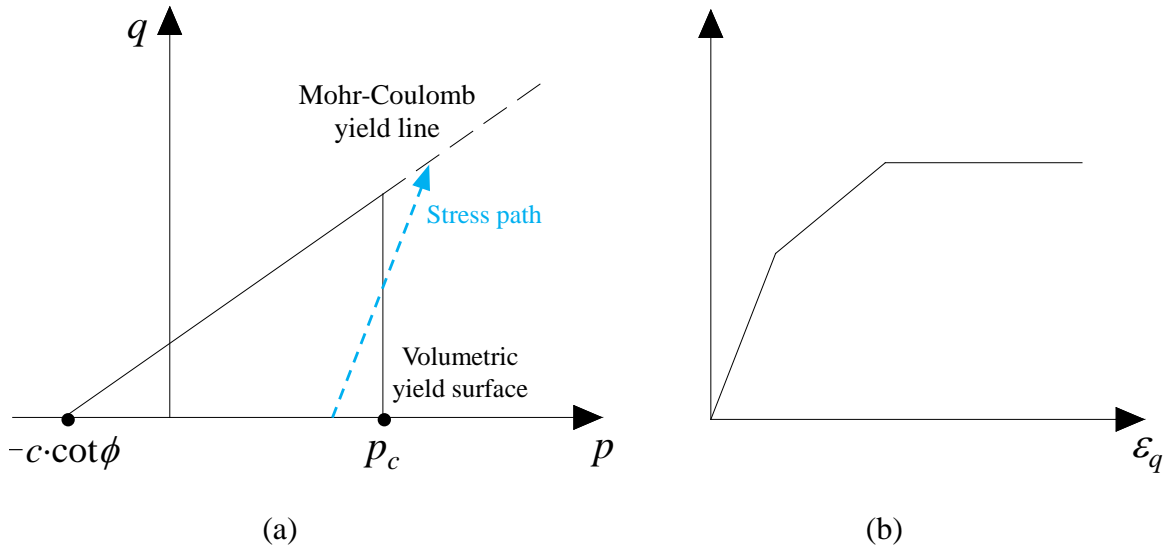
Figure 5.2: Schematic (a) yield surface and (b) stress-strain behavior of the double-yield model

The volumetric yield surface (or cap) of the double-yield model shown in Figure 5.2a is independent on the deviatoric stress and is defined as:

$$p - p_c = 0 \tag{5.10}$$

where p_c is the current cap pressure (or preconsolidation pressure).

The double-yield model has an associated volumetric flow rule and its hardening rule relates to the plastic volumetric strain ε_v^p through a defined piecewise-linear function. The prescribed piecewise-linear function is flexible, but needs to be calibrated based on the results of physical tests. The bulk modulus K in the double-yield model is proportional to the derivative of cap hardening function as:

$$K = R \frac{dp_c}{d\varepsilon_v^p} \tag{5.11}$$

where R is a constant.

Eq. (5.11) indicates that the elastic modulus of double-yield model is dependent on a piecewise-linear function of the cap pressure which explains the varied slope of the stress-strain curve in the elastic region as shown in Figure 5.2b. Compared with the Mohr-Coulomb model, the double-yield model involves a volumetric yield surface which enable accounting the plastic volumetric strain due to the mean stress. The double-yield model has been adopted in some studies to simulate the mechanical performance of considerably compressible backfill material (Antonov 2005; Lagger et al. 2016).

5.2.3 Soft Soil model

The Soft Soil model is an advanced Cam-Clay type model (Brinkgreve 1996, 2005) based on the critical state concept (Roscoe et al. 1958) and captures the irreversible void change accompanying the soil deformation. Figure 5.3a shows the relation between the volumetric strain ε_v and mean stress p in the Soft Soil model. It is postulated that ε_v linearly reduces with the increase of p along a normal consolidation line (NCL) in the semi-logarithmic space. The NCL has a slope of λ^*. For unloading and reloading, ε_v varies following an elastic swelling line (SL) with a slope of κ^*. In the figure, p_r is a reference value of mean stress. ε_v^n is the reference volumetric strain corresponding to $(p_r + c \cdot \cot\phi)$ on the NCL and ε_v^s is the reference volumetric strain corresponding to $(p_r + c \cdot \cot\phi)$ on the SL. The equations for NCL and SL in the Soft Soil model are given as:

(a)

(b)

(c)
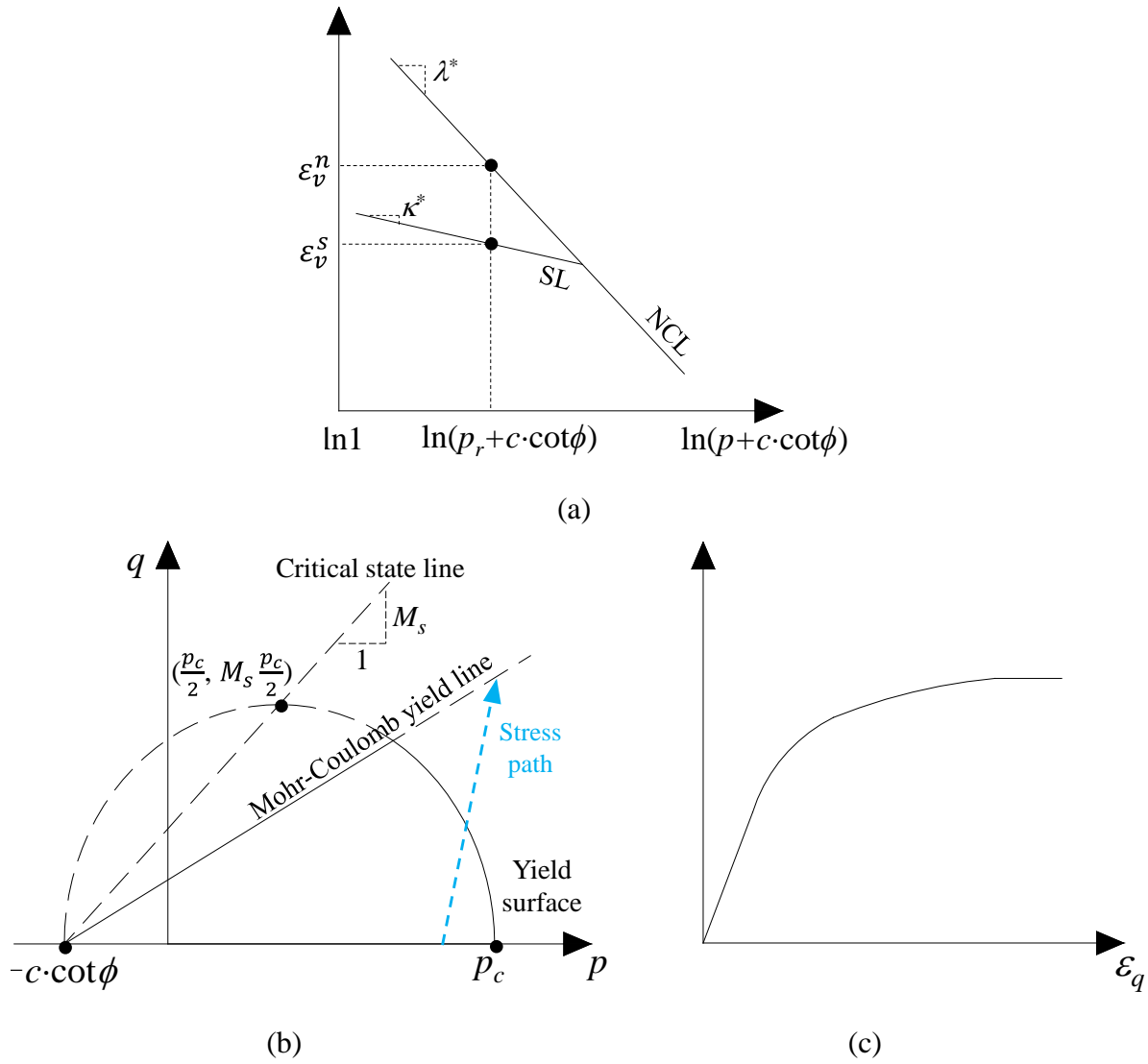
Figure 5.3: Schematic (a) logarithmic relation between the volumetric strain and mean stress, (b) yield surface, and (c) stress-strain behavior of the Soft Soil model

$$\varepsilon_v = \varepsilon_v^n - \lambda^* \cdot \ln\left(\frac{p+c\cdot\cot\phi}{p_r+c\cdot\cot\phi}\right) \tag{5.12}$$

$$\varepsilon_v = \varepsilon_v^s - \kappa^* \cdot \ln\left(\frac{p+c\cdot\cot\phi}{p_r+c\cdot\cot\phi}\right) \tag{5.13}$$

Figures 5.3b and c show the yield surface and stress-strain relation of the Soft Soil model. The yield surface consists of the envelope of the Mohr-Coulomb model and an elliptical cap. The elliptical cap has an apex on a critical state line as shown in Figure 5.3b and its formulation is expressed as:

$$\frac{q^2}{M_s^2(p+c\cdot\cot\phi)} + (p - p_c) = 0 \tag{5.14}$$

where M_s is the slope of the critical state line in p-q space which can be calculated based on the flow rule of the Modified Cam-Clay model (Burland 1965; Brinkgreve 1996) as:

$$M_s = 3\sqrt{\frac{(1-K_0)^2}{(1+2K_0)^2} + \frac{(1-K_0)(1-2v)\left(\frac{\lambda^*}{\kappa^*}-1\right)}{(1+2K_0)(1-2v)\frac{\lambda^*}{\kappa^*}-(1-K_0)(1+v)}} \tag{5.15}$$

where K_0 is the coefficient of earth pressure at-rest in normally consolidated condition.

The Soft Soil model employs an associated flow rule for the volumetric yield surface. The hardening of the volumetric yield surface attributed to the plastic volumetric strain ε_v^p is defined as:

$$\frac{dp_c}{d\varepsilon_v^p} = \frac{p_c}{\lambda^*-\kappa^*} \tag{5.16}$$

The elastic modulus in the Soft Soil model is mean stress-dependent expressed as:

$$K = \frac{p+c\cdot\cot\phi}{\kappa^*} \tag{5.17}$$

The Soft Soil model can be considered as a combination of the Mohr-Coulomb criterion and the Modified Cam-Clay model. The critical state line in the Soft Soil model controls the shape of yield surface while the shear strength is defined by the Mohr-Coulomb envelope. The Soft Soil model has been used in a few studies to analyze the compressibility of soft clay (Neher et al. 2001; Kahlström 2013), but has rarely been applied for mining backfill.

5.3 Comparisons between numerical models and laboratory tests

The capability of constitutive models presented above in describing the compressibility of mining backfill is identified by modeling one-dimensional consolidation and consolidated drained compression triaxial tests in the literature using FLAC^{3D} (Itasca 2019).

5.3.1 Comparison with one-dimensional consolidation tests

Pierce (1999) conducted one-dimensional consolidation tests on Golden Giant paste backfill. The backfill samples were made by mixing the tailings with 3% binder by weight and cured for 28 days.

Samples were casted in a rigid metal cylinder which also acted as a confining ring in the consolidation tests. The backfill samples have a diameter of 75 mm and a height of around 37.5 mm. The measured properties include a density ρ of 2013 kg/m³, a porosity of 49%, a cohesion c of 40 kPa and a friction angle ϕ of 41°. During the consolidation tests of Pierce (1999), a porous stone was put under the cylinder to allow drainage and a platen was placed on the top of the cylinder for the incremental load. Figure 5.4a shows the physical model of the test. The loading path has four stages involving an increasing from 0 to 4 kN in an increment of 0.5 kN, a decreasing from 4 to 1 kN in an increment of 1 kN, an increasing from 1 to 6 kN in an increment of 1 kN and an increasing from 6 to 12 kN in an increment of 2 kN. Figure 5.4b shows the laboratory results of applied stress-compressive strain curve in one-dimensional consolidation tests reported by Pierce (1999).

(a)   (b)
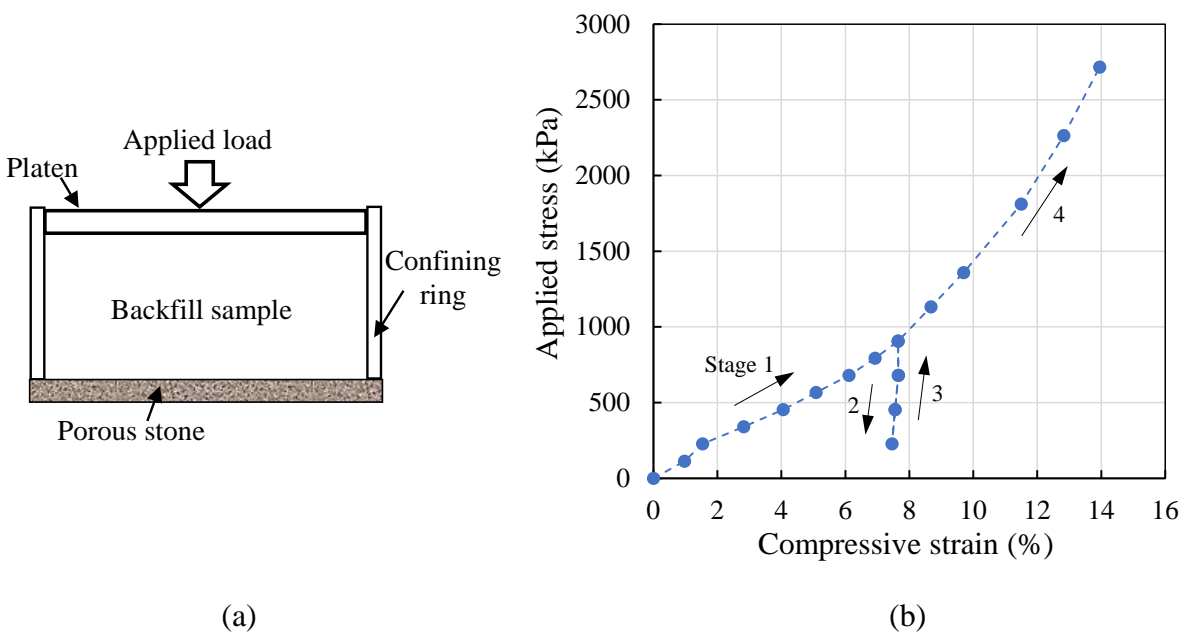
Figure 5.4: (a) Physical model and (b) stress-strain curve of one-dimensional consolidation tests on Golden Giant paste backfill with a binder content of 3% and a curing time of 28 days conducted by Pierce (1999)

Figure 5.5 shows a numerical model of one-dimensional consolidation test constructed with FLAC^{3D} which involves a backfill sample, a cylinder (cell) and a loading platen. The platen is built to allow loading on a displacement boundary of the top surface. The numerical model shown in Figure 5.5 has the identical dimensions as the physical model of Pierce (1999). The mesh size of

the numerical model is 3 mm based on the sensitivity analyses. Both the cylinder and platen are modeled as linear elastic material with a Young's modulus of 200 GPa and a Poisson's ratio of 0.3. The Mohr-Coulomb, double-yield, and Soft Soil models are applied for the backfill sample to make comparisons. Interface elements are applied between the cylinder and backfill. The normal and shear stiffness of the interface are determined based on an equation recommended in the FLAC^{3D} manual (Itasca 2019). The interface friction angle δ is taken as 2/3 of ϕ while its cohesion c_i is assumed equal to c of backfill (Canadian Geotechnical Society 1978; Bowles 1996). The displacements on the bottom of the model are restricted and other boundaries are set free. The same loading path in Pierce (1999) tests is applied in the numerical simulations while the average normal displacement on the top of platen is recorded to calculate the compressive strain for different applied stresses.
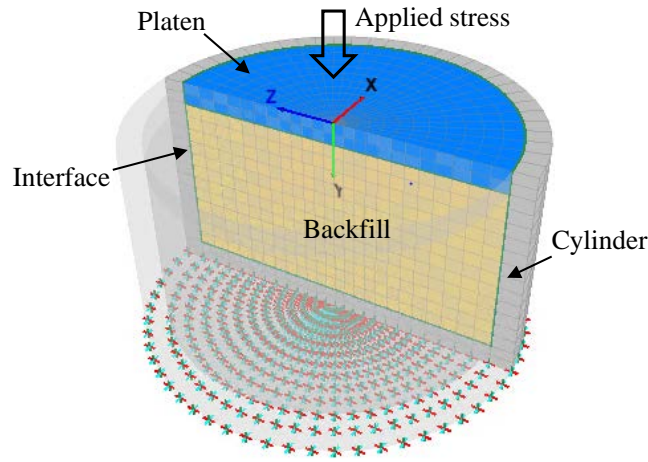
Figure 5.5: A numerical model of one-dimensional consolidation tests built with FLAC^{3D}

In the numerical simulations, the Poisson's ratio of backfill is related to its friction angle through $v = (1 - \sin\phi)/(2 - \sin\phi)$ by considering a unique value of at-rest earth pressure coefficient K_0 (Duncan and Bursey 2013; Yang et al. 2018). The tensile strength T of backfill is taken as 1/10 of its uniaxial compressive strength (UCS) (Mitchell and Wong 1982). The initial value of void ratio e_{ini} is calculated based on the measured porosity. However, some parameters remain unknown including K and shear modulus G for the Mohr-Coulomb model, R and the piecewise-linear function of p_c for the double-yield model, λ^*, κ^* and p_c for the Soft Soil model. These parameters are determined by calibrating the numerical results based on part of laboratory results of Pierce (1999) associated with the loading paths 1 and 2 as shown in Figure 5.4b. Table 5.1 summarizes

all parameters applied for different constitutive models. Numerical models with the calibrated parameters are then called the calibrated models which are further applied to predict the other part of laboratory results associated with the loading paths 3 and 4.

Table 5.1: Parameters of different constitutive models applied for backfill in numerical simulations of one-dimensional consolidation tests with $\rho = 2013$ kg/m^3, $\delta = 27°$, $c_i = 40$ kPa

Constitutive models	Parameters										
Mohr-Coulomb	K (kPa)	G (kPa)	ϕ (°)	c (kPa)	ψ (°)	T (kPa)					
	5388	3141	41	40	0	17.6					
Double-yield	K_{max} (GPa)	G_{max} (GPa)	ϕ (°)	c (kPa)	ψ (°)	T (kPa)	R				
	50	29.2	41	40	0	17.6	24.1				
	Prescribed piecewise-linear function for cap (kPa) hardening in terms of (ε_v^p, P_c) (0, 0); (0.008, 12); (0.0094, 14.2); (0.0103, 15.5); (0.0119, 30.5); (0.0178, 69.59); (0.0181, 72); (0.0246, 87.5); (0.0273, 92.46); (0.0301, 97.5); (0.0336, 120); (0.0393, 144.71); (0.0449, 169.2); (0.0479, 187); (0.0492, 193.73); (0.0573, 237); (0.0592, 246.89); (0.0611, 257); (0.0631, 285.97); (0.0689, 294.84); (0.0714, 310); (0.0741, 325); (0.0889, 455.85)										
Soft Soil	ν	ϕ (°)	c (kPa)	ψ (°)	T (kPa)	κ^*	λ^*	K_0	p_c (kPa)	e_{ini}
	0.26	41	40	0	17.6	0.0052	0.051	0.34	127	0.961

Note: K_{max} and G_{max} denote the upper limits of the bulk and shear modulus. K and G for the Mohr-Coulomb model, R and piecewise-linear function of p_c for the double-yield model, λ^*, κ^*, and p_c for the Soft Soil model are calibrated based on the experimental results.

Figure 5.6 shows the comparisons between the laboratory results of one-dimensional consolidation tests reported by Pierce (1999) and the numerical results by applying the Mohr-Coulomb (Figure 5.6a), double-yield (Figure 5.6b), and Soft Soil (Figure 5.6c) models for backfill. In Figure 5.6a, one sees the compressive strain of the Mohr-Coulomb model linearly increases as the applied stress increases. For the unloading stage, the stress-strain curve of the Mohr-Coulomb model is almost parallel to that in the loading stage. The minor scatter between the curves of loading and unloading is attributed to the yield of fill-wall interface. However, the experimental strain shows nonlinear relation with the applied stress in the test while only a small component of compressive strain is reversible at the unloading stage. The poor agreement between numerical and laboratory results is explained as that the Mohr-Coulomb model simulates a constant elastic modulus and does not capture the volumetric yield of backfill.

(a)

(b)

(c)
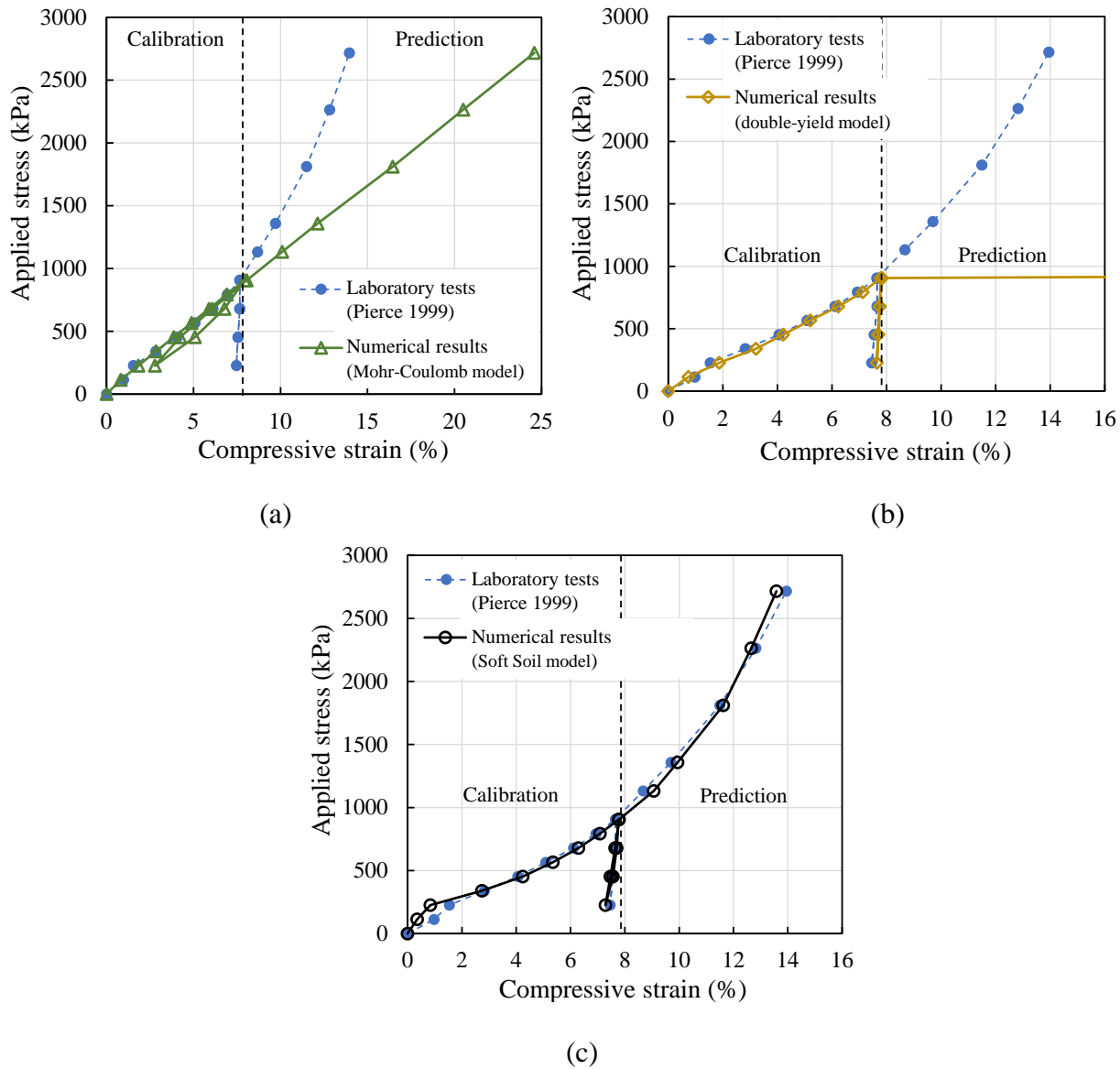
Figure 5.6: Comparisons between the experimental results of one-dimensional consolidation tests reported by Pierce (1999) and the numerical results by applying the (a) Mohr-Coulomb; (b) double-yield and (c) Soft Soil models for backfill with parameters in Table 5.1

Figure 5.6b shows that the calibrated results of the double-yield model correlate well with the laboratory results, but the predicted compressive strain steeply increases as the applied stress further increases. It is because the prescribed piecewise-linear function of the cap pressure in the double-yield mode is calibrated based on part of laboratory results. The prescribed function is flexible and can result in good fit between the numerical and test results. However, when the applied stress exceeds the range of prescribed function, the double-yield model demonstrates

infinite plastic volumetric strain as shown in Figure 5.6b. The predictive capability of the double-yield model is thus limited when the test data for calibration is insufficient. For the Soft Soil model, Figure 5.6c illustrates that both the described and predicted numerical results agree well with the laboratory results. Minor difference between the described results of the Soft Soil model and test results is seen when the applied stress is smaller than 230 kPa. It is because that the cementation in backfill increases its primary stiffness at a small stress level. As the applied stress increases, the cement bond yields as shown by a drop of fill stiffness in Figure 5.6c. The mechanical behavior of cemented backfill then approaches an uncemented condition. In the Soft Soil models, the large primary stiffness caused by the cement bond at the small stress level can be pseudo-simulated by using an overconsolidation state though their mechanisms are different. The Soft Soil model is thus deemed capable of describing the compressibility of lightly cemented or uncemented backfill in a confined compression condition.

5.3.2 Comparison with consolidated drained triaxial compression tests

Rankine (2004) conducted consolidated drained triaxial compression tests on Cannington paste backfill. The backfill samples have a diameter of 38 mm, a height of 76 mm, a cement content of 2%, a solid content of 74% by weight and were cured for 28 days. The density of backfill is 2091 kg/m^3 and the porosity is 51.2%. Figure 5.7 shows the physical model and deviatoric stress-strain curve of consolidated drained triaxial compression tests under confining pressures of 100, 200, 500 kPa performed by Rankine (2004).

σ_1

σ_3 σ_3

(a)   (b)
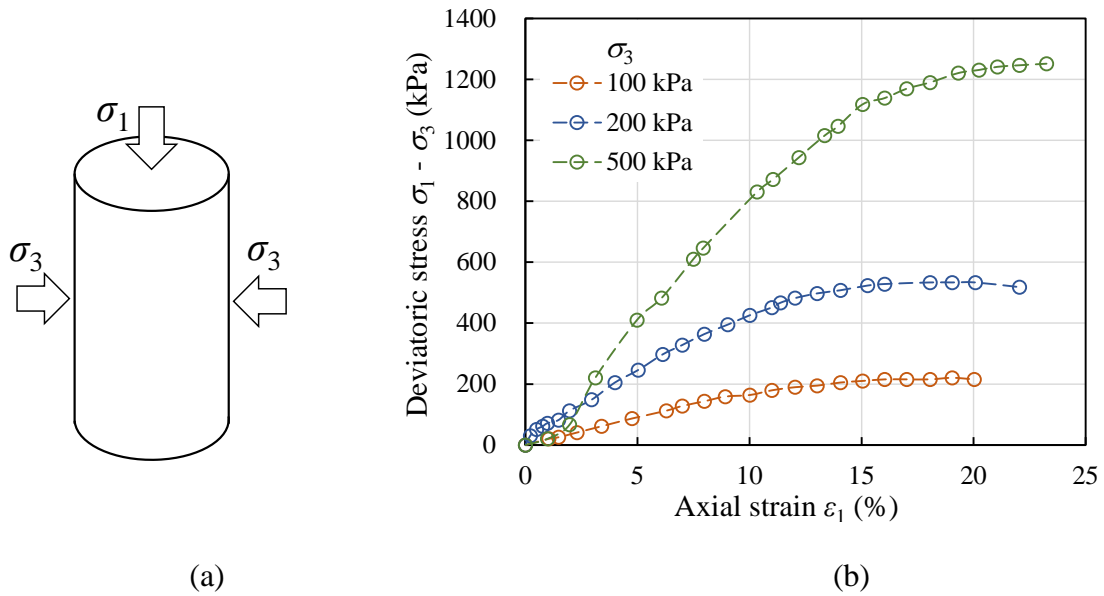
Figure 5.7: (a) Physical model and (b) deviatoric stress-strain curve under different confining pressures of consolidated drained triaxial compression tests on Cannington paste backfill with a cement content of 2% and a curing time of 28 days performed by Rankine (2004)

Figure 5.8 illustrates a numerical model of backfill sample built with FLAC^{3D} in simulations of consolidated drained triaxial compression tests. The numerical model has same sizes as the samples of Rankine (2004) while the mesh size of the numerical model is 2 mm based on the sensitivity analyses. The Mohr-Coulomb, double-yield, and Soft Soil models are applied for backfill. The normal displacements on the bottom of the numerical model are restricted. The initial state is modeled by applying the confining stress normal to the surface of the sample after which the displacement is reset to zero. A normal velocity of 1×10^{-7} m/step is then applied on the top surface to simulate the compression. The normal stress and the axial displacement on the top surface of the numerical model are recorded during the calculation.
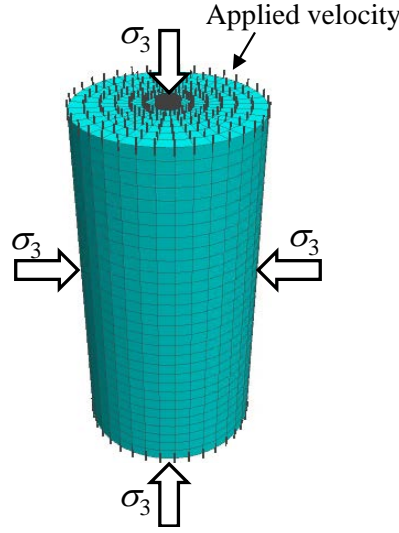
Figure 5.8: A numerical model of consolidated drained triaxial compression tests built with FLAC^{3D}

In the simulations, the Poisson's ratio is related to the friction angle of backfill considering a unique value of the at-rest earth pressure coefficient K_0. The ratio of tensile strength T to UCS of backfill is taken as 0.41 according to the experimental results of Rankine (2004). e_{ini} is calculated as 1.05 based on the measured porosity. Calibrations based on the laboratory results under confining pressures of 100 and 200 kPa are performed to obtain some unknown parameters involving c and ϕ, K and G for the Mohr-Coulomb model, R and the piecewise-linear function of p_c for the double-yield model, λ^*, κ^* and p_c for the Soft Soil model. Table 5.2 shows model parameters used for numerical simulations. The calibrated numerical models are then applied to predict the laboratory results of Rankine (2004) under a confining pressure of 500 kPa.

Table 5.2: Parameters of different constitutive models applied for backfill in numerical simulations of consolidated drained triaxial compression tests with $\rho = 2091$ kg/m^3

Constitutive models	Parameters						
Mohr-Coulomb	K (kPa)	G (kPa)	ϕ (°)	c (kPa)	ψ (°)	T (kPa)	
	2935	1203	32	14.73	0	21.8	
Double-yield	K_{max} (GPa)	G_{max} (GPa)	ϕ (°)	c (kPa)	ψ (°)	T (kPa)	R
	50	20.5	32	14.73	0	21.8	2

Prescribed piecewise-linear function for cap (kPa) hardening (ε_v^p, P_c)

(0, 0); (0.052, 50); (0.103, 100); (0.155, 150); (0.196, 190); (0.2, 200); (0.218, 250); (0.237, 300); (0.256, 350); (0.274, 400); (0.312, 500); (0.376, 670); (0.383, 690); (0.387, 700)

Soft Soil	ν	ϕ (°)	c (kPa)	ψ (°)	T (kPa)	κ^*	λ^*	K_0	p_c (kPa)	e_{ini}
	0.32	32	14.73	0	21.8	0.0078	0.135	0.47	50	1.05

Note: c and ϕ, K and G for the Mohr-Coulomb model, R and the piecewise-linear function of p_c for the double-yield model, λ^*, κ^* and p_c for the Soft Soil model are calibrated based on the experimental results.

Figure 5.9 shows the comparisons between the laboratory results of consolidated drained triaxial compression tests conducted by Rankine (2004) and numerical results under different confining pressures by applying the Mohr-Coulomb (Figure 5.9a), double-yield (Figure 5.9b), and Soft Soil (Figure 5.9c) models for backfill. Figure 5.9a illustrates that the calibrated and predicted strength of the Mohr-Coulomb model are close to the laboratory results. However, the elastic modulus of the Mohr-Coulomb model is constant while the stiffness of mining backfill increases as the confining pressure increases. The Mohr-Coulomb model thus largely underestimates the stress magnitude at a given strain under a confining pressure of 500 kPa. Meanwhile, it overestimates the strain at failure under a confining pressure of 500 kPa by predicting a value of 38% while the experimental result shows a value of 20%.
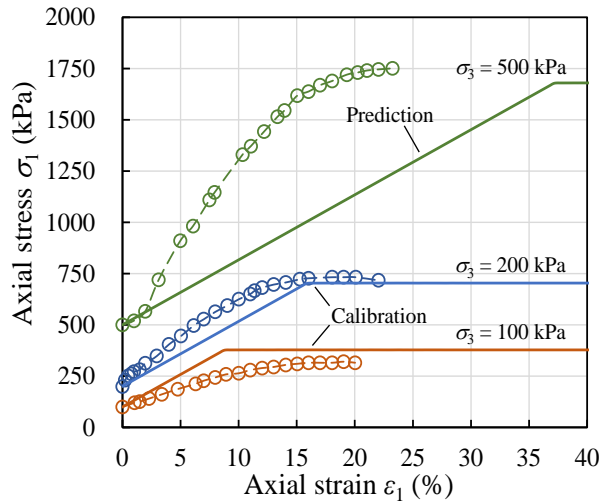
(a)
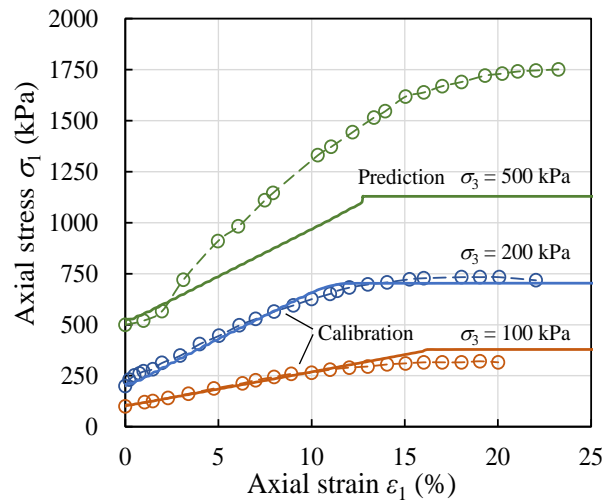
(b)
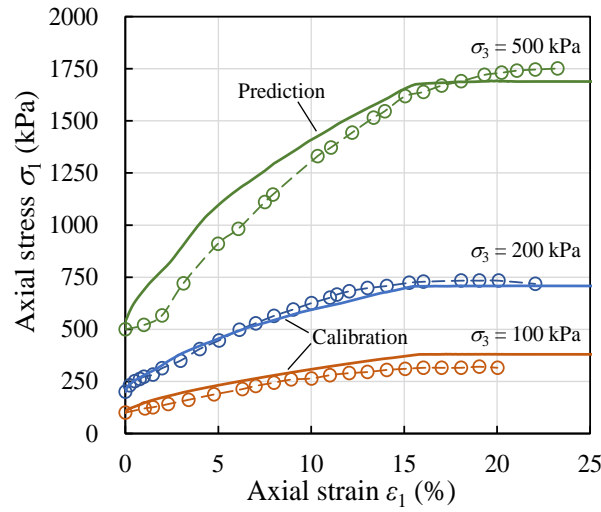
(c)

Figure 5.9: Comparisons between the experimental results (dash lines with points) of consolidated drained triaxial compression tests reported by Rankine (2004) and the numerical results (solid lines) under different confining pressures by applying the (a) Mohr-Coulomb; (b) double-yield and (c) Soft Soil models for backfill with parameters in Table 5.2

Figure 5.9b shows that the double-yield model can reasonably describe the laboratory results for the confining pressures of 100 and 200 kPa. However, the predicted strength and stiffness of the double-yield model under a confining pressure of 500 kPa are very different from the experimental results. It is explained as that the infinite volumetric plastic strain occurs once the applied stress exceeds the upper bond of prescribed piecewise-linear function of the cap in the double-yield model. The predictive capability of the double-yield model is thus limited. Figure 5.9c shows that the described and predicted results of the Soft Soil model reasonably agree with the laboratory results. Based on the comparisons between numerical results and laboratory tests, the Soft Soil model is identified superior to the Mohr-Coulomb and the double-yield model in describing the compressibility of mining backfill with slight cementation (or uncemented backfill). In order to further exhibit the applicability of the Soft Soil model, it will be benchmarked with respect to the Mohr-Coulomb model in modeling a typical backfilled stope overlying a sill mat at different mine depths.

5.4   Simulations of backfilled stope overlying a sill mat

In underhand cut-and-fill mining, uncemented or lightly cemented backfill is used to fill the mined-out upper stope overlying a sill mat. During the extraction of underlying stope, the sill mat will act as an artificial roof which makes the stress distribution within the overlying backfilled stope significant for its stability. Sobhi and Li (2017) analyzed this problem with PLAXIS^{2D} only using the Mohr-Coulomb constitutive model to simulate the backfilled stope. The compressibility of backfill under the rock-wall closure associated underlying extraction was thus not properly considered by Sobhi and Li (2017). In this section, the problem of a backfilled stope overlying a sill mat at different mine depths D of 200 and 1000 m are numerically investigated with FLAC^{3D}. Emphasis is placed on the comparisons between numerical results predicted by applying the Mohr-Coulomb and Soft Soil models. Figure 5.10 shows a physical model and a plane strain numerical model ($D = 200$ m) of the problem. The symmetry plane ($x = 0$) is taken into account by considering half of the model. The excavations have a width B of 6 m. The overlying stope has a height H of 10 m and is filled with uncemented backfill. A gap of 0.5 m is left on the top of the backfill to represent the poor contact between fill and stope roof. The sill mat has a height H_s of 3 m, while the underlying stope is 13.5 m in height. The domain size of the numerical model is a distance from the origin to the boundaries of the model. Based on the sensitivity analyses, the numerical model is constructed with the optimal domain and mesh sizes of 300 and 0.25 m
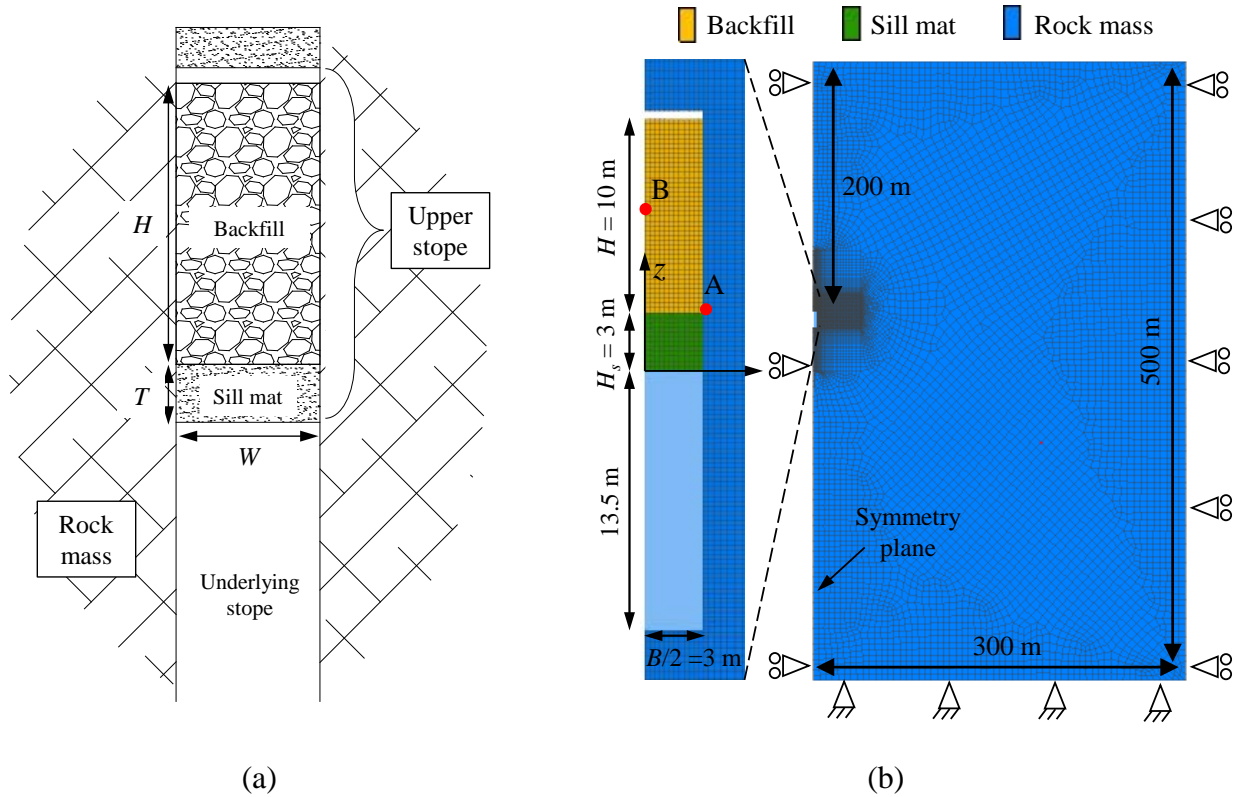
Figure 5.10: (a) Physical model and (b) numerical model built with FLAC^{3D} of an undercut below a sill mat with overlying backfill

The rock mass and sill mat obey the Mohr-Coulomb model while the overlying backfill is modeled with different constitutive models. The rock mass is characterized by unit weight $\gamma_R = 27$ kN/m^3, Young's modulus $E_R = 42$ GPa, Poisson's ratio $\nu_R = 0.25$, cohesion $c_R = 9.4$ MPa, friction angle $\phi_R = 38°$, and dilation angle $\psi_R = 0°$. The sill mat is characterized by unit weight $\gamma_s = 20$ kN/m^3, Young's modulus $E_s = 1.5$ GPa, Poisson's ratio $\nu_s = 0.3$, cohesion $c_s = 5$ MPa, friction angle $\phi_s = 35°$, and dilation angle $\psi_s = 0°$. Table 5.3 provides the material parameters for the overlying uncemented backfill in which same parameters are applied in the Mohr-Coulomb and Soft Soil models where possible. The shear strength parameters (i.e., c_i and δ) of fill-rock interfaces are considered equal to those of backfill by assuming rough rock walls.

Table 5.3: Parameters of the Mohr-Coulomb and Soft Soil models applied for overlying uncemented backfill with unit weight $\gamma = 18$ kN/m^3

Constitutive models	Parameters									
Mohr-Coulomb	K (MPa)	G (MPa)	ϕ (°)	c (kPa)	ψ (°)	T (kPa)				
	250	115	35	0	0	0				
Soft Soil	v	ϕ (°)	c (kPa)	ψ (°)	κ^* (×10⁻³)	λ^* (×10⁻³)	T (kPa)	K_0	p_c (kPa)	e_{ini}
	0.3	35	0	0	0.2	1	0	0.43	1	0.9

In the numerical model, the displacement along the third direction (y-axis) is constrained to simulate a two-dimensional plane strain condition. The top boundary of the numerical model is set free to simulate the ground surface while normal displacement is restricted on the lateral boundaries. For the bottom boundary, the displacements are constrained in all directions. Numerical simulations are conducted at mine depths D of 200 and 1000 m respectively. The lateral earth pressure coefficient $K_r = 2$ is employed by considering the typical stress regime of the Canadian Shield (Herget 1988). In numerical simulations, overlying stope is excavated after obtaining the initial equilibrium state. The displacement is then reset to zero and overlying stope is sequentially backfilled with 1 m per layer. This is followed by excavating the underlying stope in one step to expose the sill mat. Figure 5.11 shows the displacement distributions in the numerical model at each step as references with the Soft Soil model at a mine depth of 200 m.

(a) (b) (c)
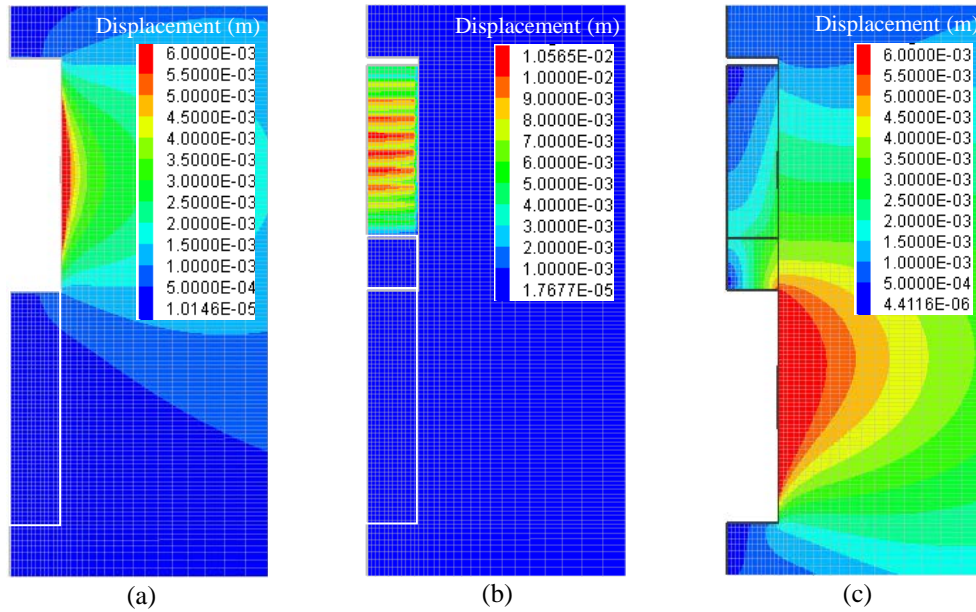
Figure 5.11: Distributions of the displacement with the Soft Soil model at a mine depth of 200 m for different simulation steps of (a) excavating the overlying stope, (b) backfilling the mined-out overlying stope and (c) extracting the underlying stope

Figure 5.12 shows the iso-contours of bulk modulus in the overlying backfill after placement by applying different constitutive models. In the figure, one sees the bulk modulus of the Mohr-Coulomb model is 250 MPa and is a constant independent on the stope height. The bulk modulus of the Soft Soil model around the middle height of the stope is around 250 MPa, but its value moderately increases along the height of the backfilled stope. It is because that the elastic modulus of the soft soil model is mean stress dependent as given by Eq. (5.17).

(a)   (b)
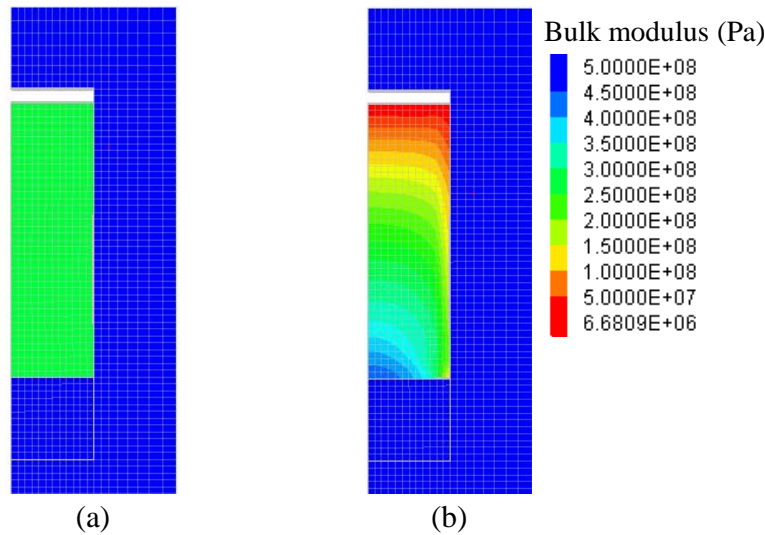
Figure 5.12: Distributions of the bulk modulus in overlying backfill after placement simulated with the (a) Mohr-Coulomb and (b) Soft Soil models

Figure 5.13 illustrates the variation of the vertical and horizontal stresses along the vertical central line (VCL) of the overlying backfill before the excavation of underlying stope. Results shown in Figure 5.13 are independent on different mine depths because the backfill is placed after the rock-walls displacement (i.e., delayed placement). In the figure, one sees that both the vertical and horizontal stresses increase smoothly along the stope height while the arching effect is evident by comparing with the overburden stresses. The stress distributions in the backfilled stope prior to the underlying excavation by applying the Mohr-Coulomb and Soft Soil models are almost identical. At the lower part of the stope, the stress state of the Soft Soil model is slightly larger than that of

the Mohr-Coulomb model. The results shown in Figure 5.13 agree well with the results reported by Sobhi and Li (2017).
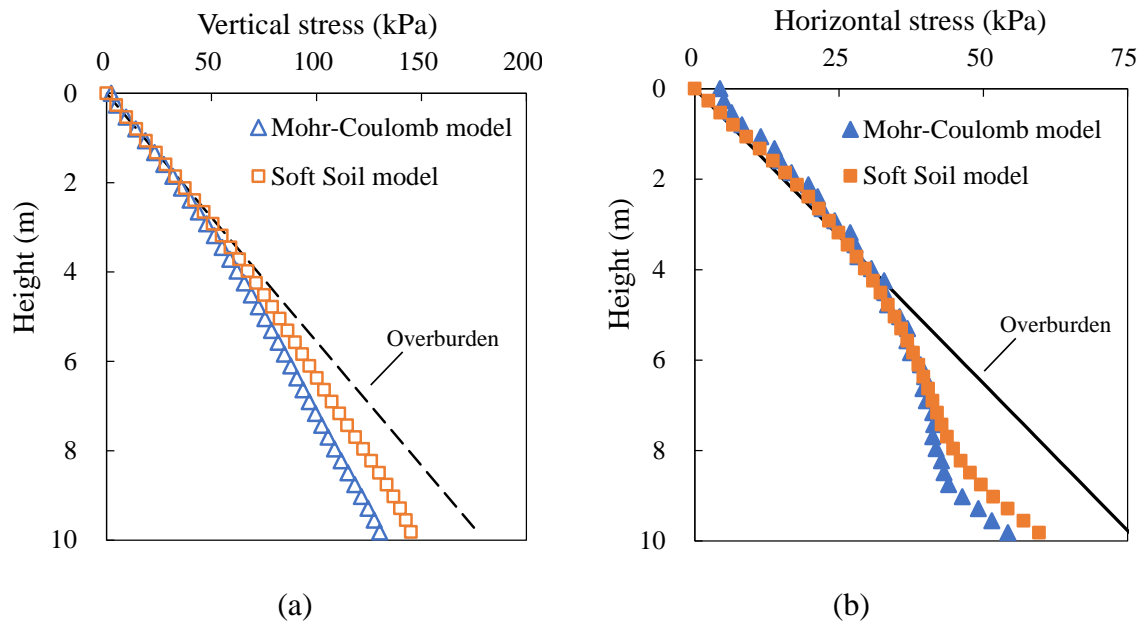
Figure 5.13: Variation of the (a) vertical and (b) horizontal stresses along the VCL of overlying backfilled stope before the underlying extraction

Figure 5.14 shows the variation of vertical and horizontal stresses along the VCL of overlying backfill after excavating the underlying stope at a mine depth $D = 200$ m. Under the influence of rock-wall closure associated with the underlying extraction, the vertical and horizontal stresses in the overlying backfill increase compared to the results shown in Figure 5.13. However, the vertical and horizontal stresses of the Soft Soil model are smaller than those of the Mohr-Coulomb model below the stope height of 2 m. The value of vertical stress at the bottom of overlying backfill is 256 kPa for the Mohr-Coulomb model and is 169 kPa for the Soft Soil model. The different results of two constitutive models are explained as that the Soft Soil model simulates plastic volumetric strain of backfill under the compression from rock walls. The backfill needs to be compacted with certain amount of compressive strain before it can sustain large compressive stress. This feature is not captured by the Mohr-Coulomb model which can thus overestimate the stress state in the overlying stope when the rock-wall closure is small at a shallow mine depth. Since the stability of sill mat largely depends on the stresses within the overlying backfill, using the Mohr-Coulomb model may further cause an inaccurate estimation on the required strength of sill mat.
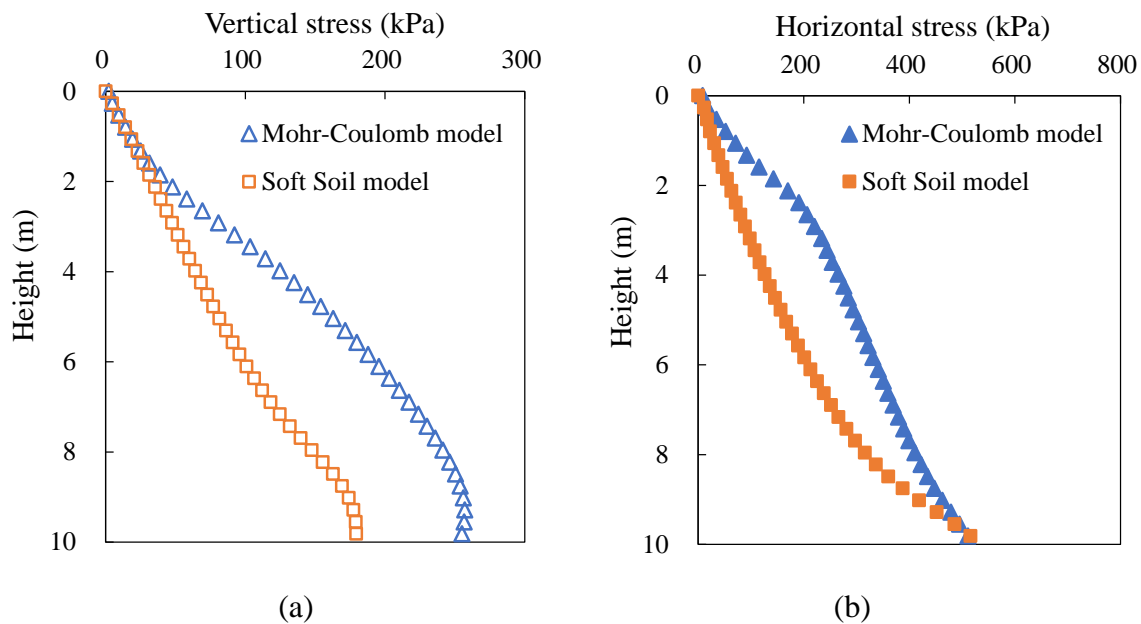
Figure 5.14: Variation of the (a) vertical and (b) horizontal stresses along the VCL of overlying backfill after excavating the underlying stope at a mine depth of 200 m

Figure 5.15 shows the variation of vertical and horizontal stresses along the VCL of overlying backfill after the excavation of underlying stope at a mine depth $D = 1000$ m. As the mine depth increases from 200 to 1000 m, the rock-wall closure associated with underlying excavation becomes larger which increases the vertical and horizontal stresses within the overlying backfill. The stress distribution predicted by the Soft Soil model is similar to that of the Mohr-Coulomb model above the stope height of 6 m as shown in Figure 5.15. However, the stresses of the Soft Soil model rapidly increase as the stope height increases. At the bottom of overlying backfill, the vertical and horizontal stresses of the Soft Soil model reach 2.2 and 7.5 MPa which are significantly larger than the values of 0.9 and 2.5 MPa as predicted by the Mohr-Coulomb model. The different results of two constitutive models shown in Figure 5.15 are attributed to that the Soft Soil model accounts the volumetric hardening and pressure-dependent behavior of backfill. With significant rock-wall closure at a large mine depth, the mining backfill demonstrates large volumetric plastic strain during which it becomes harder with large elastic modulus resulting in an increase in stresses generated by rock-wall closure. The Mohr-Coulomb model does not simulate the volumetric hardening of backfill which thus underestimates the stresses in backfilled stopes when the walls convergence is significant at a large mine depth.
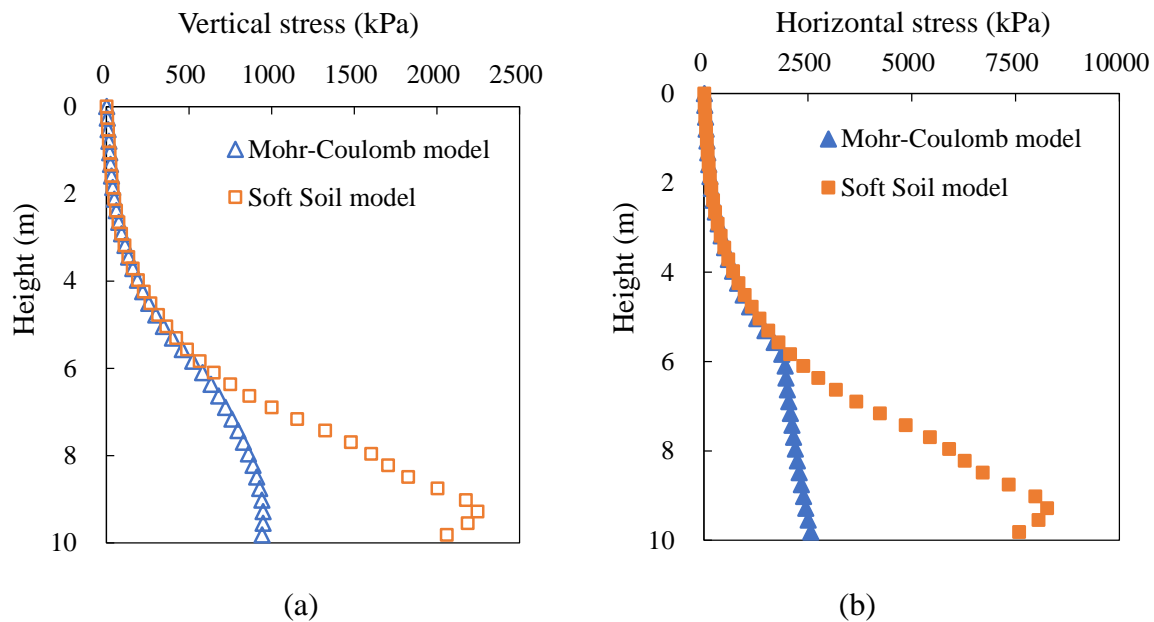
Figure 5.15: Variation of the (a) vertical and (b) horizontal stresses along the VCL of overlying backfill after excavating the underlying stope at a mine depth of 1000 m

Numerical simulations have shown that the Mohr-Coulomb and the Soft Soil models predict similar stress distributions in an isolated backfilled stope when the rock-wall closure is absent. However, the stresses within backfill simulated with two constitutive models can be different when closure of surround rock walls is applied. In this condition, the commonly used Mohr-Coulomb model can under- or overestimate the stresses due to the neglection of volumetric yield and pressure-dependent behavior of backfill. The Soft Soil model is deemed more applicable for simulating uncemented or lightly cemented backfill when its compressibility or closure resistance is a dominant factor.

5.5 Discussion

By comparing the numerical results against the experimental results of one-dimensional consolidation and consolidated drained triaxial compression tests, the Soft Soil model is identified as capable of describing the compressibility of mining backfill. Nonetheless, The Soft Soil model should not be applied for backfill with a very large cohesion. This is partially because that its elliptical yield surface crosses the p-axis at a value of $c \cdot \cot \phi$ on the left side and has an apex on the critical state line as shown in Figure 5.3b. It implies that the lower bond of preconsolidation pressure in the Soft Soil model is determined by the value of cohesion. When a large cohesion is

applied, the backfill modeled with the Soft Soil model is over-consolidated with a significant preconsolidation pressure which can be unrealistic in some conditions. Another reason is that the slope of critical state line (Eq. (5.15)) in the Soft Soil model is calculated based on the flow rule of the Modified Cam-Clay model which considers a nil cohesion (Burland 1965; Brinkgreve 1996). Therefore, the Soft Soil model is deemed applicable for modeling the uncemented or lightly cemented backfill with a small (or nil) cohesion value.

For cemented backfill, cementation increases its primary stiffness at low stress condition by binding together fill particles. Experimental results show that the cement bond can yield as the applied stress increases after which the mechanical behavior of cemented backfill approaches an uncemented condition (Stewart et al. 1986; Pierce 1999). The results in Figure 5.6c show that the effect of cementation on fill stiffness at low stress levels can be pseudo-simulated using an over-consolidated state in the Soft Soil model. However, one should be aware that the mechanisms of cementation and overconsolidation are different. More effort is needed to investigate the effect of cement content and curing time on the compressibility of mining backfill and incorporate it in a constitutive model (Stewart et al. 1986; Liu and Cater 1999; Jafari et al. 2020).

In numerical simulations, the Poisson's ratio of backfill relates to the friction angle as $v = (1 - \sin\phi)/(2 - \sin\phi)$ which is based on a unique value of at-rest earth pressure coefficient K_0. (Duncan and Bursey 2013; Yang et al. 2018). Such equation is practical in numerical modeling with an elastoplastic model. Previous studies have proposed several forms of empirical equation to define the relationship between v and ϕ (Duncan et al. 1991; Yang 2016). More works are needed to investigate this aspect based on experimental results. Meanwhile, since the stress-strain curve of soil-like material is highly nonlinear, how to determine the Poisson's ratio of backfill based on the experimental results for numerical modeling is a problem and needs to be studied in future works.

The Soft Soil model postulates a perfectly plastic behavior when the stress state reaches the Mohr-Coulomb yield line. The post-peak behavior of backfill is affected by the cement content and confining pressure level (Belem et al. 2000; Fall et al. 2007). Experimental results show that mining backfill with large cement content demonstrates strain softening under small confining pressures at the post-peak stage. The large confining pressure can also result in a strain hardening behavior of mining backfill. The post-peak behavior of backfill is not analyzed in this study.

This study focusses on modeling the compressibility of backfill in the long-term condition while the pore water pressure is not considered. More effort is thus necessary to evaluate the hydraulic conductivity and the effects of pore water pressure and drainage condition on the compressibility of backfill in the short-term condition (Pariseau 1995; Godbout et al. 2007; Fall et al. 2009).

The simulations of a backfilled stope overlying a sill mat indicate the applicability of Soft Soil model and the significance of modeling fill compressibility. The commonly used Mohr-Coulomb model tends to under- or overestimate the stress states in a backfilled stope when the walls closure is applied due to the poor description of the fill compressibility. Though the capability of the Soft Soil model has been checked against some consolidation and triaxial tests, field measurements are still needed when available to make further verifications.

5.6 Conclusions

The Mohr-Coulomb, double-yield, and Soft Soil constitutive models are recalled and evaluated for the capability of describing the compressibility of mining backfill. Numerical results with different constitutive models in FLAC^{3D} are compared with one-dimensional consolidation and consolidated drained triaxial compression tests made on lowly cemented backfills available in the literature. Part of the experimental results is used to calibrate some model parameters and the calibrated models are applied to predict the other part of the test results. Based on the comparisons, the Soft Soil model shows the satisfactory description of the experimental results while its prediction is also quite good. The prevalently used Mohr-Coulomb model demonstrates poor correlations with the experimental results due to the neglection of volumetric yield and pressure-dependent behavior of backfill. The double-yield model accurately describes the experimental results based on the calibration, but its predictive capability is limited when the test results are insufficient.

The comparisons between Soft Soil and Mohr-Coulomb models in simulating a backfilled stope overlying a sill mat at different mine depths show similar stress distributions when the rock-wall closure is absent. However, when the rock-wall closure associated with the underlying extraction is applied, application of the Soft Soil model shows that the Mohr-Coulomb model tends to overestimate the stresses in backfill at a shallow mine depth and underestimate the stresses at a large mine depth due to the poor description of the fill compressibility. The Soft Soil model is

recommended to describe the compressibility of uncemented or lightly cemented backfill with small cohesions under external compressions associated with rock-wall closure.

5.7 Appendix: Sensitivity analyses of domain and mesh sizes in the numerical simulations

Sensitivity analyses are conducted to determine the optimal mesh size for the numerical models of consolidation and triaxial tests in this study. For the numerical model of a backfilled stope overlying a sill mat, both optimal domain and mesh sizes are determined based on the sensitivity analyses.

The physical and numerical models of one-dimensional consolidation test are illustrated in Figure 5.4a and Figure 5.5. The material parameters are provided in Table 5.1. Figure 5.16 shows the variation of compressive strain under an applied stress of 500 kPa with different constitutive models as function of mesh size. The values of mesh size vary between 20 to 2 mm. The numerical results are considered stable when the mesh size is smaller than 5 mm.
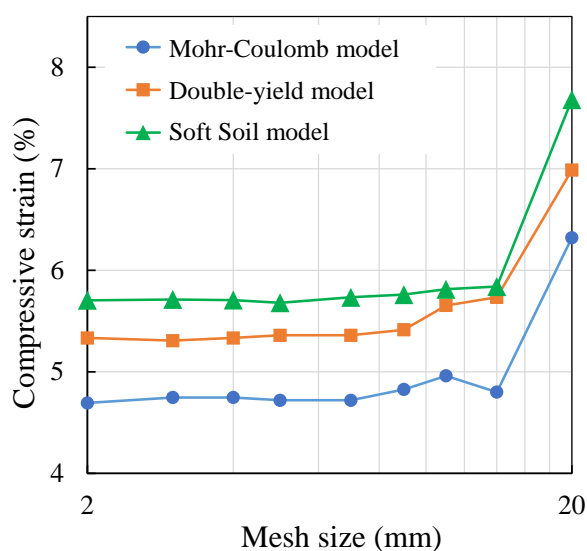
Figure 5.16: Variation of compressive strain under an applied stress of 500 kPa in one-dimensional consolidation simulations as function of mesh size

For the numerical simulations of consolidated drained triaxial compression tests, the physical and numerical models are shown in Figure 5.7a and Figure 5.8 while the material parameters are provided in Table 5.2. Figure 5.17 shows the variation of axial stress under an axial strain of 5%

and a confining pressure of 200 kPa with different constitutive models as function of mesh size. The values of mesh size range from 10 to 1 mm. The numerical results are considered stable when the mesh size reduces to 3 mm.
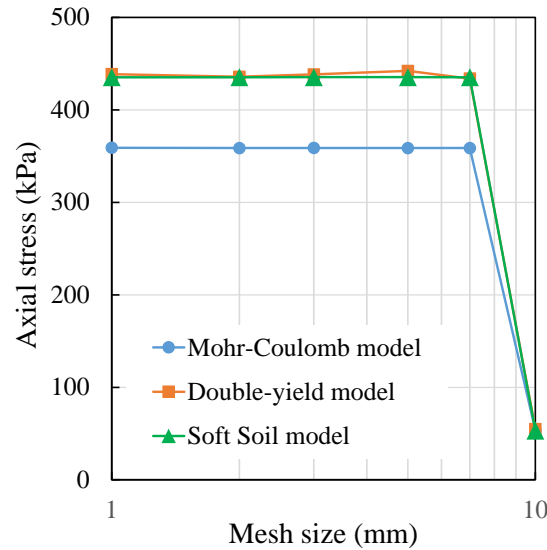
Figure 5.17: Variation of axial stress under an axial strain of 5% and a confining pressure of 200 kPa in triaxial compression simulations as function of mesh size

For the numerical model of a backfilled stope overlying a sill mat shown in Figure 5.10, Mohr-Coulomb model is applied for backfill to conduct the sensitivity analyses at a mine depth of 1000 m. The material parameters are provided in Table 5.3. During the sensitivity analyses, two indicators are analyzed for different domain and mesh sizes. One is the total displacement of surrounding rock mass at Point A in Figure 5.10b (one corner of sill mat) after extracting the overlying stope. The other indicator is the horizontal stress after excavating the underlying stope at Point B in Figure 5.10b which is at the middle height on the VCL of backfill. Figure 5.18 shows the variation of total displacement at Point A and horizontal stress at Point B as functions of domain size ranging from 35 to 550 m. The numerical results become stable when the domain size is larger than 200 m.

(a)   (b)
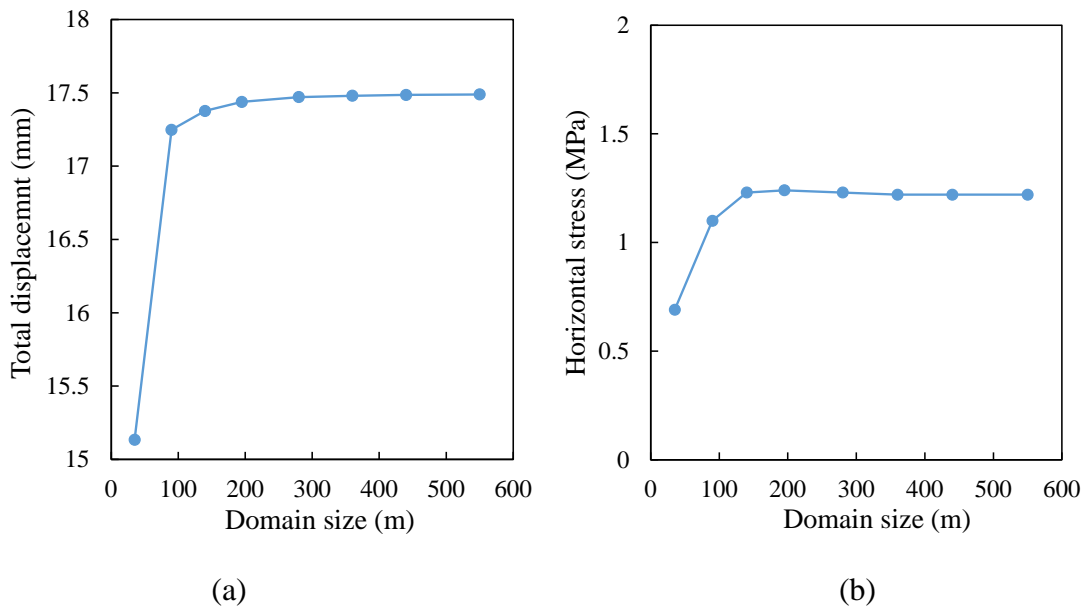
Figure 5.18: Variation of (a) total displacement at Point A after extracting the overlying stope and

(b) vertical stress at Point B after excavating the underlying stope as functions of domain size

Figure 5.19 shows the variation of total displacement at Point A and horizontal stress at Point B as functions of mesh size which ranges from 5 to 0.1 m. The numerical results become stable when the mesh size reduces to 0.5 m.

(a)   (b)
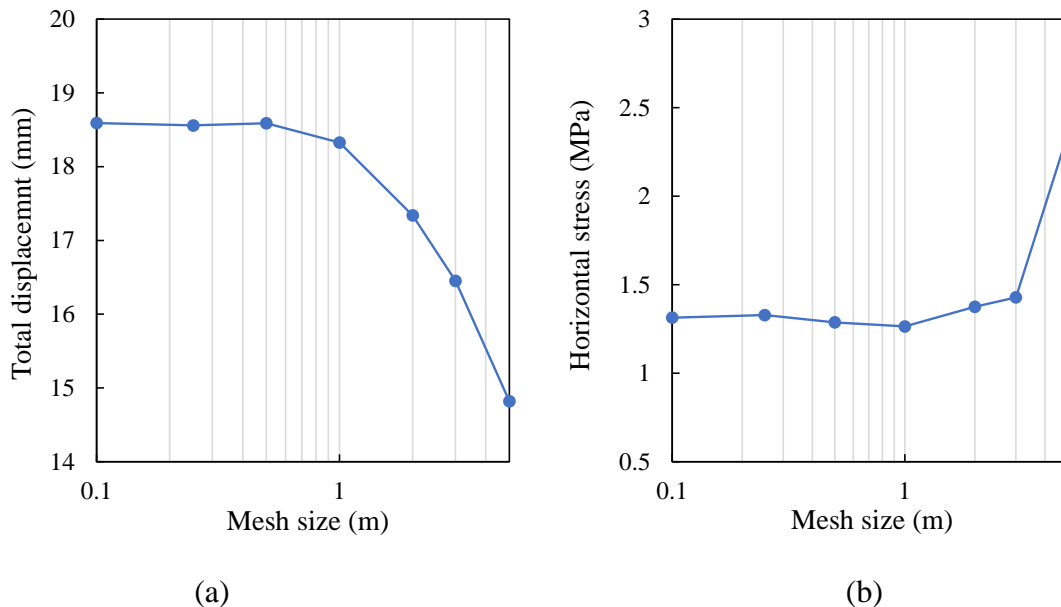
Figure 5.19: Variation of (a) total displacement at Point A after extracting the overlying stope and

(b) horizontal stress at Point B after excavating the underlying stope as functions of mesh size

Acknowledgements

5.8　References

Aubertin, M., Li, L., Arnoldi, S., Belem, T., Bussière, B., Benzaazoua, M., & Simon, R. (2003). Interaction between backfill and rock mass in narrow stopes. *Proceedings of 12th Panamerican Conference on Soil Mechanics and Geotechnical Engineering and 39th U.S. Rock Mechanics Symposium*. Cambridge, Massachusetts, United States of America, 1157–1164.

Antonov, D. (2005). *Optimization of the use of cement in backfilling operations*. (Ph.D. thesis, École Polytechnique de Montréal).

Belem, T., Benzaazoua, M., & Bussière, B. (2000). Mechanical behaviour of cemented paste backfill. *Proceedings of 53rd Canadian Geotechnical Conference*. Montreal, Canada, Canadian Geotechnical Society, 373–380.

Benzaazoua, M., Bussière, B., Demers, I., Aubertin, M., Fried, É., & Blier, A. (2008). Integrated mine tailings management by combining environmental desulphurization and cemented paste backfill: Application to mine Doyon, Quebec, Canada. *Minerals Engineering*, 21(4), 330–340.

Bowles, L. (1996). *Foundation analysis and design*. 5th ed. New York: McGraw-hill.

Brinkgreve, R.B.J. (1996). *Geomaterial models and numerical analysis of softening*. (Ph.D. thesis, Delft University of Technology).

Brinkgreve, R.B.J. (2005). Selection of soil models and parameters for geotechnical engineering application. *Proceedings of Geo-Frontiers Congress*. Austin, Texas, United States, American Society of Civil Engineers, 69–98.

Burland, J.B. (1965). Correspondence on the yielding and dilation of clay. *Géotechnique*, 15(2), 211–214.

Canadian Geotechnical Society. (1978). *Canadian foundation engineering manual*. Canada, BiTech Publishers Ltd.

Clark, I.H. (1991). The cap model for stress path analysis of mine backfill compaction processes. *Proceedings of 7th International Conference on Computer Methods and Advances in Geomechanics*. Cairns, Australia, 1293–1298.

Coulomb, C.A. (1773). Sur une Application des regles de mximus et mnimus a qelques poblemes de satique rlatits a l'architecture. *Academie Royale des Sciences, Memoires de Mathermatiques et de Physique par Divers Sowans*, 7, 343–382.

Cui, L., & Fall, M. (2015). A coupled thermo–hydro-mechanical–chemical model for underground cemented tailings backfill. *Tunnelling and Underground Space Technology*, 50, 396–414.

Duncan, J.M., Williams, G.W., Sehn, A.L., & Seed, R.B. (1991). Estimation earth pressures due to compaction. *Journal of Geotechnical Engineering*, 117(12), 1833–1847.

Duncan, J.M., & Bursey, A. (2013). Soil modulus correlations. In *Foundation engineering in the face of uncertainty: Honoring Fred H. Kulhawy*. ASCE, 321-336.

Emad, M.Z., Mitri, H.S., & Henning, J.G. (2012). Effect of blast vibrations on the stability of cemented rockfill. *International Journal of Mining, Reclamation and Environment*, 26(3), 233–243.

Falaknaz, N., Aubertin, M., & Li, L. (2015). Numerical investigation of the geomechanical response of adjacent backfilled stopes. *Canadian Geotechnical Journal*, 52(10), 1507–1525.

Fall, M., Belem, T., Samb, S., & Benzaazoua, M. (2007). Experimental characterization of the stress–strain behaviour of cemented paste backfill in compression. *Journal of Materials Science*, 42(11), 3914–3922.

Fall, M., Adrien, D., Célestin, J., Pokharel, M., & Touré, M. (2009). Saturated hydraulic conductivity of cemented paste backfill. *Minerals Engineering*, 22(15), 1307–1317.

Fourie, A.B., Gürtunca, R.G., De Swardt, G., & Wendland, E. (1993). An evaluation of four constitutive models for the simulation of backfill behaviour. *Proceedings of 5th International Symposium on Mining with Backfill*. Johannesburg, South Africa, 33–38.

Godbout, J., Bussière, B., & Belem, T. (2007). Evolution of cemented paste backfill saturated hydraulic conductivity at early curing time. *Proceedings of the Diamond Jubilee Canadian Geotechnical Conference and the 8th Joint CGS/IAH-CNC Groundwater Conference*. Ottawa.

Hassani, F., & Archibald, J. (1998). *Mine backfill*. Canadian Institute of Mine, Metallurgy and Petroleum.

Helinski, M., Fahey, M., & Fourie, A. (2007). Numerical modeling of cemented mine backfill deposition. *Journal of Geotechnical and Geoenvironmental Engineering*, 133(10), 1308–1319.

Herget, G. (1988). *Stresses in rock*. Rotterdam: AA Balkema.

Hiramatsu, Y., & Oka, Y. (1962). Analysis of stress around a circular shaft or drift excavated in ground in a three dimensional stress state. *Journal of Mining and Metallurgy Institute of Japan*, 78, 93–98.

Hiramatsu, Y., & Oka, Y. (1968). Determination of the stress in rock unaffected by boreholes or drifts, from measured strains or deformations. *International Journal of Rock Mechanics and Mining Sciences & Geomechanics Abstracts*, 5(4), 337–353.

Itasca. (2019). *FLAC3D—Fast Lagrangian analysis of continua in 3 dimensions; user's guide*. version 7.0. Minneapolis, MN: Itasca Consulting Group.

Jafari, M., Shahsavari, M., & Grabinsky, M. Experimental Study of the Behavior of Cemented Paste Backfill under High Isotropic Compression. (2020). *Journal of Geotechnical and Geoenvironmental Engineering*, 146(11), 06020019.

Jafari, M., Shahsavari, M., & Grabinsky, M. (2021). Drained Triaxial Compressive Shear Response of Cemented Paste Backfill (CPB). *Rock Mechanics and Rock Engineering*, 1–17.

Kahlström, M. (2013). *Plaxis 2D comparison of Mohr-Coulomb and soft soil material models*. (Master's thesis, Luleå University of Technology).

Keita, A.M.T., Jahanbakhshzadeh, A., & Li, L. (2021a). Numerical analysis of the stability of arched sill mats made of cemented backfill. *International Journal of Rock Mechanics and Mining Sciences*, 140, 104667.

Kortnik, J. (2021). Green mining–use of hydraulic backfill in the Velenje Coal Mine. *Proceedings*

of the 13th International Symposium on Mining with Backfill. Katowice, Poland, 422–432.

Labuz, J.F., & Zang, A. (2012). Mohr–Coulomb failure criterion. *Rock Mechanics and Rock Engineering*, 45(6), 975–979.

Lagger, M., Henzinger, M.R., & Schubert, W. (2016). Numerical investigations on pea gravel using a nonlinear constitutive model. *Proceedings of ISRM International Symposium-EUROCK*. Cappadocia, Yurkey, 521–526.

Li, L. (1997) *Étude expérimentale du comportement hydromécanique d'une fracture*. (Ph.D. Thesis, Paris 7).

Li, L., Aubertin, M., Simon, R., Bussière, B., & Belem, T. (2003). Modeling arching effects in narrow backfilled stopes with FLAC. *Proceedings of 3rd International Symposium on FLAC and FLAC3D Numerical Modelling in Geomechanics*. Sudbury, Canada, 211–219.

Li, L., Aubertin, M., & Shirazi, A. (2010). Implementation and application of a new elastoplastic model based on a multiaxial criterion to assess the stress state near underground openings. *International Journal of Geomechanics*, 10(1), 13–21.

Li, L., & Aubertin, M. (2014). An improved method to assess the required strength of cemented backfill in underground stopes with an open face. *International Journal of Mining Science and Technology*, 24(4), 549–558.

Liu, G., Li, L., Yang, X., & Guo, L. (2017). Numerical analysis of stress distribution in backfilled stopes considering interfaces between the backfill and rock walls. *International Journal of Geomechanics*, 17(2), 06016014.

Liu, M.D., & Carter, J.P. (1999). Virgin compression of structured soils. *Géotechnique*, 49(1), 43–57.

Mitchell, R.J., & Wong, B.C. (1982). Behaviour of cemented tailings sands. *Canadian Geotechnical Journal*, 19(3), 289–295.

Mohr, O. (1900). Welche Umstände bedingen die Elastizitätsgrenze und den Bruch eines Materials. *Zeitschrift des Vereins Deutscher Ingenieure*, 46, 1572–1577.

Neher, H., Wehnert, M., & Bonnier, P. (2001). An evaluation of soft soil models based on trial

embankments. *Proceedings of 10th International Conference on Computer Methods and Advances in Geomechanics*. Tucson, Arizona, United States of America. Rotterdam: AA Balkema, 373–379.

Newman, C.R., & Agioutantis, Z.G. (2018). Stress Redistribution Around Single and Multiple Stope-and-Fill Operations. *Proceedings of 52nd US Rock Mechanics/Geomechanics Symposium*. Seattle, United States of America, American Rock Mechanics Association.

Oliver, P.H., & Landriault, D. (1989). The convergence resistance of mine backfills. *Proceedings of 4th International Symposium on mining with backfill.* Montreal, Canada. Rotterdam, AA Balkema, 433–436.

Pagé, P., Li, L., Yang, P., & Simon, R. (2019). Numerical investigation of the stability of a base-exposed sill mat made of cemented backfill. *International Journal of Rock Mechanics and Mining Sciences*, 114, 195–207.

Pariseau, W.G. (1995). Coupled three-dimensional finite element modeling of mining in wet ground. *Proceedings of 3rd Canadian Conference. on Computer Applications in the Mineral Industry*. Montreal, Québec, Canada, 283–292.

Pierce, M.E. (1999). *Laboratory and numerical analysis of the strength and deformation behaviour of paste backfill*. (Master's thesis, Queen's University).

Pietruszczak, S. (2010). *Fundamentals of plasticity in geomechanics*. Boca Raton: CRC Press.

Pirapakaran, K., & Sivakugan, N. (2007). Arching within hydraulic fill stopes. *Geotechnical and Geological Engineering*, 25(1), 25–35.

Potvin, Y., Thomas, E., & Fourie, A. (2005). *Handbook on mine fill*. Perth, Australia: Australian Centre for Geomechanics publication.

Qi, C., & Fourie, A. (2019). Numerical investigation of the stress distribution in backfilled stopes considering creep behaviour of rock mass. *Rock Mechanics and Rock Engineering*, 52(9), 3353–3371.

Raffaldi, M.J., Seymour, J.B., Richardson, J., Zahl, E., & Board, M. (2019). Cemented paste backfill geomechanics at a narrow-vein underhand cut-and-fill mine. *Rock Mechanics and*

Rock Engineering, 52(12), 4925–4940.

Rankine, R.M.A. (2004). *The geotechnical characterisation and stability analysis of BHP Billiton's Cannington Mine paste fill*. (Ph.D. thesis, James Cook University).

Roscoe, K.H., Schofield, A.N., & Wroth, C.P. (1958). On the yielding of soils. *Géotechnique*, 8(1), 22–53.

Salençon, J. (1969). Contraction Quasi-Statique D'une Cavite a Symetrie Spherique Ou Cylindrique Dans Un Milieu Elastoplastique. *Ann Ponts Chaussees*, 4, 231–236.

Sobhi, M.A., & Li, L. (2017). Numerical investigation of the stresses in backfilled stopes overlying a sill mat. *Journal of Rock Mechanics and Geotechnical Engineering*, 9(3), 490–501.

Stephan, G. (2011). Cut-and-fill mining. *In: SME Mining Engineering Handbook*. 3rd ed. Littleton.

Stewart, J.M., Clark, I.H., & Morris, A.N. (1986). Assessment of fill quality as a basis for selecting and developing optimal backfill systems for South African gold mines. *Proceedings of International Conference on Gold*. Johannesburg, South Africa, 255–270.

Vasichev, S. (2019). Ground control with backfill and caving in deep-level mining of gently dipping ore bodies. *Proceedings of International Conference on Urban Construction and Subsurface Management. Exploration and Mining Technologies. Economics. Geoecology*. Novosibirsk, Russia, 012022.

Wang, R., Zeng, F., & Li, L. (2021). Stability analyses of side-exposed backfill considering mine depth and extraction of adjacent stope. *International Journal of Rock Mechanics and Mining Sciences*, 142, 104735.

Yang, P. (2016). *Investigation of the geomechanical behavior of mine backfill and its interaction with rock walls and barricades*. (Ph.D. thesis, École Polytechnique de Montréal).

Yang, P., Li, L., & Aubertin, M. (2018). Theoretical and numerical analyses of earth pressure coefficient along the centerline of vertical openings with granular fills. *Applied Sciences*, 8(10), 1721.

Zhao, T., Ma, S., & Zhang, Z. (2018). Ground control monitoring in backfilled strip mining under the metropolitan district: case study. *International Journal of Geomechanics*, 18(7), 05018003.

CHAPTER 6   ARTICLE 4: A MODEL FOR DESCRIBING AND PREDICTING THE CREEP STRAIN OF ROCKS FROM THE PRIMARY TO THE TERTIARY STAGE

Ruofan Wang, Li Li, and Richard Simon

Abstract: Rocks under applied stresses can exhibit more or less degree of creep. Over the years, a large number of creep models have been proposed for rocks. However, few models account for friction angle and time to delayed failure. In most cases, curve fitting technique is applied to all of the available experimental results to obtain the required model parameters. The ability of the calibrated model (i.e., the model with the obtained model parameters) to predict the creep behavior under untested stress conditions remains unknown. In this paper, a new model, called ubiquitous-corrosion-Coulomb (UCC) creep model, is proposed. Distinction is made between the linear visco-elastic and non-linear creep strain rate. Subcritical crack growth is related to the non-linear creep strain rate and delayed failure of rocks. The effect of friction angle and confining stresses on the rate of creep strain and time to failure are accounted. With the UCC model, the localization of micro cracks on the failure plane in creep tests making an angle of $45° - \phi/2$ with the major principal stress σ_1 is explained by the fact that among the numerous micro cracks, the cracks along this orientation are the first ones becoming instable. To test the capability of the UCC creep model against experimental results available in the literature, the required model parameters are first obtained by applying the curve-fitting technique on a part of the available experimental results. The predictability of the calibrated model is then tested against another part of the available experimental results, which are not used in the previous curve-fitting process. The results showed that the proposed UCC creep model can be used to describe and predict the creep strain and time to failure of rocks.

Key-words: Rock mechanics; Rheological model; Creep; Time to failure; Description; Prediction

6.1 Introduction

When a rock is submitted to a sufficiently high (but below its peak strength) and constant load, it may deform continuously with time. This strain evolution is well known as creep behavior (Hardy et al. 1969). Most rocks can exhibit a more or less degree of creep. Soft rocks usually demonstrate more pronounced creep phenomenon than hard rocks (Cristescu and Hunsche 1998). Under high stress or thermal conditions, hard rocks can also show significant creep behavior (Malan et al. 1997; Malan 1999). An excessive deformation due to creep can affect the designed function of rock infrastructures and increase the cost of rehabilitation. This is the case when the project is in a soft or weak rock, in a deep mine, or for radioactive waste storage (Verstrynge et al. 2011; Ma et al. 2012; Paraskevopoulou and Diederichs 2018). In extreme cases, structure instability can take place (Xu et al. 2014). It is thus important to well understand the creep behavior and characterize the creep deformation around a rock infrastructure. This requires a model that is able to describe and further predict the creep process of rock under different stress conditions.

Figure 6.1 schematically shows the creep behavior of rock. Upon an instantaneous loading, one first sees an instantaneous elastic deformation. After then, the rock can continue to deform with time while the load is maintained constant. Creep takes place and generally exhibits three stages from the start to the failure of the rock: primary (or transient creep) stage, secondary (or steady creep) stage and tertiary (or accelerating) stage (Goodman 1989; Amitrano and Helmstetter 2006; Farmer 2012).

The primary stage is featured by a creep strain rate very high at the beginning and progressively decreased with time. The secondary stage is characterized by a creep strain rate almost constant with time. In the tertiary stage, the creep strain rate accelerates and usually ends by the failure of the rock. The total strain, ε_t, can then be calculated as the sum of the strains at different stages:

$$\varepsilon_t = \varepsilon_e + \varepsilon_{pc} + \varepsilon_{sc} + \varepsilon_{tc} \tag{6.1}$$

where ε_e denotes the instantaneous elastic strain; ε_{pc}, ε_{sc} and ε_{tc} are the creep strains of the primary, secondary and tertiary creep stages, respectively.
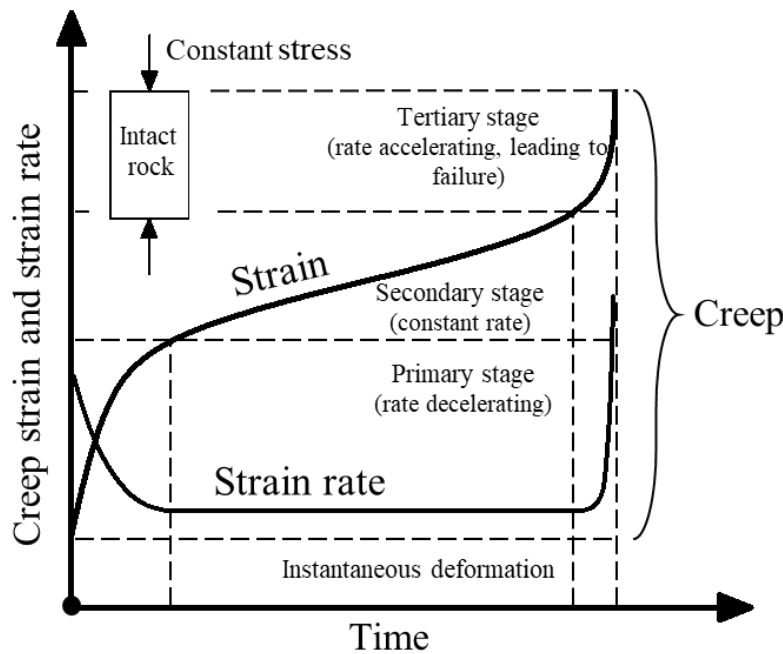
Figure 6.1: A schematic presentation of creep behavior of rock (modified based on Goodman 1989)

A number of studies have been reported on the creep behavior of rocks. Ngwenya et al. (2001) and Amitrano and Helmstetter (2006) have shown that the strain rate of the secondary creep stage increases as the deviatoric stress increases and decreases as the confining pressure increases. Experimental results (Lajtai and Schmidtke 1986; Cristescu and Hunsche 1998) show that the tertiary creep stage only occurs when the applied stress exceeds a certain critical value, known as the long-term strength of the rock. The time to failure decreases as the applied stress and steady-state rate increase (Campanella and Vaid 1974; Hao et al. 2017; Paraskevopoulou et al. 2018).

Figure 6.2a illustrates that during the primary and secondary creep stages, acoustic emissions (AE) took place through almost the whole sample., indicating the cracking or/and crack propagation during the two creep stages. These results can explain the occurrence of irreversible strains caused by micro crack propagations when the rocks were submitted to loading and unloading conditions (Li and Xia 2000; Sterpi and Gioda 2009; Zhao et al. 2017). During the tertiary creep stage, the AE coalesce around a plane and end by the formation of a failure plane, as shown in Figure 6.2a

Figure 6.2b shows the typical failures of a brittle rock in creep and conventional compressive tests, respectively (Brantut et al. 2013; Liu et al. 2016). The high similarity between the shapes of failure

indicates that the failure of the rock is controlled by shear in the creep tests as in the conventional compressive tests.
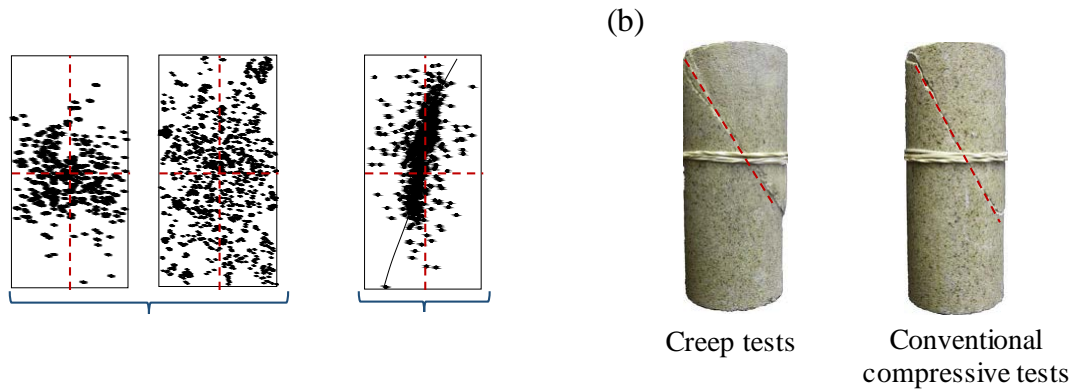
Figure 6.2: (a) AE observed during the three stages of a creep test (taken from Hirata et al. 1987 for the primary stage and Lei et al. 2003 for the secondary and tertiary stages); (b) typical failures of a rock submitted to creep and conventional compression tests (taken from Brantut et al. 2013)

Over the year, a number of models have been proposed to describe the creep behavior of rocks. They can generally be divided into empirical (Jeffieys 1958; Mirza 1978; Maruyama et al. 1990; Penny and Marriott 1995; Lockner 1998; Aydan et al. 2003; Wang and Li 2019), and rheological model-based formulations (Lo and Yuen 1981; Boukharov et al. 1995; Tomanovic 2006; Fahimifar et al. 2015; Paraskevopoulou et al. 2018; Wang and Li 2018; Xu et al. 2018). The empirical models for rocks were mostly initially proposed to describe the creep behavior of metals (Andrade 1910; Lomnitz 1957; Garofalo 1965). The formulations were established based on observed time-creep strain data to phenomenally describe the strain evolution. The empirical models are simple, but the model parameters do not have any physical meaning. Friction angle is neglected. Stresses are absent or only deviatoric stress is involved. These formulations can only be used to describe the obtained experimental data. They cannot be applied to predict the creep behavior of rocks under different stress states.

The rheological models were developed to reflect the mechanical behavior of rocks submitted to mechanical solicitations. Elastic spring, dashpot, and plastic slider are the commonly used elements in the classic and fundamental one-dimensional rheological models to simulate the elasticity, viscosity and plasticity of materials (Goodman 1989; Jaeger et al. 2009). The models are able to

describe the visco-elastic creep strain of the primary or/and secondary creep stages, but fail to describe the irreversible creep strains caused by micro crack propagations. This is the case for the Maxwell, Kelvin-Voigt, generalized Kelvin-Voigt and Burgers creep models (Jaeger et al. 2009). When a plastic slider element is incorporated, the models can describe the plasticity and triggering of the tertiary creep stage, but fail to characterize the time to failure of the tertiary creep stage. This is the case of the CVISC (Paraskevopoulou 2016) and Bingham creep models (Farmer 2012). To note that the Bingham creep model stipulates that the creep strain is possible only when the applied load exceeds a certain threshold. This may not reflect the reality as many short and long-term creep tests on rocks showed that creep can take place even in very low applied stresses (Ito 1991; Bérest et al. 2015; Nopola and Roberts 2016; Zhao et al. 2017). Similar to the empirical formulations, the fundamental rheological models omit the friction angle and confining stress. This is a typical feature of frictionless materials like metals, not that of geomaterials like rocks. It does not correspond to the experimental observations on rocks (Ngwenya et al. 2001; Brantut et al. 2013).

Maranini and Yamaguchi (2001) proposed an elastic-visco-plastic model by considering mean stress dependency of shear and bulk modulus. Friction angle is neglected. Perzyna (1966) proposed a theory of overstress, in which the material has an elasto-visco behavior when the stress point is below the elastic surface. When the applied stress point exceeds the elastic surface and below the yield surface, the rock exhibits an elasto-visco-plastic behavior. The confining pressure dependency of creep strain rate was not considered. The model cannot be used to describe or predict the tertiary creep stage of rocks.

Yahya et al. (2000) proposed an internal state variable elasto-visco-plastic model based on a viscoplastic model proposed by Aubertin et al. (1991a) to describe the stress-strain relationship under testing conditions of constant strain rate and time-strain relationship under constant stress (creep) or constant strain (relaxation) test conditions. Shao et al. (2006) developed a damage evolution model by associating the creep deformation to the propagation of sub-critical micro cracks. These models are much more powerful to describe the creep behavior of rocks under different conditions. However, these models involve a large number of model parameters and require a large quantity of tests (ideally under divers stress conditions). For most cases, all of the available experimental results have to be used to obtain the required model parameters. The good agreements between the model and experimental results are of descriptive nature, not predictive

nature (Zhang et al. 2012; Zhao et al. 2017; Liu et al. 2016; Tang et al. 2017; Mansouri and Ajalloeian 2018). In addition, the localization of micro cracks on the failure plane making an angle of $45°−\phi/2$ with the major principal stress σ_1 in creep tests has not been explained by previous studies (Kemeny 1991; Chandler and Martin 1995; Miura et al. 2003; Myer et al. 1992; Shao et al. 2006).

In this study, a new creep model is proposed to describe and predict the creep strains of the three creep stages and time to failure for rocks under different stress states. Distinction is made between linear visco-elastic and non-linear creep strain rate. The non-linear creep strain rate and delayed failure are considered associated with the growth of micro cracks. For a given rock with some available experimental results, the required model parameters are first obtained by applying the curve-fitting technique on a part of the available experimental results. The calibrated model (i.e., the model with the obtained model parameters) is then applied to the other part of the available experimental results (not participating in the previous curve-fitting process) to test the predictability of the calibrated model.

6.2   A new creep model

In the previous section, it has been shown that the creep strain of rocks can be caused by micro crack developments under an applied stress. Friction angle, deviatoric stress and confining pressure should be involved in the models to reflect the frictional feature of geomaterials. More work is also needed to better describe the strain of the tertiary accelerating creep stage. Here, a new creep model, called UCC (standing for Ubiquitous-Corrosion-Coulomb) creep model is proposed.

The Coulomb criteria is involved in the new model for the clear physical meaning of the material parameters (cohesion and friction angle) and its simplicity. Regarding the stress corrosion, its presence is reflected by the AE activities recorded throughout tested samples (Figure 6.2). The growth of micro cracks is considered as the origin of the AE activities, change in the internal stresses and one source for the creep strain. It is a mechanism responsible for the creep behavior under a stress lower than the peak strength but higher than a threshold (Freiman 1984; Damjanac and Fairhurst 2010). Its process can be affected by several aspects, including chemical reaction, stress states, mineral composition and initial geometry of grains (Charles 1959; Potyondy 2007).

In this study, a simple geometry of cracks is considered while the creep strain and time to delayed failure associated with the crack propagation will be analyzed.

Figure 6.3 shows a schematic presentation of the UCC creep model. The model is composed of a generalized Kelvin-Voigt model, a Newton dashpot and a Ubiquitous-Corrosion (UC) element. The generalized Kelvin-Voigt model is responsible for the instantaneous deformation and creep strain of the primary stage ε_{pc}. The Newton dashpot is used to describe the visco-elastic strain ε_{sc}^{v} of the secondary creep stage. The UC element is introduced to represent the creep strain caused by the micro crack propagation ε_{sc}^{c} of the secondary creep stage. It is also responsible for the strain of the tertiary creep stage ε_{tc}. The total axial strain of the UCC creep model can still be written as Eq. (6.1).

In the following subsections, the formulation and development of the UCC model will be shown by considering conventional triaxial compression test conditions (i.e. $\sigma_1 \geq \sigma_2 = \sigma_3$; where σ_1, σ_2 and σ_3 are the major, intermediate and minor principal stresses, respectively).
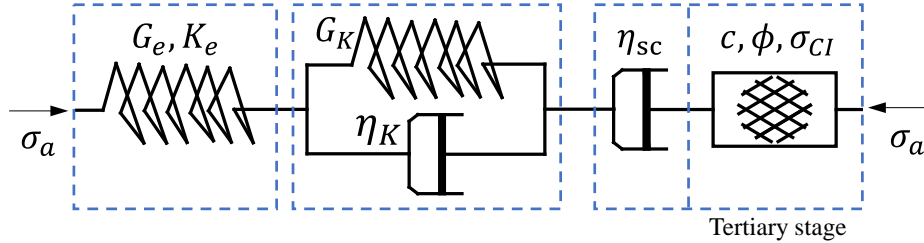
Figure 6.3: A schematic presentation of the UCC creep model

6.2.1 Instantaneous deformation

As discussed above, the instantaneous deformation of rocks under a stress below its short-term strength can be represented by a spring in the generalized Kelvin-Voigt model as shown in Figure 6.3. Possible irreversible instantaneous deformation resulted from the closure of initial cracks or pores is not considered by this element

According to the Hooke's law, the total axial elastic strain ε_1^{e} in conventional triaxial compression tests can be expressed as follows:

$$\varepsilon_1^e = \frac{\sigma_1 + 2\sigma_3}{9K_e} + \frac{\sigma_1 - \sigma_3}{3G_e} \tag{6.2}$$

where K_e and G_e are bulk and shear modulus, respectively. The axial elastic strain ε_1^e associated with the confining pressure (σ_3) is expressed as follows:

$$\varepsilon_1^e = \frac{\sigma_3}{3K_e} \tag{6.3}$$

The axial instantaneous strain ε_e caused by the applied deviatoric stress σ_a ($= \sigma_1 - \sigma_3$) can then be obtained by subtracting Eq. (6.3) from Eq. (6.2) as follows:

$$\varepsilon_e = \frac{\sigma_1 - \sigma_3}{9K_e} + \frac{\sigma_1 - \sigma_3}{3G_e} \tag{6.4}$$

6.2.2 Primary creep stage

The Kelvin-Voigt visco-elastic body is used here to reflect the primary creep stage as shown in Figure 6.3. The axial creep strain ε_{pc} of the primary creep stage under a conventional triaxial compression test condition is given as

$$\varepsilon_{pc} = \frac{\sigma_1 - \sigma_3}{3G_K}\left[1 - exp\left(-\frac{G_K \cdot t}{\eta_K}\right)\right] \tag{6.5}$$

where t denotes time; G_K and η_K are the shear modulus and viscosity coefficient of the Kelvin-Voigt body, respectively.

6.2.3 Secondary creep stage

As shown in Figure 6.3, the Newton dashpot and UC element are combined for reflecting the creep strain of the secondary creep stage.

The Newton dashpot is characterized by the viscosity coefficient η_{sc}, while the UC element by the cohesion c, internal frictional angle ϕ and crack initiation stress σ_{CI} (under compression conditions). The secondary creep strain rate $\dot{\varepsilon}_{sc}$ is decomposed into rates of visco-elastic creep strain ($\dot{\varepsilon}_{sc}^v$) and creep strain attributed to micro crack propagations ($\dot{\varepsilon}_{sc}^c$). The rate of visco-elastic creep strain $\dot{\varepsilon}_{sc}^v$ is contributed by the visco-elasticity (Ladanyi 1974; Aydan et al. 2014) and is represented by Newton dashpot. Regarding the rate of creep strain due to the micro crack

propagations $\dot{\varepsilon}_{sc}^c$, it is related to the UC element. The secondary creep strain rate $\dot{\varepsilon}_{sc}$ can then be expressed as follows:

$$\dot{\varepsilon}_{sc} = \dot{\varepsilon}_{sc}^v + \dot{\varepsilon}_{sc}^c \tag{6.6}$$
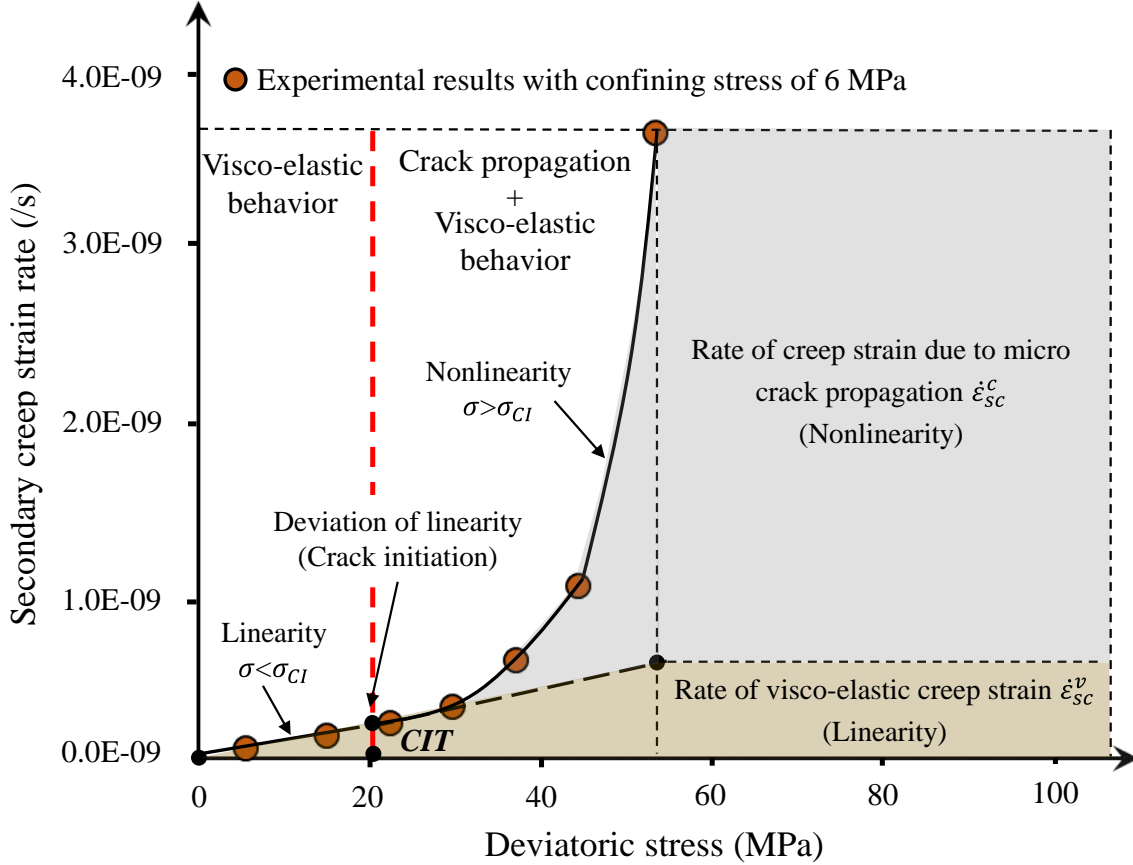
Figure 6.4: Variation of the creep strain rates during the secondary stage as a function of the deviatoric stress (experimental results taken from Zhao et al. 2017)

As previously mentioned, creep strain associated with the subcritical crack growth has been illustrated by the AE activities observed during the creep tests until the failure of the rock (Ngwenya et al. 2001; Lei et al. 2003; Brantut et al. 2013). However, crack propagation can only take place when the applied stress exceeds a threshold value, known as crack initiation threshold (CIT) (Aubertin et al. 2000; Diederichs et al. 2004; Damjanac and Fairhurst 2010; Li et al. 2017). When the applied stress is below the CIT, no crack growth takes place. In this condition, creep occurs nevertheless (Ito 1991; Bérest et al. 2015; Nopola and Roberts 2016; Zhao et al. 2017) and is attributed to the visco-elastic behavior under small stresses (Ladanyi 1974; Ohring 1995;

Weijermarset al. 1997; Aydan et al. 2014). The rate of visco-elastic creep strain under small stresses is considered linearly related to the deviatoric stress, as shown in Figure 6.4. When the applied stress is higher than the CIT, micro cracks develops and the creep strain of rocks is the result of micro cracks propagations and visco-elastic behavior. The relationship between the creep strain rate and deviatoric stress becomes nonlinear, as shown in Figure 6.4. This is the physical basis of the UCC creep model for the creep strain of the secondary creep stage.

The value of the CIT depends on the type and mineralogy of rocks. It is determined as the start of deviation of the axial stress-radial strain curve from the linearity, start of acoustic emission, or start of dilation. Table 6.1 presents a summary of the CIT for different rocks under uniaxial and triaxial compression test conditions. Its value generally varies from 0.3 to 0.7 of the short-term peak strength. In the absence of CIT measurement, a value equaling to 0.5 times the short-term strength is commonly suggested (Lajtai and Schmidtke 1986; Aubertin et al. 2000).

Table 6.1: A summary of the CIT values for different rocks under compressive conditions.

Rocks	Ratios of CIT over short-term strength	Compression conditions	References
Granite; marble; aplite	30 to 70%	Triaxial	Brace et al. (1966)
Argillaceous quartzite	40 to 60%	Triaxial	Hallbauer et al. (1973)
Granite and anorthosite	≤ 60%	Uniaxial	Lajtai and Schmidtke (1986)
Igneous; metamorphic; sedimentary	40 to 60%	Uniaxial	Aydan et al. (1994)
Lac du Bonnet granite	~30%	Triaxial	Martin (1997)
Granitoid rocks	35 to 50%	Uniaxial	Diederichs et al. (2004)
Crystalline rocks	40 to 60%	Both uniaxial and triaxial	Damjanac and Fairhurst (2010)
Jurassic limestone; Cobourg limestone	~40%	Uniaxial	Paraskevopoulou et al. (2018)
Low porosity rocks	30 to 70%	Uniaxial	Li et al. (2017)

Note: The CIT and short-term strength are in deviatoric stresses

6.2.3.1 Linear visco-elastic creep strain rate

As rock under a stress state below the CIT is visco-elastic, the Newton dashpot with viscosity coefficient η_{sc} can be applied to describe the rate of the linear visco-elastic creep strain $\dot{\varepsilon}_{sc}^{v}$ during

the secondary creep stage. Viscosity coefficient is independent on confining pressure (Jaeger 2009). The rate of linear visco-elastic creep strain $\dot{\varepsilon}_{sc}^{v}$ can then be expressed as follows (Jaeger 2009; Paraskevopoulou 2016):

$$\dot{\varepsilon}_{sc}^{v} = \frac{\sigma_1 - \sigma_3}{3\eta_{sc}} \tag{6.7}$$

The comparisons between Eq.(6.7) and the rate of the linear visco-elastic creep strain $\dot{\varepsilon}_{sc}^{v}$ of rocks reported in the literature are shown in Figure 6.5. The model parameters are obtained by applying the curve-fitting technique on part of experimental results and are shown in Table 6.2. The calibrated model is then used to predict other part of the experimental results.

(a)

(b)

(c)
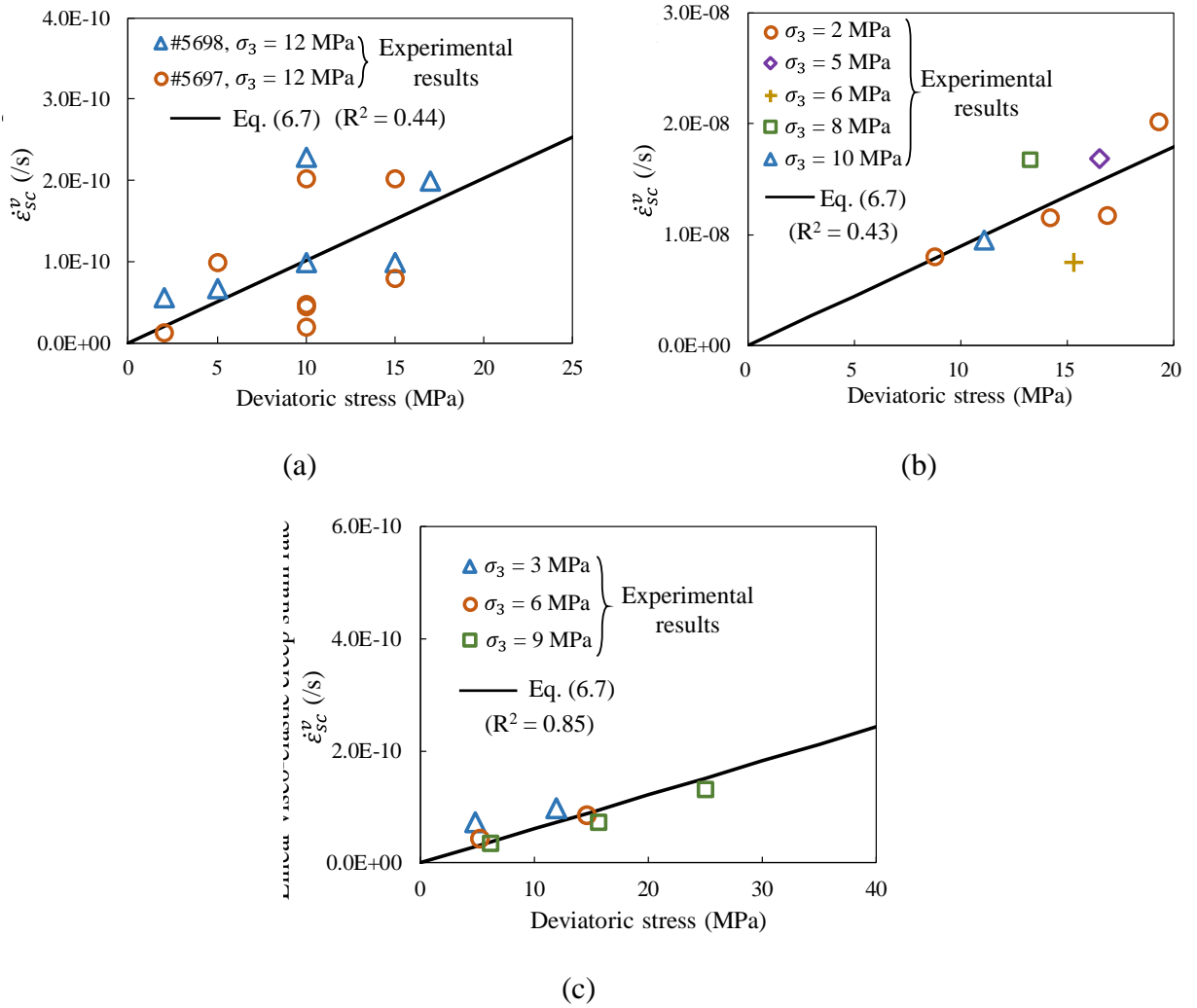
Figure 6.5: Variation of the measured rates of linear visco-elastic creep strain $\dot{\varepsilon}_{sc}^{v}$ with the deviatoric stress: (a) on Bure clayey rock (data taken from Gasc-Barbier et al. 2004); (c) on a rock

salt (data taken from Wang et al. 2014) (a) on a lherzolite rock (data taken from Zhao et al. 2017) with model description and prediction using parameters in Table 6.2

Table 6.2: Model parameters for Eq.(6.7) used in Figure 6.5

	Model description	Model prediction	η_{sc} (Pa·s)
Figure 6.5a	σ_3 = 12 MPa (#5697)	σ_3 = 12 MPa (#5698)	3.30×10^{16}
Figure 6.5b	σ_3 = 2 MPa	σ_3 = 5, 6, 8 and 10 MPa	3.71×10^{14}
Figure 6.5c	σ_3 = 6 MPa	σ_3 = 3 and 9 MPa	5.51×10^{16}

To test the model (Eq. (6.7)), experimental data of creep tests under stresses lower than the CIT of the rock are necessary to obtain the model parameter (η_{sc}) in relation with visco-elastic creep strain.

Figure 6.5 shows the variation of the measured rates of visco-elastic creep strain $\dot{\varepsilon}^v_{sc}$ as a function of the deviatoric stress ($\sigma_1 - \sigma_3$) under different confining stresses when the applied stress on a Bure clayey rock (Figure 6.5a), a rock salt (Figure 6.5b) and a lherzolite (Figure 6.5c) is below the CIT. CIT is considered as the start point of creep strain due to micro crack propagations ε^c_{sc} (Ladanyi 1974; Aydan et al. 2014; Nopola and Roberts 2016) and the measured creep strain below the CIT is considered as visco-elastic creep strain ε^v_{sc}. It should be noted that the experimental results shown in the figure were taken from published papers (Gasc-Barbier et al. 2004; Wang et al. 2014; Zhao et al. 2017), in which no distinction was made between ε^v_{sc} and ε^c_{sc}. In addition, no measurements or observations were reported in the papers to allow the determination of CIT. Thus, a value of CIT equaling to 50% of the short-term strength (Lajtai and Schmidtke 1986; Aubertin et al. 2000) was initially taken for all of the three cases. However, a nonlinearity and confining stress dependency were observed in the case of lherzolite, indicating a largely overestimate of the CIT value. A value of CIT equaling to 30% of the short-term strength is finally taken for the case of lherzolite (Figure 6.5c). Relatively good agreements are obtained between the experimental results and the proposed model (Eq. (6.7)) in the three cases. The relationship between $\dot{\varepsilon}^v_{sc}$ and the deviatoric stress can be considered as more or less linear, despite the important dispersion of the experimental data; these are probably due to imprecise measurements of the too small rates of visco-elastic creep strains under small stresses lower than CIT (Ohring 1995; Weijermarset al. 1997).

6.2.3.2 Non-linear creep strain rate attributed to micro cracks propagation

As mentioned in Section 6.2, subcritical micro cracks growth takes place and results in non-linear creep strain rate once the applied stress exceeds the CIT. The rates of non-linear creep strain due to subcritical crack propagations $\dot{\varepsilon}_{sc}^c$ can be obtained by subtracting the rate of linear visco-elastic creep strain from the rate of total creep strain. $\dot{\varepsilon}_{sc}^c$ is thus considered to be proportional to the subcritical crack growth velocity V_c (Shao et al. 2006), which is usually related to the stress intensity factor K_i through a power law function as follows (Charles 1958; Aubertin et al. 2000):

$$V_c = A_1 \left(\frac{\langle K_i - K_t \rangle}{K_c - K_t} \right)^{n_1} \tag{6.8}$$

where A_1 and n_1 are two material parameters; K_t is the threshold of stress intensity factor for crack extension; K_c is the critical value of K_i, corresponding to the maximum velocity of crack growth; $\langle X \rangle = (X + |X|)/2$ is the Macaulay brackets.

Eq. (6.8) is difficult to be directly applied because it requires the knowledge of initial crack length to calculate the stress intensity factor. To overcome this difficulty, the following expression can be used to obtain the subcritical crack growth velocity V_c by considering the similarity between the microscopic and macroscopic conditions (Aubertin et al. 2000; Li et al. 2017):

$$V_c = A_2 \left(\frac{\langle \sigma_a - \sigma_{CI} \rangle}{\sigma_c - \sigma_{CI}} \right)^n \tag{6.9}$$

where A_2 and n are material parameters; σ_a is the applied deviatoric stress ($\sigma_1 - \sigma_3$); σ_{CI} is the value of CIT; σ_c denotes the short-term strength in terms of deviatoric stress as follows (Kranz 1980):

$$\sigma_c = \sigma_{STF} - \sigma_3 \tag{6.10}$$

where σ_{STF} is the short-term strength under confining pressure σ_3, expressed as follows according to the Mohr-Coulomb criterion:

$$\sigma_{STF} = \frac{1 + \sin \phi}{1 - \sin \phi} \cdot \sigma_3 + 2c \cdot \frac{\cos \phi}{1 - \sin \phi} \tag{6.11}$$

Since $\dot{\varepsilon}_{sc}^c$ is proportional to the subcritical crack growth velocity V_c (Eq. (6.9)), it can be written as:

$$\dot{\varepsilon}_{sc}^c = A_{sc} \left(\frac{\langle \sigma_1 - \sigma_3 - \sigma_{CI} \rangle}{\sigma_{STF} - \sigma_3 - \sigma_{CI}} \right)^n \tag{6.12}$$

where A_{sc} (s^{-1}) is a material parameter.

Introducing Eqs. (6.10) and (6.11) into Eq. (6.12) leads to a power law function for the non-linear creep strain rate caused by micro cracks propagation $\dot{\varepsilon}_{sc}^c$ as follows:

$$\dot{\varepsilon}_{sc}^c = A_{sc}[f^*(\sigma_1, \sigma_3, c, \phi)]^n \tag{6.13}$$

where $f^*(\sigma_1, \sigma_3, c, \phi)$ (noted as f^* for simplification) is a function of normalized stress expressed as follows:

$$f^* = \frac{\langle \sigma_a - \sigma_{CI} \rangle}{\sigma_c - \sigma_{CI}} \tag{6.14}$$

or

$$f^* = \frac{\langle (1 - \sin\phi) \cdot (\sigma_1 - \sigma_3) - 2m \cdot (\sigma_3 \cdot \sin\phi + c \cdot \cos\phi) \rangle}{2(1-m)(\sigma_3 \cdot \sin\phi + c \cdot \cos\phi)} \tag{6.15}$$

after considering $\sigma_{CI} = m \cdot \sigma_c$ ($0.3 \leq m \leq 0.7$).

Function f^* is defined to describe the non-linear creep strain rate caused by micro crack propagations $\dot{\varepsilon}_{sc}^c$ during the secondary creep stage. Its value ranges from 0 to 1 ($0 \leq f^* < 1$). When its value equals to 0, the applied deviatoric stress is lower than or equal to the CIT and $\dot{\varepsilon}_{sc}^c$ is zero. When its value is higher than zero and lower than one, the $\dot{\varepsilon}_{sc}^c$ increases as the value of f^* increases. When the value of f^* is equal to one (i.e. $\sigma_a = \sigma_c$), failure occurs instantaneously without any delay. The rock does not exhibit secondary creep stage. Thus, the value of f^* should be smaller than but not equal to one.

To test the capacity of the model (Eq. (6.13)), the experimental data should contain measured cohesion and friction angle. Alternatively, the ratio between the applied stress and short-term (peak) strength should be available to obtain an estimation of the value of f^*. The model parameters A_{sc} and n can then be obtained through curve-fitting on experimental results.

Figure 6.6 shows the variation of the non-linear creep strain rates due to micro crack propagation $\dot{\varepsilon}_{sc}^c$ of different rocks as a function of f^*, using experimental results available in the literature. The description and prediction using the power law function of the model (Eq. (6.13)) are also presented in the figure with model parameters shown in Table 6.3. In most of the previous studies, only the rates of total creep strain were reported. $\dot{\varepsilon}_{sc}^c$ have to be obtained by subtracting the rate of visco-elastic creep strain $\dot{\varepsilon}_{sc}^v$ calculated with Eq. (6.7) from the rate of the total creep strain as illustrated

in Figure 6.4. For the shist (Figure 6.6c) and lherzolite (Figure 6.6d), the rates of visco-elastic creep strain can be estimated by using the viscosity coefficients $\eta_{SC}^{(c)}$ obtained by applying the curve-fitting technique on the experimental results below the CIT point. For the other rocks (Figure 6.6a, b, e, and f), the viscosity coefficient of similar rocks $\eta_{SC}^{(r)}$ is used because there are no experimental results below the CIT point. Parameters A_{sc} and n in Figure 6.6 are obtained by using calibration (curve-fitting) technique on the experimental results of one confining pressure. The calibrated model is then used to predict the experimental results under different confining pressures. For the cases of Figure 6.6a, b, e, and f, the cohesion and friction angle are not available while the ratio σ_a/σ_c can be found in the respective references (Heap et al. 2009, 2011; Brantut et al. 2012, 2013). The values of f^* for these figures are estimated by Eq. (6.14) considering $\sigma_{CI} = \sigma_c/2$ (i.e., $m = 0.5$).

(a)

(b)

(c)

(d)

(e) (f)
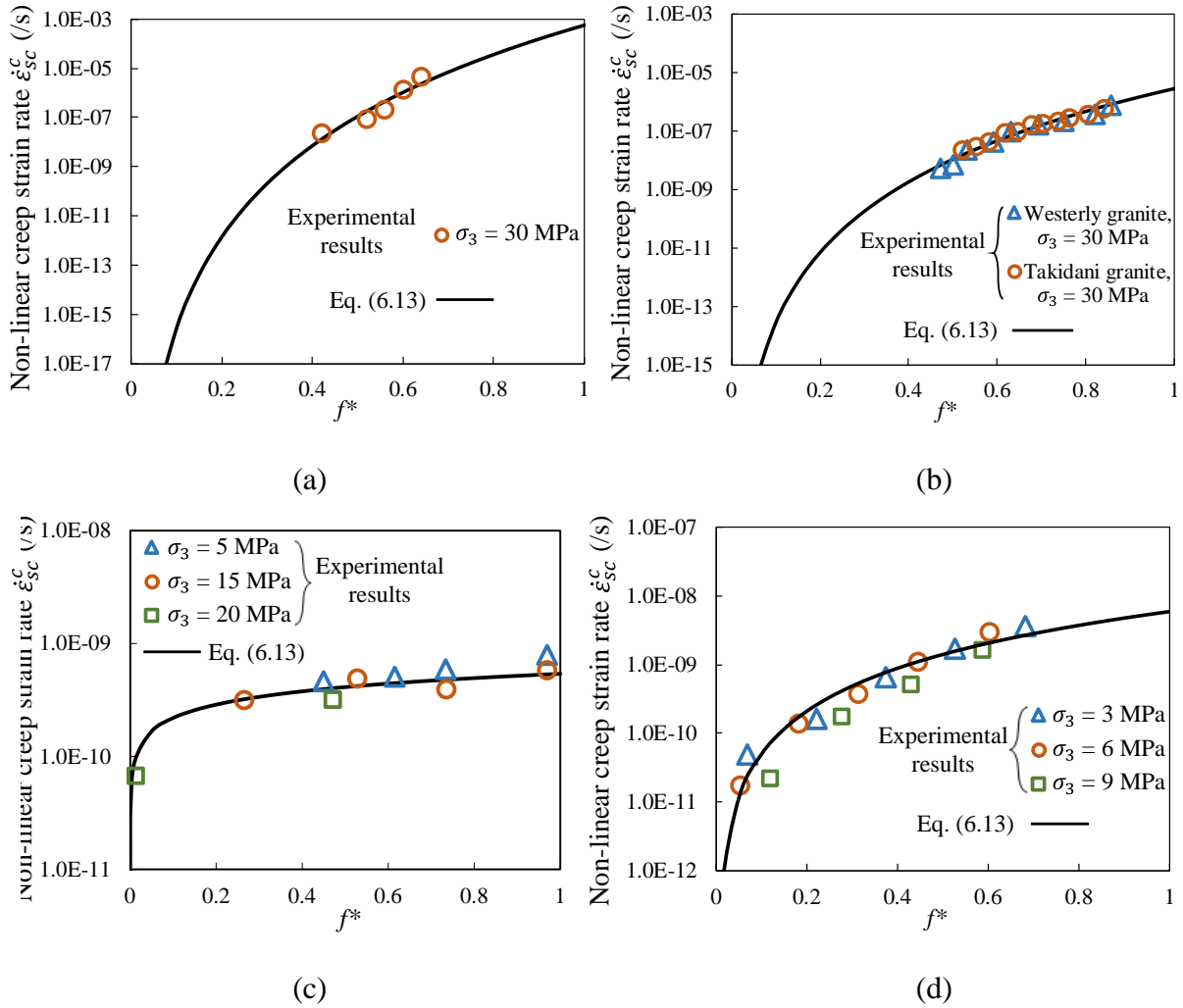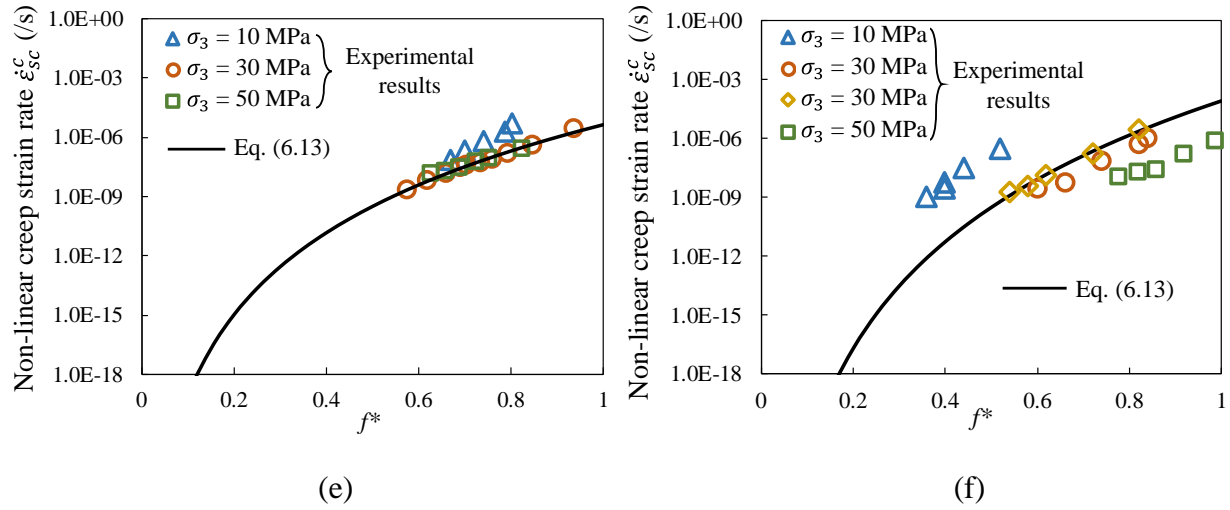
Figure 6.6: Variation of the non-linear creep strain rates $\dot{\varepsilon}_{sc}^{c}$ with the normalized stress: (a) on Tavel limestone (data processed based on Brantut et al. 2013); (b) on Westerly granite and Takidani granite (data processed based on Brantut et al. 2012, 2013); (c) on a schist (data processed based on Liu et al. 2016); (d) on a lherzolite (data processed based on Zhao et al. 2017); (e) on Etna basalt (data processed based on Heap et al. 2011); (f) on Darley Dale sandstone (data processed based on Heap et al. 2009) with model description and prediction using parameters in Table 6.3

Table 6.3: Model parameters for Eq.(6.13) used in Figure 6.6

	Model description	Model prediction	A_{sc} (/s)	n	η_{sc} (Pa·s)	m	c (MPa)	ϕ (°)
Figure 6.6a	$\sigma_3 = 30$ MPa		5.46×10^{-4}	12.3	5.84×10^{16}	0.5		
Figure 6.6b	Westerly granite	Takidani granite	2.66×10^{-6}	8.03	5.50×10^{18}	0.5		
Figure 6.6c	$\sigma_3 = 15$ MPa	$\sigma_3 = 5, 20$ MPa	5.40×10^{-10}	0.391	7.99×10^{16}	0.5	6.09	34.76
Figure 6.6d	$\sigma_3 = 6$ MPa	$\sigma_3 = 3, 9$ MPa	5.87×10^{-9}	2.07	5.51×10^{16}	0.3	14.2	35.4
Figure 6.6e	$\sigma_3 = 30$ MPa	$\sigma_3 = 10, 50$ MPa	4.62×10^{-6}	13.7	5.50×10^{18}	0.5		
Figure 6.6f	$\sigma_3 = 30$ MPa	$\sigma_3 = 10, 50$ MPa	8.27×10^{-5}	18	1.51×10^{17}	0.5		

Note: η_{sc} in Figure 6.6a is taken from Chin and Rogers (1987); in Figure 6.6b, e, f are from Paraskevopoulou et al. 2018; in Figure 6.6c, d are calculated based on the experimental results under applied stress lower than CIT.

The results show that the calibrated power law function (Eq. (6.13)) with the calibrated parameters predicts well the non-linear creep strain rate attributed to micro crack propagations $\dot{\varepsilon}_{sc}^{c}$ as shown

in Figure 6.6b for Takidani granite under confining pressure of 30 MPa, Figure 6.6c for the confining pressures of 5 and 20 MPa, Figure 6.6d for the confining pressures of 3 and 9 MPa, Figure 6.6e for the confining pressures of 10 and 50 MPa. However, for Darley Dale sandstone (Figure 6.6f), the experimental results under the different confining stresses show scatter from the analytical results. More work is necessary to understand these results. Possible reasons can be the inaccuracy associated with a viscosity coefficient of similar rocks taken from the literature (Paraskevopoulou et al. 2018) and varied CIT value from $0.5\sigma_c$ under different confining stresses.

6.2.3.3 Total creep strain of the secondary creep stage

Considering the visco-elastic creep strain (Eq. (6.7)) and creep strain attributed to micro crack propagations (Eq. (6.13)) leads to the total creep strains of the secondary creep strain as follows:

$$\varepsilon_{sc} = \left[\frac{\sigma_1 - \sigma_3}{3\eta_{sc}} + A_{sc}\left(\frac{\langle \sigma_1 - \sigma_3 - \sigma_{CI}\rangle}{\sigma_c - \sigma_{CI}}\right)^n\right] \cdot t \tag{6.16}$$

Figure 6.7 shows the variation of the measured rates of the secondary creep stage as a function of the deviatoric stress taken from Zhao et al. (2017). The model parameters of Eq. (6.16) shown in Table 6.4 were first obtained by calibration (or curve-fitting) based on the experimental results under the confining pressure of 3MPa. The calibrated model (Eq. (6.16) with the obtained model parameters) is then applied to predict the experimental results under the confining pressure of 6 MPa. The quite good agreements between the model and experimental results indicate that the proposed model can be used to describe and predict the creep strain rates of rocks under different stress states.
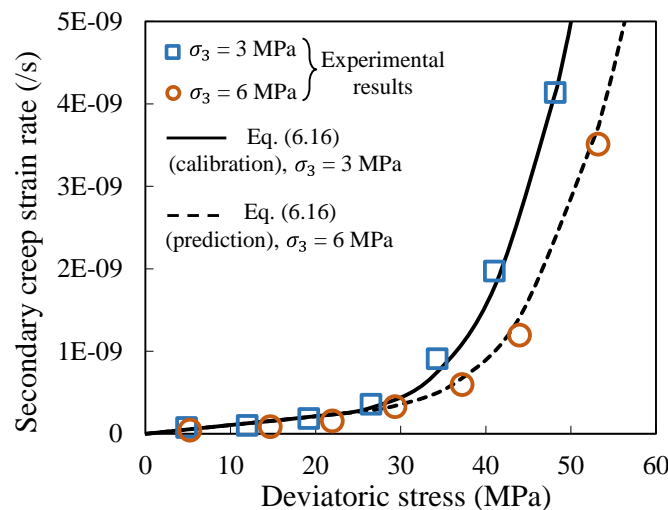
Figure 6.7: Variation of the secondary creep strain rate with the deviatoric stress under different confining stresses (data taken from Zhao et al. 2017) with model description and prediction using parameters in Table 6.4

Table 6.4: Model parameters for Eq.(6.16) used in Figure 6.7

Model description	Model prediction	A_{sc} (/s)	n	η_{sc} (Pa·s)	m	c (MPa)	ϕ (°)
$\sigma_3 = 3$ MPa	$\sigma_3 = 6$ MPa	1.35×10^{-8}	3.58	3.12×10^{16}	0.3	14.2	35.4

6.2.4 Time to failure

In Figure 6.2, one sees that the subcritical cracks propagation is randomly and almost uniformly distributed throughout the rock as indicated by the AE activities before the tertiary (accelerating) creep stage. During the tertiary creep stage, the coalescence of the AE activities appears around an inclined critical plane (Lei et al. 2003; Heap et al. 2009), which finally becomes the plane of failure as the case of a rock submitted to conventional triaxial compression test conditions (Brantut et al. 2013; Liu et al. 2016). This is a typical feature of frictional geomaterials. In addition, the time to failure of the tertiary creep stage of rocks depends on the applied stress (Campanella and Vaid 1974; Das and Scholz 1981; Paraskevopoulou et al. 2018). The UC element shown in Figure 6.3 is proposed here to capture these features, including the time to failure of rocks when the rock is submitted to a stress state higher than the CIT but lower than the peak strength.

With the growth of subcritical cracks, the contact area in intact rock decreases and the internal stress on the area of intact rock increases (Ashby and Sammis 1990). Delayed failure occurs when the internal stress state reaches a critical state defined by the Mohr-Coulomb criterion. This is the physical basis of the UCC creep model for time to failure. Moreover, the following assumptions are made in the model:

1) The effect of interactions between micro cracks on stress state is not considered.

2) The area affected by cracks is independent on the initial angle of its inclination.

3) The reduction speed of the contact area is proportional to subcritical crack growth velocity V_c.

4) At failure, the Mohr-Coulomb criterion applies.

Figure 6.8 shows a simplified two-dimensional micro element from a rock sample in creep process with the presence of only one micro crack. The rock around the micro crack can be divided into three zones based on assumptions:

1) Subcritical crack extension zone where the crack continues to extend resulting in decrease of the contact area;

2) Affected zone. In this area, the contact area decreases and stresses increase due to subcritical crack extension;

3) Intact zone. This area is far enough from the subcritical crack extension zone. The rock in this zone is in stationary (secondary) creep stage.

With the propagation of micro crack, the affected zone can eventually fail due to that the increased stresses reach the Mohr-Coulomb failure line. The coalescence of the failed affected zones due to the micro cracks propagation leads to the failure of the whole rock.

**Affected zone $S(t)$,
contact area reduces and stresses increase**
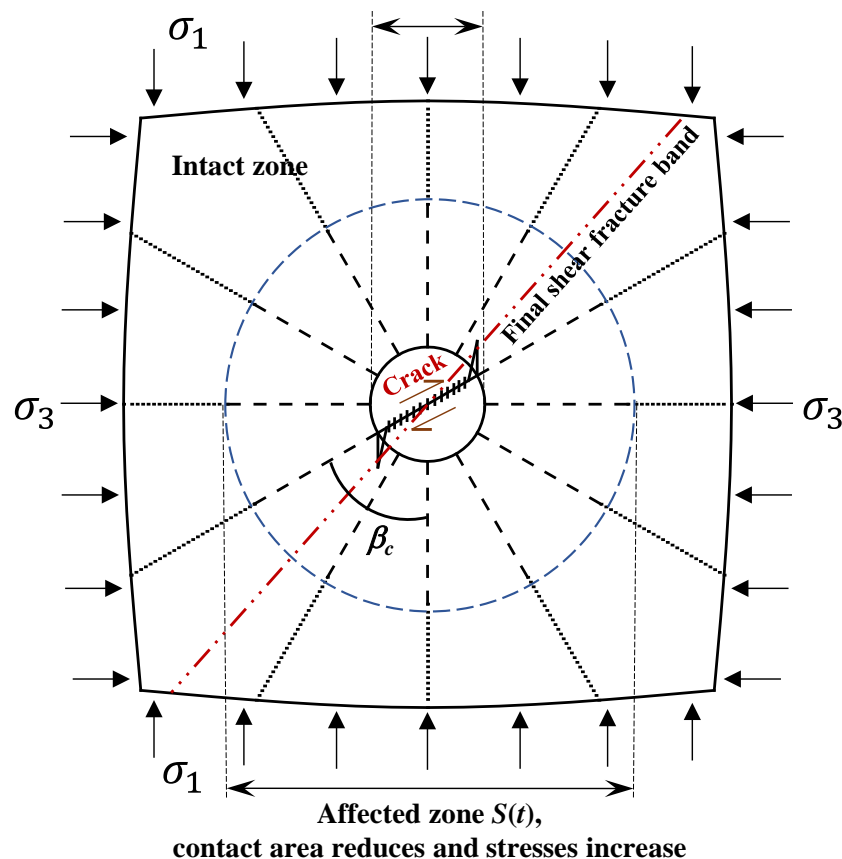
Figure 6.8: The simplified model based on the micro element from a rock sample with the presence of one micro crack in the tertiary creep stage of creep process

Now, one considers a micro crack making an angle of β_c (°) with the major principal stress σ_1. Along the crack plane, the normal ($\sigma_t^{\beta_c}$) and shear ($\tau_t^{\beta_c}$) stresses can be represented by a point on the Mohr circle of the stress state (σ_3, σ_1), which makes an angle of θ_c (= $2\beta_c$) with the normal stress axis as shown in Figure 6.9. At a given time t, they can be expressed as follows within the affected zone:
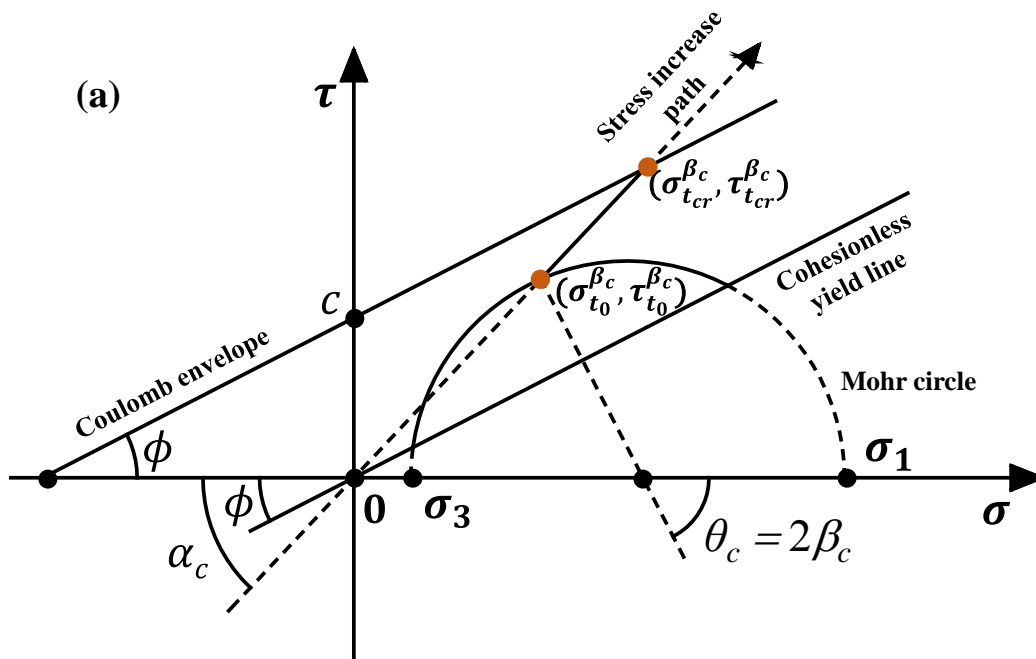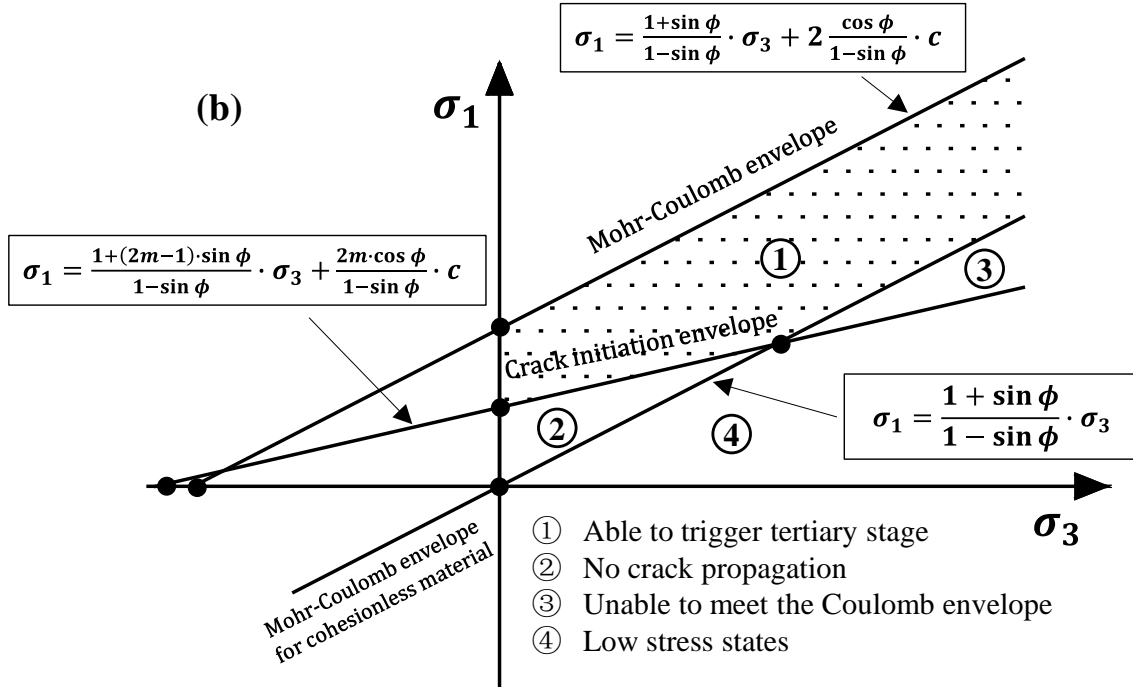
Figure 6.9: Illustration of (a) internal stress path associated with the crack extension in Mohr plane and (b) stress criteria for the occurrence of the tertiary creep stage.

$$\tau_t^{\beta_c} = \frac{F_\tau^{\beta_c}}{S(t)} \tag{6.17}$$

$$\sigma_t^{\beta_c} = \frac{F_\sigma^{\beta_c}}{S(t)} \tag{6.18}$$

where $F_\tau^{\beta_c}$ (N) and $F_\sigma^{\beta_c}$ (N) are the constant shear and normal forces, respectively; $S(t)$ (m^2) is the contact area of the affected zone.

As micro crack propagates with time, $S(t)$ reduces and the initial internal stress state can change. The initial normal stress $\sigma_{t_0}^{\beta_c}$ and shear stress $\tau_{t_0}^{\beta_c}$ along the crack plane can be expressed as:

$$\sigma_{t_0}^{\beta_c} = \frac{1}{2} \cdot [\sigma_1 + \sigma_3 - (\sigma_1 - \sigma_3) \cdot \cos\theta_c] \tag{6.19}$$

$$\tau_{t_0}^{\beta_c} = \frac{1}{2} \cdot (\sigma_1 - \sigma_3) \cdot \sin\theta_c \tag{6.20}$$

Figure 6.9a shows the evolution of the stress state from $(\sigma_{t_0}^{\beta_c}, \tau_{t_0}^{\beta_c})$ to $(\sigma_t^{\beta_c}, \tau_t^{\beta_c})$ when time passes from t_0 to t, following a line making an angle of α_c with the normal stress axis:

$$\tan \alpha_c = \frac{d\tau_t^{\beta c}}{d\sigma_t^{\beta c}} = \frac{F_\tau^{\beta c}}{F_\sigma^{\beta c}} = \frac{\tau_{t_0}^{\beta c}}{\sigma_{t_0}^{\beta c}} \tag{6.21}$$

Eq. (6.21) indicates the stress path line cross the origin point in Figure 6.9a. Therefore, one sees that the stress path line can meet the Coulomb criterion envelope only when the applied stress is higher than the CIT and the value of angle α_c is larger than the friction angle ϕ.

Figure 6.9b shows the different zones surrounded by the Mohr-Coulomb envelop ($\sigma_1 = \frac{1+\sin\phi}{1-\sin\phi} \cdot \sigma_3 + 2\frac{\cos\phi}{1-\sin\phi} \cdot c$), the CIT line ($\sigma_1 = \frac{1+(2m-1)\cdot\sin\phi}{1-\sin\phi} \cdot \sigma_3 + \frac{2m\cdot\cos\phi}{1-\sin\phi} \cdot c$) and the cohesionless yield line ($\sigma_1 = \frac{1+\sin\phi}{1-\sin\phi} \cdot \sigma_3$). When the cohesion is very low, Zone 1 (susceptible to the tertiary creep) will be very thin and close to the peak strength line. This means that the stresses applied on low cohesion rocks must be carefully controlled to observe a tertiary creep stage. This explains why low cohesion rocks such as rock salts usually exhibit ductile behavior and much less brittle behavior and shear failure (Paraskevopoulou and Diederichs 2018).

Considering the case when the internal stresses increase along the stress path and meet the Coulomb envelop at time t_{cr} leads to the following expressions:

$$\begin{cases} \tau_{t_{cr}}^{\beta c} = \sigma_{t_{cr}}^{\beta c} \cdot \tan \alpha \\ \tau_{t_{cr}}^{\beta c} = \sigma_{t_{cr}}^{\beta c} \cdot \tan \phi + c \end{cases} \tag{6.22}$$

where $\tau_{t_{cr}}^{\beta c}$ and $\sigma_{t_{cr}}^{\beta c}$ are the critical shear and normal stresses along the crack plane upon failure, respectively.

From Eq. (6.22), one can express the critical shear stress $\tau_{t_{cr}}^{\beta c}$ as follows:

$$\tau_{t_{cr}}^{\beta c} = \frac{\tan \alpha_c}{\tan \alpha_c - \tan \phi} \cdot c \tag{6.23}$$

Introducing Eqs.(6.19),(6.20), (6.21) ($\tan \alpha_c = \frac{\tau_{t_0}^{\beta c}}{\sigma_{t_0}^{\beta c}}$) into Eq. (6.23) leads to:

$$\tau_{t_{cr}}^{\beta c} = \frac{(\sigma_1-\sigma_3)\cdot\sin\theta_c}{(\sigma_1-\sigma_3)\cdot\sin\theta_c - [\sigma_1+\sigma_3-(\sigma_1-\sigma_3)\cdot\cos\theta_c]\cdot\tan\phi} \cdot c \tag{6.24}$$

Then, the time to failure $t_f^{\beta_c}$ along a micro crack plane with an angle of β_c ($= \theta_c/2$) as shown in Figure 6.8 can be written as:

$$t_f^{\beta_c} = \frac{\tau_{t_{cr}}^{\beta_c} - \tau_{t_0}^{\beta_c}}{V_\tau^{\beta_c}} \tag{6.25}$$

where $V_\tau^{\beta_c}$ is the increasing rate of shear stress, expressed as follows:

$$V_\tau^{\beta_c} = \frac{\partial \tau_t^{\beta_c}}{\partial t} = -\frac{F_\tau^{\beta_c}}{S(t)} \cdot \frac{1}{S(t)} \cdot \dot{S}(t) \tag{6.26}$$

where $\dot{S}(t)$ denotes the decrease rate of the contact area $S(t)$. Considering Eq. (6.9), $\dot{S}(t)$ can be given as the following expression:

$$\dot{S}(t) = A_{tc} \left(\frac{\langle \sigma_a - \sigma_{CI} \rangle}{\sigma_c - \sigma_{CI}} \right)^n \tag{6.27}$$

where A_{tc} (s^{-1}) is a material parameter.

To avoid the shear stress growth rate becoming an overly complicated function of θ_c and t, the reduction in the contact area of the affected zone (Figure 6.8) associated with the crack growth is considered as very small and the value of $S(t)$ in Eq. (6.26) is roughly considered equal to $S(t_0)$. Eq. (6.26) can then be simplified as follows:

$$V_\tau^{\beta_c} = \frac{\partial \tau_t^{\beta_c}}{\partial t} = -\tau_{t_0}^{\beta_c} \cdot \frac{1}{S(t_0)} \cdot \dot{S}(t) \tag{6.28}$$

To make the analytical solution possible, one assumes the initial contact area to be unity at the beginning of the creep t_0 (i.e., $S(t_0) = 1$). One should note that the value of contact area here does not affect the model because the model parameters can be calibrated based on the experimental results. Introducing Eqs. (6.20), (6.24), (6.27) and (6.28) into Eq. (6.25), $t_f^{\beta_c}$ can be expressed as:

$$t_f^{\beta_c} = \frac{\frac{2}{\Gamma(\theta_c)} \cdot c - 1}{A_{tc} \left(\frac{\langle \sigma_a - \sigma_{CI} \rangle}{\sigma_c - \sigma_{CI}} \right)^n} \text{ or } t_f^{\beta_c} = \frac{\frac{2}{\Gamma(\theta_c)} \cdot c - 1}{A_{tc} \left(\frac{\langle (1 - \sin \phi) \cdot (\sigma_1 - \sigma_3) - 2m \cdot (\sigma_3 \cdot \sin \phi + c \cdot \cos \phi) \rangle}{2(1 - m)(\sigma_3 \cdot \sin \phi + c \cdot \cos \phi)} \right)^n} \tag{6.29}$$

where function $\Gamma(\theta)$ is expressed as follows:

$$\Gamma(\theta) = (\sigma_1 - \sigma_3) \cdot \sin \theta_c - [\sigma_1 + \sigma_3 - (\sigma_1 - \sigma_3) \cdot \cos \theta_c] \cdot \tan \phi \tag{6.30}$$

Eq. (6.29) varies for different inclination angles of the micro cracks. The time to failure of rocks t_f corresponds to the minimum value of $t_f^{\beta c}$ (Eq. (6.29)) which can be obtained by imposing $\frac{d\, t_f^{\beta c}}{d\theta_c} = 0$. This leads to:

$$\frac{d\,\Gamma(\theta_c)}{d\theta_c} = (\sigma_1 - \sigma_3) \cdot \cos\theta_{cr} - (\sigma_1 - \sigma_3) \cdot \sin\theta_{cr} \cdot \tan\phi = 0 \tag{6.31}$$

where θ_{cr} is the critical angle of the stress state in Mohr plane for t_f, corresponding to the critical plane β_{cr} in the rock sample. Based on Eq. (6.31), the latter can then be identified as:

$$\beta_{cr} = \frac{\theta_{cr}}{2} = 45° - \frac{\phi}{2} \tag{6.32}$$

This angle is the same as that in conventional triaxial compression tests. This explains well why the failure plane where micro cracks localized during the tertiary creep stage is very similar to that of conventional triaxial compression tests as illustrated in Figure 6.2b. But the meaning is that among the numerous micro cracks, the cracks making an angle of $45°-\phi/2$ with the major principal stress σ_1 will be the first becoming instable.

The time to failure of rocks t_f can then be calculated as:

$$t_f = \frac{\frac{2}{(\sigma_1-\sigma_3)\cdot\cos\phi - [\sigma_1+\sigma_3-(\sigma_1-\sigma_3)\cdot\sin\phi]\cdot\tan\phi}\cdot c-1}{A_{tc}\left(\frac{\langle\sigma_a-\sigma_{CI}\rangle}{\sigma_c-\sigma_{CI}}\right)^n} \tag{6.33}$$

The tertiary creep strain of UCC model can be written as:

$$\varepsilon_{tc} = C(\sigma_1, \sigma_3, \phi) \cdot \langle t - t_f \rangle^0 \cdot F(t) \tag{6.34}$$

where $C(\sigma_1, \sigma_3, \phi)$ is an additional criterion for tertiary creep stage (see the cohesionless yield line in Figure 6.9), given as:

$$C(\sigma_1, \sigma_3, \phi) = \langle \sigma_1 - \frac{1+\sin\phi}{1-\sin\phi} \cdot \sigma_3 \rangle^0 \tag{6.35}$$

If the Mohr circle is below the cohesionless yield line, it will be impossible for the stress state points to reach the Coulomb envelope even though the stresses can increase with the reduction of the contact area.

Function $F(t)$ is introduced to control the shape of time-creep strain curve in the tertiary (accelerating) creep stage. It can be given as:

$$F(t) = \gamma_{tc} \cdot \left(\frac{t}{t_f}\right)^{\lambda_{tc}} \tag{6.36}$$

where γ_{tc} and λ_{tc} are two parameters.

To test the model (Eq. (6.33)), the experimental data under different confining stresses are necessary to perform calibration and prediction. Figure 6.10 shows the time to failure of Barre granite as a function of deviatoric stress under different confining stresses, obtained in laboratory tests by Kranz (1980). The model parameters of the UCC creep model shown in Table 6.5 are first obtained by applying calibration technique on the experimental results under a confining pressure of 0.1 MPa (solid line). The UCC creep model along with the obtained model parameters are then used to predict the time to failure under a confining pressure of 101 MPa (dash line). It can be seen that the agreements between the experimental results and the model description and prediction are quite good. The UCC creep model can thus be used to describe and predict the time to failure of rocks under different stress conditions.
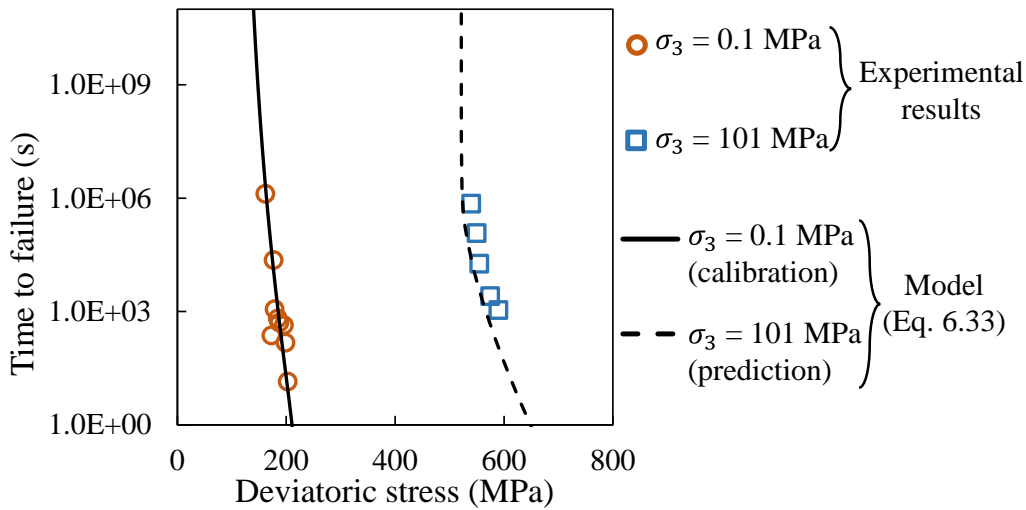
Figure 6.10: Variation of the time to failure with deviatoric stress under different confining stresses (experimental results taken from Kranz 1980) with model description and prediction using parameters in Table 6.5

Table 6.5: Model parameters for Eq.(6.33) used in Figure 6.10

Model description	Model prediction	A_{tc} (/s)	n	m	c (MPa)	ϕ (°)
$\sigma_3 = 0.1$ MPa	$\sigma_3 = 101$ MPa	0.25	18.71	0.5	44.3	46.1

6.2.5 Total axial strain

Introducing Eqs. (6.4), (6.5), (6.16) and (6.34) into Eq. (6.1), the total axial strain of the UCC creep model can be given as:

$$\varepsilon_t = \frac{\sigma_1 - \sigma_3}{9K_e} + \frac{\sigma_1 - \sigma_3}{3G_e} + \frac{\sigma_1 - \sigma_3}{3G_K}\left[1 - \exp\left(-\frac{G_K \cdot t}{\eta_K}\right)\right] + \left[\frac{(\sigma_1 - \sigma_3)}{3\eta_{sc}} + A_{sc}\left(\frac{\langle\sigma_1 - \sigma_3 - \sigma_{CI}\rangle}{\sigma_c - \sigma_{CI}}\right)^n\right] \cdot t + C(\sigma_1, \sigma_3, \phi) \cdot$$
$$\langle t - t_f\rangle^0 \cdot F(t) \tag{6.37}$$

6.3 Application of the UCC creep model

6.3.1 Parameter identification

To use the proposed UCC creep model (Eq. (6.37)), parameters K_e, G_e, G_K, η_K, η_{sc}, A_{sc}, A_{tc}, n, γ_{tc}, and λ_{tc} need to be identified.

K_e and G_e can be obtained from elastic modulus E and Poisson's ratio υ as follows:

$$K_e = \frac{E}{3(1 - 2\upsilon)} \tag{6.38}$$

$$G_e = \frac{E}{2(1 + \upsilon)} \tag{6.39}$$

In absence of E and υ, their values can also be obtained by curve-fitting technique on instantaneous strain as a function of stress.

Parameters G_K and η_K can be obtained by fitting the UCC creep model with measured total creep strains as a function of time under one or several stress states at the primary creep stage.

Parameter η_{sc} can be obtained by curve-fitting on the measured rates of visco-elastic creep strain. The creep strain under a stress state lower than the CIT is visco-elastic creep strain. The measured CIT should be used as long as it is available. In absence of its measurement, its value can typically be taken as 50% of the short-term strength (Lajtai and Schmidtke 1986; Aubertin et al. 2000).

However, the ratio between the CIT and short-term strength can range from 30 to 70%, as shown in Table 6.1.

Parameters A_{sc} and n are obtained by fitting the model with measured rates of creep strain due to micro cracks propagation which are obtained by subtracting the rate of visco-elastic creep strain from the rate of total creep strain.

Parameter A_{tc} can be obtained by fitting the model with measured time to failure under one or several confining pressure levels. Parameters γ_{tc} and λ_{tc} are obtained by fitting the model with the measured total creep strain as a function of time at the tertiary creep stage.

6.3.2 Sample application

Zhao et al. (2017) conducted a series of creep tests on lherzolite cylinder rock samples having a diameter of 50 mm and a height of 100 mm. Axial loads were exercised through a servo-controlled creep test machine. The axial strains were measured by a linear variable displacement transducer (LVDT). Cyclic increment loading and unloading creep tests were conducted. The axial pressure was loaded at a rate of 0.03 MPa/s until the targeted stress level, which was maintained constant for a duration of 90 h. After that, unloading was processed until a zero deviatoric stress. A repos period of 20 to 30 h was applied before applying a new load.

According to Zhao et al. (2017), fifteen triaxial compression tests were performed under the confining pressures of 0, 3, 6, 9 and 12 MPa, respectively. However, they only presented the experimental results under the confining pressure of 6 MPa at different deviatoric stress levels as shown in Figure 6.11. These results will be used to test the description and prediction ability of the proposed UCC creep model.
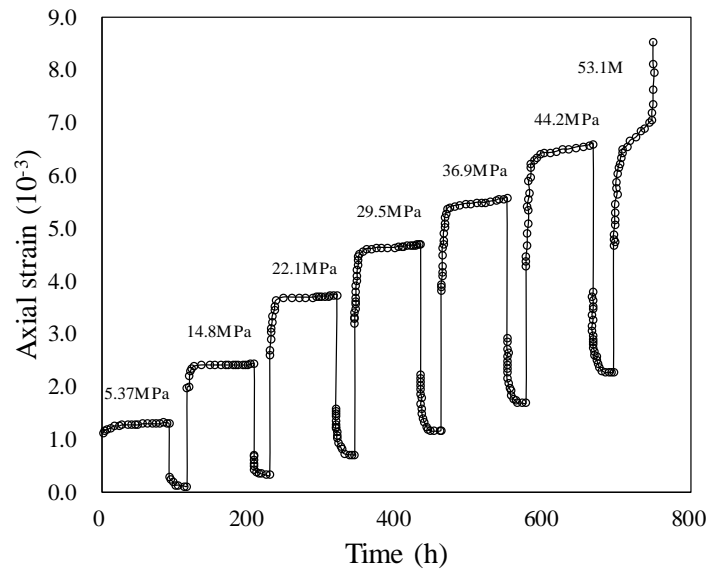
Figure 6.11: Axial strain data under the confining pressure of 6 MPa and different deviatoric stresses (data taken from Zhao et al. 2017)

Table 6.6 shows the required model parameters, obtained by applying the curve-fitting technique on the experimental results under the deviatoric stresses of 14.8 MPa (below the CIT, 20.8 MPa), 36.9 MPa and 44.2 MPa (above the CIT). It is interesting to note that the obtained bulk and shear modulus are quite close to those presented by Zhao et al. (2017). These parameters are then used in the UCC creep model to predict the creep behavior of the rock under other deviatoric stresses.

The description and prediction of the UCC creep model using the model parameters shown in Table 6.6 are plotted on Figure 6.12. It can be seen that the model description of the experimental results under deviatoric stresses of 14.8, 36.9 and 44.2 MPa are very good while the prediction of the calibrated model (i.e., Eq. (6.37)) on the experimental results under other deviatoric stresses are also quite good.

Table 6.6: Material parameters obtained by applying the curve-fitting technique on the experimental results of the 2th, 5th and 6th stress levels with the confining pressure of 6 MPa, reported by Zhao et al. (2017)

c (MPa)	ϕ (°)	K_e (GPa)	G_K (GPa)	G_e (GPa)	η_K (GPa · h)	η_{sc} (GPa · h)
14.2	35.4°	6.90	6.87	4.06	19.73	9.96×10^3

A_{sc} (h^{-1})	A_{tc} (h^{-1})	n	γ_{tc}	λ_{tc}	m
$7.76{\times}10^{-6}$	0.034	2.78	$1.1{\times}10^{-4}$	195	0.3
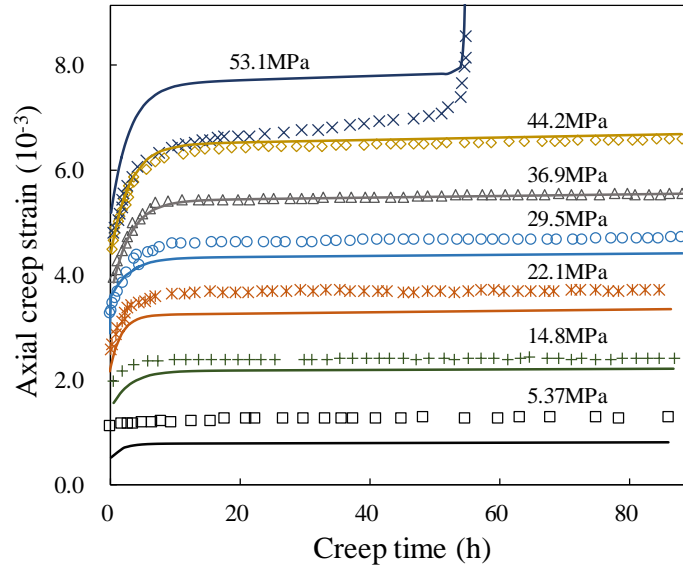
Figure 6.12: Experimental results (points) of the strain evolution of a cylinder rock under different axial stresses at the confining pressure of 6 MPa (data taken from Zhao et al. 2017); the solid lines correspond to the three descriptions and four predictions of the UCC creep model using the model parameters given in Table 6.6

6.4 Discussion

In this study, a new creep model, called ubiquitous-corrosion-Coulomb (UCC) creep model is proposed to describe and predict the creep strain and time to failure of rocks. The results show that the UCC creep model is applicable to describing and predicting the creep strain and time to failure of rocks under different stress states. However, some hypotheses involved in the model need to be discussed:

1) The application of the model requires the knowledge of CIT. For a given rock, the CIT value can be determined as the start of deviation of the axial stress-radial strain curves from the linearity, start of acoustic emission, or start of dilation. The measured value should be used in the model as long as it is available. In absence of its measurement, it can be simply taken as

50% of the short-term strength for most cases (Lajtai and Schmidtke 1986; Aubertin et al. 2000). However, the ratio between the CIT and short-term strength can range from 30 to 70%, as shown in Table 6.1.

2) The ratio between the CIT and short-term strength was taken as the constant under varied confining pressures in this study. Experimental results have shown that this ratio can be dependent on confining pressures (Taheri et al. 2020). This may explain the important pressure dependency shown in Figure 6.6f. The dependency of the ratio between the CIT and short-term strength needs to be considered in future.

3) The change in the internal stresses was only attributed to the reduction of the contact area, which was in turn associated with the extension of micro cracks. In the future, more work is necessary to take into account the interaction between micro cracks (Ashby and Sammis 1990; Li et al. 2018).

4) The distribution of initial cracks and the space orientations of micro cracks were not considered in this study. They should be further studied in future.[49]

5) In this study, the relationship between the applied stress and the micro crack extension velocity was described by Eq. (6.8). This is an equation based on the crack extension in the glass which is homogeneous and isotropic. However, most rocks are of non-homogeneous and anisotropic properties. Therefore, this relationship will need to be further investigated in future study.

6) In this study, the affected zone of cracks was considered as independent on the initial inclination angle of micro cracks. More work is needed to investigate its validity and impact on the proposed model.

7) In Eq. (6.28), a simplification has been made by assuming a negligible effect of the crack extension on $S(t)$. $S(t)$ was loosely considered to be equal to $S(t_0)$, which was assumed to be unity area. This simplifying assumption is necessary to avoid overly complicated derivations. Other forms of $S(t)$ are expected to be studied in future to improve the model.

In this study, the tests of the capacity of the model were made by using limited data available in the literature. More experimental works are needed on a wider range of rocks. Moreover, the UCC creep model was developed by considering conventional triaxial compression test conditions. It is

known that the intermediate principal stress can affect the mechanical behavior of rocks. An improvement of the UCC creep model is expected by taking the intermediate principal stress into consideration. Its validation requires in turn more creep tests under true triaxial compression test conditions.

Finally, in order for the proposed model to be useful in practice, its implementation in a numerical code is necessary (Julien et al. 1998; Boulianne et al. 2004).

6.5 Conclusions

In this paper, a new model called ubiquitous-corrosion-Coulomb (UCC) creep model is proposed to represent and predict creep strain and time to failure of rocks under different stress states. Distinction is made between the linear visco-elastic and non-linear creep strain rate. Subcritical crack growth is related to the non-linear creep strain rate and delayed failure of rocks. The effects of friction angle and confining pressure on the rate of creep strain and the time to failure are accounted in the model. The similarity between the failure plane of creep tests and that observed in conventional triaxial compression tests is mathematically shown. With the UCC creep model, the localization of micro cracks on the failure plane in creep tests making an angle of $45°-\phi/2$ with the major principal stress σ_1 is explained by the fact that among the numerous micro cracks, the cracks along this orientation are the first becoming instable. To test the description and prediction capability of the UCC creep model against experimental results available in the literature, the model parameters were first obtained by applying the curve-fitting technique on a part of the available experimental results. The obtained model parameters were then used in the model (i.e. calibrated model) to predict another part of the available experimental results. The results showed that proposed UCC creep model is able to describe and predict the creep strain and time to failure in creep process of rocks under different stress states.

Acknowledgements

6.6 References

Amitrano, D., & Helmstetter, A. (2006). Brittle creep, damage, and time to failure in rocks. *Journal of Geophysical Research*, 111(B11201), 1-17.

Andrade, E.N.D.C. (1910). On the viscous flow in metals, and allied phenomena. *Proceedings of the Royal Society of London*, *Series A*. The Royal Society, 1-12.

Ashby, M.F., & Sammis, C.G. (1990). The damage mechanics of brittle solids in compression. *Pure and Applied Geophysics*, 133(3), 489-521.

Aubertin, M., Gill, D., & Ladanyi, B. (1991a). An internal variable model for the creep of rock salt. *Rock Mechanics and Rock Engineering*, 24(2), 81-97.

Aubertin, M., Li, L., & Simon, R. (2000). A multiaxial stress criterion for short-and long-term strength of isotropic rock media. *International Journal of Rock Mechanics and Mining Sciences*, 37(8): 1169-1193.

Aydan, O., Seiki, T., Jeong, G., & Tokashiki, N. (1994). Mechanical behaviour of rocks, discontinuities and rock masses. *Proceedings of International Symposium Pre-failure Deformation Characteristics of Geomaterials*. Sapporo, 1161-1168.

Aydan, O., Tokashiki, N., Ito, T., Akagi, T., Ulusay, R., & Bilgin, H. (2003). An experimental study on the electrical potential of nonpiezoelectric geomaterials during fracturing and sliding. *Proceedings of 10th ISRM Congress, International Society for Rock Mechanics*. South Africa, 73-78.

Aydan, Ö., Ito, T., Özbay, U., Kwasniewski, M., Shariar, K., Okuno, T., Özgenoğlu, A., Malan, DF., & Okada, T. (2014). ISRM suggested methods for determining the creep characteristics of rock. *Rock Mechanics and Rock Engineering*, 47(1), 275–290.

Bérest, P., Béraud, J., Gharbi, H., Brouard, B., DeVries, K. (2015). A very slow creep test on an Avery Island salt sample. *Rock Mechanics and Rock Engineering*; 48(6), 2591-2602.

Boukharov, G., Chanda, M., & Boukharov, N. (1995). The three processes of brittle crystalline rock creep. *International Journal of Rock Mechanics and Mining Sciences*, 32(4), 325-335.

Boulianne, M., Simon, R., & Aubertin, M. (2004). A numerical investigation of the creep (viscoplastic) behaviour of circular opening and pillar in rock salt. *Proceedings of 57th Canadian geotechnical conference and the 5th joint CGS-IAH conference*. Quebec City, 25-32.

Brace, W., Paulding, Jr. B., Scholz, C. (1966). Dilatancy in the fracture of crystalline rocks. *Journal of Geophysical Research*, 71(16), 3939-3953.

Brantut, N., Baud, P., Heap, M., & Meredith, P. (2012). Micromechanics of brittle creep in rocks. *Journal of Geophysical Research*, 117(B08412).

Brantut, N., Heap, M., Meredith, P., & Baud, P. (2013). Time-dependent cracking and brittle creep in crustal rocks: A review. *Journal of Structural Geology*, 52, 17-43.

Campanella, R., & Vaid, Y. (1974). Triaxial and plane strain creep rupture of an undisturbed clay. *Canadian Geotechnical Journal*, 11(1), 1-10.

Chandler, N.A., & Martin, C.D. (1995). An analysis of laboratory and long-term rock strength using a sliding crack model. *Proceedings of the 35th US Symposium on Rock Mechanics (USRMS)*. American Rock Mechanics Association, 741-747.

Charles, R. (1958). Static fatigue of glass. I. *Journal of Applied Physics*, 29(11), 1549-1553.

Charles, R. (1959). The strength of silicate glasses and some crystalline oxides. *Proceedings of International Conference on the Atomic Mechanisms of Fracture*. Swampscott, Massachusetts, 225–49.

Chin, H., & Rogers, J. (1987). Creep parameters of rocks on an engineering scale. *Rock Mechanics and Rock Engineering*, 20(2), 137-146.

Cristescu, N., & Hunsche, U. (1998). *Time effects in rock mechanics*. New York: Wiley.

Damjanac, B., & Fairhurst, C. (2010). Evidence for a long-term strength threshold in crystalline rock. *Rock Mechanics and Rock Engineering*, 43(5), 513-531.

Das, S., & Scholz, C. (1981). Theory of time-dependent rupture in the earth. *Journal of Geophysical Research*, 86(B7), 6039-6051.

Diederichs, M., Kaiser, P., & Eberhardt, E. (2004). Damage initiation and propagation in hard rock during tunneling and the influence of near-face stress rotation. *International Journal of Rock Mechanics and Mining Sciences*, 41(5), 785-812.

Fahimifar, A., Karami, M., & Fahimifar, A. (2015). Modifications to an elasto-visco-plastic constitutive model for prediction of creep deformation of rock samples. *Soils and Foundations*, 55(6), 1364-1371.

Farmer, I.W. (2012). *Engineering behaviour of rocks*. Springer Science & Business Media.

Freiman, S. (1984). Effects of chemical environments on slow crack growth in glasses and ceramics. *Journal of Geophysical Research*, 89(B6), 4072-4076.

Garofalo, F. (1965). *Fundamentals of creep and creep-rupture in metals*. Macmillan.

Gasc-Barbier, M., Chanchole, S., & Bérest, P. (2004). Creep behavior of Bure clayey rock. *Applied Clay Science*, 26(1-4), 449-458.

Goodman, R. (1989). *Introduction to rock mechanics*. New York: Wiley.

Hallbauer, D., Wagner, H., & Cook, N. (1973). Some observations concerning the microscopic and mechanical behaviour of quartzite specimens in stiff, triaxial compression tests. *International Journal of Rock Mechanics and Mining Sciences*, 10(6), 713-726.

Hao, S., Liu, C., Wang, Y., & Chang, F. (2017). Scaling law of average failure rate and steady-state rate in rocks. *Pure and Applied Geophysics*, 174(6), 2199-2215.

Hardy, H.R., Kim, R. Y., Stefanko, R., & Wang, Y. J. (1969). Creep and microseismic activity in geologic materials. *Proceedings of the 11th US Symposium on Rock Mechanics (USRMS)*. American Rock Mechanics Association, 377-414.

Heap, M., Baud, P., Meredith, P., Bell, A., & Main, I. (2009). Time-dependent brittle creep in Darley Dale sandstone. *Journal of Geophysical Research*, 114(B07203).

Heap, M., Baud, P., Meredith, P., Vinciguerra, S., Bell, A., & Main, I. (2011). Brittle creep in basalt and its application to time-dependent volcano deformation. *Earth and Planetary Science Letters*, 307(1-2): 71-82.

Hirata, T., Satoh, T., & Ito, K. (1987). Fractal structure of spatial distribution of microfracturing in rock. *Geophysical Journal International*, 90(2), 369-374.

Ito, H. (1991). On rheological behaviour of in situ rock based on long-term creep experiments. *Proceedings of 7th ISRM Congress*. Aachen, Germany.

Jaeger, J.C., Cook, N.G.W., & Zimmerman, R. (2009). *Fundamentals of rock mechanics*. John Wiley & Sons.

Jeffieys, H. (1958). A modification of Lomnitz's law of creep in rocks. *Geophysical Journal International*, 1(1), 92-95.

Julien, M.R., Foerch, R., Aubertin, M., & Cailletaud, G. (1998). Some aspects of the numerical implementation of SUVIC-D. *Proceedings of 4th Conference on the Mechanical Behavior of Salt*. Trans Tech Publications, Clausthal-Zellerfeld, Germany, 389-404.

Kemeny, J. M. (1991). A model for non-linear rock deformation under compression due to sub-critical crack growth. *International Journal of Rock Mechanics and Mining Sciences*, 28, 459-467.

Kranz, R.L. (1980). The effects of confining pressure and stress difference on static fatigue of granite. *Journal of Geophysical Research*, 85(B4), 1854-1866.

Ladanyi, B. (1974). Use of the long-term strength concept in the determination of ground pressure on tunnel linings. *Proceedings of the 3rd Congress of International Society of Rock Mechanics on Advances in Rock Mechanics*. Washington, National Academy of Science.

Lajtai, E., & Schmidtke, R. (1986). Delayed failure in rock loaded in uniaxial compression. *Rock Mechanics and Rock Engineering*, 19(1), 11-25.

Lei, X., Kusunose, K., Satoh, T., & Nishizawa, O. (2003). The hierarchical rupture process of a fault: an experimental study. *Physics of the Earth and Planetary Interiors*, 137(1-4), 213-228.

Li, L., Aubertin, M., & Simon, R. (2017). The MSDP$_u$ multiaxial criterion for the strength of rocks and rock masses. *Rock Mechanics and Engineering*. CRC Press, 409-436.

Li, X., Qi, C., Shao, Z., & Qu, X. (2018). Static shear fracture influenced by historic stresses path and crack geometries in brittle solids. *Theoretical and Applied Fracture Mechanics*, 96, 64-71.

Li, Y., & Xia, C. (2000). Time-dependent tests on intact rocks in uniaxial compression. *International Journal of Rock Mechanics and Mining Sciences*, 37(3), 467-475.

Liu, H., Xie, H., He, J., Xiao, M., & Zhuo, L. (2016). Nonlinear creep damage constitutive model for soft rocks. *Mechanics of Time-Dependent Materials*, 21(1), 73-96.

Lo, K.Y., & Yuen, C.M.K. (1981). Design of tunnel lining in rock for long-term time effects. *Canadian Geotechnical Journal*, 18(1), 24–39.

Lockner, D.A. (1998). A generalized law for brittle deformation of Westerly granite. *Journal of Geophysical Research*, 103(B3), 5107-5123.

Lomnitz, C. (1957). Linear dissipation in solids. *Journal of Applied Physics*, 28(2), 201-205.

Ma, L., Liu, X., Fang, Q., Xu, H., Xia, H., Li, E., Yang, S., & Li, W. (2012). A new elasto-viscoplastic damage model combined with the generalized Hoek–Brown failure criterion for bedded rock salt and its application. *Rock Mechanics and Engineering*, 46(1), 53-66.

Malan, D.F. (1999). Time-dependent behaviour of deep level tabular excavations in hard rock. *Rock Mechanics and Engineering*, 32(2), 123-155.

Malan, D.F., Vogler, U.W., & Drescher, K. (1997). Time-dependent behaviour of hard rock in deep level gold mines. *Journal of the Southern African Institute of Mining and Metallurgy*, 97(3), 135-147.

Mansouri, H., & Ajalloeian, R. (2018). Mechanical behavior of salt rock under uniaxial compression and creep tests. *International Journal of Rock Mechanics and Mining Sciences*, 110, 19-27.

Maranini, E., & Yamaguchi, T. (2001). A non-associated viscoplastic model for the behaviour of granite in triaxial compression. *Mechanics of Materials*, 33(5), 283-293.

Martin, C.D. (1997). Seventeenth Canadian geotechnical colloquium: the effect of cohesion loss and stress path on brittle rock strength. *Canadian Geotechnical Journal*, 34(5), 698-725.

Maruyama, K., Tanaka, C., & Oikawa, H. (1990). Long-term creep curve prediction based on the modified theta projection concept. *Journal of Pressure Vessel Technology, Transactions of the ASME*, 112(1), 92-97.

Mirza, U. (1978). *Investigation into the design criteria for underground openings in rocks which exhibit rheological behaviour*. (Ph.D. thesis, University of Newcastle upon Tyne).

Miura, K., Okui, Y., & Horii, H. (2003). Micromechanics-based prediction of creep failure of hard rock for long-term safety of high-level radioactive waste disposal system. *Mechanics of Materials*, 35(3-6), 587-601.

Myer, L.R., Kemeny, J.M., Zheng, Z., Suarez, R., Ewy, R.T., & Cook, N.G.W. (1992). Extensile cracking in porous rock under differential compressive stress. *Applied Mechanics Reviews*, 45(8), 263-280.

Ngwenya, B.T., Main, I.G., Elphick, S.C., Crawford, B.R., & Smart, B.G.D. (2001). A constitutive law for low-temperature creep of water-saturated sandstones. *Journal of Geophysical Research*, 106(B10), 21811-21826.

Nopola, J., & Roberts, L. (2016). Time-dependent deformation of Pierre Shale as determined by long-duration creep tests. *Proceedings of 50th US Rock Mechanics/Geomechanics Symposium*. American Rock Mechanics Association, 584-591.

Ohring, M. (1995). *Engineering materials science*. Elsevier.

Paraskevopoulou, C., & Diederichs, M. (2018). Analysis of time-dependent deformation in tunnels using the Convergence-Confinement Method. *Tunnelling and Underground Space Technology*, 71, 62-80.

Paraskevopoulou, C., Perras, M., Diederichs, M., Loew, S., Lam, T., & Jensen, M. (2018). Time-dependent behaviour of brittle rocks based on static load laboratory tests. *Geotechnical and Geological Engineering*, 36(1), 337-376.

Paraskevopoulou, C. (2016). *Time-dependency of rocks and implications associated with tunneling*. (Ph.D. thesis, Queen's University).

Penny, R., & Marriott, D. (1995). *Design for creep*. Springer Science & Business Media.

Perzyna, P. (1966). Fundamental problems in viscoplasticity. *Advances in Applied Mechanics*, 9, 243-377.

Potyondy, D.O. (2007). Simulating stress corrosion with a bonded-particle model for rock. *International Journal of Rock Mechanics and Mining Sciences*, 44(5), 677-691.

Shao, J., Chau, K., & Feng, X. (2006). Modeling of anisotropic damage and creep deformation in brittle rocks. *International Journal of Rock Mechanics and Mining Sciences*, 43(4), 582-592.

Sterpi, D., & Gioda, G. (2009). Visco-plastic behaviour around advancing tunnels in squeezing rock. *Rock Mechanics and Rock Engineering*, 42(2), 319-339.

Taheri, A., Zhang, Y., & Munoz, H. (2020). Performance of rock crack stress thresholds determination criteria and investigating strength and confining pressure effects. *Construction and Building Materials*, 243, 118263.

Tang, H., Wang, D., Huang, R., Pei, X., & Chen, W. (2017). A new rock creep model based on variable-order fractional derivatives and continuum damage mechanics. *Bulletin of Engineering Geology and the Environment*, 77(1), 375-383.

Tomanovic, Z. (2006). Rheological model of soft rock creep based on the tests on marl. *Mechanics of Time-Dependent Materials*, 10(2), 135-154.

Verstrynge, E., Schueremans, L., & Van Gemert, D. (2011). Time-dependent mechanical behavior of lime-mortar masonry. *Materials and Structures*, 44(1), 29-42.

Wang, G., Zhang, L., Zhang, Y., & Ding, G. (2014). Experimental investigations of the creep-damage-rupture behaviour of rock salt. *International Journal of Rock Mechanics and Mining Sciences*, 66, 181-187.

Wang, R., & Li, L. (2019). A non-stationary power law model to predict the secondary creep rate of rocks. *Proceedings of 8th International Conference on Case Histories in Geotechnical*

Engineering. American Society of Civil Engineers (ASCE), Philadelphia, United States, 476-483.

Wang, R., & Li, L. (2018). Burgers creep model used for describing and predicting the creep behaviour of a rock under uniaxial and triaxial compression test conditions. *Proceedings of the 71st Canadian Geotechnical Conference*. Edmonton, Canada, 572.

Weijermars, R., Alekseev, V. B., Cuevas, J., Vigneresse, J. L., & Schmid, S. (1997). *Principles of rock mechanics*. Amsterdam: Alboran Science Publishing.

Xu, M., Jin, D., Song, E., & Shen, D. (2018). A rheological model to simulate the shear creep behavior of rockfills considering the influence of stress states. *Acta Geotechnica*, 13(6), 1313-1327.

Xu, T., Xu, Q., Deng, M., Ma, T., Yang, T., & Tang, C. (2014). A numerical analysis of rock creep-induced slide: a case study from Jiweishan Mountain, China. *Environmental Earth Sciences*, 72(6), 2111-2128.

Yahya, O., Aubertin, M., & Julien, M. (2000). A unified representation of the plasticity, creep and relaxation behavior of rocksalt. *International Journal of Rock Mechanics and Mining Sciences*, 37(5), 787-800.

Zhang, H., Wang, Z., Zheng, Y., Duan, P., & Ding, S. (2012). Study on tri-axial creep experiment and constitutive relation of different rock salt. *Safety Science*, 50(4), 801-805.

Zhao, Y., Wang, Y., Wang, W., Wan, W., & Tang, J. (2017). Modeling of non-linear rheological behavior of hard rock using triaxial rheological experiment. *International Journal of Rock Mechanics and Mining Sciences*, 93, 66-75.

CHAPTER 7   GENERAL DISCUSSION

In this thesis, the implications of rock walls instantaneous closure due to adjacent excavation and time-dependent creep deformation on the stability, minimum required cohesion (c_{min}) and mechanical behavior of side-exposed backfill have been investigated mainly based on the numerical simulations with FLAC^{3D}. The proposed numerical and analytical solutions have been verified by comparing with some previous solutions, laboratory test results, and in-situ measurements in the literature. The outcomes of this thesis lead to an improved design of mining backfill and the optimized backfilling and mining operations. However, these investigations are based on some important assumptions and have some limitations which have been addressed in Chapters 3 to 6. The main assumptions, limitations and some aspects of this study are further summarized as follows.

- The numerical model for geotechnical problem should be stable and reliable. The FLAC^{3D} in this study has been validated as shown in Appendices A and B by comparing the numerical results of different constitutive models with analytical solutions. The domain size and mesh size of a numerical model are important to ensure stable numerical results. When the closure of rock walls is not considered, the domain size may be small due to fixed rock walls. In this project however, rock-wall closure is considered. Large numerical model is necessary. With a large numerical model, fine mesh can be applied in the area of interests (around excavations) while coarse mesh can be used in the outer part of the model by using a method developed and described in Appendix C. In numerical simulations, sensitivity analyses should be conducted case by case to determine the optimal domain and mesh sizes.

- The numerical model of the side-exposed backfill in this project was simplified from the engineering practice of backfilled stopes in underground mines. In the model, both the primary and secondary stopes were simplified as a vertical rectangular prism. However, in practice, a stope usually has irregular geometry with inclinations (Thompson et al. 2009, 2017). The vicinity of an underground backfilled stope can have various excavations such as drifts, declines, and previous stopes which were also not considered.

- The backfill and rock mass were assumed homogeneous and isotropic. In practice, both of them can be non-homogeneous and anisotropic due to segregation and different pouring stages for

the backfill and geological discontinuities for rock mass (Grabinsky and Bawden 2007; Wittke 2014). The numerical model can be improved by overcoming these limitations.

- In the numerical model for analyzing the stability of side-exposed backfill, the adjacent secondary stope was excavated in one step which is close to a sublevel stoping or long-hole stoping mining. In underground mine, the secondary stope could also be extracted in layers such as the vertical retreat mining that can result in a sequential exposure of backfill in the primary stope (Hamrin 2001; Darling 2011). More work is desired to study the effect of different mining methods and mine sequences on the stability of backfill.

- The neighboring workings around a backfilled stope can cause blasting vibrations and affect the stability of backfill upon exposure (Emad et al. 2012, 2018). The effect of blasting on the stability and required strength of side-exposed backfill needs to be considered in future work.

- In numerical simulations, the backfill was simulated in dry condition while the presence of water was not considered. This assumption is reasonable for backfill upon exposure because that in practice, the backfill is usually exposed after a long curing time (typically 28 days) when it is fully drained. However, in numerical simulations of time-dependent stability of backfill where the time factor and creep behavior of rocks are considered, more work is needed to analyze the dissipation of excess pore water pressure during curing time (Godbout et al. 2007; El Mkadmi et al 2014).

- The minimum required cohesion c_{min} of side-exposed backfill was determined mainly by evaluating the coalescence of yield zones within backfill. The yield zone development as an instability criterion was verified by comparing with centrifugal model tests of side-exposed backfill conducted by Mitchell (1986). The displacement of backfill is not a main instability criterion because that there is not a limiting displacement value and the variation trend of displacement depends on the selected axis scale.

- When determining the c_{min} of side-exposed backfill, its mechanical parameters including cohesion, friction angle, and Young's modulus, were all considered as independent parameters. According to the experimental results, these parameters may be coupling. Belem et al. (2000) reported that the friction angle of backfill can decrease with the increase of its cohesion and cement content. And a stiffer fill is usually of a higher cohesion (Gonano and Kirkby 1977;

Fall et al. 2007). The combined effect of these mechanical parameters can affect the stability and c_{min} of side-exposed backfill and should be studied in future.

- In the numerical model developed for analyzing the time-dependent stability of side-exposed backfill, the CVISC model was applied for describing the creep behavior of rock mass. The CVISC model exhibits the linear relationship between the stress and long-term creep strain rate which captures the creep behavior of rocks when the applied stress is low. However, the CVISC model cannot reflect the non-linear creep strain rate when the applied stress exceeds the crack initiation threshold (Brantut et al. 2013; Aydan et al. 2014; Wang et al. 2019). The CVISC model is also not able to predict the time to delayed failure and creep strains of rocks in the tertiary creep stage. This may cause an underestimation of walls creep deformation applied on backfill when the exposure time is very long. More work is needed to introduce the developed creep model in Chapter 6 in a numerical code and apply it to evaluate the stability of side-exposed backfill.

- The developed creep model for rocks involves the value of crack initiation threshold (CIT). For a given rock, the CIT value can be identified as the start of acoustic emission, start of deviation of the axial stress-radial strain curves from the linearity, or start of dilation. When the measured CIT value is not available, it was commonly taken as a constant 50% of the short-term strength for most cases (Lajtai and Schmidtke 1986; Aubertin et al. 2000). However, some experiential results have shown that the ratio between the CIT and short-term strength of rocks can range from 30 to 70% (Brace et al. 1966; Aydan et al. 1994; Damjanac and Fairhurst 2010; Li et al. 2017). Moreover, this ratio also demonstrates dependency on confining pressures (Taheri et al. 2020). More work is needed to investigate the CIT value of rocks and its evolution with confining pressure.

- Another limitation refers to the linear evolution of backfill parameters during curing time in numerical simulations. The evolution of the backfill properties during curing time can be more complex than a linear function (Belem et al. 2000). Yilmaz (2018) reported that the UCS and elastic modulus of cemented backfill increase as the applied compressive stress increases during curing time due to the reduced porosity. More work is needed to consider this aspect in

numerical simulations because that the creep deformation of rock walls compresses the backfill and can lead to an increase in compression stresses within backfilled stope during curing time.

- The Mohr-Coulomb elasto-plastic model was applied for cemented backfill when evaluating its stability upon side exposure. Numerical results show that when the rock mass exhibits creep deformation, the stress states in a backfilled stope can significantly increases. In this condition, the volumetric yield under high isotropic loading and pressure dependent behavior of backfill (Pierce 1999; Rankine 2004) can not be represented by the Mohr-Coulomb model. Meanwhile, experimental results show that mining backfill with large cement content demonstrates strain softening under small confining pressures (Belem et al. 2000; Fall et al. 2007). The large confining pressure can also result in a strain hardening behavior of mining backfill. The post-peak behavior of backfill is not involved in the Mohr-Coulomb elastic perfectly plastic model.

- According to the comparisons of different constitutive models in simulating the one-dimensional consolidation and consolidated drained triaxial compression tests, the Soft Soil model is deemed applicable to modeling the compressibility of uncemented or lightly cemented backfill with a small cohesion value. More effort is needed to apply the Soft Soil model to analyze the stability of side-exposed backfill under the influence of rock-wall closure. However, one should note that the Soft Soil model cannot describe the effect of cementation on fill stiffness at low stress levels. It is also not able to represent the yielding of cement bond. More work is thus needed to investigate the effect of strong cementation on the compressibility of mining backfills and incorporate it in a constitutive model (Stewart et al. 1986; Liu and Cater 1999; Jafari et al. 2020).

- In numerical simulations in Chapters 3 and 5, the Poisson's ratio of backfill was related to its friction angle as $v = (1 - \sin\phi)/(2 - \sin\phi)$ to ensure a unique value of at-rest earth pressure coefficient (Duncan and Bursey 2013; Yang et al. 2018). This relationship should be further validated based on experimental results. Since the stress-strain curve of geomaterial is highly nonlinear, how to determine the Poisson's ratio of backfill based on the experimental results is a problem and needs to be studied in future works.

- The creep behavior of rocks is related the temperature. The rocks exhibit larger creep deformation under a given stress state when the temperature increases (Farmer 2012; Brantut

et al. 2013). The effect of temperature on the creep behavior of rocks is not considered in this project.

- More experimental works and in-situ measurements are desirable to validate the developed analytical and numerical solutions in this project.

CHAPTER 8   CONCLUSIONS AND RECOMMENDATIONS

8.1   Conclusions

The primary objective of the thesis is to evaluate the stability and mechanical behavior of backfill upon vertical exposure considering the closure of rock walls caused by the stope extraction and time-dependent creep deformation of rocks. The objective was achieved mainly based on numerical simulations with FLAC^{3D}. The solutions were verified with experimental results and some in-situ measurements in the literature. The study can be useful for the design of mining backfill and the optimizations of backfilling and mining operations. The main conclusions are recalled as follows:

- Pillar recovery needs stable backfill upon vertical exposure in open stoping mining. Three-dimensional numerical model was developed using FLAC^{3D} to evaluate the stability and determine the minimum required cohesion (c_{min}) of side-exposed backfill associated with rock walls instantaneous closure during adjacent extraction. The instability and c_{min} were determined by analyzing the coalescence of yield zones within backfill. Numerical results show that the dominant failure mechanism can be sliding or horizontal crushing failure. When the mine depth and rock-wall closure are small, wedge sliding failure is governing and rock-wall closure improves the stability of side-exposed backfill. The c_{min} becomes even smaller than those obtained with solutions considering fixed rock walls. The c_{min} decreases as the mine depth, fill stiffness, rock pressure coefficient, and fill-rock interface strength (friction angle and adhesion) increase. Increased rock mass stiffness, stope height and width result in an increase in c_{min}. When mine depth and rock-wall closure are large, the crushing failure becomes dominant. The c_{min} increases as the mine depth, stope height and length, fill stiffness and rock pressure coefficient increase. It decreases when the stope width and rock mass stiffness increase, and is insensitive to the varied strength of fill-rock interface. In all cases, the stability of side-exposed backfill improves when its internal frictional angle increases. The numerical model and instability criterion were verified with some centrifugal model tests in the literature.

- The time-dependent stability of side-exposed backfill associated with creep behavior of rock mass is another significant issue for mining engineers to design backfill and to optimize the mining and backfilling schedule. However, this problem has never been investigated before. To fill this gap, numerical simulations were performed using FLAC^{3D}. The creep deformation

of rock walls and mechanical parameters evolution of backfill during curing time were considered. Numerical results show that the empty time of primary stope does not significantly affect the stability and c_{min}. When mine depth is small and the rock exhibits little creep, it deserves to wait longer time before excavating adjacent stope in order for the backfill to gain more strength. When the mine depth is large or/and the rock exhibits heavy creep, the instability of side-exposed backfill can be dictated by crushing failure. Simply increasing the binder content may not be the best choice because a stronger backfill means also a harder backfill which is prone to be crushed. Rather, a softer backfill can be better through the use of lower binder content or/and with a shorter curing time. Once the adjacent secondary stope is mined out, it should be filled as soon as possible to prevent failure of side-exposed backfill. An optimization of the sizes of primary and secondary stopes is necessary to minimize the overall mining cost. The soft rock mass with small stiffness and viscosity coefficient leads to the decrease of c_{min} at a shallow mine depth, but requires a larger c_{min} to prevent crushing when the walls creep deformation is significant at a large mine depth. The applicability of numerical model was verified by comparing with the in-situ measurement of creep deformation in a tunnel.

- The compressibility of mining backfill governs its resistance to the closure of surrounding rock mass. Finding an appropriate constitutive model to better represent the compressibility of mining backfill in numerical simulations is challenging. Numerical modeling was conducted to compare the Mohr-Coulomb elasto-plastic model, double-yield model, and Soft Soil model in simulating the one-dimensional consolidation and consolidated drained triaxial compression tests made on lowly cemented backfills in the literature. The results show that the Soft Soil model can satisfactorily describe the experimental results while the application of the Mohr-Coulomb model and double-yield model shows poor description on the compressibility of the backfill submitted to large and cycle loading. The additional simulations of a backfilled stope overlying a sill mat indicate that the Soft Soil and Mohr-Coulomb models result in similar stress distributions when the rock-wall closure is absent. However, when the rock-wall closure due to underlying extraction is applied, application of the Soft Soil model shows that the Mohr-Coulomb model tends to overestimate the stresses in the backfill when the mine depth is small and underestimate the stresses when the mine depth is large due to the poor description of fill

compressibility. Thus, the Soft Soil model can be applied to describe the compressibility of uncemented or lightly cemented backfill with small cohesions under external compressions associated with rock-wall closure.

- The CVISC model used in time-dependent stability analyses cannot represent the tertiary creep stage of rocks. In most previous studies, curve fitting technique was applied on all experimental results of creep strain to calibrate the creep model which makes its predictive capability unknown. Therefore, a new creep model was developed to represent and predict creep strain and time to failure of rocks. The secondary creep strain rate of rocks was decomposed into the linear visco-elastic creep strain rate under a stress lower than the crack initiation threshold (CIT) and the non-linear creep strain rate under a stress higher than CIT. Subcritical crack growth is related to the non-linear creep strain rate and delayed failure of rocks. With the proposed creep model, the localization of micro cracks on the failure plane in creep tests making an angle of $45°-\phi/2$ with the major principal stress σ_1 is explained by the fact that among the numerous micro cracks, the cracks along this orientation are the first becoming instable. The developed creep model was calibrated based on part of experimental results of creep strain and time to failure available in the literature. The calibrated model was then applied to predict another part of the experimental results. The quite good agreements between the creep model and experimental results indicate that it is applicable to describing and predicting the creep strain and time to failure of rocks.

8.2 Recommendations

In addition to the outcomes presented in the thesis, recommendations are given on several aspects as following for further research to better understand the stability and geomechanical behavior of backfill associated with the closure of surrounding rock mass:

- The developed analytical and numerical models were verified with some experimental results and in-situ measurements available in the literature. Nonetheless, more experimental works are highly recommended to validate the proposed solutions.

- It is preferable to consider the influence of real irregular geometry and inclination angles of stopes on the stability of side-exposed backfill. The non-homogeneity and anisotropy of backfill and surrounding rock mass require further study.

- In the numerical model for stability evaluation of side-exposed backfill, the secondary stope is excavated in one step to simulate the sublevel stoping or long-hole stoping mining. The effect of varied mining methods and different mining sequences on the stability and required strength of backfill should be analyzed.

- The blasting vibrations caused by neighboring workings around backfilled stope may affect its stability upon exposure (Emad et al. 2012, 2018). More work is desirable on this aspect. It is also recommended to investigate the dissipation of excess pore water pressure in backfill during curing time and its effect on the compression stresses in the stope generated by the walls creep deformation.

- It is useful to analyze the combined effect of mechanical parameters of backfill including cohesion, friction angle, Young's modulus and involve it in the numerical modeling of side-exposed backfill. It is recommended to investigate the volumetric yield and pressure dependent behavior of backfill in the stope associated with the compression stresses generated by the rock walls closure. More realistic evolution of backfill parameters with curing time needs to be studied and considered in numerical modeling.

- The CVISC model used to simulate creep behavior of rocks cannot represent the tertiary creep stage. It is preferable to introduce the developed creep model in Chapter 6 in a numerical code and apply it to analyze the time-dependent stability of side-exposed backfill.

- The developed creep model for rocks was generally applied by considering a constant crack initiation threshold (CIT) as 0.5 of the short-term peak strength (Lajtai and Schmidtke 1986; Aubertin et al. 2000). More experimental work is needed to evaluate the value of CIT for different rocks. In particular, the variation of the CIT value for different confining pressures is desirable to be investigated.

- The Soft Soil model is recommended to be applied to analyze the stability of side-exposed backfill under the influence of rock-wall closure.

- More experimental work is desirable to study the post-peak behavior of cemented backfill with varied cement contents and curing time. It is also recommended to conduct laboratory tests to study the effect of cementation on the compressibility of cemented backfill.

- It is valuable to define and validate the relationship between the friction angle and the Poisson's ratio of mining backfills based on more experimental works.

- More work is required to investigate the influence of temperature on the creep behavior of rocks.

BIBLIOGRAPHY

Adachi, T., & Takase, A. (1981). Prediction of long term strength of soft sedimentary rock. *Proceedings of International Symposium on Weak Rock*. Tokyo, Japan, 99–104.

Alejano, L.R., Alonso, E., Rodriguez-Dono, A., & Fernandez-Manin, G. (2010). Application of the convergence-confinement method to tunnels in rock masses exhibiting Hoek-Brown strain-softening behaviour. *International Journal of Rock Mechanics and Mining Sciences*, 47(1), 150–160.

Amaratunga, L., & Yaschyshyn, D. (1997). Development of a high modulus paste fill using fine gold mill tailings. *Geotechnical & Geological Engineering,* 15(3), 205-219.

Amitrano, D., & Helmstetter, A. (2006). Brittle creep, damage, and time to failure in rocks. *Journal of Geophysical Research: Solid Earth*, 111, 1–17.

Anderson, T. (2014). A comparison of shallow and deep mining. *Proceedings of the 7th International Conference on Deep and High Stress Mining*. Sudbury, Canada, Australian Centre for Geomechanics, 181–187.

Andrade, E.N.D.C. (1910). On the viscous flow in metals, and allied phenomena. *Proceedings of the Royal Society of London*, *Series A*. The Royal Society, 1–12.

Andrade, E.N.D.C. (1914). The flow in metals under large constant stresses. *Proceedings of the Royal Society of London. Series A, Containing Papers of a Mathematical and Physical Character*, 90(619), 329–342.

Antonov, D. (2005). *Optimization of the use of cement in backfilling operations*. (Ph.D. thesis, École Polytechnique de Montréal).

Aref, K., Hassani, F., & Churcher, D. (1989). A study on liquefaction potential of paste backfill. *Innovations in Mining Backfill Technology*, 15–23.

Ashby, M.F., & Sammis, C.G. (1990). The damage mechanics of brittle solids in compression. *Pure and Applied Geophysics*, 133(3), 489–521.

Askew, J., McCarthy, P.L., & Fitzgerald, D.J. (1978). Backfill research for pillar extraction at ZC/NBHC. *Proceedings of 12th Canadian Rock Mechanics Symp*. Sudbury, Canada, Canadian Institute of Mining and Metallurgy, 100–110.

Aubertin, J.D., Hoentzsch, S., Diederichs, M.S., & Milton, H. (2018). Influence of the creep law on pillar response based on numerical simulations of an underground salt mine. *Proceedings of 52nd U.S. rock mechanics/geomechanics symposium*. Seattle, Washington, American Rock Mechanics Association.

Aubertin, M., Gill, D., & Ladanyi, B. (1991a). An internal variable model for the creep of rocksalt. *Rock Mechanics and Rock Engineering,* 24(2), 81–97.

Aubertin, M., Gill, D. E., & Ladanyi, B. (1991b). A unified viscoplastic model for the inelastic flow of alkali halides. *Mechanics of Materials,* 11(1), 63–82.

Aubertin, M., Bussiere, B., & Chapuis, R.P. (1996). Hydraulic conductivity of homogenized tailings from hard rock mines. *Canadian Geotechnical Journal*, 33(3), 470–482.

Aubertin, M., Sgaoula, J., Servant, S., Julien, M., & Gill, D. (1998). An up-to-date version of SUVIC-D for modeling the behavior of salt. *Series on rock and soil mechanics*, 205–220.

Aubertin, M., Li, L., & Simon, R. (2000). A multiaxial stress criterion for short-and long-term strength of isotropic rock media. *International Journal of Rock Mechanics and Mining Sciences*, 37(8), 1169–1193.

Aubertin, M., Li, L., Arnoldi, S., Belem, T., Bussière, B., Benzaazoua, M., & Simon, R. (2003). Interaction between backfill and rock mass in narrow stopes. *Proceedings of 12th Panamerican Conference on Soil Mechanics and Geotechnical Engineering and 39th U.S. Rock Mechanics Symposium*. Cambridge, Massachusetts, United States of America, 1157–1164.

Aubertin, M. (2013). Waste rock disposal to improve the geotechnical and geochemical stability of piles. *Proceedings of the world mining congress*. Montreal, Canada.

Aydan, O., Seiki, T., Jeong, G., & Tokashiki, N. (1994). Mechanical behaviour of rocks, discontinuities and rock masses. *Proceedings of International Symposium Pre-failure Deformation Characteristics of Geomaterials*. Sapporo, 1161–1168.

Aydan, O., & Nawrocki, P. (1998). Rate-dependent deformability and strength characteristics of rocks. *Proceedings of International symposium on the geotechnics of hard soils-soft rocks*. Naples, Italy, 403–411.

Aydan, O., & Kawamoto, T. (2000). The assessment of mechanical properties of rock masses through RMR rock classification system. *Proceedings of the GeoEng 2000 symposium*. Sydney, Australia.

Aydan, O., Ito, T., Özbay, U., Kwasniewski, M., Shariar, K., Okuno, T., Özgenoğlu, A., Malan, D.F., & Okada, T. (2014). ISRM suggested methods for determining the creep characteristics of rock. *Rock Mechanics and Rock Engineering*, 47(1), 275–290.

Aydan, O., Tokashiki, N., Ito, T., Akagi, T., Ulusay, R., & Bilgin, H. (2003). An experimental study on the electrical potential of nonpiezoelectric geomaterials during fracturing and sliding. *Proceedings of 10th ISRM Congress*. South Africa, International Society for Rock Mechanics, 73–78.

Barla, G., Barla, M., & Martinotti, M. (2010). Development of a new direct shear testing apparatus. *Rock Mechanics and Rock Engineering, 43*(1), 117–122.

Barla, G., Bonini, M., & Debernardi, D. (2010). Time dependent deformations in squeezing tunnels. *Proceedings of the 12th ISSMGE international conference of international association for computer methods and advances in geomechanics*. Goa, India, 4265–4275.

Barrett, J.R., & Cowling, R. (1980). Investigations of cemented fill stability in 1100 orebody, Mount Isa Mines, Ltd., Queensland, Australia. *Mining Technology IMM Transactions section A*, 89, A118–A128.

Barrett, J.R., Coulthard, M.A., & Dight, P.M. (1978). Determination of fill stability. *Proceedings of 12th Canadian Rock Mechanics Symp*. Sudbury, Canada, Canadian Institute of Mining and Metallurgy, 85–91.

Been, K., Brown, E., & Hepworth, N. (2002). Liquefaction potential of pastefill at Neves Corvo Mine. *Portugal, Mining Technology, 111*(1), 47–58.

Behera, S., Prashant, C., Mishra, D., Mandal, P., Verma, A., Mohanty, S., Mishra, K., & Singh, P. (2019). Slump test: laboratory and numerical simulation–based approach for consistency of mill tailings paste. *Current Science, 117*(2), 235.

Belem, T., Benzaazoua, M., & Bussière, B. (2000). Mechanical behaviour of cemented paste backfill. *Proceedings of 53rd Canadian Geotechnical Conference*. Montreal, Canada,

Canadian Geotechnical Society, 373–380.

Belem, T., Bussière, B., & Benzaazoua, M. (2001). The effect of microstructural evolution on the physical properties of paste backfill. *Proceedings of Tailings and Mine Waste*. Balkema, Rotterdam.

Belem, T., El Aatar, O., Bussière, B., Benzaazoua, M., Fall, M., & Yilmaz, E. (2006). Characterisation of self-weight consolidated paste backfill. *Proceedings of the 9th International Seminar on Paste and Thickened Tailings*. Perth, 333–345.

Belem, T., & Benzaazoua, M. (2008). Design and application of underground mine paste backfill technology. *Geotechnical and Geological Engineering, 26*(2), 147–174.

Benz, T., & Schwab, R. (2008). A quantitative comparison of six rock failure criteria. *International Journal of Rock Mechanics and Mining Sciences*, 45(7), 1176–1186.

Benzaazoua, M., Bussière, B., Demers, I., Aubertin, M., Fried, É., & Blier, A. (2008). Integrated mine tailings management by combining environmental desulphurization and cemented paste backfill: Application to mine Doyon, Quebec, Canada. *Minerals Engineering, 21*(4), 330–340.

Bérest, P., Béraud, J., Gharbi, H., Brouard, B., & DeVries, K. (2015). A very slow creep test on an Avery Island salt sample. *Rock Mechanics and Rock Engineering, 48*(6), 2591–2602.

Bérest, P., Gharbi, H., Brouard, B., Brückner, D., DeVries, K., Hévin, G., Hofer, G., Spiers, C., & Urai, J. (2019). Very slow creep tests on salt samples. *Rock Mechanics and Rock Engineering*, 52(9), 2917–2934.

Bieniawski, Z. T. (1970). Time-dependent behaviour of fractured rock. *Rock Mechanics, 2*(3), 123–137.

Bieniawski, Z.T. (1989). *Engineering rock mass classifications: a complete manual for engineers and geologists in mining, civil, and petroleum engineering*. New York: Wiley.

Blight, G.E., & Clarke, I.E. (1983). Design and properties of stiff fill for lateral support of pillars. *Proceedings of International Symp on Mining with Backfill*. Lulea, Sweden, 303–307.

Bonini, M., Debernardi, D., Barla, M., & Barla, G. (2009). The mechanical behaviour of clay shales and implications on the design of tunnels. *Rock Mechanics and Rock Engineering*, 42(2), 361–388.

Börgesson, L. (1981). Mechanical properties of hydraulic backfill. *Proceedings of Conference on the Application of Rock Mechanics to Cut and Fill Mining*. London, The Institution of Mining and Metallurgy, 193–203

Borquez, G. (1981). Sequence of the Analysis of a Block Caving Mining Method. *Design and Operation of Caving and Sublevel Stoping Mines. SME of AIME*. New York, 283–297.

Boukharov, G., Chanda, M., & Boukharov, N. (1995). The three processes of brittle crystalline rock creep. *International Journal of Rock Mechanics and Mining Sciences*, 32(4), 325–335.

Boulianne, M., Simon, R., & Aubertin, M. (2004). A numerical investigation of the creep (viscoplastic) behaviour of circular opening and pillar in rock salt. *Proceedings of 57th Canadian geotechnical conference and the 5th joint CGS-IAH conference*. Quebec City, 25–32.

Bowles, L. (1996). *Foundation analysis and design*. New York: McGraw-hill.

Brace, W., Paulding, Jr. B., Scholz, C. (1966). Dilatancy in the fracture of crystalline rocks. *Journal of Geophysical Research*, 71(16), 3939–3953.

Brady, A.C, & Brown, J.A (2002). Hydraulic fill at Osborne mine. *Proceedings of the 8th Underground Operators' Conference*. Townsville, Australia, 161–165.

Brady, B.H., & Brown, E.T. (2004). *Rock mechanics: for underground mining*: Springer science & business media.

Brantut, N., Baud, P., Heap, M., & Meredith, P. (2012). Micromechanics of brittle creep in rocks. *Journal of Geophysical Research*, 117(B08412).

Brantut, N., Heap, M., Meredith, P., & Baud, P. (2013). Time-dependent cracking and brittle creep in crustal rocks: A review. *Journal of Structural Geology, 52*, 17-43.

Brinkgreve, R.B.J. (1996). *Geomaterial models and numerical analysis of softening*. (Ph.D. thesis, Delft University of Technology).

Brinkgreve, R.B.J. (2005). Selection of soil models and parameters for geotechnical engineering application. *Proceedings of Geo-Frontiers Congress*. Austin, Texas, United States, American Society of Civil Engineers, 69–98.

Brown, E.T. (2012). Progress and challenges in some areas of deep mining. *Mining Technology*, 121(4), 177–191.

Brummer, R. (1991). Paste-the fill of the future. 1. *Canadian Mining Journal*, 112, 31–5.

Bullock, R.L. (2011). Comparison of underground mining methods. *SME Mining Engineering Handbook*. USA: Society for Mining, Metallurgy, and Exploration, Inc, 385–403.

Burland, J.B. (1965). Correspondence on the yielding and dilation of clay. *Géotechnique*, 15(2), 211–214.

Bussière, B. (2007). Colloquium 2004: Hydrogeotechnical properties of hard rock tailings from metal mines and emerging geoenvironmental disposal approaches. *Canadian Geotechnical Journal, 44*(9), 1019-1052.

Caceres, C., Moffat, R., & Pakalnis, R. (2017). Evaluation of flexural failure of sill mats using classical beam theory and numerical models. *International Journal of Rock Mechanics and Mining Sciences*, 99, 21–27.

Campanella, R., & Vaid, Y. (1974). Triaxial and plane strain creep rupture of an undisturbed clay. *Canadian Geotechnical Journal*, 11(1), 1–10.

Canadian Geotechnical Society. (1978). *Canadian foundation engineering manual*. Canada, BiTech Publishers Ltd.

Cao, S., Yilmaz, E., & Song, W. (2018). Evaluation of viscosity, strength and microstructural properties of cemented tailings backfill. *Minerals*, 8(8), 352.

Carranza-Torres, C. (2004). Elasto-plastic solution of tunnel problems using the generalized form of the Hoek-Brown failure criterion. *International Journal of Rock Mechanics and Mining Sciences*, 41(3), 480–481.

Chai, S. (2020). *Analytical and Numerical Studies on the Stresses in Backfilled Stopes and the Stability of Side-Exposed Backfill in Inclined Stopes.* (Master's thesis, Polytechnique

Montréal).

Chandler, N.A., & Martin, C.D. (1995). An analysis of laboratory and long-term rock strength using a sliding crack model. *Proceedings of the 35th US Symposium on Rock Mechanics (USRMS)*. American Rock Mechanics Association, 741–747.

Chang, K., Ge, L., & Lin, H. (2015). Slope creep behavior: observations and simulations. *Environmental Earth Sciences, 73*(1), 275–287.

Chapuis, R.P., & Aubertin, M. (2003). On the use of the Kozeny Carman equation to predict the hydraulic conductivity of soils. *Canadian Geotechnical Journal, 40*(3), 616–628.

Charles, R. (1958). Static fatigue of glass. I. *Journal of Applied Physics*, 29(11), 1549–1553.

Charles, R. (1959). The strength of silicate glasses and some crystalline oxides. *Proceedings of International Conference on the Atomic Mechanisms of Fracture*. Swampscott, Massachusetts, 225–49.

Chin, H.P., & Rogers, J.D. (1987). Creep parameters of rocks on an engineering scale. *Rock Mechanics and Rock Engineering*, 20(2), 137–146.

Clark, I.H. (1991). The cap model for stress path analysis of mine backfill compaction processes. *Proceedings of 7th International Conference on Computer Methods and Advances in Geomechanics*. Cairns, Australia, 1293–1298.

Cooke, R. (2006). Thickened and paste tailings pipeline systems: Design procedure–Part 1. *Proceedings of the 9th International Seminar on Paste and Thickened Tailings*. Perth, Australia.

Coulomb, C.A. (1773). Sur une Application des regles de mximus et mnimus a qelques poblemes de satique rlatits a l'architecture. *Academie Royale des Sciences, Memoires de Mathermatiques et de Physique par Divers Sowans*, 7, 343–382.

Coulthard, M.A. (1980). Numerical analysis of fill pillar stability: Three dimensional linearly elastic finite element calculations. *Technical Report*. Australia, Division of Applied Geomechanics, Commonwealth Scientific and Industrial Research Organization;.

Coulthard, M.A. (1999). Applications of numerical modelling in underground mining and

construction. *Geotechnical and Geological Engineering*, 17(3-4), 373–385.

Coulthard, M.A., & Dight, P.M. (1980). Numerical analysis of failed cemented fill at ZC/NBHC Mine, Broken Hill. *Proceedings of 3rd Australia-New Zealand conference on geomechanics*. Wellington, Institution of Professional Engineers New Zealand, 145–151.

Counter, D. (2014). Kidd Mine–dealing with the issues of deep and high stress mining–past, present and future*. Proceedings of the seventh international conference on deep and high stress mining*. Perth, Australia.

Cowling, R., Grice, A., & Isaacs, L. (1988). Simulation of hydraulic filling of large underground mining excavations. *Proceedings of 6th International Conference on Numerical Methods in Geomechanics*. Innsbruck, Austria.

Cristescu, N., & Hunsche, U. (1998). *Time effects in rock mechanics*. New York: Wiley.

Cui, L., & Fall, M. (2015). A coupled thermo–hydro-mechanical–chemical model for underground cemented tailings backfill. *Tunnelling and Underground Space Technology*, 50, 396–414.

Cundall, P., Shillabeer, J.H., & Herget, G. (1978). Modelling to predict rock fill stability in transverse pillar extraction. *Proceedings of 12th Canadian Rock Mechanics Symp*. Sudbury, Canada, Canadian Institute of Mining and Metallurgy, 92–99.

Cundall, P., Carranza-Torres, C., & Hart, R. (2003). A new constitutive model based on Hoek-Brown criterion. *Proceedings of 3rd International Symp on FLAC and FLAC3D Numerical Modelling in Geomechanics*. Sudbury, Canada, 17–25.

Damjanac, B., & Fairhurst, C. (2010). Evidence for a long-term strength threshold in crystalline rock. *Rock Mechanics and Rock Engineering, 43*(5), 513–531.

Darling, P. (2011). *SME mining engineering handbook*. Denver: Society for Mining, Metallurgy and Exploration.

Das, S., & Scholz, C. (1981). Theory of time-dependent rupture in the earth. *Journal of Geophysical Research*, 86(B7), 6039–6051.

Diederichs, M., Kaiser, P., & Eberhardt, E. (2004). Damage initiation and propagation in hard rock during tunneling and the influence of near-face stress rotation. *International Journal of Rock Mechanics and Mining Sciences*, 41(5), 785–812.

Dirige, A.P.E., McNearny, R.L., & Thompson, D.S. (2009). The effect of stope inclination and wall rock roughness on back-fill free face stability. *Proceedings of the 3rd Canada–US Rock Mechanics Symposium*. Toronto.

Dirige, A.P.E., & De Souza, E. (2013). Mechanics of failure of paste backfill face exposure during adjacent mining. *Proceedings of 23rd World Mining Congress*. Montreal, Canada.

Duncan, J.M., Williams, G.W., Sehn, A.L., & Seed, R.B. (1991). Estimation earth pressures due to compaction. *Journal of Geotechnical Engineering*, 117(12), 1833–1847.

Duncan, J.M., & Bursey, A. (2013). Soil modulus correlations. *Foundation engineering in the face of uncertainty: Honoring Fred H. Kulhawy*. ASCE, 321–336.

Durrheim, R.J., & Riemer, K. (2012). History of endeavours to mitigate the rockburst risk in South African mines. *Proceedings of International Mining History Congress*. Johannesburg, South Africa.

Dusseault, M.B., & Fordham, C.J. (1993). Time-dependent behavior of rocks. *In: Hudson JA (ed) Rock testing and site characterization*. Pergamon, 119–149.

El Mkadmi, N., Aubertin, M., & Li, L. (2014). Effect of drainage and sequential filling on the behavior of backfill in mine stopes. *Canadian Geotechnical Journal*, 51(1), 1–15.

Emad, M.Z., Mitri, H.S., & Henning, J.G. (2012). Effect of blast vibrations on the stability of cemented rockfill. *International Journal of Mining, Reclamation and Environment, 26*(3), 233–243.

Emad, M.Z., Mitri, H.S., & Kelly, C. (2014). Effect of blast-induced vibrations on fill failure in vertical block mining with delayed backfill. *Canadian Geotechnical Journal, 51*(9), 975–983.

Emad, M.Z., Mitri, H.S., & Kelly, C. (2015). State-of-the-art review of backfill practices for sublevel stoping system. *International Journal of Mining, Reclamation and Environment, 29*(6), 544–556.

Emad, M.Z., Mitri, H.S., & Kelly, C. (2018). Dynamic model validation using blast vibration monitoring in mine backfill. *International Journal of Rock Mechanics and Mining Sciences*, 107, 48–54.

Fahimifar, A., Karami, M., & Fahimifar, A. (2015). Modifications to an elasto-visco-plastic constitutive model for prediction of creep deformation of rock samples. *Soils and Foundations, 55*(6), 1364–1371.

Fairhurst, C. (2017). Some challenges of deep mining. *Engineering, 3*(4), 527–537.

Falaknaz, N. (2014). *Analysis of the geomechanical behavior of two adjacent backfilled stopes based on two and three dimensional numerical simulations* (Ph.D. thesis, École Polytechnique de Montréal).

Falaknaz, N., Aubertin, M., & Li, L. (2015). Numerical investigation of the geomechanical response of adjacent backfilled stopes. *Canadian Geotechnical Journal, 52*(10), 1507–1525.

Fall, M., & Nasir, O. (2010). Mechanical behaviour of the interface between cemented tailings backfill and retaining structures under shear loads. *Geotechnical and Geological Engineering*, 28, 779–790.

Fall, M., Adrien, D., Célestin, J., Pokharel, M., & Touré, M. (2009). Saturated hydraulic conductivity of cemented paste backfill. *Minerals Engineering*, 22(15), 1307–1317.

Fall, M., Belem, T., Samb, S., & Benzaazoua, M. (2007). Experimental characterization of the stress-strain behaviour of cemented paste backfill in compression. *Journal of Materials Science*, 42(11), 3914–3922.

Fall, M., Célestin, J., Pokharel, M., & Touré, M. (2010). A contribution to understanding the effects of curing temperature on the mechanical properties of mine cemented tailings backfill. *Engineering Geology*, 114(3-4), 397–413.

Fang, K., & Fall, M. (2018). Effects of curing temperature on the shear behaviour of cemented paste backfill-rock interface. *International Journal of Rock Mechanics and Mining Sciences*, 112, 184–192.

Fang, K., & Fall, M. (2019). Chemically induced changes in the shear behaviour of the interface between rock and tailings backfill undergoing cementation. *Rock Mechanics and Rock Engineering*, 52, 3047–3062.

Fang, K., & Fall, M. (2020). Shear behavior of the interface between rock and cemented backfill: effect of curing stress, drainage condition and backfilling rate. *Rock Mechanics and Rock Engineering*, 53, 325–336.

Fang, K., & Fall, M. (2021). Shear behaviour of rock–tailings backfill interface: effect of cementation, rock type, and rock surface roughness. *Geotechnical and Geological Engineering*, 39, 1753–1770.

Farmer, I.W. (2012). *Engineering behaviour of rocks*. Springer Science & Business Media.

Farsangi, P.N. (1996). *Improving cemented rockfill design in open stoping*. (Ph.D. thesis, McGill University).

Feng, X.T., Chen, B.R., Yang, C., & Zhou, H. (2006). Intelligent analysis of rheological characteristic of rock materials. *Proceedings of EUROCK 2006—Multiphysics coupling and long term behaviour in rock mechanics*. Taylor & Francis Group, London, 275–280.

Ferraris, C.F., & de Larrard, F. (1998). Modified slump test to measure rheological parameters of fresh concrete. *Cement, Concrete and Aggregates*, 20(2), 241–247.

Fourie, A.B., Gürtunca, R.G., De Swardt, G., & Wendland, E. (1993). An evaluation of four constitutive models for the simulation of backfill behaviour. *Proceedings of 5th International Symposium on Mining with Backfill*. Johannesburg, South Africa, 33–38.

Freiman, S. (1984). Effects of chemical environments on slow crack growth in glasses and ceramics. *Journal of Geophysical Research: Solid Earth, 89*(B6), 4072–4076.

Fuenkajorn, K., & Phueakphum, D. (2010). Effects of cyclic loading on mechanical properties of Maha Sarakham salt. *Engineering Geology, 112*(1-4), 43–52.

Garofalo, F. (1965). *Fundamentals of creep and creep-rupture in metals*. New York: Macmillan.

Gasc-Barbier, M., Chanchole, S., & Bérest, P. (2004). Creep behavior of Bure clayey rock. *Applied Clay Science*, 26(1-4), 449–458.

Ghirian, A., & Fall, M. (2015). Coupled behavior of cemented paste backfill at early ages. *Geotechnical and Geological Engineering*, 33(5), 1141–1166.

Godbout, J., Bussière, B., & Belem, T. (2007). Evolution of cemented paste backfill saturated hydraulic conductivity at early curing time**. *Proceedings of 60th Canadian geotechnical conference and the 8th joint CGS/IAH-CNC groundwater conference*. Ottawa, 2230–2236.

Gonano, L.P., & Kirkby, R.W. (1977). In situ investigation of cemented rockfill in the 1100 orebody, Mount Isa Mine, Queensland. *Technical Report*. Australia: Division of Applied Geomechanics, Commonwealth Scientific and Industrial Research Organization.

Goodman, R. (1989). *Introduction to rock mechanics*. New York: Wiley.

Grabinsky, M.W., & Bawden, W.F. (2007). In situ measurements for geomechanical design of cemented paste backfill systems. *Proceedings of 9th International Symp on Mining with Backfill*. Montreal, Canada, Canadian Institute of Mining, Metallurgy and Petroleum, 1–8.

Grabinsky, M.W. (2010). In situ monitoring for ground truthing paste backfill designs. *Proceedings of the 13th International Seminar on Paste and Thickened Tailings*. Perth, Australia, Australian Centre for Geomechanics, 85–98.

Green, H.W. (1984). "Pressure solution" creep: some causes and mechanisms. *Journal of Geophysical Research: Solid Earth*, 89(B6), 4313–4318.

Grice, A.G. (2005). Introduction to hydraulic fill. *Handbook on Mine Fill*, 66–80.

Grice, A.G. (2001). Recent mine fill developments in Australia. *Proceedings of the 7th international symposium on mining with Backfill: Minefill*. Seattle, Society for Mining, Metallurgy and Exploration.

Grice, T. (1998). Underground mining with backfill. *Proceedings of 2nd Annual Summit-Mine Tailings Disposal Systems*. Brisbane, Australia, 24–25.

Griggs, D. (1939). Creep of rocks. *The Journal of Geology*, 47(3), 225–251.

Guler, G. (1998). *Analysis of the rock mass behaviour as associated with Ventersdorp Contact Reef stopes, South Africa*. (Master's thesis, University of the Witwatersrand, Johannesburg).

Gupta, A.K., & Paul, B. (2017). Comparative analysis of different materials to be used for

backfilling in underground mine voids with a particular reference to hydraulic stowing. *International Journal of Oil, Gas and Coal Technology, 15*(4), 425–434.

Hallbauer, D., Wagner, H., & Cook, N. (1973). Some observations concerning the microscopic and mechanical behaviour of quartzite specimens in stiff, triaxial compression tests. *International Journal of Rock Mechanics and Mining Sciences*, 10(6), 713–726.

Hamrin, H. (2001). Underground mining methods and applications. *Underground mining methods: Engineering fundamentals and international case studies*. Society for Mining, Metallurgy and Exploration, 3–14.

Hao, S.W., Zhang, B.J., Tian, J.F., & Elsworth, D. (2014). Predicting time-to-failure in rock extrapolated from secondary creep. *Journal of Geophysical Research: Solid Earth, 119*(3), 1942–1953.

Hao, S.W., Liu, C., Wang, Y., & Chang, F. (2017). Scaling law of average failure rate and steady-state rate in rocks. *Pure and Applied Geophysics*, 174(6), 2199–2215.

Hardy, H.R., Kim, R.Y., Stefanko, R., & Wang, Y.J. (1969). Creep and microseismic activity in geologic materials. *Proceedings of the 11th US Symposium on Rock Mechanics (USRMS)*. American Rock Mechanics Association, 377–414.

Hartman, H.L. (1992). *SME mining engineering handbook, 2nd edn*. Littleton: Society for Mining, Metallurgy, and Exploration.

Haruna, S., & Fall, M. (2020). Time-and temperature-dependent rheological properties of cemented paste backfill that contains superplasticizer. *Powder Technology, 360*, 731–740.

Hasanpour, R., Rostami, J., & Barla, G. (2015). Impact of advance rate on entrapment risk of a double-shielded TBM in squeezing ground. *Rock Mechanics and Rock Engineering*, 48(3), 1115–1130.

Hassani, F., & Archibald, J. (1998). *Mine backfill 1998*. Canadian Institute of Mining, Metallurgy and Petroleum.

Heap, M., Baud, P., Meredith, P.G., Bell, A., & Main, I. (2009). Time-dependent brittle creep in Darley Dale sandstone. *Journal of Geophysical Research*, 114(B07203).

Heap, M.J., Baud, P., Meredith, P.G., Vinciguerra, S., Bell, A., & Main, I. (2011). Brittle creep in basalt and its application to time-dependent volcano deformation. *Earth and Planetary Science Letters, 307*(1-2), 71–82.

Heap, M.J., Baud, P., & Meredith, P.G. (2009). Influence of temperature on brittle creep in sandstones. *Geophysical Research Letters*, 36(19), L19305.

Helinski, M., Fahey, M., & Fourie, A. (2007). Numerical modeling of cemented mine backfill deposition. *Journal of Geotechnical and Geoenvironmental Engineering*, 133(10), 1308–1319.

Henderson, A., Revell, M., Landriault, D., & Coxon, J. (2005). Paste fill. *Handbook on Mine Fill*. Australian Centre for Geomechanics, 83–97.

Herget, G., & De Korompay, V. (1978). In-situ drainage properties of hydraulic backfills. *Proceedings of 12th Canadian Rock Mechanics Symposium*. Sudbury, Ontario, 23–25.

Herget, G. (1988). *Stresses in rock*. Rotterdam: AA Balkema.

Hiramatsu, Y., & Oka, Y. (1962). Analysis of stress around a circular shaft or drift excavated in ground in a three dimensional stress state. *Journal of Mining and Metallurgy Institute of Japan*, 78, 93–98.

Hiramatsu, Y., & Oka, Y. (1968). Determination of the stress in rock unaffected by boreholes or drifts, from measured strains or deformations. *International Journal of Rock Mechanics and Mining Sciences & Geomechanics Abstracts*, 5(4), 337–353.

Hirata, T., Satoh, T., & Ito, K. (1987). Fractal structure of spatial distribution of microfracturing in rock. *Geophysical Journal International*, 90(2), 369–374.

Hoek, E., & Brown, E.T. (1997). Practical estimates of rock mass strength. *International Journal of Rock Mechanics and Mining Sciences*, 34(8), 1165–1186.

Hoek, E., Kaiser, P.K., & Bawden, W.F. (2000.). *Support of underground excavations in hard rock*. Rotterdam: AA Balkema.

Hoek, E., & Brown, E.T. (2019). The Hoek–Brown failure criterion and GSI–2018 edition. *Journal of Rock Mechanics and Geotechnical Engineering*, 11(3), 445–463.

Innocente, J.C., Paraskevopoulou, C., & Diederichs, M.S. (2021). Estimating the long-term

strength and time-to-failure of brittle rocks from laboratory testing. *International Journal of Rock Mechanics and Mining Sciences, 147*, 104900.

Itasca. (2013). *FLAC3D—Fast lagrangian analysis of continua in 3 dimensions, user's guide, version 5.01*. Minneapolis: Itasca Consulting Group.

Itasca. (2019). *FLAC3D—Fast Lagrangian analysis of continua in 3 dimensions; user's guide, version 7.0*. Minneapolis: Itasca Consulting Group.

Ito, H. (1991). On rheological behaviour of in situ rock based on long-term creep experiments. *Proceedings of 7th ISRM Congress*. Aachen, Germany.

Jaeger, J.C. (1969). *Elasticity, fracture and flow: with engineering and geological applications*. London: Chapman and Hall.

Jaeger, J.C., Cook, N.G.W., & Zimmerman, R. (2009). *Fundamentals of rock mechanics*. John Wiley & Sons.

Jafari, M., Shahsavari, M., & Grabinsky, M. (2020). Experimental study of the behavior of cemented paste backfill under high isotropic compression. *Journal of Geotechnical and Geoenvironmental Engineering*, 146(11), 06020019.

Jafari, M., Shahsavari, M., & Grabinsky, M. (2021). Drained Triaxial Compressive Shear Response of Cemented Paste Backfill (CPB). *Rock Mechanics and Rock Engineering*, 1–17.

Jahanbakhshzadeh, A., Aubertin, M., & Li, L. (2017). A new analytical solution for the stress state in inclined backfilled mine stopes. *Geotechnical and Geological Engineering*, 35(3), 1151–1167.

Jahanbakhshzadeh, A., Aubertin, M., & Li, L. (2018a). Analysis of the stress distribution in inclined backfilled stopes using closed-form solutions and numerical simulations. *Geotechnical and Geological Engineering*, 36(2),1011–1036.

Jahanbakhshzadeh, A., Aubertin, M., & Li, L. (2018b). Three-dimensional stress state in inclined backfilled stopes obtained from numerical simulations and new closed-form solution. *Canadian Geotechnical Journal*, 55(6), 810–828.

Jalbout, A., & Simser, B. (2014). Rock mechanics tools for mining in high stress ground conditions

at Nickel Rim South Mine. *Proceedings of the Seventh International Conference on Deep and High Stress Mining*. Perth, Australian Centre for Geomechanics, 189–208.

Jaouhar, E.M., Li, L., & Aubertin, M. (2018). An analytical solution for estimating the stresses in vertical backfilled stopes based on a circular arc distribution. *Geomechanics and Engineering*, 15(3), 889–898.

Jeffieys, H. (1958). A modification of Lomnitz's law of creep in rocks. *Geophysical Journal International*, 1(1), 92–95.

Johnson, J., Seymour, J., Martin, L., Stepan, M., Arkoosh, A., & Emery, T. (2015). Strength and elastic properties of paste backfill at the Lucky Friday Mine, Mullan, Idaho. *Proceedings of the 49th US Rock Mechanics/Geomechanics Symposium*. San Francisco, American Rock Mechanics Association.

Julien, M.R., Foerch, R., Aubertin, M., & Cailletaud, G. (1998). Some aspects of the numerical implementation of SUVIC-D. *Proceedings of 4th Conference on the Mechanical Behavior of Salt*. Clausthal-Zellerfeld, Germany, Trans Tech Publications, 389–404.

Kahlström, M. (2013). *Plaxis 2D comparison of Mohr-Coulomb and soft soil material models*. (Master's thesis, Luleå University of Technology).

Kamali-Asl, A., Ghazanfari, E., Newell, P., & Stevens, M. (2018). Elastic, viscoelastic, and strength properties of Marcellus Shale specimens. *Journal of Petroleum Science and Engineering*, 171, 662–679.

Karim, R., Simangunsong, G.M., Sulistianto, B., & Lopulalan, A. (2013). Stability analysis of paste fill as stope wall using analytical method and numerical modeling in the Kencana underground gold mining with long hole stope method. *Procedia Earth and Planetary Science*, 6, 474–484.

Keita, A.M.T., Jahanbakhshzadeh, A., & Li, L. (2021a). Numerical analysis of the stability of arched sill mats made of cemented backfill. *International Journal of Rock Mechanics and Mining Sciences*, 140, 104667.

Keita, A.M.T., Jahanbakhshzadeh, A., & Li, L. (2021b). Numerical analysis of the failure mechanisms of sill mats made of cemented backfill. *International Journal of Geotechnical Engineering*, 1–13.

Kemeny, J.M. (1991). A model for non-linear rock deformation under compression due to sub-critical crack growth. *International Journal of Rock Mechanics and Mining Sciences*, 28, 459–467.

King, R.G., Jager, A.J., Roberts, M.K.C., & Turner, P.A. (1989). Rock mechanics aspects of stoping without back-area support. *Research Report*. CSIR, Pretoria.

Koohestani, B., Darban, A.K., & Mokhtari, P. (2018). A comparison between the influence of superplasticizer and organosilanes on different properties of cemented paste backfill. *Construction and Building Materials*, 173, 180–188.

Kortnik, J. (2021). Green mining–use of hydraulic backfill in the Velenje Coal Mine. *Proceedings of the 13th International Symposium on Mining with Backfill*. Katowice, Poland, 422–432.

Kranz, R.L. (1980). The effects of confining pressure and stress difference on static fatigue of granite. *Journal of Geophysical Research: Solid Earth*, 85(B4), 1854–1866.

Kuganathan, K. (2002). A method to design efficient mine backfill drainage systems to improve safety and stability of backfill bulkheads and fills. *Proceedings of 8th AUSIMM Underground Operators Conference: Growing our Underground Operations*. Townville, Australia.

Kuganathan, K. (2005). Rock fill in mine fill. *Handbook on Mine Fill*. Perth, Australian Centre for Geomechanics, 101–115.

Kuganathan, K., & Sheppard, I. (2001). A non-segregating 'Rocky Paste Fill' (RPF) produced by co-disposal of cemented de-slimed tailings slurry and graded rockfill. *Proceedings of the Minefill 2001: 7th International Symposium on Mining with Backfill*. Seattle, Society for Mining, Metallurgy and Exploration.

Labuz, J.F., & Zang, A. (2012). Mohr–Coulomb failure criterion. *Rock Mechanics and Rock Engineering*, 45(6), 975–979.

Ladanyi, B. (1974). Use of the long-term strength concept in the determination of ground pressure on tunnel linings. *Proceedings of the 3rd Congress of International Society of Rock Mechanics on Advances in Rock Mechanics*. Washington, National Academy of Science.

Ladanyi, B., & Gill, D. (1988). Design of tunnel linings in a creeping rock. *International Journal*

of Mining and Geological Engineering, 6(2), 113–126.

Lagger, M., Henzinger, M.R., & Schubert, W. (2016). Numerical investigations on pea gravel using a nonlinear constitutive model. *Proceedings of ISRM International Symposium-EUROCK*. Cappadocia, Yurkey, 521–526.

Lajtai, E.Z., & Schmidtke, R.H. (1986). Delayed failure in rock loaded in uniaxial compression. *Rock Mechanics and Rock Engineering*, 19(1), 11–25.

Lei, X., Kusunose, K., Satoh, T., & Nishizawa, O. (2003). The hierarchical rupture process of a fault: an experimental study. *Physics of the Earth and Planetary Interiors*, 137(1-4), 213–228.

Lessard, G. (2011). Essais d'infiltration sur la halde à stériles Petit-Pas de la mine Tio, Havre-St-Pierre. *Rapport de maîtrise.* Département des génies civil, géologique et des mines. École Polytechnique de Montréal, Canada.

Li, L. (1997) *Étude expérimentale du comportement hydromécanique d'une fracture*. (Ph.D. Thesis, Paris 7).

Li, L., Aubertin, M., Simon, R., Bussière, B., & Belem, T. (2003). Modeling arching effects in narrow backfilled stopes with FLAC. *Proceedings of 3rd International Symposium on FLAC and FLAC3D Numerical Modelling in Geomechanics*. Sudbury, Canada, 211–219.

Li, L., Aubertin, M., & Belem, T. (2005). Formulation of a three dimensional analytical solution to evaluate stresses in backfilled vertical narrow openings. *Canadian Geotechnical Journal, 42*(6), 1705–1717.

Li, L., & Aubertin, M. (2008). An improved analytical solution to estimate the stress state in subvertical backfilled stopes. *Canadian Geotechnical Journal, 45*(10), 1487–51496.

Li, L., & Aubertin, M. (2009). Numerical investigation of the stress state in inclined backfilled stopes. *International Journal of Geomechanics, 9*(2), 52–562.

Li, L., Aubertin, M., & Shirazi, A. (2010). Implementation and application of a new elastoplastic model based on a multiaxial criterion to assess the stress state near underground openings. *International Journal of Geomechanics*, 10(1), 13–21.

Li, L., & Aubertin, M. (2012). A modified solution to assess the required strength of exposed

backfill in mine stopes. *Canadian Geotechnical Journal*, 49(8), 994–1002.

Li, L. (2014a). Generalized solution for mining backfill design. *International Journal of Geomechanics*, 14(3), 04014006.

Li, L. (2014b). Analytical solution for determining the required strength of a side-exposed mine backfill containing a plug. *Canadian Geotechnical Journal*, 51(5), 508–519.

Li, L., & Aubertin, M. (2014). An improved method to assess the required strength of cemented backfill in underground stopes with an open face. *International Journal of Mining Science and Technology*, 24(4), 549–558.

Li, L., Aubertin, M., & Simon, R. (2017). The MSDP$_u$ multiaxial criterion for the strength of rocks and rock masses. *Rock Mechanics and Engineering*. CRC Press, 409–436.

Li, X., Qi, C., Shao, Z., & Qu, X. (2018). Static shear fracture influenced by historic stresses path and crack geometries in brittle solids. *Theoretical and Applied Fracture Mechanics*, 96, 64–71.

Li, Y., & Xia, C. (2000). Time-dependent tests on intact rocks in uniaxial compression. *International Journal of Rock Mechanics and Mining Sciences*, 37(3), 467–475.

Lingga, B.A. (2018). *Investigation of cemented rockfill properties used at a Canadian diamond mine*. (Master's thesis, University of Alberta).

Liston, D. (2014). Utilisation of cemented rockfill, cemented hydraulic fill and paste to successfully achieve ore production expansion to 2 Mtpa at Chelopech Mine. *Proceedings of the Eleventh International Symposium on Mining with Backfill*. Perth, Australian Centre for Geomechanics, 407–420.

Liu, G., Li, L., Yang, X., & Guo, L. (2016a). Stability analyses of vertically exposed cemented backfill: A revisit to Mitchell's physical model tests. *International Journal of Mining Science and Technology*, 26(6), 1135–1144.

Liu, G., Li, L., Yang, X., & Guo, L. (2016b). A numerical analysis of the stress distribution in backfilled stopes considering nonplanar interfaces between the backfill and rock walls. *International Journal of Geotechnical Engineering*, 10(3), 271–282.

Liu, G., Li, L., Yang, X., & Guo, L. (2017). Numerical analysis of stress distribution in backfilled stopes considering interfaces between the backfill and rock walls. *International Journal of Geomechanics*, 17(2), 06016014.

Liu, G., Li, L., Yang, X., & Guo, L. (2018). Required strength estimation of a cemented backfill with the front wall exposed and back wall pressured. *International Journal of Mining and Mineral Engineering, 9*(1), 1–20.

Liu, H., Xie, H., He, J., Xiao, M., & Zhuo, L. (2016). Nonlinear creep damage constitutive model for soft rocks. *Mechanics of Time-Dependent Materials*, 21(1), 73–96.

Liu, M.D., & Carter, J.P. (1999). Virgin compression of structured soils. *Géotechnique*, 49(1), 43–57.

Lo, K.Y., & Yuen, C.M.K. (1981). Design of tunnel lining in rock for long-term time effects. *Canadian Geotechnical Journal*, 18(1), 24–39.

Lockner, D. (1993). Room temperature creep in saturated granite. *Journal of Geophysical Research: Solid Earth, 98*(B1), 475–487.

Lockner, D.A. (1998). A generalized law for brittle deformation of Westerly granite. *Journal of Geophysical Research*, 103(B3), 5107–5123.

Lomnitz, C. (1957). Linear dissipation in solids. *Journal of Applied Physics*, 28(2), 201–205.

Ma, L., Liu, X., Fang, Q., Xu, H., Xia, H., Li, E., Yang, S., & Li, W. (2012). A new elasto-viscoplastic damage model combined with the generalized Hoek–Brown failure criterion for bedded rock salt and its application. *Rock Mechanics and Engineering*, 46(1), 53–66.

Malan, D.F., Vogler, U.W., & Drescher, K. (1997). Time-dependent behaviour of hard rock in deep level gold mines. *Journal of the Southern African Institute of Mining and Metallurgy*, 97(3), 135–147.

Malan, D.F., & Basson, F.R.P. (1998). Ultra-deep mining: the increased potential for squeezing conditions. *Journal of the Southern African Institute of Mining and Metallurgy*, 98(7), 353–363.

Malan, D.F. (1999). Time-dependent behaviour of deep level tabular excavations in hard rock. *Rock Mechanics and Rock Engineering*, 32(2), 123–155.

Malan, D.F. (2002). Manuel Rocha medal recipient simulating the time-dependent behaviour of excavations in hard rock. *Rock Mechanics and Rock Engineering*, 35(4), 225–254.

Malan, D.F., Napier, J.A.L., & Janse V.R. (2007). Stope deformation measurements as a diagnostic measure of rock behaviour: a decade of research. *Journal of the Southern African Institute of Mining and Metallurgy*, 107(11), 743–765.

Mansouri, H., & Ajalloeian, R. (2018). Mechanical behavior of salt rock under uniaxial compression and creep tests. *International Journal of Rock Mechanics and Mining Sciences*, 110, 19–27.

Maranini, E., & Yamaguchi, T. (2001). A non-associated viscoplastic model for the behaviour of granite in triaxial compression. *Mechanics of Materials, 33*(5), 283–293.

Marston, A. (1930). The theory of external loads on closed conduits in the light of the latest experiments. *Proceedings of the Ninth Annual Meeting of the Highway Research Board*. Washington, D.C.

Martin, C.D. (1997). Seventeenth Canadian geotechnical colloquium: the effect of cohesion loss and stress path on brittle rock strength. *Canadian Geotechnical Journal*, 34(5), 698–725.

Maruyama, K., Tanaka, C., & Oikawa, H. (1990). Long-term creep curve prediction based on the modified theta projection concept. *Journal of Pressure Vessel Technology, Transactions of the ASME*, 112(1), 92–97.

Marx, H., Lack, D., & Krauke, W. (2005). Substantial aspects of the recycling of industrial wastes as backfilling Material in Salt Mines. *Proceedings of the Mining and Sustainable Development – 20th World Mining Congress & Expo*. Teheran, Iran.

Mbonimpa, M., Aubertin, M., Chapuis, R., & Bussière, B. (2002). Practical pedotransfer functions for estimating the saturated hydraulic conductivity. *Geotechnical and Geological Engineering, 20*(3), 235–259.

McClay, K.R. (1977). Pressure solution and Coble creep in rocks and minerals: a review. *Journal*

of the Geological Society, 134(1), 57–70.

Mirza, U. (1978). *Investigation into the design criteria for underground openings in rocks which exhibit rheological behaviour*. (Ph.D. thesis, University of Newcastle upon Tyne).

Mitchell, R., Smith, J., & Libby, D. (1975). Bulkhead pressures due to cemented hydraulic mine backfills. *Canadian Geotechnical Journal, 12*(3), 362–371.

Mitchell, R.J., & Wong, B.C. (1982). Behaviour of cemented tailings sands. *Canadian Geotechnical Journal*, 19(3), 289–295.

Mitchell, R.J., Olsen, R.S., & Smith, J.D. (1982). Model studies on cemented tailings used in mine backfill. *Canadian Geotechnical Journal*, 19(1), 14–28.

Mitchell, R.J. (1991). Sill mat evaluation using centrifuge models. *Mining Science and Technology, 13*(3), 301–313.

Mitchell, R.J. (1986). Centrifuge model tests on backfill stability. *Canadian Geotechnical Journal*, 23(3), 341–345.

Mitchell, R.J. (1989). Model studies on the stability of confined fills. *Canadian Geotechnical Journal*, 26(2), 210–216.

Miura, K., Okui, Y., & Horii, H. (2003). Micromechanics-based prediction of creep failure of hard rock for long-term safety of high-level radioactive waste disposal system. *Mechanics of Materials*, 35(3-6), 587–601.

Mohr, O. (1900). Welche umstände bedingen die elastizitätsgrenze und den bruch eines materials. *Zeitschrift des Vereins Deutscher Ingenieure*, 46, 1572–1577.

Myer, L.R., Kemeny, J.M., Zheng, Z., Suarez, R., Ewy, R.T., & Cook, N.G.W. (1992). Extensile cracking in porous rock under differential compressive stress. *Applied Mechanics Reviews*, 45(8), 263–280.

Nasir, O., & Fall, M. (2008). Shear behaviour of cemented pastefill–rock interfaces. *Engineering Geology*, 101(3), 146–153.

Neher, H., Wehnert, M., & Bonnier, P. (2001). An evaluation of soft soil models based on trial embankments. *Proceedings of 10th International Conference on Computer Methods and*

Advances in Geomechanics. Tucson, Arizona, United States of America, Rotterdam: AA Balkema, 373–379.

Nejati, H.R., Ghazvinian, A., Moosavi, S.A., & Sarfarazi, V. (2014). On the use of the RMR system for estimation of rock mass deformation modulus. *Bulletin of Engineering Geology and the Environment*, 73(2), 531–540.

Newman, C.R., & Agioutantis, Z.G. (2018). Stress Redistribution Around Single and Multiple Stope-and-Fill Operations. *Proceedings of 52nd US Rock Mechanics/Geomechanics Symposium*. Seattle, United States of America, American Rock Mechanics Association.

Ngwenya, B.T., Main, I.G., Elphick, S.C., Crawford, B.R., & Smart, B.G.D. (2001). A constitutive law for low-temperature creep of water-saturated sandstones. *Journal of Geophysical Research: Solid Earth*, 106(B10), 21811–21826.

Nieto, A. (2011). Soft-Rock (Underground) Mining: Selection Methods. *In SME Mining Engineering Handbook.* Society for Mining, Metallurgy & Exploration.

Niroshan, N., Sivakugan, N., & Veenstra, R.L. (2018). Flow characteristics of cemented paste backfill. *Geotechnical and Geological Engineering, 36*(4), 2261–2272.

Nopola, J., & Roberts, L. (2016). Time-dependent deformation of Pierre Shale as determined by long-duration creep tests. *Proceedings of 50th US Rock Mechanics/Geomechanics Symposium*. American Rock Mechanics Association, 584–591.

Nordlund, E. (2013). Deep hard rock mining and rock mechanics challenges. *Proceedings of the Seventh International Symposium on Ground Support in Mining and Underground Construction*. Perth, Australia.

Obert, L., Duvall, W.I., & Windes, S.L. (1946). *Standardized tests for determining the physical properties of mine rock*. US Bureau of Mines.

Ohring, M. (1995). *Engineering materials science*. Elsevier.

Oliver, P.H., & Landriault, D. (1989). The convergence resistance of mine backfills. *Proceedings of 4th International Symposium on mining with backfill.* Montreal, Canada. Rotterdam, AA Balkema, 433–436.

Ortlepp, W. (2005). RaSiM comes of age—a review of the contribution to the understanding and control of mine rockbursts. *Proceedings of the 6th international symposium on rockburst and seismicity in mines,* Perth, Australia.

Pagé, P., Li, L., Yang, P., & Simon, R. (2019). Numerical investigation of the stability of a base-exposed sill mat made of cemented backfill. *International Journal of Rock Mechanics and Mining Sciences*, 114, 195–207.

Pałac-Walko, B., & Pytel, W. (2014). The effect of the presence of salt formations above extracted copper ore as determined by numerical modelling. *Proceedings of the seventh international conference on deep and high stress mining*. Australian Centre for Geomechanics, Perth, 409–420.

Palarski, J., Plewa, F., & Strozik, G. (2014). Filling of voids in coal longwall mining with caving–technical, environmental and safety aspects. *Proceedings of the Eleventh International Symposium on Mining with Backfill*. Perth, Australia.

Paraskevopoulou, C. (2016). *Time-dependency of rocks and implications associated with tunneling*. (Ph.D. thesis, Queen's University).

Paraskevopoulou, C., & Diederichs, M. (2018). Analysis of time-dependent deformation in tunnels using the Convergence-Confinement Method. *Tunnelling and Underground Space Technology*, 71, 62–80.

Paraskevopoulou, C., Perras, M., Diederichs, M., Loew, S., Lam, T., & Jensen, M. (2018). Time-dependent behaviour of brittle rocks based on static load laboratory tests. *Geotechnical and Geological Engineering*, 36(1), 337–376.

Pariseau, W.G. (1995). Coupled three-dimensional finite element modeling of mining in wet ground. *Proceedings of 3rd Canadian Conference. on Computer Applications in the Mineral Industry*. Montreal, Québec, Canada, 283–292.

Pariseau, W.G. (2007). Fitting failure criteria to laboratory strength tests. *International Journal of Rock Mechanics and Mining Sciences*, 44(4), 637–646.

Penny, R., & Marriott, D. (1995). *Design for creep*. Springer Science & Business Media.

Peregoedova, A. (2012). *Étude expérimentale des propriétés hydrogéologiques des roches stériles à une échelle intermédiaire de laboratoire.* (Master's thesis, École Polytechnique de Montréal).

Perzyna, P. (1966). Fundamental problems in viscoplasticity. *Advances in Applied Mechanics*, 9, 243–377.

Pierce, M.E. (1999). *Laboratory and numerical analysis of the strength and deformation behaviour of paste backfill.* (Master thesis, Queen's University).

Pietruszczak, S. (2010). *Fundamentals of plasticity in geomechanics.* Boca Raton: CRC Press.

Pirapakaran, K., & Sivakugan, N. (2007). Arching within hydraulic fill stopes. *Geotechnical and Geological Engineering, 25*(1), 25–35.

Potvin, Y., Thomas, E., & Fourie, A. (2005). *Handbook on mine fill.* Perth, Australia: Australian Centre for Geomechanics publication.

Potyondy, D.O. (2007). Simulating stress corrosion with a bonded-particle model for rock. *International Journal of Rock Mechanics and Mining Sciences*, 44(5), 677–691.

Qi, C., & Fourie, A. (2019). Numerical investigation of the stress distribution in backfilled stopes considering creep behaviour of rock mass. *Rock Mechanics and Rock Engineering*, 52(9), 3353–3371.

Quesnel, W., De Ruiter, H., & Pervik, A. (1989). The assessment of cemented rockfill for regional and local support in a rockburst environment. *Proceedings of the 4th International Symposium on Mining with Backfill.* Montreal.

Raffaldi, M.J., Seymour, J.B., Richardson, J., Zahl, E., & Board, M. (2019). Cemented paste backfill geomechanics at a narrow-vein underhand cut-and-fill mine. *Rock Mechanics and Rock Engineering*, 52(12), 4925–4940.

Ranjith, P.G., Zhao, J., Ju, M., De Silva, R.V.S., Rathnaweera ,T.D., & Bandara, A.K. (2017). Opportunities and challenges in deep mining: a brief review. *Engineering*, 3(4), 546–551.

Rankine, K.J. (2005). *An investigation into the drainage characteristics and behaviour of hydraulically placed mine backfill and permeable minefill barricades.* (Ph.D. thesis, James

Cook University).

Rankine, K.J., Sivakugan, N., & Cowling, R. (2006). Emplaced geotechnical characteristics of hydraulic fills in a number of Australian mines. *Geotechnical and Geological Engineering, 24*(1), 1–14.

Rankine, R.M., & Sivakugan, N. (2007). Geotechnical properties of cemented paste backfill from Cannington Mine, Australia. *Geotechnical and Geological Engineering, 25*(4), 383–393.

Rankine, R.M. (2004). *The geotechnical characterisation and stability analysis of BHP Billiton's Cannington Mine paste fill*. (Ph.D. thesis, James Cook University).

Roberts, D., Tolfree, D., & McIntire, H. (2007). Using confinement as a means to estimate pillar strength in a room and pillar mine. *Proceedings of the 1st Canada-US Rock Mechanics Symposium*. Vancouver, Canada.

Roscoe, K.H., Schofield, A.N., & Wroth, C.P. (1958). On the yielding of soils. *Géotechnique*, 8(1), 22–53.

Sainsbury, D.P, & Sainsbury, B.L. (2014). Design and implementation of cemented rockfill at the Ballarat Gold Project. *Proceedings of the Eleventh International Symposium on Mining with Backfill*. Perth, Australia.

Sainsbury, D.P., & Urie, R. (2007). Stability analysis of horizontal and vertical paste fill exposures at the Raleigh Mine. *Proceedings of 9th International Symp on Mining with Backfill*. Montreal, Canada, Canadian Institute of Mining, Metallurgy and Petroleum.

Salencon, J. (1969). Contraction quasi-statique d'une cavité a symétrie sphérique ou cylindrique dans un milieu elastoplastique. *Ann Ponts Chaussées*, 4, 231–236.

Salvoldi, B., van der Spuy, B., & Wilson, S. (2019). Optimisation of cemented aggregate backfill at New Luika Gold Mine. *Proceedings of the 22nd International Conference on Paste, Thickened and Filtered Tailings*. Cape Town, South Africa.

Saw, H., Prentice, S., & Villaescusa, E. (2011). Characterisation of cemented rock fill materials for the Cosmos nickel mine, Western Australia. *Proceedings of International Conference on Advances in Construction Materials through Science and Engineering*. Hong Kong, China.

Seymour, J.B., Raffaldi, M.J., Abraham, H., Johnson, J.C., & Zahl, E.G. (2017). Monitoring the in situ performance of cemented paste backfill at the Lucky Friday Mine. *Proceedings of 12th International Symp on Mining with Backfill*. Denver, United States of America, 19–22.

Shao, J., Chau, K., & Feng, X. (2006). Modeling of anisotropic damage and creep deformation in brittle rocks. *International Journal of Rock Mechanics and Mining Sciences*, 43(4), 582–592.

Sharifzadeh, M., Tarifard, A., & Moridi, M.A. (2013). Time-dependent behavior of tunnel lining in weak rock mass based on displacement back analysis method. *Tunnelling and Underground Space Technology*, 38, 348–356.

Shrestha, B.K., Tannant, D.D., Proskin, S., Reinson, J., & Greer, S. (2008). Properties of cemented rockfill used in an open pit mine. *Proceedings of 61st Canadian Geotechnical Conference and the 9th Joint CGS/IAH-CNC Groundwater Conference*. Edmonton, Canada, 609–616.

Simon, D., & Grabinsky, M. (2013). Apparent yield stress measurement in cemented paste backfill. *International Journal of Mining, Reclamation and Environment, 27*(4), 231–256.

Sivakugan, N. (2008). Drainage issues and stress developments within hydraulic fill mine stopes. *Australian journal of civil engineering, 5*(1), 61–70.

Sivakugan, N., Rankine, K., Lovisa, J., & Hall, W. (2013). Flow rate computations in hydraulic fill mine stopes. *Indian Geotechnical Journal*, 43(3), 195–202.

Sivakugan, N., Veenstra, R., & Naguleswaran, N. (2015). Underground mine backfilling in Australia using paste fills and hydraulic fills. *International journal of geosynthetics and ground engineering*, 1(2), 1–7.

Sobhi, M.A., & Li, L. (2015). A numerical study of the stresses in backfilled stopes overlying a sill mat. *Proceedings of the 13th ISRM International Congress of Rock Mechanics*. Montreal, Canada.

Sobhi, M.A., & Li, L. (2017). Numerical investigation of the stresses in backfilled stopes overlying a sill mat. *Journal of Rock Mechanics and Geotechnical Engineering*, 9(3), 490–501.

Stebbins, S.A., & Schumacher, O.L. (2001). Cost estimating for underground mines. *In: Underground mining methods: Engineering fundamentals and international case studies.*

Colorado: Society for Mining, Metallurgy, and Exploration, 49–72.

Stephan, G. (2011). Cut-and-fill mining. *In: SME Mining Engineering Handbook*. 3rd ed. Littleton.

Sterpi, D., & Gioda, G. (2009). Visco-plastic behaviour around advancing tunnels in squeezing rock. *Rock Mechanics and Rock Engineering*, 42(2), 319–339.

Stewart, J.M., Clark, I.H., & Morris, A.N. (1986). Assessment of fill quality as a basis for selecting and developing optimal backfill systems for South African gold mines. *Proceedings of International Conference on Gold*. Johannesburg, South Africa, 255–270.

Sulem, J., Panet, M., & Guenot, A. (1987). Closure analysis in deep tunnels. *International Journal of Rock Mechanics and Mining Sciences & Geomechanics Abstracts*, 24(3), 145–154.

Sulistianto, B., Kramadibrata, S., Saptono, S., & Rismayanti, R. (2010). Laboratory Study for Determining Long-term Shear Strength of Rock. *Proceedings of* International Symposium on Earth Science and Technology. Fukuoka, Japan.

Taheri, A., Zhang, Y., & Munoz, H. (2020). Performance of rock crack stress thresholds determination criteria and investigating strength and confining pressure effects. *Construction and Building Materials*, 243, 118263.

Talbot, A.N., Brown, H.A., & Richart, F.E. (1923). *The strength of concrete: its relation to the cement aggregates and water*. University of Illinois Bulletin.

Tan, Z., Bernal, S.A., & Provis, J.L. (2017). Reproducible mini-slump test procedure for measuring the yield stress of cementitious pastes. *Materials and Structures*, 50(6), 1–12.

Tang, H., Wang, D., Huang, R., Pei, X., & Chen, W. (2017). A new rock creep model based on variable-order fractional derivatives and continuum damage mechanics. *Bulletin of Engineering Geology and the Environment*, 77(1), 375–383.

Tesarik, D.R., Seymour, J.B., & Jones, F.M. (2003). Determination of in situ deformation modulus for cemented rockfill. *Proceedings of the 10th ISRM Congress*. Sandton, South Africa, 1209–1220.

Tesarik, D.R., Seymour, J.B., & Yanske, T.R. (2009). Long-term stability of a backfilled room-and-pillar test section at the Buick Mine, Missouri, USA. *International Journal of Rock Mechanics*

and Mining Sciences, 46(7), 1182–1196.

Thompson, B.D., Grabinsky, M.W., Bawden, W.F., & Counter, D.B. (2009). In-situ measurements of cemented paste backfill in long-hole stopes. *Proceedings of the 3rd CANUS rock mechanics symposium*. Toronto, 197–198.

Thompson, B.D., Bawden, W.F., & Grabinsky, M. (2012). In situ measurements of cemented paste backfill at the Cayeli Mine. *Canadian Geotechnical Journal*, 49(7), 755–772.

Thompson, B.D., Bawden, W.F., Brzeczka, B., & Grabinsky, M.W. (2017). In-Situ Backfill Monitoring–Lessons Learned and a New Case Study. *Proceedings of 12th International Conference on Mining with Backfill*. Denver, USA.

Ting, C.H., Shukla, S.K., & Sivakugan, N. (2011). Arching in soils applied to inclined mine stopes. *International Journal of Geomechanics*, 11(1), 29–35.

Tomanovic, Z. (2006). Rheological model of soft rock creep based on the tests on marl. *Mechanics of Time-Dependent Materials*, 10(2), 135–154.

Vasichev, S. (2019). Ground control with backfill and caving in deep-level mining of gently dipping ore bodies. *Proceedings of International Conference on Urban Construction and Subsurface Management. Exploration and Mining Technologies. Economics. Geoecology*. Novosibirsk, Russia, 012022.

Veenstra, R.L. (2013). *A design procedure for determining the in situ stresses of early age cemented paste backfill*. (Ph.D. thesis, University of Toronto).

Verstrynge, E., Schueremans, L., & Van Gemert, D. (2011). Time-dependent mechanical behavior of lime-mortar masonry. *Materials and Structures*, 44(1), 29–42.

Wagner, H. (2019). Deep mining: a rock engineering challenge. *Rock Mechanics and Rock Engineering*, 52(5), 1417–1446.

Wang, G., Zhang, L., Zhang, Y., & Ding, G. (2014). Experimental investigations of the creep-damage-rupture behaviour of rock salt. *International Journal of Rock Mechanics and Mining Sciences*, 66, 181–187.

Wang, J.J., Zhang, H.P., Tang, S.C., & Liang, Y. (2013). Effects of particle size distribution on

shear strength of accumulation soil. *Journal of Geotechnical and Geoenvironmental Engineering*, 139(11), 1994–1997.

Wang, R., & Li, L. (2018). Burgers creep model used for describing and predicting the creep behaviour of a rock under uniaxial and triaxial compression test conditions. *Proceedings of the 71st Canadian Geotechnical Conference*. Edmonton, Canada, 572.

Wang, R., & Li, L. (2019). A non-stationary power law model to predict the secondary creep rate of rocks. *Proceedings of 8th international conference on case histories in geotechnical engineering*. Philadelphia, American Society of Civil Engineers, 476–483.

Wang, R., Li, L., & Simon, R. (2019). A model for describing and predicting the creep strain of rocks from the primary to the tertiary stage. *International Journal of Rock Mechanics and Mining Sciences*, 123, 104087.

Wang, R., Zeng, F., & Li, L. (2021). Stability analyses of side-exposed backfill considering mine depth and extraction of adjacent stope. *International Journal of Rock Mechanics and Mining Sciences*, 142, 104735.

Weijermars, R., Alekseev, V.B., Cuevas, J., Vigneresse, J.L., & Schmid, S. (1997). *Principles of rock mechanics*. Amsterdam: Alboran Science Publishing.

Williams, D.J., & Walker, L. (1985). Laboratory and field strength of mine waste rock. *Technical report*. University of Queensland. Department of Civil Engineering.

Williams, D.J., & Kuganathan, V. (1992). Co-disposal of coal mine tailings and coarse reject. *Proceedings of third Large Open Pit Mining Conference*. Mackay, Australia.

Wittke, W. (2014). *Rock mechanics based on an anisotropic jointed rock model (AJRM)*. Berlin: Ernst & Sohn.

Xie, H., Gao, M., Zhang, R., Peng, G., Wang, W., & Li, A. (2019). Study on the mechanical properties and mechanical response of coal mining at 1000 m or deeper. *Rock Mechanics and Rock Engineering*, 52(5), 1475–1490.

Xu, M., Jin, D., Song, E., & Shen, D. (2018). A rheological model to simulate the shear creep behavior of rockfills considering the influence of stress states. *Acta Geotechnica*, 13(6), 1313–1327.

Xu, T., Xu, Q., Deng, M., Ma, T., Yang, T., & Tang, C. (2014). A numerical analysis of rock creep-induced slide: a case study from Jiweishan Mountain, China. *Environmental Earth Sciences*, 72(6), 2111–2128.

Xu, T., Zhou, G., Heap, M.J., Yang, S., Konietzky, H., & Baud, P. (2018). The modeling of time-dependent deformation and fracturing of brittle rocks under varying confining and pore pressures. *Rock Mechanics and Rock Engineering*, 51(10), 3241–3263.

Xu, W.Y., Nie, W.P., Zhou, X.Q., Shi, C., Wang, W., & Feng, S.R. (2011). Long-term stability analysis of large-scale underground plant of Xiangjiaba hydro-power station. *Journal of Central South University*, 18(2), 511–520.

Yahya, O., Aubertin, M., & Julien, M. (2000). A unified representation of the plasticity, creep and relaxation behavior of rocksalt. *International Journal of Rock Mechanics and Mining Sciences*, 37(5), 787–800.

Yan, B., Lai, X., Jia, H., Yilmaz, E., & Hou, C. (2021). A solution to the time-dependent stress distribution in suborbicular backfilled stope interaction with creeping rock. *Advances in Civil Engineering*, 2021, 5533980.

Yang, L., Mei, J., Sheng, X., Yang, W., & Li, J. (2021). Cracking and Creep Behavior of Rocks Considering Propagation and Interaction of Adjacent Cracks Under Hydro-Mechanical Coupling. *Rock Mechanics and Rock Engineering*, 1–12.

Yang, P. (2016). *Investigation of the geomechanical behavior of mine backfill and its interaction with rock walls and barricades*. (Ph.D. thesis, École Polytechnique de Montréal).

Yang, P., & Li, L. (2017). Evolution of water table and pore-water pressure in stopes with submerged hydraulic fill. *International Journal of Geomechanics*, 17(9), 04017052.

Yang, P., Li, L., & Aubertin, M. (2017). A new solution to assess the required strength of mine backfill with a vertical exposure. *International Journal of Geomechanics*, 17(10), 04017084.

Yang, P., Li, L., & Aubertin, M. (2018). Theoretical and numerical analyses of earth pressure coefficient along the centerline of vertical openings with granular fills. *Applied Sciences*, 8(10), 1721.

Yilmaz, E. (2018). Stope depth effect on field behaviour and performance of cemented paste backfills. *International Journal of Mining, Reclamation and Environment*, 32(4), 273–296.

Yumlu, M., & Guresci, M. (2007). Paste backfill bulkhead monitoring: A case study from Inmet's Cayeli Mine, Turkey. *Proceedings of 9th International Symp on Mining with Backfill*. Montreal, Canada, Canadian Institute of Mining, Metallurgy and Petroleum, 146–155.

Zhang, H., Wang, Z., Zheng, Y., Duan, P., & Ding, S. (2012). Study on tri-axial creep experiment and constitutive relation of different rock salt. *Safety Science*, 50(4), 801–805.

Zhang, J., Zhang, Q., Sun, Q., Gao, R., Germain, D., & Abro, S. (2015). Surface subsidence control theory and application to backfill coal mining technology. *Environmental Earth Sciences*, 74(2), 1439–1448.

Zhao, Y., Wang, Y., Wang, W., Wan, W., & Tang, J. (2017). Modeling of non-linear rheological behavior of hard rock using triaxial rheological experiment. *International Journal of Rock Mechanics and Mining Sciences*, 93, 66–75.

Zhao, T., Ma, S., & Zhang, Z. (2018). Ground control monitoring in backfilled strip mining under the metropolitan district: case study. *International Journal of Geomechanics*, 18(7), 05018003.

Zhao, X., Fourie, A., & Qi, C. (2019). An analytical solution for evaluating the safety of an exposed face in a paste backfill stope incorporating the arching phenomenon. *International Journal of Minerals, Metallurgy and Materials*, 26(10), 1206–1216.

Zheng, J., & Li, L. (2020). Experimental study of the "short-term" pressures of uncemented paste backfill with different solid contents for barricade design. *Journal of Cleaner Production*, 275, 123068.

APPENDIX A VALIDATION OF FLAC^{3D}

A1 Validation of the Mohr-Coulomb model in FLAC^{3D}

FLAC^{3D} can be validated using the simulation of a cylindrical hole in the infinite rock mass that obeys Mohr-Coulomb (MC) criterion. The schematic of the physical model for the problem is illustrated in Figure A-1a. The radius of the hole a_r is 1 m while the distance of AB denotes the domain size of the model. The corresponding numerical model built using the radcylinder mesh (radial grid ratio 1.1) with FLAC^{3D} is shown in Figure A-1b. Only one quarter of the full model is constructed by considering symmetric planes. Displacements along y-axis (third direction) are restricted to simulate a plane strain condition while the normal displacements are prohibited on the left and the bottom boundary. Moreover, a stress P_0 is applied on the top and the right boundary of the model to represent the in-situ stress in the rock mass.

<table>
<tr><td>(a)</td><td>(b)</td></tr>
</table>
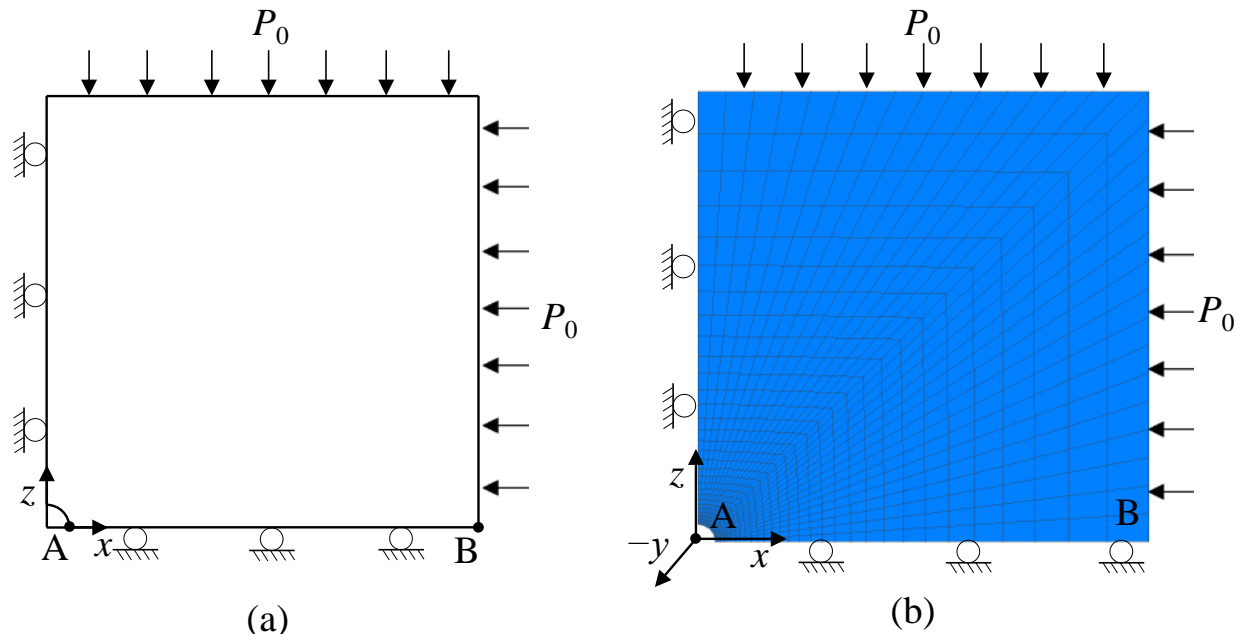
Figure A-1: Schematic of (a) physical model and (b) numerical of a cylindrical hole in an infinite MC medium

Numerical results of the radial stress σ_r, tangential stress σ_θ and radial displacement U along line AB are analyzed. Effects of different modeling parameters (conditions) will be studied including the mesh size, domain size, strain mode (small/large), flow rules (different dilation angles ψ), third dimension of the model (y direction), and the grid number in y direction. The numerical program

of the simulation is summarized in Table A-1. In addition to parameters defined in Table A-1, the numerical model has a Young's modulus E of 6.5 GPa, a cohesion c of 3 MPa, a friction angle ϕ of 35°, a Poisson's ratio ν of 0.25, and a tensile strength T of 10 GPa. The applied stress P_0 is 40 MPa,

Table A-1: Varied parameters applied in the simulation to validate FLAC^{3D} with the MC model

Case	Mesh size (m)	Domain size (m)	Strain mode	ψ (°)	Third dimension (m)	Grid in y direction
1	VAR	10	small	0	0.1	1
2	VAR	VAR	small	0	0.1	1
3	VAR	10	large	0	0.1	1
4	VAR	10	small	35	0.1	1
5	VAR	10	small	0	VAR	1
6	VAR	10	small	0	0.1	VAR

The numerical results will be further compared with the analytical solution proposed by Salencon (1969) to validate the FLAC^{3D} code. According to Salencon (1969) solution, the radius of the yield zone around the cylinder hole R_0 is

$$R_0 = a \left(\frac{2}{K_p+1} \frac{P_0 + \frac{q_{MC}}{K_p-1}}{P_{iner} + \frac{q_{MC}}{K_p-1}} \right)^{1/(K_p-1)} \tag{A.1}$$

where P_{iner} is the internal pressure; $q_{MC} = 2c \cdot \tan(45° + \phi/2)$; $K_p = (1 + \sin\phi)/(1 - \sin\phi)$.

Moreover, the stresses and radial displacement in the elastic zone are given as:

$$\sigma_r = P_0 - (P_0 - \sigma_{re})\left(\frac{R_0}{r}\right)^2 \tag{A.2}$$

$$\sigma_\theta = P_0 + (P_0 - \sigma_{re})\left(\frac{R_0}{r}\right)^2 \tag{A.3}$$

$$U = \frac{R_0{}^2}{2G}\left(P_0 - \frac{2P_0 - q_{MC}}{K_p+1}\right)\frac{1}{r} \tag{A.4}$$

where r is a polar coordinate; G is the shear modulus; σ_{re} is the radial stress at the elastic-plastic interface and is expressed as:

$$\sigma_{re} = \frac{1}{K_p+1}(2P_0 - q_{MC}) \tag{A.5}$$

Moreover, the stresses and radial displacement in the plastic zone are given as:

$$\sigma_r = -\frac{q_{MC}}{K_p-1} + \left(P_{iner} + \frac{q_{MC}}{K_p-1}\right)\left(\frac{r}{a}\right)^{(K_p-1)} \tag{A.6}$$

$$\sigma_\theta = -\frac{q_{MC}}{K_p-1} + K_p\left(P_{iner} + \frac{q_{MC}}{K_p-1}\right)\left(\frac{r}{a}\right)^{(K_p-1)} \tag{A.7}$$

$$U = \frac{r}{2G}\left[(2\upsilon - 1)\left(P_0 + \frac{q_{MC}}{K_p-1}\right) + \frac{(1-\upsilon)(K_p{}^2-1)}{K_p+K_\psi}\left(P_{iner} + \frac{q_{MC}}{K_p-1}\right)\left(\frac{R_0}{a}\right)^{(K_p-1)}\left(\frac{R_0}{a}\right)^{(K_\psi+1)} + \left(\frac{(1-\upsilon)(K_pK_\psi+1)}{K_p+K_\psi} - \right.\right.$$

$$\upsilon\left)\left(P_{iner} + \frac{q_{MC}}{K_p-1}\right)\left(\frac{r}{a}\right)^{(K_p-1)}\right] \tag{A.8}$$

where $K_\psi = (1 + \sin\psi)/(1 - \sin\psi)$.

A1.1 Effect of mesh size

Figure A-2 shows the tangential and radial stress distribution along the line AB for Case 1 in Table A-1 with different mesh sizes ranging from 2 m to 0.0025 m. It is found that both radial and tangential stresses moderately converge as the mesh size reduces. Applying smaller mesh size will also illustrate stress gradient better than using larger mesh size. The stresses around the cylinder hole become stable when the mesh size is smaller than 0.1m.
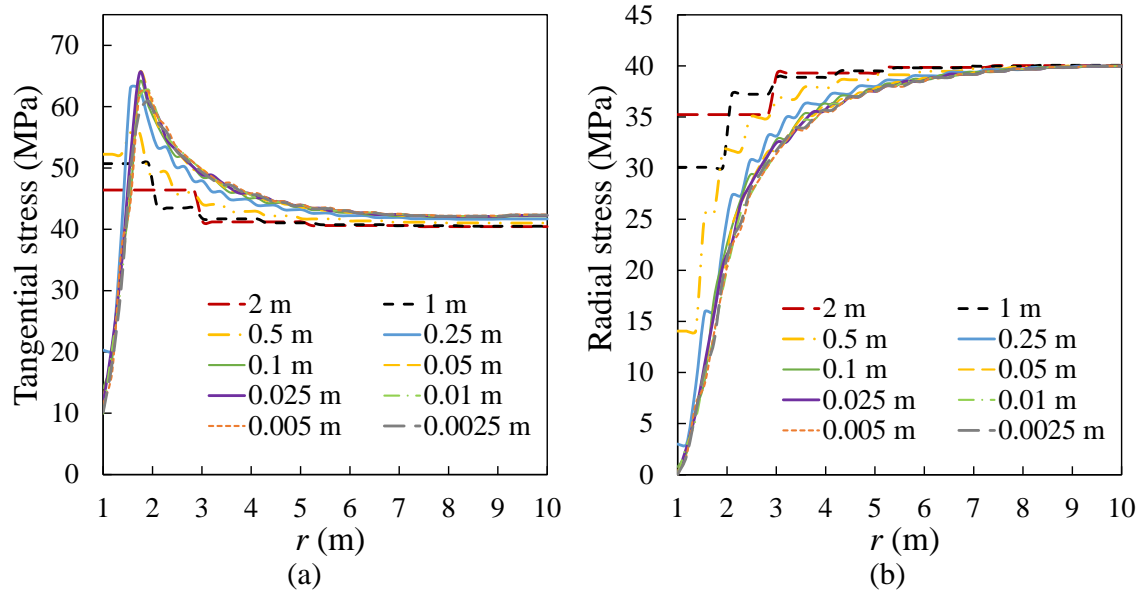
Figure A-2: Distributions of (a) tangential stress and (b) radial stress along line AB around a cylindrical hole with different mesh sizes (Case 1 in Table A-1)

In practice, the displacement on the inner boundary of the hole is usually of interests. Therefore, the radial displacements at the point A with different mesh sizes are illustrates in Figure A-3. One can see that as the mesh size becomes smaller than 0.1 m, the radial displacements around the cylinder hole converge which agrees with the trend of stress distribution shown in Figure A-2. Nevertheless, the radial displacement still shows slight increasing as the mesh size further decreases form 0.1 m to 0.0025 m. The optimal mesh for this case to ensure the stable numerical results and a reasonable runtime is thus determined as 0.1 m.
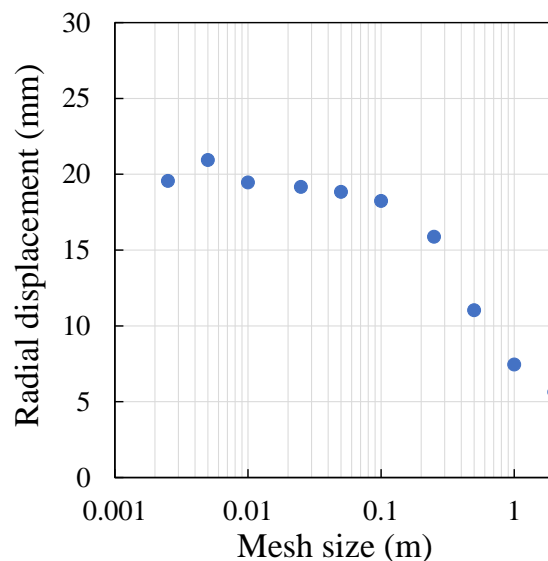
Figure A-3: Radial displacements at the point A for Case 1 in Table A-1

A1.2 Effect of domain size

Radial displacements at the point A for Case 2 in Table A-1 with different domain sizes are shown in Figure A-4. It is found when the domain size is 5 m, numerical results show some scatters. Moreover, As the domain size increase to 10 m, the displacements tend to become stable. Therefore, the optimal domain size of the model can be determined as 10 m.
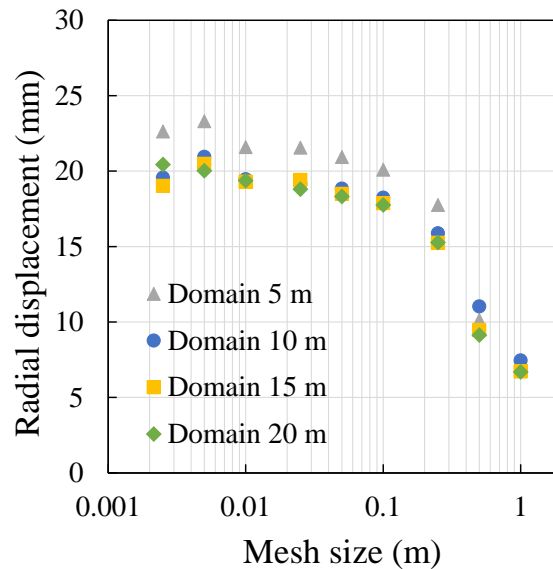
Figure A-4: Radial displacements at the point A for Case 2 in Table A-1

A1.3 Effect of strain mode

Numerical modeling with FLAC^{3D} can be conducted with the small strain or large strain modes. The geometry remains same as the numerical model displaces with the small strain mode while the coordinates of gridpoints will update according to the deformation with the large strain mode. Figure A-5 shows that the radial displacement at the point A with the small strain model is slightly larger than that with the large strain mode when the mesh size is larger than 0.25 m. As the mesh size further reduces, applying different strain modes generally has no obvious influence on the results.
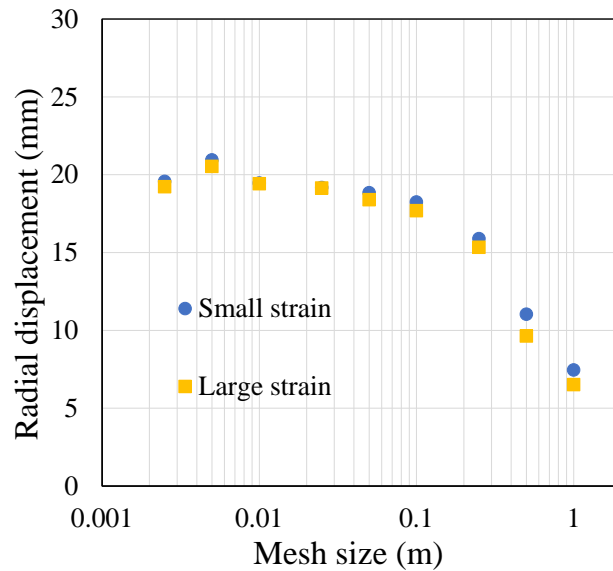
Figure A-5: Radial displacements at the point A for Case 3 in Table A-1

A1.4 Effect of Associated flow rule

Associated flow rule is applied for Case 4 in Table A-1 by considering that ψ equals to ϕ. Figure A-6 shows that the numerical results with associated flow rule tend to become stable when the mesh size decreases to 0.1 m. This tendency is quite similar to results with non-associated flow rule shown in Figure A-5.
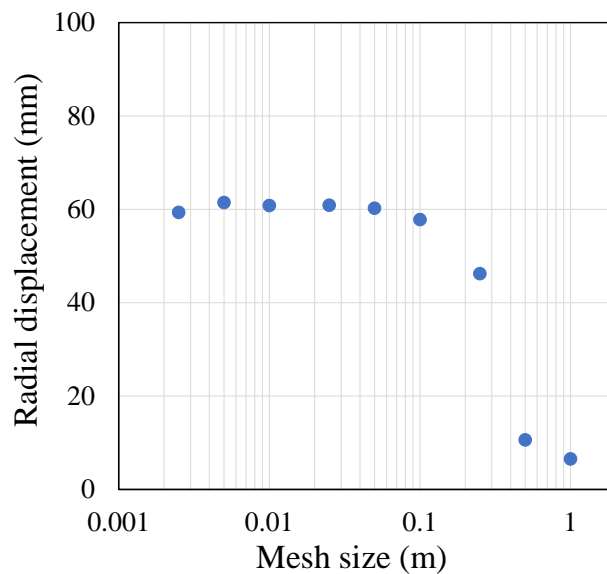
Figure A-6: Radial displacements at the point A for Case 4 in Table A-1

A1.5 Effect of third dimension

Dimensions along *y*-axis including 5, 2, 1, 0.5, 0.1 and 0.05 m are applied for Case 5 in Table A-1. Figure A-7 shows that different third dimensions have minor effect on the numerical results of radial displacement at the point A. The radial displacement slightly increases with the reduction of mesh size from 0.1 m to 0.0025 m for different third dimensions.
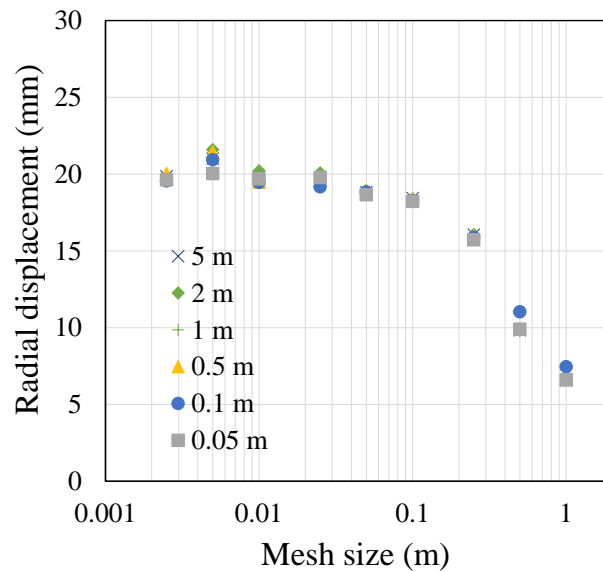
Figure A-7: Radial displacements at the point A for Case 5 in Table A-1

A1.6 Effect of grid number in third direction

The grid number in third direction varies in Case 6 to make that the element has the same size along all three (*x*, *y*, *z*) directions. This means that the element around the cylinder hole in this case is close to a regular cube. The comparison between radial displacement at the point A of Case 6 and Case 1 are illustrated in Figure A-8. It is found that the radial displacement of Case 6 becomes stable when the mesh size reduces to 0.1 m which is similar to the results of Case 1. However, as the mesh size further decreases from 0.1 m to 0.0025 m, the results for Case 6 dose not show a slight increasing tendency. This is because the aspect ratio of the elements tends to be 1 for Case 6 while for Case 1, the aspect ratio decreases significantly as the mesh size decreases due to the constant grid number in the third direction. A value of aspect ratio far from 1 means that the element is significantly stretched and influences the accuracy of the results. Therefore, the aspect ratio of elements in FLAC^{3D} should be close to 1 to ensure stable and accurate results.
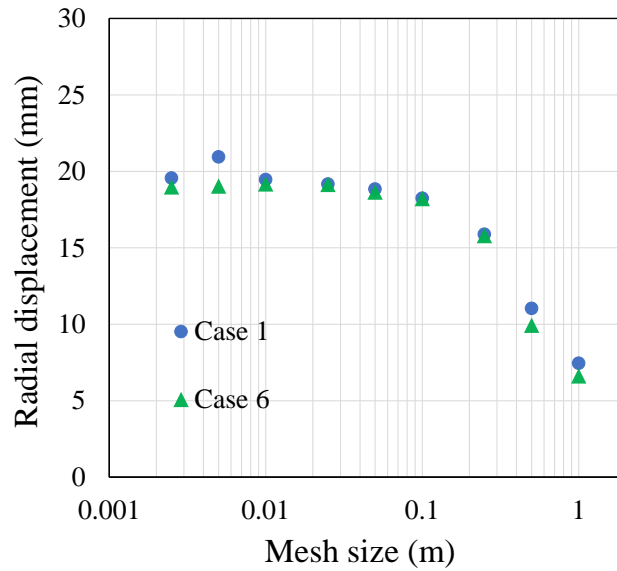
Figure A-8: Comparisons between radial displacements at the point A for Case 1 and Case 6 in
Table A-1

A1.7 Comparison between numerical and analytical results

According to above analyses, the optimal values of domain and mesh size are determined as 10 m
and 0.1 m. The mesh size along third direction is 0.1 m to ensure that the aspect ratio of elements
around the cylinder hole is close to 1. Figure A-9 shows the comparisons between numerical results
of tangential stress, radial stress, and radial displacement along the line AB using optimal modeling
parameters with analytical solutions of Salencon (1969). Both associated and non-associated flue
rules are applied. Quite good agreements can be seen between numerical and analytical solutions.
FLAC^{3D} is thus validated with the MC model and can be applied to simulate other problems.
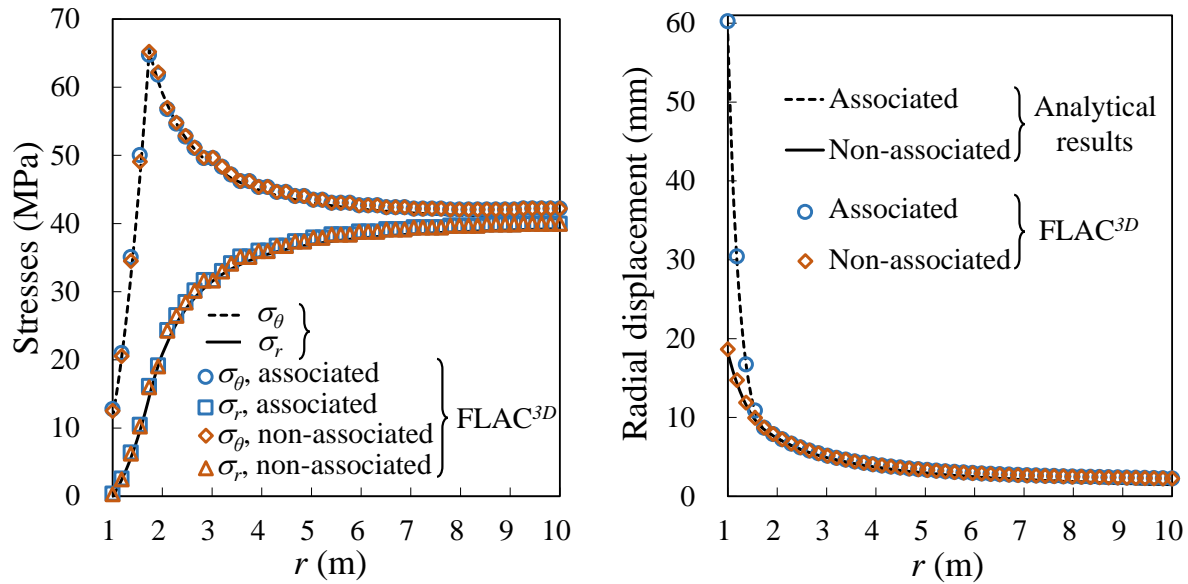
Figure A-9: Comparisons between numerical results with analytical result of Salencon (1969) of (a) stresses distribution and (b) radial displacement along line AB around a cylinder hole in a Mohr-Coulomb material

A2 Validation of the Hoek-Brown model with strain softening in FLAC^{3D}

The Hoek-Brown (HB) model with strain softening in FLAC^{3D} can be validated by simulating the problem of a cylindrical hole in an infinite rock mass. Optimal modeling parameters including the domain size and mesh size of the numerical model are determined based on the sensitivity analyses. The numerical results of stresses and radial displacement around the hole with optimal domain and mesh size are then compared with the analytical solutions proposed by Carranza-Torres (2004). Figure A-10a shows the physical model of the problem while the numerical plane-strain model (in x-z plane) built using the Cshell mesh (radial grid ratio 1.1) with FLAC^{3D} is illustrated in Figure A-10b. Only one quarter of the full model is constructed by considering symmetric planes. The radius of the hole a_r is 1 m and the distance between origin and point B is the domain size of the model All displacements in the third direction (y-axis) are restricted. The normal displacement is restricted on the left and bottom boundaries. Moreover, a normal stress $P_0 = 100$ MPa is applied on the outer circumference of the model to represent the in-situ stress in the rock mass.
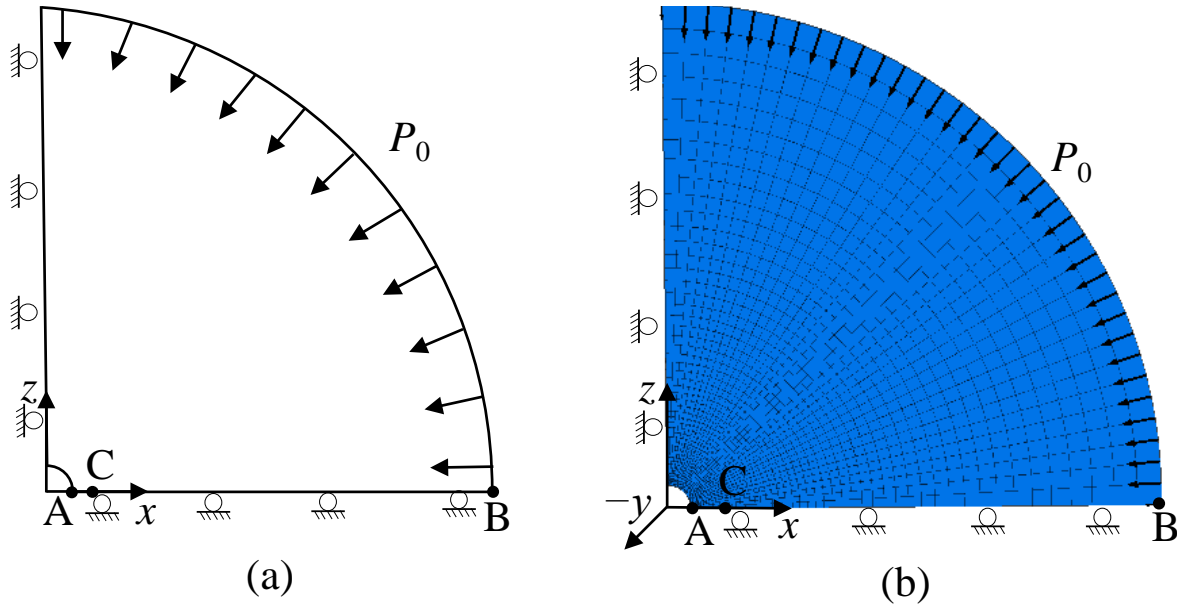
Figure A-10: Schematic of (a) physical model and (b) numerical model of a cylindrical hole in an infinite rock mass obeying HB model with strain softening

Mechanical parameters for rock mass involve a Young's modulus $E_R = 42$ GPa, a Poisson's ratio $v_R = 0.22$, a shear modulus $G_R = 17.2$ GPa, a bulk modulus $K_R = 25$ GPa, a dilation angle $\psi_R = 0°$, the uniaxial compressive stress (UCS) $\sigma_{ci} = 150$ MPa, GSI = 75, Hoek-Brown parameters of $a = 0.5$, $m_i = 25$, $m_b = 10.24$, $s = 0.06$. Strain softening behavior of rock mass is achieved by changing σ_{ci} and m_b based on the plastic confining strain component e_3^p. Residual value of σ_{ci} and m_b are calculated by (Cundall et al. 2003):

$$\sigma_{ci}^r = (1 - \beta)\sigma_{ci} \tag{A.9}$$

$$m_b^r = (1 - \beta)m_b \tag{A.10}$$

where β_s ($0 \leq \beta_s \leq 1$) is a parameter controlling the transition between the peak and the residual strength. e_3^p is given by (Cundall et al. 2003):

$$e_3^p = -\frac{\beta\sigma_{ci}}{2G_R}\left(\frac{\eta+1}{\eta}\right)\left(m_b\frac{\sigma_3}{\sigma_{ci}} + s\right)^a \frac{K_{\psi R}}{K_{\psi R}+2} \tag{A.11}$$

where $K_{\psi R} = (1 + \sin\psi_R)/(1 - \sin\psi_R)$; η ($\eta > 0$) is a parameter controlling the slope of stress-strain curve in the softening stage. The rock mass is perfectly-ductile when $\eta \to 0$ and perfectly-brittle when $\eta \to \infty$. In this case, $\beta = 0.85$, $\eta \to \infty$.

According to Carranza-Torres (2004) solutions, the radial and tangential stresses around a cylinder hole in the infinite HB material with strain softening are expressed as:

$$\sigma_r = \left(\tilde{S}_r - \frac{s}{(m_b^r)^{1/a}}\right)(m_b^r)^{(1-a)/a}\sigma_{ci}^r \tag{A.12}$$

$$\sigma_\theta = \left(\tilde{S}_\theta - \frac{s}{(m_b^r)^{1/a}}\right)(m_b^r)^{(1-a)/a}\sigma_{ci}^r \tag{A.13}$$

The variables in above equations are given as (Carranza-Torres 2004):

$$\tilde{S}_r = \left[\tilde{P}_i^{cr\,1-a} + (1-a)\tilde{\mu}\cdot\ln(\frac{r}{r_{pl}})\right]^{1/(1-a)} \tag{A.14}$$

$$\tilde{S}_\theta = \tilde{S}_r + \tilde{\mu}\cdot\tilde{S}_r^{\;a} \tag{A.15}$$

$$r_{pl} = a\cdot\exp\left[\frac{\tilde{P}_i^{cr\,1-a}-\tilde{P}_i^{\;1-a}}{(1-a)\tilde{\mu}}\right] \tag{A.16}$$

$$\tilde{\mu} = (m_b^r)^{(2a-1)/a} \tag{A.17}$$

$$\tilde{P}_i = \frac{P_{iner}}{(m_b^r)^{(1-a)/a}\sigma_{ci}^r} + \frac{s}{(m_b^r)^{1/a}} \tag{A.18}$$

$$\tilde{P}_i^{cr} = \frac{P_{iner}^{cr}}{(m_b^r)^{(1-a)/a}\sigma_{ci}^r} + \frac{s}{(m_b^r)^{1/a}} \tag{A.19}$$

$$P_i = \frac{P_{iner}}{(m_b)^{(1-a)/a}\sigma_{ci}} + \frac{s}{(m_b)^{1/a}} \tag{A.20}$$

$$P_i^{cr} = \frac{P_{iner}^{cr}}{(m_b)^{(1-a)/a}\sigma_{ci}} + \frac{s}{(m_b)^{1/a}} \tag{A.21}$$

For $a = 0.5$, $\quad P_i^{cr} = \left[\frac{1-\sqrt{1+16S_0}}{4}\right]^2 \tag{A.22}$

$$P_{iner}^{cr} = \left[P_i^{cr} - \frac{s}{(m_b)^{1/a}}\right](m_b)^{(1-a)/a}\sigma_{ci} \tag{A.23}$$

$$S_0 = \frac{P_0}{(m_b)^{(1-a)/a}\sigma_{ci}} + \frac{s}{(m_b)^{1/a}} \tag{A.24}$$

$$\tilde{S}_0 = \frac{P_0}{(m_b^r)^{(1-a)/a}\sigma_{ci}^r} + \frac{s}{(m_b^r)^{1/a}} \tag{A.25}$$

The radial displacement around a cylinder hole in the infinite HB material with strain softening is given as (Carranza-Torres 2004):

$$U = \frac{1}{1-A_1}(\chi_H{}^{A_1} - A_1 \cdot \chi_H)U(1) + \frac{1}{1-A_1}(\chi_H - \chi_H{}^{A_1})U'(1) + \frac{r_{pl}}{8\tilde{G}_R}\frac{A_2-A_3}{1-A_1}\chi_H(ln\chi_H)^2 +$$

$$\frac{r_{pl}}{2\tilde{G}_R}\left[\frac{A_2-A_3}{(1-A_1)^2}\sqrt{\tilde{P}_i{}^{cr}} - \frac{1}{2}\frac{A_2-A_1A_3}{(1-A_1)^3}\right] \times [\chi_H{}^{A_1} - \chi_H + (1-A_1)\chi_H ln\chi_H] \tag{A.26}$$

The variables in above equations are given as (Carranza-Torres 2004):

$$\chi_H = \frac{r}{r_{pl}} \tag{A.27}$$

$$\tilde{G}_R = \frac{G_R}{(m_b^r)^{(1-a)/a}\sigma_{ci}^r} \tag{A.28}$$

$$A_1 = -K_\psi \tag{A.29}$$

$$A_2 = 1 - \nu_R - \nu_R \cdot K_\psi \tag{A.30}$$

$$A_3 = \nu_R - (1 - \nu_R)K_\psi \tag{A.31}$$

$$U(1) = \frac{r_{pl}}{2\tilde{G}_R}(\tilde{S}_0 - \tilde{P}_i^{cr}) \tag{A.32}$$

$$U'(1) = A_1 U(1) + \frac{r_{pl}}{2\tilde{G}_R}[1 - \nu_R(1-A_1)](\tilde{P}_i^{cr} - \tilde{S}_0) - \frac{r_{pl}}{2\tilde{G}_R}[A_1 + \nu_R(1-A_1)](\tilde{P}_i^{cr} + \tilde{\mu}\tilde{P}_i^{cr^a} - \tilde{S}_0) \tag{A.33}$$

A2.1 Effect of domain size

Figure A-11 shows the variation of the radial displacement at points A ($r = 1.5$ m) and C ($r = 3$ m) with different domain sizes ranging from 5 m to 90 m. These domain sizes correspond to 2.5 to 45 times of the diameter of the hole. The radial displacement tends to become stable when the domain size is larger than 17 m. Therefore, the optimal domain size should be 17 m. In this case, a conservative domain size of 41 m is used for further study of the effect of the mesh size.
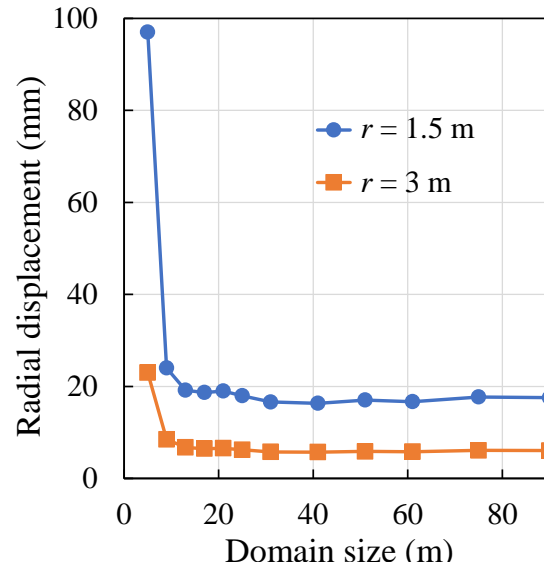
Figure A-11: Variation of the radial displacements at points of A (r = 1.5 m) and C (r = 3 m) with different domain sizes

A2.2 Effect of mesh size

Figure A-12 shows the variation of the radial displacement at points A (r = 1.5 m) and C (r = 3 m) with different mesh sizes ranging from 2 m to 0.0025 m. Results indicate that the radial displacement tends to converge when the mesh size reduces to 0.1 m. The radial displacement slightly increases as the mesh size further decreases from 0.1 m to 0.0025 m. A value of 0.025 m is thus determined as the optimal mesh size to ensure the stable result.
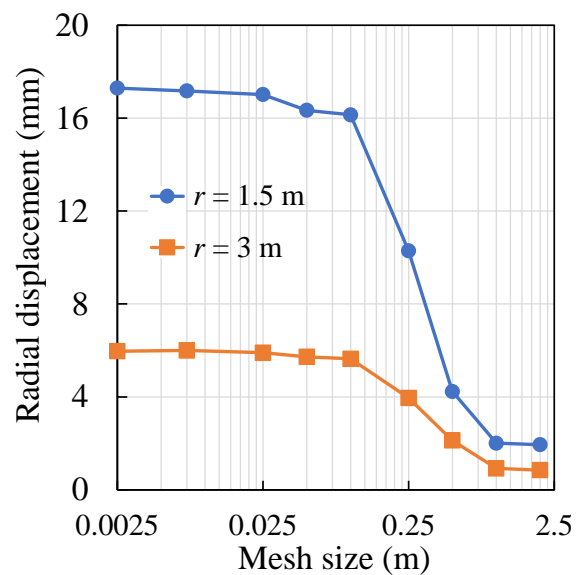
Figure A-12: Variation of the radial displacements at points of A ($r = 1.5$ m) and C ($r = 3$ m) with different mesh sizes

A2.3 Comparison between numerical and analytical results

Figure A-13 shows comparisons between numerical results of the tangential stress σ_θ, radial stress σ_r, and radial displacement U along line AB considering domain size of 41 m and mesh size of 0.025 m with the analytical solution proposed by Carranza-Torres (2004). In the figure, the numerical results show quite good agreement with the analytical results. This indicates that the Hoek-Brown model with strain softening in FLAC^{3D} is validated.
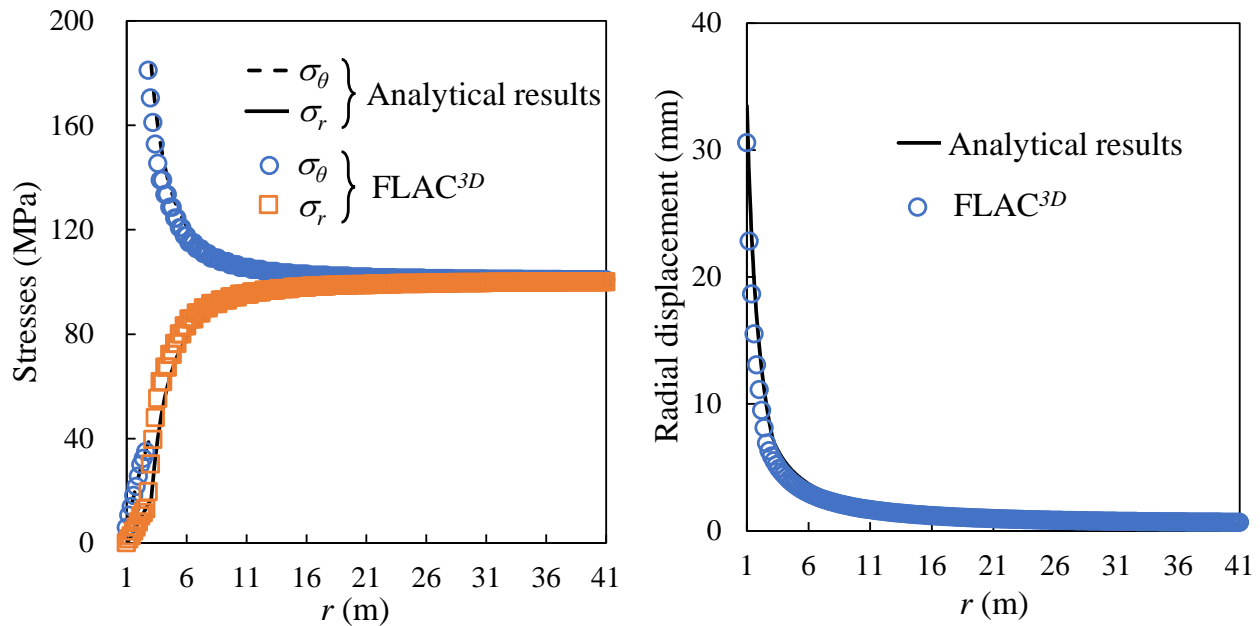
Figure A-13: Comparisons between numerical results with analytical result of Carranza-Torres (2004) of (a) stresses distribution and (b) radial displacement along line AB around a cylinder hole in Hoke-Brown material with strain softening

A3 Validation of the linear elastic model in FLAC^{3D}

FLAC^{3D} can also be validated against analytical solutions of stresses and displacements around an infinite cylinder hole in the infinite linear elastic material. The problem can be analyzed in a plane strain condition. The physical model of this problem is shown in Figure A-14. The origin locates at the central point of the model. In the figure, a_r is the radius of the hole. Domain size is the distance from the hole to the model boundary. r and θ are the cylindrical coordinates. The model is characterized by Young's modulus E and Poisson's ratio v.
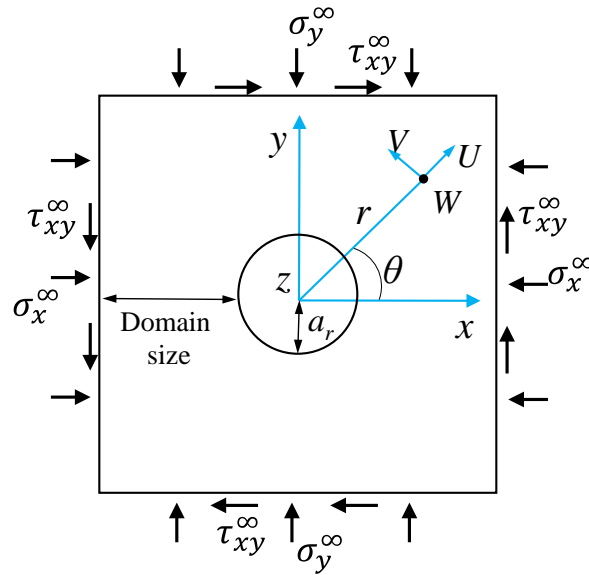
Figure A-14: Physical plane strain model of a cylinder hole in an infinite linear elastic material

When the infinite hole is subject to a stress field composed of $\sigma_x^\infty, \sigma_y^\infty, \sigma_z^\infty, \tau_{xy}^\infty, \tau_{xz}^\infty, \tau_{yz}^\infty$, the analytical solutions for stresses around the hole are given as (Hiramatsu and Oka 1962, 1968):

$$\sigma_r = \frac{\sigma_x^\infty + \sigma_y^\infty}{2}\left(1 - \frac{a^2}{r^2}\right) + \frac{\sigma_x^\infty - \sigma_y^\infty}{2}\left(1 + 3\frac{a^4}{r^4} - 4\frac{a^2}{r^2}\right)\cos 2\theta + \tau_{xy}^\infty\left(1 + 3\frac{a^4}{r^4} - 4\frac{a^2}{r^2}\right)\sin 2\theta \quad \text{(A.34)}$$

$$\sigma_\theta = \frac{\sigma_x^\infty + \sigma_y^\infty}{2}\left(1 + \frac{a^2}{r^2}\right) - \frac{\sigma_x^\infty - \sigma_y^\infty}{2}\left(1 + 3\frac{a^4}{r^4}\right)\cos 2\theta - \tau_{xy}^\infty\left(1 + 3\frac{a^4}{r^4}\right)\sin 2\theta \quad \text{(A.35)}$$

$$\sigma_z = -2v\left(\sigma_x^\infty - \sigma_y^\infty\right)\frac{a^2}{r^2}\cos 2\theta - 4v\tau_{xy}^\infty\frac{a^2}{r^2}\sin 2\theta + \sigma_z^\infty \quad \text{(A.36)}$$

$$\tau_{r\theta} = -\frac{\sigma_x^\infty - \sigma_y^\infty}{2}\left(1 - 3\frac{a^4}{r^4} + 2\frac{a^2}{r^2}\right)\sin 2\theta + \tau_{xy}^\infty\left(1 - 3\frac{a^4}{r^4} + 2\frac{a^2}{r^2}\right)\cos 2\theta \quad \text{(A.37)}$$

$$\tau_{\theta z} = \left(-\tau_{xz}^\infty\sin\theta + \tau_{yz}^\infty\cos\theta\right)\left(1 + \frac{a^2}{r^2}\right) \quad \text{(A.38)}$$

$$\tau_{zr} = \left(\tau_{xz}^{\infty}\cos\theta + \tau_{yz}^{\infty}\sin\theta\right)\left(1 - \frac{a^2}{r^2}\right) \tag{A.39}$$

where σ_r is the radial stress; σ_θ is the tangential stress; σ_z is the normal stress along third direction (z-axis); $\tau_{r\theta}$, $\tau_{\theta z}$, and τ_{zr} are the shear stresses around infinite cylinder hole based on cylindrical coordinates.

The analytical solutions for displacements around the infinite cylinder hole had been given by Li (1997) as follows:

$$U = \frac{1}{E}\left\{\frac{\sigma_x^{\infty}+\sigma_y^{\infty}}{2}(1+v) + \left[-(1+v)\frac{a^2}{r^2} + 4(1-v^2)\right]\left(\frac{\sigma_x^{\infty}-\sigma_y^{\infty}}{2}\cos 2\theta + \tau_{xy}^{\infty}\sin 2\theta\right)\right\}\frac{a^2}{r} \tag{A.40}$$

$$V = -\frac{(1+v)}{E}\left[\frac{a^2}{r^2} + 2(1-2v)\right]\left(\frac{\sigma_x^{\infty}-\sigma_y^{\infty}}{2}\sin 2\theta - \tau_{xy}^{\infty}\cos 2\theta\right)\frac{a^2}{r} \tag{A.41}$$

$$W = \frac{2(1+v)}{E}\left(\tau_{xz}^{\infty}\cos\theta + \tau_{yz}^{\infty}\sin\theta\right)\frac{a^2}{r} \tag{A.42}$$

where U, V and W are the components of displacement in the directions of r, θ, and z (third direction) respectively.

Figure A-15 shows the corresponding plane strain numerical model built with FLAC^{3D}. In the numerical model, hole radius $a = 1$ m, $E = 10$ GPa, $v = 0.25$. The applied stress components include $\sigma_x^{\infty} = 15$ MPa, $\sigma_y^{\infty} = 10$ MPa, and $\tau_{xy}^{\infty} = 3$ MPa. The displacement along the third direction (z-axis) is restricted. In order to ensure stable numerical results, the domain size and mesh size of the numerical model need to be determined based on the sensitivity analyses.
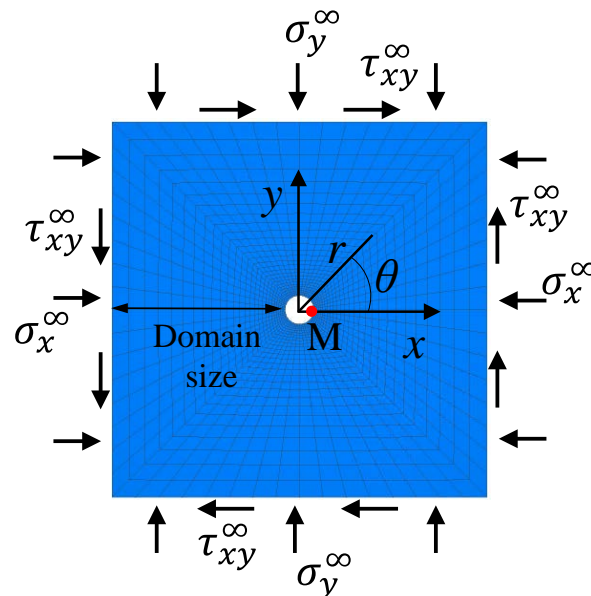
Figure A-15: Plane strain numerical model of a cylinder hole in an infinite linear elastic material built with FLAC^{3D}

A3.1 Effect of domain size

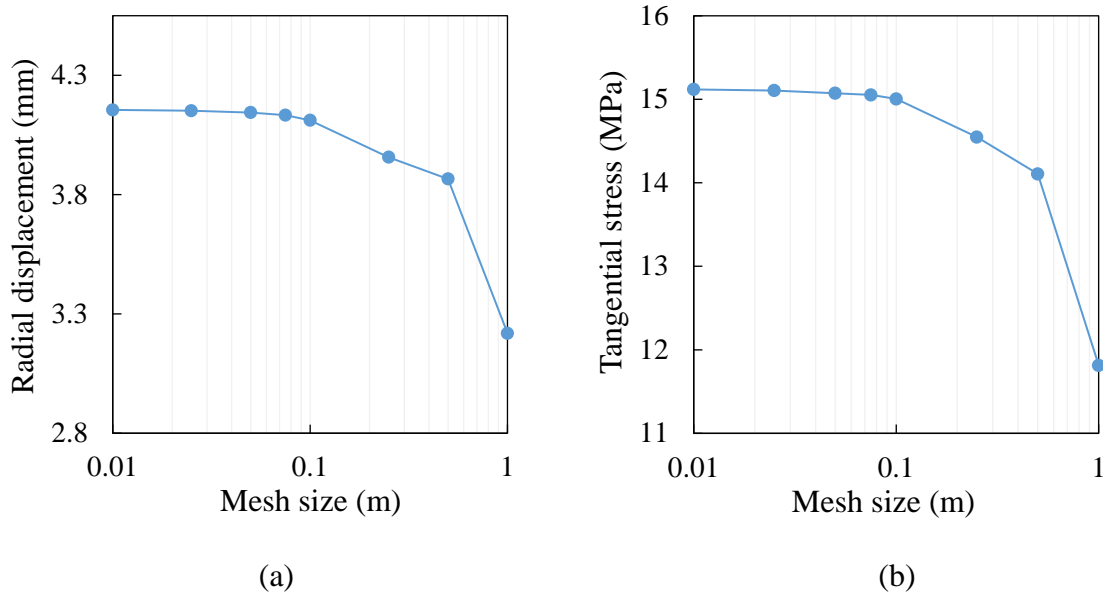The numerical results of radial displacement and tangential stress are obtained at point M in Figure A-15. Figure A-16 shows the variations of radial displacement and tangential stress at point M as functions of domain size. The variation of numerical results reduces as the domain size increases from 1 to 20 m and become stable when the domain size is larger than 10 m. Therefore, the optimal domain size is determined as 12 m that is 6 times of the size of the hole.

(a)   (b)
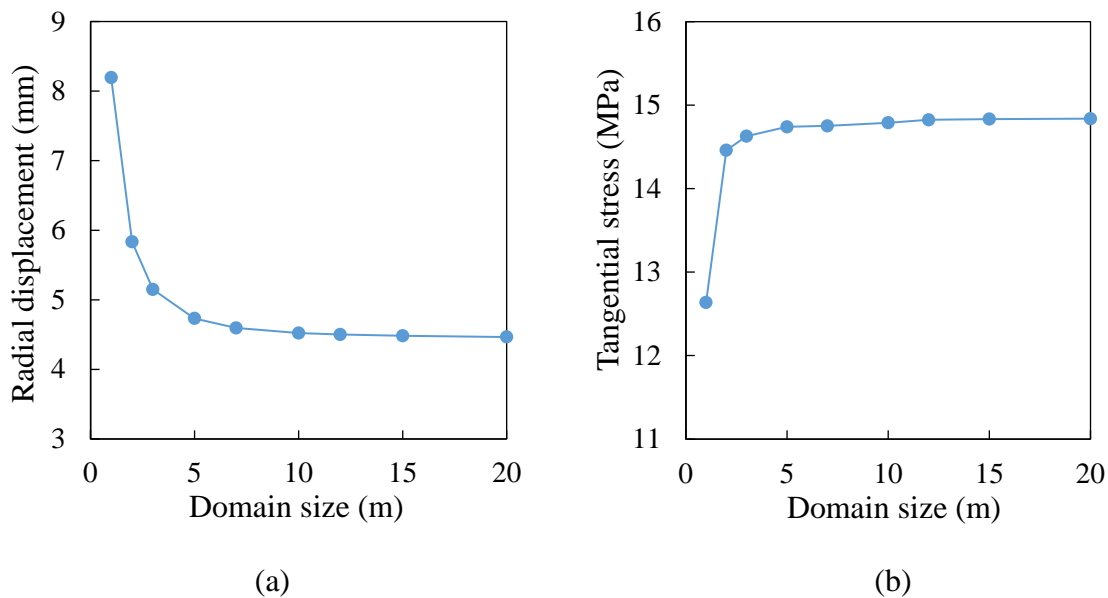
Figure A-16: Variations of radial displacement and tangential stress at point M as functions of domain size

A3.2 Effect of mesh size

Figure A-17 shows the variations of radial displacement and tangential stress at point M as functions of mesh size. The mesh size ranges from 1 to 0.01 m. The numerical results become stable when the mesh size is smaller than 0.1 m. Further reduction of the mesh size will not greatly change the results. Therefore, the optimal mesh size is determined as 0.05 m to ensure stable results.

(a)   (b)

Figure A-17: Variations of radial displacement and tangential stress at point M as functions of
mesh size

A3.3 Comparison between numerical and analytical results

Numerical simulations are conducted by using the optimal domain and mesh sizes. Figure A-18 shows the comparisons between the numerical results of σ_r, σ_θ, $\tau_{r\theta}$, U, V long x-axis with the analytical solutions. The good correlations between the numerical and analytical results validate the FLAC^{3D}.

(a)   (b)
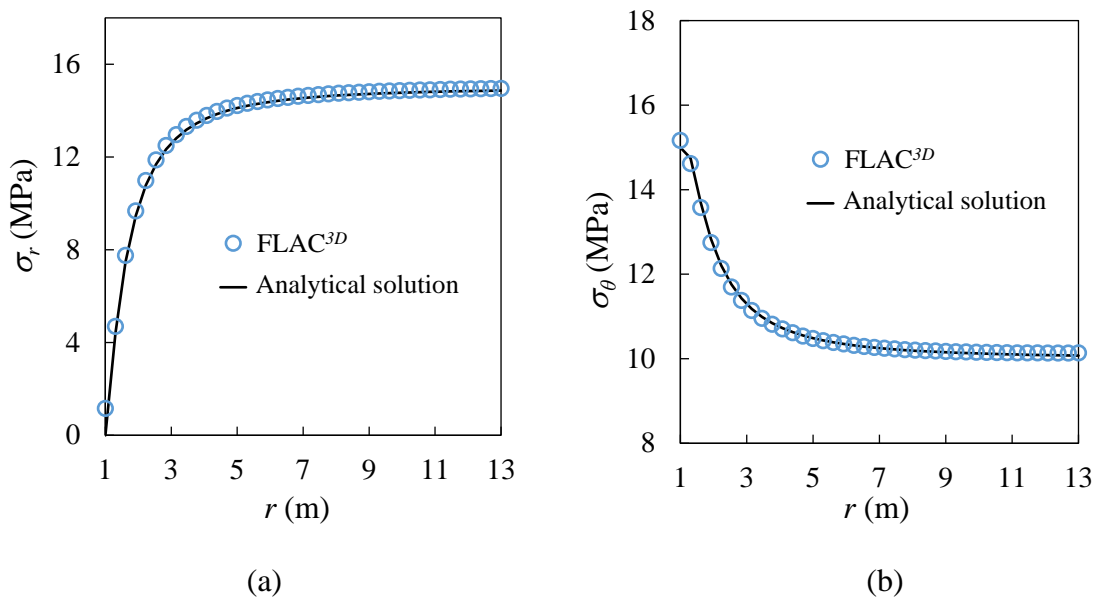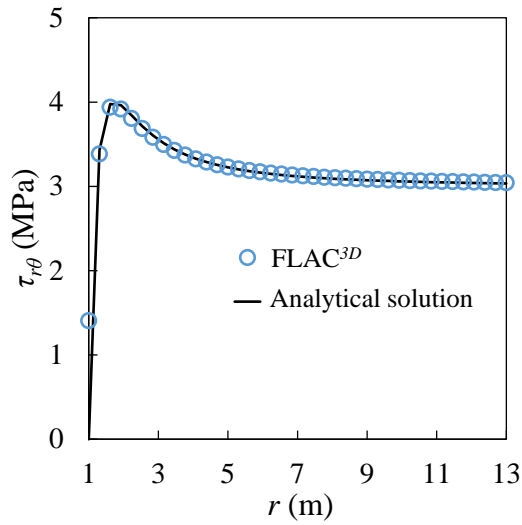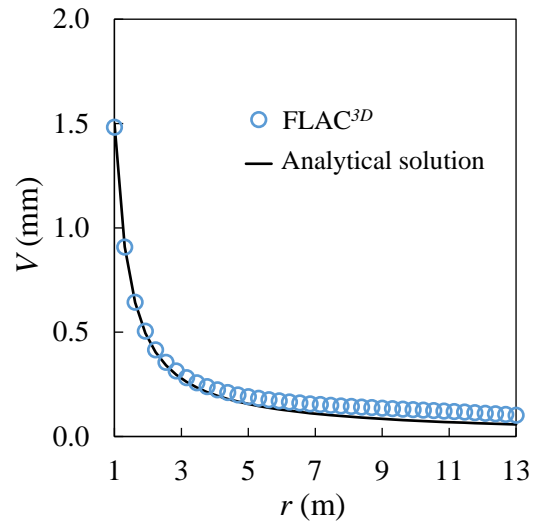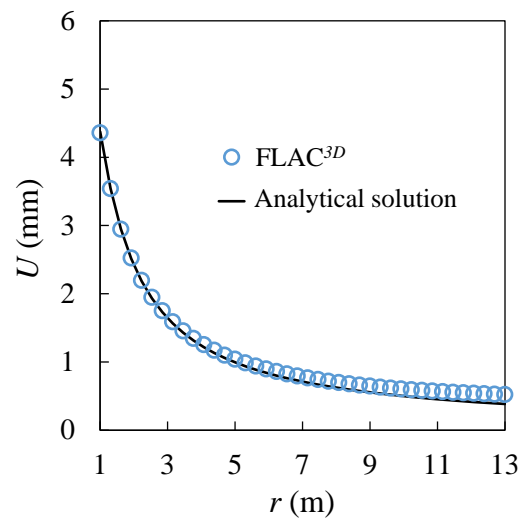
Figure A-18: Comparisons between the numerical results and the analytical results of (a) σ_r, (b) σ_θ, (c) $\tau_{r\theta}$, (d) V, (e) U long x-axis around a cylinder hole in the linear elastic material

APPENDIX B   THE BURGERS-CREEP VISCOPLASTIC MODEL AND ITS VALIDATION IN FLAC^{3D}

B1 The Burgers-creep viscoplastic model in FLAC^{3D}

The Burgers-creep viscoplastic (CVISC) model is a creep constitutive model commonly used to model the creep behavior of rocks. The CVISC model consists of the Burgers model and the MC model. The Burgers model is composed of a Kelvin-Voigt element and a Maxwell element. The schematic of the CVISC model is shown in Figure B-1. The constitutive equations of the Burgers models are defined as (Jaeger 1969):
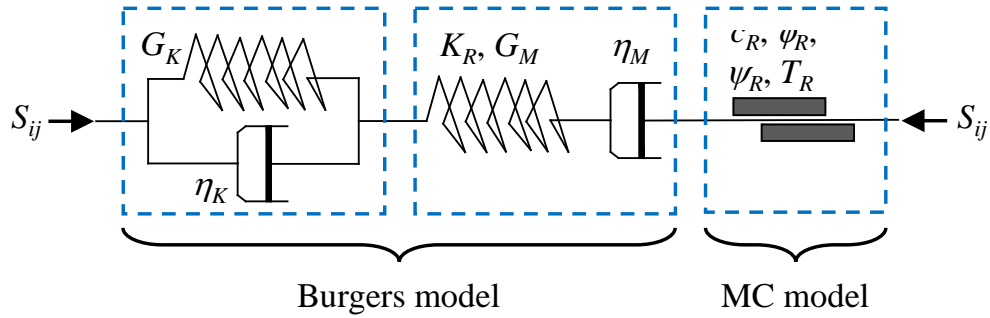
Figure B-1: Schematics of the CVISC model in FLAC^{3D}

$$\varepsilon_{ij} = \frac{\sigma_m}{3K_R} + \frac{S_{ij}}{2G_M} + \frac{S_{ij} \cdot t}{2\eta_M} + \frac{S_{ij}}{2G_K} \cdot \left[1 - exp\left(-\frac{G_K \cdot t}{\eta_K} \right) \right] \tag{B.1}$$

where t (s) denotes time; ε_{ij} is the strain tensor; S_{ij} is the deviatoric stress tensor; σ_m is the spherical stress tensor; G_M (Pa) and η_M (Pa·s) are the shear modulus and viscosity coefficient of the Maxwell element; G_K (Pa) and η_K (Pa) are the shear modulus and viscosity coefficient of the Kelvin-Voigt element; K_R (Pa) is the bulk modulus. In addition to above parameters, the CVISC model in FLAC^{3D} involves a cohesion c_R (Pa), an internal friction angle ϕ_R (°), a dilation angle ψ_R (°) and a tensile strength T_R (Pa).

The strain-time curve of the CVISC model is shown in Figure B-2. When the CVISC model is submitted to a stress state below MC failure criterion, the mechanical behavior is governed by the Burgers model as shown in Figure B-2a. The instantaneous strain is captured by the Maxwell's spring element while the primary creep stage is captured by the Kelvin-Voigt element. The linear viscoelastic strain with time at a constant strain rate for the secondary creep stage of the rock mass

is described by the Maxwell's dashpot element. The tertiary creep state cannot be described by the CVISC model. However, instantaneous (time-independent) plastic strain following the MC elasto-plastic model occurs if the stress state exceeds the MC yield criterion as shown in Figure B-2b.
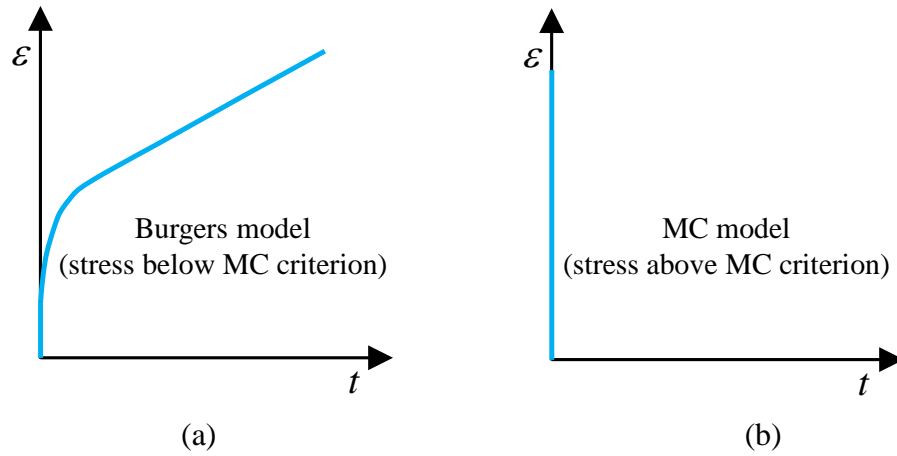

Figure B-2: Stain-time curve of the CVISC model under a stress state (a) below the MC criterion and (b) above the MC criterion

Table B-1 presents viscoelastic parameters for modeling some typical rocks with the CVISC model reported in literatures. In the table, E_M and E_K are Young's modulus of elastic springs in Kelvin-Voigt and Maxwell elements of the CVISC model that can be used in one-dimensional condition.

Table B-1: Viscoelastic parameters for some typical rocks reported in the literature

Rocks	G_M or E_M (Pa)	η_M (Pa·s)	G_K or E_K (Pa)	η_K (Pa·s)	References
Rock Salt	7.20×10^9	5.37×10^{15}	2.64×10^{10}	7.60×10^{14}	
	8.41×10^9	4.96×10^{15}	2.19×10^{10}	1.17×10^{15}	Zhang et al. (2012)
	1.20×10^{10}	8.39×10^{15}	2.39×10^{10}	5.58×10^{14}	
	3.41×10^9	1.57×10^{17}	1.93×10^9	1.14×10^{15}	Pałac-Walko and Pytel (2014)
	1.36×10^9	3.46×10^{16}	7.54×10^9	7.82×10^{14}	Mansouri and Ajalloeian (2018)
Shale	1.92×10^7	4.22×10^{13}	3.07×10^7	1.07×10^{12}	Bonini et al. (2009)
	3.50×10^9	2.10×10^{16}	3.50×10^8	4.20×10^{18}	Sharifzadeh et al. (2013)
	1.63×10^{10}	9.19×10^{15}	3.32×10^{11}	6.84×10^{14}	Kamali-Asl et al. (2018)
	2.53×10^{10}	2.61×10^{16}	2.62×10^{11}	2.66×10^{14}	
Schist	5.76×10^8	8.82×10^{14}	4.98×10^8	1.34×10^{14}	Barla et al. (2010)
Sandstone	6.50×10^9	1.51×10^{17}	5.23×10^{11}	1.56×10^{16}	Xu et al. (2011)

Argillaceous rock	2.17×10^9	3.60×10^{15}	3.29×10^9	1.49×10^{13}	Feng et al. (2006)
Limestone	2.20×10^8	5.96×10^{16}	1.99×10^8	4.00×10^{13}	Chin and Rogers (1987)
	1.05×10^7	1.74×10^{15}	4.08×10^8	1.73×10^{19}	Paraskevopoulou et al (2018)
	1.66×10^8	1.78×10^{14}	5.18×10^8	1.53×10^{16}	
Diorite	1.09×10^{10}	2.80×10^{12}	1.09×10^{10}	1.02×10^{12}	Qi and Fourie (2019)

Note: Corresponding values in the table from the studies of Pałac-Walko and Pytel (2014), Mansouri and Ajalloeian (2018) and Kamali-Asl et al. (2018) are for E_M and E_K.

B2 Validation of the CVISC model in FLAC^{3D}

The applicability and capability of the CVISC model in FLAC^{3D} can be validated by comparing it with experimental results. Mansouri and Ajalloeian (2018) conducted conventional uniaxial creep tests on the rock salt specimens that have a diameter of 58 mm and a height of 116 mm. The tests were performed at room temperature using a hydraulic press to maintain the constant load while the axial creep strain was measured with dial-gauges for 14 days. Figure B-3a shows the physical model of Mansouri and Ajalloeian (2018) creep tests. The numerical model of the creep tests is built with FLAC^{3D} as illustrated in Figure B-3b. Vertical displacements are not allowed at the bottom of the numerical model while a uniform compressive stress is applied on the top to represent the constant load. The CVISC model is applied for the numerical model and the axial strain is calculated based on the average vertical displacement at the top recorded during the creep calculation.
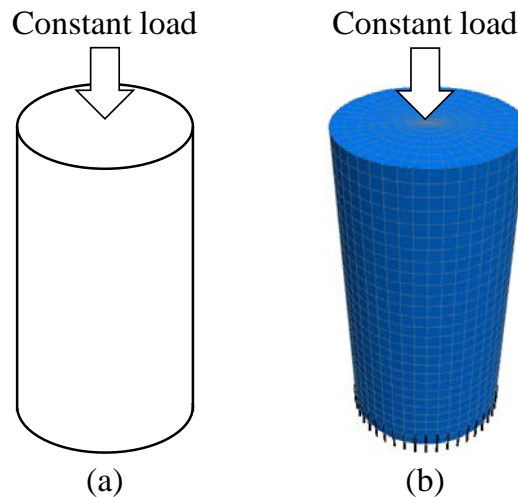
Figure B-3: (a) The physical model of conventional uniaxial creep tests conducted by Mansouri and Ajalloeian (2018); (b) the numerical model built with FLAC^{3D}

Figure B-4 illustrates the creep strain-time curve of Mansouri and Ajalloeian (2018) test under an applied stress of 15 MPa. The material viscoelastic parameters of the CVISC model can be determined by calibrating the analytical solutions based on the experimental results. The calibrated viscoelastic parameters include K_R, G_K, η_K, G_M, and η_M, which are shown in Table B-2. The other material parameters of $c_R = 8.5$ MPa, $\phi_R = 35°$, $\psi_R = 0°$, $T_R = 1.5$ MPa are assumed based on the reported UCS which do not affect the numerical results of creep strain-time curve. Before comparing the numerical results with the analytical results, sensitivity analyses are needed to determine the optimal values of some modeling parameters for the numerical model shown in Figure B-3b. These parameters include the mesh size, initial timestep t_i, latency, *lfob* and *ufob*. The sensitivity analyses are provided as follows.
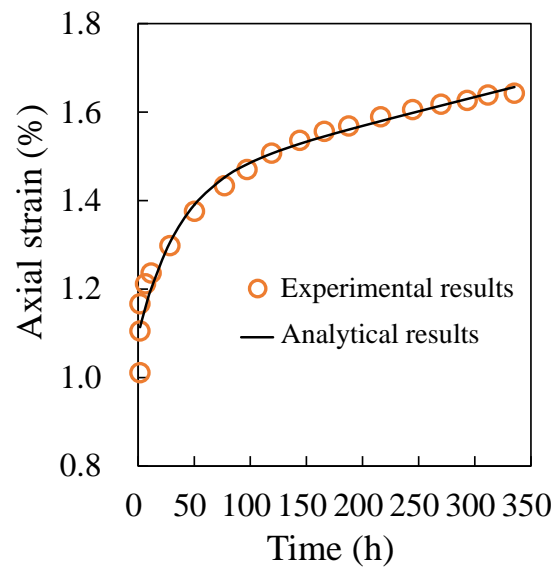
Figure B-4: Experimental results of Mansouri and Ajalloeian (2018) and the calibrated analytical results of the CVISC model

Table B-2: Viscoelastic parameters for rock salt calibrated by comparing the analytical solution of CVISC model with experimental results of Mansouri and Ajalloeian (2018)

K_R (GPa)	G_K (GPa)	η_K (Pa·s)	G_M (GPa)	η_M (Pa·s)
1.13	1.45	1.84×10^{14}	0.53	2.81×10^{15}

B2.1 Sensitivity analyses of mesh size

Sensitivity analyses are conducted using the calibrated material parameters and different modeling parameters. The applied constant stress on the top surface of the numerical model is same as the test of Mansouri and Ajalloeian (2018) which is 15 MPa. Figure B-5 shows the numerical results of creep strain-time curve with different mesh sizes ranging from 15 to 1.5 mm. The results are almost superposed which indicates that the mesh size has little effect on the creep strain of the numerical model. Based on these results, 3 mm is determined as the optimal mesh size for the numerical model.
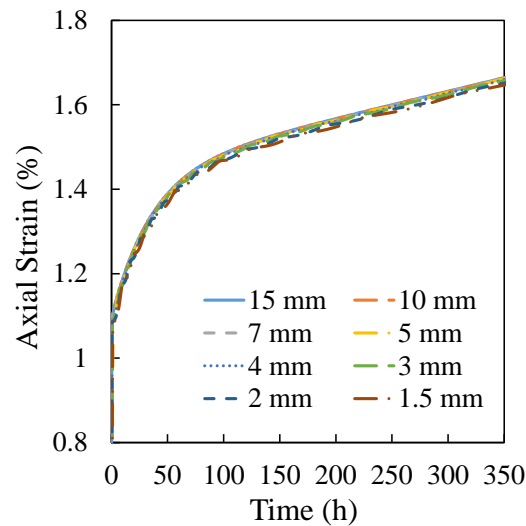
Figure B-5: Numerical results of creep strain-time curve with different mesh sizes

B2.2 Sensitivity analyses of initial timestep

Figure B-6 shows the numerical results of creep strain-time curve with different initial timestep t_i. The creep strain-time curve of numerical model gradually converge as t_i reduces from 1000 to 60 s. When t_i becomes smaller than 60 s, the numerical results become stable and superposed. Based on the results shown in Figure B-6. The optimal initial timestep t_i is determined as 30 s.
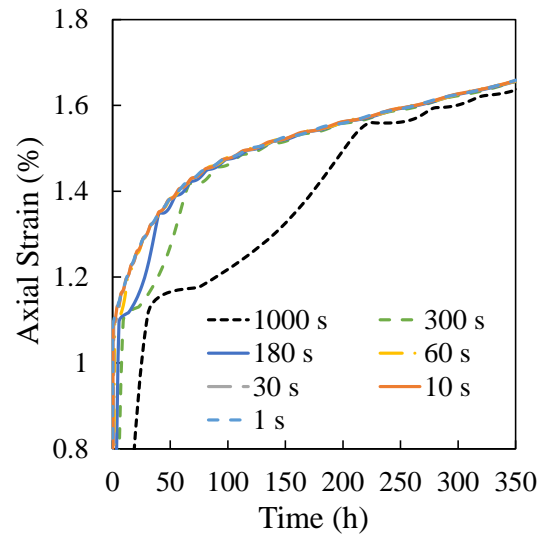
Figure B-6: Numerical results of creep strain-time curve with different initial timestep t_i

B2.3 Sensitivity analyses of latency

The latency is the minimum number of steps that need to be calculated before that the timestep can be adjusted. Figure B-7 illustrates the numerical results of creep strain-time curve with different latency ranging from 1 to 500 steps. It can be seen that when the latency is 1 step, the numerical results are slightly unstable between 250 to 350 h. This is because that when the latency is small, the timestep can be adjusted very frequently which affects the stability of the results. Based on the results shown in Figure B-7, the optimal value for the latency is determined as 100 steps.
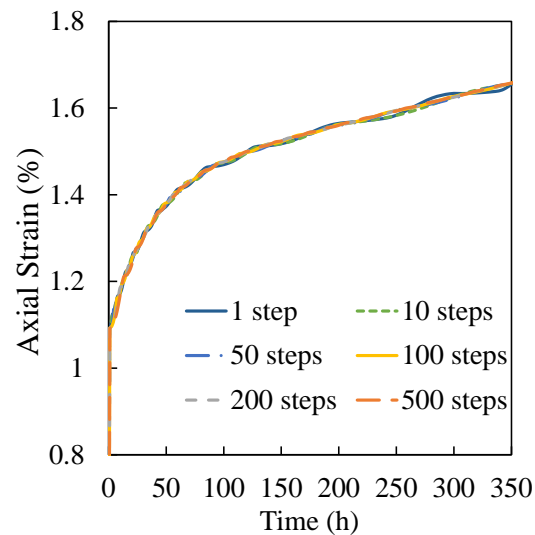
Figure B-7: Numerical results of creep strain-time curve with different latency

B2.4 Sensitivity analyses of *lfob* and *ufob*

The *lfob* and *ufob* are lower limit and upper limit of the unbalanced force ratio (UFR) respectively. The timestep is increased by multiplying 1.05 if UFR falls below *lfob*, and decreased by multiplying 0.95 if UFR exceeds *ufob*. Figure B-8 shows the numerical results of creep strain-time curve with different *lfob* (Figure B-8a) and *ufob* (Figure B-8b). The results are almost superposed for different *lfob* and *ufob* which indicate that these parameters have little effect on the creep strain of the numerical model. Based on the results in Figure B-8, the optimal values of *lfob* and *ufob* are determined as 1×10^{-5} and 3×10^{-5} respectively.

(a)

(b)
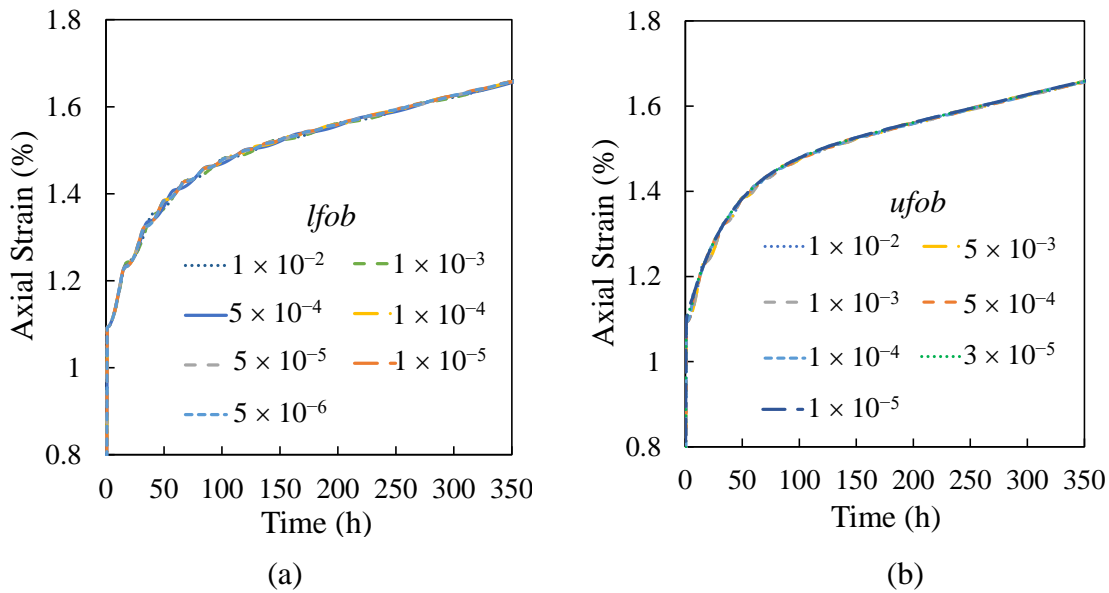
Figure B-8: Numerical results of creep strain-time curve with different (a) *lfob* and (b) *ufob*

B2.5 Comparison between numerical results of the CVISC model with the experimental and analytical results

Based on above sensitivity analyses, the optimal values of mesh size, t_i, latency, *lfob* and *ufob* are determined for the optimal numerical model. In addition, the maximum timestep t_m for the CVISC model in FLAC^{3D} needs to be defined to ensure the quasi-static equilibrium for the numerical model during the creep calculation (Itasca 2013). Its value can be calculated based on an equation recommended in FLAC^{3D} manual. In this case, the value for t_m is set as 1000 s. By using the calibrated material parameters and optimal modeling parameters, the numerical results of creep strain-time curve are obtained and are compared with analytical and experimental results of

Mansouri and Ajalloeian (2018) as shown in Figure B-9. Quite good agreement is obtained between numerical, analytical and experimental results which validate the applicability and capability of the CVISC model in FLAC^{3D}.
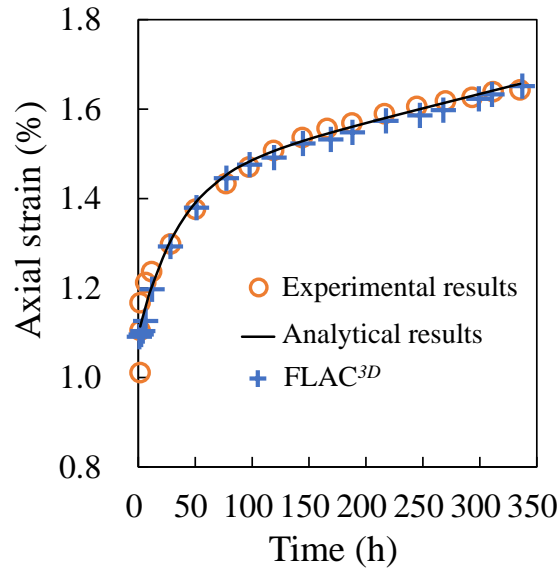
Figure B-9: Comparison between the numerical results of creep strain-time curve of CVISC model in FLAC^{3D} with analytical results and experimental results of Mansouri and Ajalloeian (2018)

B3 Effect of viscoelastic parameters on the creep strain of CVISC model

The effects of viscoelastic parameters on the creep strain of the CVISC model are investigated by changing one parameter in one case. In the simulations, other parameters are obtained from Table B-2. Figure B-10 shows the variation of the creep strain-time curve of the CVISC model for different shear modulus G_K (Figure B-10a) and viscosity coefficient η_K (Figure B-10b) of the Kelvin-Voigt element. The results show that the increase of G_K results in the decrease of duration of the primary creep stage. As the η_K increases, the creep strain rate in the primary creep stage reduces while the duration of the primary creep stage increases. However, the variation of G_K and η_K do not affect the instantaneous strain and the secondary creep stage of the numerical model.
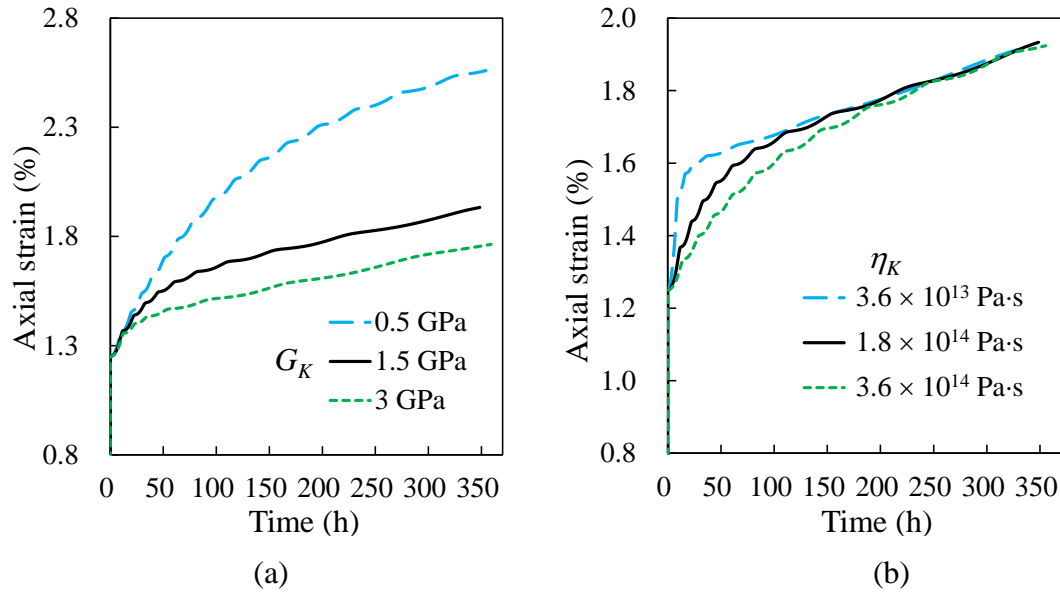
Figure B-10: Numerical results of creep strain-time curve with different (a) G_K and (b) η_K

Figure B-11 shows the variation of the creep strain-time curve of the CVISC model for different shear modulus G_M (Figure B-11a) and viscosity coefficient η_M (Figure B-11b) of the Maxwell element. The results show that the increase of G_M causes the decrease of the instantaneous strain. However, it does not influence the creep strain of the CVISC model. As the η_M increases, the creep strain rate in the secondary creep stage reduces. Therefore, the viscosity coefficient of the Maxwell element affects the rate of long-term creep deformation of the CVISC model.
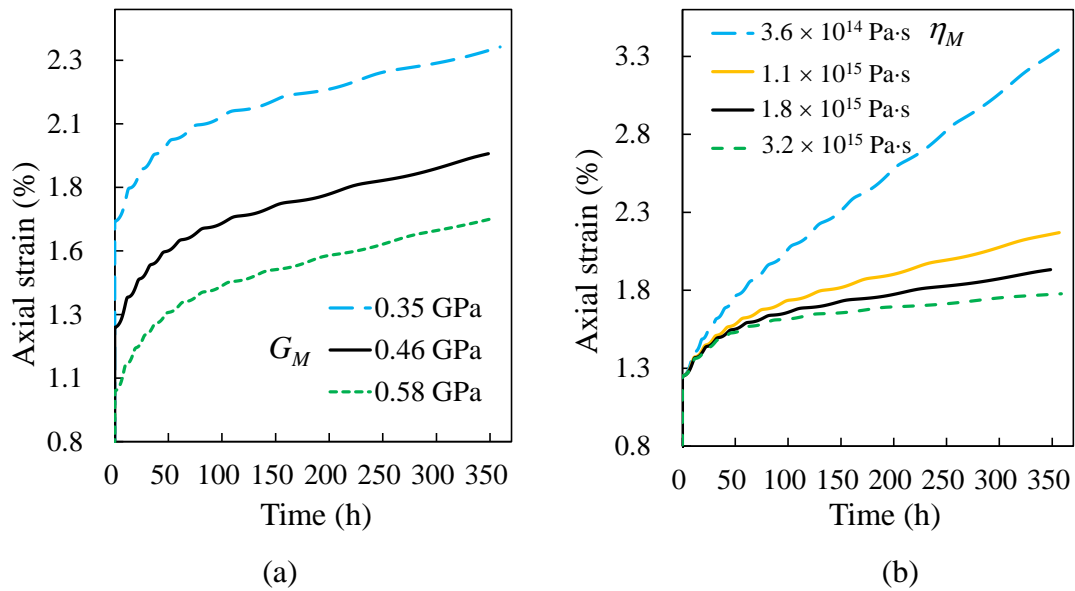
Figure B-11: Numerical results of creep strain-time curve with different (a) G_M and (b) η_M

B4 Comparison between the CVISC and MC models in static simulation

In order to verify that the mechanical behavior of CVISC model is governed by the MC model in the static simulation, the simulations of uniaxial constant strain rate compression are conducted. In the simulations, the CVISC and MC models are applied to the numerical model shown in Figure B-3b respectively. The related parameters in the MC model are set as same as those of the CVISC model. On the top of the numerical model, a constant velocity of 1×10^{-5} mm/step is applied to simulate the compression. The vertical stress on the top surface is monitored during the simulation. Figure B-12 shows the comparison between the numerical results of stress-strain curve of CVISC and MC models. The results show that as the axial strain increases, the vertical stress of two model increases with the same slope. The CVISC and MC models also reach a same strength of 32 MPa when the axial strain is larger than 2.5%. The results in Figure B-12 verifies that the mechanical of CVISC model is governed by the MC model in static simulations.
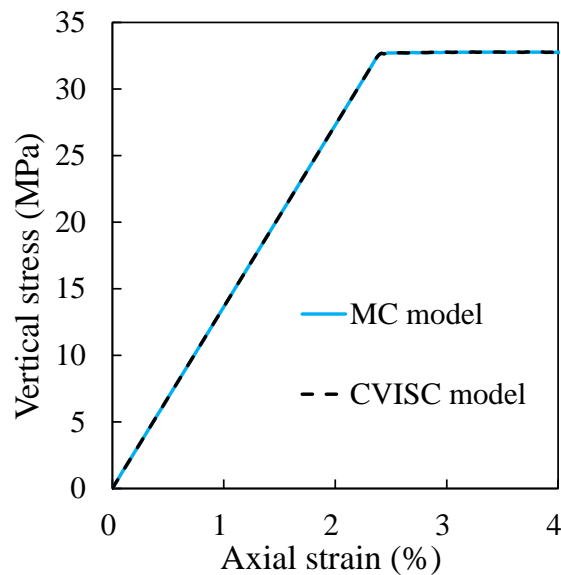
Figure B-12: Comparison between the numerical results of stress-strain curve of CVISC and MC models in a static simulation

B5 Conclusions

- The CVISC model in FLAC^{3D} is validated.

- In the CVISC model, G_K and η_K affect the duration and creep strain rate of the primary creep stage. G_M affects the instantaneous deformation while η_M affects the long-term creep strain rate of the secondary creep stage. The CVISC model is not able to capture the tertiary creep stage.

- The CVISC model reduces to the Mohr-Coulomb model in the static simulations.

APPENDIX C   METHOD OF APPLYING VARIED MESH SIZES FOR DIFFERENT AREAS IN NUMERICAL MODEL

C1 Introduction

The mesh size of a numerical model could affect the accuracy of numerical results and the calculation time. When the mesh size is coarse, the convergency can be fast, but the numerical results may be unstable because high gradients of stress or displacement cannot be reflected by the coarse mesh. However, when the mesh size is very fine, particularly for a large model, the numerical simulation may be very time-consuming. Therefore, a method can be used by applying fine mesh in the area of interests such as area around underground excavations while using coarse mesh for other parts of the numerical model. It can ensure the stable numerical results with a reasonable run time. In this section, the problem of a cylindrical hole in a rock mass that obeys Mohr-Coulomb criterion is simulated. Varied mesh sizes are used for different parts of the numerical model. The Numerical results are compared with the analytical solutions proposed by Salencon (1969) to validate this method.

C2 Description of the method

The physical model of the problem is same as that shown in Figure A-1a. The radius of the hole is 1 m. Figure C-1 shows the numerical model of a cylindrical hole in a rock mass. It has the same material parameters and boundary conditions as those presented in Appendix A1. The material parameters involve Young's modulus E of 6.5 GPa, cohesion c of 3 MPa, friction angle ϕ of 35°, Poisson's ratio v of 0.25, and tensile strength T of 10 GPa. Displacements along y-axis (third direction) are restricted. The normal displacements are prohibited on the left and the bottom boundary. The normal stress $P_0 = 40$ MPa is applied on the top and right surface. Based on the sensitivity analyses conducted in Appendix A1, a domain size of 20 m is used for the numerical model. In the numerical model, fine mesh of a 0.05 m size and 1.05 radial grid ratio is applied for the area within a distance of D_f around the excavated hole. For the outer part of the numerical model, coarse mesh is used, whose size follows an integer ratio χ to that of the fine mesh to reduce the discontinuity.
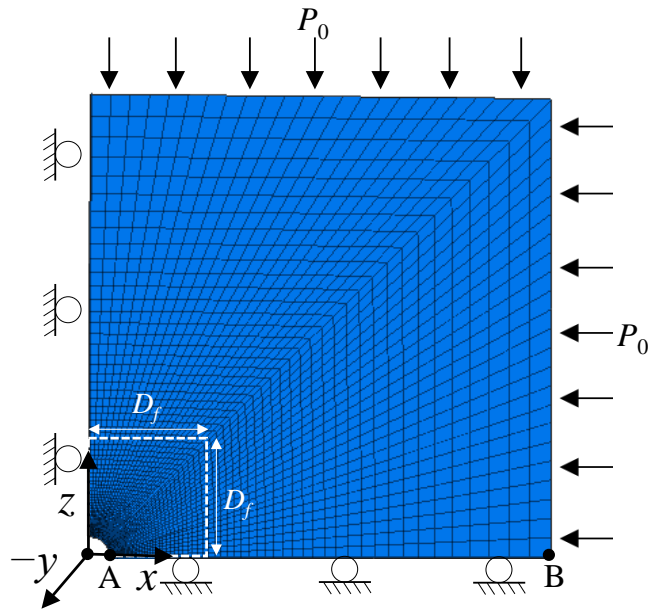
Figure C-1: Numerical model of the problem of a cylindrical hole in the rock mass with a range of D_f around the excavated hole for the fine mesh

Different values of D_f and χ are studied. D_f ranges from 2 to 7 m while χ ranges from 1 to 6. It should be noted that when χ equals to 1, the mesh sizes for the area around the hole and outer part of the numerical model are same. Figure C-2 illustrates an example of numerical model with D_f = 7 m and χ = 4.
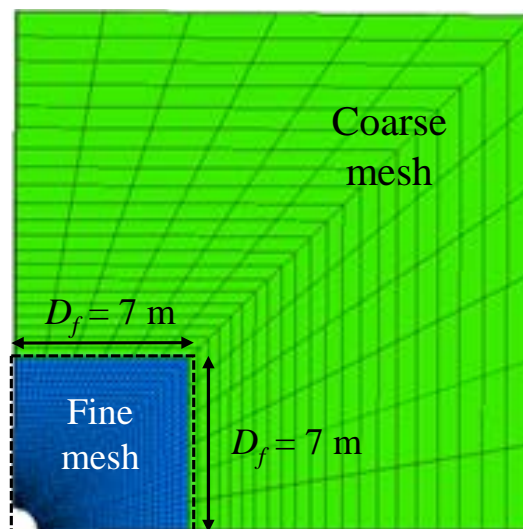

Figure C-2: Illustration of a numerical model with D_f = 7 m and χ = 4

C3 Results

Figure C-3 shows the numerical results of radial displacement at the point A (see Figure C-1) as a function of χ for different values of D_f. From the figure, one can see that for different D_f and χ the results are almost stable. The good agreement is also seen between the numerical results and the analytical solution of Salencon (1969). This suggests that the value of D_f ranging from 2 to 7 m and the value of χ ranging from 1 to 6 are all applicable.
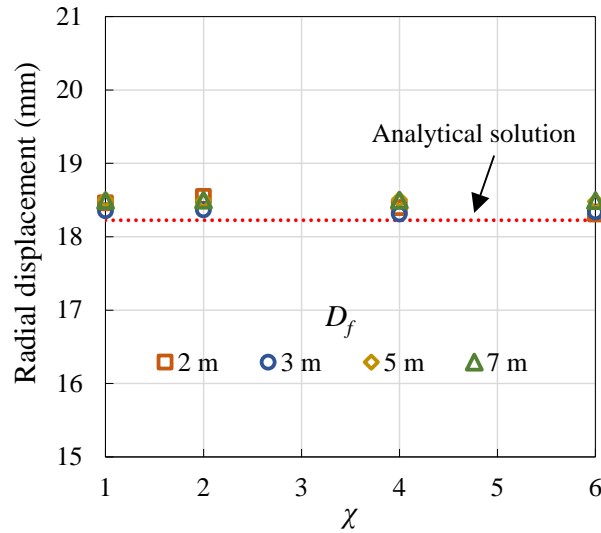
Figure C-3: Radial displacement at point A as a function of χ for different values of D_f

Figures C-4 to C-7 show the comparisons between the analytical and numerical results of radial displacement, radial and tangential stresses along line AB for D_f of 2 m (Figure C-4), 3 m (Figure C-5), 5 m (Figure C-6), 7 m (Figure C-7). It can be seen that the numerical results are stable and agree quite well with the analytical solutions. These results verify the method of applying different mesh sizes in different areas in a numerical model. To save the runtime, a small D_f with a large χ are preferred. Therefore, based on the numerical results, a D_f of 2 m and χ of 6 can be used to ensure stable numerical results and largely reduce the calculation time.

(a)   (b)
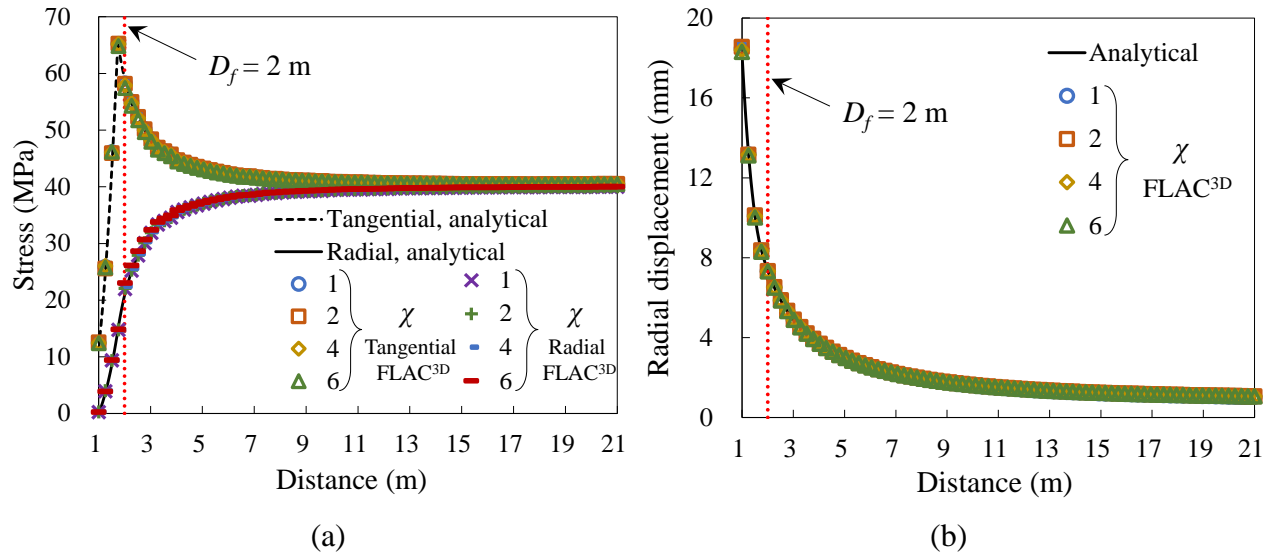
Figure C-4: Comparisons between the analytical and numerical results of (a) radial and tangential stresses, (b) radial displacement along the line AB for $D_f = 2$ m with different χ

(a)   (b)
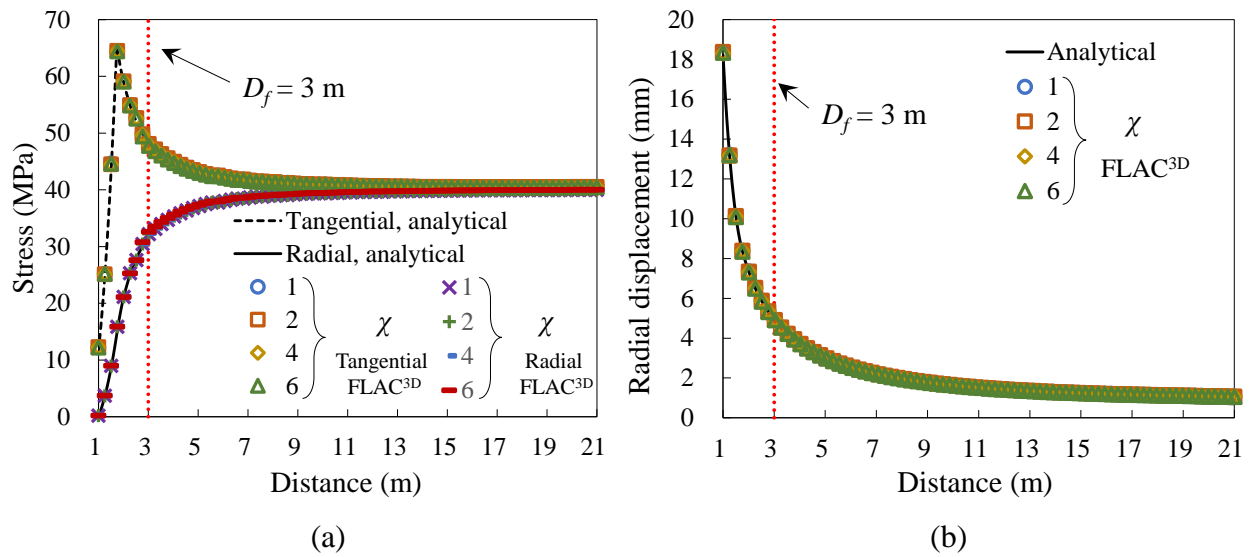
Figure C-5: Comparisons between the analytical and numerical results of (a) radial and tangential stresses, (b) radial displacement along the line AB for $D_f = 3$ m with different χ

(a)

(b)
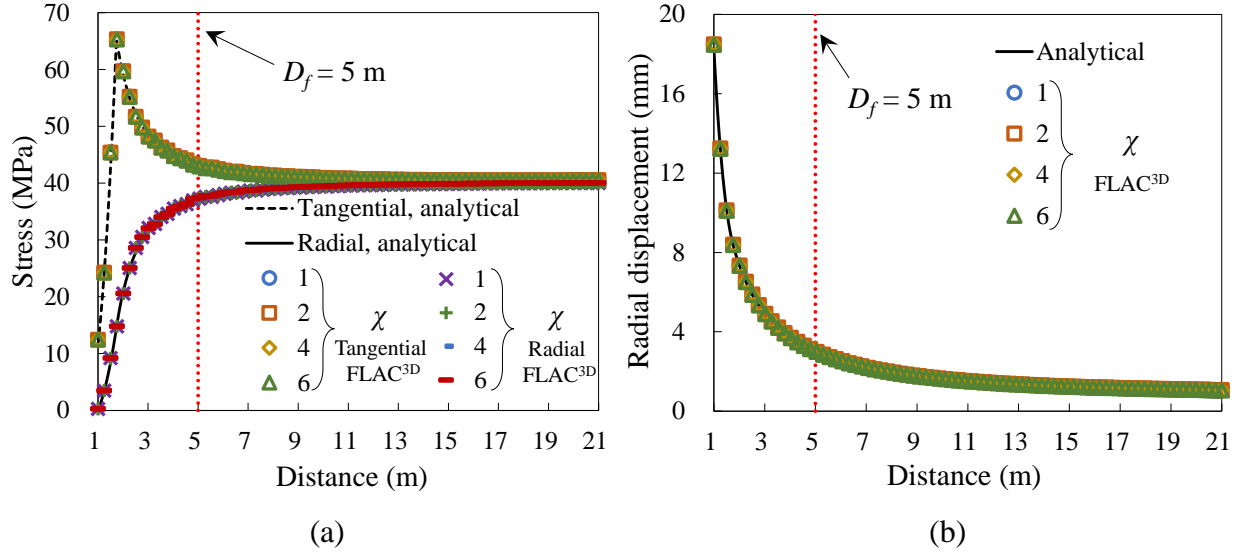
Figure C-6: Comparisons between the analytical and numerical results of (a) radial and tangential stresses, (b) radial displacement along the line AB for $D_f = 5$ m with different χ
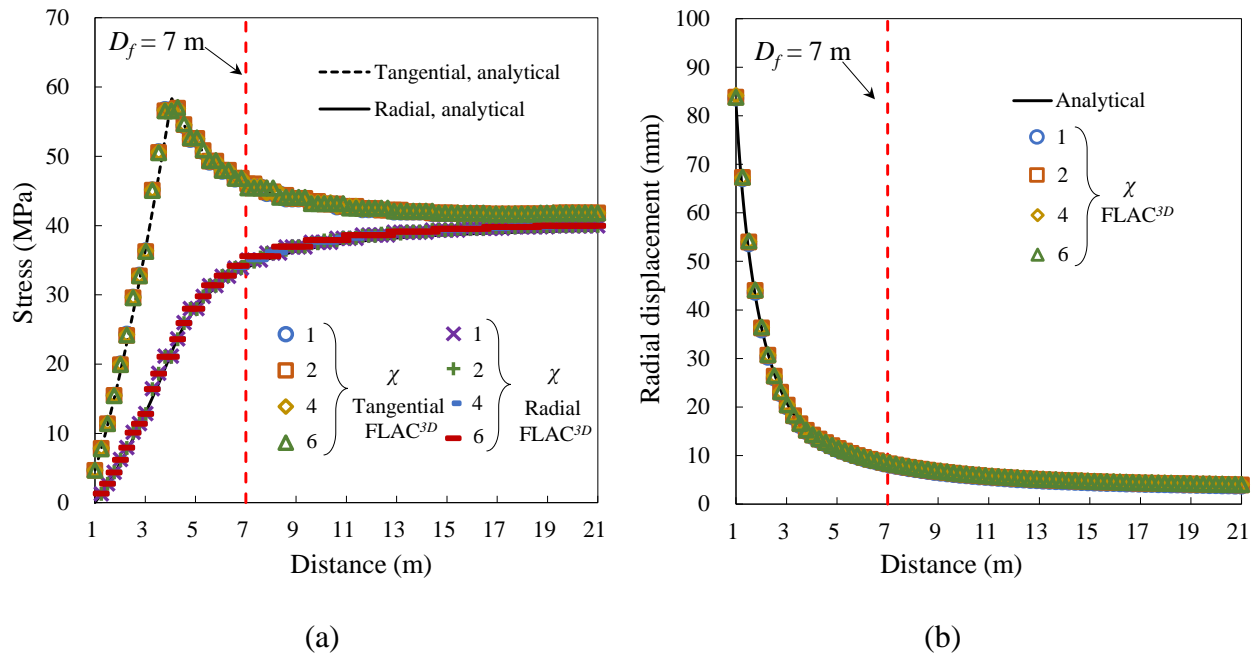

(a)

(b)
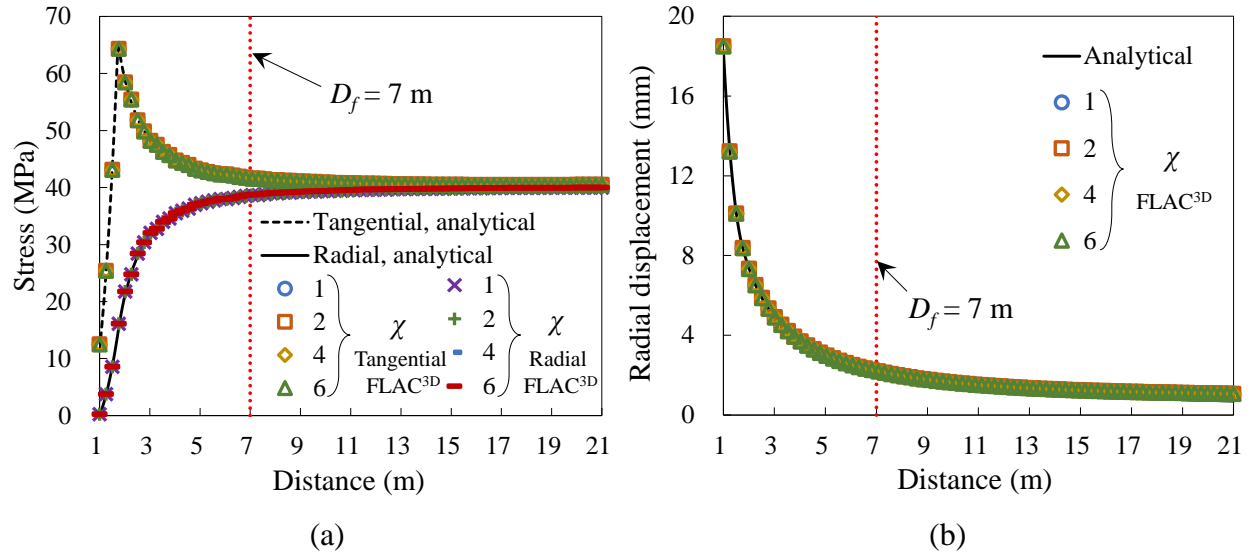
Figure C-7: Comparisons between the analytical and numerical results of (a) radial and tangential stresses, (b) radial displacement along the line AB for $D_f = 7$ m with different χ

The range of fine mesh in a numerical model depends on the ranges of high gradients of stress and displacement. And it should be determined case by case. Here, additional numerical simulations are conducted by considering the smaller c of 1.5 MPa and the smaller ϕ of 25°. Figure C-8 shows the radial displacement at the point A as a function of χ with D equaling 2 and 7 m. From the figure, one sees that numerical results are not stable when $D_f = 2$ m while radial displacement at the point A gradually decreases as the χ increase. When $D_f = 7$, the numerical results become stable. The

reasons are that the radius of the yield area around the hole increases form 1.74 to 4.05 m as c decreases from 3 MPa to 1.5 MPa and ϕ decreases from 35° to 25°. The yield area in a numerical model around the excavation typically demonstrates large displacement and high gradient of stresses compared to the elastic area. Therefore, a D_f of 2 m for the fine mesh in the model is too small to ensure a stable result.
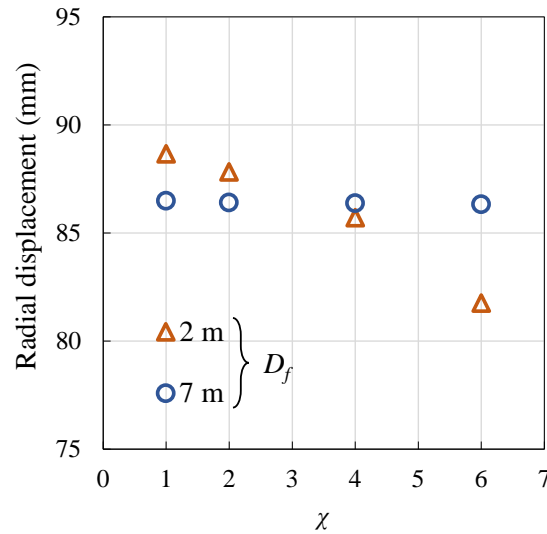
Figure C-8: Radial displacement at point A with $c = 1.5$ MPa and $\phi = 25°$ as a function of χ for D_f equaling 2 and 7 m respectively

Figure C-9 shows the comparisons between the analytical and numerical results of radial displacement, radial and tangential stresses along line AB with $c = 1.5$ MPa, $\phi = 25°$ and $D_f = 7$ m. In the figure, the numerical results show good agreements with analytical solutions for different χ ranging from 1 to 6. Therefore, in this case with reduced shear strength, a D_f of 7 m and a χ of 6 can be used.

Figure C-9: Comparisons between the analytical and numerical results of (a) radial and tangential stresses, (b) radial displacement along the line AB with $c = 1.5$ MPa, $\phi = 25°$ and $D_f = 7$ m for different χ

C4 Conclusions

Different areas in a numerical model can be built with varied mesh sizes. In the area of interest, the fine mesh should be used to ensure accurate results. In the outer part of the model (e.g., area far from excavation), coarse mesh can be used to save the run time. This method has been verified by comparing the numerical and analytical results of the problem of a cylindrical hole in a rock mass that obeys MC criterion. It is also concluded that the range of fine mesh should be sufficiently large to reflect the high gradients of displacements and stresses. The ratio of coarse mesh size to fine mesh size should follow an integer ratio and should not be too large to avoid significant discontinuity.

.

APPENDIX D SENSITIVITY ANALYSES AND ADDITIONAL RESULTS RELATED TO CHAPTER 3

This section presents the sensitivity analyses, additional results of yield zones development of side-exposed backfill related to Chapter 3.

The effects of domain size, range of fine mesh, mesh size and filling layers on the numerical results are investigated to determine optimal values of these parameters. Figure D-1 shows the schematic of the model for evaluating the stability of side-exposed backfill by considering the extraction of adjacent secondary stope. In the figure, AA' is the vertical central line (VCL) of the primary stope. EE' is a vertical line in the primary stope close to the open face. M is central point on a side wall of the primary stope. MM' is a line in the surrounding rock mass and is perpendicular to the side wall. D_f represents the range for area with fine mesh. In the model, H_D, B_D and L_D are applied with the same value which is considered as the domain size of the model.
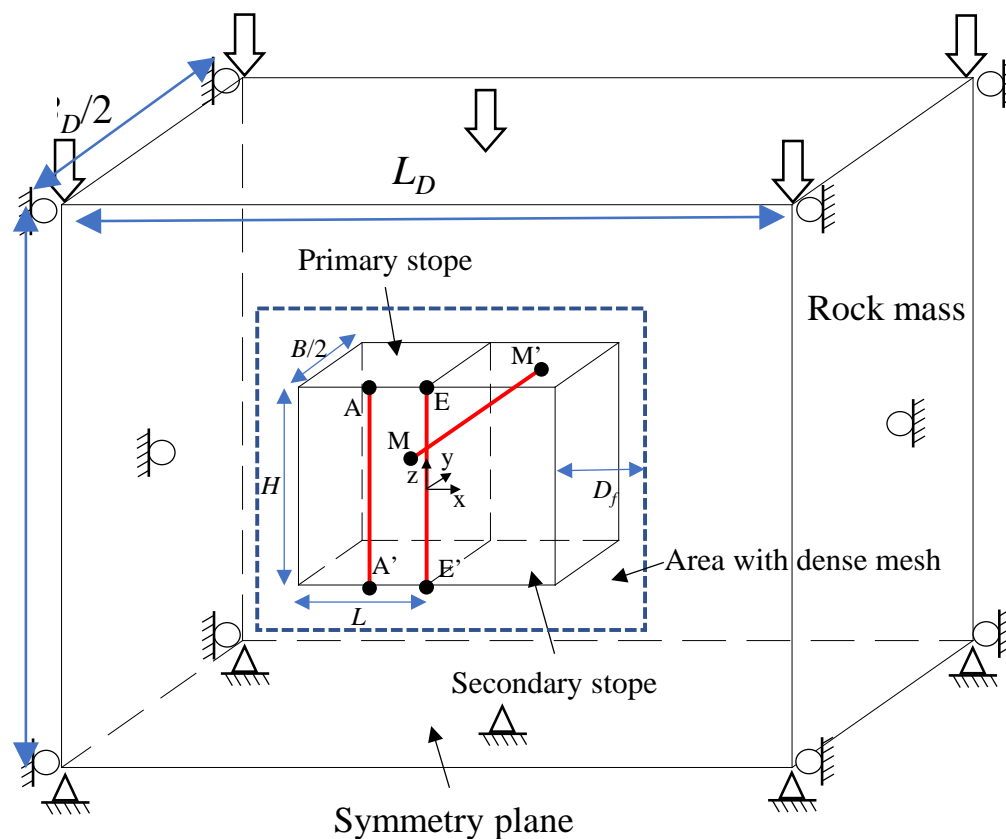
Figure D-1: Schematic of the model for evaluating the stability of side-exposed backfill considering the extraction of adjacent secondary stope

In the sensitivity analyses, the size of stope and the mine depth D are applied as the largest value to ensure that the domain size and D_f of the model are conservative. The applied values are 60 m for H, 25 m for B, 25 m for L and 2000 m for D. In case that the model height is limited, a surcharge is applied on the top surface to represent the overburden stress. The simulations for sensitivity analyses are conducted with 4 steps which are presented in Chapter 3. In sensitivity analyses, the rock mass is characterized by γ_R = 27 kN/m^3, bulk modulus K_R = 7.15 GPa, shear modulus G_R = 4.92 GPa, ψ_R = 0°, GSI = 75, σ_{ci} =150 MPa, m_i = 25, m_b = 10.23, s = 0.062 and a = 0.5. The backfill is characterized by γ = 18 kN/m^3, bulk modulus K = 300 MPa, shear modulus G = 113 MPa, c = 2 MPa, ϕ = 30°, and ψ = 0°. Numerical results are obtained after different simulations steps for the sensitivity analyses. Theses numerical results include:

- The horizontal displacement (y-displacement) of rock mass along the horizontal line MM' after excavating the primary stope (step 2);

- The vertical (σ_{zz}) and horizontal (σ_{yy}) stresses along the VCL AA' after backfilling the excavated primary stope (step 3);

- The total displacement, vertical (σ_{zz}) and horizontal (σ_{yy}) stresses along the vertical line EE' close to the open face after excavating the adjacent secondary stope (step 4).

In the follows, the variation of above numerical results for different domain sizes, ranges for fine mesh, mesh sizes and filling layers will be shown and analyzed to determine the optimal modeling parameters. It should be noted that when analyzing the effects of domain size, range for fine mesh, and mesh size, the excavated primary stope is backfilled in one step (one layer). When studying the effect of filling layers, different layers are used to fill the primary stope.

D1 Effect of domain size

Different domain sizes including 80 m, 120 m, 240 m, 420 m, 640 m, 900 m, 1200 m, 1600 m are applied for the numerical model. Numerical results are obtained from numerical models with different domain sizes after each simulation step.

D1.1 Excavating the primary stope

Figure D-2 shows the horizontal displacement (y-displacement) of rock mass along 50 m on the line MM' (Figure D-2a) and the horizontal displacement (y-displacement) at the point M (Figure

D-2b) after excavating the primary stope (step 2) for different domain sizes. Figure D-2 indicates that when the domain size is larger than 240 m, the numerical results become stable.
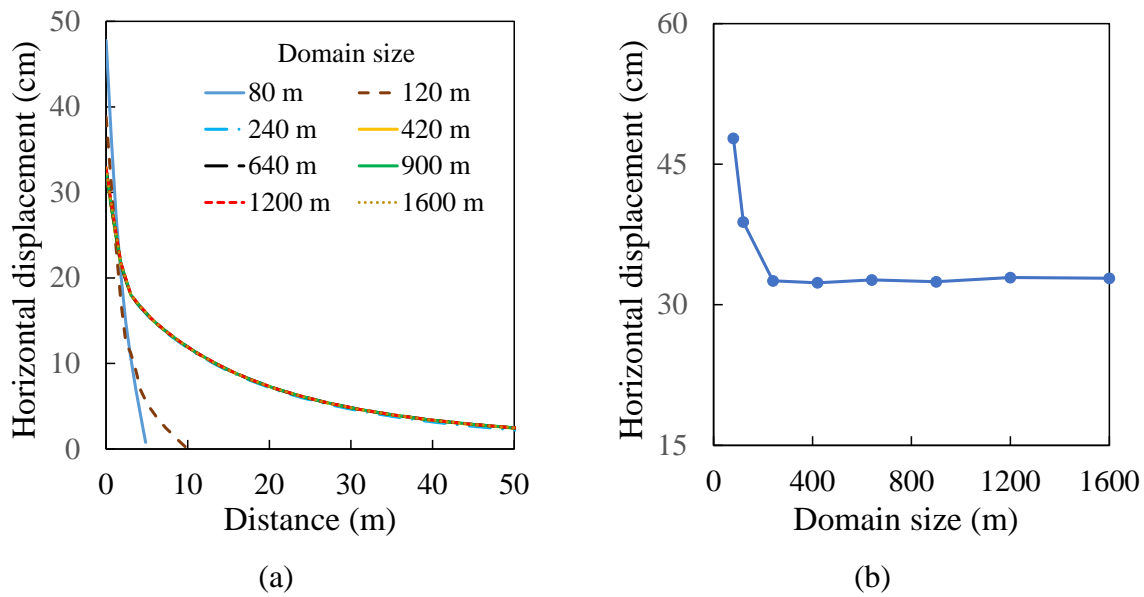

Figure D-2: (a) Horizontal displacement (*y*-displacement) of rock mass along the horizontal line MM' and (b) horizontal displacement (*y*-displacement) at the point M after excavating the primary stope (step 2) for different domain sizes

D1.2 Backfilling the primary stope

Figure D-3 shows the distributions of vertical (σ_{zz}) and horizontal (σ_{yy}) stresses along the vertical central line AA' in backfill after backfilling the primary stope (step 3) for different domain sizes. From the figure, one sees that the domain size does not significantly affect the stress distribution in the backfilled primary stope. This is because that the backfill is placed after the displacement of rock walls. Figure D-3 indicates that the numerical results become very stable when the domain size is larger than 240 m.
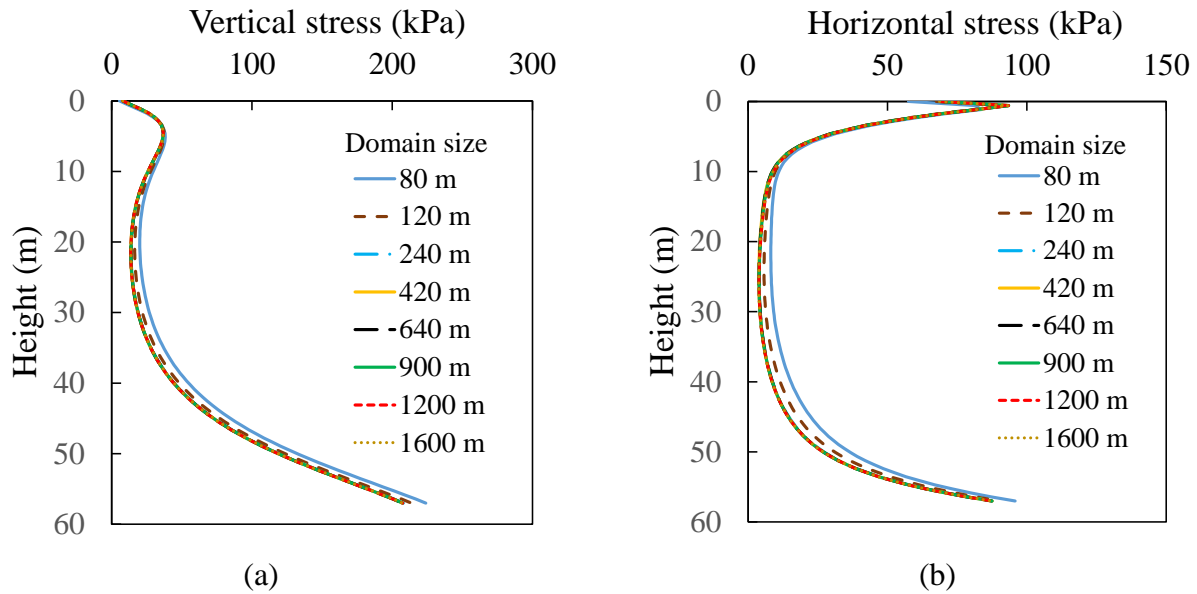
Figure D-3: Distributions of the vertical (σ_{zz}) and horizontal (σ_{yy}) stresses along the vertical central line AA' in backfill after backfilling the primary stope (step 3) for different domain sizes

D1.3 Excavating the secondary stope

Figure D-4 shows the total displacement of side-exposed backfill along the line EE' (Figure D-4a) and the total displacement at the center of open face (Figure D-4b) after excavating the secondary stope (step 4) for different domain sizes. From Figure D-4a, one sees that the results become superposed for domain size larger than 420 m. Moreover, the displacement at the center of open face shown in Figure D-4a becomes stable when the domain size is larger than 240 m. Therefore, results in Figure D-4 suggest that the domain size of the numerical model should be larger than 420 m.
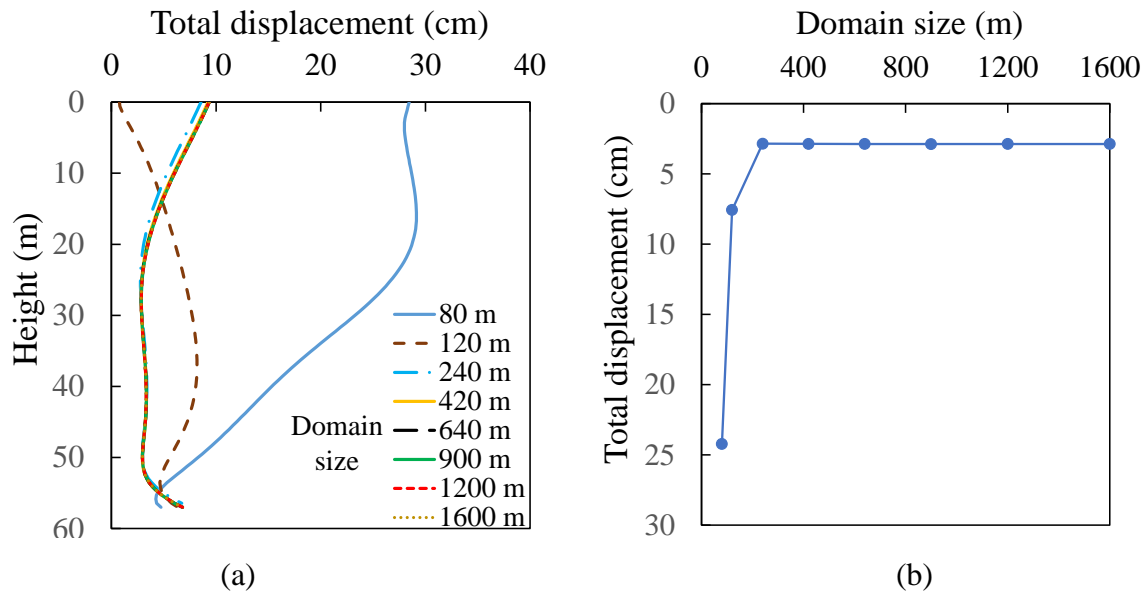
Figure D-4: (a) Total displacement of side-exposed backfill along the vertical line EE' and (b) total displacement at the center of open face after excavating the secondary stope (step 4) for different domain sizes

Figure D-5 shows the distributions of vertical (σ_{zz}) and horizontal (σ_{yy}) stresses along the line EE' in the side-exposed backfill after excavating the secondary stope (step 4) for different domain sizes. Results show that both the vertical and horizontal stresses become stable when the domain size is larger than 240 m.
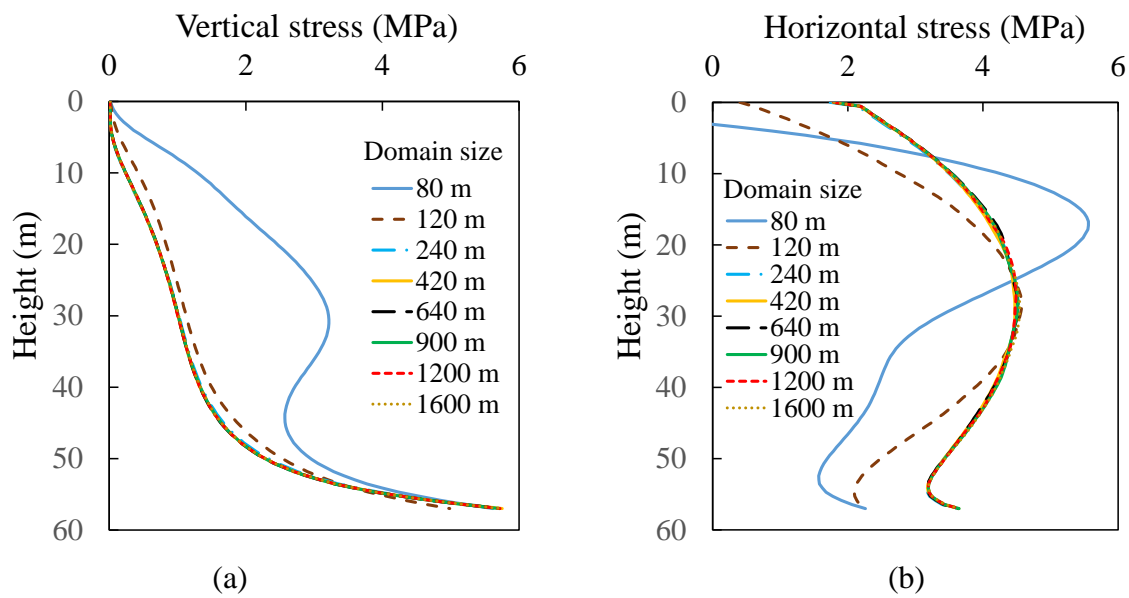
Figure D-5: Distributions of the vertical (σ_{zz}) and horizontal (σ_{yy}) stresses along the vertical line EE' in the side-exposed backfill after excavating the secondary stope (step 4) for different domain sizes

According to the above sensitivity analyses, the domain size of the numerical model should be larger than 420 m to ensure the stable numerical results. To be conservative, a value of 900 m is determined as the optimal value of domain size and will be used hereafter.

D2 Effect of range for fine mesh

Different ranges for fine mesh D_f including 5 m, 15 m, 25 m, 35 m, 45 m, and 55m are applied to investigate their influence on the results. In the numerical model, coarse mesh is applied for the area out of this range. The ratio χ of coarse mesh size to the fine mesh size is 2.

D2.1 Excavating the primary stope

Figure D-6 shows the horizontal displacement (y-displacement) of rock mass along the line MM' and the horizontal displacement (y-displacement) at the point M after excavating the primary stope (step 2) for different D_f. The numerical results become stable when D_f increases to 25 m.

(a)   (b)
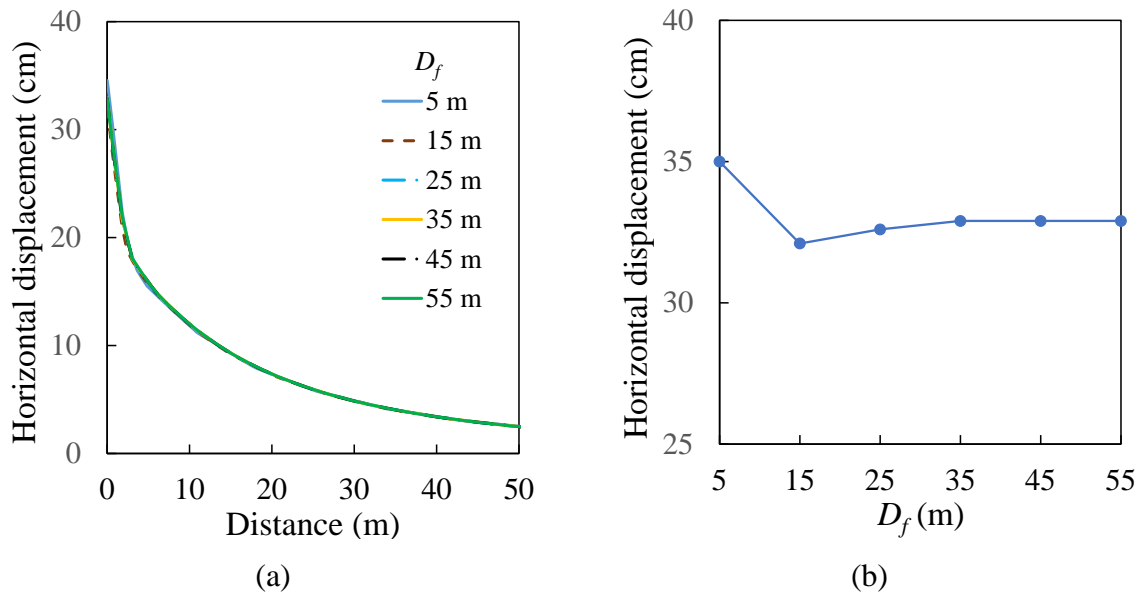
Figure D-6: (a) Horizontal displacement (y-displacement) of rock mass along the horizontal line MM' and (b) horizontal displacement (y-displacement) at the point M after excavating the primary stope (step 2) for different D_f

D2.2 Backfilling the primary stope

Figure D-7 shows the distributions of vertical (σ_{zz}) and horizontal (σ_{yy}) stresses along the vertical central line AA' in the backfill after backfilling the primary stope (step 3) for different D_f. It can be seen that the range for fine mesh D_f has very little effect on the stresses in the backfilled stope. This has been explained as that the excavated primary stope is backfilled after the displacement of surrounding rock mass.
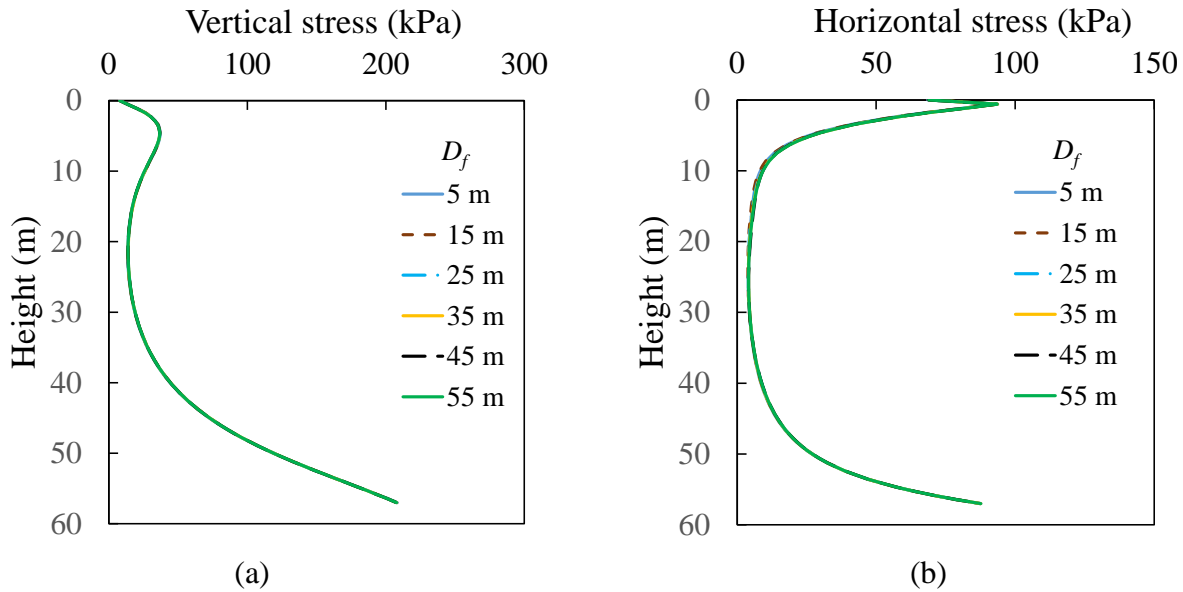

Figure D-7: Distributions of the vertical (σ_{zz}) and horizontal (σ_{yy}) stresses along the vertical central line AA' in the backfill after backfilling the primary stope (step 3) for different D_f

D2.3 Excavating the secondary stope

Figure D-8 illustrates the total displacement along the line EE' and the total displacement at the center of open face after excavating the secondary stope (step 4) for different D_f. It is found that the effect of D_f on the displacement of side-exposed backfill after adjacent extraction is very minor. According to Figure D-8, the numerical results are considered stable when D_f increases to 15 m.
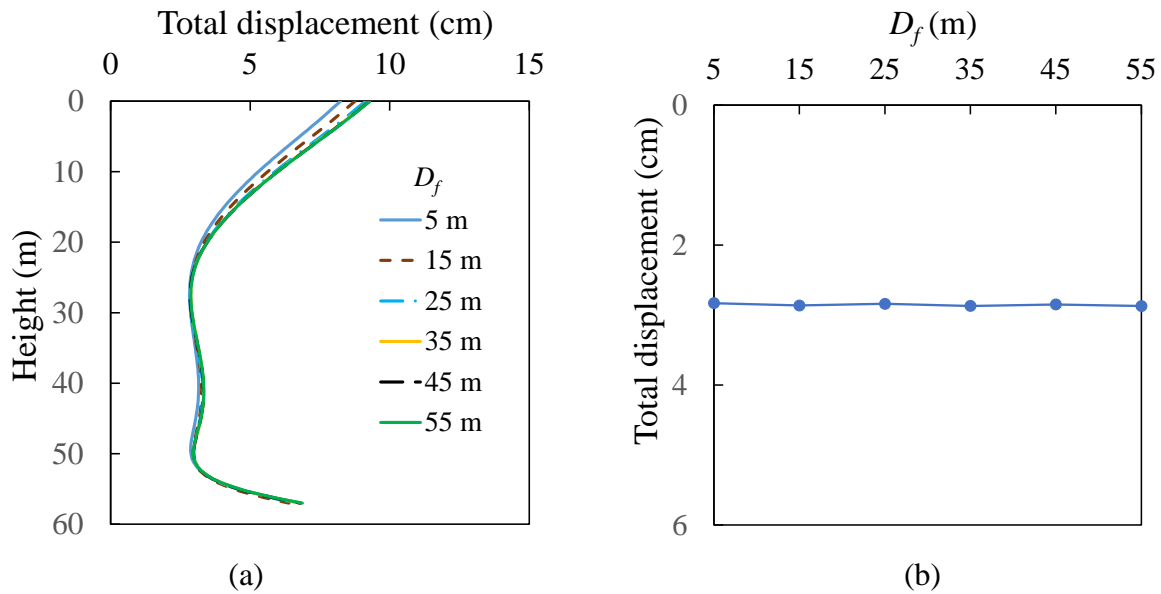
Figure D-8: (a) Total displacement along the vertical line EE' and (b) total displacement at the center of open face after excavating the secondary stope (step 4) for different D_f

Figure D-9 shows the distributions of vertical (σ_{zz}) and horizontal (σ_{yy}) stresses along the line EE' in the side-exposed backfill after excavating the secondary stope (step 4) for different D_f. From Figure D-9a, one can see that D_f does not show significant influence on the vertical stress in the backfill after adjacent extraction. However, Figure D-9b shows that when D_f is 5 and 15 m, the horizontal stress in the side-exposed backfill is not stable. Therefore, Figure D-9 suggests that the range of fine mesh D_f for the numerical model should be 25 m or larger.
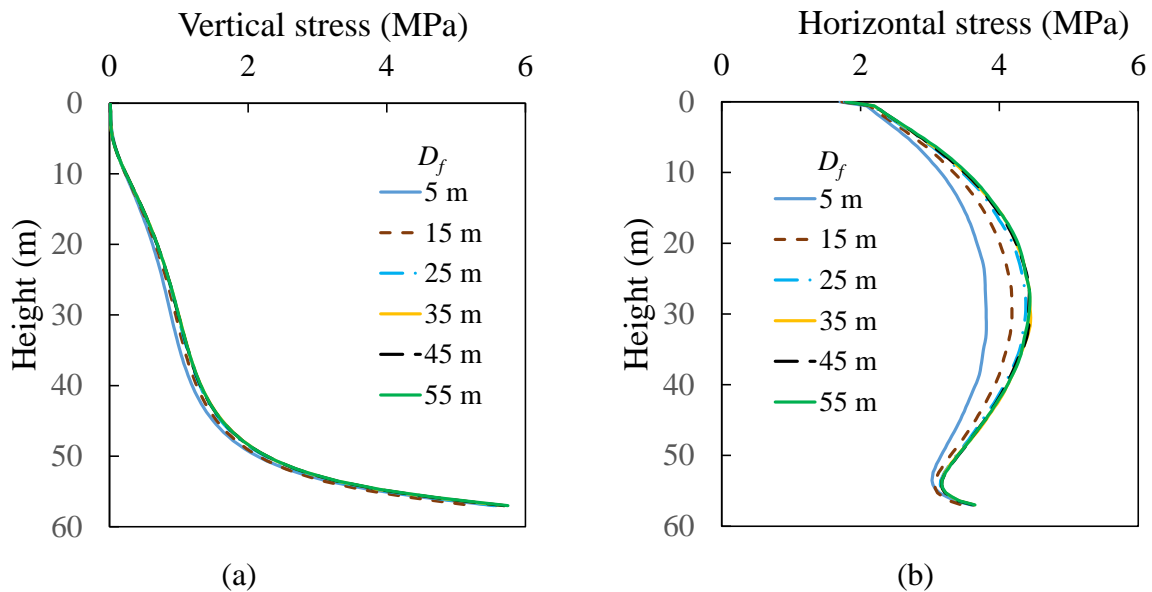
Figure D-9: Distributions of the vertical (σ_{zz}) and horizontal (σ_{yy}) stresses along the vertical line EE' in the side-exposed backfill after excavating the secondary stope (step 4) for different D_f

According to the above sensitivity analyses, the range for fine mesh for the numerical model should be 25 m or larger. A conservative value of 45 m is thus determined as the optimal value for D_f.

D3 Effect of mesh size

Different mesh sizes including 4 m, 3 m, 2 m, 1.5 m, 1 m, 0.75 m, 0.5 m, and 0.4 m are applied for stopes and rock mass within a range of 45 m around the excavations. Coarse mesh is used for other parts out of this area.

D3.1 Excavating the primary stope

Figure D-10 shows the horizontal displacement (y-displacement) of rock mass along the line MM' and the horizontal displacement (y-displacement) at the point M after excavating the primary stope (step 2) for different mesh sizes. It can be seen that as the mesh size decreases, the numerical results converge. When the mesh size reduces to 0.75 m, the numerical results become stable. Further reducing the mesh size does not greatly change the results.

(a)   (b)
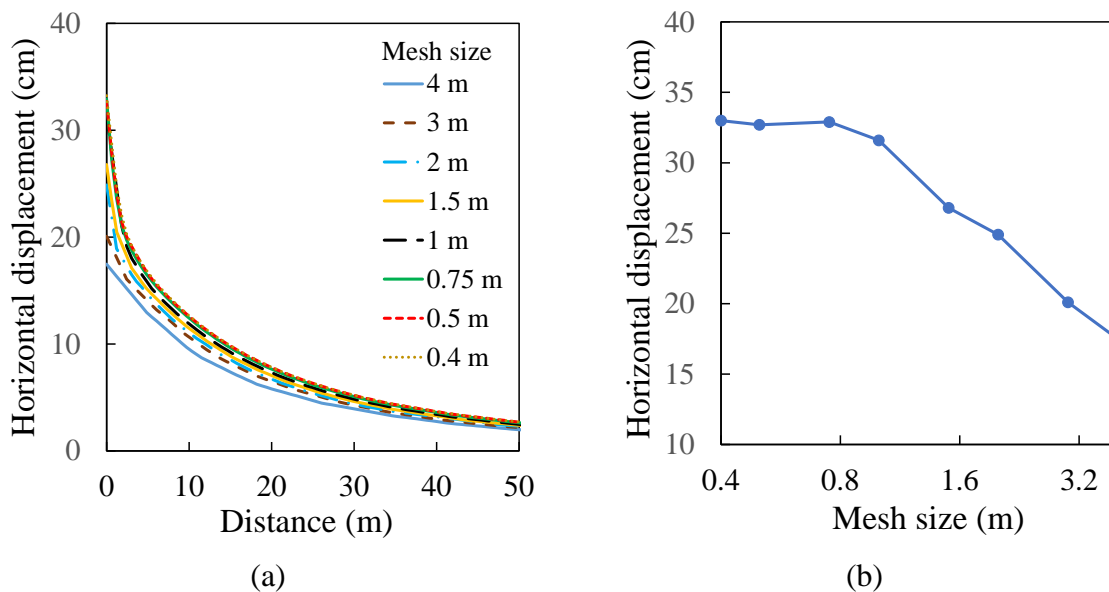
Figure D-10: (a) Horizontal displacement (y-displacement) of rock mass along the horizontal line MM' and (b) horizontal displacement (y-displacement) at the point M after excavating the primary stope (step 2) for different mesh sizes

D3.2 Backfilling the primary stope

Figure D-11 illustrates the distributions of vertical (σ_{zz}) and horizontal (σ_{yy}) stresses along the vertical central line AA' in the backfill after backfilling the primary stope (step 3) for different mesh sizes. It can be seen that mesh size affects the stress distribution in the backfilled stope. The numerical results become stable when the mesh size reduces to 0.75 m.
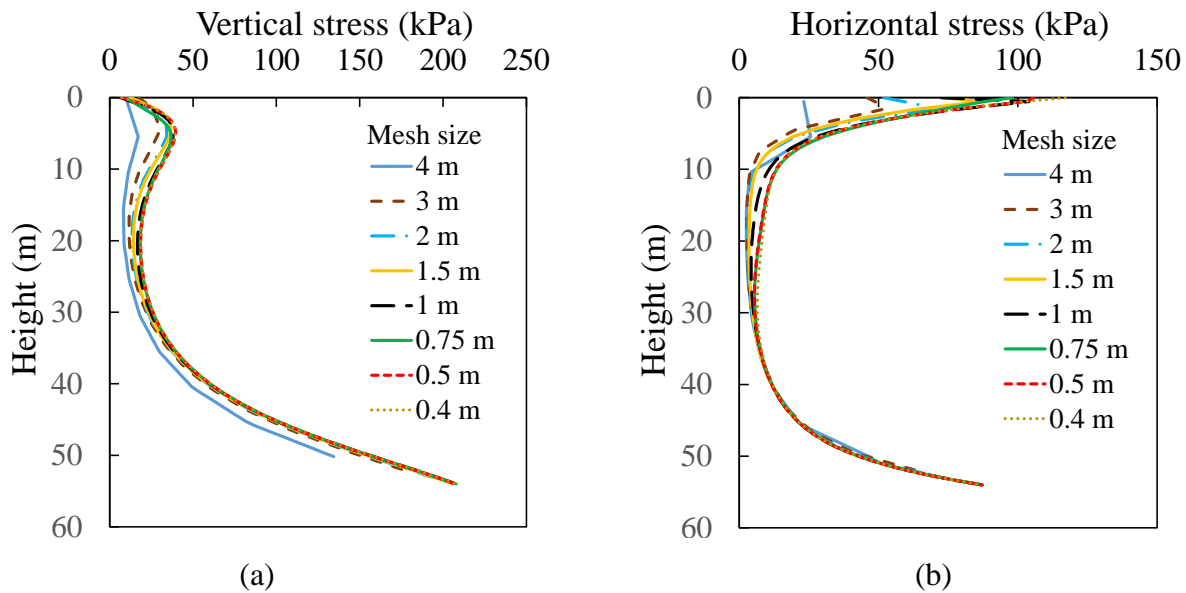

Figure D-11: Distributions of the vertical (σ_{zz}) and horizontal (σ_{yy}) stresses along the vertical central line AA' in the backfill after backfilling the primary stope (step 3) for different mesh sizes

D3.3 Excavating the secondary stope

Figure D-12 shows the total displacement along the line EE' and the total displacement at the center of open face after excavating the secondary stope (step 4) for different mesh sizes. From the figure, one can see that the displacement of side-exposed backfill after adjacent extraction becomes stable when the mesh size is smaller than 1.5 m.
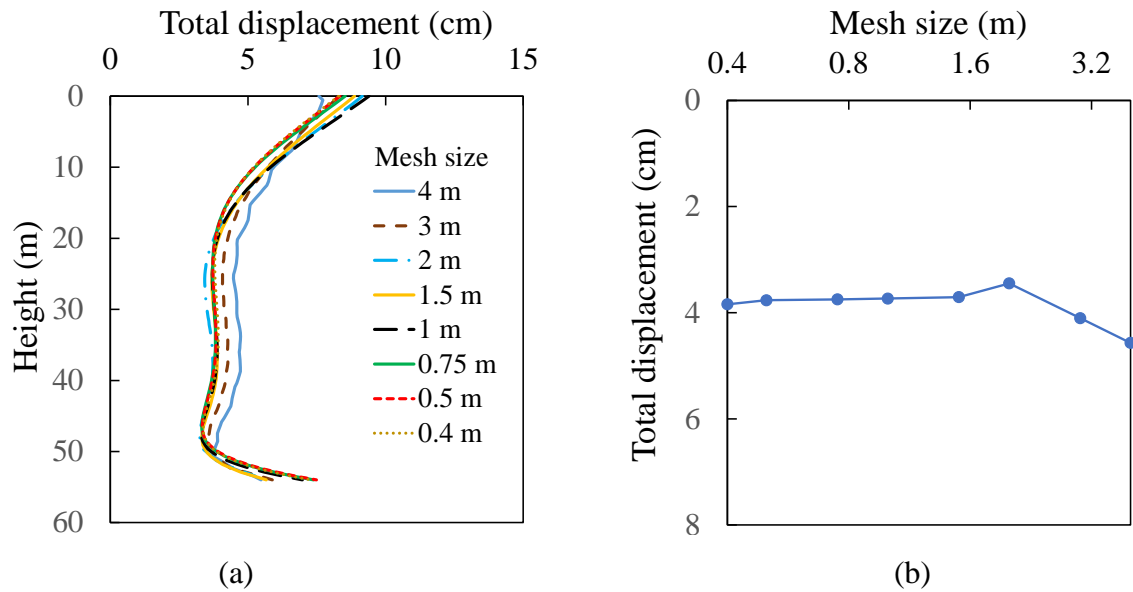
Figure D-12: (a) Total displacement along the vertical line EE' and (b) total displacement at the center of open face after excavating the secondary stope (step 4) for different mesh sizes

Figure D-13 illustrates the distributions of vertical (σ_{zz}) and horizontal (σ_{yy}) stresses along the line EE' in the side-exposed backfill after excavating the secondary stope (step 4) for different mesh sizes. It can be seen that both the vertical and horizontal stresses in the side-exposed backfill after excavating the adjacent secondary stope become stable when the mesh size reduces to 0.75 m. Further reduction of the mesh size does not greatly change the results.
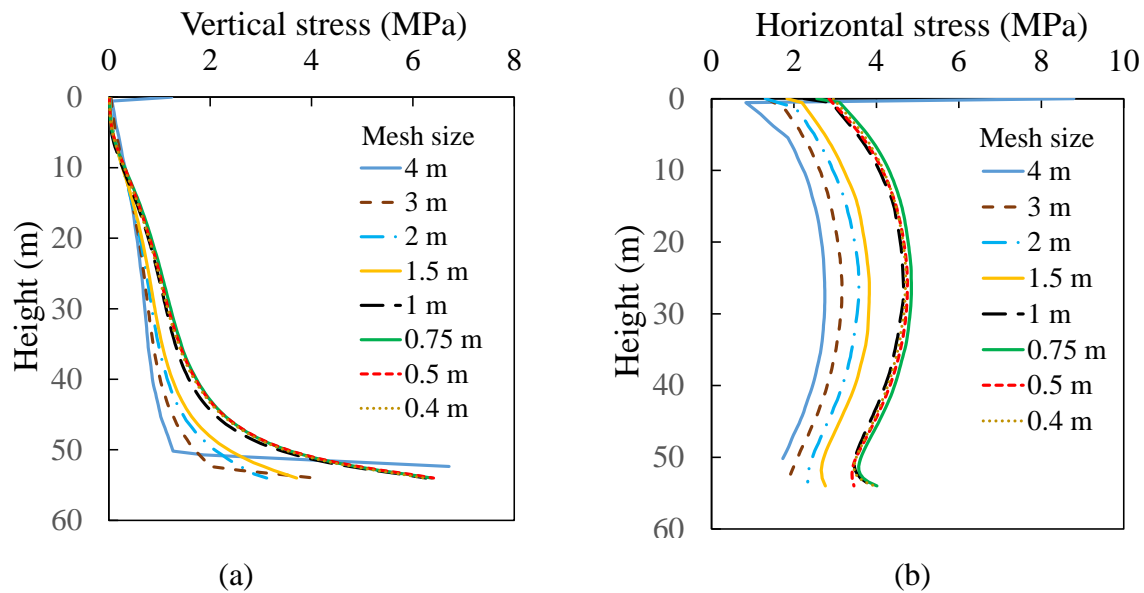
Figure D-13: Distributions of the vertical (σ_{zz}) and horizontal (σ_{yy}) stresses along the vertical line EE' in the side-exposed backfill after excavating the secondary stope (step 4) for different mesh sizes

Based on the sensitivity analyses, the fine mesh size used for the stopes and rock mass around excavations should not exceed 0.75 m to ensure the stable numerical results. Therefore, 0.5 m is determined as the optimal mesh size for numerical modeling.

D4 Effect of filling layers

The filling layers affect the equilibrium state of the placed backfill. The thickness of filling layer should be sufficiently small to represent a realistic condition. Therefore, the effects of different filling layer thicknesses including 60 m, 30 m, 20 m, 10 m, 5 m, 2 m, and 1 m are investigated. These filling layers thicknesses correspond to different filling layers of 1, 2, 3, 6, 12, 30, and 60 respectively. Figure D-14 shows the distributions of vertical (σ_{zz}) and horizontal (σ_{yy}) stresses along the vertical central line AA' in the backfill after backfilling the primary stope (step 3) for different filling layer thicknesses. It can be seen that filling layer affects the stresses distribution in the backfilled stope while as its thickness reduces, the numerical results gradually stabilize. When the thickness of filling layer decreases to 2 m, the numerical results become stable. The optimal value for filling layer thickness is thus determined as 2 m.
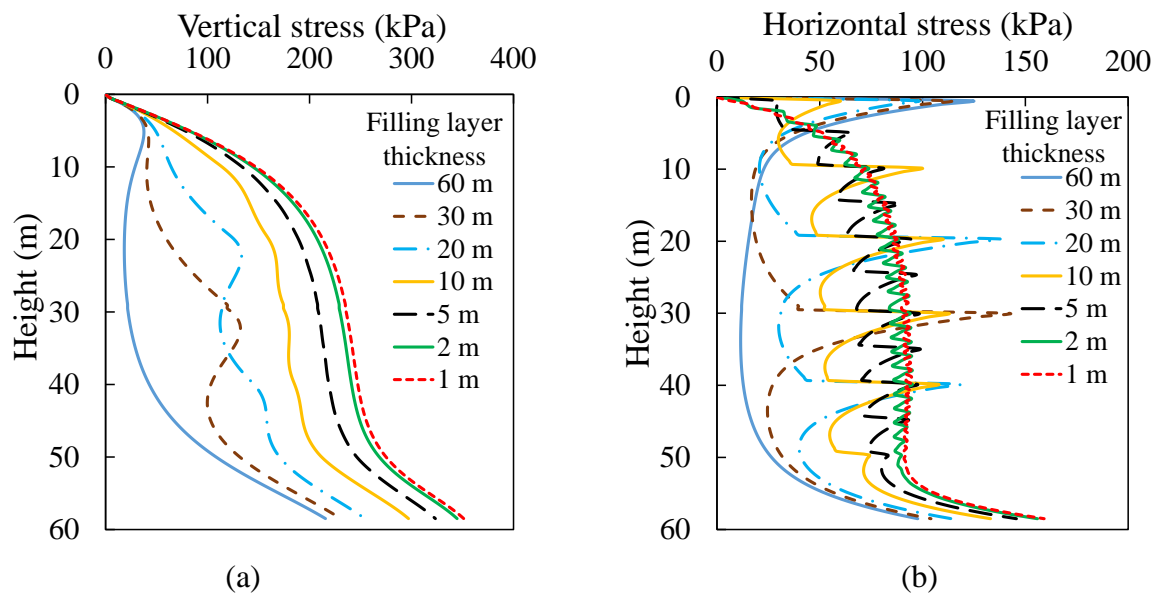

(a)   (b)

Figure D-14: Distributions of the vertical (σ_{zz}) and horizontal (σ_{yy}) stresses along the vertical central line AA' in the backfill after backfilling the primary stope (step 3) for different filling layer thicknesses

D5 Numerical results of yield zones development in side-exposed backfill

In Chapter 3, the coalescence of yield zones is the major instability criterion to evaluate the stability and determine c_{min} of side-exposed backfill. In the follows, some additional results of yield zones development in side-exposed backfill as the cohesion reduces for different stope geometries, mechanical properties of backfill, rock mass and fill-rock interface are presented. For one failure mechanism, the trends of yield zones development at different mine depths are similar. Therefore, results at two mine depths with two different failure mechanisms of sliding and crushing failure will be presented for each case as examples.

Failed: (shear) (tensile)

c = 26 kPa c = 23 kPa c = 22 kPa

(a)

c = 240 kPa c = 230 kPa c = 220 kPa c = 170 kPa

(b)
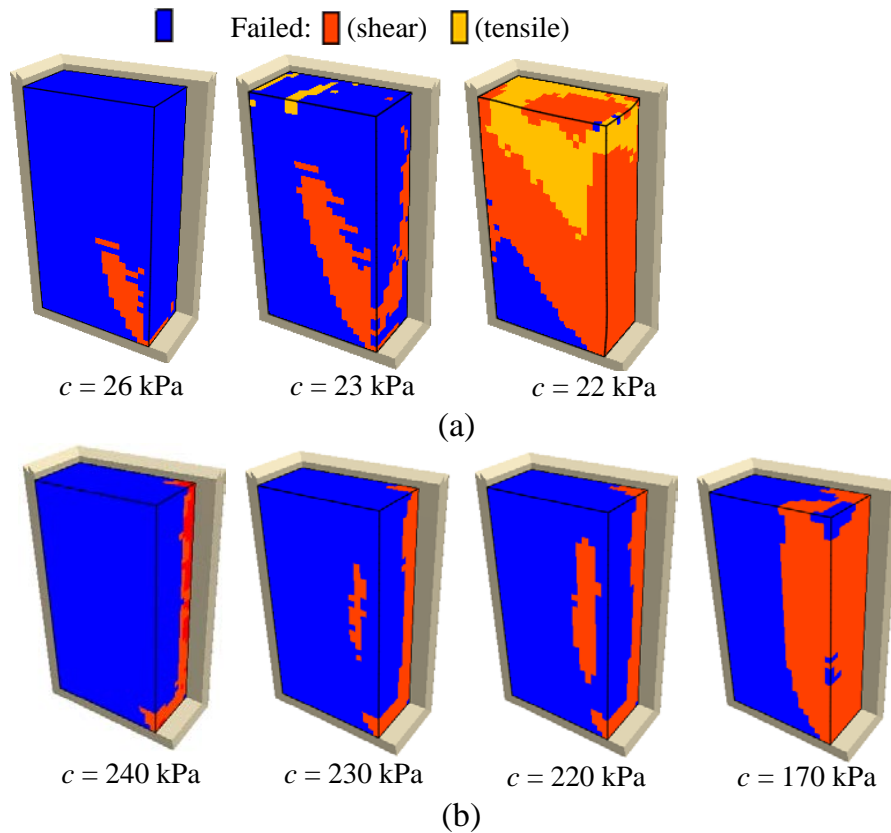
Figure D-15: Yield zones development of side-exposed backfill for Case 1 in Chapter 3 with H = 20 m as c reduces (a) at D = 100 m governed by sliding failure and (b) at D = 1000 m governed by crushing failure
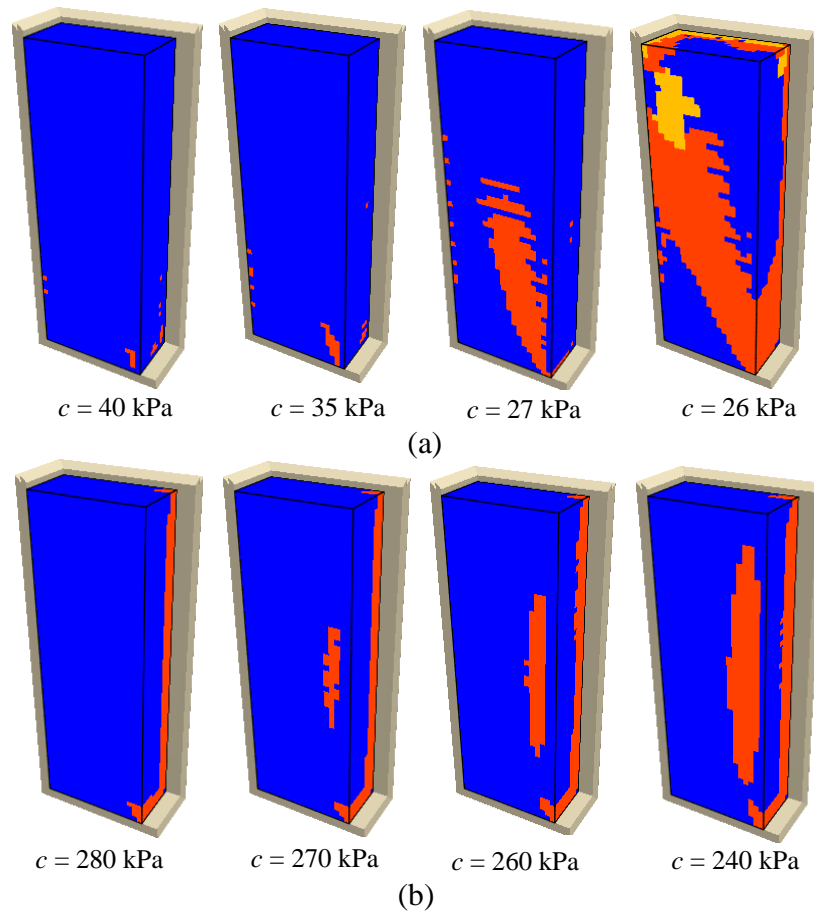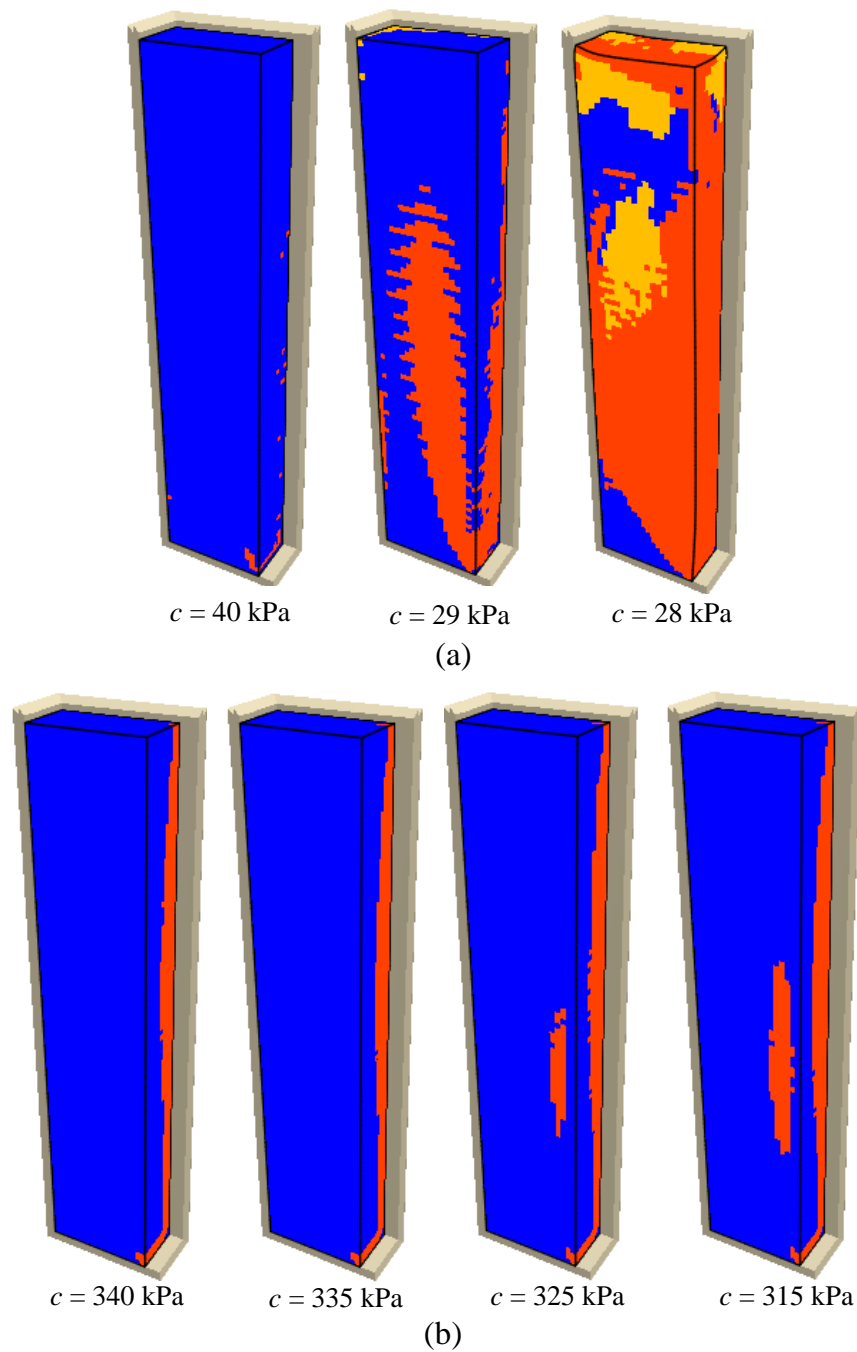
$c = 40$ kPa $c = 35$ kPa $c = 27$ kPa $c = 26$ kPa

(a)

$c = 280$ kPa $c = 270$ kPa $c = 260$ kPa $c = 240$ kPa

(b)

Figure D-16: Yield zones development of side-exposed backfill for Case 1 in Chapter 3 with $H = 30$ m as c reduces (a) at $D = 100$ m governed by sliding failure and (b) at $D = 1000$ m governed by crushing failure

$c = 40$ kPa $c = 29$ kPa $c = 28$ kPa

(a)

$c = 340$ kPa $c = 335$ kPa $c = 325$ kPa $c = 315$ kPa

(b)

Figure D-17: Yield zones development of side-exposed backfill for Case 1 in Chapter 3 with $H = 50$ m as c reduces (a) at $D = 100$ m governed by sliding failure and (b) at $D = 1000$ m governed by crushing failure

$c = 50$ kPa $c = 30$ kPa $c = 28$ kPa

(a)

$c = 360$ kPa $c = 347$ kPa $c = 335$ kPa $c = 310$ kPa

(b)
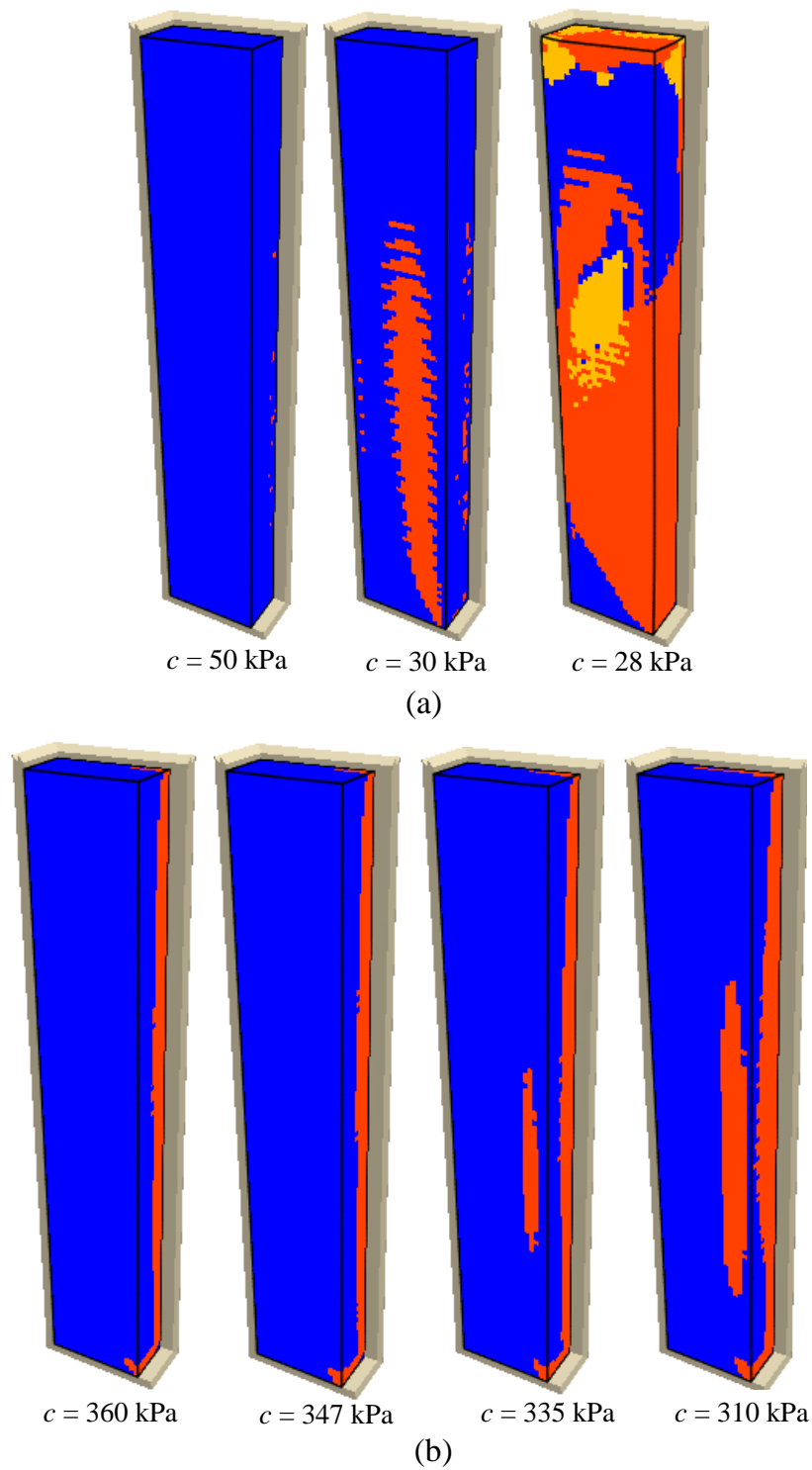
Figure D-18: Yield zones development of side-exposed backfill for Case 1 in Chapter 3 with $H = 60$ m as c reduces (a) at $D = 100$ m governed by sliding failure and (b) at $D = 1000$ m governed by crushing failure
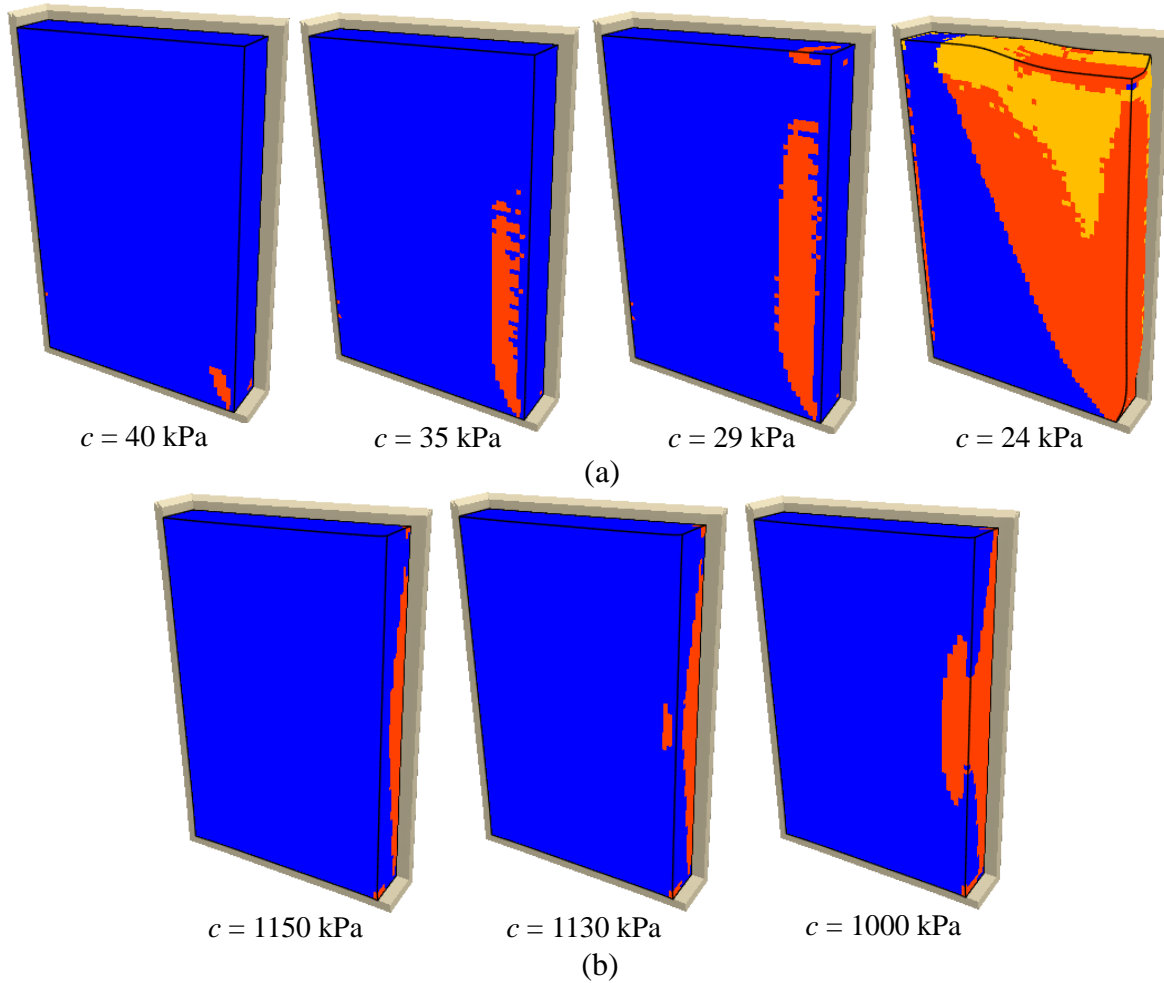
$c = 39$ kPa $c = 36$ kPa $c = 35$ kPa

(a)

$c = 230$ kPa $c = 180$ kPa $c = 174$ kPa

(b)
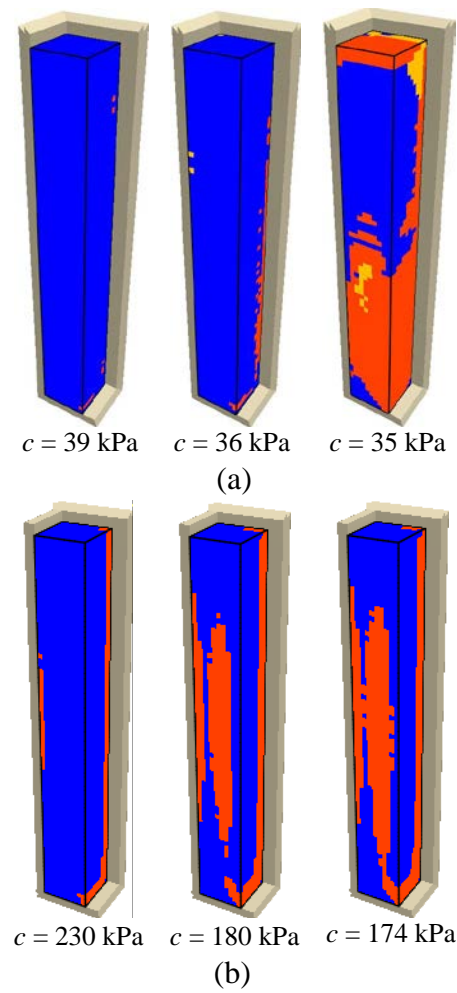
Figure D-19: Yield zones development of side-exposed backfill for Case 2 in Chapter 3 with $L = 5$ m as c reduces (a) at $D = 100$ m governed by sliding failure and (b) at $D = 1000$ m governed by crushing failure

$c = 40$ kPa $c = 26$ kPa $c = 24$ kPa

(a)

$c = 450$ kPa $c = 440$ kPa $c = 430$ kPa $c = 350$ kPa

(b)
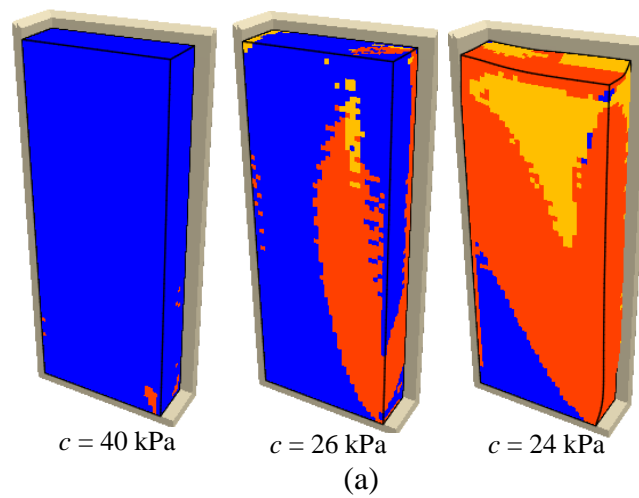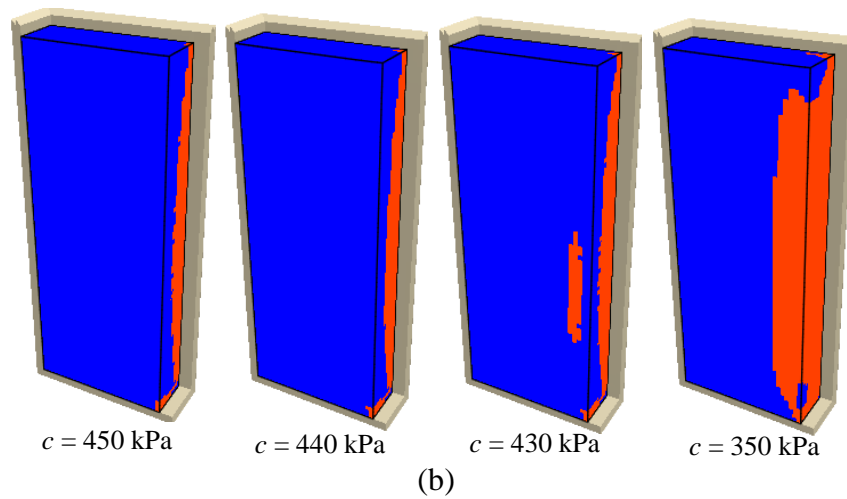
Figure D-20: Yield zones development of side-exposed backfill for Case 2 in Chapter 3 with $L = 15$ m as c reduces (a) at $D = 100$ m governed by sliding failure and (b) at $D = 1000$ m governed by crushing failure


$c = 40$ kPa $c = 27$ kPa $c = 24$ kPa

(a)

$c = 1060$ kPa $c = 1050$ kPa $c = 1000$ kPa

(b)
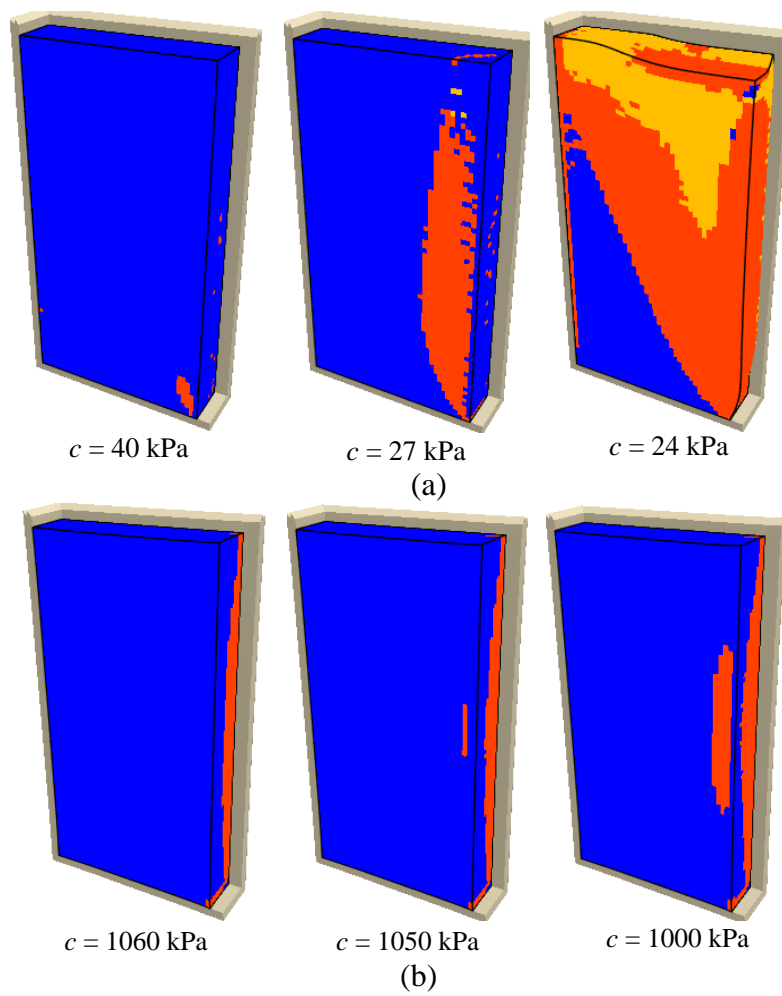
Figure D-21: Yield zones development of side-exposed backfill for Case 2 in Chapter 3 with $L =$ 20 m as c reduces (a) at $D = 100$ m governed by sliding failure and (b) at $D = 1500$ m governed by crushing failure

| $c = 40$ kPa | $c = 35$ kPa | $c = 29$ kPa | $c = 24$ kPa |

(a)

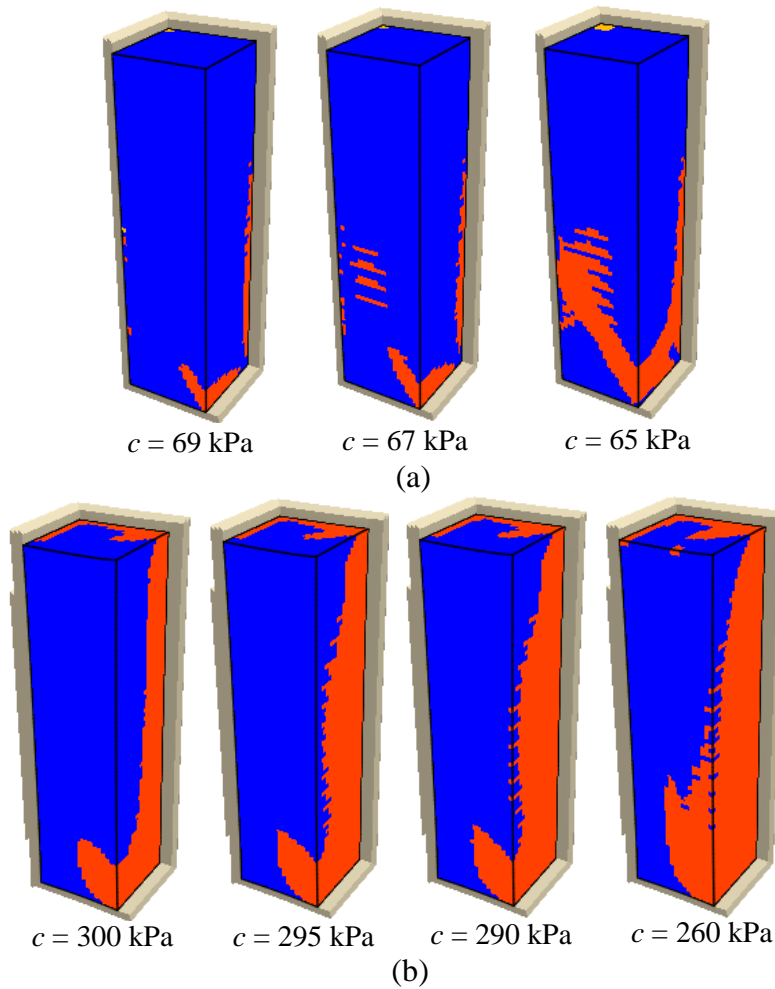| $c = 1150$ kPa | $c = 1130$ kPa | $c = 1000$ kPa |

(b)

Figure D-22: Yield zones development of side-exposed backfill for Case 2 in Chapter 3 with $L =$ 25 m as c reduces (a) at $D = 100$ m governed by sliding failure and (b) at $D = 1500$ m governed by crushing failure
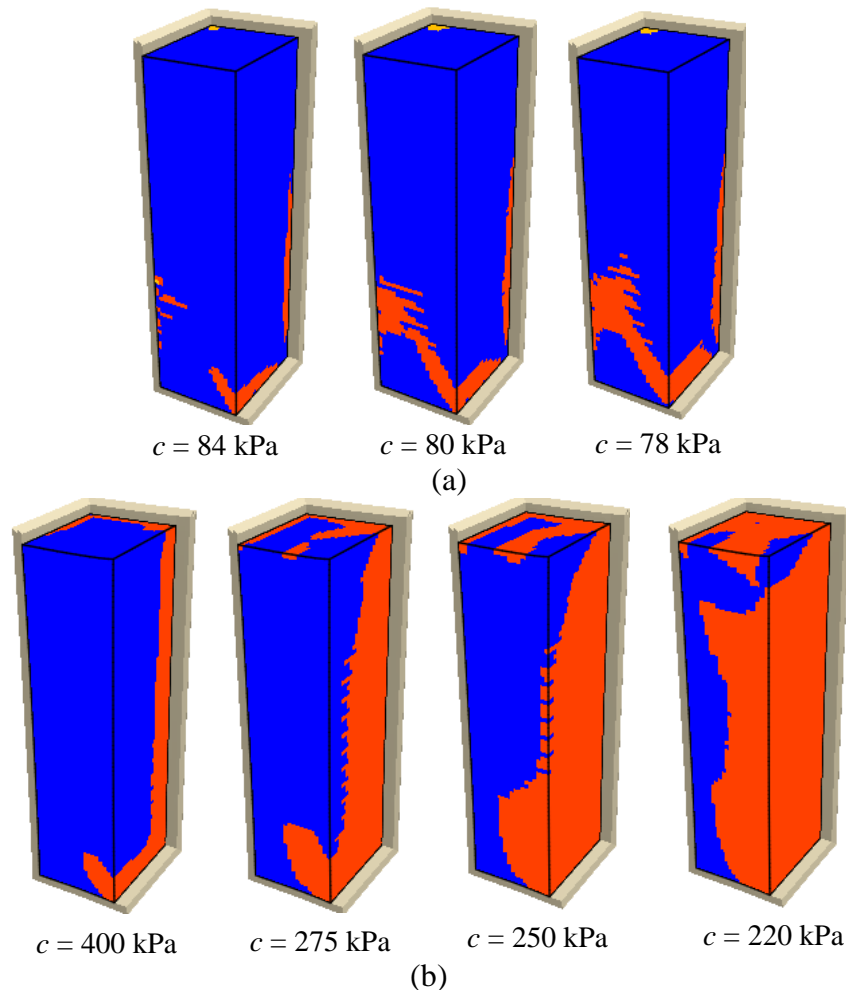
$c = 800$ kPa $c = 795$ kPa $c = 790$ kPa
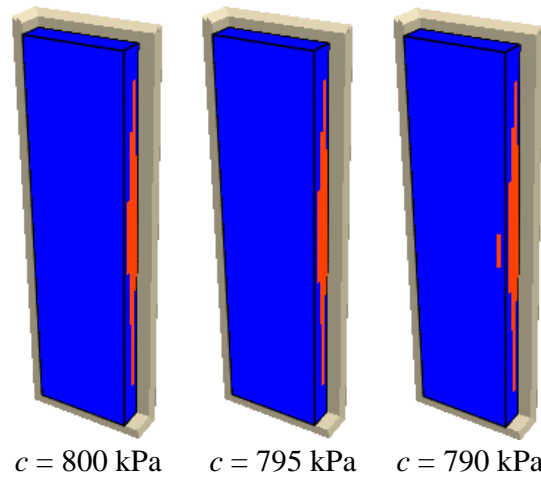
Figure D-23: Yield zones development of side-exposed backfill for Case 3 in Chapter 3 with $B =$ 5 m as c reduces at $D = 1000$ m governed by crushing failure

$c = 53$ kPa $c = 49$ kPa $c = 45$ kPa

(a)
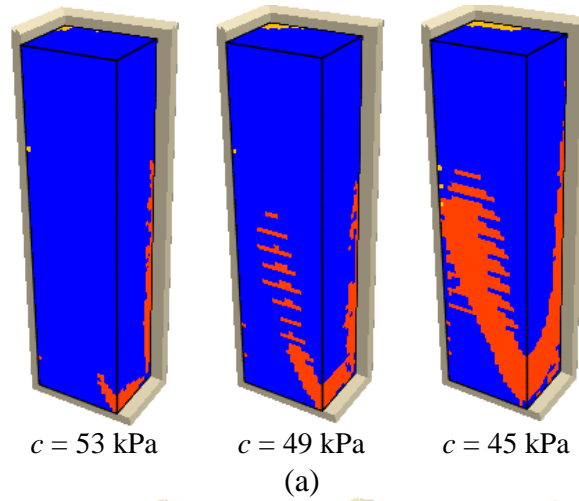
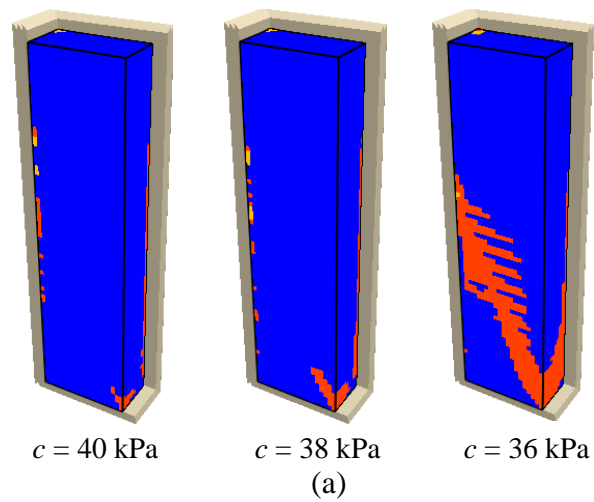$c = 300$ kPa $c = 195$ kPa $c = 190$ kPa $c = 170$ kPa
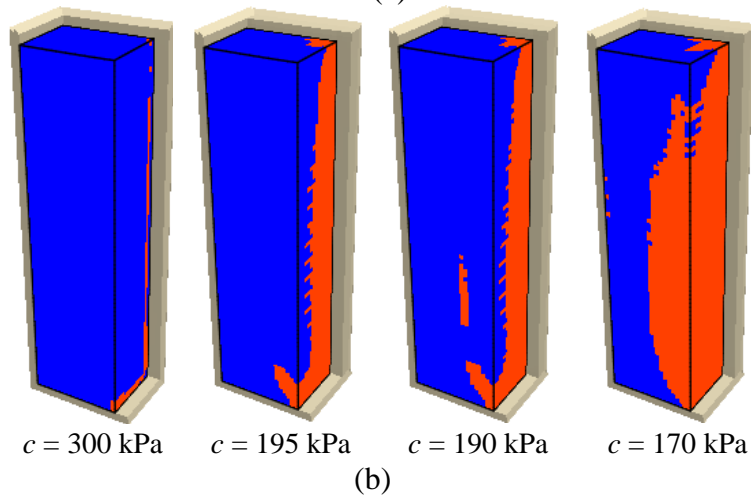
(b)

Figure D-24: Yield zones development of side-exposed backfill for Case 3 in Chapter 3 with $B =$ 15 m as c reduces (a) at $D = 100$ m governed by sliding failure and (b) at $D = 1000$ m governed by crushing failure

$c = 69$ kPa $\qquad$ $c = 67$ kPa $\qquad$ $c = 65$ kPa

(a)

$c = 300$ kPa $\qquad$ $c = 295$ kPa $\qquad$ $c = 290$ kPa $\qquad$ $c = 260$ kPa

(b)

Figure D-25: Yield zones development of side-exposed backfill for Case 3 in Chapter 3 with $B =$ 20 m as c reduces (a) at $D = 100$ m governed by sliding failure and (b) at $D = 1500$ m governed by crushing failure
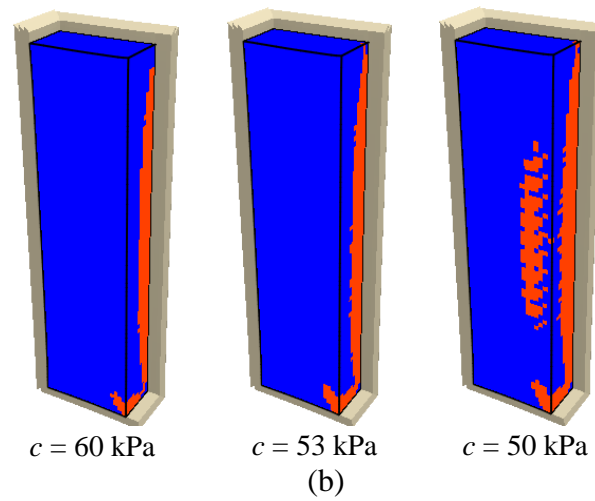
$c = 84$ kPa $\quad\quad$ $c = 80$ kPa $\quad\quad$ $c = 78$ kPa

(a)

$c = 400$ kPa $\quad$ $c = 275$ kPa $\quad$ $c = 250$ kPa $\quad$ $c = 220$ kPa

(b)

Figure D-26: Yield zones development of side-exposed backfill for Case 3 in Chapter 3 with $B = 25$ m as c reduces (a) at $D = 100$ m governed by sliding failure and (b) at $D = 1500$ m governed by crushing failure
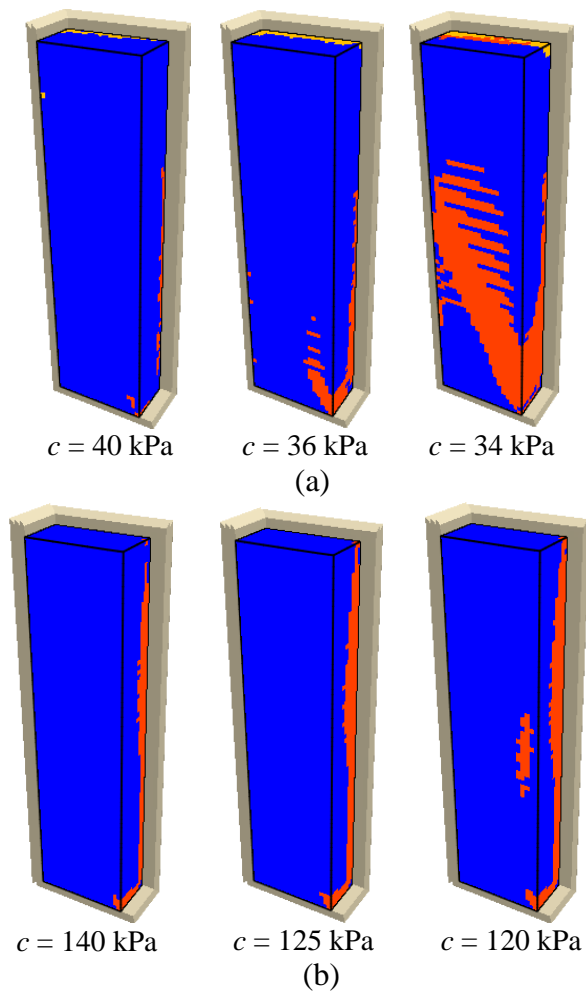

$c = 40$ kPa $\quad\quad$ $c = 38$ kPa $\quad\quad$ $c = 36$ kPa

(a)

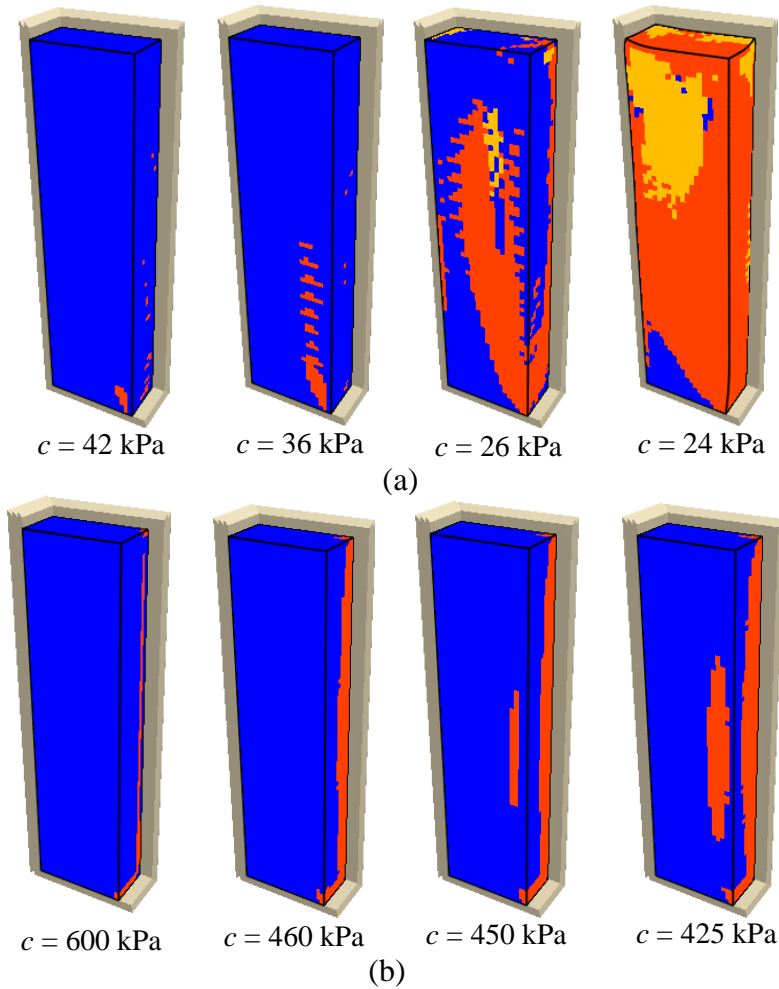c = 60 kPa c = 53 kPa c = 50 kPa

(b)

Figure D-27: Yield zones development of side-exposed backfill for Case 4 in Chapter 3 with E = 10 MPa as c reduces (a) at D = 100 m governed by sliding failure and (b) at D = 1500 m governed by crushing failure


c = 40 kPa c = 36 kPa c = 34 kPa

(a)

c = 140 kPa c = 125 kPa c = 120 kPa

(b)

Figure D-28: Yield zones development of side-exposed backfill for Case 4 in Chapter 3 with $E =$ 100 MPa as c reduces (a) at $D = 100$ m governed by sliding failure and (b) at $D = 1000$ m governed by crushing failure


$c = 42$ kPa $c = 36$ kPa $c = 26$ kPa $c = 24$ kPa

(a)

$c = 600$ kPa $c = 460$ kPa $c = 450$ kPa $c = 425$ kPa

(b)

Figure D-29: Yield zones development of side-exposed backfill for Case 4 in Chapter 3 with $E =$ 500 MPa as c reduces (a) at $D = 100$ m governed by sliding failure and (b) at $D = 1000$ m governed by crushing failure

$c = 40$ kPa $c = 38$ kPa $c = 36$ kPa

(a)

$c = 370$ kPa $c = 365$ kPa $c = 360$ kPa

(b)
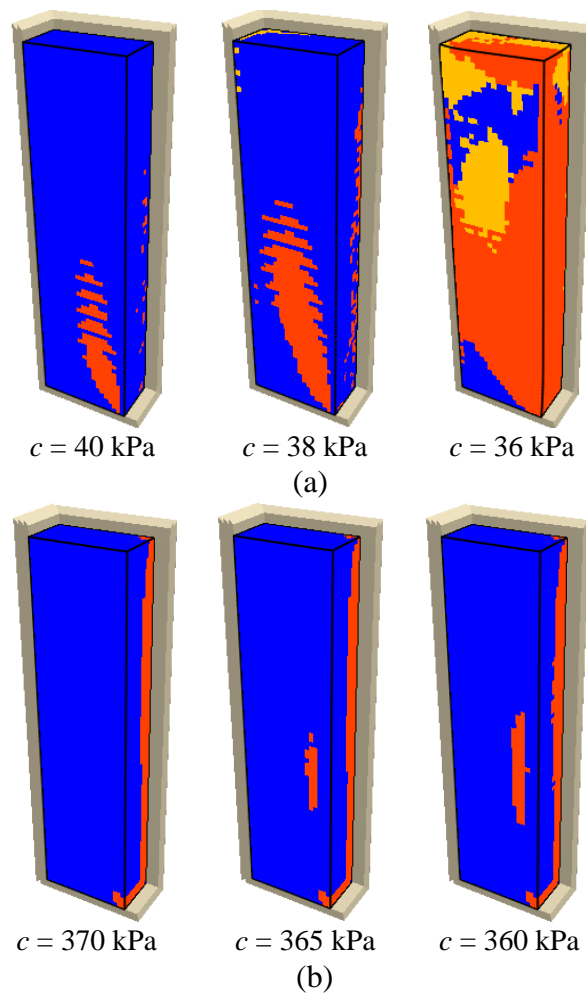
Figure D-30: Yield zones development of side-exposed backfill for Case 5 in Chapter 3 with $\phi = 20°$ as c reduces (a) at $D = 100$ m governed by sliding failure and (b) at $D = 1000$ m governed by crushing failure

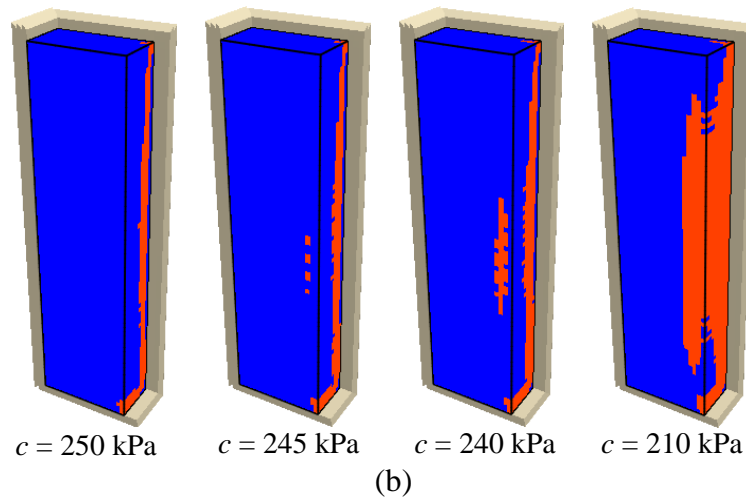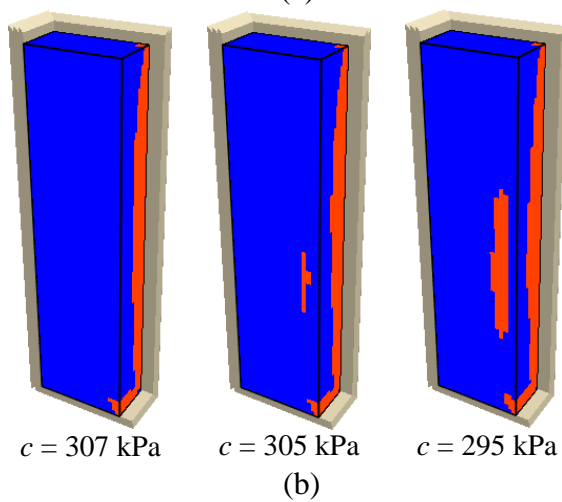$c = 21$ kPa $c = 20$ kPa $c = 19$ kPa

(a)

c = 250 kPa   c = 245 kPa   c = 240 kPa   c = 210 kPa
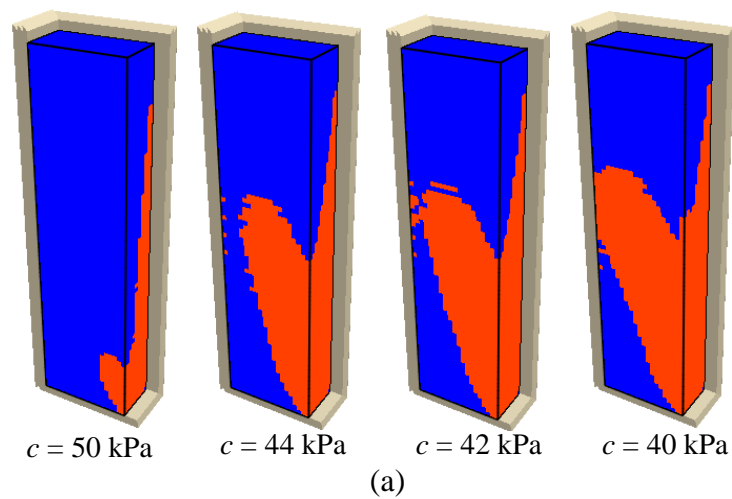
(b)
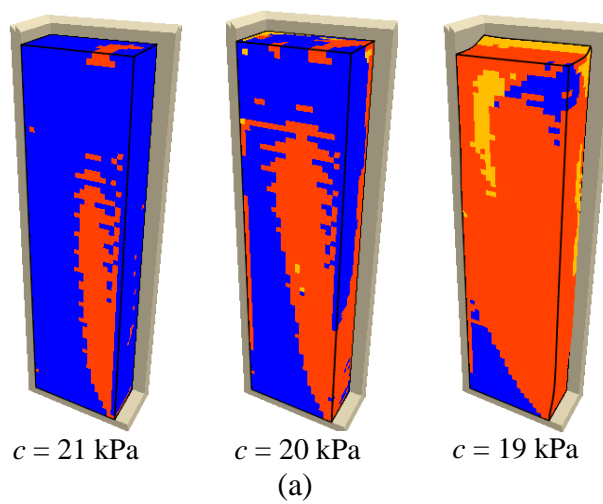
Figure D-31: Yield zones development of side-exposed backfill for Case 5 in Chapter 3 with $\phi = 40°$ as c reduces (a) at $D = 100$ m governed by sliding failure and (b) at $D = 1000$ m governed by crushing failure

c = 50 kPa   c = 44 kPa   c = 42 kPa   c = 40 kPa

(a)

c = 307 kPa   c = 305 kPa   c = 295 kPa

(b)

Figure D-32: Yield zones development of side-exposed backfill for Case 6 in Chapter 3 with $r_s =$ 0 as c reduces (a) at $D = 100$ m governed by sliding failure and (b) at $D = 1000$ m governed by crushing failure
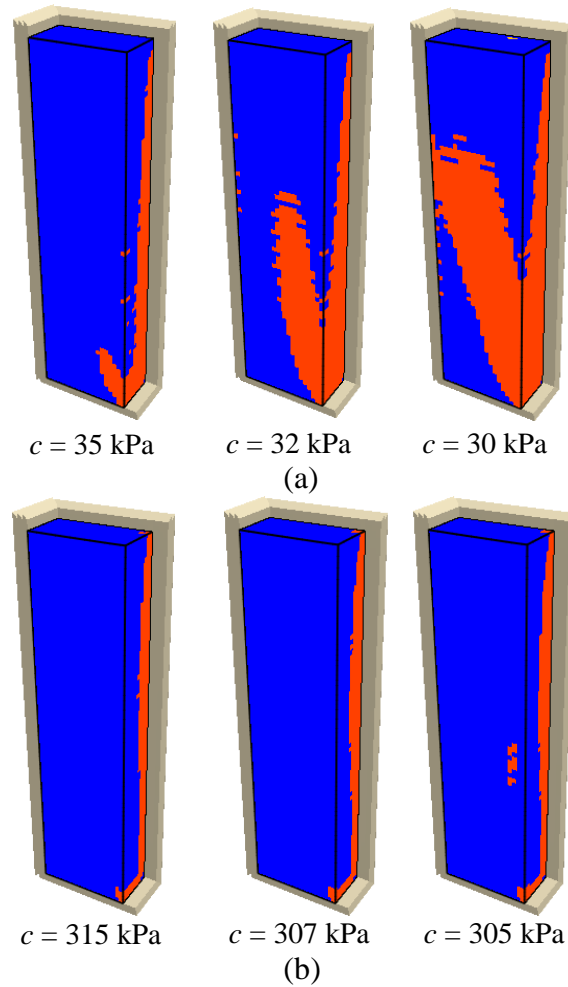

$c = 35$ kPa $c = 32$ kPa $c = 30$ kPa

(a)

$c = 315$ kPa $c = 307$ kPa $c = 305$ kPa

(b)

Figure D-33: Yield zones development of side-exposed backfill for Case 6 in Chapter 3 with $r_s =$ 0.5 as c reduces (a) at $D = 100$ m governed by sliding failure and (b) at $D = 1000$ m governed by crushing failure
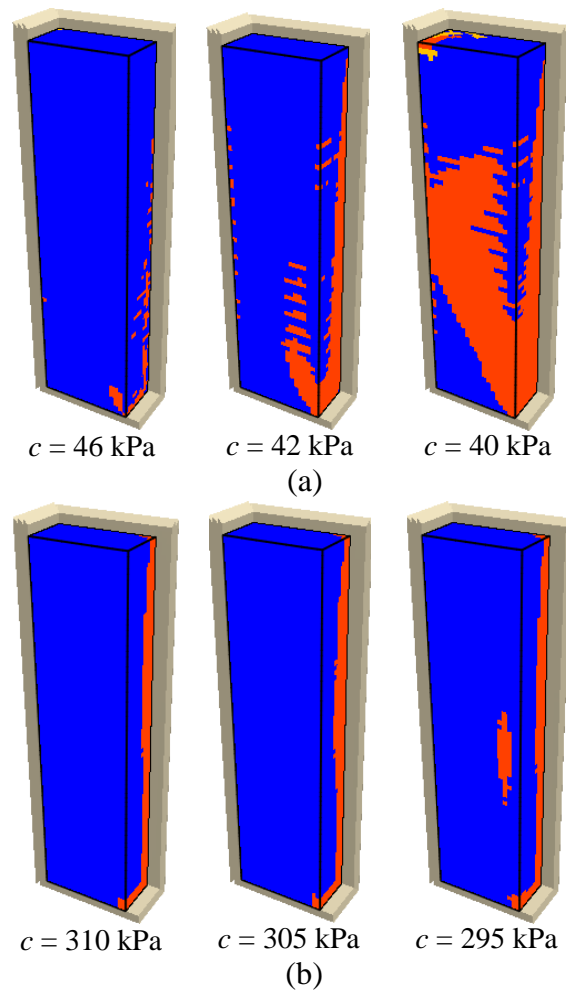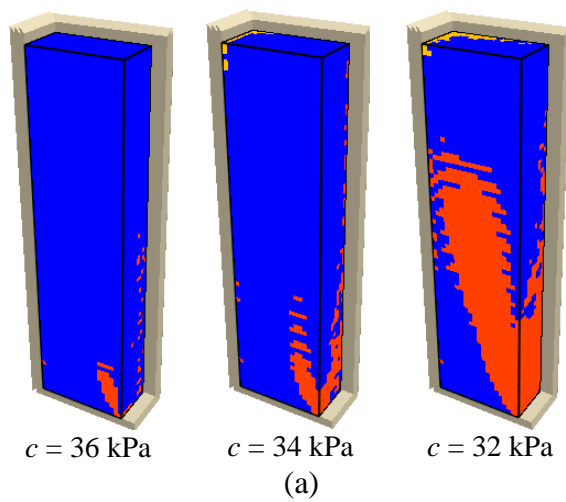
$c = 46$ kPa $c = 42$ kPa $c = 40$ kPa

(a)

$c = 310$ kPa $c = 305$ kPa $c = 295$ kPa

(b)

Figure D-34: Yield zones development of side-exposed backfill for Case 7 in Chapter 3 with $r_a = $ 1/3 as c reduces (a) at $D = 100$ m governed by sliding failure and (b) at $D = 1000$ m governed by crushing failure
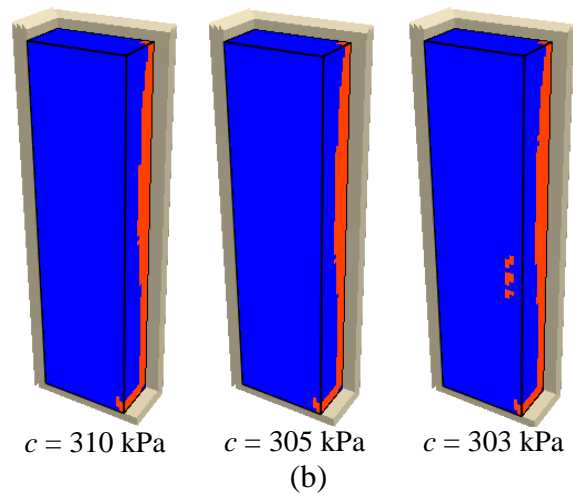

$c = 36$ kPa $c = 34$ kPa $c = 32$ kPa

(a)

$c = 310$ kPa $c = 305$ kPa $c = 303$ kPa

(b)

Figure D-35: Yield zones development of side-exposed backfill for Case 7 in Chapter 3 with r_a = 2/3 as c reduces (a) at $D = 100$ m governed by sliding failure and (b) at $D = 1000$ m governed by crushing failure

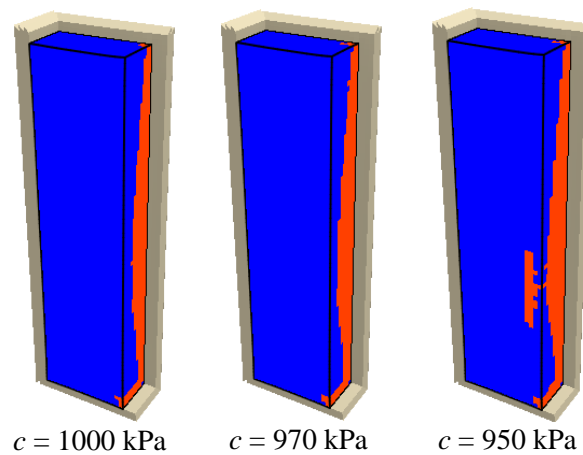$c = 1000$ kPa $c = 970$ kPa $c = 950$ kPa

Figure D-36: Yield zones development of side-exposed backfill for Case 8 in Chapter 3 with E_r = 12 GPa as c reduces at $D = 1000$ m governed by crushing failure
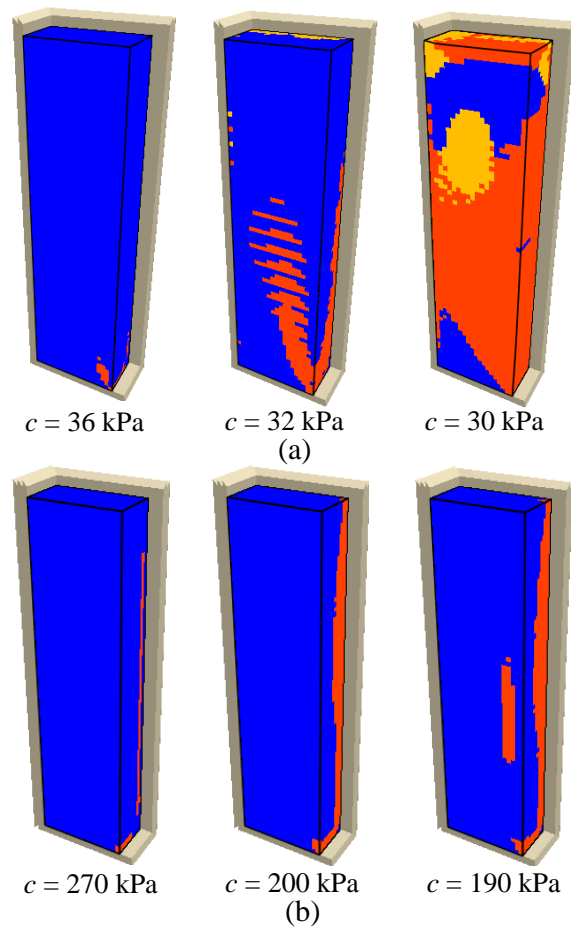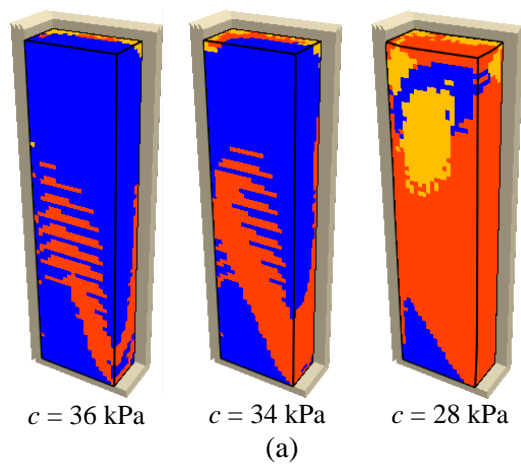
c = 36 kPa c = 32 kPa c = 30 kPa

(a)

c = 270 kPa c = 200 kPa c = 190 kPa

(b)

Figure D-37: Yield zones development of side-exposed backfill for Case 8 in Chapter 3 with E_r = 72 GPa as c reduces (a) at D = 100 m governed by sliding failure and (b) at D = 1000 m governed by crushing failure

c = 36 kPa c = 34 kPa c = 28 kPa

(a)

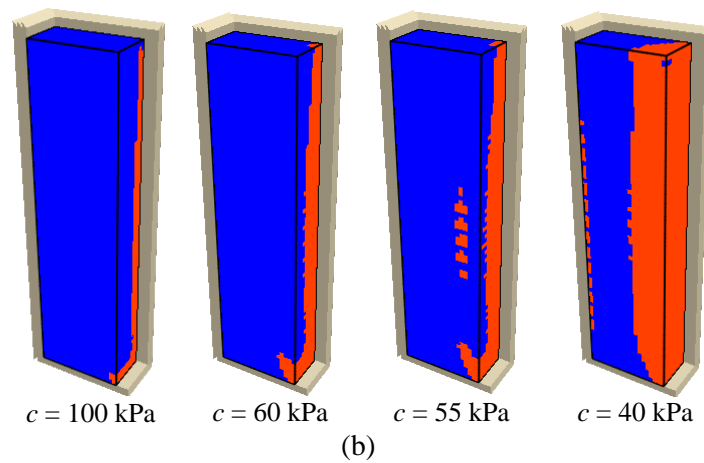$c = 100$ kPa $c = 60$ kPa $c = 55$ kPa $c = 40$ kPa

(b)

Figure D-38: Yield zones development of side-exposed backfill for Case 9 in Chapter 3 with $K_r = 0.5$ as c reduces (a) at $D = 100$ m governed by sliding failure and (b) at $D = 1000$ m governed by crushing failure

$c = 34$ kPa $c = 32$ kPa $c = 30$ kPa

(a)

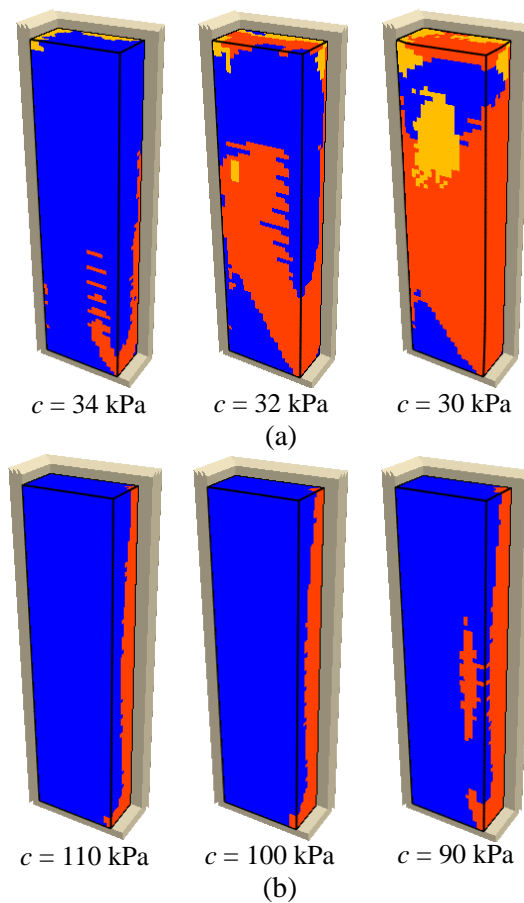$c = 110$ kPa $c = 100$ kPa $c = 90$ kPa

(b)

Figure D-39: Yield zones development of side-exposed backfill for Case 9 in Chapter 3 with $K_r = 1$ as c reduces (a) at $D = 100$ m governed by sliding failure and (b) at $D = 1000$ m governed by crushing failure

APPENDIX E   COMPARISONS BETWEEN NUMERICAL AND ANALYTICAL SOLUTIONS RELATED TO CHAPTER 3

Several analytical solutions considering immobile surrounding rocks were developed to estimate the minimum required cohesion of side-exposed backfill and have been reviewed in Chapter 2. In the following, the solutions proposed by Mitchell et al. (1982), Li and Aubertin (2012, 2014), Li et al. (2014a) and Yang et al. (2017) will be compared with the numerical results considering immobile rock mass in Chapter 3.

Numerical results of the minimum required cohesion c_{min} considering immobile rock mass and different stope geometries for Cases 1–3 in Chapter 3 are compared with analytical solutions as shown in Figure E-1. In the figure, one sees that the numerical results of c_{min} moderately increases with the increase of stope height H, and significantly grows as the stope width B increases. As the stope length L increases from 5 to 15 m, the value of c_{min} slightly decreases, followed by an almost constant trend as L further increasing. In all cases, numerical results are in a range between the predicted results of Li and Aubertin (2012) and Yang et al. (2017). In Figure E-1a, analytical solutions of Mitchell et al. (1982), Li and Aubertin (2012, 2014) predict an increasing trend for c_{min} as H increases which agrees with numerical results. Moreover, one sees in Figure E-1b that L has small effect on the value of c_{min}. This trend agrees with those predicted by analytical solutions of Mitchell et al. (1982) and Yang et al. (2017). The variation trend of numerical c_{min} with stope width agrees well with the analytical solutions as shown in Figure E-1c. Based on the comparisons between numerical and analytical results, the applicability of numerical models in Chapter 3 is considered partly verified by previous analytical solutions.
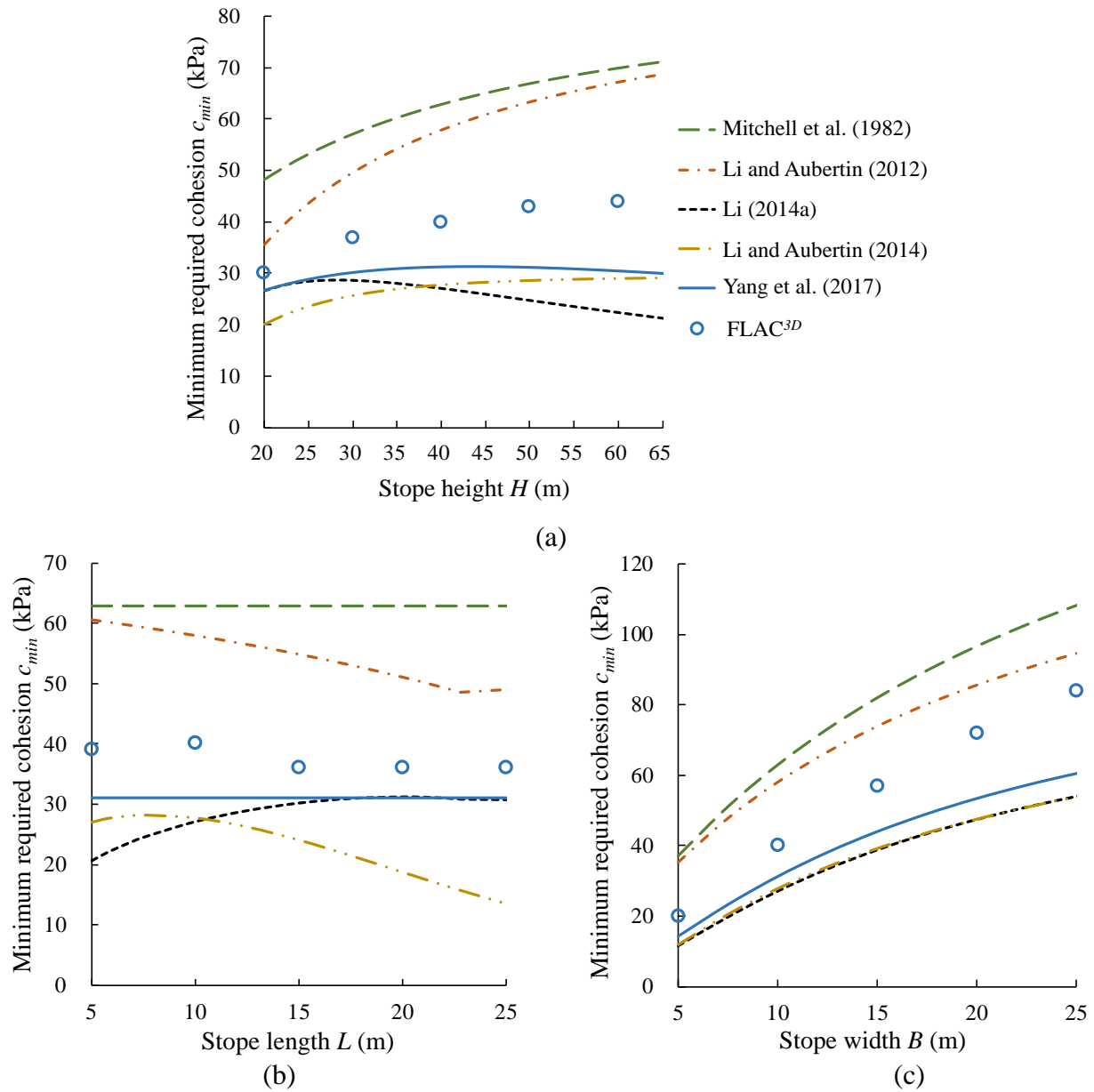
Figure E-1: Comparisons between analytical solutions and numerical results of the minimum required cohesion c_{min} considering immobile rock mass in Chapter 3 for different: (a) stope heights H (Case 1), (b) stope lengths L (Case 2) and (c) stope widths B (Case 3)

APPENDIX F   SENSITIVITY ANALYSES AND ADDITIONAL RESULTS RELATED TO CHAPTER 4

F1 Sensitivity analyses

Sensitivity analyses were conducted to determine the optimal domain size, range of fine mesh, mesh size and values of t_i, latency, *lfob* and *ufob* for the numerical model in Chapter 4. The numerical model in Chapter 4 had a similar schematic as shown in Figure D-1. In this numerical model, the distance between the stope boundaries to the boundaries of the numerical model is considered as the domain size. For the sensitivity analyses of the domain size and range of fine mesh, the largest dimensions of stopes and the largest mine depth D are used to ensure conservative results. The applied values are 50 m for H, 14 m for B, 8 m for L_b, 12 m for L_s, and 500 m for D. The simulations for sensitivity analyses are conducted with 7 steps presented in Chapter 4 with t_d $= 0$, $t_c = 28$ days, and $t_e = 0$. In sensitivity analyses, the rock mass is characterized by $\gamma_R = 27$ kN/m^3, $K_R = 8.67$ GPa, $G_M = 5.2$ GPa, $G_K = 3$ GPa, $\eta_K = 3 \times 10^{14}$ Pa·s, $\eta_M = 5 \times 10^{15}$ Pa·s, $c_R = 3.5$MPa, $\phi_R = 35°$, $\psi_R = 0°$, $T_R = 150$ kPa. The backfill is characterized $\gamma = 18$ kN/m^3, bulk modulus $K = 50$ MPa, shear modulus $G = 18.8$ MPa, $c = 1.5$ MPa, $\phi = 30°$, and $\psi = 0°$. Numerical results of horizontal stress σ_{yy} and total displacement along a vertical line EE' (see Figure D-1) on the open face after side exposure (Step 6 in Chapter 4) are obtained for the sensitivity analyses.

Figure F-1 shows the variations of the horizontal stress and total displacement along a vertical line on the open face for different domain sizes. The domain size ranges from 15 to 500 m. The numerical results become stable when the domain size is larger than 100 m. Further increasing of the domain size does not change the results. In the numerical modeling in Chapter 4, the domain size is applied as 500 m to be conservative.
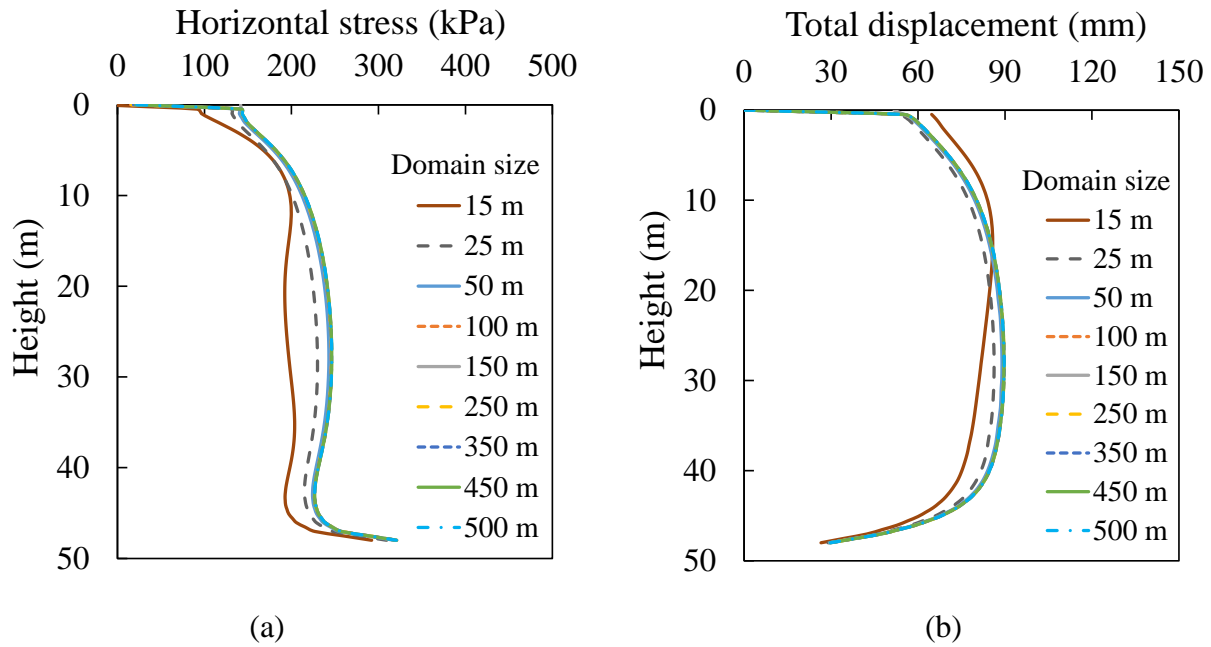
Figure F-1: The variations of (a) horizontal stress and (b) total displacement along a vertical line on the open face after side exposure for different domain sizes

Figure F-2 illustrates the variations of the horizontal stress and total displacement along a vertical line on the open face for different ranges of fine mesh around stopes. The numerical results become stable when the range of fine mesh is larger than 5 m. The optimal range of fine mesh around stopes in Chapter 4 is thus determined as 10 m.
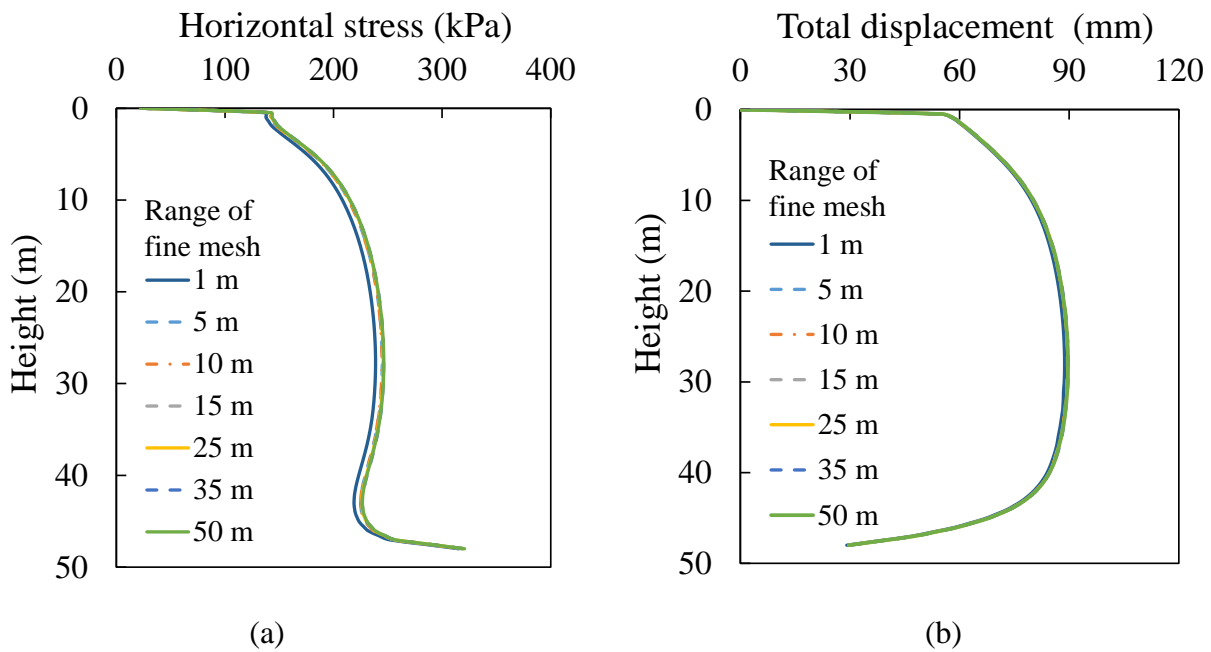
Figure F-2: The variations of (a) horizontal stress and (b) total displacement along a vertical line on the open face after side exposure for different ranges of fine mesh around stopes

The optimal value of initial timestep t_i in creep calculation is analyzed before the determination of optimal mesh size. Figure F-3 shows the variations of vertical and horizontal stresses along the VCL of backfill after a curing time t_c = 28 days (Step 5 in Chapter 4) for different initial timesteps t_i. It can be seen that t_i has little effect on the results at least within a range of 1 to 300 s. The optimal value of t_i used in numerical simulations in Chapter 4 is thus determined as 30 s.

(a)   (b)
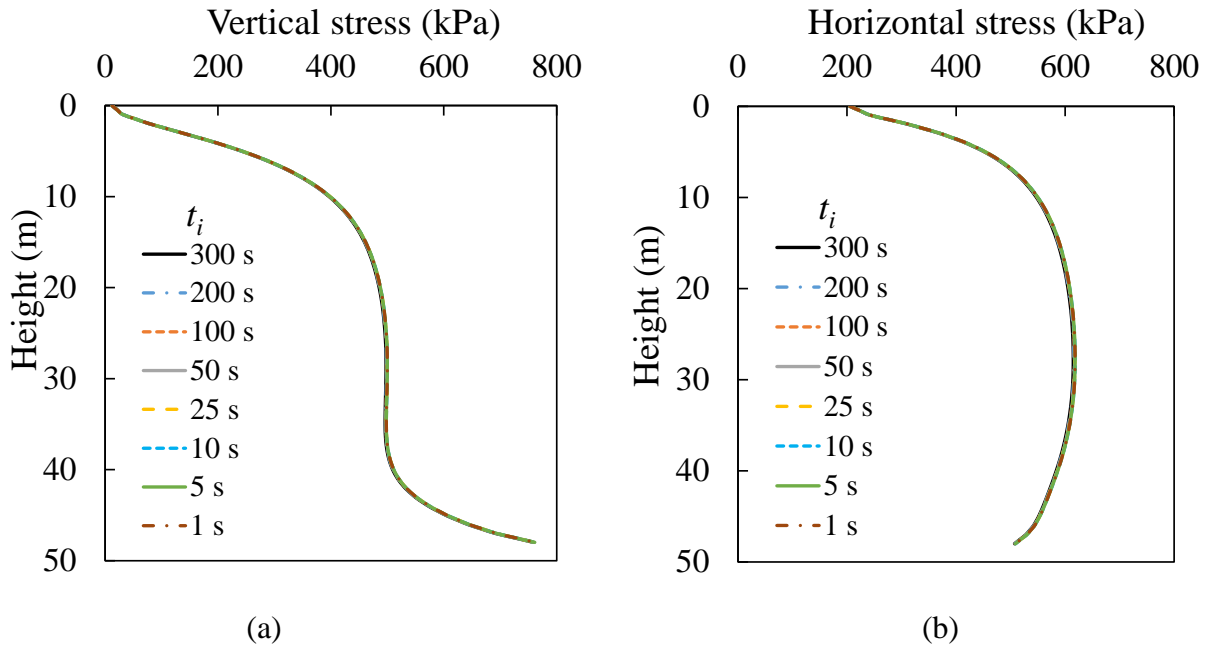
Figure F-3: The variations of (a) vertical and (b) horizontal stresses along the VCL of backfill after a curing time t_c = 28 days for different initial time steps t_i

The dimesons of stope reduce when determining the optimal mesh size. In this case, H = 40 m, B =10 m, L_b = 8 m, L_s = 8 m. The mine depth and other material parameters remain the same. Figure F-4 shows the variations of the horizontal stress and total displacement along a vertical line on the open face after side exposure (Step 6 in Chapter 4) for different mesh sizes. The numerical results become stable when the mesh size is smaller than 0.8 m. Further decreasing of the mesh size does not greatly change the results. Therefore, the optimal mesh size for numerical simulations in Chapter 4 is determined as 0.5 m.

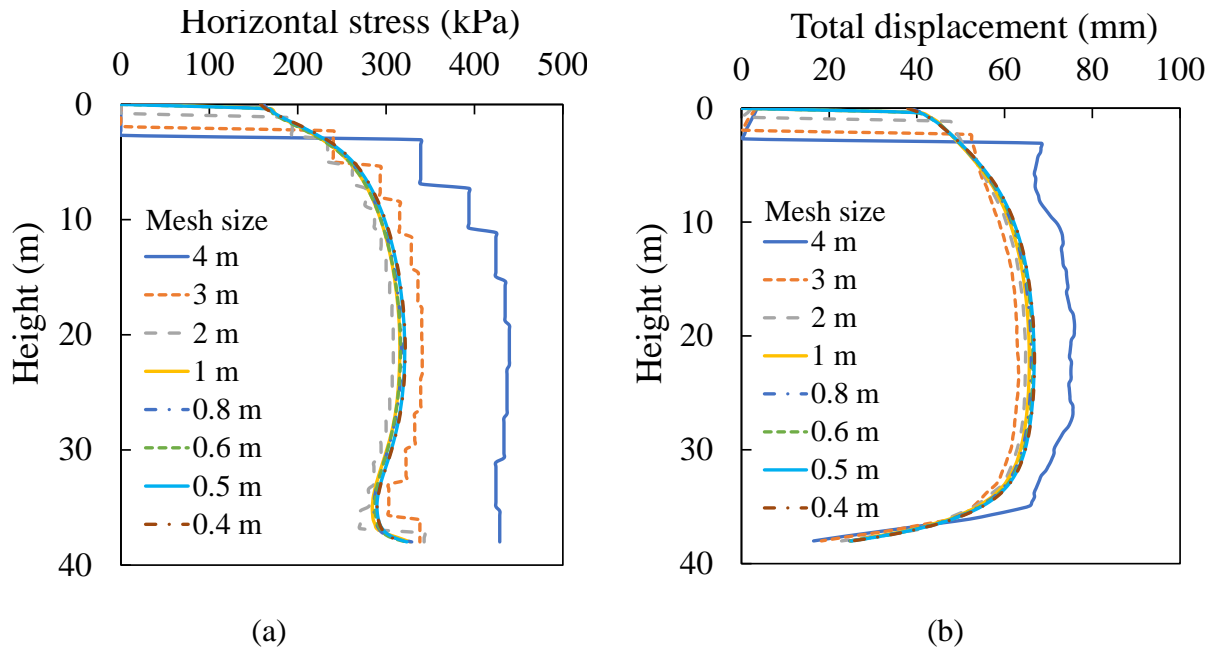(a)   (b)

Figure F-4: The variations of (a) horizontal stress and (b) total displacement along a vertical line on the open face after side exposure for different mesh sizes

Figure F-5 shows the variations of vertical and horizontal stresses along the VCL of backfill after a curing time t_c = 28 days (Step 5 in Chapter 4) for different values of *lfob*. The values of *ufob* are taken as 3 times of the corresponding values of *lfob*. Figure F-5 shows that different values of *lfob* ranging form 1×10^{-4} to 1×10^{-7} (3×10^{-4} to 3×10^{-7} for *ufob*) do not significantly affect the results. The values of *lfob* and *ufob* used in numerical simulations in Chapter 4 are thus determined as 1×10^{-6} and 3×10^{-6} respectively.
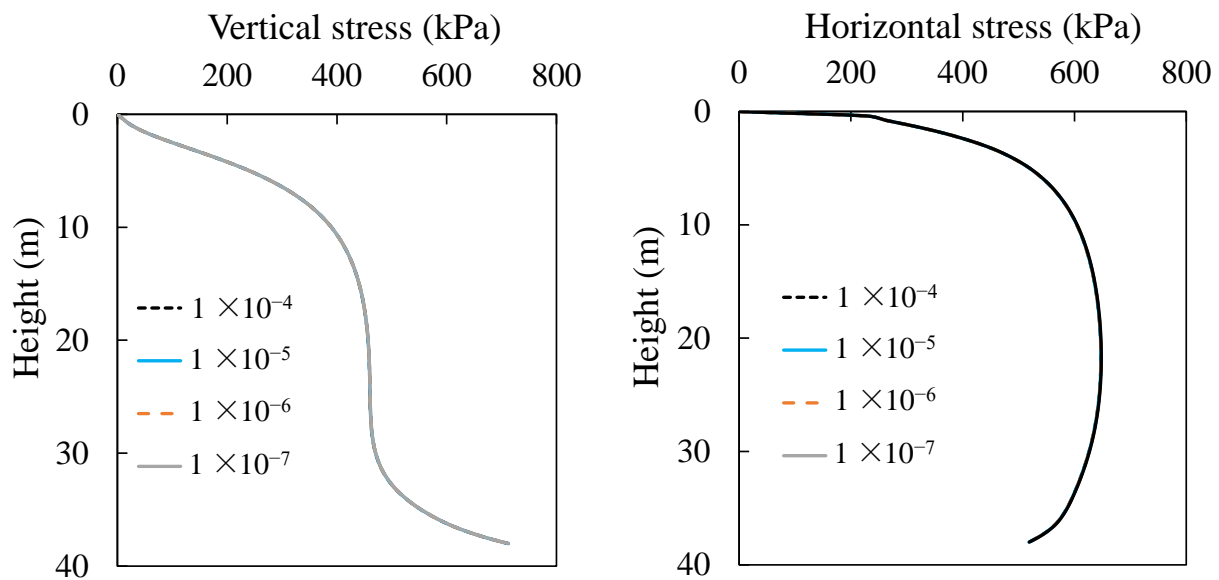
Figure F-5: The variations of (a) vertical and (b) horizontal stresses along the VCL of backfill after a curing time t_c = 28 days for different values of *lfob*

Figure F-6 shows the variations of vertical and horizontal stresses along the VCL of backfill after a curing time t_c = 28 days for different steps of latency. It is found that within 1 to 400 steps, the latency does not have a significant influence on the results. The value of latency used in numerical simulations in Chapter 4 is thus determined as 50 steps.
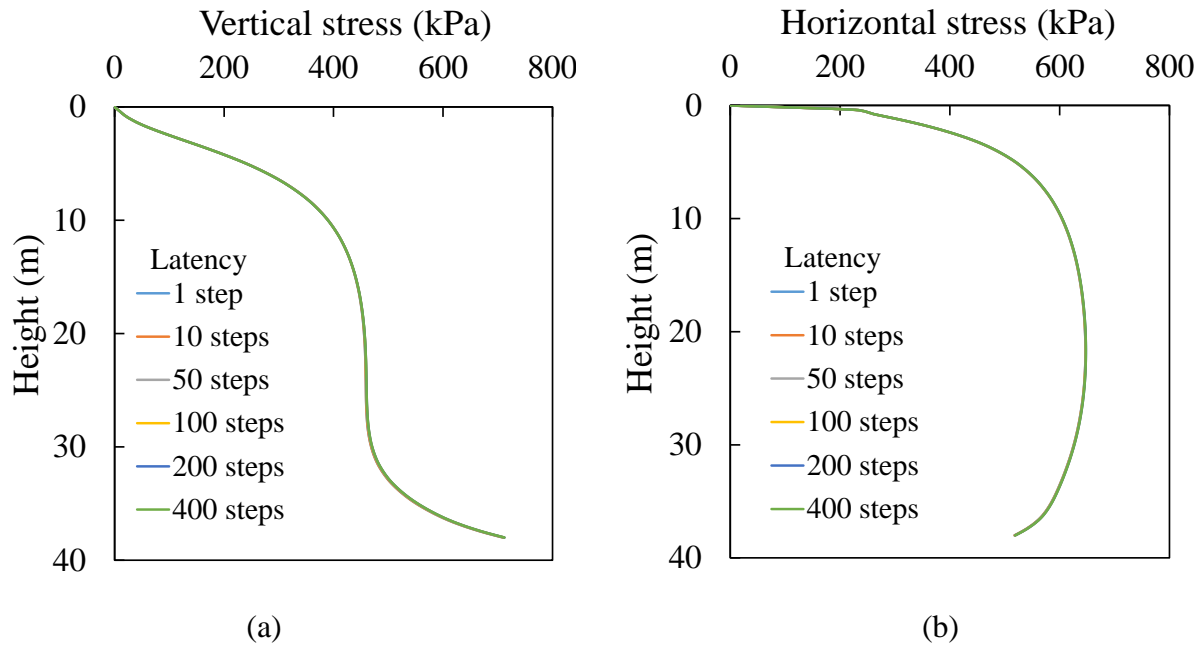

(a)   (b)

Figure F-6: The variations of (a) vertical and (b) horizontal stresses along the VCL of backfill after a curing time t_c = 28 days for different steps of latency

F2 Additional results

Figure F-7 shows the iso-contours of horizontal stress (σ_{yy}, along normal direction of side walls) in the backfilled primary stope before side exposure (Step 5) for the reference case as curing time t_c increases from 1 to 28 days. The horizontal stress in the backfilled primary stope shows an increasing trend as t_c increases. However, the increasing of stress is not obvious when t_c is smaller than 3 days because the stiffness of backfill in the model is set increasing for 28 days after filling and remains low when t_c = 3 days. As t_c exceeds 7 days, the horizontal stress in the backfilled stope significantly increases, especially around the mid-height of the stope where a value of 680 kPa is reached for t_c = 28 days compared with 40 kPa for t_b = 0 day. This is because the creep deformation

of surrounding rock mass increases with time which results in larger compressive strain in backfill. Meanwhile, the backfill becomes harder with larger elastic modulus as curing time increases which leads to larger compressive stress with the same closure. The increase of stresses in backfilled stope with t_c shown in Figure F-7 is thus a combined effect of backfill hardening and increase of walls closure.
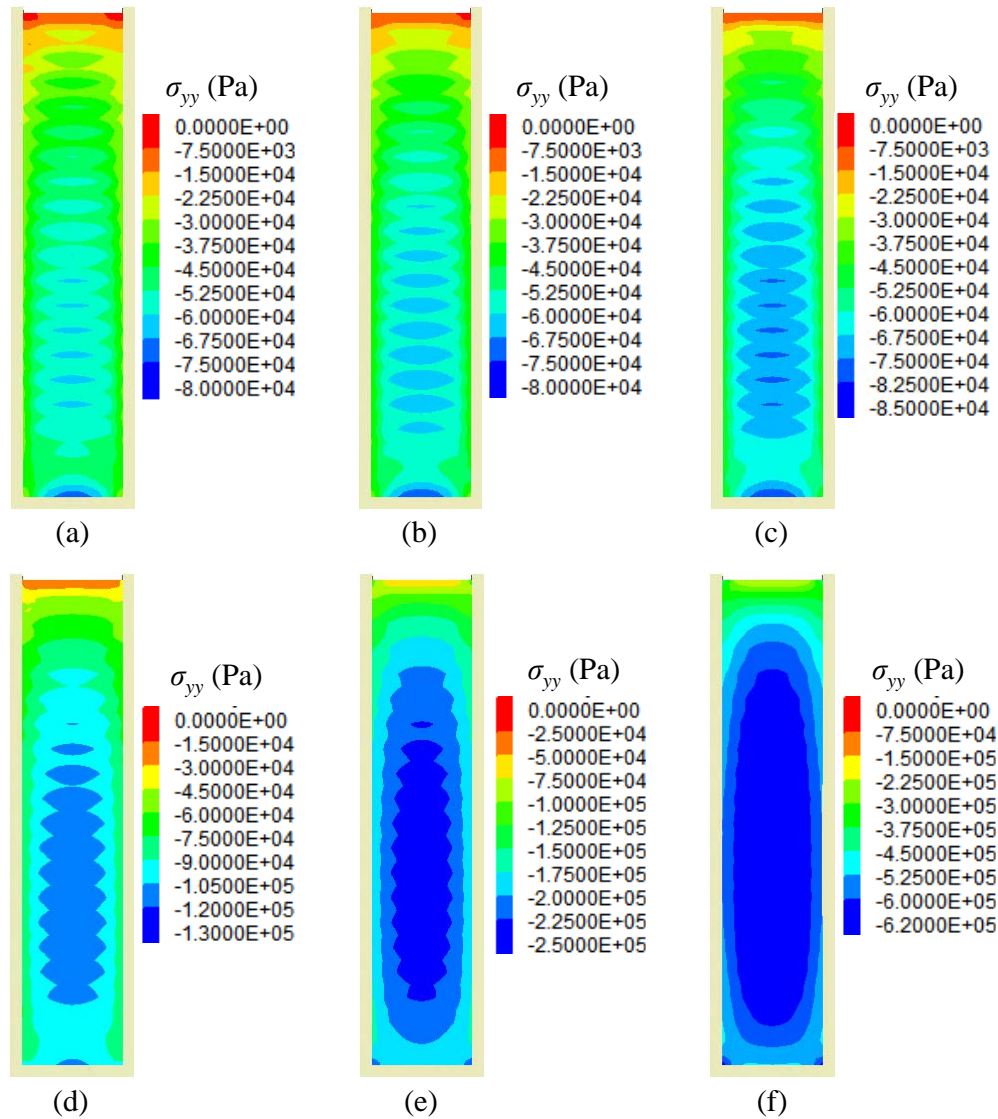

Figure F-7: iso-contours of horizontal stress (σ_{yy}) in a backfilled stope before side exposure for the reference case after a curing time t_c of (a) 0 day (without creep), (b) 1 day, (c) 3 days, (d) 7 days, (e) 14 days, and (f) 28 days.

The instability and the minimum required cohesion c_{min} of side-exposed backfill in Chapter 4 are determined by mainly evaluating the coalescence of yield zones. The development of yield zones

within backfill for the sliding and horizontal crushing failure by considering creep deformation of rock walls is similar to that with the consideration of rock-wall instantaneous closure presented in Appendix D. The developments of yield zones for side-exposed backfill in different cases in Chapter 4 are thus not further shown.

APPENDIX G FISH PROGRAM FOR BACKFILL PARAMETERS EVOLUTION WITHIN CURING TIME IN FLAC^{3D}

A FISH program in the creep simulations of FLAC^{3D} (Itasca 2013) in Chapter 4 for the evolution of Young's modulus E, cohesion c, tensile strength T of backfill (group of "backfill") with curing time t_c will be given as an example in this section. In the program, $t_c = 35$ days, $\gamma = 18$ kN/m^3, $E = 300$ MPa, $v = 0.3$, $c = 300$ kPa, $\phi = 30°$, $\psi = 0°$, $T = $ UCS/10. The FISH program is provided as follows:

```
define parameters_evolution ; defining the name of the program

    ; defining time and the parameters of backfill

    global creep_time_total = 3.02E6 ; curing time (3.02 × 10⁶ s,
    i.e., 35 days)

    global creep_time_one_day = 8.64E4 ; 8.64 × 10⁴ s for the
    duration of 1 day (24 h)

    global backfill_density = 1800 ; density of backfill

    global young_final = 300e6 ; final value of Yong's modulus of
    backfill

    global backfill_poisson = 0.3 ; Poisson's ratio of backfill

    global cohesion_final = 300e3 ; final value of cohesion of
    backfill

    global backfill_friction = 30 ; internal friction angle of
    backfill

    global backfill_dilation = 0 ; dilation angle of backfill

    global bulk_final = young_final/(3*(1 – 2* backfill_poisson)) ;
    final value of bulk modulus of backfill

    global shear_final = young_final/(2*(1 + backfill_poisson)) ;
    final value of shear modulus of backfill
```

```
global backfill_friction_rad = backfill_friction*3.1416/180 ;
radian of internal friction angle of backfill

global  tension_final  =  cos(backfill_friction_rad)/(1  –
sin(backfill_friction_rad))* cohesion_final/5 ; final value of
tensile strength of backfill

global bulk_increment = bulk_final /28 ; increment of bulk
modulus of backfill every 24 h

global shear_increment = shear_final /28 ; increment of shear
modulus of backfill every 24 h

global cohesion_increment = cohesion_final/28 ; increment of
cohesion of backfill every 24 h

global tension_increment = tension_final /28 ; increment of
tensile strength of backfill every 24 h

global backfill_bulk = 0 ; bulk modulus of backfill (varies
with time)

global backfill_shear = 0 ; shear modulus of backfill (varies
with time)

global backfill_cohesion = 0 ; cohesion of backfill (varies
with time)

global backfill_tension = 0 ; tensile strength of backfill
(varies with time)

local times_evolution = 28 ; parameters updating  times (varies
based on curing time)

global creep_time = 0 ; initial time

; updating the parameters of backfill every 24 h during the
creep calculation for 28 days

loop while times_evolution # 0

    creep_time = creep_time + creep_time_one_day
```

```
        backfill_bulk = backfill_bulk + bulk_increment

        backfill_shear = backfill_shear + shear_increment

        backfill_cohesion = backfill_cohesion + cohesion_increment

        backfill_tension = backfill_tension + tension_increment

        command

            property  bulk  @backfill_bulk   shear  @backfill_shear
            cohesion @backfill_cohesion friction @backfill_friction
            dilation  @backfill_dilation  tension  @backfill_tension
            density @backfill_density range group backfill

            solve age @creep_time

        end_command

        times_evolution = times_evolution - 1

    end_loop

end

set gravity 0 0 -10

; interacting the program with FLAC³ᴰ

@parameters_evolution

; completing the creep calculation with full curing time

solve age @creep_time_total
```